Black Sea Journal of Engineering and Science

Volume 8 | Issue 2



ISSN: 2619 - 8991

BS Journals

BLACK SEA JOURNAL OF ENGINEERING AND SCIENCE

(BSJ ENGIN SCI)

Black Sea Journal of Engineering and Science (BSJ Eng Sci) is a double-blind peer-reviewed, open-access international journal published electronically 6 times (January, March, May, July, September, and November) in a year by since January 2018. It publishes, in English and Turkish, full-length original research articles, innovative papers, conference papers, reviews, mini-reviews, rapid communications or technical note on advances in a wide range of scientific disciplines from all fields of engineering and science and from any source.

ISSN 2619 - 8991

Phone: +90 362 408 25 15

Fax: +90 362 408 25 15

Email: bsjsci@blackseapublishers.com

Web site: http://dergipark.gov.tr/bsengineering

Sort of publication: Periodically 6 times (January, March, May, July, September, and November) in a year

Publication date and place: March 15, 2025 - Samsun, TÜRKİYE

Publishing kind: Electronically

OWNER

Assoc. Prof. Dr. Uğur ŞEN

DIRECTOR IN CHARGE

Prof. Dr. Hasan ÖNDER

EDITOR BOARDS

EDITOR IN CHIEF

Prof. Dr. Hasan ÖNDER, Ondokuz Mayis University, TÜRKİYE

Assoc. Prof. Dr. Uğur ŞEN, Ondokuz, Mayis University, TÜRKİYE

SECTION EDITORS*

Prof. Dr. Berna KILIÇ, Section Editor of Fisheries Engineering, Ege University, TÜRKİYE

Prof. Dr. Bülent YANIKTEPE, Section Editor of Aerospace Engineering, Osmaniye Korkut Ata University, TÜRKİYE

Prof. Dr. Çiğdem TAKMA, Section Editor of Statistics, Ege University, TÜRKİYE

Prof. Dr. Çiğdem TAKMA, Section Editor of Statistics, Ege University, FRANCE

Prof. Dr. Dilek KUT, Section Editor of Textile Engineering, Uludağ University, TÜRKİYE

Prof. Dr. Erkan YALÇIN, Section Editor of Biology, Ondokuz Mayıs University, TÜRKİYE

Prof. Dr. Ertan BUYRUK, Section Editor of Mechanical Engineering, Sivas Cumhuriyet University, TÜRKİYE

Prof. Dr. Fauziatul FAJAROH, Section Editor of Chemical Engineering, Universitas Negeri Malang, INDONESIA

Prof. Dr. Fuad ALHAJOMAR, Section Editor of Electrical and Electronics Engineering, University of South Wales, UNITED KINGDOM

Prof. Dr. Gökhan CİVELEKOĞLU, Section Editor of Environmental Engineering, Akdeniz University, TÜRKİYE

Prof. Dr. Hasan TANAK, Section Editor of Physics, Amasya University, TÜRKİYE

Prof. Dr. Hasan TEMİZ, Section Editor of Food Engineering, Ondokuz Mayis University, TÜRKİYE

Prof. Dr. Hojjat SADEGHİ-ALİABADİ, Section Editor of Chemistry, Isfahan University, IRAN

Prof. Dr. Hüseyin PEKER, Section Editor of Forest Engineering, Artvin Çoruh University, TÜRKİYE

Prof. Dr. İbrahim Özgür DENEME, Section Editor of Civil Engineering, Aksaray University, TÜRKİYE

Prof. Dr. Nilüfer YURTAY, Section Editor of Computer Engineering, Sakarya University, TÜRKİYE

Prof. Dr. Özgür Hakan AYDOĞMUŞ, Section Editor of Mathematics, Social Sciences University of Ankara, TÜRKİYE

Assoc. Prof. Dr. Belgin KARABACAKOĞLU, Section Editor of Chemical Engineering, Eskişehir Osmangazi University, TÜRKİYE

Assoc. Prof. Dr. Bülent BOSTANCI, Section Editor of Geomatics Engineering, Erciyes University, TÜRKİYE

Assoc. Prof. Dr. Edit MİKÓ, Section Editor of Agricultural Engineering, University of Szeged, HUNGARY

Assoc. Prof. Dr. Ergün EKİCİ, Section Editor of Industrial Engineering, Çanakkale Onsekiz Mart University, TÜRKİYE

Assoc. Prof. Dr. Helal Uddin MOLLA, Section Editor of Physics, Rajshahi University of Engineering and Technology, BANGLADESH

Assoc. Prof. Dr. Kadyrbay CHEKİROV, Section Editor of Biology, Kyrgyz Turkish Manas University, KYRGYZSTAN
Assoc. Prof. Dr. Lukman ABDULRA'UF, Section Editor of Chemistry, Kwara State University, NIGERIA
Assoc. Prof. Dr. Mehmet EBEOĞLUGİL, Dokuz Eylül University, TÜRKİYE
Assoc. Prof. Dr. Mohammad KHAJEH MEHRIZI, Section Editor of Textile Engineering, Yazd University, IRAN
Assoc. Prof. Dr. Silvio DE OLİVEİRA JUNIOR, Section Editor of Mechanical Engineering, University of São Paulo, BRAZIL
Assoc. Prof. Dr. Sinan AKISKA, Section Editor of Geological Engineering, Ankara University, TÜRKİYE
Asst. Prof. Dr. Francis INEGBEDİON, Section Editor of Industrial Engineering, University of Benin, NIGERIA
Asst. Prof. Dr. Jun-wei LİM, Section Editor of Environmental Engineering, Universiti Teknologi Petronas, MALAYSIA
Asst. Prof. Dr. Mehmet GÜÇYETMEZ, Section Editor of Electrical and Electronics Engineering, Kırşehir Ahi Evran University, TÜRKİYE
Asst. Prof. Dr. Mehmet ÖZDEMİR, Section Editor of Mining Engineering, Kütahya Dumlupınar University, TÜRKİYE
Asst. Prof. Dr. Muhammad GULİSTAN, Section Editor of Mathematics, Hazara University, PAKISTAN
Asst. Prof. Dr. Sedat KARADAVUT, Section Editor of Agricultural Engineering, Trakya University, TÜRKİYE
Asst. Prof. Dr. Xinyi WANG, Section Editor of Geomatics Engineering, Henan Polytechnic University, CHINA
Asst. Prof. Ranjith RAJ A, Section Editor of Metallurgical and Materials Engineering, Sri Venkateswara College of Engineering, INDIA

* The ranking is arranged alphabetically within the academic title

STATISTIC EDITOR
Prof. Dr. Mehmet TOPAL, Kastamonu University, TÜRKİYE
ENGLISH EDITOR
Asst. Prof. Dr. Betül ÖZCAN DOST, Ondokuz Mayis University, TÜRKİYE
TURKISH EDITOR
Prof. Dr. Serkan ŞEN, Ondokuz Mayis University, TÜRKİYE

REVIEWERS OF THE ISSUE*

Prof. Dr. Baha ŞEN, National Defense University, Department of Computer Engineering, Information and Computing Sciences, TÜRKİYE

Prof. Dr. Fatih ÜÇKARDEŞ, Adıyaman University, Department of Biostatistics and Medical Informatics, Biostatistics, TÜRKİYE

Prof. Dr. Metin Hakan SEVERCAN, Niğde Ömer Halisdemir University, Department of Civil Engineering, Reinforced Concrete Buildings, TÜRKİYE

Prof. Dr. Özgür AVŞAR, Eskişehir Technical University, Department of Civil Engineering, Structural Dynamics, TÜRKİYE

Prof. Dr. Salih TERZİOĞLU, Karadeniz Technical University, Department of Forest Botany, Forest Botany, TÜRKİYE

Prof. Dr. Şana SUNGUR, Hatay Mustafa Kemal University, Department of Chemistry, Chemical Sciences, TÜRKİYE

Assoc. Prof. Dr. Ahmet UÇAR, Ankara University, Department of Animal Science, Aniaml Science, TÜRKİYE

Assoc. Prof. Dr. Ayla GÜLCÜ, Bahçeşehir University, Department of Software Engineering, Software Engineering, TÜRKİYE

Assoc. Prof. Dr. Aytaç ALTAN, Zonguldak Bülent Ecevit University, Department of Electrical Electronics Engineering, Control Theoryand Applications, TÜRKİYE

Assoc. Prof. Dr. Cihangir BOZTEPE, İnönü University, Department of Biomedical Engineering, Polymerisation Mechanisms, TÜRKİYE

Assoc. Prof. Dr. Hadi GENCELİ, Yıldız Technical University, Department of Mechanical Engineering, Energy Generation, Conversion and Storage, TÜRKİYE

Assoc. Prof. Dr. Hasan ARSLANOĞLU, Çanakkele Onsekiz Mart University, Department of Chemistry, Chemical Engineering, TÜRKİYE

Assoc. Prof. Dr. Hilal AYCI, Gazi University, Department of Architecture, Built Environment and Design, TÜRKİYE

Assoc. Prof. Dr. Mehmet Akif Boz, Yozgat Bozok University, Department of Animal Science, Aniaml Science, TÜRKİYE

Assoc. Prof. Dr. Meryem Göksel SARAÇ, Cumhuriyet University, Department of Hotel Restaurant and Catering Services, Food Chemistry and Food Sensory Science, TÜRKİYE

Assoc. Prof. Dr. Mesut ŞİMŞEK, Hatay Mustafa Kemal University, Department of Geography, Geomorphology and Earth Surface Processes, TÜRKİYE

Assoc. Prof. Dr. Mustafa Cem KASAPBAŞI, Istanbul Ticaret University, Department of Computer Engineering, Information Systems, TÜRKİYE

Assoc. Prof. Dr. Mustafa KARAOĞLAN, Dokuz Eylül University, Department of Mechanical Engineering, Mechanical Engineering, TÜRKİYE

Assoc. Prof. Dr. Serdar GENÇ, Kırşehir Ahi Evran University, Department of Agricultural Biotechnology, Biometry, TÜRKİYE

Assoc. Prof. Dr. Serhat Berat EFE, Bandırma Onyedi Eylül University, Department of Electrical Engineering, Power Plants, TÜRKİYE

Assoc. Prof. Dr. Tamer SARAÇYAKUPOĞLU, Turkish Aerospace Industries, Aerospace Engineering, TÜRKİYE

Assoc. Prof. Dr. Yılmaz KAYA, Batman University, Department of Computer Engineering, Software, TÜRKİYE

Assist. Prof. Dr. Aydan YAMAN, Aksaray University, Department of Geomatics Engineering, Photogrametry, TÜRKİYE

Assist. Prof. Dr. Barış BAYRAK, Kafkas University, Department of Civil Engineering, Reinforced Concrete Buildings, TÜRKİYE

Assist. Prof. Dr. Birkut GÜLER, Giresun University, Department of Machinery and Metal Technologies, Biomass Energy Systems, TÜRKİYE

Assist. Prof. Dr. Cengiz HARK, İnönü University, Department of Computer Engineering, Natural Language Processing, TÜRKİYE

Assist. Prof. Dr. Demet ÇANGA BOĞA, Niğde Ömer Halisdemir University, Department of Numerical Methods, Biometry, TÜRKİYE

Assist. Prof. Dr. Dilara ÖRGÜL, Selçuk University, Department of Pharmacology, Pharmacology and Pharmaceutical Sciences, TÜRKİYE

Assist. Prof. Dr. Ebru GÜL, Çankırı Karatekin University, Department of Forest Engineering, Forestry Sciences, TÜRKİYE

Assist. Prof. Dr. Emine Nazlı HAYIRLI ÖZYOL, Hitit University, Department of Basic Medical Sciences, Histology and Embryology, TÜRKİYE

Assist. Prof. Dr. Ersin DURSUN, Tokat Gaziosmanpasa University, Department of Forestry and Forest Products, Forestry Sciences, TÜRKİYE

Assist. Prof. Dr. Esra DEMiRTÜRK, Çukurova University, Department of Pharmacology, Pharmaceutical Biotechnology, TÜRKİYE

Assist. Prof. Dr. Esra YAVUZ, Şırnak University, Department of Accounting and Tax, Biometry, TÜRKİYE

Assist. Prof. Dr. Fatih TURAN, Eskişehir Technical University, Department of Mechanical Engineering, Dynamics Vibration and Vibration Control, TÜRKİYE

Assist. Prof. Dr. Fatih UÇKAYA, Alanya Alaaddin Keykubat University, Nursing Department, Medicinal and Biomolecular Chemistry, TÜRKİYE

Assist. Prof. Dr. Güneş MUTLU AVİNÇ, Muş Alparslan University, Department of Architecture, Architectural Design, TÜRKİYE

Assist. Prof. Dr. Habibullah BiLGE, Bolu Abant İzzet Baysal University, Department of Mechanical Engineering, Mechanical Vibrations and Noise, TÜRKİYE

Assist. Prof. Dr. Hatice Nur HALiPÇİ TOPSAKAL, İstanbul Atlas University, Department of Medical Services and Techniques, Microbiology, TÜRKİYE

Assist. Prof. Dr. Meltem KASAPOĞLU ÇALIK, İstanbul Gedik University, Department of Chemical Technology, Materials Science and Technologies, TÜRKİYE

Assist. Prof. Dr. Meral ÖZARSLAN YATAK, Gazi University, Deptartment of Electrical and Electronics Engineering, Control Theoryand Applications, TÜRKİYE

Assist. Prof. Dr. Merve BECİT KIZILKAYA, Afyonkarahisar Health Sciences University, Department of Pharmacology, Basic Pharmacology, TÜRKİYE

Assist. Prof. Dr. Osman Serdar GEDİK, Ankara Yıldırım Beyazıt University, Department of Computer Engineering, Computer Vision, TÜRKİYE

Assist. Prof. Dr. Ömer Faruk NEMUTLU, Bingöl University, Department of Civil Engineering, Earthquake Engineering, TÜRKİYE

Assist. Prof. Dr. Öznur DOĞAN ULU, İnönü University, Scientific and Technological Research Center, Inorganic Chemistry, TÜRKİYE

Assist. Prof. Dr. Rüya KILIÇ DEMİRCAN, Sinop University, Department of Civil Engineering, Civil Engineering, TÜRKİYE

Assist. Prof. Dr. Seçil GENÇ, Ondokuz Mayıs University, Department of Electrical and Electronic Engineering, Electrical Energy Generation, TÜRKİYE

Assist. Prof. Dr. Seda ÇEKEN, İstanbul University, Department of Aviation Psychology, Applied and Developmental Psychology, TÜRKİYE

Assist. Prof. Dr. Seyhan ÖZTÜRK, Ondokuz Mayıs University, Department of Chemistry, Reaction Kinetics and Dynamics, TÜRKİYE

Assist. Prof. Dr. Sevinç ŞENER (ATEŞ), Akdeniz University, Department of Horticulture, Agricultural Water Management, TÜRKİYE

Assist. Prof. Dr. Simge SERTKAYA KÖYBAŞI, Balıkesir University, Department of Environmental Engineering, Environmental Pollution and Prevention, TÜRKİYE

Assist. Prof. Dr. Şeyda PARLAR, Konya Technical University, Department of Geology, General Geology, TÜRKİYE

Assist. Prof. Dr. Şule KIZIL, Lokman Hekim University, Department of Basic Medical Sciences, Histology and Embryology, TÜRKİYE

Assist. Prof. Dr. Taner UÇKAN, van Yüzüncü Yıl University, Department of Computer Engineering, Natural Language Processing, TÜRKİYE

Assist. Prof. Dr. Tuğba Nurcan YÜKSEL, Tekirdağ Namık Kemal University, Department of Pharmacology, Basic Pharmacology, TÜRKİYE

Assist. Prof. Dr. Volkan ATEŞ, Kırıkkale University, Department of Electrical and Electronics Engineering, Query Processing and Optimisation, TÜRKİYE

Assist. Prof. Dr. Yağmur NALBANT ATAK, Atılım University, Department of Mechanical Engineering, Chemical Thermodynamics and Energetics, TÜRKİYE

Assist. Prof. Dr. Yaşar ERBAŞ, Bartın University, Department of Civil Engineering, Solid Mechanics, TÜRKİYE

Assist. Prof. Dr. Yılmaz KAYA, Ondokuz Mayıs University, Department of Agricultural Biotechnology, Industrial Biotechnology, TÜRKİYE

Assist. Prof. Dr. Yunus Onur YILDIZ, Sinop University, Department of Mechanical Engineering, Mechanical Engineering, TÜRKİYE

Dr. Ahmet ERDOĞAN, İnönü University, Department of Mechanical Engineering, Computational Methods in Fluid Flow, TÜRKİYE

Dr. Arif TUNCAL, International Science and Technology University, Department of Aviation Systems and Technologies, Air-Space Transportation, POLAND.

Dr. Aslı TAŞ, Nevşehir Haci Bektaş Veli University, Department of Architecture, Built Environment and Design, TÜRKİYE

Dr. Beyza ONUR, Karabük University, Department of Architecture, Built Environment and Design, TÜRKİYE

Dr. Hanife ERDOĞAN GENÇ, Eastern Black Sea Forestry Research Institute, Department of Silviculture and Forest Botany Research, Forest Biodiversity, TÜRKİYE

Dr. Hasan YILMAZ, Akdeniz University, Department of Agricultural Machinery and Technologies Engineering, Biomass Energy Systems, TÜRKİYE

Dr. Hauwa ABUBAKAR, Abubakar Tafawa Balewa University Bauchi, Department of Computer Science, Machine Learning Algorithms, NIGERIA

Dr. Majeed SOUFIAN, University of Exeter, Department of Computer Science, Computer Vision, UK

Dr. Nur Laila HAMIDAH, Institut Teknologi Sepuluh Nopember, Departement of Engineering Physics, Biomass Energy Systems, INDONESIA

Dr. Ozan İNCE, Fırat University, Department of Civil Engineering, Earthquake Engineering, TÜRKİYE

Dr. Ömer MERCİMEK, Ankara University, Department of Civil Engineering, Reinforced Concrete Buildings, TÜRKİYE

Dr. Sura NAWFAL, University of Mosul, Department of Computer Engineering, Computer Vision, IRAQ

Dr. Tuğçe BiLGİN, Süleyman Demirel University, Department of Geography, Geomorphology and Earth Surface Processes, TÜRKİYE

---

* The ranking is arranged alphabetically within the academic title

Volume 8, Issue 2 (2025)

Table of Contents

Research Articles

1. INVESTIGATION OF HORST-GRABEN STRUCTURES AROUND GÜLŞEHIR (NEVŞEHIR-CENTRAL ANATOLIA) WITH PSINSAR AND LIDAR
Ramazan DEMİRCİOĞLU, Osman OKTAR……268-277

2. INVESTIGATION OF GEOLOGICAL STRUCTURES BETWEEN ACIPINAR-HANOBASI-ALTINKAYA (AKSARAY-TÜRKİYE) ABOUT SATELLITE-BASED TECTONIC LINEAMENTS
Ramazan DEMİRCİOĞLU……278-284

3. 2023 KAHRAMANMARAŞ DEPREMLERİ SONUCU HASAR GÖREN 11 KATLI BETONARME BİR YAPININ DEPREM PERFORMANSININ DEĞERLENDİRİLMESİ
Enes EKİNCİ, Alper ÖZMEN……285-297

4. *Arachis Hypogaea* BİTKİSİ KULLANILARAK YEŞİL SENTEZİ GERÇEKLEŞTİRİLEN GÜMÜŞ NANOPARTİKÜLLERİN ANTİMİKROBİYAL VE ANTİ QUORUM SENSING AKTİVİTELERİNİN TESPİTİ
Taylan AKTAŞ……298-309

5. EFFECT OF ADDITION OF PURE TITANIUM POWDER ON MECHANICAL PROPERTIES IN ROTARY FRICTION WELDING
Mehmet Erbil ÖZCAN……310-314

6. COMPARISON OF TOTAL PHENOLIC COMPOUNDS AND ANTIOXIDANT CAPACITIES OF ETHANOL AND METHANOL EXTRACTS OF *Pistacia Vera* L., *Prunus Dulcis* AND *Rhus Coriaria* L. LEAVES
Lale DUYSAK, Barış ÖZORMAN……315-322

7. PERFORMANCE EVALUATION OF TRANSFORMER-BASED PRE-TRAINED LANGUAGE MODELS FOR TURKISH QUESTION-ANSWERING
Mert İNCİDELEN, Murat AYDOĞAN……323-329

8. ANALYSIS OF THE IMPACT OF RGB-TO-ACHROMATIC COLOR SPACE TRANSFORMATIONS ON SINGLE-IMAGE SUPER-RESOLUTION PERFORMANCE
Hürkal HÜSEM, Zeynep GÜRKAŞ AYDIN, Önder DEMİR……330-340

9. UZAKTAN EĞİTİMDEN YÜZ YÜZE EĞİTİME: KTÜ KANUNİ KAMPÜSÜ MEKÂNSAL İMGELERİ
Hare KILIÇASLAN, Esra BABUL KOÇ……341-353

10. EXAMINATION OF DISTANCE BASED REGRESSION METHODS FOR DIFFERENT DATA STRUCTURES IN ANIMAL SCIENCE
Burcu KURNAZ, Hasan ÖNDER……354-362

11. A COMPARATIVE ASSESSMENT ON THE NOVEL LONG-TERM REAL-TIME SINGLE OBJECT TRACKING 5TECHNIQUES USING YOLO-NAS AND YOLO11
Cevahir PARLAK……363-370

12. CLASSIFICATION OF VIBRATION DATA FROM BROWNFIELD MILLING MACHINES USING MACHINE LEARNING
Rasim ÇEKİK, Abdullah TURAN……371-380

13. ENHANCED THERMAL, MECHANICAL, AND ELECTRICAL PROPERTIES OF EPOXY COMPOSITES REINFORCED WITH CDS/MWCNT NANOHYBRIDS SYNTHESIZED VIA HYDROTHERMAL METHOD

Hakan ŞAHAL, Ercan AYDOĞMUŞ……381-390

14. DITTRICHIA VISCOSA METHANOL EXTRACT-CONTAINING NANOEMULSION AND NANOEMULSION-BASED GEL FORMULATIONS: PREPARATION AND IN VITRO CHARACTERIZATION STUDIES

Farnaz SHARIFLOO, Afife Busra UGUR KAPLAN, Yasar Furkan KILINBOZ, Meltem CETIN……391-397

15. EFFECT OF DIFFERENT SUBSTRATES ON H_2S AND N_2 PRODUCTION IN BIOGAS PRODUCTION

Cevat FİLİKCİ, Tamer MARAKOĞLU……398-404

16. UTILIZATION OF WASTE HEAT IN CLOSED BRAYTON CYCLE: A THERMODYNAMIC ANALYSIS WITH VARIOUS WORKING FLUIDS

Gamze SOYTÜRK……405-417

17. OPTIMIZING VISUAL INSTRUCTION DETECTION IN AUTONOMOUS MOBILE ROBOTS USING YOLOV8 AND TENSORRT ACCELERATION

İbrahim SHAMTA, Funda DEMİR……418-427

18. APPLYING PERMANOVA FOR MULTIVARIATE ANALYSIS OF VARIANCE IN HEALTH STUDIES

Fahrettin KAYA……428-434

19. TUNNELING NANOTUBE (TNT) MEDIATED INTERCELLULAR CROSSTALK AND AUTOPHAGY IN HYPOXIA-INDUCED MESENCHYMAL STEM CELLS

Gizem İLTER AKTAŞ, Şeyma KİPEL, Leyla Didem KOZACI, Habibe Meltem ÖZGÜNER……435-443

20. SAHA VERİLERİ IŞIĞINDA BETONARME BİNA DEPREM PERFORMANSININ GÜVENİLİR TAHMİNİ

Abdullah DİLSİZ, Polat GÜLKAN……444-454

21. OPTIMIZATION-BASED PID CONTROLLER DESIGN FOR DC-DC BOOST CONVERTERS IN HYBRID RENEWABLE ENERGY SYSTEMS

Mustafa GUNES, Funda DEMIR……455-461

22. DETERMINATION OF ELEMENTAL CONTENT OF *Allium pervariensis* PLANT USING ICP-OES (INDUCTIVELY COUPLED PLASMA OPTICAL EMISSION SPECTROSCOPY) METHOD

İdris YOLBAŞ……462-465

23. ANALYSIS OF COMPRESSIVE STRENGTH OF STANDARD POURED MICROSILICA ADDED REACTIVE POWDER CONCRETE

Yakup Murat ÇEBİ, Arif Emre SAĞSÖZ……466-472

24. OPTIMIZING MICROWAVE DRYING OF BLACK CARROT PRETREATED WITH OSMOTIC DEHYDRATION: TAGUCHI-BASED DESIRABILITY FUNCTION APPROACH

Mehmet GULDANE……473-479

25. IMPACT ANALYSIS OF BUILDING STRUCTURE ON BUILDING ENVELOPE DESIGN IN THE CONTEXT OF SUSTAINABILITY

Merve ERTOSUN YILDIZ, Mehmet Akif YILDIZ……480-495

26. KAMUSAL ALANLARIN SÜRDÜRÜLEBİLİRLİĞİ: CAMİ AVLUSUNUN AFET SONRASI ESNEK KULLANIMI ÜZERİNE BİR İNCELEME

Melih AK, Ceyda FESCİ, Ebru Melis ÖZDEMİR, Bedizhan BAŞKAN4, Hilal AYCI.....496-506

27. RECONSTRUCTION OF METAL OBJECTS - 3D PHOTOGRAMMETRY AND CLAY COATING

Hasan Kemal SURMEN.....507-516

28. PRODUCTION OF PURE PVC, GRAPHENE AND CARBON NANOTUBE-DOPED PVC ELECTROSPUN NANOFIBER MEMBRANES: A HIGHLY EFFECTIVE METHOD FOR REMOVING ACID BLUE 74 DYE FROM WASTEWATER

Vildan ÖZKAN, Pınar BOZBEYOĞLU.....517-523

29. FROM SIMULATORS TO SKIES: ENGINEERING AND EDUCATIONAL ADVANCEMENTS IN PILOT TRAINING: A BIBLIOMETRIC PERSPECTIVE

Ayşe Aslı YILMAZ.....524-536

30. TRADITIONAL USEGE AND PRODUCTION TECHNIQUES OF NATURAL PLANT TAXA IN TAŞKÖPRÜ AND KAYAÜSTÜ PLATEAUS (GÜMÜŞHANE)

Arzu Ergül BOZKURT, Nebahat ÇIMEN, Diren UYCAN SARAÇ.....537-545

Reviews

31. A SOLUTION TO WASTE ECONOMY AND WATER SCARCITY; AIR CONDITIONING WASTEWATER

Hülya SAYĞI.....546-557

32. THERMAL SLAM: HARNESSING TEMPERATURE VARIATIONS TO ENHANCE OBJECT DETECTION AND TRACKING PERFORMANCE

Fathia SALEM, Osman Serdar GEDİK.....558-568

Black Sea Journal of Engineering and Science
doi: 10.34248/bsengineering.1480728

Open Access Journal
e-ISSN: 2619 – 8991

Research Article
Volume 8 - Issue 2: 268-277 / March 2025

INVESTIGATION OF HORST-GRABEN STRUCTURES AROUND GÜLŞEHIR (NEVŞEHIR-CENTRAL ANATOLIA) WITH PSINSAR AND LIDAR

Ramazan DEMİRCİOĞLU[1]*, Osman OKTAR[2]

[1]*Aksaray University, Department of Emergency Aid and Disaster Management, 68100, Aksaray, Türkiye*
[2]*Aksaray University, Department of Geomatics Engineering, 68100, Aksaray, Türkiye*

Abstract: This study examined horst-graben structures in the study area using the Interferometric Synthetic Aperture Radar (PSInSAR) method, and the movements in the line of sight (LOS) were determined. Both field and PSInSAR and Lidar studies were evaluated together. Accordingly, the uplift observed in the horst-graben structures, and the descending movements observed in the grabens continue today. It has been observed that the faults forming the Horst and Graben structures are active. The structures determined by the field studies agree with the data obtained from the PSInSAR and Lidar studies. It has been determined that these structures continue to develop even today. The region continues to expand under the extensional tectonic regime.

Keywords: Türkiye, Central Anatolia, Horst-graben, GNSS, PSInSAR, Lidar

***Corresponding author:** Aksaray University, Department of Emergency Aid and Disaster Management, 68100, Aksaray, Türkiye
E mail: ra.demircioglu@gmail.com (R. DEMİRCİOĞLU)
Ramazan DEMİRCİOĞLU https://orcid.org/0000-0003-0616-0331
Osman OKTAR https://orcid.org/0000-0001-6764-0561

Received: May 08, 2024
Accepted: October 28, 2024
Published: March 15, 2025

Cite as: Demircioğlu M, Oktar O. 2025. Investigation of horst-graben structures around Gülşehir (Nevşehir-Central Anatolia) with PSInSAR and Lidar. BSJ Eng Sci, 8(2): 268-277.

1. Introduction

The study area is located in the central Central Anatolian region (Figure 1). During the Neotectonic Era, specifically during the Late Miocene–Pliocene period. As a result of this transition, horst-graben formations and regular faulting were formed, extending in the NE-SW direction. The study area is northwest of the Ecemiş Fault Zone and east of the Tuzgölü Fault Zone, where both directional and normal faults are active. According to Koçyiğit (2003), Central Anatolia experienced an extensional tectonic regime oriented in the east-northeast and west-southwest directions during the neotectonic period. This conclusion is based on the geometry of morphotectonic structures and earthquake focal point solutions. In a separate study, Çiner et al. (2015) reported that basalt ages and cosmogenic data from the Kızılırmak River terraces in the Cappadocia Region indicated the valley was excavated by 160 meters over the last 2 million years. Additionally, they found that the regional uplift rate of the river in the Central Anatolian Plateau is approximately 0.08 mm per year, which has shown significant changes over time.

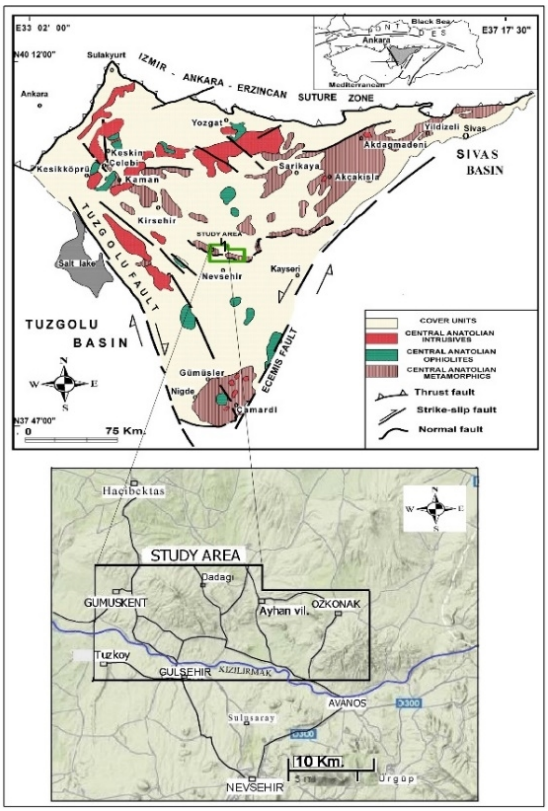


Figure 1. The study area.

The purpose of this study is to use the PSInSAR approach to determine the horst-graben structure and fault in the

This work is licensed (CC BY-NC 4.0) under Creative Commons Attribution 4.0 International License

studied area and reveal the motions of the region with the highest concentration of active faults. There are also studies on this subject. Some of them are (Biggs et al., 2007; Yavaşoğlu et al., 2011; Shirzaei and Bürgmann, 2013; Zheng et al., 2013; Rosu et al., 2015; Wang and Jónsson, 2015; Gürsoy et al., 2017; He et al., 2018; Scott et al., 2020; Poyraz and Hastaoğlu, 2020; Wang et al., 2022; Eski and Sözbilir, 2024). The research area has been the subject of numerous studies, including works by (Aydın, 1984; Atabey et al., 1988; Göncüoğlu et al., 1993; Temiz and Gökten, 2016; Koçak et al., 2021), sedimentological investigations by Atabey (1989), and structural geology studies by (Göncüoğlu et al., 1993; Dirik and Göncüoğlu, 1996; Koçyiğit, 2003; Doğan, 2011). Finding the faults' surface deformations and tectonic movements that result in the local graben and horst structures is the aim of this investigation.

One unique aspect of this research is that there have been no previous geophysical and geodetic investigations on the horst-graben structures within the study region, which were identified through field investigations. Our findings indicate that detailed studies of geology and structural geology are supported by the velocity information derived from the analysis results.

2. Materials and Methods

Field studies were used to identify the Horst-Graben formations in the research zone, and PSInSAR was used to track the movement of the line of sight (LOS) in the area. In line with the findings of the Stanford Method for Persistent Scatterers (StaMPS)/MIT study (Hooper et al., 2018), PSInSAR analyses were performed on the examined region and compared to field study data.

To further illustrate the faults and morphology of the horst-graben structure in the research area, a cross-section was made. For a more thorough assessment of the fault morphology in the cross-section, Lidar data (from equatorstudios.com) were acquired, and a cross-section was generated using these data. This cross-section was produced using the Global Mapper program's data evaluation capabilities.

2.1. PSInSAR Analyses

To analyse crustal movement, Hooper et al. (2007) created the StaMPS software and used the PSInSAR technology, which was a novel approach. These techniques identify pixels with little phase change by employing spatial correlation of the interferometric phase. It can analyse any terrain in this way, even if structures or other things are present. Through the use of interferogram adaptation maps, fixed target sites are found. Establishing the correlation threshold value is the most basic evaluation technique.

The permanent scatterer (PS) point is designated for a target when it yields a fit value greater than the mean value. To increase the number of PS points, PSInSAR studies with at least 12 SAR images are advised (Hooper et al. 2018; Zhang et al., 2021; Zhou et al., 2022). Each image's pixel amplitude data are used to create the time series. It is possible to identify highly suited targets by creating many sets of interferograms. For this purpose, a collection of differential interferograms is produced using a single master image. It is advised to utilise a DEM while creating interferograms to reduce the influence of topography.

2.2. PSInSAR Data Acquisition

Images from the European Space Agency's Sentinel-1 satellite were used in the PSInSAR analysis. The dates of the Sentinel-1A synthetic aperture radar (SAR) images are shown in Table 1, and the approximate coverage of the SAR (track 14) images is shown in Figure 2. In this study, 36 Sentinel-1 SAR images were used. The features of SAR images are interferometric wide (IW), C band, and track number 14, taken between January 2020 and December 2022.

SAR images were provided free of charge by the Copernicus Open Access Hub (URL-1).

Table 1. The Sentinel-1A synthetic aperture radar (SAR) images

2020.01.20	2021.01.14	2022.01.21
2020.02.13	2021.02.19	2022.02.26
2020.03.20	2021.03.15	2022.03.22
2020.04.13	2021.04.20	2022.04.15
2020.05.19	2021.05.14	2022.05.21
2020.06.24	2021.06.19	2022.06.14
2020.07.18	2021.07.13	2022.07.20
2020.08.23	2021.08.18	2022.08.23
2020.09.16	2021.09.23	2022.09.18
2020.10.22	2021.10.17	2022.10.24
2020.11.15	2021.11.22	2022.11.17
2020.12.21	2021.12.16	2022.12.11

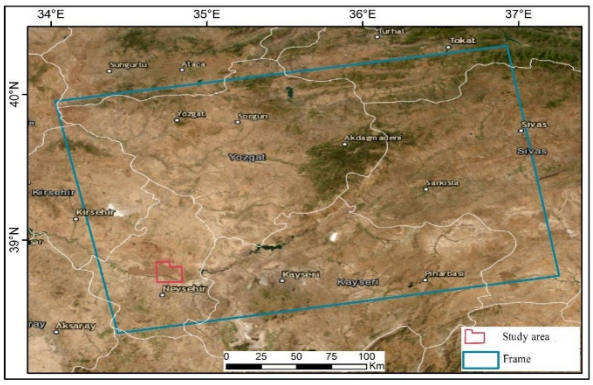


Figure 2. The blue box indicates the approximate coverage of the Sentinel-1A satellite radar images, track number 14.

3. Results

The research area's geological and geodetic investigations were assessed jointly. New information regarding the horst-graben structures in the area was discovered because of these investigations.

3.1. Study Area Geology and Structural Geology

The research region has rocks that are Paleozoic to Quaternary in age. The Kırşehir Massif's metamorphic units, which date from the Paleozoic to the Mesozoic era, make up the basement. Palaeocene-Quaternary aged units cover it in an unconformable manner (Figure 3). The studied region was originally impacted by compressional forces in roughly SW-NE directions, and subsequently in SE-NW directions throughout the Middle-Late Miocene period (Koçyiğit, 2003; Koçyiğit and Doğan, 2016; Demircioğlu, 2014).

In the Late Miocene-Pliocene period, the extensional tectonic regime is effective in the region, since there is no structure (reverse fault, fold, and inclined layers) to give any compressional tectonism in the units in the study area.

One of the signs that this extensional tectonic regime will continue is the cause of the activity on the Tuzgölü fault to the west of the study region and the Salanda fault within the study area. Additionally, there is a correlation between the significant fault strikes and the estimated principal stress orientations. The Kızılırmak valley in the study region is the greatest place to view the remnants of the extensional tectonic regime, which is believed to be continuing now. The data used in this study pertain to the extensional tectonic regime and are from the Pleistocene-Holocene, the younger units.

Local uplifts (Hırka horst) and basin formation continue with the extension. Although there are uplifts in Hırka Mountain and its surroundings (between Hırka Mountain and Ziyaret Hill), which are composed of Massif units, there are subsidences in the south of Hırka Horst, in the Kızılırmak valley (Kızılırmak Graben), and the north of Hırka Horst, around Kuyulukışla Village (Kuyulukışla Graben) (Figure 4).

Yüksekli, Dadağı, Salanda, Gülşehir, and Tuzköy faults are the main geological structures influencing the uplift and subsidance in the studied region. Based on these findings, the Neotectonic period is when the area acquired a horst-graben structure. Important neotectonic period structural components are the Kuyulukışla and Kızılırmak grabens, as well as the Hırka and Ziyarettepe horsts. The formation of the terrace systems in the valley is mostly due to the influence of climate conditions, specifically the Pleistocene Glacial period (Doğan et al., 2009).

In the research area, all fault types-normal, reverse, thrust, and strike-slip—can be observed. Every direction has faults, and the Massif contains every kind of rock. Poly-phase deformation is the cause of these faults. There is a lot of faulting within the cover units, particularly in the region known as the Ayhan fault zone. Because of the influence of the compressional tectonic regime, there is an impressive density of thrust and reverse faults in this region. These faultings are present in rocks of the Ayhan group that are from the Late Paleocene to the Middle Eocene. On the other hand, younger units have a lower fault density because they undergo less deformation. The Late Miocene (Messinian)–Pliocene dating units have typically seen normal faulting because of the dominance of the extensional tectonic regime in the region (Figure 3).

The Hırka and Gezgintepe horsts were formed during this period by strike-slip faults with vertical displacement and normal faults (Salanda, Dadağı).

Grabens named Kuyulukışla and Kızılırmak formed in the space between these horsts. The region is still affected by the extensional tectonic regime. There were notable errors during this time. These important faults comprise the horst-graben structure.

The Salanda fault zone is a right-lateral strike-slip fault that also has a vertical displacement component. It is a strike-slip (transtensional) fault developing in an extensional tectonic regime.

There are visible portions of the Salanda fault (Figure 3, 4). There are two distinct fault strikes on the fault: N40-80^{0}E and N45^{0}W-N82^{0}W. According to Demircioğlu and Oktar (2024), there are fault plane dips to the southwest and southeast with angles varying from 58 to 72 degrees (Demircioğlu, 2014). The vicinity of Eski Yaylacık hamlet is one of the research area's most visible locations (Figure 5). They stretch about between Gümüşkent Town and Eskiyaylacık villages in the direction of N580W. The fault in this region is roughly 10 kilometres long. Here, it creates the point where the basement units and the Yüksekli formation meet (Figure 3).

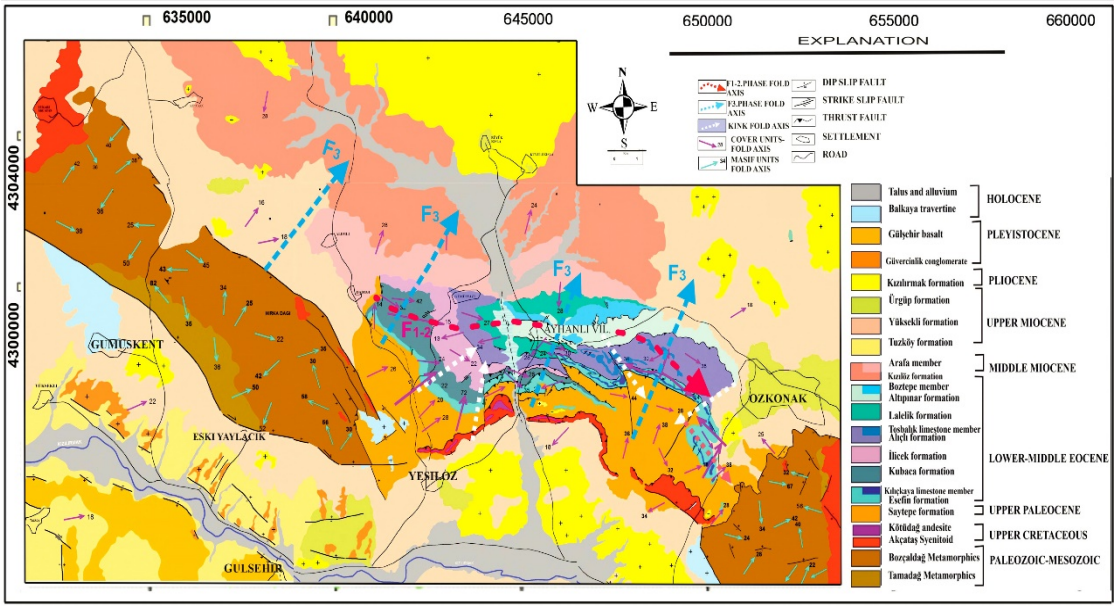


Figure 3. Geology-structural geological map of the study area (Modified from Demircioğlu, 2014).

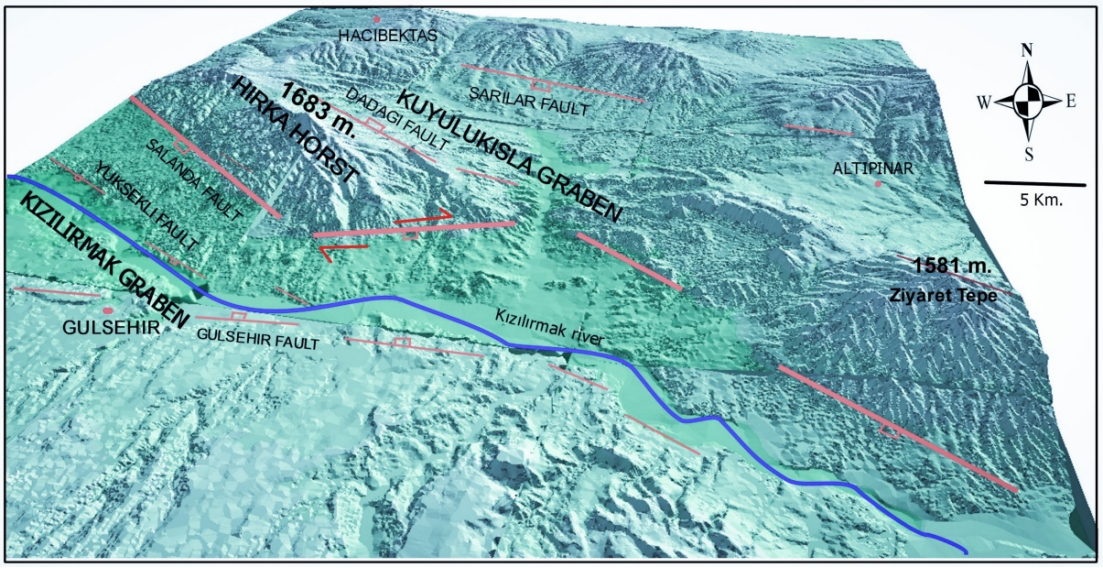


Figure 4. Morphotectonic view of the Salanda, Yüksekli, Gülşehir, Dadağı, and Sarılar faults (Modified from Demircioğlu, 2014).



Figure 5. View of the Salanda fault (Demircioğlu and Oktar, 2024).

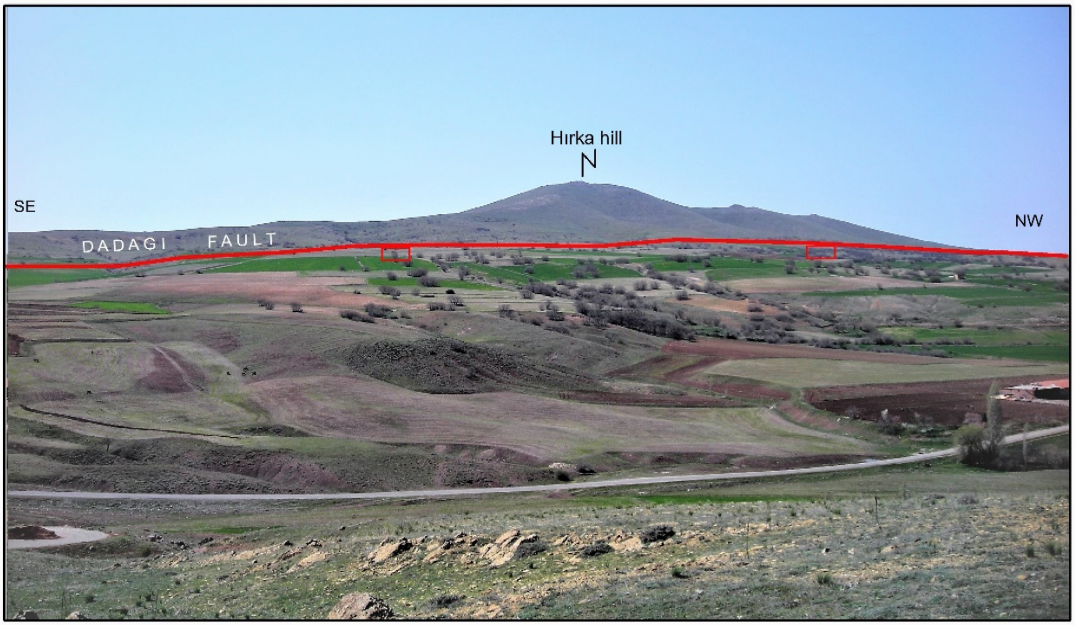


Figure 6. General view of the Dadağı fault (Alemli village).

Apart from the typical flaw, there's a lateral slip on the right side. They stretch between the villages of Yeşilöz and Eskiyaylacık in the N58-720W direction. This section of the Salanda fault is roughly 7 kilometres long. They can be observed between Dondurma Hill and Yeşilöz Village in the northeast-southwest direction. Another way to think of this region is as a transfer fault. In this area, it is around 4 miles long. Present travertine developments are depending on this fault (Salanda) (Figure 5). This fault caused the formation of travertines, particularly in the northwest and northeast of Gümüşkent and in the area surrounding Balkaya Hill. Along the fault line, there are numerous water sources. The Dadağı fault is located in the portion of the massif that faces east (Figure 6).

They stretch between Höyük Tepe and Akçataş Village's east in N60–680W directions (Figure 3, 4). The fault plane has a northeastern slope with dip angles that range from 52 to 65 degrees. It is about 15 km. long in this region. Around Höyük Tepe, at the southeast tip of the Dadağı fault, are travertine deposits.

The Salanda fault forms the boundary of the Massif's southwest region. In addition to this fault, they have led to the Massif rising and turning into a horst (Hırka horst). The Yüksekli fault (Figure 7) is one of the major faults of the Horst-graben complex. Along the route that connects Avanos District and Yüksekli Village, they outcrop fairly well. This fault and the Salanda fault are roughly aligned. It's a typical error. The Güvercinlik conglomerates are hung on a terrace-shaped, Pleistocene-aged Yükseklı fault. Compared to the Salanda fault, it is smaller. The Kızılırmak River is to the east of it.

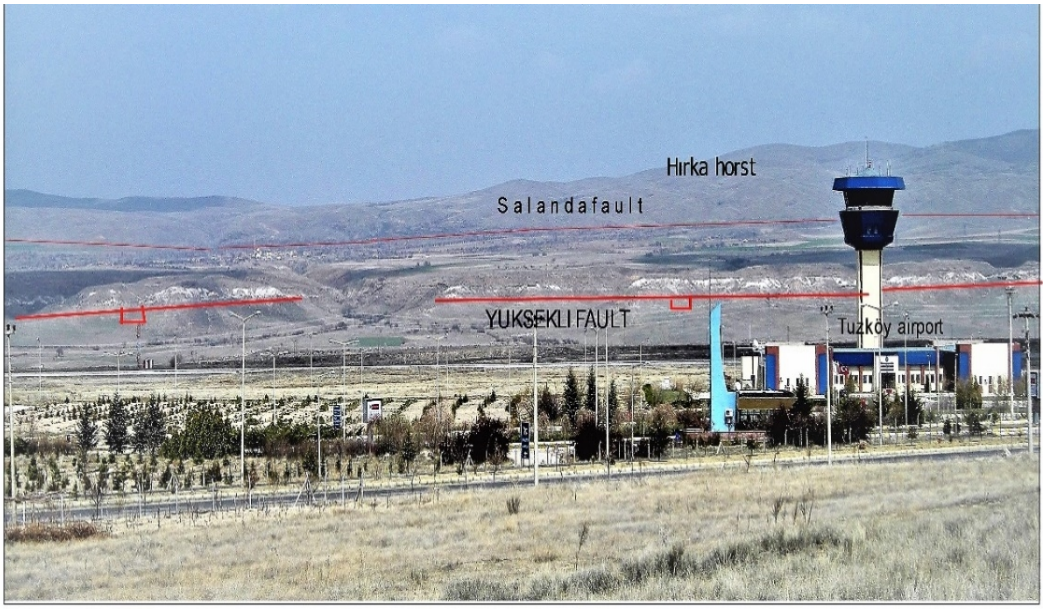


Figure 7. A view from the Yüksekli Fault (South of Yüksekli village).



Figure 8. General view of the Gülşehir fault (north of Gülşehir).

One of the faults seen in the Kızılırmak Valley is the Gülşehir fault. A typical fault delineates the valley's southern boundary. They can be viewed facing N60 to N700W. The fault planes have a northeastern dip, and their dip angles range from 56 to 620.

Additionally, the Pleistocene-aged Güvercinlik conglomerates were suspended by the Gülşehir fault. The Kızılırmak is currently resting on its current bed due to this problem. That is to say, the southern side of the Kızılırmak Valley, is the youngest fault. The Yüksekli fault is the youngest fault on the north side.

Gülşehir and its surroundings are the best places to see. It is located in the western part of the valley (Figure 8).

The research area's basement units have risen and taken on the shape of a horst structure due to faulting that is believed to be the result of the regional extensional regime. The horst structure was developed by basement units under the influence of the extensional tectonic regime in the latter Miocene and later periods, particularly with the Salanda, Yüksekli, and Dadağı faults. The Yüksekli and Gülşehir faults emerged in the direction roughly parallel to the Salanda and Dadağı faults as a result of the extension continuing (Figure 9).

The Sarılar fault, a normal fault that strikes around N800W and dips to the southwest, is located in the northernmost portion of the research region (Figure 4).

The Yüksekli and Salanda fault planes and faults have a southwest slope direction. The Dadağı and Gülşehir faults have fault planes that are inclined northeast. This suggests that under the same tectonic regime, synthetic and antithetic faults evolved.

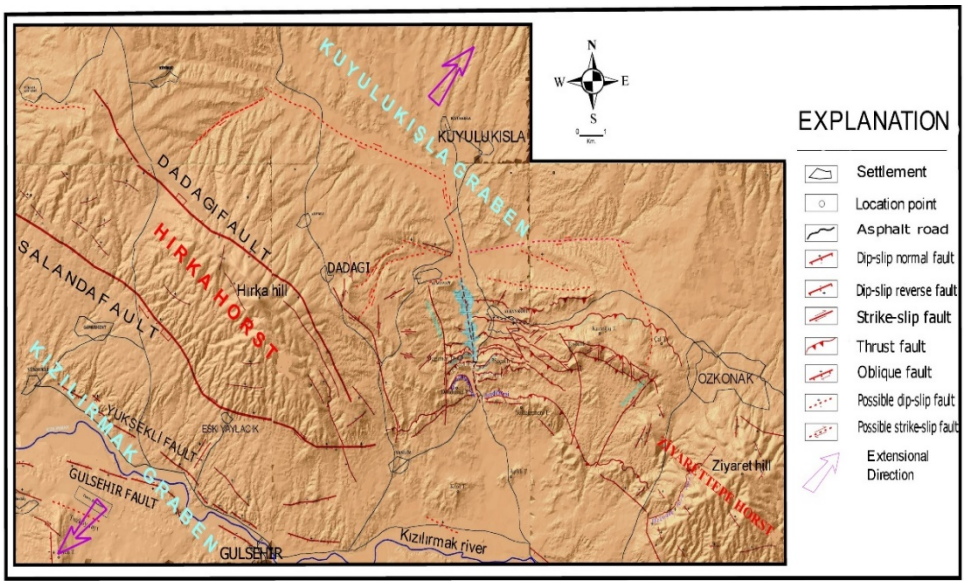


Figure 9. General view of the faults in the study area (Modified from Demircioğlu, 2014).

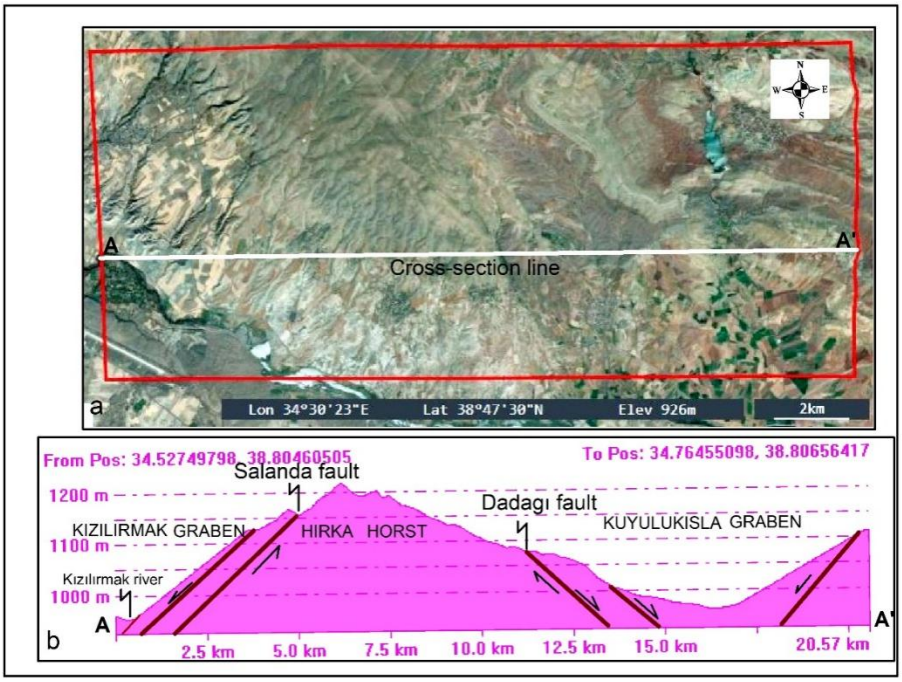


Figure 10. (a) Lidar image of the study area (from the Equator website, 2023), (b) Cross section obtained from the Lidar image.

Due to the extensional regime, the plain areas that remained between the normal faults produced the Kızılırmak graben, named after the Kızılırmak River, and the Kuyulukışla graben, named after Kuyulukışla Village (Demircioğlu, 2014).

Horst-graben structures were created during the Neotectonic period as a result of tension forces orientated northeast-southwest, according to the strikes of the normal faults. Due to the influence of these faults, the Kızılırmak, which originated in this region, altered its bed and eventually settled in its current location (Figure 10). A lidar image of the study area has been acquired and the faults are shown in the cross sections of this image (Figure 10).

These flaws have caused the Kızılırmak River's river bed to shift over time. Pebbles created from the sediments of the Kızılırmak River can be seen along the route between Avanos and Gülsehir.

3.2. Results of PSInSAR Analysis

First, the program Sentinel Application Platform (SNAP) was used to obtain interferograms. Next, data from the Shuttle Radar Topography Mission (SRTM) were utilised to eliminate the effect of topography on the interferograms. Lastly, movements in the LOS direction were obtained by using these interferograms to calculate PS points using StaMPS software. The SAR photos were analysed to ascertain the LOS direction movements occurring in the Salanda Fault. In the PSInSAR analysis, the master image was selected to be the temporal and spatial centre of all images (Figure 11).

After the SAR photos were analysed, the image was identified as the master image. A total of 333452 PS points were generated for the research region. Figure 11 displays the annual velocities in the LOS direction of the research area along with their standard deviations. In Figure 11, the horizontal axis displays the longitude value and the vertical axis the latitude value. In Figure 11, blue colours indicate uplift and red colours indicate subsidence.

Horst-graben regions were identified using PSInSAR data (Figure 11). Horst-graben regions were identified using PSInSAR data (Figure 11). These results indicate that elevation levels are found in the horst portions and decreasing values in the graben parts. Additionally, these values agree with field findings (Figure 12).

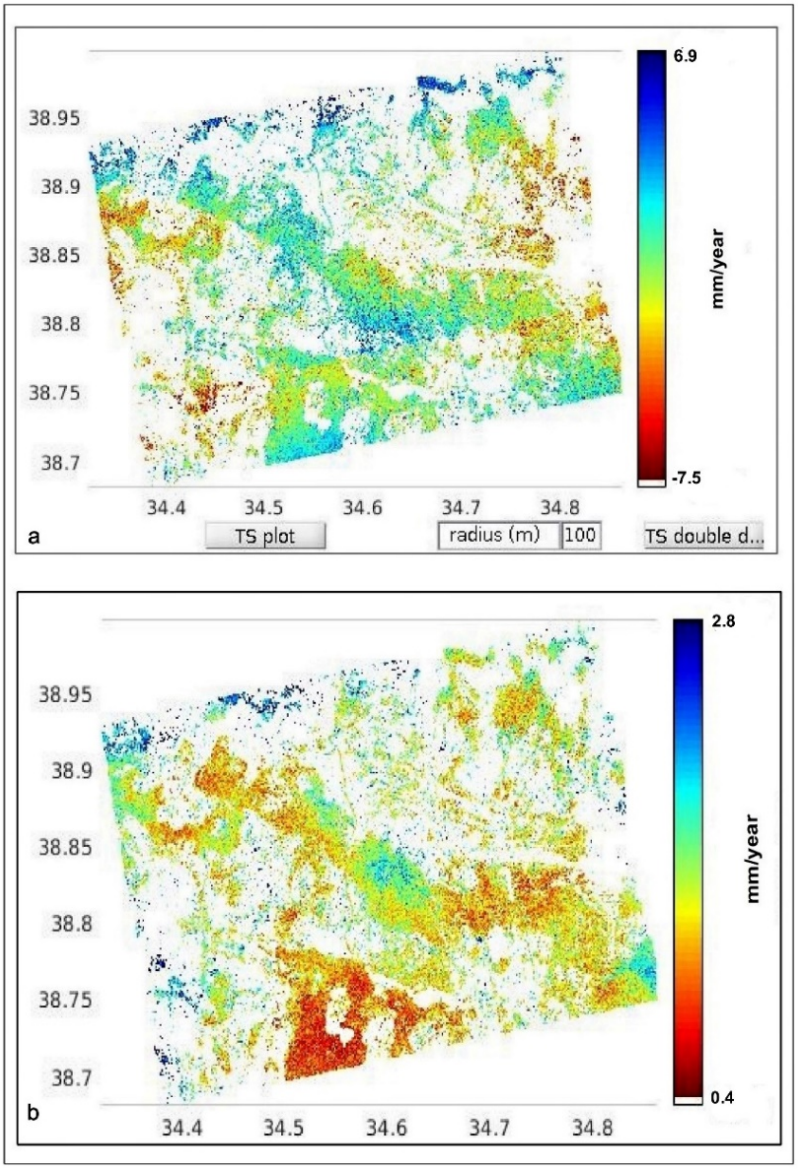


Figure 11. (a) PSInSAR results of the study area. Annual velocity in the LOS direction, (b) Standard deviations of the annual velocities in the LOS direction.

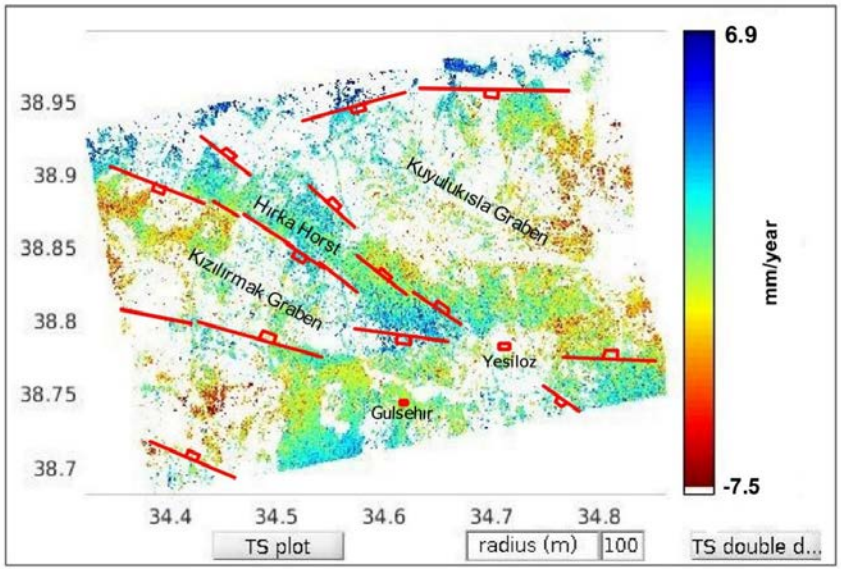


Figure 12. Horst-graben structures and PSInSar.

4. Discussion

After the research region's annual velocities in the LOS direction were assessed, the PSInSAR analysis's findings revealed that annual uplift values of up to 7.1 mm and annual subsidence values of up to -7.5 mm had been discovered. According to Demircioğlu and Oktar (2024), these values were determined at very similar values on different measurement dates. Doğan et al. (2009) estimated that throughout the past two million years, the river digging rate along the Kızılırmak valley has been 0.08 mm/year based on field data. It was discovered that the maximum rate of excavation was 0.11 mm/year. The SAR images from this study's final three years showed an average uplift value of 6.9 mm/year.

This study is a significant improvement over the data obtained from previous studies. The evaluations made at the locations of the faults forming the Kızılırmak and Kuyulukışla grabens indicate significant uplift and subsidence values for the faults. The faults contain both horizontal and vertical movement elements. As the amount of horizontal slip is significantly reduced, the fault will not be recognised as oblique. Scholz et al. (1986) found that there are higher movement values compared to intracontinental faulting. Their study looked at the amount of movement and the tendency to cause earthquakes. As a result, these faults are likely to generate earthquakes.

5. Conclusion

In this study, the PSInSAR approach was used to determine the vertical and line-of-sight motions on the faults forming the Kızılırmak and Kuyulukışla grabens. In addition, PSInSAR data were used to evaluate the actual number and amount of movements on the faults forming the grabens and horsts. The 33452 PS points generated over the study area were used to generate precise movement information about the area. The amount of movement in these places is very high due to field observations, elevations in the fault zone, and areas where the fault crosses. In terms of tectonic activity, geomorphic indices (Demircioglu and Coşkuner, 2022) indicate moderate to high activity. PSInSAR data, field observations, and geomorphic index analyses indicate significant active faults.

Author Contributions

The percentages of the authors' contributions are presented below. All authors reviewed and approved the final version of the manuscript.

	R.D.	O.O.
C	50	50
D	50	50
S	50	50
DCP	50	50
DAI	50	50
L	50	50
W	50	50
CR	50	50
SR	50	50
PM	50	50
FA	50	50

C=Concept, D= design, S= supervision, DCP= data collection and/or processing, DAI= data analysis and/or interpretation, L= literature search, W= writing, CR= critical review, SR= submission and revision, PM= project management, FA= funding acquisition.

Conflict of Interest

The authors declared that there is no conflict of interest.

Ethical Consideration

Ethics committee approval was not required for this study because of there was no study on animals or humans.

References

Atabey E, Tarhan N, Yusufoğlu H, Canpolat M. 1988. Hacıbektaş, Gülşehir, Kalaba (Nevşehir) Himmetdede (Kayseri) arasının jeolojisi, MTA Rapor No: 8523, Ankara, Türkiye.

Atabey E. 1989. Aksaray-H19 quadrangle, 1:100,000 scale geological map and explanatory text. Maden Tetkik Arama Yayınları Ankara, Türkiye, ss: 64.

Aydın N. 1984. Orta Anadolu masifinin Gümüşkent B.(Nevşehir) Dolayında jeolojik petrografik incelemeler. MTA Jeoloji Etüdleri Daire Bşk. Saydamer – Gün Kitaplığı Arşiv No: 206, Ankara, Türkiye, ss: 72.

Biggs J, Wright T, Lu Z, Parsons B. 2007. Multi-interferogram method for measuring interseismic deformation: Denali Fault, Alaska. Geophysical J Int, 170(3): 1165-1179. https://doi.org/10.1111/j.1365-246X.2007.03415.x

Çiner A, Doğan U, Yıldırım C, Akçar N, Ivy-Ochs S, Alfimov V, Schlüchter C. 2015. Quaternary uplift rates of the Central Anatolian Plateau, Turkey: insights from cosmogenic isochron-burial nuclide dating of the Kızılırmak River terraces. Quaternary Sci Rev, 107: 81-97.

Demircioğlu R, Coşkuner B. 2022. Salanda fay zonu'nun Kesikköprü (Kırşehir) ve Yeşilöz (Nevşehir) arasında kalan kesiminin göreceli tektonik aktivitesinin jeomorfik indislerle incelenmesi. Pamukkale Üniv Müh Bil Derg, 8(3): 464-482.

Demircioğlu R, Oktar O. 2024. Investigation of Salanda fault zone, between Yesiloz and Gumuskent (Nevsehir-Turkey) with PSInSAR. Geofísica Int, 63(2): 865-879. https://doi.org/10.22201/igeof.2954436xe.2024.63.2.1733

Demircioğlu R. 2014. Geology and structural features of the Kirşehir massif and cover units in the Gülşehir-Özkonak (Nevşehir) region. PhD Thesis, Selçuk University, Institute of

Science, Konya, Türkiye, pp: 241.

Dirik K, Göncüoğlu MC. 1996. Neotectonic characteristics of the Central Anatolia. Int Geol Rev, 38: 807-817.

Doğan U, Koçyiğit A, Wijbrans J. 2009. Evolutionary history of the Kızılırmak River, Cappadocia Section: implication for the initiation of Neotectonic regime in Central Anatolia, Turkey. 62nd Geological Congress of Turkey, April 13-17, Ankara, Türkiye, pp: e2020JD034411. https://doi.org/10.1029/2020JD034411

Doğan U. 2011. Climate-controlled river terrace formation in the Kızılırmak Valley, Cappadocia section, Turkey: inferred from Ar-Ar dating of Quaternary basalts and terraces stratigraphy. Geomorphol J, 126: 66-81. https://doi.org/10.1016/j.geomorph.2010.10.028

Eski S, Sözbilir H. 2024. Gediz (Alaşehir) grabeni'nde gelişen a-sismik yüzey deformasyonların kökeni. Türkiye Jeol Bült, 67(4): 31-62. https://doi.org/10.25288/tjb.1342834

Göncüoğlu MC, Yalınız K, Kuşçu I, Köksal S, Dirik K. 1993. Orta Anadolu masifinin orta bölümünün jeolojisi, Bolum 3: Orta Kızılırmak Tersiyer Baseninin Jeolojik evrimi. T.P.A.O. Rapor No: 3313, Ankara, Türkiye, ss: 48.

Gürsoy Ö, Kaya Ş, Çakir Z, Tatar O, Canbaz O. 2017. Determining lateral offsets of rocks along the eastern part of the North Anatolian Fault Zone (Turkey) using the spectral classification of satellite images and field measurements. Natural Hazards Risk, 8: 1276-1288. https://doi.org/10.1080/19475705.2017.1318794

He P, Wen Y, Xu C, Chen Y. 2018. High-quality three-dimensional displacement fields from new-generation SAR imagery: application to the 2017 Ezgeleh, Iran, earthquake. J Geodesy, 93: 573-591. https://doi.org/10.1007/s00190-018-1183-6

Hooper A, Bekaert D, Hussain E, Spaans K. 2018. Stamps/Manual, VeStamps4.1b, School of Environment, University of Leeds, Leeds, UK, pp: 135.

Hooper A, Pa S, Howard Z. 2007. Persistent scatterer interferometric synthetic aperture radar for crustal deformation analysis, with application to Volcán Alcedo, Galápagos. J Geophysical Res: Solid Earth, 112: B07407. https://doi.org/10.1029/2006JB004763

Koçak İ, Temiz U, Öksüz N. 2021. Salanda Fay zonu (SFZ) ile ilişkili traverten oluşumlarının paleoiklimsel önemi. Müh Bil Araş Derg, 3: 218-225. https://doi.org/10.46387/bjesr.963704.

Koçyiğit A, Doğan U. 2016. Strike-slip neotectonic regime and related structures in the Cappadocia region: a case study in the Salanda basin, Central Anatolia, Turkey. Turkish J Earth Sci, 25(5): 393-417. https://doi.org/10.3906/yer-1512-9

Koçyiğit A. 2003. Orta Anadolu'nun genel neotektonik özellikleri ve depremselliği. Türkiye Petrol Jeologları Dern Bült, 5(Özel Sayı): 1-26.

Poyraz F, Hastaoglu K. 2020. Monitoring of tectonic movements of the Gediz Graben by the PSInSAR method and validation with GNSS results. Arabian J Geosci, 13: 844. https://doi.org/10.1007/s12517-020-05834-5

Rosu AM, Pierrot-Deseilligny M, Delorme A, Binet R, Klinger Y. 2015. Measurement of ground displacement from optical satellite image correlation using the free open-source software MicMac. ISPRS J Photogrammetry Remote Sens, 100: 48-59. https://doi.org/10.1016/j.isprsjprs.2014.03.002

Scholz C.H, Aviles CA, Wesnousky SG. 1986. Scaling differences between large interplate and intraplate earthquakes. Bull Seism Soc Amer, 76: 65-70. https://doi.org/10.1785/BSSA0760010065

Scott C, Bunds M, Shirzaei M, Toke N. 2020. Creep along the Central San Andreas Fault from surface fractures, topographic differencing, and InSAR. J Geophys Res: Solid Earth, 125: e2020JB019762 https://doi.org/10.1029/2020JB019762

Shirzaei M, Bürgmann R. 2013. Time-dependent model of creep on the Hayward fault from joint inversion of 18 years of InSAR and surface creep data. Türkiye Petrol Jeologları Dern Bült, 5(Özel Sayı): 1-25.

Temiz U, Gökten Y.E. 2016. 10 Ocak 2016 Hacıduraklı-Çiçekdağı (Kırşehir) depremi (Mw = 5.0); ilgili yapılar ve tektonik ortam, Orta Anadolu. Geological Bull Turkey, 59: 155-166. https://doi.org/10.25288/tjb.298218

URL-1: https://equatorstudios.com (accessed date: january 14, 2024).

Wang T, Jónsson S. 2015. Improved SAR amplitude image offset measurements for deriving three-dimensional coseismic displacements. IEEE J Selected Topics Appl Earth Observat Remote Sens, 8(7): 3271-3278. https://doi.org/10.1109/JSTARS.2014.2387865

Wang Z, Lawrence J, Ghail R, Mason P, Carpenter A, Agar S, Morgan T. 2022. Characterizing micro-displacements on active faults in the Gobi Desert with time-series InSAR. Appl Sci, 12(9): 4222. https://doi.org/10.3390/app12094222

Yavaşoğlu H, Tarı E, Tüysüz O, Çakır Z, Ergintav S. 2011. Determining and modelling tectonic movements along the central part of the North Anatolian Fault (Turkey) using geodetic measurements. J Geodynamics, 51(5): 339-343. https://doi.org/10.1016/j.jog.2010.07.003

Zhang X, Feng M, Zhang H, Wang C, Tang Y, Xu J, Wang C. 2021. Detecting rock glacier displacement in the central himalayas using multi-temporal InSAR. Remote Sens, 13(23): 4738. https://doi.org/10.3390/rs13234738

Zheng M, Fukuyama K, Sanga-Ngoie K. 2013. Application of InSAR and GIS techniques to ground subsidence assessment in the Nobi Plain, Central Japan. Sensors, 14(1): 492-509. https://doi.org/10.3390/s140100492

Zhou L, Zhao Y, Zhu Z, Ren C, Yang F, Huang L, Li X. 2022. Spatial and temporal evolution of surface subsidence in Tianjin from 2015 to 2020 based on SBAS-InSAR technology. J Geodesy Geoinfo Sci, 5(1): 60-72. http://jggs.chinasmp.com/EN/Y2022/V5/I1/60

Black Sea Journal of Engineering and Science
doi: 10.34248/bsengineering.1472055

Open Access Journal
e-ISSN: 2619 – 8991

Research Article
Volume 8 - Issue 2: 278-284 / March 2025

INVESTIGATION OF GEOLOGICAL STRUCTURES BETWEEN ACIPINAR-HANOBASI-ALTINKAYA (AKSARAY-TÜRKİYE) ABOUT SATELLITE-BASED TECTONIC LINEAMENTS

Ramazan DEMİRCİOĞLU[1]*

[1]*Aksaray University, Faculty of Health Sciences, Department of Emergency Aid and Disaster Management, 42250, Aksaray, Türkiye*

Abstract: The region between Aksaray, Central Anatolia, and Altınkaya (Türkiye) is included in the study area. The area's basement comprises ophiolites, igneous rocks from the Late Cretaceous period, and metamorphic rocks from the Palaeozoic to Mesozoic ages. Late Cretaceous-Quaternary sedimentary units were formed in the area Tuzgolü Basin. The Late Cretaceous-Mio-Pliocene sedimentary rocks in the study area have undergone polyphase deformation under compressive and extensional tectonic regimes. As a result of these deformations the folded, faulted and fractured structures have been developed in the rocks of the area. These structures have formed lineations. In this study, the relationship between the tectonic lineaments identified in the field and those obtained by computer processing of Landsat 8 images was evaluated. The lineament densities obtained by satellite were N40-500E, N50-600E, N30-400W, N40-500W and N80-900W. Similarly, the lineament densities obtained from field studies were determined as N40-500E, N50-600E, N40-500W, N30-400W and N80-900W. The lineaments belonging to the Tuzgölü fault and the structural geological structures determined in the field are in significant agreement.

Keywords: Türkiye, Tuzgolu basin, Aksaray, Acıpınar-Altınkaya, Lineament

***Corresponding author:** Aksaray University, Faculty of Health Sciences, Department of Emergency Aid and Disaster Management, 42250, Aksaray, Türkiye
E mail: ra.demircioglu@gmail.com (R. DEMIRCIOĞLU)
Ramazan DEMİRCİOĞLU https://orcid.org/0000-0003-0616-0331

Received: April 22, 2024
Accepted: November 26, 2024
Published: March 15, 2025

Cite as: Demircioğlu R. 2025. Investigation of geological structures between Acipinar-Hanobasi-Altinkaya (Aksaray-Türkiye) about satellite-based tectonic lineaments. BSJ Eng Sci, 8(2): 278-284.

1. Introduction

The study area is located in the Tuzgölü basin in Central Anatolia, northeast of the Tuzgölü fault zone (Figure 1). It covers the area between Acıpınar and Altınkaya towns in Aksaray province. Important studies have been carried out in different fields of geology in and around the study area.

The study area, it's around have been thoroughly examined by various researchers over the years. Erol (1969), Arıkan (1975), Uygun (1981), Görür et al. (1984), Atabey et al. (1987), Dellaloğlu (1997), and Uçar (2008) also conducted sedimentological studies. Additionally, Çemen et al. (1999) analyzed the geodynamic evolution of the Tuzgölü basin, Dirik and Erol (2003) examined the morphotectonic features of the area and its surroundings, and Koçyiğit (2000, 2003) investigated the seismic characteristics of Central Anatolia.

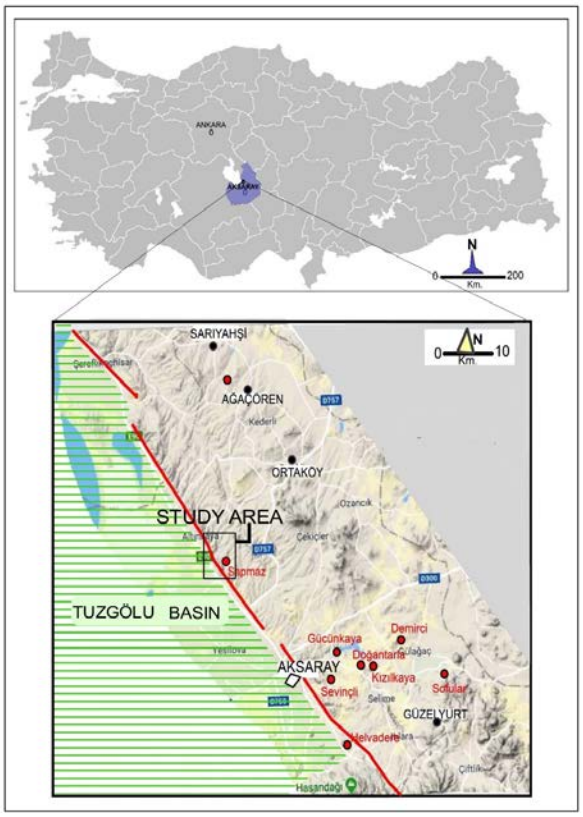


Figure 1. Map of the study area's location.

This work is licensed (CC BY-NC 4.0) under Creative Commons Attribution 4.0 International License

Some researchers, such as Şaroğlu et al. (1992) and Emre (1991), conducted active fault mapping studies in Some researchers, such as Şaroğlu et al. (1992) and Emre (1991), conducted active fault mapping studies in Türkiye to assess the earthquake-generating potential of the Tuzgölü fault zone, which passes through the study area. Kürçer (2012), Kürçer and Gökten (2011), and Kürçer and Gökten (2014) also realised palaeoseismological studies on segments of the Tuzgölü fault zone.

Recently, remote sensing studies with satellite and aerial photographs have increased. One of these studies is the determination of tectonic lineaments obtained by remote sensing studies. Lineament studies are very important in geological studies. In particular, there are many studies on the relationship between mining areas and tectonic lineaments. Some of these studies are Shirazi et al. (2022), Cherai et al. (2022), Sassioui et al. (2023), Dutra et al. (2023), Nouri and Arian (2023). For geothermal areas, linearity studies are important. Some of the related studies are Arrofi et al. (2022), Mahwa et al. (2023), and Heriawan et al. (2020). There are also studies on the relationship between geological structures and tectonic linearity. Some of them are Benaafi et al. (2017), Akram et al. (2019), Redouane et al. (2022), Skakni et al. (2022), Ahmadi et al. (2023), and Baruah et al. (2023).

The purpose of this study is to compare satellite-based tectonic lineaments with the lineament structures in a specific area. This comparison has not been performed in any other study. This study looks at lineaments belonging to faults, folded structures, and shear fractures observed in the Late Cretaceous-Miocene aged units between Acıpınar and Altınkaya. These lineaments were compared with those obtained by processing satellite images. This study found that the lineaments collected from satellite-based methods and field studies are generally compatible.

2. Materials and Methods

To begin with, the study area underwent comprehensive field evaluations that took into account prior research. Through a combination of on-site and remote sensing methods that utilized satellite imagery, the tectonic lineaments of the region were determined. The Landsat-8 OLI satellite image was initially processed in the ENVI program within a computer environment. From there, the resultant image was transferred to the ArcGis program after taking into account the threshold values in the Geomatica program, revealing the lineaments. Linearities obtained from both field and satellite studies were used to create rose diagrams, which were generated using the Rockwork program. A visual representation of these processes can be found in Figure 2.

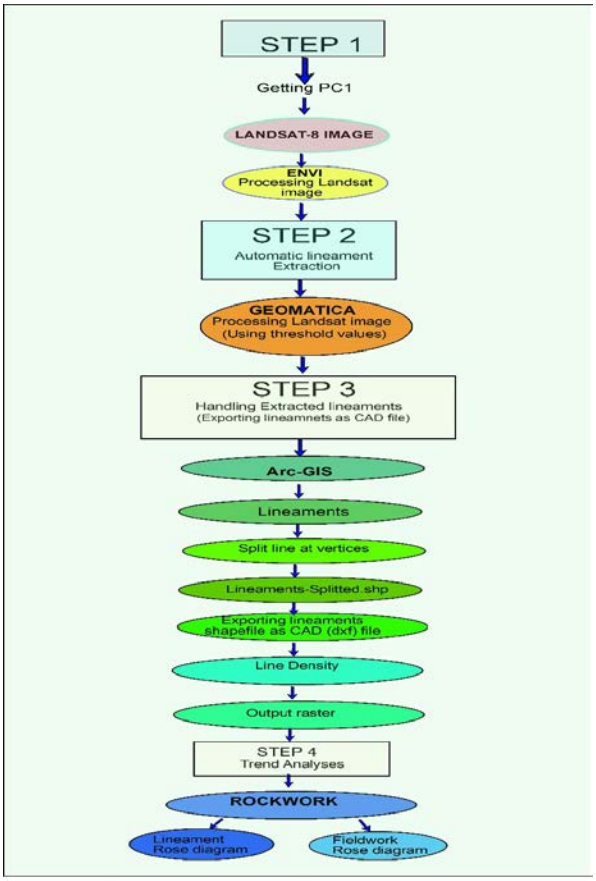


Figure 2. Flowchart of the lineament map generation.

Through the acquisition of data, an assessment was conducted on the tectonic lineaments in the area spanning from Acıpınar to Altınkaya. This was accomplished by analyzing both field and satellite-based lineaments. The lineaments extracted from the Landsat-8 satellite image were cross-referenced with those found in field research, which are related to various faults and fractures.

2.1. Geological Setting

2.1.1. Stratigraphy

The study area and its surroundings cover the region between Acıpınar and Altınkaya in Aksaray province. Late Cretaceous-Mio-Pliocene aged rocks outcrop in this area (Figure 3).

Although not visible in the study area, the Kirsehir massif's Paleozoic-Mesozoic aged metamorphites, Late Cretaceous aged ophiolites, and plutonic rocks form the surrounding and study area's basement. The Kızıltepe Formation, consisting of late Cretaceous-aged sedimentary rocks, is the oldest unit in the study area, with burgundy-red-colored conglomerates, sandstones, and siltstones indicating a terrestrial environment (Figure 3). The Asmabogazi Formation overlays this unit unconformably, starting with conglomerates and continuing with sandstones containing *Orbitoides* fossils and limestones containing Rudist and *Hippurites* towards the top, indicating a terrestrial-marine environment (Uçar, 2008). These unit's sandstone, mudstone, and marl succession sometimes have thin coaly levels. Dellaloglu

(1997) set the unit's age as Miocene based on the palaeontological studies on the coal levels. The Miocene aged Cihanbeyli formation covers this unit angularly, with sandstone, siltstone, and mudstone levels present towards the top, including tuffaceous levels. Dellaloğlu (1997) and Toprak and Rojay (1997) set the late Miocene-Pliocene age for this unit based on palaeontological and radiometric ageing studies on the units and tuffaceous levels, respectively. The Sapmaz formation, of the Miocene-Pliocene aged, is laterally vertically transitional with this unit (Uçar, 2008). Finally, all these units are unconformably overlaid by Quaternary aged alluvium (Figure 3).

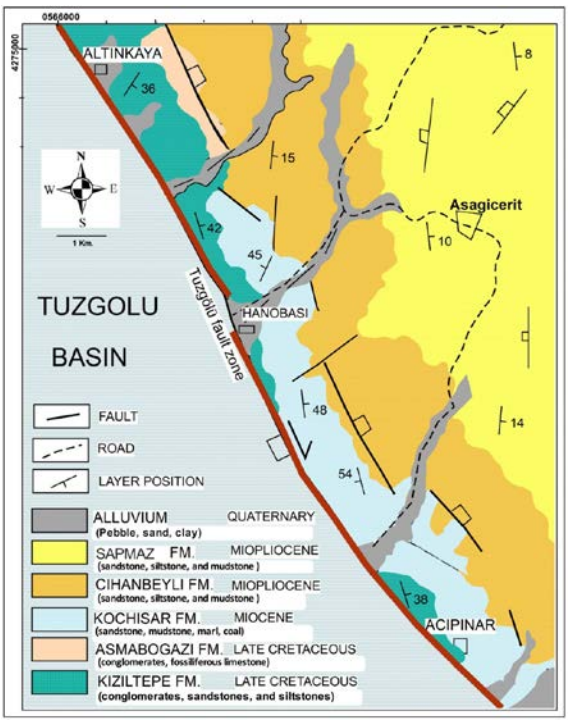


Figure 3. Geological map of the research region and its environs.

2.1.2. Structural geology

The Tuzgölü basin boasts numerous geological studies, with a particular focus on the Koçhisar-Aksaray segment of the Tuzgölü fault zone. Here, the fault segment's strikes tend to vary between N30 and 45^{0}W. The study area features northwest-southeast horst and graben structures, including the Hanobasi horst and Asagıcerit graben (Figure 3). The Late Cretaceous-Mio-Pliocene aged rocks in these areas have undergone significant deformation, attributable to the closure of the Inner Tauride Ocean and the ensuing compressive tectonic regime. The formation of folded structures, faults, and shear fractures were realised in this period. In more recent times, during the late Miocene and early Pliocene, the area has experienced the effects of the extensional tectonic regime, leading to the formation of the Tuzgölü fault zone and normal faults that possess a directional thrust fault character and a vertical thrust component (Kürçer and Gökten, 2014).

3. Results

3.1. Geological Structures Presenting Linearity

The Tuzgolu Fault Zone is the most significant linear tectonic structure in the study area. The direction of the Tuzgolu fault zone varies, and it includes the Koçhisar-Aksaray segment within the study area. Field studies show that structures like faults, fractures, and fold axes exhibit tectonic linearity, as shown in Figure 4. In Altınkaya village, the Koçhisar-Aksaray fault line is visible (Figure 4a). Similarly, the Koçhisar-Aksaray fault line is clearly visible around Acıpınar village (Figure 4b). Furthermore the fold axes of the units which exhibit folding form lineations in the study area. The shear and tension fractures also formed due to the polyphase deformation in the study area (Figure 4d, e, f).

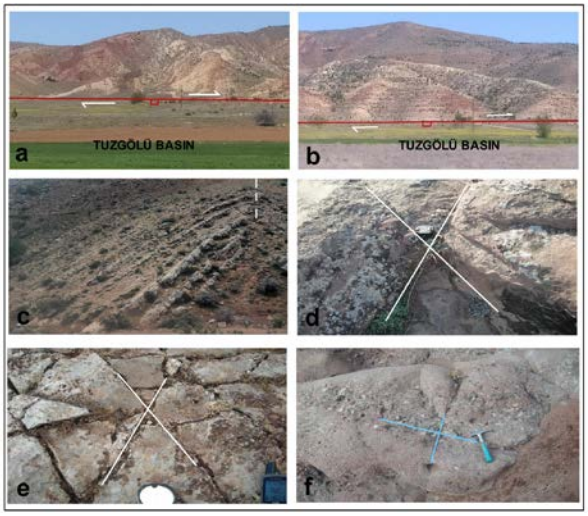


Figure 4. a-The Koçhisar-Aksaray fault line from Altınkaya village. b-The Koçhisar-Aksaray fault line from Acıpınar village c- Fold and fold axis appearance in the Asmabogazi Formation. d- Shear fractures in sandstones of the Kochisar Formation. e- Shear fractures in Asmabogazi limestones f- Tension fractures in conglomerate of the Sapmaz Formation.

In the study area, there are two types of lineations: morphological lineations caused by erosion and tectonic lineations. Additionally, there are important normal faults including the Koçhisar-Aksaray fault that forms the Hanobası horst are present. The normal faults, which have developed in parallel or semi-parallel directions to this fault, also form lineations.

3.2. Lineament maps

One of the satellite images between Acıpınar and Altınkaya is the Google Earth image where the Koçhisar-Aksaray fault is seen (Figure 5). In this image, the Koçhisar-Aksaray fault is visible. Landsat-8 OLI satellite imagery obtained from earthexplorer.usgs.gov/ web address was used to create the lineament maps (Figure 6). This image was processed in the Envi programme. Then, in Geomatica, the image was prepared for the ArcGis program by using threshold values to obtain sufficient detail. A lineament map was obtained in the

ArcGis programme (Figure 7). By superimposing the density map and lineament map of the lineaments between Acıpınar and Altınkaya, a density-lineament map of the study area was created (Figure 8).

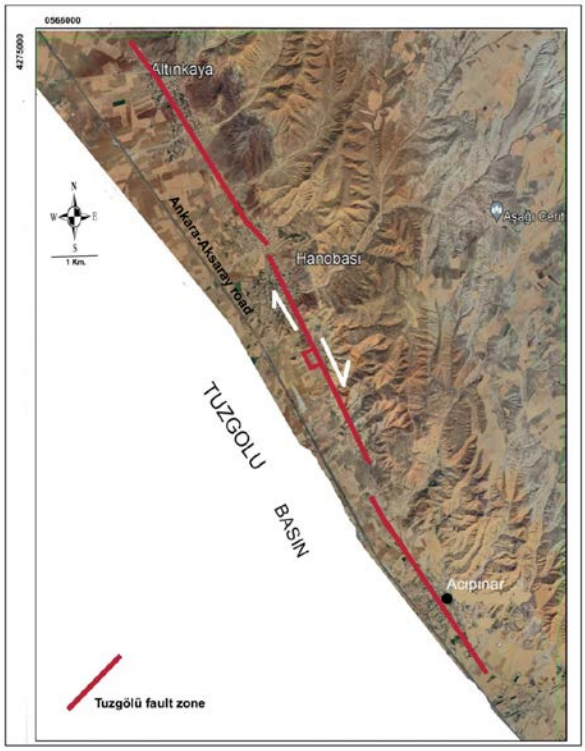


Figure 5. Google Earth image of Acıpınar-Altınkaya.

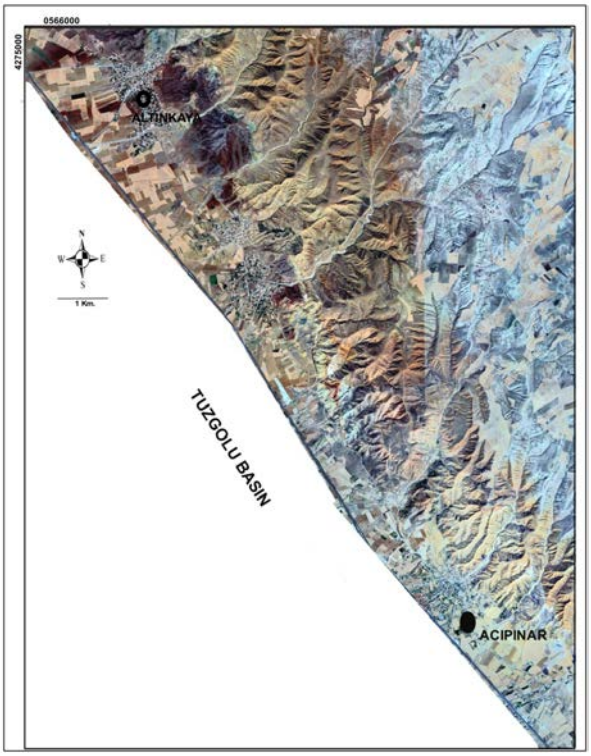


Figure 6. Landsat-8 OLI satellite image.

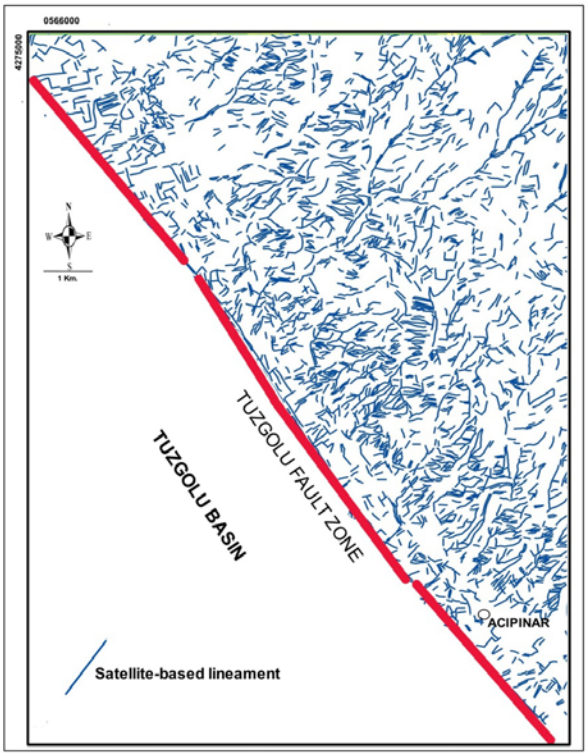


Figure 7. Tectonic lineament map between Acıpınar-Altınkaya.

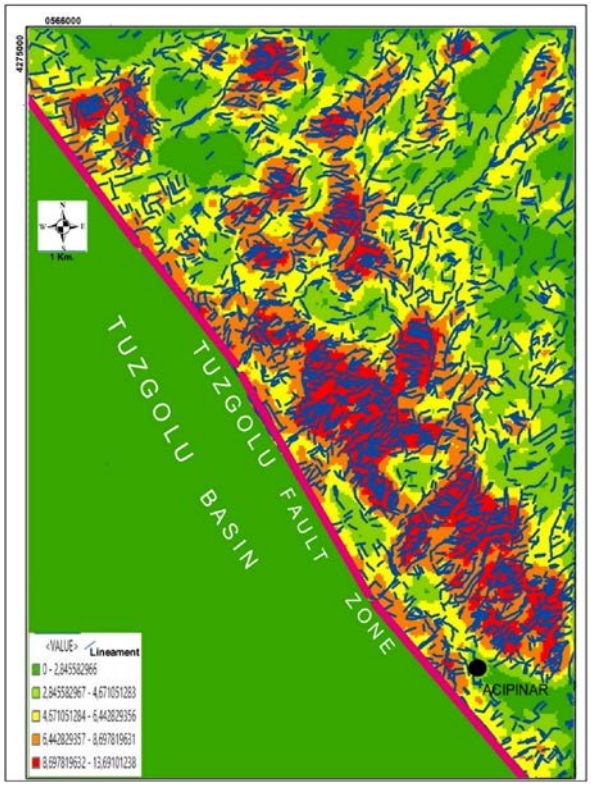


Figure 8. Lineament density and lineaments map.

3.3. Assessment of fieldwork and satellite lineaments

To ascertain the predominant distribution directions of the lineaments collected between Altınkaya and Acıpınar, rose diagrams were constructed. The length as a proportion of the total lineament length (%L) and the

length as a percentage of the total lineament population (%N) were used to produce two different types of rose diagrams.

The diagrams showed that lineaments were present in all directions, but the dominant directions were N40^0-50^{0}E, N50^0-60^{0}E, N30^0-40^{0}W, N40^0-50^{0}W, and N80^0-90^{0}W.

Furthermore, a rose diagram of the faults was created in the Rockwork programme. It was based on 67 measurements taken from faults ranging from centimetres to metres in size, which were determined in the Late Cretaceous-Mio-Pliocene aged rocks. The dominant fault directions were found to be concentrated between N40^0-50^{0}E, N50^0-60^{0}E, N30^0-40^{0}W, N40^0-50^{0}W, and N80^0-90^{0}W

Based on the measurements taken from the shear fractures in Late Cretaceous-Miocene-aged units, a rose diagram was created. The dominant fracture directions were N20^0-30^{0}E, N40^0-50^{0}E, N30^0-40^{0}W, N40^0-50^{0}W, and N80^0-90^{0}W, totaling 157 measurements.

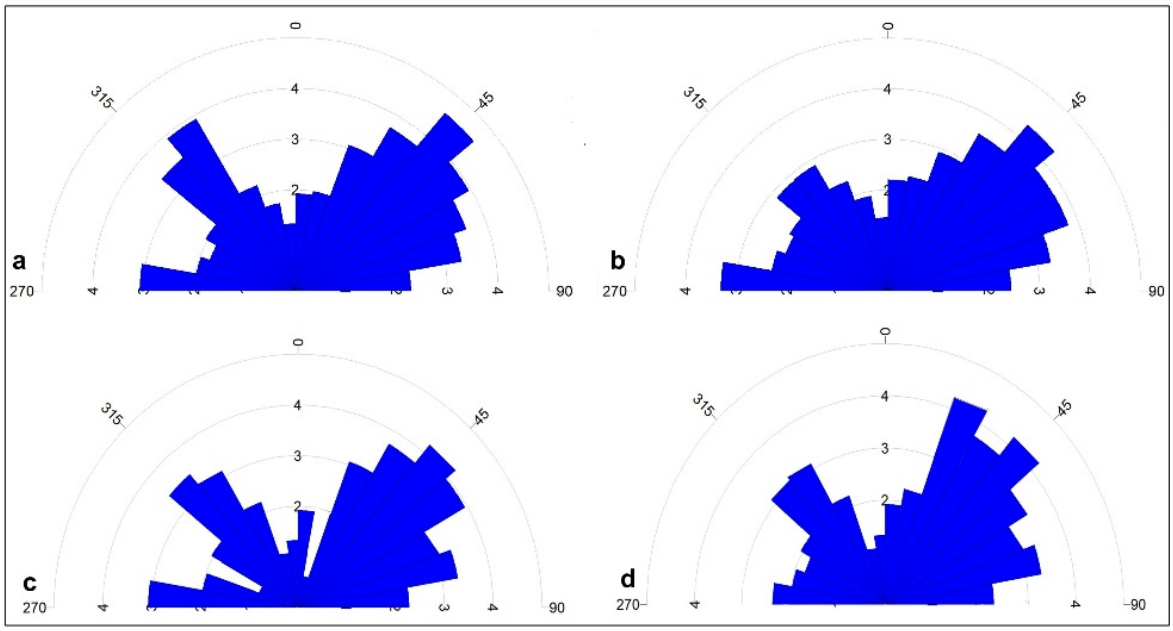


Figure 9. a- %L rose diagram b- %N rose diagram. c- Rose diagram of the faults d- Rose diagram of shear fracture in sedimentary rocks.

4. Conclusions

Lineaments in the region between Acıpınar and Altınkaya, derived from field and satellite-based surveys, were analyzed. Within the Late Cretaceous-Mio-Pliocene aged rocks in the study area, faults, fractures, and folds resulted from polyphase deformations, forming lineaments. These lineaments were assessed, particularly those located northeast of the Tuzgölü fault zone. Using the Rockwork program, rose diagrams were generated for both field and satellite-based lineaments, which revealed that the lineaments were distributed in all directions due to polyphase deformations, with the most intense directions being N40^0-50^{0}E, N50^0-60^{0}E, N30^0-40^{0}W, N40^0-50^{0}W, and N80^0-90^{0}W, according to %L and %N. A rose diagram was created based on the directional measurements of the faults determined in the field, which showed that the dominant fault directions were N40^0-50^{0}E, N50^0-60^{0}E, N40^0-50^{0}W, N30^0-40^{0}W, and N80^0-90^{0}W, similar to the fault directions of the Koçhisar-Aksaray segment. Similarly, a rose diagram was prepared for the measurements taken from the fractures in the area, revealing dominant fracture directions of N20^0-30^{0}E, N40^0-50^{0}E, N30^0-40^{0}W, N40^0-50^{0}W, and N80^0-90^{0}W, similar to the faults.

From the obtained rose diagrams, fractures have developed in all orientations due to polyphase deformation. By evaluating the fracture and fault planes in the rose diagrams, it is possible to determine the dominant compression and extension directions.

The lineaments obtained from the field surveys and satellite-based studies were found to be highly compatible.

Author Contributions

The percentages of the author' contributions are presented below. The author reviewed and approved the final version of the manuscript.

	R.D.
C	100
D	100
S	100
DCP	100
DAI	100
L	100
W	100
CR	100
SR	100
PM	100
FA	100

C=Concept, D= design, S= supervision, DCP= data collection and/or processing, DAI= data analysis and/or interpretation, L= literature search, W= writing, CR= critical review, SR= submission and revision, PM= project management, FA= funding acquisition.

Conflict of Interest

The author declared that there is no conflict of interest.

Ethical Consideration

Ethics committee approval was not required for this study because of there was no study on animals or humans.

References

Ahmadi H, Pekkan E, Seyitoğlu G. 2023. Automatic lineaments detection using radar and optical data with an emphasis on geologic and tectonic implications: a case study of Kabul Block, eastern Afghanistan. Geocarto Inter, 38(1): 2231400. https://doi.org/10.1080/10106049.2023.2231400

Akram MS, Mirza K, Zeeshan M, Ali I. 2019. Correlation of tectonics with geologic lineaments interpreted from remote sensing data for Kandiah Valley, Khyber-Pakhtunkhwa, Pakistan. J Geol Soc India, 93: 607-613. https://doi.org/10.1007/s12594-019-1224-7

Arıkan Y. 1975. Tuz Gölü havzasının jeolojisi ve petrol imkanları. M.T.A. Derg, 85: 17-37.

Arrofi D, Abu-Mahfouz IS, Prayudi SD. 2022. Investigating high permeable zones in non-volcanic geothermal systems using lineament analysis and fault fracture density (FFD): northern Konawe Regency, Indonesia. Geothermal Ener, 10(1): 1-17. https://doi.org/10.1186/s40517-022-00241-3

Atabey E, Tarhan N, Akarsu B, Taşkıran A. 1987. Şereflikoçhisar, Panlı (Ankara) Acıpınar (Niğde) yöresinin jeolojisi, maden tetkik ve arama genel müdürlüğü raporu. Derleme no; 8155, Ankara, Ankara, Türkiye, ss: 63.

Baruah M P, Goswami T K., Bezbaruah D. 2023. Understanding the tectonics of the Mikir massif, northeast India: insights from lineament analysis. Arabian J Geosci, 16(10): 545. https://doi.org/ 10.1007/s12517-023-11658-w

Benaafi M, Hariri M, Abdullatif O, Makkawi M., Al-Shaibani A. 2017. Analysis of lineaments within the Wajid Group, SW Saudi Arabia, and their tectonic significance. Arabian J Geosci, 10: 1-17. https://doi.org/10.1007/s12517-017-2860-0

Cherai,M, Marzouki A, Talbi F. 2022. Mineralization-tectonic relationship in the jbeltirremi fluorite mine (Taourirt region-eastern morocco): contribution of remote sensing for geological exploration. J Mines, Metals Fuels, 70(5): 251-257. https://doi.org/10.18311/jmmf/2022/28374

Çemen İ, Göncüoğlu MC, Dirik K.1999. Structural evolution of the Tuzgölü basin in Central Anatolia. Turkey, J Geol, 107 (6): 693-706.

Dellaloğlu A. 1997. Ankara ili-Tuz Gölü arasındaki Neotetis'in kuzey kolunun evrimi (Haymana-Tuzgölü Basenlerinin stratigrafileri ve jeoteknik evrimleri. Doktora tezi, Çukurova Üniversitesi, Adana, Türkiye, ss: 154.

Dirik K, Erol O. 2003.Tuzgölü ve çevresinin tektonomorfolojik evrimi, Orta Anadolu-Türkiye. TPJD, 5: 27-46.

Dutra LF, Louro VHA, Monteiro LVS. 2023. The southern IOCG and hydrothermal nickel mineralization trend of the Carajás Mineral Province: Airborne geophysical and remote sensing evidence for structural controls and hydrothermal signature. J Appl Geophys, 213: 105016. https://doi.org/10.1016/j.jappgeo.2023.105016

Emre Ö. 1991. Hasandağı-Keçiboyduran dağı yöresivolkanizmasının jeomorfolojisi, Tuz Gölü fay zonunun neotektonik özellikleri. Doktora tezi, İstanbul Üniversitesi, Deniz Bilimleri ve Coğrafya Enstitüsü, İstanbul, Türkiye, ss: 198.

Erol O. 1969. Tuz Gölü havzasının jeolojisi ve jeomorfolojisi. MTA Derleme rapor no; 4220, Ankara, Türkiye, ss: 43.

Görür N, Oktay FY, Seymen İ, Şengör AMC. 1984. Paleotectonic evolution of the Tuzgölü basin complex, Central Turkey. Sedimentary record of a Neo-Tethyan closure, The Geological Evolution of the Eastern Mediterranean. Geology Society Special Publication, 17, In J.E. Dixon, and A.H.F. Robertson (eds.). Oxford, UK, pp: 467-482.

Heriawan M N, Hafizsyah RA, Hanunah J S, Hede A N H, Malik D. 2020. Surface and subsurface fracture zones modeling using automatic lineament analysis and geostatistical method, with case study of Wayang Windu geothermal field, West Java, Indonesia. Earth Environ Sci, 417: 012007. https://doi.org/ 10.1088/1755-1315/417/1/012007

Koçyiğit A. 2000. General neotectonic characteristics and seismicity of Central Anatolia, Haymana-Tuzgölü-Ulukışla basenlerinin uygulamalı çalışması (workshop). URL: http://tpjd.org.tr/images/bultenler/pdf/haymana5.pdf (accesed date: March 15, 2024).

Koçyiğit A. 2003. Orta anadolunun sismisitesi ve neotektonik özellikleri. Türkiye Petrol Jeolog Der, 5: 1-26.

Kürçer A, Gökten YE. 2011. Paleoseismic Trenching on the southern part of Tuzgölü Fault Zone, Central Anatolia, Turkey. Geophysical Research Abstracts Vol. 13, EGU2011-5767, 3 – 8 April, Vienna, Austria, pp: 43.

Kürçer A. 2012. Tuz Gölü Fay Zonu'nun neotektonik özellikleri ve paleosismolojisi, Orta Anadolu, Türkiye. Doktora Tezi, Ankara Üniversitesi, Fen Bilimleri Enstitüsü, Ankara, Türkiye, ss: 318,

Kürçer A, Gökten YE. 2014. Paleosismolojik üç boyutlu sanal fotoğraflama yöntemi, örnek çalışma: Duru-2011 Hendeği, Tuz Gölü Fay Zonu, Orta Anadolu, Türkiye. Türkiye Jeoloji Bülteni, 2014: 57-61.

Mahwa J, Ping J, Leng W, Zhao J, Liu J. 2023. Tectonics and hydrogeochemical features of geothermal waters in Tangyin Rift SE Taihang Mountain. Geothermics, 109: 102657. https://doi.org/10.1016/j.geothermics.2023.102657

Nouri R, Arian M. 2023. Multifractal modelling of gold

mineralization and lineaments in the 1: 100,000 Chaapaan sheet (NW IRAN). J Mining Environ, 14(3): 973-980. https://doi.org/10.22044/jme.2023.12919.2343

Redouane M, Mhamdi H S, Haissen F, Raji M, Sadki O. 2022. Lineaments extraction and analysis using landsat 8 (OLI/TIRS) in the Northeast of Morocco. Open J Geol, 12(5): 333-357. https://doi.org/10.4236/ojg.2022.125018

Sassioui S, Lakhloufi A, Aarab A, Zouggarh A, EL HILALI M, Courba S, Larabi A. 2023. Contribution of remote sensing to mapping lineaments and ore-mineral occurrences in the Taghbalt Region, Moroccan Eastern Anti-Atlas. Iraqi Geol J, 2023: 307-323. https://doi.org/10.46717/igj.56.2D.23ms-2023-10-29

Seymen İ. 1981. Kaman (Kırşehir) dolayında Kırşehir Masifi'nin stratigrafisi ve metamorfizması, Türkiye Jeol Kurumu Bülten, 24: 7-14.

Shirazi A, Hezarkhani A, Pour AB. 2022. Fusion of lineament factor (Lf) map analysis and multifractal technique for massive sulfide copper exploration: The Sahlabad area, East Iran. Minerals, 12(5): 549. https://doi.org/10.3390/min12050549

Skakni O, Hlila R, Pour AB, Martín M, Maate A, Maate S, Hossain MS. 2022. Integrating remote sensing, GIS and in-situ data for structural mapping over a part of the NW Rif belt, Morocco. Geocarto Inter, 37(11): 3265-3292. https://doi.org/10.1080/10106049.2020.1852611

Şaroğlu F, Emre Ö, Boray A. 1992. Türkiye diri fay haritası. Maden Tetkik Arama Genel Müdürlüğü, Ankara, Türkiye, ss: 63.

Toprak V, Rojay B. 1997. Neojen peçenek havzasının jeolojik evrimi (Orta Anadolu). Selçuk Üniversitesi, Mühendislik-Mimarlık Fakültesi, Jeoloji Bölümü, 20 yıl Sempozyumu Bildiri Özleri, 12-16 Mayıs, Konya, Türkiye, ss: 125-127.

Uçar L. 2008. Hanobası-Karapınar (KB Aksaray) alanının stratigrafik incelenmesi. Geosound, 2008: 52-61.

Uygun A. 1981. Tuzgölü havzasının jeolojisi, evaporit oluşumları ve hidrokarbon olanakları. TJK İç Anadolu Sempozyumu, Ankara, Türkiye, ss: 66-71.

Black Sea Journal of Engineering and Science
doi: 10.34248/bsengineering.1588734

Open Access Journal
e-ISSN: 2619 – 8991

Araştırma Makalesi (Research Article)
Cilt 8 - Sayı 2: 285-297 / Mart 2025
(Volume 8 - Issue 2: 285-297 / March 2025)

2023 KAHRAMANMARAŞ DEPREMLERİ SONUCU HASAR GÖREN 11 KATLI BETONARME BİR YAPININ DEPREM PERFORMANSININ DEĞERLENDİRİLMESİ

Enes EKİNCİ[1]*, Alper ÖZMEN[1]

[1] *Inonu University, Faculty of Engineering, Department of Civil Engineering, 44280 Malatya, Türkiye*

Özet: 6 Şubat 2023 tarihinde meydana gelen Kahramanmaraş depremleri ülkemizde bulunan mevcut yapı stokumuzun deprem güvenliği açısından incelenmesi gerektiğini gözler önüne sermiştir. Bu çalışmada 11 katlı betonarme bir yapının 2018 Deprem Yönetmeliğine göre deprem performans analizi aşamaları detayları gösterilmiş ve yapının deprem performansı elde edilmiştir. 2018 Türkiye Bina Deprem Yönetmeliği'nde verilen esaslara uygun olarak gerçekleştirilen performans analizi sonucunda, çalışma kapsamında incelenen yapı her ne kadar kontrollü hasar performans hedefini sağlamış olsa da yapılan saha incelemesinde, yapının bazı taşıyıcı sistem elemanlarında hasarlar gözlemlenmiştir. Bu durum yapı tasarımı aşaması ile proje aplikasyonunun arasında bulunan birtakım uyumsuzluk, hata ve kusurların yapının deprem performansı üzerinde oldukça önemli etkileri olduğunu göstermiştir. Sahada yapılan mevcut durum incelemesi ve performans analizi sonucunda elde edilen bulgular, yapı tasarımı ile ilgili birtakım önerileri de bünyesinde barındıracak şekilde detaylı bir şekilde açıklanmıştır.

Anahtar kelimeler: Beton, Performans analizi, Güçlendirme, TBDY 2018, Deprem

Evaluation of the Earthquake Performance of an 11-Storey Reinforced Concrete Building Damaged After the 2023 Kahramanmaraş Earthquakes

Abstract: The earthquakes that impacted Kahramanmaraş on February 6, 2023, have highlighted the necessity to evaluate the seismic safety of the current building inventory in our nation. This research provides a comprehensive seismic performance analysis of an 11-story reinforced concrete edifice executed in compliance with the 2018 Turkish Seismic Code. During field inspections, it was observed that specific structural elements of the building sustained damage following the 2023 Kahramanmaraş earthquakes, despite the fact that the controlled damage performance target was achieved, as indicated by the performance analysis, which was conducted in accordance with the 2018 Turkish Building Seismic Code. The situation demonstrated that certain discrepancies, errors, and defects between the structural design phase and project application have a significant impact on the earthquake performance of the structure. The results from the field research and performance analysis offer comprehensive insights and propose recommendations for enhanced design practices in next building projects.

Keywords: Concrete, Performance analysis, Retrofitting, TBDY 2018, Earthquake

***Sorumlu yazar (Corresponding author):** Inonu University, Faculty of Engineering, Department of Civil Engineering, 44280 Malatya, Türkiye
E mail: enes.ekinci@inonu.edu.tr (E. EKİNCİ)
Enes EKİNCİ https://orcid.org/0000-0001-7669-887X
Alper ÖZMEN https://orcid.org/0000-0003-1335-3780

Gönderi: 20 Kasım 2024 **Received:** November 20, 2024
Kabul: 24 Aralık 2024 **Accepted:** December 24, 2024
Yayınlanma: 15 Mart 2025 **Published:** March 15, 2025

Cite as: Ekinci E, Özmen A. 2025. Evaluation of the earthquake performance of an 11-storey reinforced concrete building damaged after the 2023 Kahramanmaraş earthquakes. BSJ Eng Sci, 8(2): 285-297.

1. Giriş

Türkiye, dünya üzerindeki en aktif deprem kuşaklarından biri olan Akdeniz-Alp-Himalaya deprem kuşağında yer almakta olup, bu durum ülkenin her bölgesinde ciddi bir sismik tehlike oluşturmaktadır. Özellikle Kuzey Anadolu ve Doğu Anadolu fay hatlarının etkisinde bulunan ülkemiz, bugüne kadar birçok yıkıcı depreme sahne olmuş ve bu durum yapı güvenliğini sürekli olarak gündemde tutmuştur. Nitekim Doğu Anadolu Fayı üzerinde meydana gelen 6 Şubat 2023 tarihli iki büyük deprem (Mw 7.6 Pazarcık ve Mw 7.7 Elbistan), mevcut yapı stoğumuzun önemli bir kısmının depreme karşı yetersiz olduğunu acı bir şekilde ortaya koymuştur. Bu bağlamda, mevcut binaların deprem performanslarının değerlendirilmesi ve dayanıklılığı düşük olanların uygun yöntemlerle güçlendirilmesi, can ve mal güvenliğini sağlamak adına büyük önem arz etmektedir (Küçükaslan ve Altan, 2021). 6 Şubat tarihinde meydana gelen Kahramanmaraş depremlerinin ardından, Hatay ilinde yapılan saha araştırmaları sonrasında binaların ağır hasar almasına ve çökmesine neden olan birçok farklı problem tespit edilmiştir. Bu problemlerin en belirgin olanları ise; yetersiz kesme donatısı kullanımı, beton kalitesinin düşük olması, güçlü kiriş-zayıf kolon etkisi, kısa kolon oluşumu, yumuşak kat ve burulma etkileri olarak sıralanmıştır (Altunsu vd., 2024). Meydana gelen bu büyük depremler sonrasında yapılan bir başka araştırmada ise, araştırmacılar endüstriyel yapıların hasar durumlarını incelemiştir. Çalışmada incelenen endüstriyel yapılar; sıvı depolama tankları, silolar,

This work is licensed (CC BY-NC 4.0) under Creative Commons Attribution 4.0 International License

prefabrik betonarme yapılar ve az katlı çelik konstrüksiyon taşıyıı sisteme sahip farklı endüstriyel yapılar olarak belirlenmiştir. Çalışmadan elde edilen sonuçlar; sıvı depolama tanklarında duvar burkulması, petrol depolama tesisinde ankraj yetersizliğinden dolayı devrilme, silolarda iç basınç nedeniyle oluşan ürün deşarjlarının yaşanması ve kolon-kiriş elemanları arasındaki yetersiz bağlantılar şeklinde çok çeşitli hasar nedenlerinin gözlendiğini ortaya çıkarmıştır (Öztürk vd., 2024). Depremin yıkıcı etkilerinin incelendiği bir başka çalışmada ise Kahramanmaraş depremlerinin neden olduğu yapısal hasarlar; zemin ve taşıyıcı sistem ilişkisi açısından değerlendirilmiştir. Çalışma sonuçları yapı-zemin etkileşiminin yapıların deprem performansları üzerinde en önemli etken olduğu ve özellikle zayıf zeminlerde inşa edilecek yapılarda hasarların oldukça ağır bir şekilde gözlendiğini ortaya koymuştur. Araştırmacılar, ayrıca, depremler sonucunda elde edilen saha gözlemlerinin mevcut deprem yönetmeliğinde bulunan bazı hususlarının tekrar ele alınmasını gerekli kıldığını belirtmişlerdir (Avcil vd., 2024).

Nemutlu vd. (2023) tarafından Kahramanmaraş depremlerinin araştırıldığı bir başka çalışma ise deprem nedeniyle meydana gelen kayıpların önceden tahmin edilebilmesini mümkün kılan kayıp değerlendirilmesi metodolojisini kullanmayı amaçlamıştır. Çalışmadan elde edilen bulgular; can kayıpları tahminlerinde kullanılan modifiye edilen katsayılar ile gerçek sonuçların benzerlik gösterdiğini ortaya çıkarmıştır. Ayrıca, oldukça büyük yıkım oranına sahip şehirlerde ağır hasarlı veya yıkılmış bina sayılarının tam olarak örtüşmemesine rağmen, kayıp tahmin aşamalarının uygulanması halinde benzer sonuçların elde edilebildiği belirlenmiştir.

6 Şubat Kahramanmaraş depremleri sonrasında gerçekleştirilen saha araştırmalarına benzer olarak, çok yakın bir tarihte (2020) yaşanan Sivrice depreminin yapılar üzerindeki etkilerini inceleyen bir çalışmaya da rastlanılmıştır. Bu çalışma sonucunda elde edilen bulgular 2020 yılında meydana gelen 6.8 büyüklüğündeki Sivrice depremi sonrasında binaların hasar almalarının başlıca nedenlerinin; gevrek davranış sergileyen elemanlar, düşük beton kalitesi, kısa kolonlar, güçlü kiriş-zayıf kolon oluşumları ve büyük açıklıklı ağır konsol durumları ve donatı detaylarındaki eksiklikler olduğu belirtilmiştir (Nemutlu vd., 2021). Bu sonuçlar; depremin büyüklüğü ve merkez üssü gibi değişkenlerden bağımsız olarak, yapılarda gözlenen deprem hasarlarının oluşum nedenlerinin oldukça benzer olduğunu ve deprem dirençli şehirlere ulaşma hedefinin ancak bilimsel temellere dayalı yapı stoğunun yenilenmesi ile mümkün olabileceğini göstermiştir.

Türkiye'de depreme dayanıklı yapı tasarımı konusunda ilk yönetmelik düzenlemeleri 1940'lı yıllarda yapılmış olup, bilimsel ve teknolojik gelişmeler doğrultusunda zaman içinde revize edilmiştir. Bu bağlamda, ülkemizdeki mevcut ve yeni inşa edilecek binaların deprem güvenliğini sağlamak amacıyla 2007 yılında yürürlüğe giren Deprem Bölgelerinde Yapılacak Binalar Hakkında Yönetmelik DBYBHY-2007, 2018 yılında güncellenerek Türkiye Bina Deprem Yönetmeliği adıyla son haliyle yürürlüğe konulmuştur. Bu yeni yönetmelik gerek mevcut yapıların performans analizinde gerekse yeni tasarımlarda daha kapsamlı ve detaylı bir analiz yaklaşımı sunmaktadır (Kap vd., 2019a). Özellikle mevcut binaların deprem performansının belirlenmesi konusunda performans seviyelerini tanımlayan kriterler, doğrusal ve doğrusal olmayan analiz yöntemleri ile net bir çerçeve oluşturulmuştur (Özmen ve Sayın, 2021). 2007 ve 2018 deprem yönetmeliklerine göre deprem performans analizlerini karşılaştırmalı olarak ele alan güncel literatürde çeşitli çalışmalar bulunmaktadır.

Yalın ve Ulutaş (2021) DBYBHY-2007 ile TBDY-2018 esas alınarak mevcut bir okul binasının deprem performansını karşılaştırmalı olarak incelenmiştir. Sonuçta, 50 yılda %2 aşılma olasılığı olan depremler için yönetmelikler arasında uyumsuzluk olduğunu çıkarımında bulunmuşlardır. Küçükaslan ve ve Altan, 2021 tarafından yapılan bir çalışmada, 2007 Türk Deprem Yönetmeliği (TDY) ve 2018 Türk Bina Deprem Yönetmeliği (TBDY) kullanılarak İstanbul'daki 9 katlı betonarme bir yapının güçlendirme öncesi ve sonrasındaki sismik performansını analiz etmiştir. Çalışma sonucunda elde edilen bulgular, 2007 ve 2018 deprem yönetmeliklerinin sismik etkileri tahmin etmede aralarında farklar ortaya çıktığını göstermiştir.

Dalyan ve Şahin (2019) 5 katlı betonarme bir konut binasının taşıyıcı sistemi üzerinde doğrusal olmayan artımsal itme analizi gerçekleştirmiş ve hem DBYBHY (2007) hem de TBDY (2018) yöntemlerinden elde edilen sonuçları karşılaştırarak incelemiştir. Sarı, 2020 mevcut bir konut yapısının sismik performansını TBDY (2018) ve DBYBHY (2007) normlarına uygun olarak statik pushover analizi ile değerlendirmiştir. İncelenen konut binasının her iki kural uyarınca belirtilen performans standartlarına uygun olduğu sonucuna varmıştır. Ayrıca, Nemutlu 2019, TBDY (2018) ve DBYBHY (2007) kanunlarını Amerikan sismik kodu (ASCE 7-16) ile karşılaştırmalı olarak deprem hesaplamaları açısından analiz etmiştir. Coşkun vd., 2023 yaptıkları çalışmada, Karabük ilinde 2002 yılında inşa edilmiş betonarme bir okul binasını değerlendirmekte ve eski deprem kuralları altında güçlendirme ihtiyacını ortaya koymaktadır. Güçlendirme kararı verilirken bina yaşı, inşaat maliyet oranı ve birleşik maliyetler gibi faktörlerin de göz önünde bulundurulması gerektiğini önermişlerdir. Bu çalışmaların yanı sıra, mevcut yapıların 2018 Deprem Yönetmeliği esasları dikkate alınarak deprem performansının analiz edildiği yapıldığı çalışmalar da mevcuttur (Yüzbaşı ve Yerli, 2018; Severcan ve Sınanı, 2019; Kap vd., 2019b; Foroughi ve Yüksel, 2022; Işık ve Tuncer, 2023).

Bu çalışmada, 6 Şubat 2023 tarihinde gerçekleşen Kahramanmaraş depremlerinde hasar gören 11 katlı bir betonarme yapının, 2018 Deprem Yönetmeliği hükümlerine uygun olarak deprem performansı analiz edilmiştir. Çalışmanın temel amacı, yapının mevcut

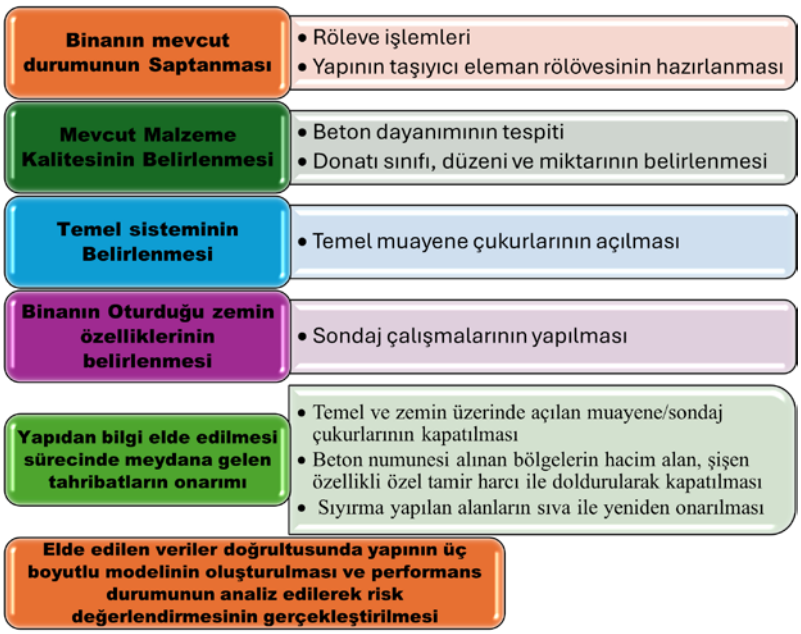
durumunu değerlendirerek sahada gözlemlenen hasarların nedenlerini ortaya koymak ve deprem performansını belirlemektir. Ayrıca, analizler sonucunda elde edilen veriler ışığında, yapı tasarım ve uygulama süreçlerinde yapılan hataların etkisi üzerinde durulmuş; gelecekte benzer yapıların depreme karşı güvenli hale getirilmesi için öneriler geliştirilmiştir. Bu çalışmayı benzerlerinden ayıran temel özellik, 2023 Kahramanmaraş depremleri sonrasında hasar görmüş mevcut bir yapının deprem performansının incelenmesine odaklanmasıdır. Mevcut hasarlı bir yapının deprem performansını, 2018 Deprem Yönetmeliği çerçevesinde değerlendiren bu çalışma, deprem sonrası gözlemlenen hasarların performans analizleri ile uyumunu ortaya koymayı amaçlamıştır.

2. Materyal ve Yöntem

Bu çalışmada, incelenen binanın deprem dayanıklılığı, Türkiye Bina Deprem Yönetmeliği 2018 (TBDY 2018) kapsamında yer alan 'Deprem Etkisi Altında Mevcut Bina Sistemlerinin Değerlendirilmesi ve Güçlendirme Tasarımı İçin Özel Kurallar' başlıklı bölümde tanımlanan Doğrusal mayan Hesap Yöntemleri doğrultusunda Deprem Hesabı'na uygun şekilde analiz edilmiştir.

Şekil 1'de özetlenen adımlara bağlı kalınarak gerçekleştirilmiştir. Bina Malatya ili Yeşilyurt ilçesi sınırlarında bulunmaktadır. Bina, bodrum, zemin ve 9 normal kat olmak üzere toplam 11 kattan oluşmaktadır. Kirişli plak döşemeli betonarme taşıyıcı sistem tarzında inşa edilen binada kat yükseklikleri bodrum katta 3 m, zemin katta 4.5 m ve normal katlarda ise 3 m'dir. Öncelikle yapının statik projesi incelenmiş ve sahada röleve çalışmaları yapılmıştır. Daha sonra, yapının deprem performansının belirlenmesinde kullanılacak önemli bilgilerin elde edilmesi için saha çalışmaları yapılmıştır. Bina ile ilgili bilgiler ve analiz parametreleri Tablo 1' de sunulmuştur.

Her bir bina tipi için bilgi seviyesi ve TBDY 2018 bölüm 15.2.12'de belirtilen bilgi seviyesi katsayıları, binaların denetiminden elde edilecek temel bilgilerin kapsamına göre belirlenecektir. Bilgi seviyeleri buna göre kapsamlı ve sınırlı olarak sınıflandırılacaktır. Yapı elemanı kapasiteleri, elde edilen bilgi seviyeleri kullanılarak hesaplanacaktır. Taşıyıcı sistem özellikleri, sınırlı bilgi düzeyinde bina üzerinde alınması gereken ölçümlerle belirlenir. Kapsamlı bilgi seviyesinde sınırlı bilgi seviyesine göre daha fazla sayıda ölçüm yapılır. Bu çalışma kapsamında incelenen yapı Kapsamlı Bilgi Düzeyi dikkate alınarak incelenmiştir. Bu bölümde anlatılan işle mler kapsamlı bilgi düzeyine göre gerçekleştirilmiştir.

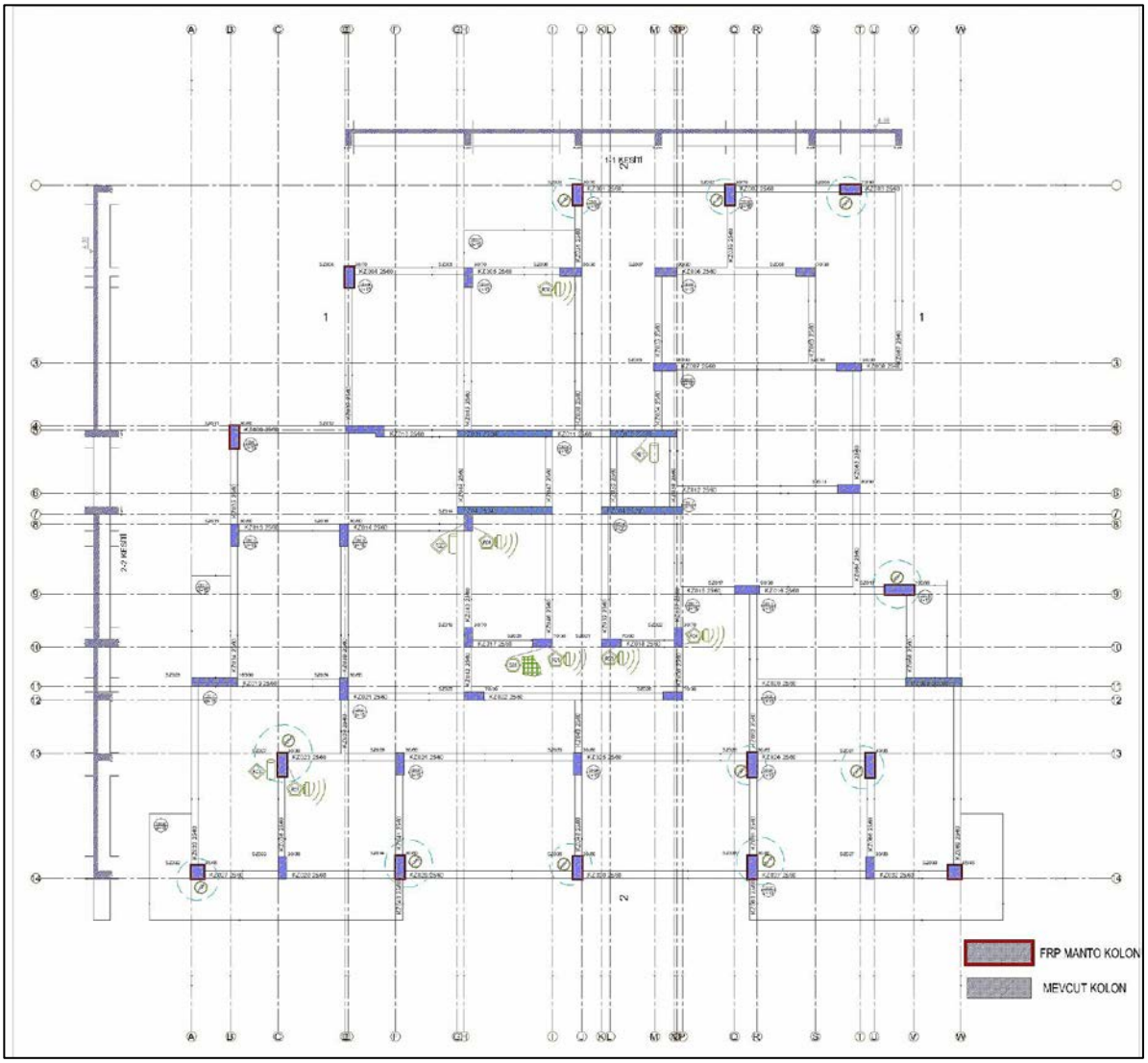


Şekil 1. TBDY 2018' e göre deprem performans analizi işlem adımları.

Binanın taşıyıcı sistem planını elde etmek amacıyla gerçekleştirilen saha çalışması kapsamında, yapısal elemanların mevcut durumu detaylı olarak incelenmiş ve taşıyıcı sistem elemanlarının boyutları, malzeme özellikleri ve bağlantı detayları tespit edilmiştir. Bu veriler, bina modelinin oluşturulmasında temel referans olarak kullanılmıştır. Elde edilen bilgiler bir bina hesaplama modeli oluşturmak için yeterli olmalı ve her kat için, tüm betonarme elemanlar ve bölme duvarların konumu, malzemesi, eksen açıklıkları, yükseklikleri ve boyutlarını içermelidir. Kat planlarında varsa kısa kolon ve hasarlı elemanlar belirtilmiştir. Binanın komşuları ile ilişkisi (ayrık, bitişik, bağlantılı/bağlantısız) belirtilmiştir. Saha çalışmalarında elde edilen örnek pafta Şekil 2'de gösterilmiştir. Bu pafta üzerinde karot alınan, sıyırma yapılan, donatı tarama yapılan ve hasarlı olan elemanlar işaretlenmiştir. Ayrıca mevcut aplikasyondan farklı olan elemanların mevcut olması halinde yine bu pafta üzerinde gösterilecektir.

Tablo 1. İncelenen yapı ile ilgili bilgiler

Binanın Adresi	Yeşilyurt, Malatya
Kat Adedi	11 (B+Z+N)
Kat Yükseklikleri	B – Z – N: 3.0m – 4.5m –3m
Binanın Toplam Yüksekliğ	31.50 m
Toplam Yapı Alanı	4675 m2
Bina Türü	Perdeli Çerçeveli Betonarme Sistem
Beton Sınıfı	C25/30
Donatı Sınıfı	S420
Tasarım Spektral İvme Katsayısı (Sds/Sd1) (DD2)	0.725 / 0.178
Tasarım Spektral İvme Katsayısı (Ss/S1)) (DD2)	0.805 / 0.223
Yerel Zemin Sınıfı	ZB
Yapı Önem Katsayısı (I)	1
Zemin Taşıma Kapasitesi	63.7 t/m2
Düşey Yatak Katsayısı	3260 t/m3
Analiz Türü	Non-Lineer Çok Modlu İtme Analizi
Kullanılan Yönetmelik Ve Standart	TBDY 2018, TS 498
Kullanılan Yazılım	İDECAD STATİK 10



Şekil 2. Saha çalışmalarından elde edilen örnek kroki.

2.1. Malzeme Özelliklerinin Belirlenmesi

2.1.1. Beton dayanımının elde edilmesi

TBDY 2018' Bölüm 15.2.5.3'de beliritlen esaslara uyularak yapı üzerinde farklı taşıyıcı elemanlardan karot örnekleri alınmıştır. Numuneler TS EN 12504-1'de belirtilen şartlara uygun olarak kolonlardan veya perdelerden alınmıştır. Mevcut betonun dayanımı; çapı ve uzunluğu 100 mm olan karotların test edilmesinden elde edilen dayanım değerleri kullanılarak herhangi bir katsayı uygulanmadan elde edilebilir. Farklı uzunluk/çap oranlarına sahip karot örneklerinden bulunan test sonuçlarının dönüştürülmesi uygun dönüştürme faktörleri kullanılarak yapılmalıdır. Elemanların kapasitesini belirlemek için, mevcut beton dayanımı (ortalamanın 0,85 katı) ve (ortalama eksi standart sapma) değerlerinde numunelerden elde edilen değerlerden büyük olanı ile belirlenecektir.

En küçük değrin istatistiksel olarak sapkın bir sonuç olup olmadığını belirlemek için, bir grup beton numunesinin test sonuçları arasında kalan sonuçların ortalaması ile en küçük değer arasındaki fark değerlendirilmelidir. Bu nedenle, değerlendirme sırasında en düşük tek değerin kalan sonuçların ortalamasının %75'inden az olması durumunda gruptaki numune sonuçları dikkate alınmaz.

Bu bilgiler dikkate alınarak, İnönü Üniversitesi Mühendislik Fakültesi İnşaat Mühendisliği Bölümü'nün imkânlarıyla söz konusu yapıdan zemin kattan 3 adet, diğer katlardan ise 2'şer adet olmak üzere toplan 23 adet karot örneği alınmıştır. Alınan karot örneklerinin sonuçları Tablo 2'de verilmiştir.

Tablo 2. Yapıdan alınan karot numunelerine ait sonuçlar

Kat No	Karot No	Silindir Ebadı		Boy / Çap	Kırılma Yükü (N)	Basınç Dayanımı (MPa)
		Çap (mm)	Yükseklik (mm)			
K-B-1	1	100	100	1	256200	32,6
K-B-2	2	100	100	1	212700	27,1
K-Z-1	3	100	100	1	200300	25,5
K-Z-2	4	100	100	1	306900	39,1
K-Z-3	5	100	100	1	247500	31,5
K-1-1	6	100	100	1	319100	40,6
K-1-2	7	100	100	1	206000	26,2
K-2-1	8	100	100	1	184600	23,5
K-2-2	9	100	100	1	172400	22,0
K-3-1	10	100	100	1	297900	37,9
K-3-2	11	100	100	1	304700	38,8
K-4-1	12	100	100	1	258600	32,9
K-4-2	13	100	100	1	301800	38,4
K-5-1	14	100	100	1	305300	38,9
K-5-2	15	100	100	1	325000	41,4
K-6-1	16	100	100	1	216900	27,6
K-6-2	17	100	100	1	307600	39,2
K-7-1	18	100	100	1	246400	31,4
K-7-2	19	100	100	1	313700	39,9
K-8-1	20	100	100	1	273900	34,9
K-8-2	21	100	100	1	253600	32,3
K-9-1	22	100	100	1	247000	31,4
K-9-2	23	100	100	1	292100	37,2
Ortalama Basınç Dayanımı		33,5				
Standart Sapma		5,94				

Ortalama basınç dayanımı: $\frac{(32,6+27,1+25,5+\cdots+37.2)}{23}$ = 33,5 MPa olarak elde edilmiştir.

Standart Sapma değeri ise:
$\sqrt{\frac{(32.6-33,5)2+(27,1-33,5)2+(25.5-33,5)2+\cdots(37.2-33.5)2}{(23-1)}}$
= 5,94 olarak elde edilmiştir.

TBDY 2018'de yer alan "Bir grup beton örneğine ait deney sonuçları arasında en küçük değer ile geriye kalan sonuçların ortalaması arasındaki farkın değerlendirilmesi ile en küçük değerin istatistiki olarak sapan bir sonuç olup olmadığı kontrol edilecektir. Bu amaçla, gruptaki numune sonuçlarının değerlendirilmesinde, en düşük tek değer, geriye kalan diğer sonuçların ortalamasının %75'inden daha düşük ise bu numune değerlendirmeye alınmaz" ibaresi uyarınca en küçük basınç dayanımı değeri olan 22 MPa'ın değerlendirmeye alınıp alınmayacağı kontrol edilmiştir. En küçük dayanım hariç diğer 22 adet karot örneğinin ortalama basınç dayanımı = 34 MPa. 22 ≤ 0,75*34 = 25,5 MPa sağlandığından en küçük basınç dayanımı değeri değerlendirmeye alınmamıştır. Sonuç olarak ortalama basınç dayanımı değeri 34 MPa olarak elde edilmiştir. Yine TBDY 2018'de yer alan "Elemanların kapasitelerinin hesaplanmasında, örneklerden elde edilen (ortalama - standart sapma) değeri ile (0,85 × ortalama) değeri arasından yüksek olan değer, mevcut beton dayanımı olarak kabul edilecektir." ibaresi uyarınca performans analizinde dikkate alınacak beton dayanım sınıfı belirlenmiştir.

Basınç dayanımı	0,85 x ort. basınç dayanımı Ort. Basınç dayanımı standart sapma	değerlerinden büyük olanı olarak seçilecektir.

Basınç dayanımı	0,85 x 34 = 28,9 MPa ✓ 34– 5,94 = 28,06 MPa	değerlerinden 28,9 MPa olarak seçilmiştir.

Beton basınç dayanımı 29 MPa olarak elde edilmiştir. Karot alımına örnek görseller, Şekil 3' te verilmiştir. TS EN 12504-1 madde 7.2'de belirtildiği üzere, karot alınan numunelerin boy/çap oranı 1 olması halinde küp basınç dayanımı olarak dikkate alınması gerektiği belirtilmiştir. Bu nedenle, 100*100 mm boyutlarına sahip olan karot numunelerinin basınç dayanımı değeri C25/30 olarak belirlenmiştir. Yapı üzerinde karot alınması işlemlerine ilişkin örnekler Şekil 3'te verilmiştir.

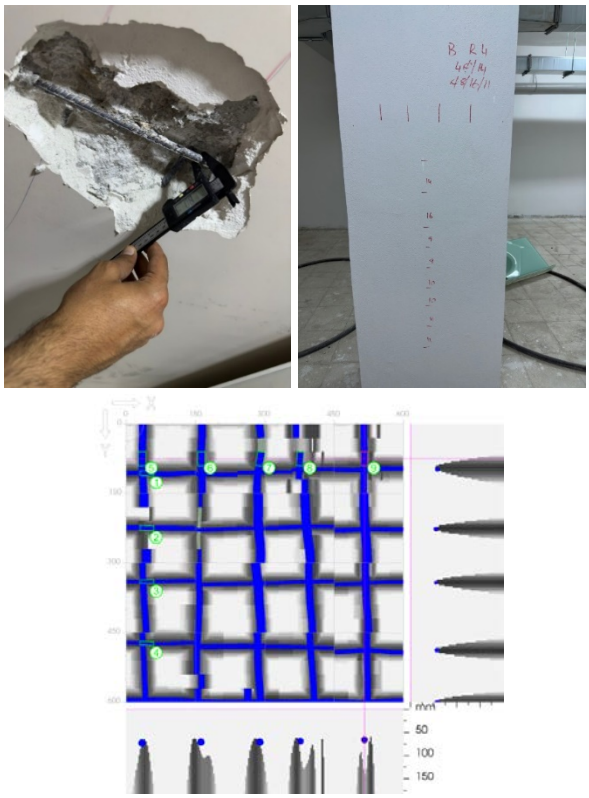


Şekil 3. Örnek karot alma işlemi.

2.1.2. Donatı detaylarının belirlenmesi

Binanın betonarme detay projelerine ulaşılabilmesi koşuluyla, donatının projesine uygun olduğunu doğrulamak için aynı miktarda betonarme eleman üzerinde TBDY 2018 Bölüm 15.2.4.2'de belirtilen işlemler uygulanacaktır. Ayrıca, beton örtüsü kaldırılmamış durumdaki perdelerin ve kolonların %20'sinde, çerçeve kirişlerin ise %10'unda enine ve boyuna donatıların miktarı ve konumları, donatı tespit cihazları yardımıyla detaylı bir şekilde belirlenecektir. Bu işlem, yapının taşıyıcı elemanlarına dair doğru ve kapsamlı bilgi sağlamak amacıyla gerçekleştirilmiştir Proje ile uygulama arasında herhangi bir uyumsuzluk tespit edilmesi durumunda, perdeler, kolonlar ve kirişler için ayrı ayrı olmak üzere donatı gerçekleşme katsayısı hesaplanacaktır. Bu hesaplamalar, mevcut durumun projedeki tasarım değerleriyle olan farklılıklarını niceliksel olarak ortaya koymak amacıyla yapılacaktır. Bu katsayı, betonarme elemanlardaki mevcut donatının projede öngörülen donatı miktarına oranını ifade etmektedir. Donatısı tespit edilmeyen elemanlara bu katsayı diğer tüm uygulanarak potansiyel donatı miktarları elde edilecektir. Betonarme projelerin ya da inşaat uygulama çizimlerinin bulunmadığı durumlarda, her katta en az iki adet olacak şekilde, kolon ve perdelerin %10'unda beton örtüsü sıyrılarak donatı tespiti yapılacaktır. Bu işlem, mevcut donatı düzeni ve miktarının doğru bir şekilde belirlenmesi amacıyla gerçekleştirilecektir. Sökülen yüzeyler yüksek mukavemetli tamir harcı ile kaplanacaktır. Ayrıca, beton örtüsü kaldırılmayan kolon ve perdelerin %30'unda ve kirişlerin %15'inde enine ve boyuna donatı miktarını ve yerini tespit etmek için donatı tespit cihazları kullanılacaktır. Bu işlem adımları dikkate alınarak yapının donatı durumunu tespit etmek amacıyla aşağıda detayları verilen işlemler gerçekleştirilmiştir.

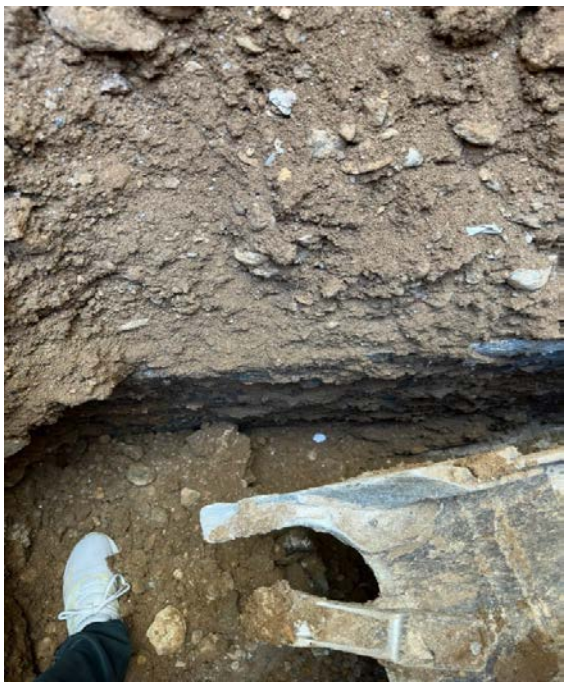
Yapının taşıyıcı sistem elemanları üzerinde donatı adet ve yerleşim detaylarının belirlenmesi amacıyla donatı taramaları ve pas payı sıyırma işlemleri gerçekleştirilmiştir. Taşıyıcı elemanların donatı yerleşimleri ve çapları, yüzey durumları, etriye kanca açıları ve elemanların net beton örtüleri gibi parametrelerin belirlenmiştir. Pas payı sıyırma işlemleri ile donatı sınıfı S420 olarak tespit edilmiştir. Donatı tespit çalışması yapılan elemanlarda boyuna donatı oranının yönetmelikte belirtilen %1 minimum donatı oranına karşılık geldiği tespit edilmiştir. Donatı tarama işlemleri ve pas payı sıyırma işlemlerine ait görseller Şekil 4'te verilmiştir. Donatı tarama işlemleri neticesinde boyuna donatı sayıları, etriye aralıkları gibi detaylar pafta üzerinde işlenmiş ve bu detaylar yapının modellenmesinde dikkate alınmıştır.



Şekil 4. Pas payı sıyırma ve donatı tarama işlemlerine ait görseller.

2.2. Temel Sisteminin Belirlenmesi

Yapı temelinin belirlenmesi amacıyla temel gözlem çukuru açılmış ve yapıda 85 cm kalınlığında bir radye temel bulunduğu tespit edilmiştir. Yapılan gözlem çukuru incelemesi sonucu yapının temelinin projeye uygun olduğu belirlenmiştir. Gözlem çukuruna ait fotoğraflar Şekil 5' de verilmiştir.



Şekil 5. Temel gözlem çukuru açılması.

2.3. Zemin Özelliklerinin Belirlenmesi

Özel bir firma tarafından yapının oturduğu zemin özelliklerinin belirlenmesi amacıyla zemin etüdü yaptırılmış ve zemine ait özellikler Tablo 3'de verilmiştir. Zemin etüt sonuçlarına göre yapının oturduğu zemin ZB sınıfı olarak tespit edilmiştir.

Tablo 3. Zemin etüt raporundan elde edilen parametreler

Koordinat	38.3379°- 38.2592°
Yeraltı Su Seviyesi (m)	Yok
Yerel Zemin Sınıfı	ZB
Deprem Yer Hareket Düzeyi	DD-2
Spektral İvme Katsayısı	Ss=0.805 S1=0.223 Sds=0.725 Sd1=0.178
En Büyük Yer İvmesi (g) ve hızı (cm/sn)	PGA=0.336 PGV=20.909
Yapı Önem Katsayısı (I)	1
Deprem Tasarım Sınıfı	DTS=1 DTS=2 DTS=3
Zemin Taşıma Kapasitesi	63.7 t/m2
Oturma Miktarı (cm)	-
Analiz Türü	Non-Lineer Çok Modlu İtme Analizi
Bina Kullanım Sınıfı	BKS=3
Sıvılaşma Potansiyeli	Sıvılaşma Yoktur
Düşey Yatak Katsayısı	3260 t/m3
Köşe Periyotları (Ta, Tb)(sn)(AFAD)	Ta=0.049 Tb=0.246

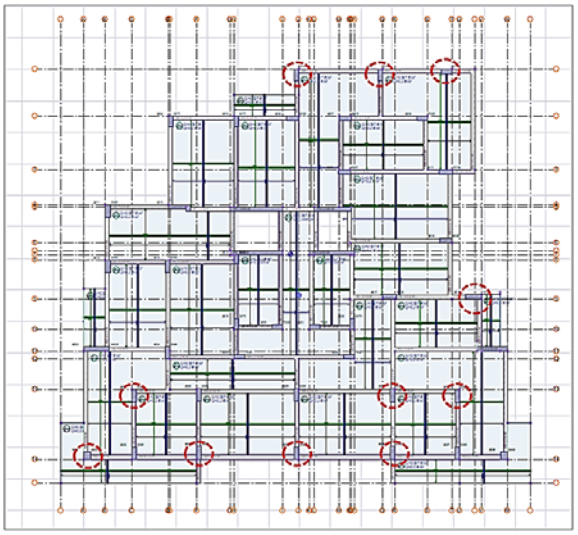
2.4. Bina Genel Durumunun Tespit Edilmesi

Binanın giriş katında birden fazla kolonda kabuk atma şeklinde hasar oluşumları gözlenmiştir. Zemin katta bulunan kolonların alt kısımlarında yeterli vibrasyon uygulaması yapılamaması segregasyon (ayrışma) oluşumuna neden olmuştur. Segregasyon oluşumunun ise deprem kuvveti etkisi altında kabuk atma hasarına zemin hazırladığı belirlenmiştir. Ayrıca, binanın giriş kısmında gözlenen hasarın da boğaz etriyesi kullanılmaması sebebiyle oluştuğu belirlenmiştir. Zemin kat kolonlarında gözlenen kabuk atma hasarları Şekil 6'da verilmiştir. Yapının statik projesi incelendiğinde, yapının y yönünde deprem perdeleriyle donatılmamış olduğu ve yapının bu yönde perde rijitliğinin yeterli düzeyde olmadığı tespit edilmiştir. Mevcut hasarların daha çok y yönünde ortaya çıkmasındaki en önemli faktörün ise bu durum olduğu düşünülmüştür. Ayrıca kabuk atma şeklinde hasar alan elemanlarda korozyon oluşumu gözlemlenmiştir. Bu durumun ortaya çıkmasına ise pas payı mesafesinin yetersiz olmasının sebep olduğu belirlenmiştir. İlgili binanın bazı kirişlerinde sıva çatlakları gözlenmiş olsa da önemli sayılabilicek bir kiriş hasarına rastlanmamıştır.



Şekil 6. Bina genel durumu ve gözlenen hasarlardan bazıları.

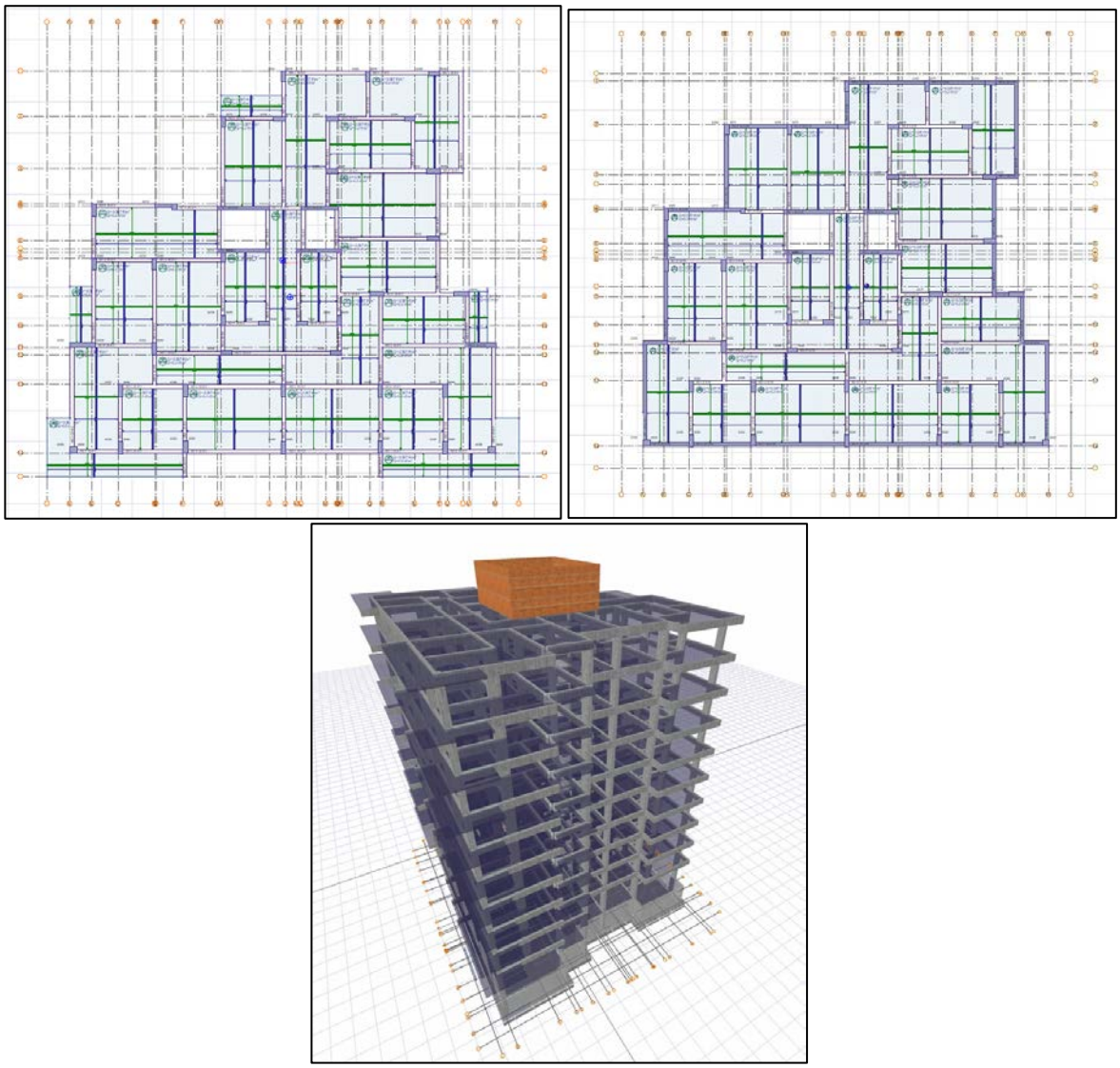
Taşıyıcı sistem elemanlarının boyut, adet ve mesafe kontrollerini içeren röleve incelemeleri yapılmıştır. Röleve çalışmaları sonrasında yapının kat planı çizilmiş ve zemin katta kabuk atma hasarı gözlenen elemanlar Şekil 7'de verilmiştir.



Şekil 7. Hasar alan elemanların proje üzerinde gösterimi.

2.5. Binanın 3D Modelinin Oluşturulması

Yapının üç boyutlu modeli İDECAD STATİK 10 programı kullanılarak oluşturulmuş olup, Şekil 8'de sunulmuştur. Modelleme sürecinde, TS 498'e göre ölü yükler, hareketli yükler ve mimari projeye uygun olarak duvar yükleri modele dâhil edilmiştir. Beton dayanımı, donatı sınıfı ve kesit özellikleri saha çalışmaları neticesinde elde edilen değerlere göre programa girilmiştir. Donatı düzenlemesi yapabilmek amacıyla öncelikle doğrusal analiz yapılmış daha sonra donatı düzenlemesi yapılarak donatı miktarları ve etriye aralıkları donatı tespit işlemi yapılan kolonlara uygulanmıştır. Geriye kalan taşıyıcı elemanlar üzerinde donatı gerçekleşme katsayısı dikkate alınmıştır. Bu projede donatı gerçekleşme katsayısı 1 olarak dikkate alınmıştır. Beton sınıfı C25/30 ve donatı sınıfı S420 olarak girilmiştir.



Şekil 8. Yapının 3D modeli ve kalıp planı.

3. Bulgular ve Tartışma

2018 TBDY'ne göre yapıda hedeflenen performans seviyesi; DD-2 (50 yılda aşılma olasılığı %10 olan deprem) için KH (Kontrollü Hasar) olarak değerlendirilmektedir. Değerlendirme ve tasarım yaklaşımı olarak ise ŞGDT (şekil değiştirmelere göre değerlendirme ve tasarım) yaklaşımı kullanılmaktadır.

3.1. Performans Hesabında Kullanılacak Analiz Yöntemleri

Yapının deprem performansı TBDY 2018'de verilen doğrusal veya doğrusal olmayan hesap yöntemleri kullanılarak bulunabilir. Düşey yüklerin ve depremlerin birleşik etkileri sonucunda yapı elemanlarında oluşacak iç kuvvetlerin, yer değiştirmelerin ve deformasyonların doğru bir şekilde hesaplanabilmesi için binanın taşıyıcı sistem modelinin yüksek hassasiyetle oluşturulması gerekmektedir. Binadan toplanan verilerin kapsamına bağlı olarak, mevcut binaların yapısal sistemlerindeki belirsizlikleri hesaplama yöntemlerine yansıtmak için TBDY 2018 Bölüm 15,2'de tanımlanan bilgi seviyesi katsayıları kullanılmıştır. İlgili yapıda bilgi düzeyi katsayısı 1 olarak dikkate alınmıştır. Eğilme etkisindeki betonarme elemanlar için çatlamış kesite ait etkin kesit rijitlikleri kullanılmıştır, bu rijitlikler TBDY 2018'in 4.5.8. Bölümüne göre hesaplanmıştır. Doğrusal olmayan hesaplama yöntemleri, mevcut veya güçlendirilmiş binaların deprem etkileri altındaki yapısal performansını belirlemek ve güçlendirme hesaplamaları için tasarlanmıştır. Bu yöntemlerin amacı, sünek davranış için plastik şekil değiştirme ve plastik dönme taleplerini ve belirli bir deprem için gevrek davranış için iç kuvvet taleplerini hesaplamaktır. Daha sonra, kesit ve bina seviyelerindeki yapısal performans, talep büyüklükleri ile deplasman ve iç kuvvet kapasiteleri değerlendirilir. TBDY 2018'e göre mevcut veya güçlendirilmiş binaların deprem performansını değerlendirmek amacıyla çeşitli doğrusal olmayan hesap yöntemleri kullanılmaktadır. Bu yöntemler arasında yer alan Tek Modlu İtme Yöntemleri, genellikle basit sistemlerin analizinde tercih edilirken, Çok Modlu İtme Yöntemleri, daha karmaşık yapılar için daha ayrıntılı sonuçlar sunar. Zaman Tanım Alanında Doğrusal Olmayan Hesap Yöntemi ise, yapının deprem anındaki dinamik tepkisini doğrudan zaman fonksiyonu

içinde inceleyerek daha hassas sonuçlar elde edilmesini sağlar.

Konut projeleri için Bina Kullanım Sınıfı (BKS) 3 olarak, bina önem katsayısı ise I=1 olarak kabul edilmiştir. DD-2 deprem düzeyine göre kısa periyot tasarım spektral ivme katsayısı (S_{DS}), AFAD İnteraktif Web Uygulaması kullanılarak yapının konum bilgileri üzerinden hesaplanmış ve 0.805 olarak belirlenmiştir. Bu parametreler, deprem yüklerinin hesaplanmasında kullanılan temel değerleri oluşturur ve yapı güvenliğinin sağlanması açısından önemli rol oynar. Yapıya ilişkin dikkate alınacak diğer temel bilgiler ise Tablo 4'te detaylandırılmıştır. Bu bilgiler, yapının deprem performans analizinde doğru bir modelleme ve hesaplama yapılmasını desteklemektedir.

Tablo 4. Deprem hesabında dikkate alınacak bazı bilgiler

Yerel Zemin Sınıfı	ZB
Deprem Yer Hareketi Düzeyi	DD2
S_s	0.805
S_1	0.223
PGA	0.336
S_{DS}	0.725

Bu çalışma kapsamında incelenen yapının deprem performansının elde edilmesinde, bina yükseklik sınıfı (BYS) 5'den küçük (BYS = 4) olduğundan doğrusal olmayan hesap yöntemlerinden doğrusal olmayan çok modlu itme analizi uygulanmıştır.

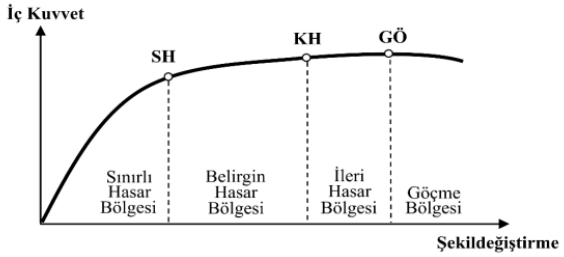
3.2. Yapının Deprem Performansının Değerlendirilmesi

Deprem Tasarım Sınıfları (DTS) 1, 2, 3, 3a, 4 ve 4a için DD-3 deprem yer hareketi düzeyinde normal bir performans hedefi bulunmamaktadır. Ancak ileri performans hedefi olarak Sınırlı Hasar (SH) hedefi belirlenmiş olup, bu durumda Şartlı Güvenlik Dayanıklılık Tasarımı (ŞGDT) yaklaşımı uygulanacaktır. Aynı DTS sınıfları için DD-2 seviyesinde, normal performans hedefi Kontrollü Hasar (KH) olarak belirlenmiş ve ŞGDT değerlendirme/tasarım yaklaşımı kullanılmaktadır; ileri performans hedefi ise bulunmamaktadır. DD-1 deprem yer hareketi düzeyinde ise normal performans hedefi tanımlanmamış olup, ileri performans hedefi olarak Kontrollü Hasar (KH) seçilmiş ve yine ŞGDT yaklaşımı uygulanmaktadır. DTS sınıfları 1a ve 2a için DD-3 seviyesinde normal bir performans hedefi bulunmazken, ileri performans hedefi olarak Sınırlı Hasar (SH) hedefi belirlenmiş ve ŞGDT değerlendirme/tasarım yaklaşımı öngörülmüştür. DD-2 düzeyinde hem normal hem de ileri performans hedefi tanımlanmamışken, DD-1 seviyesinde normal performans hedefi bulunmamakta, ancak ileri performans hedefi olarak Kontrollü Hasar (KH) belirlenmiş ve ŞGDT yaklaşımı uygulanmaktadır. Bu tablo, farklı deprem seviyeleri ve yapı tasarım sınıflarına göre gerekli performans hedeflerini ve uygulanacak analiz yöntemlerini göstermektedir.

Bina performans seviyeleri, sismik aktiviteden kaynaklanan yapısal bileşenlere verilen farklı hasar derecelerini ifade eder. Kesintisiz Kullanım (KK) Performans Seviyesi, yapısal elemanların hiç hasar görmediği veya minimum hasar gördüğü bir durumu tanımlar. Sınırlı Hasar (SH) Performans Seviyesi, yapısal sistemin doğrusal olmayan davranışının kısıtlandığı ve minimum hasarla sonuçlandığı bir durumu ifade eder. Kontrollü Hasar (KH) Performans Seviyesi, hasarın ağırlıklı olarak onarılabilir olduğu ve aşırı derecede şiddetli olmadığı, dolayısıyla can güvenliğinin sağlandığı bir senaryo ile ilgilidir. Göçmenin Önlenmesi (GÖ) Performans Seviyesi, önemli hasarların meydana geldiği, ancak binanın kısmen veya tamamen çökmesinin önlendiği bir senaryoyu tanımlar. Tablo 5'e göre çalışma kapsamında incelenen binanın DD-2 deprem düzeyinde KH performans hedefini sağlaması gerekmektedir.

Kontrollü Hasar Performans Düzeyi'nde kabul edilen binalarda bazı koşullar sağlanmalıdır. Öncelikle gevrek hasar almış elemanların güçlendirilmesi gerekmektedir. Betonarme yapılarda, her bir deprem yönü için yapılan analizlerde, ikincil kirişler hariç olmak üzere, kirişlerin en fazla %35'inin ve düşey elemanların belirli bir kısmının İleri Hasar Bölgesi'ne geçişine izin verilebilir." İkinci olarak, İleri Hasar Bölgesi'ndeki düşey elemanların her katta taşıdıkları kesme kuvveti toplam katkısı %20'nin altında olmalıdır. En üst katta bu oran %40'ı geçmemelidir. Diğer taşıyıcı elemanların ise Sınırlı Hasar veya Belirgin Hasar Bölgesi'nde kalması gerekmektedir; ancak herhangi bir katta, alt ve üst kesitlerinde eşzamanlı olarak Belirgin Hasar Sınırı'nı aşan düşey elemanların, tüm düşey elemanlar tarafından taşınan toplam kesme kuvvetine katkısı %30'u geçmemelidir.

TBDY 2018 Bölüm 15.3, yapı elemanlarının kesit düzeyinde farklı hasar durumları ve bölgelerini tanımlamaktadır. Sünek elemanlar için üç ana hasar durumu ve sınır değerleri belirlenmiştir: Sınırlı Hasar (SH), Kontrollü Hasar (KH) ve Göçme Öncesi Hasar (GÖ) (Şekil 9).



Şekil 9. TBDY 2018'e göre kesit hasar sınırlar.

Sınırlı Hasar, elemanda sınırlı elastik ötesi davranışı tanımlarken, Kontrollü Hasar, elemanın dayanımını güvenli bir şekilde sürdürebileceği bir elastik ötesi davranışı ifade eder. Göçme Öncesi Hasar ise, elemanda ileri düzeyde elastik ötesi deformasyonların oluştuğu durumu tanımlar. Bu sınıflandırma, gevrek hasar almış elemanları kapsamaz. Tanımlara göre, elemanlar kritik kesitlerdeki hasar durumlarına göre farklı hasar

bölgelerine ayrılmaktadır. Kritik kesitleri Sınırlı Hasar (SH) seviyesine ulaşmayan elemanlar Sınırlı Hasar Bölgesi'nde, SH ile Kontrollü Hasar (KH) arasında kalan elemanlar Belirgin Hasar Bölgesi'nde, KH ile Göçme (GÖ) arasında yer alan elemanlar ise İleri Hasar Bölgesi'nde sınıflandırılır. GÖ seviyesini aşan elemanlar ise Göçme Bölgesi'nde değerlendirilir.

Çalışmalar neticesinde elde edilen veriler dikkate alınarak binanın taşıyıcı sistemi İDECAD V10 yazılımında oluşturulmuş ve doğrusal olmayan çok modlu itme analizi gerçekleştirilerek yatay ve düşey taşıyıcı elemanların kesit hasar durumları elde edilmiştir. Düşey taşıyıcı elemanların hasar durumları Şekil 10a' da ve kirişlerin hasar durumları ise Şekil 10b'de sunulmuştur.

KAT	+X +0.3Y				+X-0.3Y				-X +0.3Y				-X-0.3Y			
	SH	BH	İH	GB	SH	BH	İH	GB	SH	BH	İH	GB	SH	BH	İH	GB
10	77.5	22.5	0	0	76.2	23.8	0	0	70.1	29.9	0	0	58.1	41.9	0	0
9	87.5	12.5	0	0	90.33	+9.7	0	0	91.9	8.1	0	0	79.8	20.2	0	0
8	93	7	0	0	93.5	6.5	0	0	95.3	4.7	0	0	90	10	0	0
7	95.7	4.3	0	0	9.1	3.9	0	0	97.7	2.3	0	0	98	2	0	0
6	100	0	0	0	96	4	0	0	100	0	0	0	98.1	1.9	0	0
5	98	2	0	0	96	4	0	0	100	0	0	0	98.2	1.8	0	0
4	98	2	0	0	100	0	0	0	100	0	0	0	97.1	2.9	0	0
3	100	0	0	0	100	0	0	0	100	0	0	0	97.1	2.9	0	0
2	98.5	1.5	0	0	99.2	0.8	0	0	100	0	0	0	97.4	2.6	0	0
1	86.6	13.4	0	0	88.9	11.1	0	0	86.3	13.7	0	0	875	12.5	0	0
B	100	0	0	0	100	23.8	0	0	100	0	0	0	100	0	0	0
Max.	**100**	**22.5**			**100**	**23.8**			**100**	**29.9**			**100**	**41.9**		

KAT	+Y +0.3X				+Y-0.3X				-Y +0.3X				-Y-0.3X			
	SH	BH	İH	GB	SH	BH	İH	GB	SH	BH	İH	GB	SH	BH	İH	GB
10	93.9	6.1	0	0	82.6	17.4	0	0	89.8	10.2	0	0	68.5	31.5	0	0
9	100	0	0	0	100	0	0	0	100	0	0	0	95.7	4.3	0	0
8	100	0	0	0	100	0	0	0	96	4	0	0	96.4	3.6	0	0
7	100	0	0	0	100	0	0	0	96	4	0	0	92.1	7.9	0	0
6	100	0	0	0	100	0	0	0	96.1	3.9	0	0	96.4	3.6	0	0
5	93.4	6.6	0	0	93.6	6.4	0	0	96.3	3.7	0	0	96.6	3.4	0	0
4	97.4	2.6	0	0	94.8	5.2	0	0	96.4	3.6	0	0	96.5	3.5	0	0
3	97.5	2.5	0	0	94	6	0	0	96.4	3.6	0	0	96.6	3.4	0	0
2	93.6	6.4	0	0	93.8	6.2	0	0	93.2	6.8	0	0	91.3	8.7	0	0
1	76.8	23.2	0	0	75.4	24.6	0	0	63.3	36.7	0	0	55.4	44.6	0	0
B	100	0	0	0	100	0	0	0	100	0	0	0	100	0	0	0
Max.	**100**				**100**	**24.6**			**100**	**36.7**			**100**	**44.6**		

a) Düşey elemanların hasar yüzdeleri

KAT	+Y +0.3X				+Y-0.3X				-Y +0.3X				-Y-0.3X			
	SH	BH	İH	GB	SH	BH	İH	GB	SH	BH	İH	GB	SH	BH	İH	GB
10	54.8	45.2	0	0	61.3	38.7	0	0	67.7	32.3	0	0	67.7	32.3	0	0
9	34.4	65.6	0	0	37.5	62.5	0	0	37.5	62.5	0	0	28.1	71.9	0	0
8	18.8	81.2	0	0	21.9	78.1	0	0	25	75	0	0	18.8	81.2	0	0
7	9.4	90.6	0	0	21.9	78.1	0	0	18.8	81.2	0	0	15.6	84.4	0	0
6	9.4	90.6	0	0	12.5	87.5	0	0	9.4	90.6	0	0	12.5	87.5	0	0
5	6.2	93.8	0	0	6.2	93.8	0	0	9.4	90.6	0	0	12.5	87.5	0	0
4	6.2	93.8	0	0	6.2	93.8	0	0	9.4	90.6	0	0	6.2	93.8	0	0
3	3.1	96.9	0	0	6.2	93.8	0	0	9.4	90.6	0	0	6.2	93.8	0	0
2	3.1	96.9	0	0	6.2	93.8	0	0	9.4	90.6	0	0	6.2	93.8	0	0
1	3.1	96.9	0	0	9.4	90.6	0	0	12.5	87.5	0	0	9.4	90.6	0	0
B	73.7	26.3	0	0	63.2	36.8	0	0	63.2	36.8	0	0	78.9	21.1	0	0
Max.	**73.7**	**96.9**			**63.2**	**93.8**			**67.7**	**90.6**			**78.9**	**93.8**		

KAT	+Y +0.3X				+Y-0.3X				-Y +0.3X				-Y-0.3X			
	SH	BH	İH	GB	SH	BH	İH	GB	SH	BH	İH	GB	SH	BH	İH	GB
10	82.9	17.1	0	0	77.1	22.9	0	0	85.7	14.3	0	0	85.7	14.3	0	0
9	66.7	33.3	0	0	38.9	61.1	0	0	55.6	44.4	0	0	63.9	36.1	0	0
8	41.7	58.3	0	0	36.1	63.9	0	0	33.3	66.7	0	0	36.1	63.9	0	0
7	22.2	77.8	0	0	22.2	77.8	0	0	22.2	77.8	0	0	27.8	72.2	0	0
6	13.9	86.1	0	0	13.9	86.1	0	0	16.7	83.3	0	0	22.2	77.8	0	0
5	8.3	91.7	0	0	8.3	91.7	0	0	8.3	91.7	0	0	5.6	94.4	0	0
4	5.6	94.4	0	0	5.6	94.4	0	0	5.6	94.4	0	0	5.6	94.4	0	0
3	5.6	94.4	0	0	5.6	94.4	0	0	5.6	94.4	0	0	5.6	94.4	0	0
2	5.6	94.4	0	0	5.6	94.4	0	0	5.6	94.4	0	0	5.6	94.4	0	0
1	5.6	94.4	0	0	5.6	94.4	0	0	5.6	94.4	0	0	5.6	94.4	0	0
B	36	64	0	0	40	60	0	0	40	60	0	0	48	52	0	0
Max.	**82.9**	**94.4**			**77.1**	**94.4**			**85.7**	**94.4**			**85.7**	**94.4**		

b) Kirişlerin hasar yüzdeleri

Şekil 10. Elemanların hasar yüzdeleri; a) düşey elemanların hasar yüzdeleri, b) kirişlerin hasar yüzdeleri.

Doğrusal olmayan sismik hesapların uygulanması, TBDY Bölüm 15.6.2'den türetilen birim şekildeğiştirme taleplerinin, birim şekildeğiştirme kapasiteleri ile karşılaştırılmasını ve dolayısıyla yapısal sistem performansının kesit düzeyinde değerlendirilmesini içerir. Kolon ve kirişlerde yığılı plastik davranış modelinden elde edilen plastik mafsal dönme değerlerinin, mevcut binaların performans analizi yoluyla belirlenen plastik dönme sınır değerleriyle karşılaştırılmasını içerir. Benzer şekilde, perde duvarlar ve poligonal duvarlar için yayılı plastik davranış modeli ile belirlenen beton ve donatı çeliği birim şekil değiştirme değerleri, birim şekil değiştirme sınır değerleri ile kıyaslanır. Plastik mafsal dönmesi ve birim yer değiştirme değerleri pushover analizi kullanılarak türetilmiş ve kesit performansı sınır değerlerle karşılaştırılarak değerlendirilmiştir. İzin verilen birim şekil değiştirme ve plastik dönme sınırları, TBDY bölüm 5.8.1.1, 5.8.1.2, 5.8.1.3 ve 5.8.1.4'te belirtildiği gibi belirlenir. Sünek eleman kesitleri için hasar limitleri olarak adlandırılan üç performans seviyesi belirlenmiştir. Bunlar, Göçmenin Önlenmesi (GÖ), Kontrollü Hasar (KH) ve Sınırlı Hasar (SH)' dır. Mevcut binaların performans analizinde, her bir kesit için birim şekil değiştirme ve plastik dönme sınırları hem doğrusal hem de doğrusal olmayan hesaplama yöntemleri için geçerli olan belirtilen performans seviyelerine göre belirlenir. Binanın performansı, birim şekil değiştirme ve plastik dönme talepleri yukarıda belirtilen sınır değerlere göre değerlendirilerek değerlendirilir. İncelene yapıda hedeflene performans düzeyi KH olduğundan bu bölümde KH kesit hasar sınırlarları için gerekli bilgiler paylaşılmıştır.

TBDY Madde 5.8.1.3 'e göre Kontrollü Hasar (KH) Performans Düzeyi için yayılı plastik davranış modeli 'ne göre hesaplanan beton malzemesinin birim

şekildeğiştirme sınır değeri εc (KH) ve donatı çeliğinin birim şekildeğiştirme sınır değeri εs (KH) eşitlik 1 ile hesaplanır. Aynı performans düzeyi için Yığılı plastik davranış modeli 'ne göre hesaplanan plastik dönmelerin sınır değeri θp(KH) eşitlik 2 ile hesaplanmaktadır. Ayrıca $\theta_p^{(G\ddot{O})}$ ifadesinin açılımı eşitlik 3'de verilmiştir.

$$\varepsilon_c(KH) = 0.75\left(\varepsilon_c^{(G\ddot{O})}\right);\ \varepsilon_s(KH) = 0.75\left(\varepsilon_s^{(G\ddot{O})}\right) \quad (1)$$

$$\theta_p^{(KH)} = 0.75\,\theta_p^{(G\ddot{O})} \quad (2)$$

$$\theta_p^{(G\ddot{O})} = {}^{2}/_{3}\left[(\phi_u - \phi_y)L_p\left(1 - 0.5\frac{Lp}{Ls}\right) + 4.5\phi_u d_b\right] \quad (3)$$

$\theta_p^{(G\ddot{O})}$, Göçme ötesi (GÖ) bölgesinde elemanın maruz kaldığı plastik dönmeyi ifade eder. ϕ_u, elemanın plastik kapasitesine ulaştığı noktadaki maksimum eğrilik değeri. ϕ_y akma eğriliğini, Lp plastik mafsal uzunluğu, Ls elemanın serbest uzunluğunu ve d_b donate çapını ifade eder. Bu hesaplamalardan elde edilen veriler herbir kat için Şekil 10' da yüzdelik olarak verilmiştir.

Şekil 10'dan elde edilen sonuçlar ışığında binanın performans düzeyi 2018 TBDY'nde belirlenen sınır değerler (Şekil 11) kapsamında değerlendirilmiştir. Taşıyıcı elemanlardan elde edilen değerler Şekil 11' de verilen KH performans hedefi şartlarının yerine getirdiğinden yapının performans düzeyi, Kontrollü Hasar olarak belirlenmiştir.



Şekil 11. KH performans düzeyinin sağlanması için gerekli koşullar.

Yapının performans düzeyi KH olarak elde edilmiş olsa da 2023 Kahramanmaraş depremleri sonrası yapının taşıyıcı sisteminde birtakım hasarlar gözlemlenmiştir.

Depremler sonrası binalarda gözlenen hasarların analitik performans değerlendirmeleriyle uyumsuz olabileceği, mevcut yapıların tasarım ve analiz standartlarının saha performansını tam yansıtmayabileceğine işaret etmektedir. Özellikle, Türkiye gibi yüksek sismisiteye sahip bölgelerde, binaların karmaşık zemin-yapı etkileşimleri, işçilik hataları ve çevresel etkenler nedeniyle kontrol dışı davranışlar sergileyebileceği literatürde sıklıkla vurgulanmaktadır. Örneğin, saha çalışmalarında görülen hasar, kullanılan analiz yöntemlerinin, özellikle doğrusal olmayan davranışları tam olarak yansıtmakta yetersiz kalabileceğini ve yapıların teorik olarak belirlenen performans seviyelerinin sahada farklılık gösterebileceğini göstermektedir (Yeniçelik vd., 2023; Yenidoğan, 2024). Bu bağlamda, Kahramanmaraş depremleri sonrası hasar gören yapının teorik olarak KH performans seviyesinde olsa da analiz ve gerçek hasar düzeyi arasındaki farklılığın sebeplerini incelemek önemlidir. Bu sebepler arasında yapının inşaat kalitesi, yaş ve bakım durumu, zemin özellikleri ve yapısal elemanların birbirleriyle etkileşimi yer almaktadır. Bu tür incelemeler, deprem performansı analizlerinin güncel saha verileri ışığında sürekli olarak güncellenmesi gerektiğini ve gelecekteki analiz yöntemlerinde bu etkenlerin daha doğru bir şekilde dikkate alınmasının önemini vurgular.

4. Sonuç ve Öneriler

Bu çalışmada, 6 Şubat 2023 Kahramanmaraş depremlerinde hasar gören 11 katlı bir betonarme yapının deprem performansı, Türkiye Bina Deprem Yönetmeliği 2018 (TBDY 2018) esaslarına göre analiz edilmiştir. Analiz sonucunda yapının performans düzeyi, Kontrollü Hasar olarak belirlenmiştir. Bu durum, yapının deprem etkisi altında güvenlik sınırları içinde kalabildiğini, ancak taşıyıcı sistemde gözle görülür hasarların oluşabileceğini göstermektedir. Ancak, 2023 depremleri sonrası yapılan saha gözlemlerinde, yapının bazı taşıyıcı elemanlarında beklenenden fazla hasar tespit edilmiştir. Bu uyumsuzluk, tasarım ve analiz sonuçları ile saha performansı arasındaki potansiyel farklılıkları gündeme getirmektedir. Örnek vermek gerekirse, yapıda gözlenen hasar oluşumlarının neredeyse tümünde düğüm noktalarında boğaz etriyesi kullanılmadığı tespit edilmiştir. Bu kritik bölgelerde kullanılması gereken boğaz etriyesinin kullanılmaması ve bu nedenle kabuk atma hasarlarının gözlenmiş olması yapının deprem performansının tasarlandığı şekilde değil inşa edildiği şekilde olacağı gerçeğini gözler önüne sermektedir. Diğer bir yandan, kabuk atma hasarı oluşan kolonlarda yapılan incelemelerde donatı korozyonunun mevcut olduğu ve yeterli pas payı mesafesinin bırakılmadığı tespit edilmiştir. İşçilikten kaynaklanan problemlere ek olarak, yapının y yönünde deprem perdeleriyle donatılmadığı ve bu nedenle yapının bu yönde rijitliğinin yeterli düzeyde olmadığı tespit edilmiştir. Yapıda meydana gelen hasarların daha çok y yönünde oluşması da bu çıkarımı doğrular niteliktedir.

Çalışmada elde edilen bulgular, analiz yöntemleri ve yönetmelik esaslarının teorik olarak yeterli bir güvenlik sağlamasına karşın, pratik uygulamalarda işçilik kalitesi, malzeme kullanımı, zemin-yapı etkileşimi gibi faktörlerin performans üzerinde etkili olduğunu ortaya koymuştur.

Yapının performans analizinde doğrusal olmayan çok modlu itme analizinin kullanılması, TBDY 2018'e uygun bir yaklaşım sergilese de saha koşullarının birebir yansıtılamaması, gerçek performansın analiz sonuçlarından sapmasına yol açmaktadır. Bu nedenle, binaların performans analizlerinin sahadaki gerçek davranışlarıyla uyumluluğunun artırılması için kullanılan modelleme teknikleri, yapı detayları ve işçilik kalitesinin daha ayrıntılı bir şekilde ele alınması gerekmektedir.

Bu bağlamda, Kahramanmaraş depremlerinden elde edilen saha gözlemleri, gelecekte yapılacak deprem dayanıklılığı çalışmalarında referans niteliği taşımaktadır. Özellikle, benzer yapısal özelliklere sahip binaların depreme karşı dayanıklılığı artırmak adına tasarım sürecinde sahadan elde edilen verilerin analiz süreçlerine entegre edilmesi önemlidir. Ayrıca, bu tür analizler, ülkemizde mevcut yapı stokunun deprem performansını iyileştirmek ve depreme dayanıklı tasarım hedeflerini sağlamak için kritik bilgiler sunmaktadır.

Katkı Oranı Beyanı

Yazarların katkı yüzdeleri aşağıda verilmiştir. Yazarlar makaleyi incelemiş ve onaylamıştır.

	E.E.	A.Ö.
K.	60	40
T	40	60
Y	40	60
VTI	60	40
VAY	40	60
KT	40	60
YZ	60	40
KI	50	50
GR	70	30
PY	60	40
FA	50	50

K= kavram, T= tasarım, Y= yönetim, VTI= veri toplama ve/veya işleme, VAY= veri analizi ve/veya yorumlama, KT= kaynak tarama, YZ= Yazım, KI= kritik inceleme, GR= gönderim ve revizyon, PY= proje yönetimi, FA= fon alımı.

Çatışma Beyanı

Yazarlar bu çalışmada hiçbir çıkar ilişkisi olmadığını beyan etmektedirler.

Etik Onay Beyanı

Bu araştırmada hayvanlar ve insanlar üzerinde herhangi bir çalışma yapılmadığı için etik kurul onayı alınmamıştır.

Destek ve Teşekkür Beyanı

Laboratuvar imkânlarını kullandığımız İnönü Üniversitesi'ne teşekkür ederiz.

Kaynaklar

Altunsu E, Güneş O, Öztürk S, Sorosh S, Sarı A, Beeson S.T. 2024. Investigating the structural damage in Hatay province after Kahramanmaraş-Türkiye earthquake sequences. Engin Failure Analy, 157: 107857.

Avcil F, Işık E, İzol R, Büyüksaraç A, Arkan E, Arslan MH, Harirchian E. 2024. Effects of the February 6 2023 Kahramanmaraş earthquake on structures in Kahramanmaraş city. Natural Hazards. 120(3): 2953-2991.

Coşkun ME, Gürsoy Ş, Garıp ZŞ. 2023. Betonarme bir okul binasında güçlendirme ilkelerinin 2007 ve 2019 Türk deprem yönetmeliklerine göre karşılaştırılması. Gümüşhane Üniv Fen Bilim Derg, 13(1): 127-144.

Dalyan İ, Şahin B. 2019. Mevcut betonarme bir binanın 2007 ve 2018 deprem yönetmeliklerine göre deprem yükleri altındaki taşıyıcı sistem perfomansının değerlendirilmesi. Türk Deprem Araş Derg, 1(2): 134-147.

Foroughı S, Yüksel B. 2022. TBDY 2018'e göre doğrusal olmayan hesap yöntemleri ile betonarme yapı sistemlerinin performans analizi. Osmaniye Korkut Ata Üniv Fen Bilim Enstit Derg, 5(1): 33-55.

Işık G, Tuncer F. 2023. Bursa'da yıkım kararı verilen tescilli betonarme yapıların deprem performans analizleri etkinliğinin tartışılması. Kent Akad, 16(1): 297-317.

Kap T, Özgan E, Uzunoğlu MM. 2019a. Betonarme bir okul binasının 2018 deprem yönetmeliğine göre incelenmesi. Düzce Üniv Bilim Teknol Derg, 7(3): 1140-1150.

Kap T, Özgan E, Uzunoğlu MM. 2019b. Taşıma gücü zayıf zeminde inşa edilmiş betonarme bir binanın performans analizi. Düzce Üniv Bilim Teknol Derg, 7(1): 795-809.

Küçükaslan N, Altan MF. 2021. Güçlendirilen mevcut bir yapının tdy 2007 ile 2018 yeni türkiye bina deprem yönetmeliğine göre performansının tekrar incelenmesi. Afyon Kocatepe Üniv Uluslararası Mühen Teknol Uygulamalı Bilim Derg, 4(1): 18-36.

Nemutlu ÖF. 2019. 2007-2018 Türk deprem yönetmeliklerinin ve Amerikan deprem yönetmeliğinin deprem hesapları açısından karşılaştırılması. Yüksek Lisans Tezi, İstanbul Teknik Üniversitesi, Fen Bilimleri Enstitüsü, İstanbul, Türkiye, ss: 112.

Nemutlu OF, Balun B, Sari A. 2021. Damage assessment of buildings after 24 January 2020 Elazığ-Sivrice earthquake. Earthquak Struct, 20(3): 325-335.

Nemutlu ÖF, Sarı A, Balun B. 2023. 06 Şubat 2023 Kahramanmaraş depremlerinde(mw 7.7-mw 7.6) meydana gelen gerçek can kayıpları ve yapısal hasar değerlerinin tahmin edilen değerler ile karşılaştırılması. Afyon Kocatepe Üniv Fen Müh Bilim Derg, 23(5) 1222-1234.

Özmen A, Sayın E. 2021. Deprem etkisinde çok katlı betonarme bir binanın tdy-2007 ve tbdy-2018 deprem yönetmeliklerine göre eşdeğer deprem yüklerinin karşılaştırılması. Osmaniye Korkut Ata Üniv Fen Bilim Enstit Derg, 4(2): 124-133.

Öztürk S, Altunsu E, Güneş O, Sarı A. 2024. Investigation of industrial structure performances in the Hatay and Gaziantep provinces during the Türkiye earthquakes on February 6 2023. Soil Dynam Earthquak Engin, 179 :108569.

Sarı O. 2020. Mevcut Konut Türü Bir Binanın DBYBHY–2007 ve TBDY–2018 Deprem yönetmeliklerine göre deprem performansının değerlendirilmesi. Yüksek Lisans Tezi, Burdur Mehmet Akif Ersoy Üniversitesi, Fen Bilimleri Enstitüsü, Burdur, Türkiye, ss: 103.

Severcan MH, Sınanı B. 2019. Mevcut betonarme yapilarin deprem performansinin analizi. Niğde Ömer Halisdemir Üniv Müh Bilim Derg, 8(2): 936-947.

Yalın M, Ulutaş H. 2021. Mevcut okul türü bir binanın deprem performansının 2007 ve 2018 deprem yönetmeliklerine göre değerlendirilmesi. Niğde Ömer Halisdemir Üniv Müh Bilim Derg, 10(2): 648-661.

Yeniçelik N, Er Ş, Sıcacık EA. 2023. Farklı beton ve çelik sınıfı kullanımının yapıların zaman tanım alanında analiz sonuçlarına etkilerinin incelenmesi (Ocak 2020 Elazığ depremi örneği). Inter J Engin Res Develop, 15(3): 166-178.

Yenıdoğan C. 2024. 6 Şubat 2023 depremleri ve saha gözlemlerine dayalı bina hasarları hakkında ön değerlendirme. Turkish J Civil Engin, 35(5): 75-113.

Yüzbaşı J, Yerlı HR. 2018. Betonarme yapıların deprem etkisi altında performans analizlerinin yapılması ve güçlendirilmesi. Çukurova Ünivi Müh-Mim Fak Derg, 33(2): 273-286.

Black Sea Journal of Engineering and Science
doi: 10.34248/bsengineering.1604007

Open Access Journal
e-ISSN: 2619 – 8991

Araştırma Makalesi (Research Article)
Cilt 8 - Sayı 2: 298-309 / Mart 2025
(Volume 8- Issue 2: 298-309 / March 2025)

Arachis Hypogaea BİTKİSİ KULLANILARAK YEŞİL SENTEZİ GERÇEKLEŞTİRİLEN GÜMÜŞ NANOPARTİKÜLLERİN ANTİMİKROBİYAL VE ANTİ QUORUM SENSING AKTİVİTELERİNİN TESPİTİ

Taylan AKTAŞ[1]*

[1]*Kırşehir Ahi Evran University, Çiçekdağı Vocational School, Department of Veterinary, 40700, Kırşehir, Türkiye*

Özet: Yer fıstığı (*Arachis hypogaea* L.), ağırlıklı olarak Akdeniz bölgesi olmak üzere Türkiye ve Amerika Birleşik Devletleri'nde dikkate değer bir öneme sahip, dünya çapında yetiştirilen önemli bir tarım ürünüdür. Bu araştırmada Osmaniye ilinden elde edilen yer fıstığı, araştırma çalışmalarımızın ana malzemesi olarak kullanılmıştır. Nanopartiküller, çağdaş bilimsel araştırmalar içinde çeşitli disiplinlerde kullanılmaktadır. Bu alanlardaki en kritik araştırmalar arasında, özellikle çeşitli mikroorganizmalar üzerindeki ölümcül etkileri nedeniyle antibiyotiklerin incelenmesi bulunmaktadır. Bu çalışmada *A. hypogaea* bitkisine ait tohum ve kabuklar ile gümüş nanopartiküllerin (AgNP) yeşil sentezi gerçekleştirilmiştir. Sentezlenen AgNP'ler; antimikrobiyal ve anti-quorum sensing aktivite açısından analiz edilmiştir. Antimikrobiyal aktivite analizi amacıyla çalışmada 22 adet patojen mikroorganizma kullanılmıştır. Sonuç olarak; AgNP'lerin antimikrobiyal aktivitelerinde istatistiksel açıdan anlamlı farklar tespit edilmiştir ($P<0,05$). Çalışmada kullanılan *Chromobacterium violaceum*, AgNP'lerin en yüksek antimikrobiyal aktivite gösterdiği mikroorganizma olmuştur. AgNP'lerin *C. violaceum* üzerinde göstermiş oldukları antimikrobiyal etki, anti-quorum sensing aktiviteninde olduğunu sonuçlarda göstermiştir. Fıstık ve kabuk ile yeşil sentezi gerçekleştirilen AgNP'ler, Anti-QS açısından istatistiksel olarak anlamlı farklara da neden olmuştur ($P<0,05$). 2,5 µl/ml konsantrasyondaki yaş, çiğ ve kavrulmuş yer fıstığı tohumu ile yeşil sentezi gerçekleştirilmiş AgNP'lerde zon çapları sırasıyla 19,2 mm, 18,6 mm, 19,4 mm iken, yer fıstığı kabuğu ile yeşil sentezi gerçekleştirilmiş AgNP'lerde sırasıyla 16,8 mm, 16,8 mm, 14,8 mm'dir. Özellikle mikroorganizmaların antibiyotiklere ve diğer terapötik ajanlara karşı önemli ölçüde yüksek direnç seviyeleri sergilediği gerçeği ışığında hem ekonomik olarak uygulanabilir hem de etkili olan bu malzemeler ilaç sektöründe ve diğer alanlarda dikkate alınmayı hak etmektedir.

Anahtar kelimeler: *Arachis hypogaea*, Antimikrobiyal aktivite, Quorum sensing, Gümüş nanopartikül

Detection of Antimicrobial and Anti-Quorum Sensing Activities of Silver Nanoparticles Performed by Green Synthesis Using the *Arachis hypogaea* Plant

Abstract: Peanuts (*Arachis hypogaea* L.) are an important agricultural crop grown worldwide, with notable significance in Türkiye and the United States, particularly in the Mediterranean region. In this research, peanuts obtained from Osmaniye province were used as the main material for our studies. Nanoparticles are utilized in a variety of disciplines within contemporary scientific research. Among the most critical research areas is the study of antibiotics, especially due to their lethal effects on various microorganisms. In this study, the green synthesis of silver nanoparticles (AgNPs) from the seeds and shells of the *A. hypogaea* plant was carried out. Synthesized AgNPs were analyzed for antimicrobial and anti-quorum sensing activity. For the purpose of antimicrobial activity analysis, 22 pathogenic microorganisms were used in the study. As a result, statistically significant differences were found in the antimicrobial activity of AgNPs ($P<0.05$). *Chromobacterium violaceum*, used in the study, was the microorganism in which AgNPs showed the highest antimicrobial activity. The antimicrobial effect of AgNPs on *C. violaceum* was demonstrated to be related to anti-quorum sensing activity. AgNPs synthesized from peanut seeds and shells also caused statistically significant differences in terms of anti-QS ($P<0.05$). In AgNPs synthesized from green and raw peanut seeds at a concentration of 2.5 µl/ml, the zone diameters were 19.2 mm, 18.6 mm, and 19.4 mm, respectively, whereas for AgNPs synthesized from green peanuts with shells, the diameters were 16.8 mm, 16.8 mm, and 14.8 mm, respectively. Especially in light of the fact that microorganisms exhibit significantly high levels of resistance to antibiotics and other therapeutic agents, these materials, which are both economically viable and effective, deserve consideration in the pharmaceutical industry and other fields.

Keywords: *Arachis hypogaea*, Antimicrobial activity, Quorum sensing, Silver nanoparticle

***Sorumlu yazar (Corresponding author):** Kırşehir Ahi Evran University, Çiçekdağı Vocational School, Department of Veterinary, 40700, Kırşehir, Türkiye
E mail: taylanaktas@gmail.com (T. AKTAŞ)
Taylan AKTAŞ https://orcid.org/0000-0003-1323-8459

Gönderi: 19 Aralık 2024 **Received:** December 19, 2024
Kabul: 23 Ocak 2025 **Accepted:** January 23, 2024
Yayınlanma: 15 Mart 2025 **Published:** March 15, 2025

Cite as: Aktaş T. 2025. Detection of antimicrobial and anti-quorum sensing activities of silver nanoparticles performed by green synthesis using the *Arachis hypogaea* plant. BSJ Eng Sci, 8(2): 298-309.

This work is licensed (CC BY-NC 4.0) under Creative Commons Attribution 4.0 International License

1. Giriş

Nanoteknoloji ve nanobilim, ağırlıklı olarak 1-100 nm ölçeğindeki parçacıkları kapsayan ve böylece hem atomik hem de atom altı katmanlardaki tüm kümeleri ele alan kavramsal bir çerçevenin iki temel boyutunu temsil eder (Horikoshi ve Serpone, 2013). Gümüşün içsel ve fizikokimyasal özelliklerine ek olarak, bu ve diğer metalik maddelerde malzemeler nano ölçeğe geçerken yüzey-hacim oranlarındaki önemli değişiklik, nanopartiküllerin doğasında bulunan dönüştürücü özelliklerin ortaya çıkmasıyla sonuçlanır (Liu vd., 2012).

Gümüş nanopartiküller (AgNP), mikrobiyal varlıklarla önemli etkileşimi kolaylaştıran, dikkate değer ölçüde geniş yüzey alanlarına atfedilebilen önemli antimikrobiyal özellikler sergiler. Bu nanopartiküller hücresel zara yapışır ve bakteri hücrelerinin içine sızabilir. Bakteri zarı, kükürt içeren proteinlerden oluşur ve gümüş nanopartiküller, DNA gibi fosfor içeren moleküllerle etkileşime girmenin yanı sıra hücre içi olarak bu proteinlerle etkileşime girer (Singh vd., 2015). Gümüş nanopartiküller bakteriyel hücresel yapılarla etkileşime girdiğinde, bakteri popülasyonlarının toplandığı merkezi bölgede lokalize bir düşük moleküler ağırlıklı bölge oluştururlar, böylece DNA üzerinde gümüş iyonlarına karşı koruyucu bir etki sağlarlar (Kumar vd., 2014). Nanopartiküller, solunum zincirini hedefli bir eğilim sergiler ve bozulmuş hücresel bölünmenin bir sonucu olarak hücre ölümleri gerçekleşir (Kim vd., 2013). Bununla birlikte, nanopartiküller bakteri hücreleri içinde gümüş iyonlarını serbest bırakır, böylece bakterisit etkinliklerini arttırır (Singh vd., 2015). Yer fıstığı, izoflavonlar, polikozanol, skualen ve bir dizi ek fitosterol dahil olmak üzere önemli bir fitokimyasal rezervuar görevi görür (Isanga ve Zhang, 2007). Ayrıca, *A. hypogaea*'nın farklı genotipleri, farklı salisilik asit, p-kumarik asit ve daidzein (bir izoflavon olarak sınıflandırılır) konsantrasyonları sergiler (Rodriguez vd., 2015). Genel olarak çeşitli hastalıklarla ilgili risklerin azaltılmasına katkıda bulunduklarını gösteren önemli kanıtlar vardır (Lopes vd., 2011). Bu çalışmanın amacı, önemli besin özellikleriyle tanınan *A. hypogaea* tohum ve kabukları ile yeşil sentez yaklaşımı kullanılarak elde edilen gümüş nanopartiküllerin mikrobiyolojik etkinliğini değerlendirmektir. Bu bağlamda, nanopartiküllerin çeşitli patojenik mikroorganizmalar üzerinde antimikrobiyal ve anti-quorum sensing etkiler gösterip göstermediği araştırılmıştır.

2. Materyal ve Yöntem

Bu çalışmada, fitokimyasal içeriği zengin olan *A. hypogaea* bitkisine ait tohum ve kabuk ekstraktları ile yeşil sentezi gerçekleştirilen AgNP'ler kullanılmıştır. AgNP'lerin karakterizasyonu içi UV-Vis spektrometre analizi ve Enerji Dağılımlı X-Işını Spektroskopisi (EDS) gerçekleştirilmiştir. Bunun yanı sıra AgNP'lerin morfolojik analizi ise Taramalı Elektron Mikroskobu (SEM) gerçekleştirilmiştir. AgNP'lerin antimikrobiyal aktivitelerinin tespiti için Agar Well Difüzyon (AWD) yöntemi kullanılmış olup minimal inhibisyon konsantrasyonu da (MİK) belirlenmiştir. AgNP'lerin antimikrobiyal aktivite analizi için 22 adet patojen bakteri kullanılmıştır. Anti-Quorum Sensing Aktivite (Anti-QS) analizi için AWD yönteminin yanı sıra UV-Vis spektrometri analizi de gerçekleştirilmiştir.

AgNP yeşil sentezi için Merck markasına ait kristalize $AgNO_3$ (169,87 g/mol) kullanılmıştır. Çalışmada kullanılacak olan yer fıstıkları ise Osmaniye ilinin Sumbas ilçesinden toplanmıştır. Gerçekleştirilen bilimsel çalışmada UV-Vis spektrofotometre (Jasco V-730), etüv (Elektromag M 420 P) ve Santrifüj (Nüve NF 400) kullanılmıştır. Antimikrobiyal aktivite testi için *Staphylococcus aureus* (ATCC 25923), *Bacillus thuringiensis* (ATCC 13367), *Candida albicans* (ATCC 90028), *Candida parapsilosis* (M006), *Escherichia coli* (ATCC 25922), *Klebsiella pneumoniae* (ATCC 13883), *Candida tropicalis* (M007), *Chromobacterium violaceum* (ATCC 12472), *Enterobacter aerogenes* (ATCC 51342), *Enterococcus faecalis* (ATCC 29212), *Aeromonas hydrophila* (ATCC7966), *Bacillus cereus* (709 Roma), *Bacillus subtilis* (ATCC 6633), *Listeria monocytogenes* (ATCC 35152), *Proteus vulgaris* (ATCC 29905), *Pseudomonas aeruginosa* (ATCC 27853), *Salmonella typhimurium* (ATCC 14028), *Shigella dysenteriae* (ATCC 11835), *Staphylococcus aureus* (ATCC 29213), *Staphylococcus epidermidis* (ATCC 12228), *Proteus mirabilis* (ATCC 29906), *Vibrio anguillarum* (ATCC 43312) bakterileri kullanılmıştır. Anti-quorum sensing aktivite testi için ise *Chromobacterium violaceum* (ATCC 12472) bakterisi kullanılmıştır. Kullanılan bakteriler Kırşehir Ahi Evran Üniversitesi Sağlık Hizmetleri Meslek Yüksekokulu Mikrobiyoloji Laboratuvarından temin edilmiştir.

Çalışmaların gerçekleştirilebilmesi amacıyla 25 gram toz haline getirilmiş fıstık tohumu ve kabuğu (yaş, çiğ ve kavrulmuş çeşitleri içeren), hem yer fıstığı tohumlarından hem de kabuklardan bileşiklerin ekstraksiyonunu için 30 dakika süreyle 200 mililitre deiyonize suda kaynatma işlemine tabi tutuldu. Elde edilen karışımlar daha sonra Whatman Grade No.1 (11 µm) filtre kâğıdı kullanılarak filtrelemeye tabi tutuldu ve daha sonra erlenlere aktarıldı. Elde edilen yaş, çiğ ve kavrulmuş yer fıstığı tohumu ile bu tohumlara ait kabuk ekstraktları, çalışmalar gerçekleşene kadar +4 °C'de muhafaza edildi. Yukarıda bahsedilen prosedürler, üç farklı *A. hypogaea* tohum ve kabuk örneği için ayrı ayrı yürütülmüştür.

Ekstraktlardan 10 mL alınarak üzerlerine kademeli olarak (10^{-4} ile 10^{-2} mol/L) 90 mL gümüş nitrat ($AgNO_3$, Merck; Almanya) çözeltisi eklendi. Elde edilen çözelti, 28 santigrat derece sıcaklıkta 24 saat boyunca karanlık bir ortamda tutuldu. Makroskopik inceleme yoluyla, çözelti tonunun 24 saatlik sürenin sonunda kahverengiye geçtiği kaydedildi. Oluşan bu renk değişimi, AgNP'lerin (tohum ve kabuk) oluşumunu kanıtlamaktadır (Zhang vd., 2011).

İndirgenme işlemi tamamlanmış olan bitki ekstraktı yüklü Gümüş nanopartiküller (AgNP'ler) daha sonra Falcon tüplerine aktarıldı ve dakikada 4500 devir dönme hızında

bir saat boyunca santrifüjlemeye tabi tutuldu. Santrifüjleme işleminin tamamlanmasının ardından, sıvı fazdan ayrılan AgNP'ler tüpün sınırları içinde titizlikle izole edildi. Daha sonra, ekstrakte edilen tohum ve kabuk numunelerinden türetilen gümüş nanopartiküller (AgNP'ler), aseptik tüplerde steril damıtılmış su kullanılarak 1 mM, 2 mM ve 3 mM konsantrasyonlarda hazırlandı. Yeşil sentezlenmiş gümüş nanopartiküllerin antimikrobiyal etkinliğini belirlemek için, steril petrilerde mikroorganizmaların çoğalması için elverişli ortamlar oluşturmak amacıyla Triptik Soy Agar (TSA) besiyeri kullanıldı.

Besiyeri hazırlanmadan önce cam petriler 180 °C'de 1 saat pastör fırınında bekletilerek steril edildi. Daha sonra, TSA litre başına 40 gram konsantrasyonda formüle edildi ve daha sonra otoklavlama ve sterilizasyon prosedürlerinden geçen petri kaplarına aktarıldı. Petri kaplarında bulunan ortam, çalışma sırasında 37 ^{0}C sıcaklıkta 24 saat inkübe edildi ve herhangi bir kontaminasyon belirtisi izlendi. Kontaminasyon gözlenmeyen hazırlanmış plakların her birine eküvyon çubuğu ile kullanılacak mikroorganizmalar ekildi. Ekim işlemi sonrasında; sentezlenen 1mM, 2mM ve 3mM'lık AgNP'ler kuyucukların içerisine uygulandı ve plaklar etüvde 24 saat 37 °C'de bekletildi. Sonrasında plaklarda bulunan kuyucukların etrafındaki zon çapları ölçülerek AgNP'lerin etki düzeyleri tespit edildi.

Gümüş nanoparçacıklar (AgNP'ler) için minimum inhibitör konsantrasyonun (MIC) belirlenmesi, 96 kuyu içeren steril mikroplaklar kullanılarak gerçekleştirildi. Deneyi kolaylaştırmak için, triptik soya suyu (TSB) içindeki 22 farklı mikroorganizmanın kültürlerinden türetilen çözeltiler, McFarland 0.5 bulanıklık standardına göre 1,5 x 10^6 hücre/ml'lik bir hücre konsantrasyonu elde etmek için hazırlandı. Mikroplakların ilk kuyularına 100 µl TSB ve 100 µl AgNP'lik bir başlangıç hacmi dağıtıldı, ardından 100 µl önceki kuyudan sonraki kuyuya aktarıldı. Bu seyreltme prosedürü, nihai kuyuya ulaşılana kadar sistematik olarak sürdürüldü. AgNP'ler için belirlenen konsantrasyonlar 5 µl/ml, 2.5 µl/ml, 1.25 µl/ml, 0.625 µl/ml, 0.312 µl/ml, 0.156 µl/ml, 0.078 µl/ml ve 0.039 µl/ml içeriyordu. Daha sonra, negatif kontrol görevi gören nihai kuyu hariç tüm kuyulara 10 µl mikrobiyal çözeltiler eklendi. Hazırlanan mikro plakalar, 24 saatlik bir süre boyunca 37 °C'lik sabit bir sıcaklıkta inkübe edildi. Kuluçka süresinin sona ermesinden sonra, elde edilen plaklar, 600 nm dalga boyunda ayarlanmış bir spektrofotometre kullanılarak analize tabi tutuldu. Yapılan araştırmada, tekrarlanabilirliği sağlamak için AgNP'leri içeren tüm prosedürler üç nüsha halinde gerçekleştirildi.

Çalışmada Anti-QS analizi makroskobik ve spektroskopik yöntemlerle gerçekleştirildi. Makroskopik metodolojide, *Chromobacterium violaceum*'un Triptik Soy Agar (TSA) ile formüle edilmiş agar plakalarına aşılandığı ve Gümüş Nanopartiküller (AgNP'ler) tarafından indüklenen inhibisyon bölge çaplarının ölçüldüğü AWD yaklaşımı kullanıldı. UV-Vis spektroskopi kullanılan anti-quorum sensing (anti-QS) değerlendirmesi için, başlangıçta TSB ilavesiyle steril cam tüplere bir sıvı kültür ortamı eklendi. Daha sonra, belirgin quorum sensing mekanizmaları için bilimsel literatürde kapsamlı bir şekilde belgelenmiş bakteri olan C. violaceum, TSB'de kültürlendi. Böylece bu organizmanın sıvı ortam içinde yeterli miktarlarda üretimi kolaylaştırıldı. Anti-QS analizi amacıyla her biri 2 mL TSB ortamı içeren cam tüplerde, AgNP'lerin seyreltilmesi sistematik olarak gerçekleştirildi. Dilüsyon yapılmış her tüpe, TSB içerisinde üremesi sağlanmış 200 mL *C. violaceum* bakterisi eklendi. Hazırlanan tüpler etüvde 37 °C'de 24 saat inkübasyona bırakıldı. İnkübasyon sonrasında alınan tüplere 200 mL sodyum dodesil sülfat (SDS) ve 500 ml n-bütanol eklendi. Oluşan çözelti santrifüj edilerek faz oluşumu sağlandı ve süpernatantın spektrofotometrik absorbansı ölçüldü. Çalışmada, yeşil sentezi gerçekleştirilen AgNP'lerin farklı derişimlerinin, antimikrobiyal etkileri faktöriyel anova istatistik testi ile değerlendirilmiştir. Bununla birlikte, sentezlenen AgNP'lerin mikrobiyolojik açıdan birbirleri arasındaki ilişki duncan çoklu karşılaştırma testi ile değerlendirilmiştir.

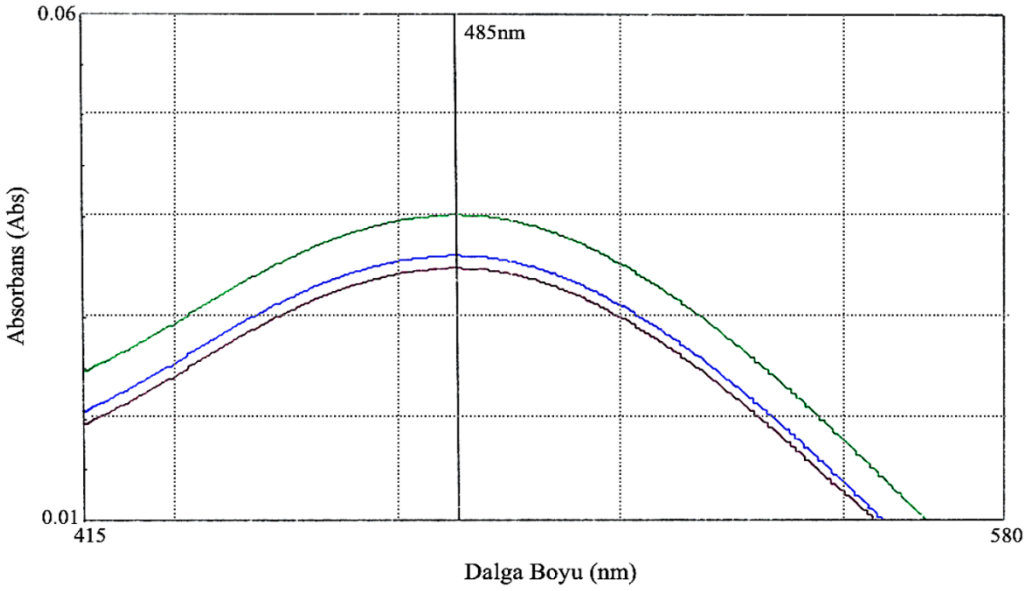
3. Bulgular

3.1. *A. hypogaea* Tohumları ve Kabukları ile Sentezlenen AgNP'lerin Karakterizasyonu

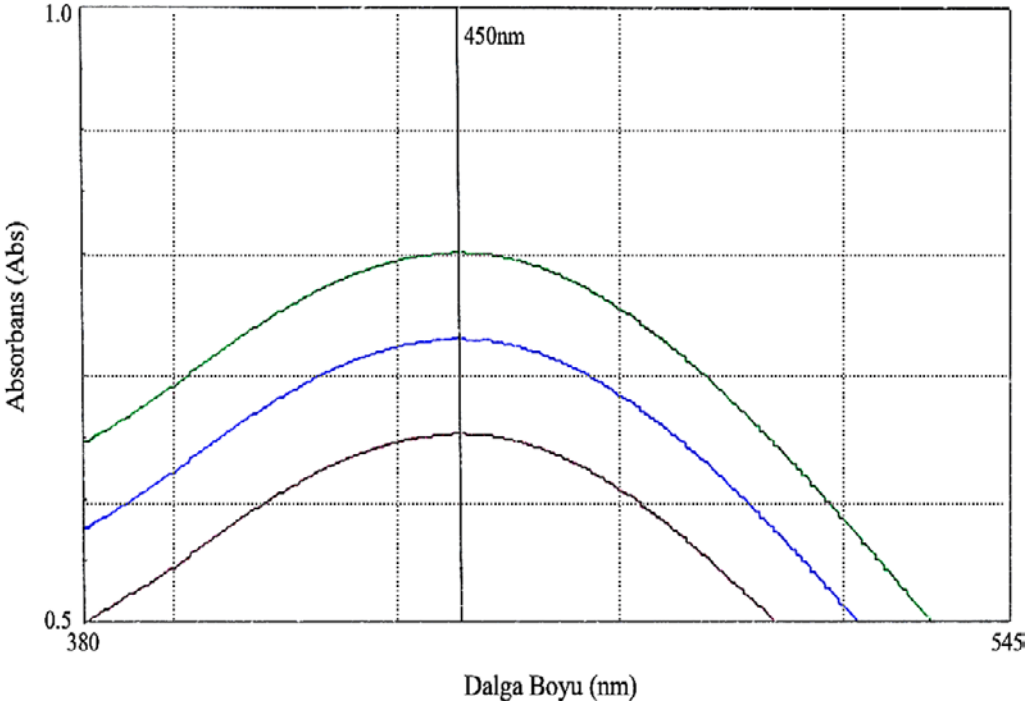
A. hypogaea bitkisinin tohum ve kabukları kullanılarak 1mM, 2mM ve 3mM konsantrasyonlarda sentezlenen gümüş nanopartiküllerin (AgNP'ler) UV-Vis spektrumlarından türetilen absorbans (abs) metrikleri Tablo 1'de tanımlanmıştır. UV-Vis spektrumlarından elde edilen absorbans metriklerinin grafik gösterimleri de Şekil 1 ve 2'de gösterilmektedir. Yapılan araştırmada, yaş, çiğ ve kavrulmuş *A. hypogaea* tohumları ve kabukları kullanılarak üretilen AgNP'lerin UV-Vis spektrumları, tohumlardan sentezlenen nanopartiküller için 485 nm'de bir absorbans zirvesi sergilerken, kabuklardan sentezlenen nanopartiküller 450 nm'de bir tepe gösterir. UV-Vis spektrumlarından alınan absorbans sonuçları (Tablo 1); *A. hypogaea* tohumları ile gerçekleştirilen AgNP yeşil sentezinin, *A. hypogaea* kabukları ile gerçekleştirilen AgNP yeşil sentezinden daha verimli olduğunu ortaya koymuştur. Bununla birlikte, 3mM $AgNO_3$ kullanan gümüş nanopartiküllerin (AgNP) biyosentezi, AgNP yeşil sentez işlemi sırasında 1mM ve 2mM $AgNO_3$ bileşiklerinin kullanımına kıyasla, UV-Vis absorbans ölçümlerinden elde edilen sonuçların kanıtladığı gibi, yaş, çiğ ve kavrulmuş olarak kategorize edilen tüm numunelerde üstün etkinlik göstermektedir.

3.2. SEM Analizi Sonuçları

A. hypogaea tohum ve kabukları ile sentezlenen AgNP'lere ait taramalı elektron mikroskobu (SEM) görüntüsü Şekil 3'te verilmiştir.



Şekil 1. *A. hypogaea* tohumu ile sentezlenen AgNP'e ait UV-Vis spektrum grafiği. Yeşil, mavi ve kahverengi absorbans eğrileri sırasıyla 1mM, 2mM ve 3mM'lık gümüş nanopartikül derişimlerini belirtmektedir. Çalışmada absorbans eğrilerinin pik yaptığı dalga boyu kullanılmıştır.

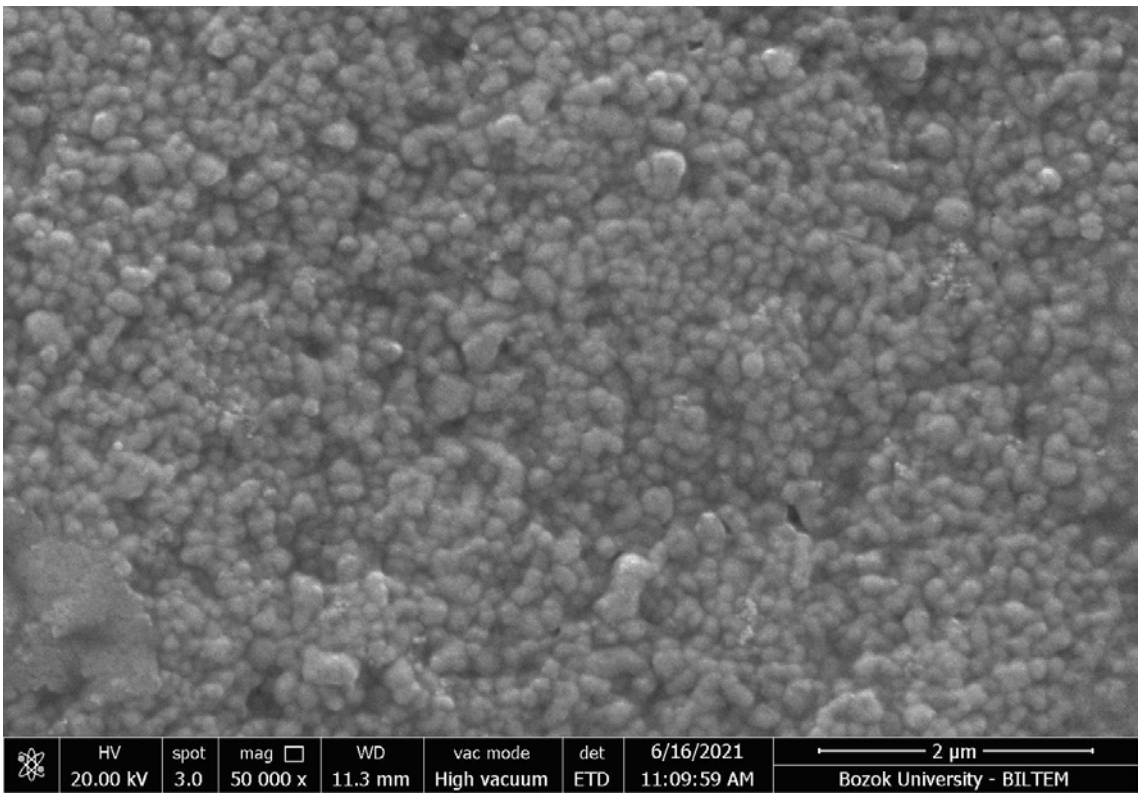


Şekil 2. *A. hypogaea* kabuğu ile sentezlenen AgNP'e ait UV-Vis spektrum grafiği. Yeşil, mavi ve kahverengi absorbans eğrileri sırasıyla 1mM, 2mM ve 3mM'lık gümüş nanopartikül derişimlerini belirtmektedir. Çalışmada absorbans eğrilerinin pik yaptığı dalga boyu kullanılmıştır.

Tablo 1. *Arachis hypogaea* tohum ve kabukları ile sentezlenen AgNP'lerin UV-Vis absorbans değerleri

AgNP Derişimi	Yer Fıstığı Tohumu (UV-Vis Abs)			Yer Fıstığı Kabuğu (UV-Vis Abs)		
	Yaş	Çiğ	Kavrulmuş	Yaş	Çiğ	Kavrulmuş
1mM	0,0433	0,0403	0,0819	0,9249	0,8031	0,7732
2mM	0,0431	0,0376	0,0802	0,9011	0,7357	0,6949
3mM	0,0328	0,0341	0,0419	0,6381	0,6522	0,6428

*absorbans (Abs) değerlerinin "0" (sıfır)'a yaklaşması daha verimli bir AgNP sentezini ifade etmektedir.



Şekil 3. *A. hypogaea* ile sentezlenen AgNP'e ait sem görüntüsü. Elde edilen gümüş nanopartiküllerin SEM görüntülerinde tespit edilen görüntüler, morfolojik açıdan küresel yapıya sahip olduklarını göstermektedir.

Bu bağlamda, SEM ile görüntülenen AgNP'lerde tespit edilen boyutlar her örnekte (tohum ve kabuk ile sentezlenen AgNP'ler için) farklılık göstermektedir.

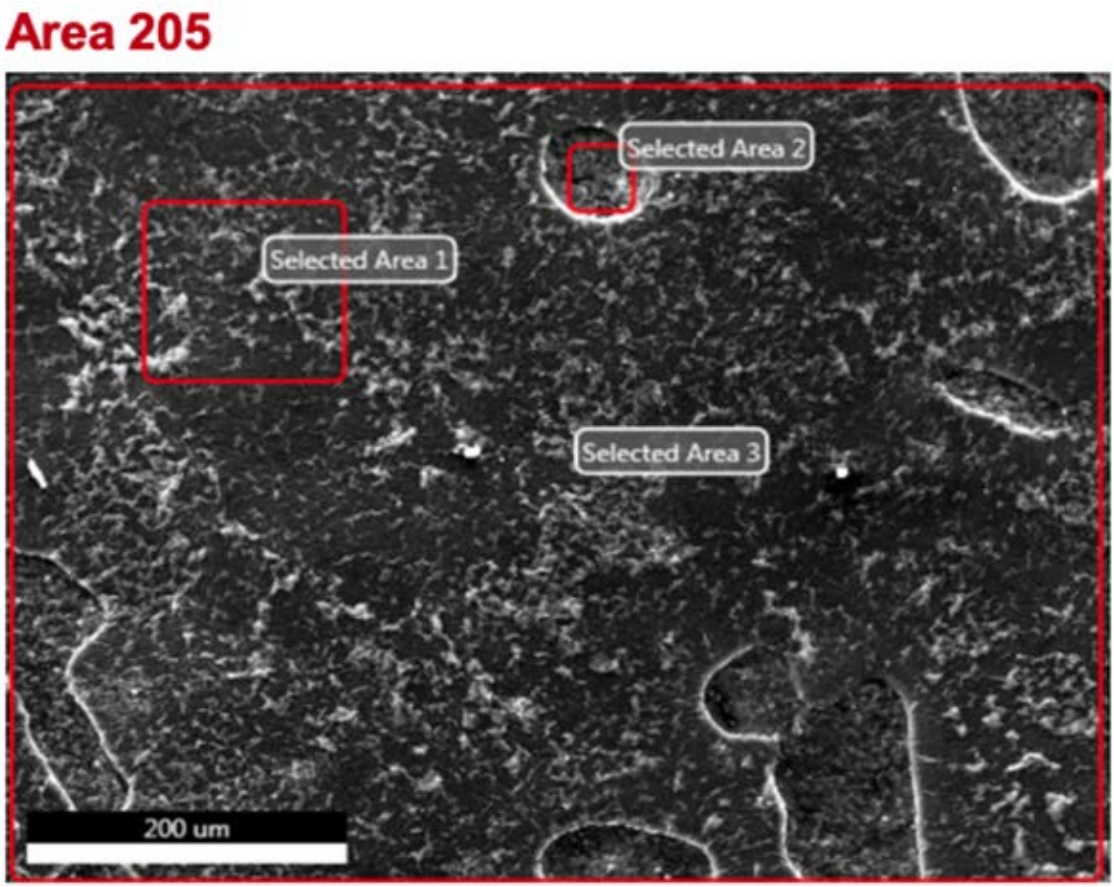
3.3. EDS Analizi Sonuçları

Arachis hypogaea'nın tohumları ve kabukları kullanılarak sentezlenen gümüş nanopartiküller (AgNP'ler) için Enerji Dispersiv Spektrum (EDS) analizinin sonuçları Şekil 4 ve 5'te sunulmaktadır. EDS analiz sonuçları, Ag (gümüş), N (azot) ve O (oksijen) gibi elementlerin tanımlanmasıyla kanıtlandığı gibi, Taramalı Elektron Mikroskobu (SEM) ile görselleştirilen bölgelerde AgNP'lerin varlığını kanıtlamaktadır. SEM ile görselleştirilen bölgeler, EDS analizi sonucu AgNP tespit edilen bölgeler dahilinde belirlenmiştir.

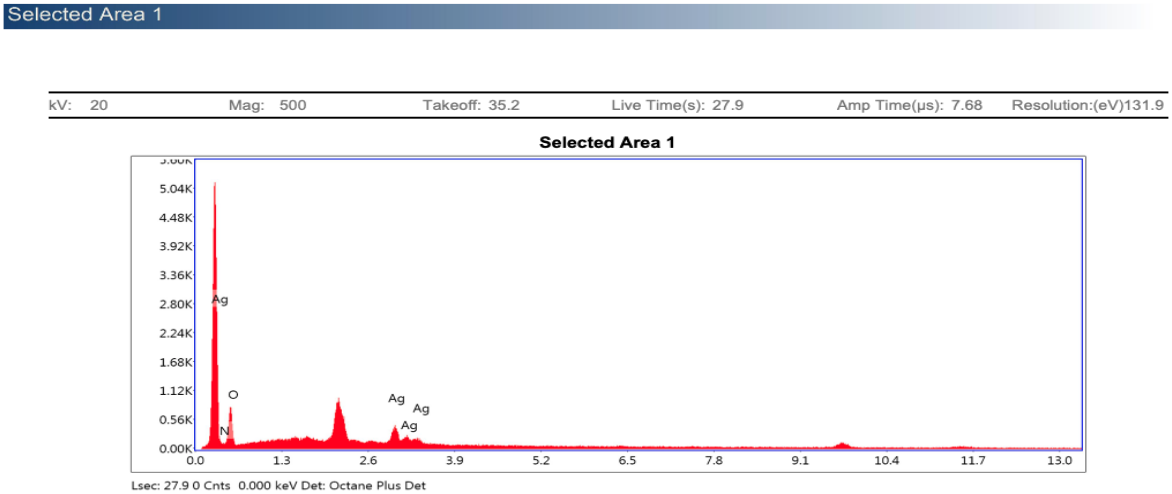
3.4. *A. hypogaea* Tohum ve Kabuğu ile Sentezlenen AgNP'lerin Antimikrobiyal Aktivite Sonuçları

Bu araştırma kapsamında yaş, çiğ ve kavrulmuş *Arachis hypogaea* tohumlarından ve kabuklarından sentezlenen 1mM, 2mM ve 3mM konsantrasyonlarındaki gümüş nanopartiküllerin (AgNP'ler) antimikrobiyal özellikleri çeşitli patojenik mikroorganizmalara karşı incelenmiştir. Sentezlenen AgNP'lerin antimikrobiyal etkilerine ilişkin inhibisyon bölgelerinin ortaya çıkan çapları, milimetre cinsinden ölçülen Tablo 2 ve 3'te sunulmuştur. Gümüş nanopartiküllerin (AgNP'ler) çeşitli mikroorganizmalara karşı antimikrobiyal etkinliği ile ilişkili bölge çapları incelendiğinde, Chromobacterium violaceum'un hem yaş hem de çiğ ve kavrulmuş tohumlardan sentezlenen AgNP'lere karşı en yüksek duyarlılığı sergilediği belirlendi. Ayrıca, üç farklı tohum türünden türetilen AgNP'lere en az duyarlılık gösteren mikroorganizmalar şunlardır: *K. pneumoniae*'ye karşı minimal aktivite sergileyen yaş yer fıstığından sentezlenen AgNP (YFAgNP); *Candida albicans*'a karşı etkisiz olan çiğ yer fıstığından sentezlenen AgNP (KFAgNP) ve Bacillus cereus'a karşı ihmal edilebilir aktivite sergileyen kavrulmuş fıstıktan sentezlenen AgNP (KFAgNP). Bununla birlikte, YFAgNP ile ilişkili antimikrobiyal aktivite istatistiksel olarak anlamlı bir azalma sağlamasa da ($P>0.05$), ÇFAgNP ve KFAgNP ile ilgili antimikrobiyal aktivite sonuçlarının belirli bölge çaplarında istatistiksel olarak anlamlı bir azalma kaydedildi ($P<0.05$).

Yaş, çiğ ve kavrulmuş yer fıstığı kabuğu kullanılarak elde edilen gümüş nanopartiküller (AgNP'ler), mikroorganizma *Chromobacterium violaceum*'a karşı en yüksek antimikrobiyal etkinliği sergiledi. Ayrıca, üç farklı fıstık kabuğundan sentezlenen AgNP'lere en az duyarlılık gösteren mikroorganizmalar şunları içerir: Yaş kabuklardan türetilen AgNP (YKAgNP) ve çiğ kabuklardan kaynaklanan AgNP (ÇKAgNP), *Candida albicans* kavrulmuş kabuklardan sentezlenen AgNP (KKAgNP) ile ilişkilendirildi ve *Salmonella typhimurium* ham kabuklardan üretilen AgNP (KKAgNP) ile ilişkilendirildi. Bununla birlikte; *A. hypogaea* kabukları ile sentezlenen tüm AgNP'lerin (YKAgNP, ÇKAgNP ve KKAgNP), *Chromobacterium violaceum* üzerindeki antimikrobiyal aktivitesi istatistiksel açıdan anlamlı artış göstermiştir ($P<0,05$).



Şekil 4. *A. hypogaea* tohumu ile sentezlenen AgNP'e ait eds görüntüsü.



eZAF Smart Quant Results

Element	Weight %	Atomic %	Net Int.	Error %	Kratio	Z	R	A	F
N K	0.02	0.03	0.04	99.99	0.00	1.1	0.94	0.44	1
O K	75.75	95.44	192.45	9.84	0.25	1.07	0.95	0.31	1
AgL	24.23	4.53	104.73	6.69	0.20	0.74	1.22	1.12	1.02

Şekil 5. *A. hypogaea* ile sentezlenen AgNP'e ait eds alan grafiği. EDS verilerinde tespit edilen element kompozisyonları, gümüşe (Ag) ait güçlü piklerin oluşu ile gümüş nanopartiküllerin varlığını destekleyici nitelik taşımaktadır.

Tablo 2. *Arachis hypogaea* tohumları ile sentezlenen AgNP'lerin antimikrobiyal aktivite zon çapları

Mikroorganizma Tür İsimleri	Gümüş Nanopartiküller (AgNP)									Kontrol		
	Yaş			Çiğ			Kavrulmuş			$AgNO_3$		
	1mM	2mM	3mM	1mM	2mM	3mM	1mM	2mM	3mM	1mM	2mM	3mM
A. hydrophila	9,4	9,8	10,6	9,8	9,8	10,2	---*	---*	8,6	9,8	9,8	10,2
B. cereus	9,2	10,2	12,2*	9,8	10,2	10,8	---*	---*	---*	9,8	10,2	10,8
B. subtilis	9,8	10,4	10,6	9,6	9,8	7,8	8,4	9,2	10,2	9,8	10,2	10,2
B. thuringiensis	12,2*	13,8*	13,8	11,8	11,8	12,8	8,2*	9,8	10,2*	11,8	11,8	12,8
C. albicans	10,6	11,8*	11,8*	---*	---*	---*	7,2*	7,6	8,2	9,2	9,6	9,8
C. parapsilosis	9,8	8,4	9,8	12,4*	12,6*	11,8	---*	7,4	7,8	7,4	8,2	9,4
C. tropicalis	10,8	11,8	12,2	11,8*	10,2	10,2	11,4	11,8	12,2	10,2	10,4	11,2
C. violaceum	17,2*	17,8*	17,8*	15,4*	15,7*	16,4*	12,8	14,2	15,8*	12,2	13,6	14,6
E. aerogenes	11,8	13,8*	12,6	10,4	11,2	11,8	6,8*	8,2*	8,4*	10,4	10,6	10,6
E. faecalis	11,8	13,4*	12,4	9,8	10,4	12,2*	8,4*	9,8	11,6	9,8	10,2	10,6
E. coli	11,6*	11,6	12,2	7,6	9,6	9,8	10,4*	10,6	12,2	8,4	10,4	11,8
K. pneumoniae	8,2	8,8	10,8	10,8	11,2*	12,2*	6,2	6,4*	8,2	8,2	9,2	9,6
L. monocytogenes	9,8	9,8	11,4	10,6	10,6	12,6*	---*	7,4*	8,2	9,4	9,6	10,2
P. mirabilis	11,8*	11,6	12,2*	11,8*	11,8	12,2	6,4*	6,4*	6,8*	9,4	10,4	10,4
P. vulgaris	10,6*	10,8*	11,8*	9,8	9,8	10,8*	6,4	6,6*	7,6	7,8	8,4	8,6
P. aeruginosa	10,2	10,4	12,2	9,2	9,4	10,2	7,2*	7,4*	7,6*	10,2	11,4	11,6
S. typhimurium	9,8	10,2	12,2*	8,4	8,4	9,8	6,2*	6,2*	6,6*	8,4	8,4	9,8
S. dysenteriae	10,8	11,2*	11,8	9,8	9,2	11,6	7,4	8,2	9,8	9,2	9,2	10,2
S. aureus (25923)	10,2*	10,4*	12,6*	8,4	7,8	7,8	---*	---*	---*	7,2	7,4	8,2
S. aureus (29213)	10,2*	11,4*	11,6*	8,4	8,8	10,6*	---*	---*	7,6	8,4	8,4	8,6
S. epidermidis	10,8	11,4	11,6	10,2	10,4	11,2	9,6	9,8	11,2	10,2	10,4	10,8
V. anguillarum	10,6*	12,2	12,8*	9,8	10,2	10,4	9,6	10,2	10,8	8,4	9,8	10,8

*= tespit edilen değerin kontrol grubuna göre istatistiksel açıdan anlamlı farklılık gösterdiğini ifade etmektedir (P<0,05), (---)= antimikrobiyal aktivite zonu gözlemlenmediğini ifade etmektedir.

Tablo 3. *Arachis hypogaea* kabukları ile sentezlenen AgNP'lerin antimikrobiyal aktivite zon çapları

Mikroorganizma Tür İsimleri	Gümüş Nanopartiküller (AgNP)									Kontrol		
	Yaş			Çiğ			Kavrulmuş			$AgNO_3$		
	1mM	2mM	3mM	1mM	2mM	3mM	1mM	2mM	3mM	1mM	2mM	3mM
A. hydrophila	7,4*	7,6*	8,2	9,4	9,8	10,2	8,2	10,2	10,4	9,8	9,8	10,2
B. cereus	8,4	8,8	9,4	8,2	8,4	8,6	10,4	11,4	11,4	9,8	10,2	10,8
B. subtilis	7,2*	7,6*	7,8*	11,4	11,6	11,8	11,8*	12,2	12,4	9,8	10,2	10,2
B. thuringiensis	11,8	12,2	14,2*	11,8	13,4	13,4	9,8	10,8	10,8	11,8	11,8	12,8
C. albicans	---*	---*	---*	---*	---*	8,2	10,4	10,6	10,8	9,2	9,6	9,8
C. parapsilosis	9,8*	10,4	11,2*	10,2	10,4	11,2	11,4*	11,6*	12,6*	7,4	8,2	9,4
C. tropicalis	9,2	9,4	9,8	8,4	8,8	9,4	11,2	12,2*	12,6	10,2	10,4	11,2
C. violaceum	16,4*	17,4*	17,8*	17,6*	17,8*	18,6*	15,6*	16,4*	16,8*	12,2	13,6	14,6
E. aerogenes	8,4*	8,8	8,8	8,2*	8,4*	8,8	9,8	10,2	10,6	10,4	10,6	10,6
E. faecalis	8,4	8,6	8,6*	9,8	10,2	10,2	9,8	10,2	10,2	9,8	10,2	10,6
E. coli	7,2	7,6*	7,8*	8,4	8,6	9,4	12,4*	12,8*	13,8*	8,4	10,4	11,8
K. pneumoniae	8,2	8,6	8,6	10,4	10,8	12,2	8,2	9,8	10,6	8,2	9,2	9,6
L. monocytogenes	9,2	9,6	10,2	10,2	10,4	11,4	11,8*	12,2*	12,4	9,4	9,6	10,2
P. mirabilis	7,8	8,2*	8,4	9,8	10,4	10,8	10,2	10,6	11,8	9,4	10,4	10,4
P. vulgaris	9,2	9,4	10,2*	9,4	10,2	10,4	11,6*	11,8*	12,4*	7,8	8,4	8,6
P. aeruginosa	8,2	8,4*	9,2	10,8	11,4	11,8	9,8	10,4	10,6	10,2	11,4	11,6
S. typhimurium	---*	8,4	8,8	10,2	10,6	10,6	7,8	8,2	8,4	8,4	8,4	9,8
S. dysenteriae	8,2	8,8	10,6	9,8	10,2	10,4	9,6	10,2	10,4	9,2	9,2	10,2
S. aureus (25923)	7,2	7,4	7,8	8,4	8,6	8,8	10,2*	11,4*	11,8*	7,2	7,4	8,2
S. aureus (29213)	8,8	9,2	9,4	10,2	10,2	10,8	10,2	10,6*	11,4*	8,4	8,4	8,6
S. epidermidis	8,6	9,2	10,2	11,6	12,2	13,8	10,2	10,4	11,2	10,2	10,4	10,8
V. anguillarum	9,8	10,2	10,6	8,2	8,6	9,2	11,2*	11,4	12,2	8,4	9,8	10,8

*= tespit edilen değerin kontrol grubuna göre istatistiksel açıdan anlamlı farklılık gösterdiğini ifade etmektedir (P<0,05), (---)= antimikrobiyal aktivite zonu gözlemlenmediğini ifade etmektedir.

YKAgNP ve ÇKAgNP'e ait antimikrobiyal aktivite sonuçlarında ise istatistiksel açıdan anlamlı düşüş tespit edilmesine karşın (P<0,05), KKAgNP'e ait antimikrobiyal aktivite sonuçlarında istatistiksel açıdan anlamlı bir düşüş tespit edilmemiştir (P>0,05).

Değişen konsantrasyonlarda (1mM, 2mM ve 3mM) sentezlenmiş gümüş nanopartiküllerin (AgNP) antimikrobiyal aktivite bölgelerinin çapları üzerindeki etkisi Faktöriyel ANOVA istatistiksel analizi kullanılarak değerlendirildi. Tüm AgNP konsantrasyonlarının

birbirleri arasında istatistiksel olarak anlamlı farklılıklar gösterdiği tespit edildi (P<0.05). Gözlenen bu değer, uygulanan her bir AgNP dozunun birbirine göre farklı etkiler sergilediğini göstermiştir. Bununla birlikte, Faktöryal ANOVA istatistiksel analizi ile AgNP'lerin sentezinde kullanılan çeşitli malzemelerin (yaş, çiğ, kavrulmuş yer fıstığı veya kabuklar dahil) mikroorganizmalar üzerinde farklı inhibitör etkiler yarattığı tespit edildi (P<0.05). Aynı istatistiksel metodoloji ile tanımlanan ek bir sonuç, çeşitli mikroorganizma sınıflandırmalarının antimikrobiyal aktivite bölgesi çaplarının gelişiminde istatistiksel olarak anlamlı bir varyasyon yarattığını göstermektedir (P<0.05).

Kontrol grubu olarak kullanılan çeşitli $AgNO_3$ konsantrasyonlarını ve bunların mikrobiyal popülasyonlar üzerindeki inhibitör etkilerini karşılaştıran istatistiksel bir analiz, Duncan testi kullanılarak yapılmıştır (Tablo 4). İstatistiksel analizden elde edilen bulgulara göre, antimikrobiyal aktivitede en yüksek etkinliği gösteren $AgNO_3$ dozu 3mM dozajıydı. Tersine, mikrobiyal organizmalar üzerinde minimal inhibitör etki sergileyen dozaj, 1mM dozu olarak tanımlandı. Duncan testi sonucuna göre farklı gruplara ayrılan her bir dozajın tanımlanması, hiçbir dozajın diğerinin yerine geçmek için uygun olmadığını ortaya koydu.

Tablo 4. $AgNO_3$'lara ait farklı dozların Duncan çoklu karşılaştırma testi tablosu

AgNP Dozları	Gruplar		
	A	B	C
1mM			9,9945
2mM		10,3001	
3mM	10,8678		

*Tabloda verilmiş olan değerler milimetre (mm) cinsinden zon çaplarını temsil etmektedir.

Tablo 5. Farklı materyaller ile sentezlenen AgNP gruplarının Duncan çoklu karşılaştırma testi tablosu

Uygulama Materyali	Gruplar		
	A	B	C
YFAgNP	11,5031		
KKAgNP		11,1031	
ÇFAgNP		10,5888	
ÇKAgNP		10,5178	
YKAgNP			9,4598
KFAgNP			9,1523

*Tabloda verilmiş olan değerler mm cinsinden zon çaplarını temsil etmektedir.

Yeşil yöntemlerle sentezlenen tüm gümüş nanopartiküller (AgNP'ler) için mikroorganizmalar üzerindeki inhibitör etkilerin istatistiksel bir değerlendirmesi (1mM, 2mM ve 3mM AgNP'ler ilgili grupları içinde eşzamanlı olarak değerlendirildi) Duncan testi kullanılarak gerçekleştirilmiştir (Tablo 5). Gümüş nanopartiküllerin (AgNP'ler) analizi yapılırken, antimikrobiyal etkinlik açısından en etkili olanın (en yüksek derecede inhibisyon sergileyen) yaş yer fıstığı kullanılarak sentezlenen YFAgNP olduğu gözlenmiştir. Bu bağlamda, mevcut araştırmanın gösterdiği genel etki hem üstün performans açısından hem de Duncan testi tarafından belirlendiği gibi toplu olarak diğer sentezlenmiş AgNP'lerden farklıdır. Bununla birlikte, mikroorganizmalara karşı antimikrobiyal etkinlik konusunda minimum etki sergileyen gümüş nanopartiküller (AgNP'ler), sırasıyla yaş kabuk ve kavrulmuş yer fıstığı kullanılarak sentezlenen YKAgNP ve KFAgNP'dir. İstatistiksel değerlendirmenin sonucunda, YKAgNP ve KFAgNP'nin karşılaştırılabilir antimikrobiyal özellikler sergilediği ve böylece fonksiyonel muadilleri olarak potansiyel değiştirilebilirliklerini gösterdiği belirlenmiştir. Tablo 5'te tanımlanan alternatif gümüş nanopartiküllerin (AgNP'ler) incelenmesi üzerine, kavrulmuş kabuk, çiğ yer fıstığı ve yaş kabuk ile sentezlenen AgNP'ler (KKAgNP, ÇFAgNP ve ÇKAgNP) arasında istatistiksel olarak anlamlı bir benzerlik gözlendi. Duncan testinden elde edilen bulgulara dayanarak, bu üç AgNP'nin sergilediği antimikrobiyal özellikler karşılaştırılabilir ve etkili bir şekilde birbirinin yerine geçebilir.

3.5. *A. hypogaea* Tohum ve Kabuğu ile Sentezlenen AgNP'lerin Minimal İnhibisyon Konsantrasyonları (MİK)

Yapılan çalışma kapsamında; antimikrobiyal aktivitesi tespit edilen AgNP'lere ait minimal inhibisyon konsantrasyonları Tablo 6 ve 7'de belirtilmiştir. MİK tablosunda bulunan değerler; AgNP'lerin dilüsyon metodu uygulanarak gerçekleştirilmiş seyreltilme seviyelerini göstermektedir. AgNP'lerin minimal inhibisyon konsantrasyonları göz önüne alındığında; sentezlenen AgNP'lerin en düşük doz ile üzerinde en fazla etkiyi gösterdikleri mikroorganizma türü *C. violaceum*'dur. Bununla birlikte; tüm AgNP'ler göz önünde bulundurulduğunda en düşük doz ile en fazla inhibisyon etkisine sahip olan AgNP'ler, 3mM'lık AgNP'lerdir. *A. hypogaea* tohumlarıyla sentezlenen AgNP'lerin minimal inhibisyon konsantrasyonları, *A. hypogaea* kabuklarıyla sentezlenen AgNP'lere göre daha düşüktür. Bu durum, tohumlar ile sentezlenen AgNP'lerin, kabuklar ile sentezlenen AgNP'lere göre daha yüksek inhibisyon etkisi gösterdiğini ifade etmektedir.

3.6. Anti-Quorum Sensing Analizi Sonuçları

Anti-Quorum Sensing aktivite (Anti-QS) iki ayrı yöntem ile analiz edilmiştir. Bu iki yöntemden birincisi olan agar difüzyon yönteminde *C. violaceum* bakterisi bulunan plaklarda (Şekil 6), AgNP'lerin zon çapları hesaplanmıştır (Tablo 8). İkinci yöntemde ise UV-spektroskopi kullanılarak Anti-QS çalışmalarında indikatör olarak kullanılan ve *C. violaceum* bakterisi tarafından üretilen "violacein" pigmenti analiz edilmiştir. *C. violaceum* bakterisinde pigmentasyonda gözlenen azalma, uygulanan maddenin (AgNP) Quorum-sensing (QS) mekanizmaları üzerinde inhibitör bir etki yarattığını göstermektedir.



Şekil 6. *A. hypogaea* ile sentezlenen AgNP'lerin anti-quorum sensing aktivitelerine ait inhibisyon zonları.

Tablo 6. *A. hypogaea* tohumları ile sentezlenen AgNP'lerin MİK tablosu

Mikroorganizma Tür İsimleri	Gümüş Nanopartiküller (AgNP)									$AgNO_3$		
	Yaş			Çiğ			Kavrulmuş					
	1mM	2mM	3mM	1mM	2mM	3mM	1mM	2mM	3mM	1mM	2mM	3mM
A. hydrophila	1,25	0,625	0,078	2,5	2,5	0,156	---	---	2,5	2,5	2,5	1,25
B. cereus	5,0	2,5	0,156	5,0	2,5	0,156	---	---	---	5,0	5,0	2,5
B. subtilis	2,5	1,25	0,156	5,0	2,5	0,156	5,0	2,5	0,625	5,0	5,0	1,25
B. thuringiensis	0,078	0,039	0,039	1,25	0,312	0,039	2,5	2,5	1,25	2,5	2,5	0,625
C. albicans	5,0	1,25	0,312	---	---	---	5,0	5,0	2,5	5,0	5,0	2,5
C. parapsilosis	2,5	2,5	0,312	5,0	2,5	0,156	---	5,0	2,5	2,5	1,25	0,156
C. tropicalis	5,0	2,5	0,625	5,0	5,0	0,625	2,5	0,625	0,625	2,5	2,5	0,312
C. violaceum	0,312	0,078	0,039	0,625	0,312	0,039	0,625	0,625	0,312	0,625	0,312	0,312
E. aerogenes	2,5	1,25	0,156	2,5	2,5	0,156	5,0	2,5	1,25	2,5	2,5	0,312
E. faecalis	5,0	0,625	0,312	5,0	5,0	2,5	2,5	1,25	1,25	5,0	5,0	2,5
E. coli	2,5	2,5	0,156	2,5	2,5	0,312	1,25	0,312	0,156	5,0	2,5	0,312
K. pneumoniae	5,0	1,25	0,312	2,5	2,5	0,312	2,5	2,5	2,5	5,0	5,0	2,5
L. monocytogenes	2,5	1,25	0,625	5,0	5,0	0,156	---	5,0	2,5	5,0	5,0	2,5
P. mirabilis	5,0	5,0	0,625	5,0	5,0	1,25	5,0	5,0	2,5	5,0	2,5	2,5
P. vulgaris	5,0	5,0	1,25	5,0	5,0	0,625	5,0	2,5	1,25	5,0	5,0	2,5
P. aeruginosa	2,5	1,25	0,312	5,0	5,0	0,156	2,5	1,25	1,25	5,0	2,5	0,625
S. typhimurium	2,5	1,25	2,5	5,0	5,0	0,156	5,0	5,0	2,5	5,0	5,0	0,625
S. dysenteriae	5,0	1,25	0,312	5,0	2,5	0,156	2,5	0,625	0,625	5,0	5,0	2,5
S. aureus (25923)	2,5	2,5	0,625	2,5	2,5	0,312	---	---	---	2,5	1,25	1,25
S. aureus (29213)	2,5	1,25	0,312	2,5	2,5	0,156	---	---	1,25	2,5	2,5	1,25
S. epidermidis	0,625	0,156	0,156	2,5	1,25	0,078	0,625	0,625	0,312	2,5	0,625	0,625
V. anguillarum	5,0	2,5	1,25	5,0	2,5	0,312	2,5	1,25	0,312	5,0	5,0	1,25

(---)= antimikrobiyal aktivite gözlemlenememesi nedeniyle MİK analizi yapılmadığını ifade etmektedir.

Tablo 7. *A. hypogaea* kabukları ile sentezlenen AgNP'lerin MİK tablosu

Mikroorganizma Tür İsimleri	Gümüş Nanopartiküller (AgNP)									$AgNO_3$		
	Yaş			Çiğ			Kavrulmuş					
	1mM	2mM	3mM	1mM	2mM	3mM	1mM	2mM	3mM	1mM	2mM	3mM
A. hydrophila	2,5	1,25	1,25	2,5	2,5	2,5	2,5	2,5	1,25	2,5	2,5	1,25
B. cereus	2,5	1,25	1,25	2,5	2,5	1,25	5	2,5	2,5	5,0	5,0	2,5
B. subtilis	5	2,5	2,5	2,5	1,25	1,25	5	2,5	2,5	5,0	5,0	1,25
B. thuringiensis	0,312	0,156	0,156	0,156	0,156	0,156	0,625	0,312	0,312	2,5	2,5	0,625
C. albicans	---	---	---	---	---	2,5	5	5	2,5	5,0	5,0	2,5
C. parapsilosis	2,5	2,5	1,25	5	5	2,5	2,5	2,5	2,5	2,5	1,25	0,156
C. tropicalis	5	2,5	2,5	2,5	2,5	2,5	5	5	2,5	2,5	2,5	0,312
C. violaceum	0,156	0,156	0,156	0,312	0,156	0,156	0,312	0,312	0,156	0,625	0,312	0,312
E. aerogenes	5	2,5	1,25	5	2,5	1,25	2,5	2,5	2,5	2,5	2,5	0,312
E. faecalis	5	1,25	0,625	2,5	2,5	1,25	5	2,5	1,25	5,0	5,0	2,5
E. coli	5	2,5	2,5	2,5	2,5	2,5	5	5	2,5	5,0	2,5	0,312
K. pneumoniae	5	2,5	1,25	5	5	2,5	5	2,5	2,5	5,0	5,0	2,5
L. monocytogenes	2,5	2,5	2,5	1,25	1,25	1,25	2,5	2,5	2,5	5,0	5,0	2,5
P. mirabilis	5	5	2,5	5	2,5	2,5	5	5	2,5	5,0	2,5	2,5
P. vulgaris	5	2,5	2,5	2,5	1,25	1,25	5	5	2,5	5,0	5,0	2,5
P. aeruginosa	2,5	2,5	1,25	5	2,5	2,5	2,5	2,5	2,5	5,0	2,5	0,625
S. typhimurium	5	5	2,5	5	5	2,5	5	2,5	2,5	5,0	5,0	0,625
S. dysenteriae	2,5	1,25	1,25	5	2,5	1,25	2,5	2,5	2,5	5,0	5,0	2,5
S. aureus (25923)	5	1,25	1,25	2,5	2,5	1,25	2,5	2,5	2,5	2,5	1,25	1,25
S. aureus (29213)	2,5	1,25	1,25	5	5	1,25	2,5	2,5	2,5	2,5	2,5	1,25
S. epidermidis	2,5	1,25	1,25	5	1,25	1,25	2,5	2,5	2,5	2,5	0,625	0,625
V. anguillarum	5	1,25	1,25	2,5	2,5	1,25	5	2,5	2,5	5,0	5,0	1,25

(---)= antimikrobiyal aktivite gözlemlenememesi nedeniyle MİK analizi yapılmadığını ifade etmektedir.

Tablo 8. *A. hypogaea* ile sentezlenen AgNP'lerin anti-quorum sensing aktivitelerine ait zon çapları

Konsantrasyon	Gümüş Nanopartiküller (AgNP)					
	Yaş		Çiğ		Kavrulmuş	
	Fıstık	Kabuk	Fıstık	Kabuk	Fıstık	Kabuk
5 µl/ml	19,8	17,8	19,6	18,6	19,6	16,4*
2,5 µl/ml	19,2	16,8*	18,6	16,8*	19,4	14,8*
1,25 µl/ml	18,8	16,4	18,4	14,6*	18,4	14,4*
0,625 µl/ml	18,8	13,6*	18,2	12,4*	17,8	12,6*

*= kabuk ile yeşil sentezi gerçekleştirilmiş AgNP'lerin, tohum ile yeşil sentezi gerçekleştirilmiş AgNP'lere göre istatistiksel açıdan anlamlı düşüşü göstermektedir (P<0,05).

Bu bağlamda, sentezlenen tüm gümüş nanopartiküllerin (AgNP'ler), anti-quorum algılama (anti-QS) aktivitesinin değerlendirilmesi için kullanılan agar difüzyon metodolojisinde etkinlik sergilediği gösterilmiştir. Gözlemlenen inhibisyon bölgeleri, *C. violaceum* bakterilerinin pigmentleri sentezleyemediği alanlar olarak kabul edilir. Sentezlenen gümüş nanopartiküller (AgNP'ler) arasında, tohum aracılı yöntemle sentezlenenler en belirgin anti-quorum algılama (QS) aktivitesini sergiledi. Bununla birlikte, daha koyu bir renk tonu ile temsil edilen inhibisyon bölgeleri, eşdeğer konsantrasyonlarda diğer toplu nanopartikül formülasyonları tarafından yürütülen anti-quorum algılama aktiviteleri ile yan yana getirildiğinde istatistiksel olarak anlamlı bir azalma sergiledi (P<0.05). AHL oluşumunu engelleyerek *Chromobacterium violaceum*'da açil homoserin lakton (AHL) sentezini etkili bir şekilde engelleyen ve sonuç olarak en belirgin anti-quorum algılama (anti-QS) aktivitesini sergileyen gümüş nanopartiküller (AgNP'ler), *Arachis hypogaea* bitkisinden türetilen yaş tohumlar kullanılarak üretilen AgNP'lerdir.

4. Tartışma

Yapılan çalışma kapsamında; yaş, çiğ ve kavrulmuş *A. hypogaea* tohum ve kabukları ile yeşil sentezi gerçekleştirilen AgNP'lerin UV-Vis spektrumları tespit edilmiştir. Bilimsel literatürdeki çalışmalarda, *A. hypogaea* kullanılarak sentezlenen gümüş nanopartiküllerin UV-Vis spektrumlarında gözlemlenen yüzey plazmon rezonansı 420 nm'lik dalga boyunda tanımlanmıştır (Padmapriya vd., 2020). *A. hypogaea*'nın tohum ve kabukları kullanılarak yeşil sentez yoluyla üretilen gümüş nanopartiküllerin (AgNP'ler) UV-Vis spektrumları, sırasıyla 485 nm ve 450 nm'de tepe dalga boyu sergilemiştir. Bu bağlamda, *Arachis hypogaea* kullanılan yeşil sentez yaklaşımında, gümüş nanopartiküllerin (AgNP) sentezine odaklanan önceki yıllarda yapılan araştırmalarla bağlantılı olarak, ultraviyole görünür (UV-Vis) spektral değerlerinin 350 nm ila 500 nm aralığında olduğu belirlendi (Saha vd., 2016; Sankaranarayanan vd., 2016). Bununla birlikte, gümüş nanopartiküllerin (AgNP'ler) yeşil sentezine ilişkin UV-Vis spektral grafiklerinde çeşitli parametrelerin

tanımlanması, kullanılan malzemelerin doğasına, gümüş nitrat konsantrasyonuna (AgNO3) ve ayrıca sıcaklık ve pH seviyelerindeki dalgalanmalara bağlı olarak değişebilir (Jagtap ve Bapat, 2013; Yang ve Li, 2013).

Arachis hypogaea tohumları ve kabukları kullanılarak üretilen gümüş nanopartiküllerin (AgNP'ler) bir dizi bakteri türüne karşı antimikrobiyal özellikleri sistematik olarak araştırılmıştır. Agar well difüzyon tekniği ile yürütülen antimikrobiyal etkinliğin analizi, yeşil metodolojilerle sentezlenen AgNP'lerin bakterilere karşı önemli antimikrobiyal aktivite sergilediğini ortaya koydu. *Ficus racemosa* bitkisini kullanan çevre dostu yöntemlerle sentezlenen AgNP'lerle ilişkili antimikrobiyal aktivite bölgelerinin maksimum çapları, sırasıyla *E. coli, B. subtilis, S. aureus ve P. aeruginosa* için 13 mm, 12 mm, 12 mm ve 9 mm'de ölçülmüştür (Garole vd., 2018). Araştırmamıza göre, gümüş nanopartiküller (AgNP'ler) için gözlemlenen antimikrobiyal aktivite bölgelerinin maksimum çapları *Escherichia coli* için 13,8 mm, *Bacillus subtilis* için 12,4 mm, *Staphylococcus aureus* için 12,6 mm ve *Pseudomonas aeruginosa* için 12,2 mm'dir. *Escherichia coli* ve *Staphylococcus aureus* gibi patojenik bakteriler üzerinde inhibitör etkiler sergileyen AgNP'lerin çalışma kapsamında diğer 20 bakteri suşu üzerinde etkisi olduğu belirlendi. Bilimsel literatür içindeki karşılaştırılabilir araştırmalar, bu bakteri taksonlarıyla ilişkili antimikrobiyal özellikleri benzer şekilde tanımlamıştır ve araştırmamızın bulguları, literatürde mevcut verilerle desteklenen antimikrobiyal aktivite olduğunu göstermiştir (Gemmell vd., 2006; Chopra, 2007). Gümüş nanopartiküllerin (AgNP'ler) belirli bakteri taksonlarına karşı sergilediği belirgin antimikrobiyal etkinliğe rağmen, diğer taksonlarda gözlemlenen azalmış antimikrobiyal etkinlik, bu tür değişkenliğin, özellikle de membran mimarileri içindeki peptidoglikan tabakasının kalınlığı ile ilgili olarak, bakteri türleri arasındaki yapısal tutarsızlıklara atfedilebileceğini ima eder (Rai vd., 2009). Başka bir araştırma, *Arachis hypogaea*'nın tohumlarından ve kabuklarından üretilen AgNP'lerin olası etki mekanizmalarını aydınlatmak için gümüş nanopartiküllerin (AgNP'ler) anti-quorum algılama (anti-QS) yeteneklerinin tanımlanmasına odaklanmaktadır. Şimdiye kadar yapılan çok sayıda araştırma, çeşitli bitkiler ve deniz algleri tarafından sergilenen anti-quorum algılama özelliklerinin aydınlatılmasına odaklanmıştır (Gao vd., 2003). Araştırmada açıklanan sonuçlar, *A. hypogaea*'nın yeşil tohumları ve kabukları kullanılarak üretilen AgNP'lerin patojen bakteri suşlarına karşı kapsamlı ve çeşitli anti-quorum algılama (QS) etkinliği sergilediğini göstermektedir. Bu bağlamda, en önemli anti-quorum algılama aktivitesini sergileyen numune, fıstık tohumu kullanılarak üretilen gümüş nanopartiküllerdir. Ayrıca, değişen konsantrasyonlarda uygulanan numunelerde optimal dozajın 5 µl/ml olduğu gösterilmiştir. Gümüş nanopartiküllerin (AgNP'ler) C. violaceum suşunda violacein pigmentinin biyosentezini inhibe ettiği gözlemlenmiştir (Adonizio vd., 2006). AgNP'lerin pigmentasyonundaki bu kısıtlama, *C. violaceum* arasında karşılıklı iletişim için bir ortam görevi gören açil homoserin lakton (AHL) sinyal molekülünün sentezinin baskılanması nedeniyle ortaya çıkmıştır. Bilimsel literatürde belgelenen araştırmaların kapsamlı bir incelemesi yapıldıktan sonra, flora veya mikrobiyal varlıklar dahil olmak üzere çeşitli biyolojik örneklerden türetilen yeşil sentezlenmiş AgNP'lerin, anti-quorum algılama (Anti-QS) aktivitesi ile ilgili olarak önemli etkinlik sergilediği anlaşılmıştır. Örnek olarak, *Carum copticum* bitkisi kullanılarak üretilen gümüş nanopartiküller (AgNP'ler), *C. violaceum* suşuna karşı anti quorum sensing (Anti-QS) etkinlikleri açısından değerlendirilmeye tabi tutuldu. (Qais vd., 2020). Araştırmanın bir sonucu olarak, violacein pigmentinin inhibisyonunun %83,2 olduğu belirlendi. Araştırmamızda, *A. hypogaea* tohumlarını kullanan yeşil bir yaklaşımla sentezlenen AgNP'ler tarafından violacein inhibisyon oranının mevcut literatürde bildirilen oranı aştığı gözlemlenmiştir. Violacein pigmentinin inhibisyonunun 5 µl/ml konsantrasyonda YFAgNP için %86,74; CFAgNP için %84,83 ve KFAgNP için %84,97 olduğu gözlenmiştir. Literatürde belgelenen çok sayıda quorum sensing inhibisyon araştırmasından elde edilen inhibisyon oranlarına ilişkin sonuçlar, araştırmamızda gözlemlenen inhibisyon oranlarından daha düşük değerler sergiler (Salini ve Pandian, 2015; Anju ve Sarada, 2016).

5. Sonuç

Bu araştırma, önemli besin özellikleriyle tanınan *A. hypogaea*'nın tohumları ve kabukları ile yeşil sentez yaklaşımı kullanılarak elde edilen gümüş nanopartiküllerin önemini aydınlatmıştır. Nanomateryaller çağdaş toplumda ve bilimsel alanda çok önemli bir rol oynamaktadır. Halen, patojen mikroorganizmaların antibiyotik tedavilerine direncinde kayda değer bir artış vardır. Bu durum, geleneksel antibiyotiklerin yerine alternatif materyallerin geliştirilmesini gerektirir. Araştırmada analiz edilen veriler; *A. hypogaea* tohumları ve kabukları kullanılarak sentezlenen gümüş nanopartiküllerin önemli antimikrobiyal özelliklere sahip olduğunu ileri sürmüştür. Bununla birlikte bulgularımız, bu AgNP'lerin yalnızca mikroorganizmalar üzerinde ölümcül bir etki göstermekle kalmayıp, aynı zamanda bakterilerin toplu olarak direnç geliştirme kapasitesini engellediğini ve direnç için gerekli strese bağlı mekanizmaları inhibe ettiğini göstermiştir. Gümüş nanopartiküller toksik olmayan özellikler sergiler, uygun maliyetlidir, çevresel olarak sürdürülebilirdir ve bakteriyel patojenlere karşı önemli etkinlik gösterir. Bu nedenle AgNP'ler gelecekteki antimikrobiyal uygulamalar için umut verici adaylar olarak konumlandırılır. Küresel olarak yaygın olarak tüketilen yer fıstığının belirli miktarlarda alındığında sağlık için faydalı olduğu ve ayrıca fıstık tohumları ile kabukları üzerinde nanomalzeme tekniklerinin uygulanmasıyla ilaç sektörünün canlı organizmalar için çeşitli avantajlar sağlayabilecek malzemeler elde edebileceği öne sürülmektedir.

Katkı Oranı Beyanı

Yazarın katkı yüzdeleri aşağıda verilmiştir. Yazar makaleyi incelemiş ve onaylamıştır.

	T.A.
K	100
T	100
Y	100
VTI	100
VAY	100
KT	100
YZ	100
KI	100
GR	100
PY	100
FA	100

K= kavram, T= tasarım, Y= yönetim, VTI= veri toplama ve/veya işleme, VAY= veri analizi ve/veya yorumlama, KT= kaynak tarama, YZ= Yazım, KI= kritik inceleme, GR= gönderim ve revizyon, PY= proje yönetimi, FA= fon alımı.

Çatışma Beyanı

Yazar bu çalışmada hiçbir çıkar ilişkisi olmadığını beyan etmektedir.

Etik Onay Beyanı

Bu araştırmada hayvanlar ve insanlar üzerinde herhangi bir çalışma yapılmadığı için etik kurul onayı alınmamıştır.

Kaynaklar

Adonizio AL, Downum K, Bennett BC, Mathee K. 2006. Anti-quorum sensing activity of medicinal plants in southern Florida. J Ethnopharmacol, 105(3): 427-435.

Anju S, Sarada J. 2016. Quorum sensing inhibiting activity of silver nanoparticles synthesized by Bacillus isolate. Int J Pharm Biol Sci, 6: 47-53.

Chopra I. 2007. The increasing use of silver-based products as antimicrobial agents: a useful development or a cause for concern? J Antimicrob Chemother, 59: 587-590.

Gao M, Teplitski M, Robinson JB, Bauer WD. 2003. Production of substances by Medicago truncatula that affect bacterial quorum sensing. Amer Phytopathol Soc, 16: 827-834.

Garole VJ, Garole DJ, Tetgure SR, Choudhary BC, Borse AU. 2018. Biosynthesis of silver nanoparticles using ficus racemosa latex and ıts antimicrobial activity. World J Pharmaceut Res, 2018: 1385-1400.

Gemmell CG, Edwards DI, Frainse AP. 2006. Guidelines for the prophylaxis and treatment of methicillin-resistant Staphylococcus aureus (MRSA) infections in the UK. J Antimicrob Chemother, 57: 589-608.

Horikoshi S, Serpone N. 2013. Introduction to nanoparticles. In: Horikoshi S, Serpone N, editors. Microwaves in nanoparticle synthesis: Fundamentals and applications. Wiley-VCH Verlag GmbH Co, Weinheim, Germany, pp: 57.

Isanga J, Zhang GN. 2007. Biologically active components and nutraceuticals in peanuts and related products: Review. Food Rev Int, 2007: 123-140.

Jagtap UB, Bapat VA. 2013. Green synthesis of silver nanoparticles using Artocarpus heterophyllus Lam. seed extract and its antibacterial activity, Ind Crop Prod, 46: 132.

Kim JA, Åberg C, de Cárcer G, Malumbres M, Salvati A, Dawson KA. 2013. Low dose of amino-modified nanoparticles induces cell cycle arrest. ACS Nano, 9: 7483-7494.

Kumar D, Kumari J, Pakrashi S, Dalai S, Raichur AM, Raichur AM, Sastry TP, Mandal AB, Chandrasekaran N, Mukherjee A. 2014. Qualitative toxicity assessment of silver nanoparticles on the fresh water bacterial isolates and consortium at low level of exposure concentration. Ecotoxicol Environ Safety, 108: 152-160.

Liu J, Wang Z, Liu FD, Kane AB, Hurt RH. 2012. Chemical transformations of nanosilver in biological environments. ACS Nano, 6: 9887-9899.

Lopes RM, Agostini-Costa TS, Gimenes MA, Silveira D. 2011. Chemical composition and biological activities of Arachis species. J Agri Food Chem, 59: 4321-4330.

Padmapriya G, Muthukumaravel A, Ashok K, Senthil J, Babu M. 2020. Antimicrobial activity of green synthesized silver nanoparticles room sprayer from *Arachis hypogaea* root nodules. Eur J Molec Clin Medic, 2: 2639-2646.

Qais FA, Shafiq A, Ahmad I, Husain F. 2020. Green synthesis of silver nanoparticles using Carum copticum: Assessment of its quorum sensing and biofilm inhibitory potential against Gram negative bacterial pathogens, Microb Pathogenesis, 144: 104172.

Rai M, Yadav A, Gade A. 2009. Silver nanoparticles as a new generation of antimicrobials. Biot Adv, 27: 76-83.

Rodriguez A, Rueksomtawin Kildegaard K, Li M, Borodina I, Nielsen J, Nielsen J. 2015. Establishment of a yeast platform strain for production of p-coumaric acid through metabolic engineering of aromatic amino acid biosynthesis. Metabolic Eng, 31: 181-188.

Saha N, Trivedi P, Gupta SD. 2016. Surface plasmon resonance (SPR) based optimization of biosynthesis of silver nanoparticles from rhizome extract of curculigo orchioides gaertn and its antioxidant potential. J Clust Sci, 27: 1893-1912.

Salini R, Pandian SK. 2015. Interference of quorum sensing in urinary pathogen Serratia marcescens by Anethum graveolens. Pathog Dis, 73(6): ffv038.

Sankaranarayanan A, Govindarasu M, Gopalu K, Shine K, Naiyf S, Jamal M, Denis K. 2016. Green synthesis of silver nanoparticles using *Arachis hypogaea* (ground nut) Root extract for antibacterial and clinical applications. J Clust Sci, 28: 995-1008.

Singh R, Shedbalkar UU, Wadhwani SA, Chopade BA. 2015. Bacteriagenic silver nanoparticles: synthesis, mechanism, and applications. Appl Microbiol Biotechnol, 99: 4579-4593.

Yang N, Li WH. 2013. Mango peel extract mediated novel route for synthesis of silver nanoparticles and antibacterial application of silver nanoparticles loaded onto non-woven fabrics, Ind Crop Prod, 48: 81.

Zhang SB, Lu QY, Yang H, Li Y, Wang S. 2011. Aqueous enzymatic extraction of oil and protein hydrolysates from roasted peanut seeds. J Amer Oil Chem Soc, 88: 727-732.

Black Sea Journal of Engineering and Science
doi: 10.34248/bsengineering.1593424

Open Access Journal
e-ISSN: 2619 - 8991

Research Article
Volume 8 - Issue 2: 310-314 / March 2025

EFFECT OF ADDITION OF PURE TITANIUM POWDER ON MECHANICAL PROPERTIES IN ROTARY FRICTION WELDING

Mehmet Erbil ÖZCAN[1]*

[1]*Fırat University, Faculty of Engineering, Department of Mechanical Engineering, 23200, Elazig, Türkiye*

Abstract: Rotary friction welding, which is a type of friction welding method, which is used as an alternative to traditional welding methods and has many advantages over traditional methods, has become a very popular method in the last twenty years. In this study, shafts with and without powder reinforcement were welded on a conventional lathe with rotary friction welding, tensile tests and temperature analyses were performed and the results were examined. Holes of variable diameters were drilled into the center of the shafts obtained from aluminum 6061 material and pure titanium powder was added, then pressed and sintered. The prepared shafts were welded with rotary friction welding method in appropriate combinations, and according to the results obtained, while the adhesion properties at constant speed were worse as the amount and volume of powder increased, the maximum temperature value obtained during welding increased as the volume of powder increased.

Keywords: Friction welding, Aluminum, Tensile test, Temperature analysis

***Corresponding author: Fırat University, Faculty of Engineering, Department of Mechanical Engineering, 23200, Elazig, Türkiye**
E mail: meozcan@firat.edu.tr (M. E. ÖZCAN)
Mehmet Erbil ÖZCAN https://orcid.org/0000-0003-1641-8279

Received: November 29, 2024
Accepted: January 07, 2025
Published: March 15, 2025

Cite as: Özcan ME. 2025. Effect of addition of pure titanium powder on mechanical properties in rotary friction welding. BSJ Eng Sci, 8(2): 310-314.

1. Introduction

In today's technology, the welding process of metallic materials is of greater importance. Considering that traditional joining methods are inadequate and have many negative aspects, it is seen that the tendency towards new solid state joining methods is increasing. One of these solid state joining methods, rotary friction welding (RFW), is a solid state joining process that can be used to join alloys that are not identical, unlike traditional welding methods. It is based on the principle that surfaces interact when one surface moves relative to another.

For friction welding, the rotational, or mechanical, motion of the method generates heat and causes the materials to be joined to soften and become viscous. In the softened state, the mechanical motion of the process mixes the materials to form a bond. When the rotational speed reaches a certain level, the opposing parts are brought into contact with each other. After this initial moment of contact, an axial pressure is applied so that the parts can reach the desired temperature and the welding process can begin. At this stage, the two materials pass from the heated area to a semi-molten state, allowing the materials to mix and adhere to each other. In order to obtain the desired temperature, the speed of the rotational motion given on one side or both sides is adjusted, and the desired welding process is performed by adjusting the pressure and other parameters.

Conventional welding methods are an important production technology in the aluminum alloy industry. In addition, critical problems may arise when focusing on heat treatable alloys such as 6061. For this reason, the choice of non-conventional welding methods in addition to conventional welding methods plays an important role in both having good weldability properties and having the desired internal structure of the material. For this reason, the coating method with rotary friction welding has become an important reason for preference in terms of overcoming the difficulties of welding with the conventional method and the difficulties of obtaining the desired properties after welding. Considering the wide application range of 6000 aluminum alloys, it is seen that there are still some points that need to be studied and clarified. In this context, the aim of this research was to investigate the behavior of the shaft made of aluminum 6061 series material in rotary friction welding and to investigate some of its mechanical properties (Meran et al., 2016).

The parameters affecting the welding quality in friction welding can be listed as the speed of the tool, the pressing force of the tool, the gap between the pipe and the tool, the pipe length (the amount of pipe end protrusion from the plate), the application time, the shoulder diameter and the temperature. Among these parameters, the two most effective parameters on weldability are the speed of the tool and the pressing force. Both of these variables directly affect the friction-based temperature during welding and cause the metallurgical properties of the weld zone to change

This work is licensed (CC BY-NC 4.0) under Creative Commons Attribution 4.0 International License

(Meran et al., 2016).

Hamade et al., (2019) conducted a feasibility and energy study showing the differences between the conventional Fusion Butt Welding (FBW) method and the Rotary Friction Welding (RFW) method for joining High-density polyethylene (HDPE) pipes and performed a cost analysis for both methods used in the study. In this cost analysis, it was shown that the energy consumption in RFW was one tenth of that of FBW.

Kasman et al. joined AA7075-T651 aluminum alloy sheets by friction stir welding method at two different rotation speeds using tools with 3 different pin geometries. Afterwards, they compared the mechanical properties and microstructures of the welded areas (Kasman et al., 2016).

Unlike traditional friction welding, it is possible to weld different materials in the friction welding method. Although much less than the problems encountered in traditional welding, some problems can occur in the joining processes performed with these methods. The problems related to friction welding of different metals are not only related to their individual properties such as hardness, melting point, etc., but also to the reactions that occur at the interface. These reactions can lead to the formation of brittle intermetallic phases or other undesirable components. The presence of intermetallic phases at the interface of Al/steel components adversely affects the bonding (Yılbas et al., 1995; Ochi et al., 1977; Hartwig and Kouptsidis, 1978; Achar et al., 1980). These intermetallic phases are FeAl, FeAl2, Fe2Al5 and FeAl3 and the intermetallic phases are stable up to high temperatures. These phases can be expected to occur at the component interface and thus affect the mechanical properties of the welded component (Fukumoto et al., 1998; Atabaki et al., 2014). The thickness of the intermetallic phase in friction welded components is an important parameter contributing to the mechanical properties and therefore should be controlled (Fukumoto et al., 1999).

When the studies in the literature are examined, although there are many studies based on the principle of melting and merging of the metal by reaching temperatures close to the recrystallization zone such as friction welding, friction stir welding, friction coating, very few studies on rotary friction welding have been found. Based on these studies, there is no study in the literature with titanium powder. In this study, after pressing pure titanium powder into the shaft to be subjected to rotary friction welding and then sintering, the welding process was performed and the obtained results were examined.

2. Materials and Methods

The properties of the spindle Al6061 and the additional powder material pure Titanium powder used in rotary friction welding are shown in Table 1 and Table 2. The experimental parameters are shown in Table 3. Pure titanium is an important material with a wide range of potential uses in many sectors. Thanks to its lightness, durability and various usage advantages, it provides advantages in many points, whether used alone or in combination.

Table 1. Chemistry composition of Al6061

Al6061	%
Si	0.40-0.8
Fe	0.7
Cu	0.15-0.40
Mn	0.15
Mg	0.8-1.2
Cr	0.04-0.35
Ni	-
Zn	0.25
Ti	0.15
Zr	-
A1	Remainder

Table 2. Mechanical properties of pure titanium

Pure Ti	%
Yield Strength	275 MPa
Tensile Strength	345 MPa
Elongation	20%
Hardness	35 Rockwell C
Density	4.5 g/cm^3

Table 3. Experimental setup

Exp. Nu.	Rotary Side	Fixed Side
1	8 mm hole, pure Ti added	Non-additive
2	8 mm hole, pure Ti added	8 mm hole, pure Ti added
3	12 mm hole, pure Ti added	12 mm hole, pure Ti added

Aluminum 6061 shafts were machined as shown in Figure 1 to prepare for the experiments.

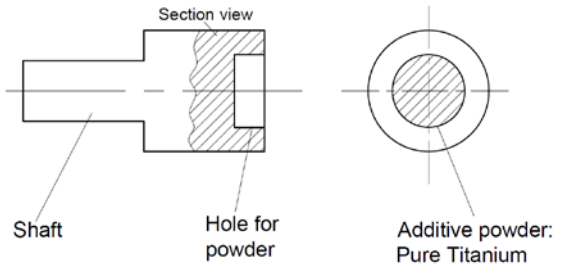


Figure 1. Preparing the samples for experiments.

As seen in Figure 1, 25 mm diameter shafts made of Aluminum 6061 material were connected to the lathe and 8 and 12 mm holes were drilled in their centers respectively and made suitable for powder pressing. A 12

mm diameter bearing area was made on the back of the shaft in accordance with the tensile tests, after the rotary friction welding process, to connect it to the tensile device. Pure Titanium powder was pressed into these shafts under a constant pressure of 50 Bar and made ready for the sintering process. The powder pressed shafts prepared in the press were taken to the sintering furnace from here and subjected to the sintering process at 400 °C (after reaching this temperature) for 90 minutes. After the sintering process, the shafts that were ready for the rotary friction welding process were subjected to experiments according to the experimental program in Figure 2 and the results of all these processes were ready to be examined.

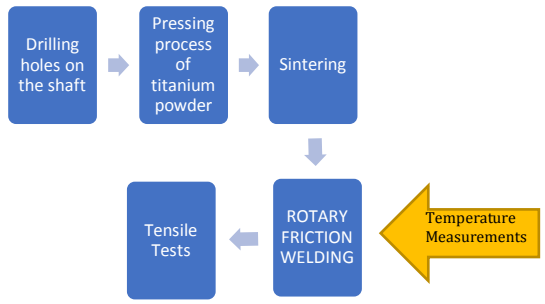


Figure 2. Overview of the experimentals.

2.1. Temperature Measurements

The rotary friction welding process was carried out at a rotation speed of 700 rpm with a powder-pressed shaft and a shaft without powder added in a hole opened with a diameter of 8 mm. In the welding process where the shaft on one side is rotary and the shaft on the other side is fixed, the shaft with powder added is connected to the lathe chuck and the shaft without powder added is connected to the moving tailstock of the machine.

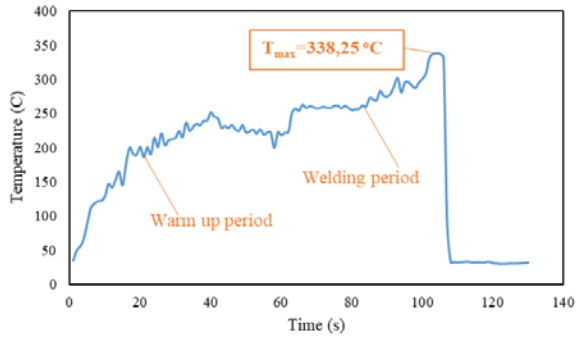


Figure 3. Temperature distribution in rotary friction welding process where the rotary shaft powder added (8 mm) and the fixed shaft without powder added.

The contact point temperature from the point of contact was measured with the help of an infrared thermometer. These obtained temperature values are shown in Figure 3. As can be seen from the graph, the temperature value starting from the moment of contact around room temperature first entered the heating period with the contact of the two shafts and then after the contact area reached the desired temperatures, the plasticized material entered the welding phase. After the flange formation and the interlocking phase of the weld, the machine was stopped and the process was completed. The maximum temperature reached during this time was 338.25 °C.

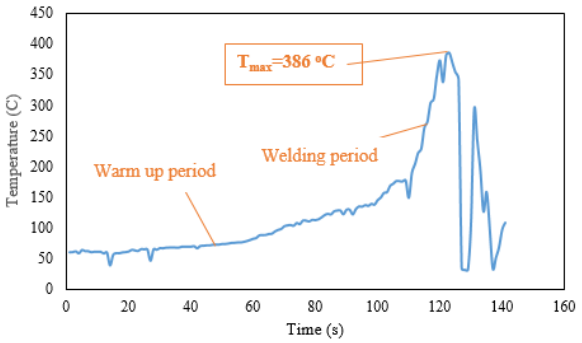


Figure 4. Temperature distribution in rotary friction welding process with rotary (8 mm) and fixed shaft (8mm) both have powder addition.

In Figure 4, the shaft with powder pressed into a hole opened with a diameter of 8 mm and the shaft with powder pressed into a shaft with a hole opened with an 8 mm hole are positioned opposite each other and the temperature values measured during the welding process are given. When these temperature values are examined, the heating period starting at around room temperature passed to the welding period with the material starting without plasticization after a period of 100 seconds and the welding process started. When compared to the welding process performed with titanium powder on one side and without powder on the other side (Figure 3), the materials plasticized later in the welding process with powder added on both shafts. The reason for this is that the melting temperature of the titanium material is 1660°C. When compared to the melting temperature of the aluminum, which is the shaft material (660 °C), the reinforcement material pure titanium, which is seen to be well above this temperature, extended this process shown as the 'warm up period' and caused the welding process to start later.

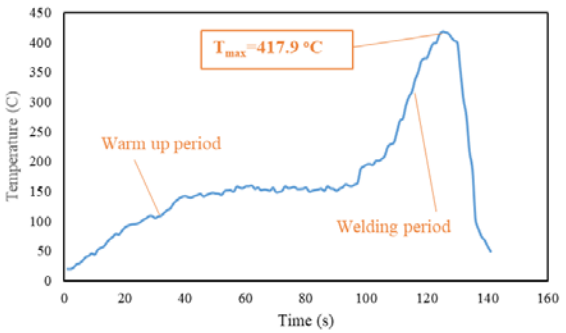


Figure 5. Temperature distribution in rotary friction welding process with rotary (12 mm) and fixed (12 mm) shaft both powder added (12 mm).

Figure 5 shows the temperature-time graphs of shafts with 12 mm diameter holes drilled into both shafts and pressed with pure titanium powder. Temperature is a function of both space and time (Ünal and Akkaş, 2022). For this reason, the temperature time graph was drawn in accordance with the obtained data. According to the graph, the process that started at room temperature entered the welding period after the first contact and heating period and the rotary friction welding process of the two shafts was completed by reaching a maximum temperature of T=417.9 ^{o}C. Since both shafts contained pure titanium powder, the heating period was longer (around 100 s) than the shafts without powder. The shafts that were plasticized later completed their heating in 40% longer time and entered into the welding period. After the welding process, the shafts were allowed to cool down to room temperature and then placed to the tensile device for tensile tests.

2.2. Tensile Tests

After the rotary friction welding process, the samples were placed to the tensile device for tensile tests. Tensile tests were carried out on the UTEST brand test device at a speed of 1 mm/min. The basic mechanical properties of the materials were determined with the tensile tests. In the experiment number 1 (1st spindle 8 mm hole powder added and 2nd spindle without powder added), the rotary friction welding process followed a very good process in terms of heating and welding properties and as a result, a good welding area was obtained. As a result, the tensile test exceeded 7000 N and then started to creep and the areas holding on to the drawing bench started to give necks and the force started to decrease. After this stage, the experiment was terminated and the graph was obtained. In the experiment number 2 (both shaft have 8 mm hole and powder added), since the melting temperature of the additional titanium powder was very high compared to the aluminum material, the adhesion was relatively more porous compared to the welding in the first experiment and as a result, the tensile test reached around 1018 N and the rupture occurred. In experiment number 3 (both shafts have 12 mm holes and powder added), shafts with 50% more powder added were used compared to the shafts used in experiments number 2. Therefore, the higher amount of titanium powder caused the heating and adhesion properties between the two shafts to be more difficult and delayed, and a weld area with more gaps was formed after welding. As a result, the force in the tensile test increased to around 800 N and then rupture occurred. Factors such as porosity in the weld zone or inadequate bonding of titanium particles to aluminum are thought to potentially play a role in the decrease in tensile strength.

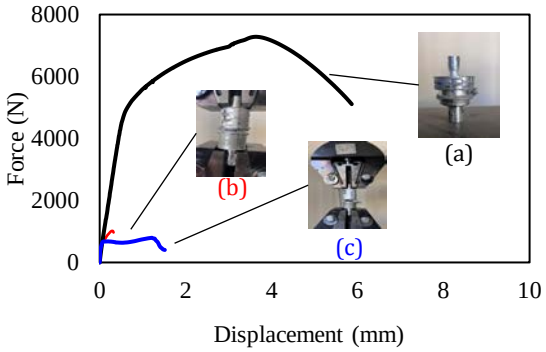


Figure 6. Tensile tests of rotary friction welded pairs. a) Non-additive b) 8 mm Ti added-8 mm Ti added pair c) 12 mm Ti added- 12 mm Ti added pair sample.

3. Results and Discussion

In this study, pure titanium powder was pressed into the shaft to be subjected to rotary friction welding and then sintered, followed by welding and the results obtained are as follows.

In the rotary friction welding process, the shafts come into contact with each other and reach temperatures close to the melting temperature, and then they are welded together with the principle of plasticization of the metal. In the study, since the pure titanium powder pressed into the shaft increases the average melting temperature, the welding process was the best in experiment number 1 (powder pressed into an 8 mm diameter hole in the moving shaft, fixed shaft without powder addition), while a relatively worse union was seen in experiment number 2 (pure titanium powder pressed into an 8 mm diameter hole in both shafts); and the least adhesion was seen in experiment number 3 (pure titanium powder added into a 12 mm diameter hole in both shafts). When the tensile test graphs are examined, in line with the results of these adhesions, the tensile force increased to 7000 N in experiment number 1, around 1000 N in experiment number 2, and in experiment number 3, separations occurred in the welding area around 800 N and the experiment was completed. It is estimated that better welded shafts can be obtained if the experiments are carried out by selecting a higher rotation speed on the bench and reaching higher melting temperatures in order to achieve better adhesion in the experiments where pure titanium powder is added. As a result of the experiments, in addition to obtaining the relevant data, the fact that the adhesion was not very good in some shaft pairs prevented further examination of the samples. For this reason, in future studies, experiments performed by changing the titanium ratio and hole diameter will yield more detailed results.

Author Contributions

The percentages of the author' contributions are presented below. The author reviewed and approved the final version of the manuscript.

	M.E.Ö.
C	100
D	100
S	100
DCP	100
DAI	100
L	100
W	100
CR	100
SR	100
PM	100
FA	100

C=Concept, D= design, S= supervision, DCP= data collection and/or processing, DAI= data analysis and/or interpretation, L= literature search, W= writing, CR= critical review, SR= submission and revision, PM= project management, FA= funding acquisition.

Conflict of Interest

The author declared that there is no conflict of interest.

Ethical Consideration

Ethics committee approval was not required for this study because of there was no study on animals or humans.

References

Achar DRG, Ruge J, Sundaresan S. 1980. Verbinden von Aluminium mit Stahl, besonders durch Schweissen. Aluminium Verl, Dusseldorf, Germany, pp: 147-149.

Atabaki, MM.; Nikodinovski, M.; Chenier, P.; Ma, J.; Harooni, M.; Kovacevic, 2014, R. Welding of aluminum alloys to steels: An overview. J Manuf Sci Prod, 14: 59-78.

Fukumoto S, Tsubakino H, Okita K, Aritashi M, Tomita T. 1999, Friction welding process of 5052 aluminium alloy to 304 stainless steel. Mater Sci Technol 15: 1080-1086.

Fukumoto S, Tsubakino H, Okita K, Aritashi M, Tomita T. 1998, Microstructure of friction weld interface of 1050 aluminium to austenitic stainless steel. Mater Sci Technol 14: 333-338.

Hamade RF, Tarek R. Andari, Ali H, Ammouri I, Jawahir S. 2019. Rotary friction welding versus fusion butt welding of plastic pipes - feasibility and energy perspective. Procedia Manuf, 33: 693-700.

Hartwig H, Kouptsidis J. 1978. Weld joints made between type AlMgSi0. 5 alloy and type X5CrNi18 9 alloy for the vacuum system of a high energy catalizer. Schweiss Schneid, 30: 45-47.

Kasman Ş, Kahraman F, Aydın A, 2016 Sürtünme karıştırma kaynak yöntemi ile birleştirilmiş AA7075-T651 alüminyum alaşımlarının farklı karıştırıcı pim geometrilerinin kaynak performansına etkisinin incelenmesi. 4th International Symposium on Innovative Technologies in Engineering and Science, 3-5 November, Antalya, Türkiye, pp: 1393.

Meran C, Korkmaz E, Aykanat E, Değirmenci S. 2016. Investigation of friction weldability of En Aw 6063 aluminium alloy tube to tube plate using an external tool. Cukurovaummfd, 31(ÖS1): 11-18.

Ochi H, Ogawa K, Yamamoto Y, Suga Y. 1977. Friction welding of aluminum alloy and steel. In: Proceedings of the 7th International Conference on Offshore and Polar Engineering, Honolulu, USA, pp: 541-545.

Ünal O, Akkaş N. 2022, Numerical analysis of temperature distribution in tandem welding process. BSJ Sci, 12: 1-21.

Yılbas BS, Sahin AZ, Kahraman N, Al-Garni AZ, 1995. Friction welding of St-Al and Al-Cu materials. J Mater Process Technol, 49: 431-443.

Black Sea Journal of Engineering and Science
doi: 10.34248/bsengineering.1592747

Open Access Journal
e-ISSN: 2619 – 8991

Research Article
Volume 8 - Issue 2: 315-322 / March 2025

COMPARISON OF TOTAL PHENOLIC COMPOUNDS AND ANTIOXIDANT CAPACITIES OF ETHANOL AND METHANOL EXTRACTS OF *Pistacia vera* L., *Prunus dulcis* AND *Rhus coriaria* L. LEAVES

Lale DUYSAK[1]*, Barış ÖZORMAN[1]

[1]*Atatürk University, Faculty of Pharmacy, Department of Biochemistry, 25030, Erzurum, Türkiye*

Abstract: *Pistacia vera* L., *Prunus dulcis*, and *Rhus coriaria* L. are among the plants frequently cultivated in the Gaziantep region of Turkey. The aim of this study is to determine the total phenolic content of ethanol and methanol extracts of the leaves of these three plants at different concentrations using DPPH (1,1-diphenyl-2-picrylhydrazyl), FRAP (Ferric Ion Reducing Antioxidant Power), and CUPRAC (Cu^{2+} Ion Reducing) methods. Ethanol and methanol extracts were obtained from the leaves of Pistacia vera L., Prunus dulcis, and Rhus coriaria L. The Folin-Ciocalteu Reagent (FCR) was used to determine the total phenolic component levels in these three plants. DPPH, FRAP, and CUPRAC techniques were used to evaluate antioxidant activities. To calculate the equivalent antioxidant capacity of the extracts, different reference sample concentrations in the range of 50, 125, and 250 g/mL were prepared. As a result, it was found that the antioxidant capacity increased with concentration. The FRAP test and total phenolic content were found to be highest in the methanol extract of the *P. vera* L. plant. It was found that the inhibition value of *P. vera* L. leaves in the ethanol extract was high. It has been determined that the ethanol extract of *R. coriaria* L. leaves has the highest reducing property for Cu^{2+} using the CUPRAC method.

Keywords: Antioxidant, *Pistacia vera* L., *Prunus dulcis*, *Rhus coriaria* L. Total phenolic content

***Corresponding author:** Atatürk University, Faculty of Pharmacy, Department of Biochemistry, 25030, Erzurum, Türkiye
E mail: lgozcu@atauni.edu.tr (L. DUYSAK)
Lale DUYSAK https://orcid.org/0000-0001-7872-3880
Barış ÖZORMAN https://orcid.org/0009-0007-4163-1211

Received: November 28, 2024
Accepted: January 07, 2025
Published: March 15, 2025

Cite as: Duysak L, Özorman B. 2025. Comparison of total phenolic compounds and antioxidant capacities of ethanol and methanol extracts of *Pistacia vera* l., *Prunus dulcis* and *Rhus coriaria* l. leaves. BSJ Eng Sci, 8(2): 315-322.

1. Introduction

Pistacia vera L. (Pistachio, *P. vera*) belongs to the Anacardiaceae family (Torun et al., 2021). Pistachio is the only species in this genus that produces edible nuts with commercial potential (Ferguson et al., 2005). Syria, Iraq, Iran and some regions of Türkiye are among the production areas of *P. vera* (Ibrahım and Mayı, 2023; Nezami and Gallego, 2023). Berries are a rich source of antioxidants including magnesium, potassium, calcium, protein, carbohydrates, dietary fibers, fat, folic acid, vitamin K, gamma-tocopherols, phytochemicals and polyphenols and flavonoids (Dreher, 2012) The antioxidant, anti-inflammatory, antimicrobial, and antiviral potential of polyphenols in pistachio has been proven by in vitro and in vivo experiments. Studies have also shown that consumption of *P. vera* plays a role in cognitive function and has beneficial effects on human skin health (Landaverde-Mejia et al., 2024; Mandalari et al., 2021) The antioxidant amounts in *P. vera* are variable and can vary significantly depending on the genetic quality of the plant, its pre-harvest and post-harvest collection, storage conditions, and different measurement methods used to measure antioxidant activity (Bolling et al., 2010; Liu, et al., 2014). *P. vera* is one of the most important export products in the Southeastern Anatolia Region of Türkiye in terms of production and export (Şimşek, 2018). Data from 2023 shows that 473 thousand tons of *P. vera* were exported worldwide. Türkiye has 32 thousand tons, which puts it in second place among exporting nations. According to 2022 data of the Food and Agriculture Organization, Türkiye ranks second in the world with 34% of the area where *P. vera* is planted (FAO, 2024).

Prunus dulcis (almond, *P. dulcis*) is a plant belonging to the Rosaceae family. It is native to Asia. It can usually be consumed fresh, dried or roasted. It is also used in cooking and confectionery. It is rich in fat. It is a rich source of polyunsaturated Fatty Acids (PUFA), especially linolenic acid, which is known for its ability to reduce the level of Low Density Lipoproteins (LDL) in the blood, preventing atherosclerotic plaques and therefore the risk of heart infarction (Berryman et al., 2011). In addition, , *P. dulcis* contain minerals such as calcium, potassium, phosphorus, and magnesium, and antioxidants, especially tocopherols. In addition to their nutritional properties, , *P. dulcis* have been reported to reduce body weight, have an effect on glucose levels, oxidative stress and inflammation, and reduce the risk of colon cancer in rats (Kamil and Chen, 2012). It has also been reported to be effective in the treatment of various skin diseases such as constipation,

This work is licensed (CC BY-NC 4.0) under Creative Commons Attribution 4.0 International License

and eczema, acne, as well as diseases such as gastro-enteritis (Kamil and Chen, 2012). Extracts of whole , *P. dulcis* kernel, brown hull, shell, green hull cover (stem), and leaves have strong free radical scavenging capacities due to the presence of flavonoids and other phenolic compounds (Esfahlan et al., 2010). Additionally, ethanolic extracts of leaves, flowers, and seeds (250 and 500 mg/kg) showed antidiabetic activity against normal and streptozotocin-induced diabetic mice (Rao, 2012). Bottone et al. reported in their study that, *P. dulcis* leaves can be considered a rich source for the extraction of bioactives with antioxidant properties and that they show particularly strong free radical scavenging capacity (Bottone, et al., 2018). According to FAO 2021 data, Türkiye ranks 7th in world almond production (FAO, 2021).

Rhus coriaria L. (*R. coriaria*) belongs to the Anacardiaceae family and is commonly known as "sumac", derived from the Syriac word "sumaga" meaning "red" (Wetherilt and Pala, 1994). *R. coriaria* leaves and fruits are generally effective in treating bacterial and fungal infections (Gabr and Alghadir, 2015; Joseph et al., 2023; Özçelik, 1987). , *R. coriaria* leaves have traditionally been used in various treatments such as mouth sores (aphtha, thrush), antiseptic, sore throat, cracked hands-feet-lips, anti-inflammatory, antidiarrheal, stomach ache, heartburn, digestive system diseases, and wound healing (Aytar, et al., 2024; Fakir et al., 2009; Özhatay and Koçak, 2011; Yücel et al., 2011). It is stated that the fresh leaves of the plant, placed on the soles of shoes, heal cracks in the skin, and the fruit is used by chewing gum for mouth sores and stomach cramps (Tuzlacı, 2006; Tuzlacı, 2011). It has been reported that the sumac plant is used in dysentery, liver diseases, and loss of appetite, as well as in hair treatment and skin diseases such as burns and dermatitis (Ali-Shtayeh et al., 2013). *R. coriaria* components fatty acids, minerals, fiber, and phytochemicals give the plant many beneficial properties. Its nutritional value keeps this plant in a fluid state as a foodstuff or functional food (Grassia et al., 2021). In addition to its nutritional value, secondary metabolites such as gallic acid and vanillic acid, which are important for therapeutic use, are found in sumac (Schulze-Kaysers et al., 2015). It is effective in preserving foods due to its antimicrobial and antioxidant properties (Gulmez et al., 2006; Joseph et al., 2023; Shabbir, 2012; Zannou et al., 2025). In Türkiye, 17.25 thousand tons of, *R. coriaria* is produced annually between 2020-2024 (TAGEM, 2020).

Manufacturers often synthesize the antioxidants utilized in in vitro and in vivo research where antioxidant activity is examined. As a result, it is uncommon for research to employ naturally occurring antioxidants. Gallic acid and Trolox, two common antioxidants, were used in this investigation (Bardakçı 2017; Duysak et al., 2024a).

The aim of this study is to compare the antioxidant activities and total phenolic contents of the three plants mentioned above, which have been briefly discussed regarding their origins, areas of use, contents, and benefits. Additionally, another aim is to investigate the potential benefits that can be obtained from the leaves of *P. vera*, *P. dulcis*, and *R. coriaria* which are considered waste and are not utilized, in order to raise awareness regarding the evaluation of waste, one of the important topics of our time.

2. Materials and Methods

2.1. Plant Materials

P. vera (60 years), *P. dulcis* (15 years), and *R. coriaria* (10 years) plant leaves were collected from Gaziantep province in Turkey. These three trees grow spontaneously after being planted and do not require separate watering. The collected leaves were dried at room temperature. The dry leaves were ground into powder using a mortar and liquid nitrogen. Ethanol and methanol extracts were prepared from the plant powders. To prepare the alcohol extracts, 50 g of dry plant powder was weighed and extracted in 250 mL of ethanol and methanol in a horizontal shaking water bath at 50ºC for 72 hours. Every 24 hours, the mixture was filtered and fresh ethanol and methanol were added. The collected filtrates were gathered in a container, and the solvents were evaporated at 50°C using an evaporator. The dried extracts were stored in airtight bottles at 4ºC for experiments.

2.2. Determination of Total Phenolic Content

The total phenolic compound amounts in the leaves of *P. vera*, *P. dulcis*, and *R. coriaria* were determined using a modified version of the method developed by Slinkard and Singleton (1977). First, a 50 ml solution of 7.5% Na_2CO_3 was prepared. After preparing the stock solutions and performing the necessary dilution procedures, 40 µL of the sample and 200 µL of the Folin & Ciocalteu reagent were added to the plate wells and left to incubate for 5 minutes. Then, after adding 160 µL of Na_2CO_3, the samples were incubated for another 30 minutes, and the absorbance was measured at 765 nm using a spectrophotometer. Using the standard graph prepared with gallic acid, the results were calculated as mg Gallic Acid Equivalent (GAE)/g.

2.3. Determination of Antioxidant Capacity

2.3.1. DPPH method

The antioxidant capacity of ethanol and methanol extracts obtained from the leaves of *P. vera*, *P. dulcis*, and *R. coriaria* were determined according to the method developed by Brand Williams (1995). This method is based on measuring the scavenging effect of antioxidants against the stable and synthetic DPPH (1,1-diphenyl-2-picrylhydrazyl) radical. In the reduction reaction that occurs in the presence of antioxidants, the DPPH solution loses its color, and the decrease in color intensity allows for easy measurement in a spectrophotometer. This method is an easy and quick way to evaluate the radical scavenging capabilities of antioxidants. DPPH, a dark purple radical, gives maximum absorbance at 517 nm. To prepare the DPPH solution, 39 mg of DPPH was dissolved in 100 mL of ethanol. Then, 210 µL of extracts and 70 µL of DPPH solution were added to each well of a 96-well

plate and shaken for about 1 minute. The samples were incubated for 30 minutes at room temperature and in the dark, and the absorbances were read at 515 nm. The standard antioxidant Trolox was used as the control sample. The results were calculated as % inhibition.

2.3.2. CUPRAC method

In the method used by Apak and colleagues, the Cu(II) Neocuproin complex is converted to Cu(I) Neocuproin through the action of antioxidant compounds in the environment, and this complex's absorbance at a wavelength of 450 nm is measured (Capanoglu, et al., 2018). To prepare the CUPRAC reagent, 0.4262 g of $CuCl_2 \bullet 2H_2O$ was weighed and dissolved in 250 mL of distilled water (10 mM). To prepare the acetate buffer, 19.27 g of NH_4Ac was dissolved in 250 mL of water. A 7.5 mM neocuproin solution was obtained by dissolving 0.039 g of neocuproin compound in a 25 mL volumetric flask with 96% pure ethanol. Then, solutions consisting of 60 µL $CuCl_2$, 60 µL acetate buffer, 60 µL neocuproin solution, and 66 µL extracts were mixed. After a 30-minute incubation, absorbances were measured at a wavelength of 450 nm. The standard antioxidant Trolox was used as the control sample. Calibration curves for the 1-100 µg/mL working range, where the absorbance graph is linear with respect to concentration, were plotted.

2.3.3. FRAP method

The antioxidant capacity measurement method based on electron transfer of ethanol and methanol extracts obtained from the leaves of *P. vera, P. dulcis,* and *R. coriaria* were determined using the method developed by Huang and colleagues (2005). First, a 300 mmol/L acetate buffer (pH=3.6) was prepared. 10 mM TPTZ was placed into a 100 mL volumetric flask, 40 mM HCl was added, and the final volume was adjusted to 100 mL. Finally, a 20 mmol/L $FeCl_3$ solution was prepared. From the prepared solutions, 2.5 mL of TPTZ, 2.5 mL of $FeCl_3$, and 25 mL of acetate buffer were taken to obtain a total of 30 mL of FRAP solution. 10 µL of the extract sample and 200 µL of the FRAP solution were added to the plate wells, and after a 30-minute incubation, their absorbance was measured at 593 nm. The standard antioxidant Trolox was used as the control sample. Calibration curves for the 1-100 µg/mL working range, where the absorbance graph is linear with respect to concentration, were plotted.

2.4. Statistical Analysis

The graphs of the obtained data were plotted using GraphPad Prism Version 10.2.2 (397) Demo version. Additionally, the comparison between plants was conducted using the Tukey test in a one-way ANOVA. The P-value was expressed as P<0.0001 (****).

3. Results and Discussion

3.1. Total Phenolic Content

The total phenolic compound amounts of ethanol and methanol extracts prepared from the leaves of *P. vera, P. dulcis,* and *R. coriaria* were determined using the Folin-Ciocalteu Reagent (FCR). Gallic acid was used as a standard phenolic compound, and it was calculated as gallic acid equivalent from the equations obtained from the calibration curves of gallic acid (Table 1).

Table 1. The R^2 and linear range values of the equations formed with standard antioxidants prepared to measure the total phenolic content, DPPH, FRAP, and CUPRAC values of the leaves of *P. vera*, *P. dulcis,* and *R. coriaria*

		R^2	Linear range
DPPH (Trolox)	Ethanol	0,997	1-50
	Methanol	0,9946	1-40
CUPRAC (Trolox)	Ethanol	0,999	1-100
	Methanol	0,9981	1-70
FRAP (Trolox)	Ethanol	0,9989	1-90
	Methanol	0,9957	1-100
Total Phenolic Content (Gallic acid)	Ethanol	0,9976	1-100
	Methanol	0,9985	1-100

The total phenolic compound amount calculated in the samples according to the regression equations of the curves was determined as GAE/g for ethanol and methanol extracts (Figure 1). The total phenolic compounds of three plants were studied at three different concentrations (50, 125, and 250 µg/mL). According to the results obtained, it was determined that the highest total phenolic content was at a concentration of 250 µg/mL. Additionally, when comparing the high concentrations of ethanol and methanol extracts, it was found that the highest phenolic content was in the methanol extract of *P. vera* leaves (P<0.0001). Various in vitro and in vivo studies have investigated the antioxidant effects of pistachio flavonoids by comparing the activity of different parts of the peanut or different extracts (lipophilic or hydrophilic). It has been proven that polyphenols and flavonoids are commonly found in all parts of the pistachio (Gentile et al., 2007). Tomaino et al. showed that pistachio shells have a higher antioxidant activity and a higher content of antioxidant phenolic compounds than kernels (Tomaino et al., 2010). It has been shown that pistachio shells, which are considered as

agricultural waste, have high antioxidant properties by evaluating the oxidation of soybean oil after the heating process and then determining the peroxide value and thiobarbituric acid value (Goli et al., 2005). In this study, the high phenolic content of the leaf extracts of the three plants may play a supportive role in the prevention of oxidative stress-related diseases such as cardiovascular diseases, diabetes, cancer, and neurodegenerative diseases.

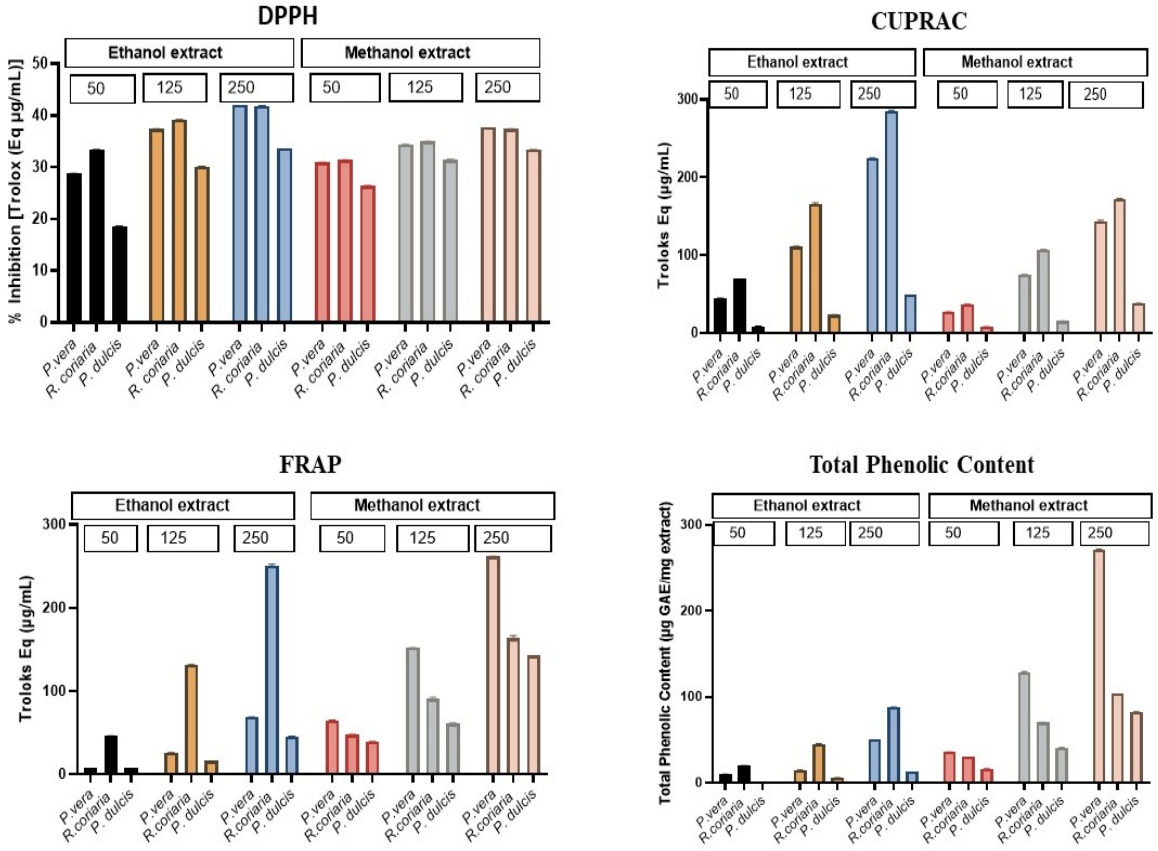


Figure 1. Total phenolic compound, DPPH, FRAP and CUPRAC values of ethanol and methanol extracts obtained from leaves of *P. vera*, *P. dulcis* and *R. coriaria* at concentrations of 50, 125 and 250 µg/mL.

3.2. Antioxidant Capacity

3.2.1. Results from DPPH radical scavenging studies

The concentration range of trolox, a standard antioxidant compound, was determined to be 1-100 µg/mL as a result of the studies conducted. A standard curve has been drawn and an equation obtained using trolox as a standard antioxidant compound (Table 1). The DPPH radical scavenging capacities of ethanol and methanol extracts prepared from the leaves of *P. vera, P. dulcis,* and *R. coriaria* at concentrations of 50, 125, and 250 µg/mL were calculated as % inhibition values. It has been determined that all three plants have the highest DPPH free radical scavenging capacity at a concentration of 250 µg/mL, and that the best effect is observed with a high dose of the ethanol extract (Figure 1). When comparing the concentration of ethanol extract at 250 µg/mL among three plants, it was found that there were differences among them, with the highest percentage of inhibition observed in the *P. vera* plant (Figure 2, $P<0.0001$). In support of our work, Hosseinzadeh et al. found in their study that the ethanol extract of *P. vera* leaves have a higher % inhibition value than the water extract (Hosseinzadeh et al., 2012). Boumaiza et al. found that all extracts tested in the DPPH assay of the *P. vera* plant exhibited good antioxidant properties. However, the antioxidant activity of the various extracts tested primarily increases based on their concentrations (Boumaiza et al., 2016).

3.2.2. Results of the copper ion reducing antioxidant capacity determination method (CUPRAC)

The conversion of ethanol and methanol extracts prepared from the leaves of *P. vera, P. dulcis,* and *R. coriaria*, as well as the Cu(II) neocuproin complex, into Cu(I) neocuproin through compounds with antioxidant effects in the medium, was carried out by measuring absorbance at 450 nm. The concentration range to be analyzed (1-100 µg/mL) was determined based on studies conducted on standard antioxidant compounds (Table 1) At the end of the study, it was observed that there is a correlation in antioxidant capacity proportional to the increasing amount of each extract, depending on the quantity of the extract. The reason for this is that as the

amount of extract increases, the quantity of active compounds in the extracts also increases. The reason for this correlation may be the many free radical scavenger groups found in plants, such as phenolic compounds with antioxidant effects (phenolic acids, flavonoids, coumarins, etc.), nitrogenous compounds (alkaloids, amines, etc.), vitamins, and terpenoids (Duysak et al., 2024b) (Figure 1).

When comparing the concentration of ethanol extract at 250 µg/mL among three plants, it was found that there were differences among them, with the best CUPRAC result observed in the *R. coriaria* plant (Figure 2) (P<0.0001). Studies have found that the leaves of *R. coriaria* exhibit high antioxidant capacity (Bursal and Köksal, 2011; Danış et al., 2014; Perna et al., 2018).

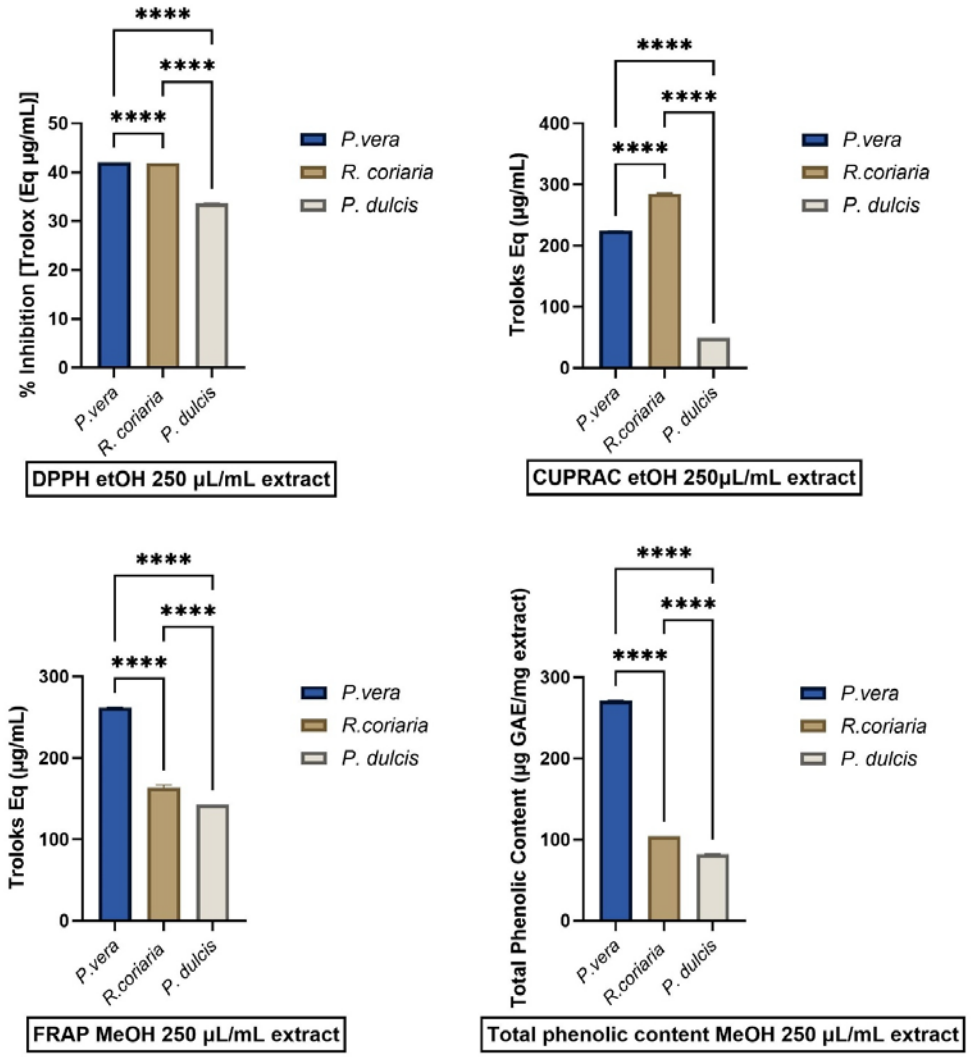


Figure 2. Comparison of the best acting solvent among plants (Statistics for antioxidant capacity and total phenolic compound measurements were made using GraphPad Prism Version 10.2.2 (397) version. Tukey test was used in one-way ANOVA for comparison among plants. p value was expressed as P<0.0001 (****).

3.2.3. Results of iron ion reducing antioxidant power (FRAP)

The analyzed concentration range (1-100 µg/mL) was determined as a result of studies on standard antioxidant compounds. As a standard antioxidant, trolox, iron (III) reducing/antioxidant potency activity reached the highest value at 100 µg/mL concentration. In line with these data, the concentration range of the extracts to be studied was determined as 1-100 µg/mL (Table 1). The iron (III) reducing/antioxidant powers of ethanol and methanol extracts prepared from *P. vera, P. dulcis,* and *R. coriaria* (50, 125 and 250 µg/mL) , standard antioxidant compounds were compared in terms of µg Trolox Equivalent Antioxidant Capacity (TEAC) (Figure 1). It was determined that the ethanol and methanol extracts prepared from the *P. vera, P. dulcis,* and *R. coriaria* had the highest iron ion reducing antioxidant power capacity, and it was determined that the methanol extract had a concentration of 250 µg/mL. When the 250 µg/mL concentration of methanol extract was compared in 3 plants, it was determined that there was a difference between them, and the best FRAP result was in the *P. vera* leaf. (Figure 2) (P<0.0001). A study showed that extracts from different parts of P. vera have antioxidant activity in various in vitro methods. It has been determined that the ethanolic extracts of leaves and fruits have higher antioxidant content (Hosseinzadeh et al., 2012). Boumaiza et al. demonstrated that the high phenolic content of *P.*

vera contributes to its antioxidant activity (Boumaiza et al., 2016). In another study, it has been shown that *P. vera* gum exhibits effective DPPH, FRAP testing for the Fe^{3+}-Fe^{2+} conversion, reducing capabilities for Cu^{2+} using the CUPRAC method (Sehitoglu et al., 2015).

4. Conclusion

The extractions of *P. vera, P. dulcis,* and *R. coriaria* were carried out separately with ethanol and methanol. The total phenolic content of the ethanol and methanol extracts of three plants, as well as their antioxidant capacities, were comparatively examined using the DPPH, FRAP, and CUPRAC methods. As a result, it has been determined that at concentrations of 50, 125, and 250 µg/mL, the antioxidant capacity increases with the concentration. The current study found that the total phenolic content and the Fe^{3+}-Fe^{2+} conversion in the FRAP test were highest in the methanol extract of the P. vera plant. In the DPPH test, it was found that the % inhibition value is present in the ethanol extract of the *P. vera* leaves. The CUPRAC method determined that the ethanol extract of R. coriaria L. leaves has the highest reducing property for Cu^{2+}. Based on this, the evaluation of the antioxidant properties of the leftover leaves of these plants, which are widely consumed for their fruits, indicates significant potential from both environmental and nutritional perspectives. In particular, the leaves of commonly consumed plants such as *P. vera* and *R. coriaria* can be used in the food industry or as natural food additives due to their high phenolic content. The evaluation of such waste will provide economic benefits and also enhance food security. In conclusion, the findings of this study can contribute to waste management strategies in the agricultural industry by investigating the antioxidant properties of plant leaves. In future studies, it is recommended that more research be conducted on the health effects and potential applications of these leaf extracts.

Author Contributions

The percentages of the author's contributions are presented below. All authors reviewed and approved the final version of the manuscript.

	L.D.	B.Ö.
C	70	30
D	80	20
S	70	30
DCP	70	30
DAI	70	30
L	50	50
W	90	10
CR	80	20
SR	90	10
PM	70	30
FA	50	50

C=Concept, D= design, S= supervision, DCP= data collection and/or processing, DAI= data analysis and/or interpretation, L= literature search, W= writing, CR= critical review, SR= submission and revision, PM= project management, FA= funding acquisition.

Conflict of Interest Statement

The authors declare that they have no conflict of interest in this study.

Ethical Approval Statement

Since this study did not involve any studies on animals or humans, ethics committee approval was not obtained.

Acnowledgements

This work was supported by TUBITAK 2209-A University Students Research Projects Support Program (number 1919B012305901).

References

Ali-Shtayeh MS, Al-Assali AA, Jamous RM.2013. Antimicrobial activity of Palestinian medicinal plants against acne-inducing bacteria. Afr J Microbiol Res, 7 (21): 2560-2573.

Aytar M, Boncooğlu RY, Erdoğan Ö, Başbülbül G, Öztürk B. 2024. Antioxidant, cytotoxicity, antimicrobial, wound healing potentials and LC-MS/MS analysis of water extract of Rhus coriaria L. (sumak) leaves. Food Biosci, 60: 104400.

Bardakçı Ö. 2017. Bazı sentetik antioksidanların 2, 2-difenil-1-pikrilhidrazil (DPPH) radikal süpürme kapasitesi yöntemi ile antioksidan aktivitelerinin araştırılması. Yüksek Lisans Tezi, Adnan Menderes Üniversitesi, Sağlık Bilimleri Enstitüsü, Farmakoloji ve Toksikoloji (Veterinerlik) Ana Bilim Dalı, Aydın, Türkiye, pp: 58.

Berryman CE, Preston AG, Karmally W, Deckelbaum RJ, Kris-Etherton PM. 2011. Effects of almond consumption on the reduction of LDL-cholesterol: a discussion of potential mechanisms and future research directions. Nutr Rev, 69(4): 171-185.

Bolling BW, McKay DL, Blumberg JB. 2010. The phytochemical composition and antioxidant actions of tree nuts. Asia Pac J Clin Nutr, 19(1): 117.

Bottone A, Montoro P, Masullo M, Pizza C, Piacente S. 2018.

Metabolomics and antioxidant activity of the leaves of Prunus dulcis Mill. (Italian cvs. Toritto and Avola). J Pharm Biomed Anal, 158: 54-65.

Boumaiza R, Snoussi A, Cirkovic-Velickovic T, Bouzouita N. 2016. Phenolic composition and antioxidant activity of different parts of *pistacia vera* L. Mediterr J Chem, 6(1): 658-664.

Brand-Williams, W, Cuvelier ME, Berset C. 1995. Use of a free-radical method to evaluate antioxidant activity. Lebensm. Wiss Technol, 28(1): 25-30.

Bursal E, Köksal E. 2011. Evaluation of reducing power and radical scavenging activities of water and ethanol extracts from sumac (Rhus coriaria L.). Food Res Int, 44(7): 2217-2221.

Capanoglu E, Kamiloglu S, Ozkan G, Apak R. 2018. Evaluation of antioxidant activity/capacity measurement methods for food products. Measure Antioxidant Activ Capacit, 2018: 273-286.

Danış Ö, Yuce-Dursun B, Çimen T, Demir S, Salan Ü, Yalçın G, Ogan A. 2014. Evaluation of Antioxidant, Radical-Scavenging and Acetylcholinesterase Inhibitory Activities of Various Culinary Herbs Cultivated in Southern Turkey. J Food Biochem, 38(6): 602-611.

Dreher ML. 2012. Pistachio nuts: composition and potential health benefits. Nutr Rev, 70(4): 234-240.

Duysak L, Kasimoğullari S, Baygutalp NK. 2024a. Determination of Total Phenolic Contents and Antioxidant Activities of Different Extracts Obtained from Morus alba L. (White Mulberry) Leaf. Pharmata, 4(2): 39-45.

Duysak L, Şekeroğulları M, Baygutalp NK. 2024b. Total phenolic content and antioxidant activity of different extracts of aronia melanocarpa L. fruit. Pharmata, 4(1): 1-6.

Esfahlan AJ, Jamei R, Esfahlan R J. 2010. The importance of almond (Prunus amygdalus L.) and its by-products. Food Chem, 120(2): 349-360.

Fakir H, Korkmaz M, Güller B. 2009. Medicinal plant diversity of western Mediterrenean region in Turkey. Appl Biosci, 3(2): 33-43.

FAO. 2021. Food and Agriculture Organization of the United Nations. https://openknowledge.fao.org/server/api/core/bitstreams/125b023c-002f-4387-9150-dc7fbbd86cbc/content (accessed date March 12, 2024).

FAO. 2024. Food and Agriculture Organization of the United Nations. URL: https://openknowledge.fao.org/server/api/core/bitstreams/4256ac5c-fef3-4f02-9965-8f7f36a22927/content (accessed date March 12, 2024)

Ferguson L, Polito V, Kallsen C. 2005. The pistachio tree; botany and physiology and factors that affect yield. Pistachio production manual, 4th ed. Davis, CA, University of California Fruit & Nut Research Information Center, California, USA, pp: 31-39.

Gabr SA, Alghadir AH. 2015. Phytochemical analysis and in vitro antifungal activities of bioactive fractions from leaves of *Rhus coriaria* (SUMAC). J Pure Appl Microbiol, 9(1): 559-565.

Gentile C, Tesoriere L, Butera D, Fazzari M, Monastero M, Allegra M, Livrea M A. 2007. Antioxidant activity of Sicilian pistachio (*Pistacia vera* L. var. Bronte) nut extract and its bioactive components. J Agric Food Chem, 55(3): 643-648.

Goli AH, Barzegar M, Sahari MA. 2005. Antioxidant activity and total phenolic compounds of pistachio (Pistachia vera) hull extracts. Food Chem, 92(3): 521-525.

Grassia M, Sarghini F, Bruno M, Cinquanta L, Scognamiglio M, Pacifico, S, Fiorentino A, Geraci A, Schicchi R, Corona O. 2021. Chemical composition and microencapsulation suitability of sumac (Rhus coriaria L.) fruit extract. Eur Food Res Technol, 247: 1133-1148.

Gulmez M, Oral N, Vatansever L. 2006. The effect of water extract of sumac (Rhus coriaria L.) and lactic acid on decontamination and shelf life of raw broiler wings. Poult Sci, 85(8): 1466-1471.

Hosseinzadeh H, Tabassi SAS., Moghadam NM, Rashedinia M, Mehri S. 2012. Antioxidant activity of *Pistacia vera* fruits, leaves and gum extracts. Iran J Pharm Res, 11(3): 879.

Huang DJ, Ou BX, Prior RL. 2005. The chemistry behind antioxidant capacity assays. J Agric Food Chem, 53(6): 1841-1856.

Ibrahım NJ, Mayı AA. 2023. Effect of cultivaris, budding dates, kinetin, and their interaction on the budding and vegetative growth characteristics of pistachio transplants "*pistacia vera* l.". J Duhok Univ, 26(2): 12-19.

Joseph G, Koltai H, Ron EZ, Azzam N, Hazan H, Raskin I, Biran D. 2023. Rhus coriaria L. (sumac) leaves harbour robust antimicrobial activity. J Herb Med, 41: 100729.

Kamil A, Chen CYO. 2012. Health benefits of almonds beyond cholesterol reduction. J Agric Food Chem, 60(27): 6694-6702.

Landaverde-Mejia K, Dufoo-Hurtado E, Camacho-Vega D, Maldonado-Celis M E, Mendoza-Diaz, S, Campos-Vega R. 2024. Pistachio (*Pistacia vera* L.) consumption improves cognitive performance and mood in overweight young adults: A pilot study. Food Chem, 457: 140211.

Liu Y, Blumberg JB, Chen C-Y O. 2014. Quantification and bioaccessibility of California pistachio bioactives. J Agric Food Chem, 62(7): 1550-1556.

Mandalari G, Barreca D, Gervasi T, Roussell MA, Klein B, Feeney MJ, Carughi A. 2021. Pistachio nuts (*Pistacia vera* L.): Production, nutrients, bioactives and novel health effects. Plants, 11(1): 18.

Nezami E, Gallego PP. 2023. History, phylogeny, biodiversity, and new computer-based tools for efficient micropropagation and conservation of Pistachio (Pistacia spp.) germplasm. Plants, 12(2): 323.

Özçelik H. 1987. Akseki yöresinde doğal olarak yetişen bazı faydalı bitkilerin yerel adları ve kullanılışları. Doğa Türk Botan Derg, 11(3): 316-321.

Özhatay N, Koçak S. 2011. Plants used for medicinal purposes in Karaman province (Southern Turkey). Istanbul J Pharm, 41, 75-89.

Perna A, Simonetti A, Grassi G, Gambacorta E. 2018. Effect of αS1-casein genotype on phenolic compounds and antioxidant activity in goat milk yogurt fortified with Rhus coriaria leaf powder. Int J Dairy Sci, 101(9): 7691-7701.

Rao H. 2012. Therapeutic applications of almonds (*Prunus amygdalus* L.): a review. J Clin Diagn Res, 6(1): 130-135.

Schulze-Kaysers N, Feuereisen M, Schieber A. 2015. Phenolic compounds in edible species of the Anacardiaceae family–a review. RSC Advances, 5(89): 73301-73314.

Sehitoglu MH, Han H, Kalin P, Gülçin İ, Ozkan A, Aboul-Enein HY. 2015. Pistachio (*Pistacia vera* L.) gum: A potent inhibitor of reactive oxygen species. J Enzyme Inhib Med Chem, 30(2): 264-269.

Shabbir A. 2012. Rhus coriaria linn, a plant of medicinal, nutritional and industrial importance: a review. J Anim Plant Sci, 22(2): 505-512.

Slinkard K, Singleton VL. 1977. Total phenol analysis: automation and comparison with manual methods. Am J Enol Vitic, 28 (1): 49-55.

Şimşek M. 2018. Production potential and development opportunities of pistachio (*Pistacia vera* L.) grown in Southeastern Turkey. Iğdır Üniv Fen Bilim Enstit Derg, 8(1): 19-22.

TAGEM 2020. Tıbbi ve aromatik bitkiler sektör politika belgesi 2020-2024. URL:

https://www.tarimorman.gov.tr/TAGEM/Belgeler/yayin/T%C4%B1bbi%20ve%20Aromatik%20Bitkiler%20SPB.pdf) (accessed date March 12, 2024).

Tomaino A, Martorana M, Arcoraci T, Monteleone D, Giovinazzo C, Saija A. 2010. Antioxidant activity and phenolic profile of pistachio (*Pistacia vera* L., variety Bronte) seeds and skins. Biochimie, 92(9): 1115-1122.

Torun AA, Bozgeyik S, Duymuş E. 2021. The effect of boron application in increasing doses on shoot boron concentration and uptake of other nutrients of pistachio (*Pistacia vera* L.). Turk J Agric Food Sci Technol, 9(5): 855-862.

Tuzlacı E. 2006. Şifa niyetine: Türkiye'nin bitkisel halk ilaçları: Alfa yayınları, İstanbul, Türkiye, ss: 848.

Tuzlacı E. 2011. Türkiye bitkileri sözlüğü (Genişletilmiş 2. baskı). Alfa Yayınları, İstanbul, Türkiye, ss: 63.

Wetherilt W.,Pala, M.1994. Herbs and spices indigenous to Turkey. Develop Food Sci, 34: 285-285.

Yücel E, Tapırdamaz A, Şengün İY, Yılmaz G, Ak A. 2011. Kisecik Kasabası Karaman ve çevresinde bulunan bazı yabani bitkilerin kullanım biçimleri ve besin öğesi içeriklerinin belirlenmesi. Biol Divers Conserv, 4(3): 71-82.

Zannou O, Oussou KF, Chabi IB, Alamou F, Awad NM, Miassi YE, Redha AA. 2025. Phytochemical and nutritional properties of sumac (Rhus coriaria): a potential ingredient for developing functional foods. J Future Foods, 5(1): 21-35.

Black Sea Journal of Engineering and Science
doi: 10.34248/bsengineering.1596832

Open Access Journal
e-ISSN: 2619 – 8991

Research Article
Volume 8 - Issue 2: 323-329 / March 2025

PERFORMANCE EVALUATION OF TRANSFORMER-BASED PRE-TRAINED LANGUAGE MODELS FOR TURKISH QUESTION-ANSWERING

Mert İNCİDELEN[1], Murat AYDOĞAN[2]*

[1]*Fırat University, Faculty of Engineering, Department of Artificial Intelligence and Data Engineering, 23200, Elazığ, Türkiye*
[2]*Fırat University, Faculty of Technology, Department of Software Engineering, 23200, Elazığ, Türkiye*

Abstract: Natural language processing (NLP) has made significant progress with the introduction of Transformer-based architectures that have revolutionized tasks such as question-answering (QA). While English is a primary focus of NLP research due to its high resource datasets, low-resource languages such as Turkish present unique challenges such as linguistic complexity and limited data availability. This study evaluates the performance of Transformer-based pre-trained language models on QA tasks and provides insights into their strengths and limitations for future improvements. In this study, variations of the mBERT, BERTurk, ConvBERTurk, DistilBERTurk, and ELECTRA Turkish pre-trained models were fine-tuned using the SQuAD-TR dataset, which is the machine-translated Turkish version of the SQuAD 2.0 dataset. The performance of these fine-tuned models was tested using the XQuAD-TR dataset. The models were evaluated using Exact Match (EM) and F1 Score metrics. Among the tested models, the ConvBERTurk Base (cased) model performed the best, achieving an EM of 57.82% and an F1 Score of 71.59%. In contrast, the DistilBERTurk Base (cased) and ELECTRA TR Small (cased) models performed poorly due to their smaller size and fewer parameters. The results indicate that case-sensitive models generally perform better than case-insensitive models. The ability of case-sensitive models to discriminate proper names and abbreviations more effectively improved their performance. Moreover, models specifically adapted for Turkish performed better on QA tasks compared to the multilingual mBERT model.

Keywords: Natural language processing, Question-answering, Transformers, BERT, ELECTRA

***Corresponding author:** Fırat University, Faculty of Technology, Department of Software Engineering, 23200, Elazığ, Türkiye
E mail: m.aydogan@firat.edu.tr (M.AYDOĞAN)
Mert İNCİDELEN https://orcid.org/0009-0002-1975-8332
Murat AYDOĞAN https://orcid.org/0000-0002-6876-6454

Received: December 05, 2024
Accepted: January 15, 2025
Published: March 15, 2025

Cite as: İncidelen M, Aydoğan M. 2025. Performance evaluation of transformer-based pre-trained language models for turkish question-answering. BSJ Eng Sci, 8(2): 323-329.

1. Introduction

With the onset of the digital age and the rise of artificial intelligence, there have been significant developments in the ability of machines to understand and use natural languages like humans. These developments have enabled the growth of the field of natural language processing (NLP) (Locke et al., 2021). NLP has emerged as an interdisciplinary field of study where computer science and linguistics intersect. NLP focuses on machines understanding and generate human language. Many tasks such as machine translation, sentiment analysis, text classification, and question-answering (QA) can be performed in the field of NLP (Khurana et al., 2023). There has been a significant increase in the amount of text data created by online sources such as social media, blogs and many other text sources (Hassani et al., 2020). Thus, a wide variety of resources have emerged for use in NLP tasks for different languages. With the increase in text data, NLP studies have also gained importance. The announcement of the Transformer architecture (Vaswani et al., 2017) and the emergence of Transformer-based pre-trained language models have led to the beginning of a new era in the field of NLP. Many pre-trained language models can be used for NLP tasks. These models are pre-trained on large-scale text data and then fine-tuned for specific NLP tasks. One of these tasks is answer extraction from text. Answer extraction is the process of extracting information about a query text from the content of texts obtained from information sources. Unlike traditional information search methods, the answer extraction method aims to obtain clear answers directly from sources instead of directing to sources where the information is available (Allam and Haggag, 2012; Yiğit and Amasyalı, 2021). Thus, effective QA systems can be developed. English datasets such as SQuAD (Stanford Question-Answering Dataset) have been a turning point for the development of QA systems. The SQuAD dataset, which is compiled from Wikipedia texts and contains more than 100,000 question-answer pairs, has become a standard for open-domain QA systems (Rajpurkar et al., 2016). SQuAD 2.0 expanded this dataset by adding unanswered questions, making it possible to evaluate the ability of QA models to handle more complex situations (Rajpurkar et al., 2018). In a high-resource language such as English, large datasets support the training, testing and

This work is licensed (CC BY-NC 4.0) under Creative Commons Attribution 4.0 International License

development processes of QA models. This has made English the most frequently studied language in the field of NLP and has led to the formation of a large literature on tasks such as QA. English QA systems have been developed with SQuAD and its derivative datasets, and the effectiveness of Transformer-based models has been proven in different fields (Raza et al., 2022; Alzubi et al., 2023; Zhu et al., 2023). NLP studies on low-resource languages such as Turkish are limited. Although pre-trained models for Turkish are widely used in different NLP tasks (Çelikten and Bulut, 2021; Türkmen et al., 2023; Arzu and Aydoğan, 2023), the lack of resources for Turkish QA tasks has limited work on this task.

The limitations in the literature on QA studies in Turkish, combined with the structural and linguistic difficulties arising from this language, make the development of QA systems more complex. In this context, there are a limited number of QA studies and datasets for Turkish. Gemirter and Goularas (2021) aimed to develop a deep learning-based Turkish QA system in their work. This capability was developed using the BERT model to develop a question and answer system. The system is designed to provide precise and concise answers to banking-related questions by using large datasets and advanced deep learning techniques. Wikipedia, news corpora, and banking sector-specific data were utilized in the study. Soygazi et al. (2021) constructed a Turkish QA dataset called THQuAD for Turkish reading comprehension evaluations. The study utilized texts consisting of Turkish Wikipedia articles and Ottoman history and Turkish-Islamic history of science datasets. Analyses were conducted on this dataset by fine-tuning language models such as BERT, ELECTRA and ALBERT. The study demonstrated how these models perform in a morphologically rich language such as Turkish. The results showed that especially ELECTRA models achieved the highest performance compared to other models, emphasizing the potential of language models in Turkish reading comprehension tasks. Akyon et al. (2021) investigated the mT5 model in multitask settings to perform automatic question generation and question answering tasks from Turkish texts. In the study, the performance of the model was evaluated on datasets such as TQuADv1, TQuADv2 and XQuAD and meaningful question-answer pairs were generated with the proposed methods. In particular, the focus was on the multitask learning approach that performs answer extraction, question generation and answering tasks simultaneously. In addition, sentence segmentation algorithms specific to the Turkish language were developed and the morphological complexities of the language were taken into account in this process. The obtained results showed that the mT5 model exhibited better performance compared to existing methods. The study focused on the applications of transformer-based models in morphologically rich languages such as Turkish. Budur et al. (2024) proposed a method to develop an efficient and effective Open Domain QA (OpenQA) system for low-resource languages. In the study, focusing on Turkish, SQuAD 2.0 dataset was translated into Turkish using machine translation approach, resulting in the creation of the SQuAD TR dataset. Models such as ColBERT-QA and DPR were customized and adapted to Turkish sources. The results indicate that these systems achieved 24-32 percent and 22-29 percent improvement in Exact Match (EM) and F1 scores, respectively.

In this study, the performance of Transformer based pre-trained language models for QA tasks is analyzed. mBERT, BERTurk Base (cased), BERTurk Base (uncased), BERTurk 128k (cased), BERTurk 128k (uncased), ConvBERTurk Base (cased), ConvBERTurk mC4 (cased), ConvBERTurk mC4 (uncased), DistilBERTurk Base (cased), ELECTRA TR Base (cased), ELECTRA TR Small (cased), ELECTRA TR mC4 (cased) and ELECTRA TR mC4 (uncased) pre-trained language models are fine-tuned using a comprehensive dataset, SQuAD-TR. The performance of the fine-tuned models on QA tasks is compared using XQuAD-TR dataset by evaluating them with metrics such as EM and F1 score. The findings of this study contribute to the growing body of research on Turkish QA systems by providing a comprehensive evaluation of Transformer-based pre-trained language models. In particular, adapting pre-trained language models based on Transformer architecture to Turkish poses many challenges due to both morphological richness and semantic parsing difficulties. In order to overcome these challenges, this paper comprehensively evaluates and performs performance analyses of different configurations of Turkish-specific models. This analysis not only identifies the most effective models for Turkish QA but also underscores the potential of Transformer architectures in addressing linguistic challenges unique to Turkish. The insights gained from this study pave the way for future research aimed at enhancing NLP tools for Turkish and other low-resource languages, ultimately advancing the development of robust QA systems.

2. Materials and Methods

2.1. Datasets

In this study, SQuAD-TR dataset is used for qa task. SQuAD-TR dataset is created by Budur et al. by translating original SQuAD 2.0 dataset from English to Turkish using machine translation (Budur et al., 2024). In addition, the performances of fine-tuned models are compared using XQuAD-TR dataset. This dataset is a Turkish QA dataset included in XQuAD (Cross-lingual Question-Answering Dataset) which was created to evaluate QA performance across different languages (Artetxe et al., 2019). Table 1 shows sample data from SQuAD-TR and XQuAD-TR datasets.

Datasets contain paragraphs from various articles and questions and answers related to these paragraphs. The answers to the questions consist of a part of the text in the paragraph. The starting positions of these answers within the paragraph are included in the datasets.

Table 1. Sample data from QA datasets

	SQuAD-TR	XQuAD-TR
Paragraph	"Beyoncé Giselle Knowles-Carter (d. 4 Eylül 1981), ABD'li şarkıcı, söz yazarı, prodüktör ve aktris. Houston, Teksas'ta doğup büyüdü, çocukken çeşitli şarkı ve dans yarışmalarında sahne aldı ve 1990'ların sonlarında R&B kız grubu Destiny's Child'ın solisti olarak ün kazandı. …"	"230.000$ bütçeyle, Apollo 11'den kalan orijinal ay yayın verileri, Nafzgerand tarafından derlendi ve restorasyon için Lowry Digital görevlendirildi. Video, tarihi meşruiyeti bozmadan, rastgele gürültüyü ve kamera sarsıntısını gidermek için işlendi. …"
Question	*"Beyonce ne zaman popüler olmaya başladı?"*	*"Kalan orijinal Apollo 11 iniş verilerini kim derledi?"*
Answer	*"1990'ların sonlarında"*	*"Nafzgerand"*

The SQuAD-TR dataset contains 113,082 questions, 63,639 answerable and 49,443 unanswerable, related to 19,980 Turkish paragraphs. Preprocessing steps were implemented to ensure the quality and suitability of the datasets for experiments focusing only on answerable questions. First, cases where the answers provided in the dataset did not match the content of the relevant paragraphs were identified and removed. Additionally, unanswerable questions were excluded to limit the scope of the analysis to answerable scenarios. These preprocessing steps aimed to eliminate inconsistencies and increase the overall reliability of the datasets for evaluating the QA model. The size and scope of the dataset provides a solid basis for comparing and evaluating the performance of models on QA tasks. Furthermore, the XQuAD-TR dataset contains 1,190 questions from 240 Turkish paragraphs. The XQuAD-TR dataset contains 1,190 questions from 240 Turkish paragraphs. After the preprocessing steps, the numbers of paragraphs and questions in the SQuAD-TR dataset and XQuAD-TR dataset are shown in Table 2.

Table 2. Datasets

	Paragraph	Question
SQuAD-TR	18273	60797
XQuAD-TR	240	1190

2.2. Methods

In the study, Transformer-based pre-trained language models were used. Transformer architecture has led to significant developments in NLP and is used for many NLP tasks (Acheampong et al., 2021). The architecture consists of encoder and decoder blocks. The encoder block takes text data and creates a representation of the text, while the decoder block uses the representations to create the target text. Positional coding takes into account the position of each word in the sentence. The architecture draws its power from the attention mechanism. The attention mechanism focuses on each word in the text and tries to understand the relationships between these words. Softmax is used to normalize the outputs (Vaswani et al., 2017). By using Transformer architecture, effective models can be created for NLP tasks by utilizing large text corpora in different languages. In this study, Transformer-based pre-trained language models developed for NLP tasks were used.

2.2.1. BERT

BERT is a pre-trained language model based on Transformer. BooksCorpus and English Wikipedia corpora were used in the pre-training phase. The model uses Masked Language Modeling (MLM) and Next Sentence Prediction (NSP) techniques. The MLM technique randomly masks a section of the text. An attempt is made to predict the masked words correctly, and the semantic relationships of these words with the words before and after them are analyzed. For the NSP technique, a sentence and its direct continuation or random sentences from the corpus are selected. Then, it is predicted whether the selected sentences are consecutive or not. This technique is used to understand the relationships between sentences in the text (Devlin et al., 2018). The NSP and the MLM techniques of the BERT model are shown in figure 1.

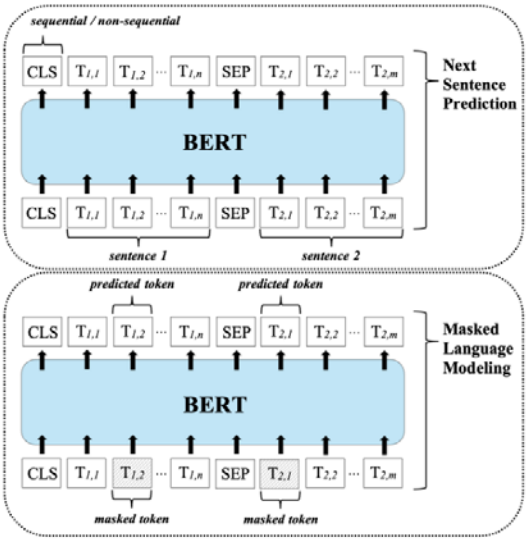


Figure 1. NSP and MLM techniques of the BERT (Devlin et al., 2018).

Thanks to its advanced natural language capabilities, the model can work effectively on various NLP tasks such as QA. For these tasks, the model is fine-tuned using relevant datasets, allowing it to be optimized for different purposes. Multilingual and Turkish customized versions of the BERT model are used in this study.

mBERT: The mBERT model is a multilingual version of the BERT model. Multilingual models can transfer learning from one language to another. Thus, tasks in low-resource languages such as Turkish can be performed using learning from different languages. The model has been trained using texts in 104 languages and can be used for NLP tasks in different languages, including Turkish.

BERTurk: BERTurk variations are BERT models specifically adapted for Turkish NLP tasks. The BERTurk model was trained on 35 GB of Turkish text data from the Wikipedia, OPUS and OSCAR corpus. There are case-sensitive "cased" and case-insensitive "uncased" versions of the models that can handle 32,000 and 128,000 unique words (Schweter, 2020).

ConvBERTurk: ConvBERT model structure aims to improve the performance and efficiency of BERT model by combining the capabilities of convolutional layers with the attention mechanism (Jiang et al., 2020). There are variations of the model specially adapted for Turkish. ConvBERTurk (cased) is a case-sensitive model trained using Turkish texts. In addition, ConvBERTurk mC4 (cased) and ConvBERTurk mC4 (uncased) variations were trained using Turkish texts from multilingual C4 corpus containing texts in many languages.

DistilBERTurk: DistilBERTurk is a faster and lighter variation of the BERT model, specifically adapted for the Turkish language. Using the distillation method, the learned knowledge from the base model is transferred from a larger teacher model to a smaller student model (Sanh et al., 2019). Thus, the model provides faster and more efficient results than the original model.

2.2.2. ELECTRA

ELECTRA is a Transformer based model that uses an approach to detect randomly changed words in the text. The architecture uses a Generator and a Discriminator. Random words are selected from the text and masked. For each masked word, the Generator generates the sentence with meaningful possible values according to the structure of the sentence. The Discriminator evaluates whether the words in the sentence generated by the Generator are the words in the original sentence (Clark et al., 2020). The structure of the language is understood in depth by using the Generator and the Discriminator. Figure 2 shows the structure of ELECTRA.

ELECTRA TR: There are different variations of the ELECTRA model specifically adapted for Turkish NLP tasks. ELECTRA Turkish Base (cased) is a case-sensitive model trained on Turkish texts, while ELECTRA TR Small (cased) is a more efficient version with fewer parameters. Both models were trained using the same data as the BERTurk model (Savci and Das, 2023). Additionally, there are both cased and uncased variations of the model trained on the Turkish part of the multilingual C4 corpus

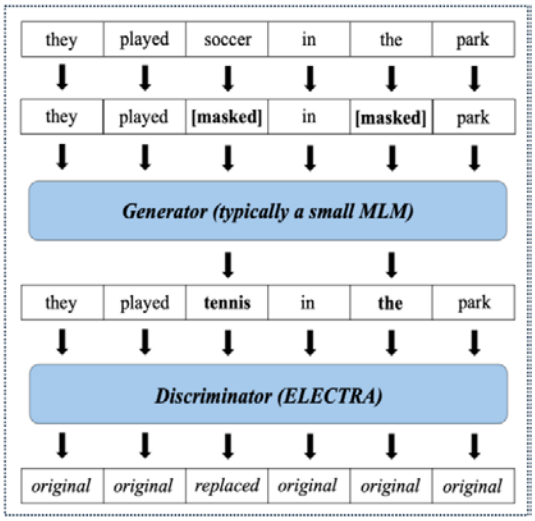


Figure 2. The ELECTRA architecture (Clark et al., 2020).

2.3. Performance Metrics

EM and F1 Score metrics were used to evaluate the performance of the models. EM is a metric based on the proportion of the model's predictions that exactly match the actual responses in the test dataset. This metric is an important and strict metric for measuring the model's ability to give correct answers that are exact matches. It has been frequently used in the literature to analyze the performance of models in QA tasks. The formula used to calculate the EM metric is given in equation 1.

$$EM\ Rate = \frac{Number\ of\ Correctly\ Answered\ Questions}{Total\ Number\ of\ Questions} \quad (1)$$

The F1 score is another commonly used metric for evaluating performance in QA tasks. It provides a balance between precision and recall, offering a single metric that reflects the accuracy of the predicted answers and their coverage of the correct answers. To calculate the F1 score, Precision and Recall results of the models are required. For these metrics, it is necessary to know the true positive (TP), false positive (FP) and false negative (FN) predictions of the model. TP refers to the number of tokens common between the correct answer and the model's prediction. FP refers to the number of tokens included in the model's prediction but not in the correct answer. FN refers to the number of tokens included in the correct answer but not in the model's prediction. The formula for the Precision metric is given in equation 2 and the formula for the Recall metric is given in equation 3.

$$Precision = \frac{TP}{TP + FP} \quad (2)$$

$$Recall = \frac{TP}{TP\ + FN} \quad (3)$$

In the study, the F1 Score used to evaluate the performance of QA models was calculated using the formula given in equation 4.

$$F1\ Score = 2\ x\ \frac{Precision\ x\ Recall}{Precision\ +\ Recall} \quad (4)$$

3. Results and Discussion

In this study, mBERT Base (cased), BERTurk Base (cased), BERTurk Base (uncased), BERTurk 128k (cased), BERTurk 128k (uncased), ConvBERTurk Base (cased), ConvBERTurk mC4 (cased), ConvBERTurk mC4 (uncased), DistilBERTurk Base (cased), ELECTRA TR Base (cased), ELECTRA TR Small (cased), ELECTRA TR mC4 (cased) and ELECTRA TR mC4 (uncased) pre-trained language models were fine-tuned using the SQuAD-TR dataset. The same parameter values were used in the fine-tuning process to ensure that the models could be evaluated under the same conditions. The parameter values used for training the models are given in Table 3.

Table 3. Fine-tuning parameters

Parameter	Value
Train Batch Size	16
Learning Rate	$3e^{-5}$
Maximum Length	512
Stride	256
Epoch	3

The training was performed with an NVIDIA Tesla V100 GPU using the Python programming language and the Transformers library. The fine-tuned models were then evaluated with the XQuAD-TR dataset. The performance of the models was evaluated using the EM and F1 Score. In the performance evaluations performed after finetuning the models, the ConvBERTurk Base (cased) model achieved the highest performance among all models with 57.82% EM and 71.59% F1 Score. As a result of the fine-tuning process, the mBERT Base (cased) model achieved 52.61% EM and 66.84% F1 Score. BERTurk 128k (cased) model showed the best performance among BERTurk variations with 57.06% EM and 71.17% F1 Score. DistilBERTurk Base (cased) model showed poor performance in Turkish QA tasks with 41.26% EM and 55.75% F1 Score. Among the ELECTRA Turkish models, the ELECTRA TR Base (cased) model achieved the best results with 57.31% EM and 71.39% F1 Score.

Among all models, the ConvBERTurk Base (cased) model performed the best, while the ELECTRA TR Small (cased) model showed the worst performance. This demonstrates that model architecture and parameter configuration significantly influence the effectiveness of pre-trained language models, particularly in complex QA tasks. Additionally, cased variations of the models were generally found to be more successful than their uncased variants. This can be attributed to the ability of cased models to better capture the semantic and syntactic intricacies of Turkish, where capitalization often conveys critical meaning.

The performance results of the fine-tuned models are presented in Table 4.

Table 4. Results of the fine-tuned models

Model	EM (%)	F1 Score (%)
mBERT Base (cased)	52.61	66.84
BERTurk Base (cased)	55.29	70.07
BERTurk Base (uncased)	52.44	67.68
BERTurk 128k (cased)	57.06	71.17
BERTurk 128k (uncased)	53.70	69.09
ConvBERTurk Base (cased)	57.82	71.59
ConvBERTurk mC4 (cased)	56.39	69.56
ConvBERTurk mC4 (uncased)	55.71	70.79
DistilBERTurk Base (cased)	41.26	55.75
ELECTRA TR Base (cased)	57.31	71.39
ELECTRA TR Small (cased)	41.18	55.19
ELECTRA TR mC4 (cased)	56.64	70.63
ELECTRA TR mC4 (uncased)	55.21	69.43

Cased models were found to be more successful than uncased models because they were able to effectively discriminate important language elements, such as proper names and abbreviations, by better managing the case sensitivity of the language. This advantage is particularly significant in Turkish, a language where orthographic case often serves as a marker of named entities, formal terms, and other contextually important elements. In particular, the ConvBERTurk Base (cased) model appears to perform best by successfully combining attentional mechanisms with convolutional layers. This architecture not only enhances the model's ability to focus on relevant portions of text but also allows it to extract features hierarchically, improving contextual understanding. In contrast, smaller models with smaller dimensions and fewer parameters showed lower performance in language comprehension and correct response extraction. Such limitations highlight the trade-off between computational efficiency and the ability to handle linguistically rich and context-dependent tasks. The fact that the mBERT model adapted to multilingual NLP tasks was not as successful as the models adapted specifically for Turkish Language, emphasizes the importance of language-specific adaptations. This finding underscores the critical need to design NLP models tailored to the unique linguistic and syntactic properties of target languages, especially for low-resource contexts. Performance comparisons of all fine-tuned models are given in Figure 3.

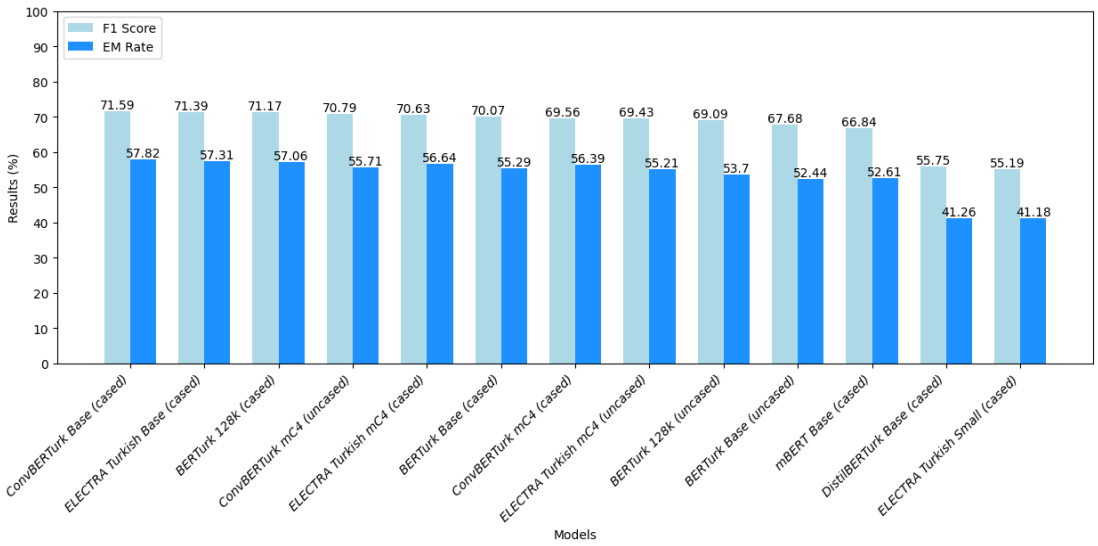


Figure 3. Performance comparisons of the fine-tuned models

4. Conclusion

This study investigated the performances of Transformer-based pre-trained language models for Turkish QA tasks. Different variations of the pre-trained language models were fine-tuned for answer extraction from Turkish texts using the SQuAD-TR dataset. As a result of the fine-tuning process, the performances of the models were tested and evaluated on the XQuAD-TR dataset. Among all models, the ConvBERTurk Base (cased) model performed the best, while the ELECTRA TR Small (cased) model showed the worst performance. Additionally, cased variations of the models were generally found to be more successful than their uncased variants. The results of this study clearly demonstrate the performance differences of Transformer-based models in Turkish QA tasks. Cased models were found to be more successful than uncased models because they were able to effectively discriminate important language elements, such as proper names and abbreviations, by better managing the case sensitivity of the language. In particular, the ConvBERTurk Base (cased) model appears to perform best by successfully combining attentional mechanisms with convolutional layers. In contrast, smaller models with smaller dimensions and fewer parameters showed lower performance in language comprehension and correct response extraction. The fact that the mBERT model adapted to multilingual NLP tasks was not as successful as the models adapted specifically for Turkish emphasizes the importance of language-specific adaptations. This research contributes to the development of efficient and accurate QA systems for low-resource languages like Turkish, paving the way for further advancements in NLP for diverse languages.

Author Contributions

The contribution percentages of the authors are given below. All authors have reviewed and approved the manuscript.

	M.İ.	M.A.
C	40	60
D	40	60
S	40	60
DCP	80	20
DAI	80	20
LS	80	20
W	60	40
CR	20	80
SR	40	60

C= concept, D= design, S= supervision, DCP= data collection, and/or processing, DAI= data analysis and/or interpretation, LS= literature search, W= writing, CR= critical review, SR= submission and revision.

Conflict of Interest

The authors declared that there is no conflict of interest.

Ethical Approval Declaration

Ethics committee approval was not required for this study because of there was no study on animals or humans.

References

Acheampong FA, Nunoo-Mensah H, Chen W. 2021. Transformer models for text-based emotion detection: a review of BERT-based approaches. Artif Intell Rev, 54(8): 5789-5829.

Akyon FC, Cavusoglu D, Cengiz C, Altinuc SO, Temizel A. 2021. Automated question generation and question answering from Turkish texts. arXiv preprint arXiv:2111.06476.

Allam AMN, Haggag MH. 2012. The question answering systems: a survey. Int J Res Rev Inf Sci (IJRRIS), 2(3).

Alzubi JA, Jain R, Singh A, Parwekar P, Gupta M. 2023. COBERT: COVID-19 question answering system using BERT. Arab J Sci

Eng, 48(8): 11003-11013.

Artetxe M, Ruder S, Yogatama D. 2019. On the cross-lingual transferability of monolingual representations. arXiv preprint arXiv:1910.11856.

Arzu M, Aydoğan M. 2023. Türkçe duygu sınıflandırma için transformers tabanlı mimarilerin karşılaştırmalı analizi. Comput Sci, 2023: 1-6.

Budur E, Özçelik R, Soylu D, Khattab O, Güngör T, Potts C. 2024. Building efficient and effective OpenQA systems for low-resource languages. arXiv preprint arXiv:2401.03590.

Clark K, Luong MT, Le QV, Manning CD. 2020. ELECTRA: pre-training text encoders as discriminators rather than generators. arXiv preprint arXiv:2003.10555.

Çelikten A, Bulut H. 2021. Turkish medical text classification using BERT. 29th Signal Processing and Communications Applications Conference (SIU), June 9-11, İstanbul, Türkiye, pp: 1-4.

Devlin J, Chang MW, Lee K, Toutanova K. 2018. BERT: pre-training of deep bidirectional transformers for language understanding. arXiv preprint arXiv:1810.04805.

Gemirter CB, Goularas D. 2021. A Turkish question answering system based on deep learning neural networks. J Intell Syst Theory Appl, 4(2): 65-75.

Hassani H, Beneki C, Unger S, Mazinani MT, Yeganegi MR. 2020. Text mining in big data analytics. Big Data Cogn Comput, 4(1): 1.

Jiang Z, Yu W, Zhou D, Chen Y, Feng J, Yan S. 2020. ConvBERT: improving BERT with span-based dynamic convolution. Adv Neural Inf Process Syst, 33: 12837-12848.

Khurana D, Koli A, Khatter K, Singh S. 2023. Natural language processing: state of the art, current trends and challenges. Multimed Tools Appl, 82(3): 3713-3744.

Locke S, Bashall A, Al-Adely S, Moore J, Wilson A, Kitchen GB. 2021. Natural language processing in medicine: a review. Trends Anaesth Crit Care, 38: 4-9.

Rajpurkar P, Jia R, Liang P. 2018. Know what you don't know: unanswerable questions for SQuAD. arXiv preprint arXiv:1806.03822.

Rajpurkar P, Zhang J, Lopyrev K, Liang P. 2016. SQuAD: 100,000+ questions for machine comprehension of text. arXiv preprint arXiv:1606.05250.

Raza S, Schwartz B, Rosella LC. 2022. CoQUAD: A COVID-19 question answering dataset system, facilitating research, benchmarking, and practice. BMC Bioinfo, 23(1): 210.

Sanh V, Debut L, Chaumond J, Wolf T. 2019. DistilBERT, a distilled version of BERT: smaller, faster, cheaper and lighter. arXiv preprint arXiv:1910.01106.

Savci P, Das B. 2023. Comparison of pre-trained language models in terms of carbon emissions, time and accuracy in multi-label text classification using AutoML. Heliyon, 9(5).

Schweter S. 2020. BERTurk-BERT models for Turkish. Zenodo, 2020: 3770924.

Soygazi F, Çiftçi O, Kök U, Cengiz S. 2021. THQuAD: Turkish historic question answering dataset for reading comprehension. 6th International Conference on Computer Science and Engineering (UBMK), September 15-17, Ankara, Türkiye, pp: 215-220.

Türkmen H, Dikenelli O, Eraslan C, Callı MC, Özbek SS. 2023. BioBERTurk: exploring Turkish biomedical language model development strategies in low-resource setting. J Healthc Inform Res, 7(4): 433-446.

Vaswani A, Shazeer N, Parmar N, Uszkoreit J, Jones L, Gomez AN, Kaiser Ł, Polosukhin I. 2017. Attention is all you need. Adv Neural Inf Process Syst, 2017: 30.

Yiğit G, Amasyalı F. 2021. Soru cevaplama sistemleri üzerine detaylı bir çalışma: veri kümeleri, yöntemler ve açık araştırma alanları. Bilisim Teknol Derg, 14(3): 239-254.

Zhu P, Yuan Y, Chen L. 2023. ELECTRA-based graph network model for multi-hop question answering. J Intell Inf Syst, 61(3): 819-834.

Black Sea Journal of Engineering and Science
doi: 10.34248/bsengineering.1597236

Open Access Journal
e-ISSN: 2619 – 8991

Research Article
Volume 8 - Issue 2: 330-340 / March 2024

ANALYSIS OF THE IMPACT OF RGB-TO-ACHROMATIC COLOR SPACE TRANSFORMATIONS ON SINGLE-IMAGE SUPER-RESOLUTION PERFORMANCE

Hürkal HÜSEM[1]*, Zeynep GÜRKAŞ AYDIN[2], Önder DEMİR[3]

[1]*Istanbul University-Cerrahpaşa, Institute of Graduate Studies, Department of Computer Engineering, 34320, Istanbul, Türkiye*
[2]*Istanbul University-Cerrahpaşa, Faculty of Engineering, Department of Computer Engineering, 34320, Istanbul, Türkiye*
[3]*Marmara University, Faculty of Technology, Department of Computer Engineering, 34840, Istanbul, Türkiye*

Abstract: Super-resolution techniques are employed to enhance the quality of digital images. Color spaces are developed to model colors in various digital environments. In the literature, several studies suggest that applying color space transformations and subsequently employing super-resolution techniques on the transformed images improve image quality. This study analyzes the impact of color space trans-formations on super-resolution applications. The analysis is conducted by performing the super-resolution process entirely in the RGB color space, followed by converting the obtained result into a different color space and comparing the quality metrics. The findings reveal that it is possible to achieve higher scores by converting RGB images into YCbCr or CIELab color spaces, despite no actual improvement in perceived image quality. Our experiments involve applying image enhancement techniques solely within the RGB color space, converting the results into alternative color spaces, and comparing them with ground truth images in Set5, Set14, BSDS100, Urban100, and DIV2K. Working in color spaces other than RGB does not lead to significant visual quality improvement. Our experiments demonstrate that solely through color space conversion, traditional metrics such as PSNR and SSIM, as well as deep learning-based metrics like DISTS and A-DISTS, can yield higher scores. Therefore, the observed improvements in quality metrics resulting from color space transformations may be misleading and may not reflect actual enhancements in image fidelity. With the A-DISTS metric that evaluates human perception, our study examines not only the impact of transformations from RGB to alternative color spaces on metrics but also evaluates the alignment of these metrics with human perception, an area that has received limited attention in the literature.

Keywords: Single-image super-resolution, Achromatic axis, Color space conversion, Image enhancement

***Corresponding author:** Istanbul University-Cerrahpaşa, Institute of Graduate Studies, Department of Computer Engineering, 34320, Istanbul, Türkiye
E mail: contact@hurkal.com (H. HÜSEM)
Hürkal HÜSEM https://orcid.org/0000-0002-5414-6481
Zeynep GÜRKAŞ AYDIN https://orcid.org/0000-0002-4125-0589
Önder DEMİR https://orcid.org/0000-0003-4540-663X

Received: December 06, 2024
Accepted: January 15, 2025
Published: March 15, 2025

Cite as: Hüsem H, Gürkaş-Aydın Z, Demir Ö. 2025. Analysis of the impact of RGB-to-achromatic color space transformations on single-image superresolution performance. BSJ Eng Sci, 8(2): 330-340.

1. Introduction

Image data captured by imaging systems, such as digital cameras, can be enhanced using various methods. Super-resolution aims to improve the data obtained by image detection systems with various techniques (Candès and Fernandez-Granda, 2014). With resolution enhancement techniques, it is possible to use more economical solutions instead of more expensive optical systems that can provide shorter exposure or high-quality images.

Color spaces are mathematically defined models developed to describe colors to determine which components can be used to obtain color. It is important to choose the appropriate color space according to the characteristics of the environment in which the image will be processed or printed to obtain true-to-life colors (Yilmaz et al., 2002). Although most of the resolution improvement studies work with RGB color space, which is modeled according to the intensity of red, green, and blue color components, it has been observed that color spaces including achromatic data along with color axes give successful results in resolution improvement studies (Dong et al., 2016; John et al., 2016; Z. Wang et al., 2021). According to Z. Wang et al. (2021), RGB color space is frequently used compared to other color spaces, and improvements made on the Y component of YCbCr (or YCC) color space in previous models are mentioned. It has been revealed that models trained using different color spaces with luminance axis other than RGB can make a significant difference in success (Z. Wang et al., 2021). John et al. (2016) show that YCbCr and CMYK models produce better PSNR results and stated that CIELab color space could also be used in resolution enhancement (John et al., 2016). Dong et al. (2016) highlighted the superior performance of the Y channel within the YCbCr color space compared to training across all axes, yet demonstrated that the best results were achieved using the RGB color space (Dong et al., 2016). Gong et al. (2017) similarly propose the use of the classified dictionary learning method in super-resolution

This work is licensed (CC BY-NC 4.0) under Creative Commons Attribution 4.0 International License

processes, recommending the L* coordinate in the CIELab color space and the Y coordinate in the YIQ system (Gong et al., 2017).

Single-image super-resolution (SISR) techniques aim to enhance the resolution of a single low-resolution image, a critical task in various image processing applications. A common practice in SISR is to convert RGB images into alternative color spaces, such as YCbCr and CIELab, assuming that this conversion improves image quality. However, the efficacy of this approach remains unclear, prompting our investigation.

Unlike previous works, which primarily focus on quantitative assessments using metrics like PSNR and SSIM, we scrutinize the perceptual quality of images resulting from color space transformations. Our methodology involves applying image enhancement techniques exclusively in the RGB color space, followed by conversion into YCbCr and CIELab for comparison with the original images. By doing so, we aim to elucidate whether the observed improvements in scores translate to tangible enhancements in visual quality.

Instead of applying resolution enhancement techniques on completely different color spaces, the color spaces of the input and output images are processed in RGB format as usual, then converted after the enhancement process. It has been demonstrated that color space transformation, when excluded from the resolution enhancement process, may independently appear to improve performance.

This study uses the Set5 (Bevilacqua et al., 2012), Set14 (Zeyde et al., 2012), BSDS100 (Martin et al., 2001), and Urban100 (Huang et al., 2015), DIV2K with unknown degradation (Agustsson and Timofte, 2017) datasets, which are frequently used in resolution enhancement studies. All images within the datasets consist of real-world high-resolution visuals paired with their corresponding synthetically generated low-resolution counterparts (Su et al., 2024).

Section II discusses the interpolation methods, neural network architectures, and transformer-based models and image quality assessment methods utilized in this study; Section III presents the experiments conducted; and Section IV provides the results and suggestions.

2. Materials and Methods

This section provides a detailed examination of the techniques and models employed in this study, alongside the image quality metrics utilized for evaluation.

2.1. Resolution Enhancement Methods

Generalizing the effect of color space conversion, interpolation methods and deep learning methods that have successful results in resolution enhancement are examined and have been studied.

2.1.1. Interpolation methods

Figure 1 shows the most widely used and known interpolation methods, which are nearest neighbor, bilinear, bicubic, and Lanczos interpolation, applied to 3D planes.

2.1.2. Nearest neighbor interpolation

The pixel value desired to be obtained in nearest neighbor interpolation takes the value of the known nearest point. Although it is the easiest interpolation method to implement and understand, created images become low quality. This is because the rectangular function is equivalent to the sinc function in the Fourier transform and there is a rapid loss in the transition gain (Fadnavis, 2014). Image distortion, called "pixelating" in nearest neighbor interpolation, is a more noticeable problem, especially as the upscaling factor is increased.

In our nearest neighbor interpolation experiments, Euclidean distance is used for distance metric.

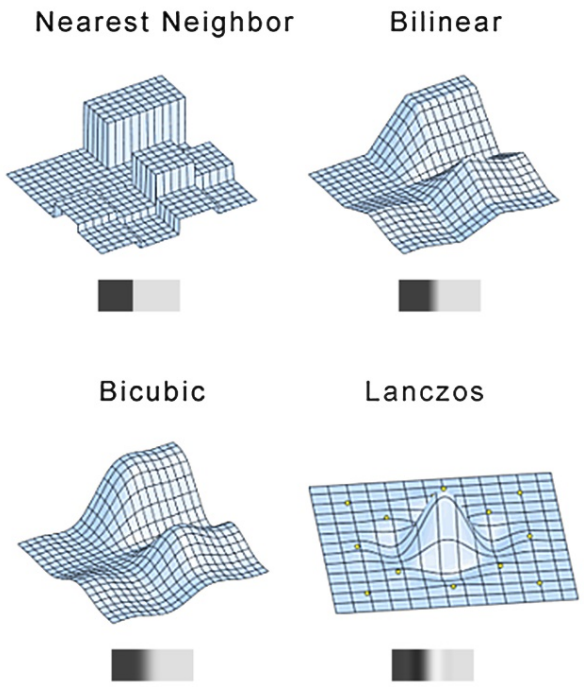


Figure 1. Demonstration of nearest neighbor, bilinear, bicubic, and Lanczos interpolation methods on examples (Getreuer, 2011).

2.1.3. Bilinear interpolation

According to the table shown in Figure 2, the data to be estimated is obtained from pairs of points. E value is obtained from A-B pairs and F value is obtained from C-D pairs. Then, P is obtained from the predicted E-F point pairs using weighted average. More realistic results are achieved than nearest neighbor interpolation (Han, 2013).

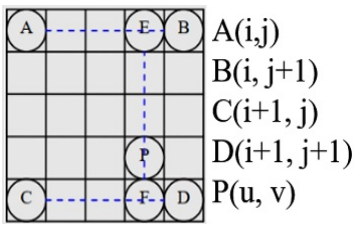


Figure 2. Application of the bilinear interpolation method on the matrix (Han, 2013).

2.1.4. Bicubic interpolation

It works similarly to the bilinear interpolation algorithm. The calculation is made here considering that it is a square matrix with 16 elements, where the points A-B-C-D are placed at the corners as shown in Figure 3. In this algorithm, the influence is expanded more than in the double linear interpolation algorithm. While calculating the point e between points A and B, a linear and non-broken curve is used by using the points A-1 and B+1 (Han, 2013).



Figure 3. Diagram of bicubic interpolation algorithm (Han, 2013).

2.1.5. Lanczos interpolation

Lanczos interpolation is a low-band filtering method close to the ideal sinc function. It is performed using the sinc filter. The computational cost is more costly than other methods because it contains trigonometric functions. The sinc function uses a windowed pruned sinc function, as shown in Figure 4 (Burger and Burge, 2008). It is more successful than the other interpolation methods mentioned in removing noises in the image.

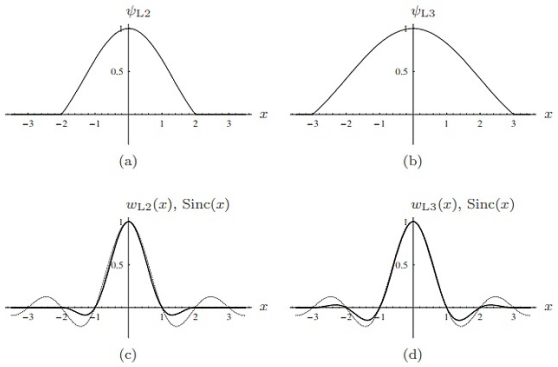


Figure 4. Lanczos window functions (a, b) and their corresponding interpolation kernels (c, d) (The original sinc function is shown as dashed.) (Burger and Burge, 2008).

2.1.6. Deep learning methods

Deep learning has introduced transformative advancements in computer vision, with architectures like Swin Transformer and GANs leading the way in feature extraction and high-resolution image synthesis. Swin Transformer excels at multi-scale feature learning through hierarchical attention mechanisms, while GANs leverage adversarial training for generating highly realistic images, exemplifying state-of-the-art deep learning applications in image processing (Ma et al., 2022; Wang et al., 2023).

2.1.7. SRGAN (Super-Resolution generative adversarial networks)

SRGAN is a generative adversarial network-based neural network that focuses on a single-image super-resolution called perceptual loss, which is the weighted sum of adversarial and content loss, with a new approach, as seen in equation 1 (Ledig et al., 2017).

$$l^{SR} = l_X^{SR} + 10^{-3} l_{Gen}^{SR} \quad (1)$$

SRGAN's discriminator network works as expected as standard GAN architecture. In a generative network, residual blocks are used to make the training process easier and to keep the previous layers connected and active. Another crucial point is the input data. Instead of using random noise, the input image is used directly.

SRGAN generates realistic textures on images but they have some artifacts (Wang et al., 2018).

In our SRGAN experiments, all parameters and network types are defined as mentioned in the original study (Ledig et al., 2017).

2.1.8. Real-ESRGAN (Enhanced super-resolution generative adversarial networks)

ESRGAN (Wang et al., 2018) tries to enhance image quality according to SRGAN results. ESRGAN uses SRGAN network architecture, adversarial loss, and perceptual loss. Besides this, residual-in-residual dense block is introduced, and batch normalization is abandoned. The idea of predicting relative realness comes from relativistic average GAN (RaGAN) (Jolicoeur-Martineau, 2018). RaGAN compares images to determine which is more realistic instead of resolving, "Is this real or fake?" (Wang et al., 2018).

Most image restoration and enhancement approaches are not good at real-world data because real-world data is more complicated than the ones generated by classical degradation models consisting of down sampling, blurring, noising, and JPEG compression. Real-ESRGAN, mainly based on ESRGAN, is focused on real-world data to overcome its complexity by using completely synthetic data while training the network. U-Net discriminator (Ronneberger et al., 2015) is used instead of a VGG-style discriminator to make local details clearer (X. Wang et al., 2021).

In our Real-ESRGAN experiments, all parameters and network types are defined as mentioned in the original study (X. Wang et al., 2021).

2.1.9. Swin2SR (SwinV2 transformer for compressed image super-resolution and restoration)

Transformer is a network architecture built for natural language processing and becomes an important advancement in this topic by using the attention mechanism (Vaswani et al., 2017). In image processing, CNNs are very useful, but Vision Transformers (ViT) achieve better results than CNNs with fewer computational resources at the training phase (Dosovitskiy et al., 2020). The idea behind ViT is the representation of the image in the transformer network.

While pixel arrays are used in CNNs, ViT uses visual tokens that represent an image split into non-overlapped patches.

CNNs use the same convolution kernel for various image sections, but this may not be a good idea for all situations because they are content-independent. The self-attention mechanism in visual transformers solves this problem, but this time, fixed-sized patches may cause border artifacts and sacrifice information over border pixels. With shallow feature extraction, deep feature extraction, and high-quality image reconstruction modules, SwinIR has fewer parameters but more successful results (Liang et al., 2021).

Swin2SR is an improved form of SwinIR (Liang et al., 2021) using SwinV2 Transformer (Liu et al., 2022) network specialized for super-resolution. With pre-normalization in the SwinV2 Transformer, more training parameters without instabilities become possible. Scaled cosine attention between queries and keys minimizes resolution gaps. With these improvements, despite using %33 fewer iterations in the training process, Swin2SR achieves similar results to SwinIR (Conde et al., 2023).

In our Swin2SR experiments, all parameters and network types are defined as mentioned in the original study (Conde et al., 2023).

2.2. Image Quality Assessments

PSNR and SSIM (Wang et al., 2004), visual comparison metrics that have been used for a long time and have become standardized in the literature, give results contrary to human perception in some techniques that show successful results. Therefore, artificial neural network-based approaches are emerging to perform better optimization in artificial neural network-based visual enhancement methods and to determine how close the proposed images are to the original forms. With LPIPS (Learned Perceptual Image Patch Similarity) (Zhang et al., 2018), DISTS (Deep Image Structure and Texture Similarity) (Ding et al., 2020) and A-DISTS (Adaptive-DISTS) (Ding et al., 2021), which are a metric developed with the idea of combining structural and textural similarity, results become very close to human interpretation.

Quality assessment metrics are divided into two categories: information-oriented and data-oriented. Knowledge-based methods such as PSNR, SSIM, FSIM (Zhang et al., 2011), VIF (Sheikh and Bovik, 2006), and GMSD (Xue et al., 2013) generally use classical distance measurements between two images. For this reason, the mentioned methods do not achieve as accurate results as DeepIQA (Bosse et al., 2017), PieAPP (Popat and Picard, 1997), LPIPS (Zhang et al., 2018), DISTS, and A-DISTS, which are data-driven methods for capturing perceptual similarities. To compare these methods, which produce values in completely different value ranges and different sizes, an approach called “Two-alternative forced choice” (2AFC) is used, in which the observer has to choose one of two options in a way that would prevent from being undecided (Ding et al., 2021).

In Figure 5, the original (a), degraded (b), and resampled original image (c) are shown. Although PSNR, SSIM, FSIM, VIF, GMSD, DeepIQA, PieAPP, and LPIPS metrics all give the result that image (b) is better than the image (c) contrary to human perception, DISTS metric is concluded that image (c) is better. However, in some cases, DISTS can reach a general conclusion over the entire image by ignoring the textures in the image. To overcome this ignorance problem, A-DISTS is developed to analyze local tissue details better with an adaptive approach.

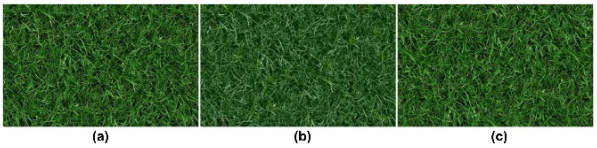


Figure 5. Original grass image (a), degradation after JPEG compression (b), resampled image (c)

The VGG neural network in DISTS does not offer sufficient sensitivity in terms of size. The convolution filters of the VGG neural network are renormalized so that the L2 norm of each filter is equal to 1. Thus, statistics are made easier to compare by ensuring that all convolution filters respond in similar intervals. A statistical feature called the dispersion index is used with A-DISTS as formulated in equation 2. In (3), $\tilde{p}_k^{(i)}$ is used to calculate the difference between X and Y images, and the pattern probability of the i^{th} dimension of the k^{th} patch is expressed. This measurement produces a value in the range of [0,1] (Ding et al., 2020).

As the PSNR and SSIM values increase, it is concluded that there are more compatible images, while results close to zero with DISTS and A-DISTS reveal that the images are more compatible. Resolution enhancement studies still include PSNR and SSIM metrics to compare with previous studies. DISTS and A-DISTS results are also included in our study, as they give the closest results to evaluating local textures and human perception according to their formulation as seen in equations 2 and 3.

$$A-\mathrm{DISTS}(X,Y)=1-\frac{1}{N}\sum_{i=0}^{M}\sum_{j=0}^{N_i}S\left(\tilde{X}_j^{(i)},\tilde{Y}_j^{(i)}\right) \quad (2)$$

$$S\left(\tilde{X}_j^{(i)},\tilde{Y}_j^{(i)}\right)=\frac{1}{K_i}\sum_{k=1}^{K_i}\left(\tilde{p}_k^{(i)}l\left(\tilde{x}_{j,k}^{(i)},\tilde{y}_{j,k}^{(i)}\right)+\tilde{q}_k^{(i)}s\left(\tilde{x}_{j,k}^{(i)},\tilde{y}_{j,k}^{(i)}\right)\right) \quad (3)$$

Another important perceptual metric is Learned Perceptual Image Patch Similarity (LPIPS). Zhang et al. introduces LPIPS designed to align closely with human visual similarity judgments. This metric leverages deep features from intermediate layers of pretrained convolutional neural networks to quantify perceptual similarity between images. These features capture both low-level visual attributes (e.g., edges, textures) and high-level semantic structures. For two images, feature maps $f_l(x_1)$ and $f_l(x_2)$ are extracted from layer l, normalized, and their L2 distances are computed in

equation 4, where w_l represents learned weights optimized to align with human perceptual judgments. The overall LPIPS distance is obtained by aggregating contributions across layers as seen in equation 5. The metric has been validated across various tasks, including super-resolution and image compression, demonstrating higher alignment with human evaluations compared to traditional metrics like PSNR and SSIM. By utilizing different architectures (e.g., AlexNet, VGG, SqueezeNet), LPIPS balances computational efficiency and perceptual fidelity, making it a robust tool for perceptual similarity assessment in computer vision (Zhang et al., 2018). In our experiments, predefined VGG network model is used to evaluate method outputs.

$$d_l(x_1, x_2) = ||w_l \odot (f_l(x_1) - f_l(x_2))||_2^2 \quad (4)$$

$$\text{LPIPS}(x_1, x_2) = \sum_l d_l(x_1, x_2) \quad (5)$$

According to the PSNR calculation in equation 6, MAX_I value depends on the maximum available value in the signal, which is 255 for RGB images for each axes (Dosselmann and Yang, 2005). However, according to John et. al., in all PSNR experiments among various color spaces, the maximum value is assumed to be 255 (John et al., 2016). Similarly, Wang et al. (2021) accepts 255 as the maximum value because of the 8-bit representation. In our study, MAX_I is used as 255, too. In the SSIM original paper, it's unclear what color space is used for the input (Nilsson and Akenine Möller, 2020; Wang et al., 2004). For both SSIM and PSNR calculations, 255 are assumed as the maximum value for all color space axes for a fair comparison within this study.

$$\text{PSNR} = 10 \cdot \log_{10}\left(\frac{\text{MAX}_I^2}{\text{MSE}}\right) \quad (6)$$

Although the PSNR calculation in resolution enhancement studies is mostly obtained by converting images in various color spaces to YCbCr color space and calculating on the Y channel, it is suggested that a clear approach is needed in this regard (Keles et al., 2021). However, in this study, in which the effect of color space change on the results is examined, the quality assessments of each color space are calculated and evaluated separately in terms of color space.

2.3. Methodology

In our experiments, all images are enhanced exclusively within the RGB color space with 4x upscaling factor. Following the super-resolution process, the upscaled and ground truth images are subsequently converted to the YCbCr and CIELab color spaces. Image Quality Assessment (IQA) metrics are then applied to both the original and enhanced images within their respective color spaces for comprehensive evaluation.

Figure 6 demonstrates the method overview.

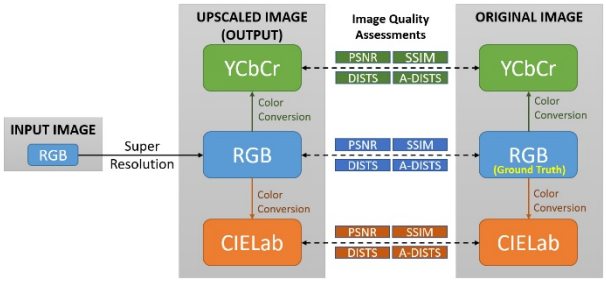


Figure 6. Method overview.

The PSNR and SSIM metrics are calculated for all axes to enable a clearer comparison of the differences between color spaces. However, many studies in the literature focus on the Y axis in the YCbCr color space, and the L* axis in the CIELab color space that include luminance information, often disregarding the chromatic components. Due to differences in how these metrics are calculated and the perspectives presented in various studies, expressing the changes in metric results as percentages is crucial for understanding the extent of improvement. In our study, the most important consideration when analyzing results should be to focus on the percentage increase in metric scores rather than their absolute values. This is because our study performs enhancements on images exclusively in the RGB color space but evaluates performance metrics on the achromatic axes of the YCbCr and CIELab color spaces.

2.3.1. Interpolation method details

In our bilinear interpolation experiments, the weighted average is used to obtain the missing value; in bicubic interpolation experiments, 4x4 pixel neighborhoods around the target pixel is used based on a cubic polynomial expansion; in Lanczos interpolation experiments, windowed sinc function utilizing 4x4 neighborhood is used.

2.3.2. SRGAN hyper-parameters and model details

The SRGAN generator network consists of 16 residual blocks, each constructed with 3×3 convolutional layers featuring 64 feature maps per layer, and employs Parametric ReLU (PReLU) as the activation function for enhancing the learning capacity of neural networks by allowing the slope of negative inputs to be learned adaptively, improving model flexibility and performance compared to standard ReLU. To upscale image resolution, two sub-pixel convolutional layers are incorporated. The discriminator network, on the other hand, is composed of 8 convolutional layers with a kernel size of 3×3, where the number of feature maps doubles at each layer, starting from 64 and increasing up to 512. Leaky ReLU (α=0.2), addresses the "dying ReLU" problem by allowing a small, non-zero gradient for negative inputs, enabling the network to learn even when activations are not strictly positive, is utilized as the activation function in the discriminator (Erdemir et al., 2020). Optimization is performed using the Adam algorithm (β1=0.9) with a learning rate set to 10^{-4} for the first 100,000 iterations and reduced to 10^{-5} for the subsequent 100,000

iterations. The loss function combines perceptual loss, which leverages content loss based on high-level feature maps of a pre-trained VGG network, with adversarial loss driven by the discriminator's ability to distinguish super-resolved images from real high-resolution images. During training, each mini-batch contains 16 images with a resolution of 96×96, derived from a dataset of 350,000 images from ImageNet. To enhance stability and avoid suboptimal convergence, the generator is initialized using the SRResNet model pre-trained with MSE loss. This carefully structured design allows SRGAN to produce photo-realistic SR images, effectively bridging the gap between low-resolution inputs and high-resolution outputs (Ledig et al., 2017).

2.3.3. Real-ESRGAN hyper-parameters and model details

The Real-ESRGAN model is designed to address complex real-world image degradations using a refined architecture and carefully tuned hyperparameters. Its generator adopts Residual-in-Residual Dense Blocks (RRDB) architecture, while the discriminator utilizes a U-Net design with spectral normalization to enhance local detail discrimination and stabilize training. The model is trained in two stages: an initial PSNR-oriented phase using L_1 loss and a combined training phase incorporating L_1, perceptual, and GAN losses with respective weights of {1, 1, 0.1}. Optimized with the Adam optimizer (β1=0.9, β2=0.999), the learning rate is set to 2×10^{-4} during the first stage and 10^{-4} in the second, with a total of 1,000,000 and 400,000 iterations respectively. The training employs high-resolution patches (256×256) from datasets such as DIV2K and Flickr2K and uses a second-order degradation model incorporating Gaussian and Poisson noise, JPEG compression, and sinc filters. Additional techniques such as Exponential Moving Average (EMA) and sharpening of ground-truth images further enhance training stability and visual sharpness, ensuring robust performance in real-world scenarios (X. Wang et al., 2021).

2.3.4. Swin2SR hyper-parameters and model details

The Swin2SR model leverages an advanced architecture optimized for compressed image super-resolution and restoration, incorporating 6 Residual Swin Transformer Blocks, each containing 6 Swin Transformer Layers with a window size of 8, 180 channels, and 6 attention heads. The training process employs an L_1 loss as the primary objective, supplemented by auxiliary and high-frequency loss functions to enhance the accuracy of low-resolution restoration and preserve fine details. Training is conducted on DIV2K and Flickr2K datasets using 192-pixel high-resolution image patches, with standard augmentations such as rotation and flipping. Optimization is performed with the Adam optimizer (β1=0.9, β2=0.999) and an initial learning rate of 2×10^{-4}. The model achieves efficient resolution enhancement through a pixel shuffle mechanism, maintaining a relatively compact size of 12 million parameters, enabling it to deliver competitive performance in restoring high-quality images from heavily compressed inputs (Conde et al., 2023).

3. Results

When the quality of the improved images is evaluated according to PSNR and SSIM measurements, as Ledig et al. mentioned, some inconsistencies stand out in various methods because these metrics are based on pixel-wise differences and cannot capture perceptual details well (Ledig et al., 2017). However, for transformer-based approaches, PSNR and SSIM metrics are still working as expected. It is observed qualitatively that better results are achieved with Swin2SR in almost all enhanced images, as seen in

Table 1.

Enhanced images on the Set5 dataset with nearest neighbor, linear, bicubic, Lanczos interpolations, SRGAN, Real-ESRGAN, and Swin2SR results are shown in Figure 7, Figure 8, and Figure 9.

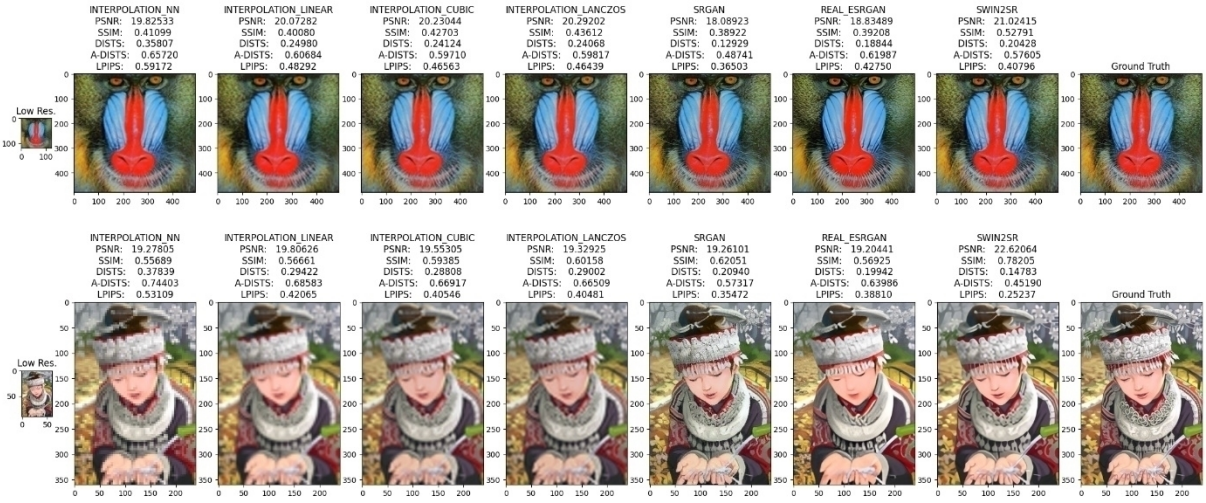


Figure 7. Interpolations, SRGAN, Real-ESRGAN, and Swin2SR results on Set14 - baboon.png and comic.png images



Figure 8. Interpolations, SRGAN, Real-ESRGAN, and Swin2SR results on Set5 dataset

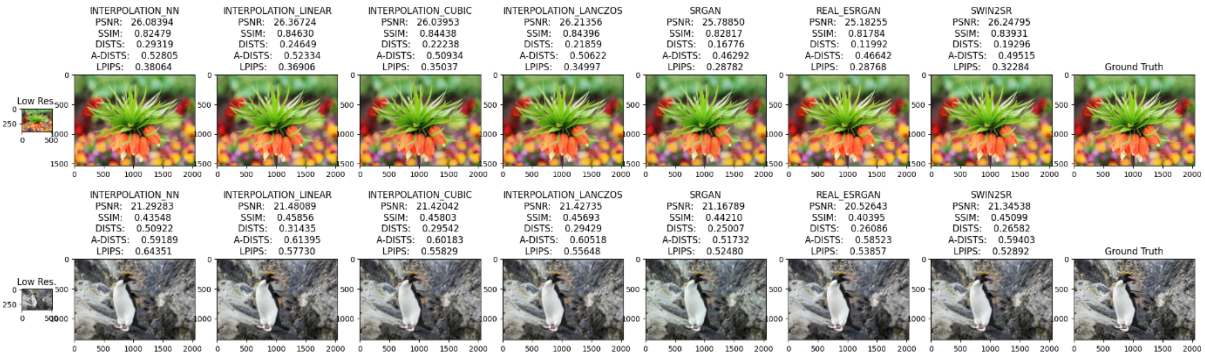


Figure 9. Interpolations, SRGAN, Real-ESRGAN, and Swin2SR results on DIV2K dataset.

The model used in Real-ESRGAN is trained with fully synthetic and noise-free data. Therefore, while it clearly shows the outlines of the objects in the images, in some cases, it is observed that "beauty filters" do smooth the image but lose the details. Besides this, there's a conflict in the baboon image between the DISTS and A-DISTS results. This is because the A-DISTS metric, which focuses much better on local patterns, is better optimized than DISTS. In such images where texture details are important, A-DISTS is a more proper metric that can be used to determine the successful method.

When the conversion to YCbCr color space is performed on SRGAN and Real-ESRGAN outputs saved by working with original images in RGB color space, it is seen that only the effect of color space change on PSNR and SSIM results is positive.

Table 1 shows the averages of PSNR, SSIM, DISTS, A-DISTS, and LPIPS values calculated before and after conversion to YCbCr and CIELab color spaces according to the methods applied to the data sets. Note that lower DISTS, A-DIST, and LPIPS values mean better results, unlike PSNR and SSIM.

Table 1. Image quality assessment scores of before and after conversion to YCbCr and CIELab color spaces (Best scores within the dataset and quality metric are marked as "*".)

Dataset	Method	Before Conversion (RGB[1])					Success of After Conversion (%)									
							YCbCr[2]					CIELab[3]				
		PSNR[4]	SSIM[5]	DISTS[6]	A-DISTS[7]	LPIPS[8]	PSNR	SSIM	DISTS	A-DISTS	LPIPS	PSNR	SSIM	DISTS	A-DISTS	LPIPS
Set5	Interpolation – NN[9]	29.03	0.86	0.26	0.48	0.34	18.7%	18.2%	28.3%	29.1%	26.7%	17.8%	18.1%	28.1%	27.8%	28.3%
	Interpolation - Linear	30.44	0.89	0.21	0.42	0.28	17.9%	16.3%	5.2%	20.6%	8.4%	17.0%	16.1%	8.0%	21.2%	13.0%
	Interpolation - Cubic	30.04	0.89	0.20	0.39	0.26	18.6%	19.1%	6.4%	23.6%	10.5%	18.5%	18.7%	8.9%	24.1%	15.0%
	Interpolation - Lanczos	30.34	0.90	0.19	0.38	0.25	18.4%	18.8%	8.7%	25.2%	12.8%	18.3%	18.4%	11.0%	25.7%	16.9%
	SRGAN[10]	31.44	0.90	0.09	0.23	*0.14	17.3%	12.0%	36.8%	43.0%	36.8%	16.9%	11.3%	39.6%	44.7%	40.9%
	Real-ESRGAN[11]	28.81	0.85	0.14	0.37	0.21	18.5%	16.5%	13.5%	26.7%	21.0%	17.8%	16.3%	19.5%	29.3%	25.1%
	Swin2SR[12]	*35.57	*0.94	*0.11	*0.24	*0.14	15.2%	6.4%	31.1%	38.6%	32.0%	14.5%	6.1%	34.6%	41.0%	36.2%
Set14	Interpolation - NN	27.07	0.82	0.26	0.50	0.37	20.1%	26.9%	25.2%	24.4%	25.6%	19.5%	26.9%	25.6%	24.0%	25.5%
	Interpolation - Linear	27.75	0.83	0.24	0.49	0.35	19.6%	25.8%	-5.2%	15.7%	10.2%	19.1%	25.8%	-4.5%	15.3%	10.7%
	Interpolation - Cubic	27.31	0.84	0.24	0.47	0.33	20.1%	25.7%	-4.3%	17.8%	11.3%	20.1%	25.8%	-3.5%	17.4%	11.5%
	Interpolation - Lanczos	27.11	0.84	0.23	0.46	0.33	20.3%	25.4%	-3.3%	18.8%	12.0%	20.3%	25.4%	-2.9%	18.2%	12.1%
	SRGAN	28.36	0.83	*0.12	0.34	*0.22	19.4%	23.5%	20.5%	28.3%	26.8%	19.1%	22.8%	21.2%	28.3%	27.6%
	Real-ESRGAN	27.80	0.81	0.15	0.44	0.27	19.5%	25.3%	3.8%	18.5%	17.0%	19.1%	25.3%	3.8%	19.1%	17.6%
	Swin2SR	*31.50	*0.89	0.14	0.34	*0.22	16.8%	14.0%	11.5%	26.3%	22.8%	16.5%	14.0%	9.9%	26.2%	22.5%
BSDS100	Interpolation - NN	25.85	0.83	0.28	0.51	0.41	22.0%	43.5%	25.2%	21.6%	24.7%	21.1%	43.3%	24.8%	20.2%	24.2%
	Interpolation - Linear	26.75	0.86	0.27	0.49	0.37	21.3%	38.7%	-4.6%	16.9%	11.6%	20.5%	38.3%	-3.5%	16.2%	11.1%
	Interpolation - Cubic	26.43	0.87	0.26	0.47	0.36	21.5%	36.8%	-4.9%	18.0%	9.8%	20.8%	36.4%	-4.1%	17.2%	9.0%
	Interpolation - Lanczos	26.50	0.87	0.26	0.47	0.35	21.5%	36.1%	-4.0%	18.8%	10.7%	20.8%	35.7%	-3.5%	18.0%	10.1%
	SRGAN	28.09	0.84	*0.12	*0.32	*0.22	20.2%	34.4%	27.4%	31.0%	27.6%	19.3%	32.6%	25.4%	30.2%	26.9%
	Real-ESRGAN	28.25	0.85	0.16	0.41	0.27	19.8%	34.7%	13.6%	24.0%	22.6%	19.1%	34.1%	13.4%	23.4%	22.1%
	Swin2SR	*31.33	*0.91	0.17	0.36	0.25	17.8%	21.7%	14.8%	27.5%	25.2%	17.0%	21.3%	15.4%	26.9%	25.2%
Urban100	Interpolation - NN	25.33	0.81	0.26	0.47	0.36	22.5%	31.6%	21.4%	21.2%	22.1%	21.6%	32.1%	20.6%	20.5%	21.9%
	Interpolation - Linear	25.84	0.82	0.26	0.46	0.35	22.0%	31.4%	1.1%	17.8%	12.9%	21.1%	31.7%	1.1%	17.5%	13.6%
	Interpolation - Cubic	25.13	0.82	0.25	0.44	0.33	22.7%	35.2%	1.7%	18.9%	14.6%	22.1%	35.4%	1.6%	18.5%	14.9%
	Interpolation - Lanczos	25.12	0.82	0.25	0.44	0.33	22.7%	34.7%	2.4%	19.4%	15.0%	22.1%	34.8%	2.2%	19.0%	15.1%
	SRGAN	26.93	0.84	*0.11	0.33	0.21	21.1%	19.7%	29.2%	29.8%	30.9%	20.2%	18.5%	28.3%	30.1%	31.1%
	Real-ESRGAN	25.69	0.82	0.13	0.38	0.25	22.0%	24.5%	12.7%	23.4%	21.2%	21.1%	24.9%	12.6%	24.0%	22.1%
	Swin2SR	*30.55	*0.91	*0.11	*0.29	*0.18	18.0%	11.1%	26.0%	30.9%	29.2%	17.2%	11.0%	26.1%	31.6%	30.6%
DIV2K (unknown deg.)	Interpolation - NN	22.93	0.57	0.41	0.59	0.54	18.1%	40.3%	28.9%	17.0%	20.6%	18.8%	40.3%	26.3%	16.5%	17.7%
	Interpolation - Linear	23.20	0.58	0.30	0.61	0.51	17.8%	37.5%	-2.5%	17.7%	14.0%	18.5%	37.1%	-3.5%	14.8%	10.8%
	Interpolation - Cubic	22.80	0.57	0.28	0.59	0.49	18.4%	41.9%	-1.6%	18.3%	13.5%	19.1%	41.5%	-2.0%	16.2%	9.9%
	Interpolation - Lanczos	22.95	0.58	0.28	0.59	0.49	19.0%	41.0%	0.3%	19.4%	14.2%	18.8%	43.7%	-0.9%	16.5%	10.9%
	SRGAN	23.00	0.57	0.23	*0.53	*0.44	18.3%	41.7%	4.4%	18.0%	16.2%	18.8%	41.3%	2.5%	27.7%	13.1%
	Real-ESRGAN	22.33	0.54	*0.21	0.58	*0.44	16.9%	47.0%	10.8%	10.9%	14.4%	19.5%	46.6%	4.9%	18.8%	10.3%
	Swin2SR	*23.29	*0.59	0.25	0.58	0.46	36.7%	38.7%	2.9%	22.2%	14.9%	18.5%	37.5%	1.1%	19.4%	10.8%
					Average (%):		20.0%	28.5%	10.9%	22.8%	18.9%	19.2%	28.3%	11.1%	23.0%	18.9%

[1] RGB: Red, Green, and Blue, [2] YCbCr: Luminance, Chrominance Blue, and Chrominance Red, [3] CIELab: Commission Internationale de l'Eclairage's standard; L* is for luminance, a* is for green to red, b* is for blue to yellow, [4] Peak Signal-to-Noise Ratio, [5] Structural Similarity Index Measure, [6] Deep Image Structure and Texture Similarity, [7] Adaptive-Deep Image Structure and Texture Similarity, [8] Learned Perceptual Image Patch Similarity, [9] Nearest Neighbor, [10] Super Resolution Generative Adversarial Networks, [11] Enhanced Super-Resolution Generative Adversarial Networks, [12] SwinV2 Transformer for Compressed Image Super-Resolution and Restoration.

4. Discussion

Our study delves into the dual impact of transforming RGB data into alternative color spaces, emphasizing not only the quantitative changes in evaluation metrics but also their correspondence to human perceptual experiences. The findings suggest that while certain transformations improve specific metrics, their perceptual relevance varies, underscoring the importance of incorporating human-centric assessments in future research. These insights highlight a critical gap in the literature, advocating for the development of methods that balance computational accuracy with perceptual validity.

Wang et al. (2021) and John et al. (2016) have highlighted the effectiveness of the YCbCr color space for improving PSNR and SSIM metrics in super-resolution tasks. Our findings corroborate these observations, demonstrating that transformations to the YCbCr space lead to higher scores in these metrics. However, similar to prior studies, we found that these improvements do not correspond to significant enhancements in perceptual image quality. Furthermore, the results obtained through transformations to the CIELab color

space align with the findings of John et al. (2016), who suggested its potential utility in resolution enhancement. Nevertheless, our experiments reveal that the contributions of these transformations are predominantly metric-specific and do not reflect tangible improvements in visual fidelity (Ding et al., 2021; John et al., 2016).

According to Dong et al. (2016), the YCbCr space allows the method to enhance only the luminance channel, which is crucial for SR tasks aiming at perceptual improvements. This focus reduces the computational load and avoids distortions in color channels (Dong et al., 2016).

Xu et al. (2020) propose a super-resolution reconstruction method that integrates $L_{2/3}$ sparse regularization with color channel constraints. By converting low-resolution images to the YCbCr color space, the luminance channel is enhanced using the sparse model, while the chrominance channels are refined to reduce color artifacts (Xu et al., 2020). Note that this study applies x2 upscaling factor to only five images that listed in Table 2, PSNR and SSIM metrics are applied on Y channel solely.

Table 2. Bicubic interpolation and proposed method of Xu et al. (2020), x2 upscaling factor with YCbCr color space

	PSNR [1]			SSIM [2]		
Image	Bicubic Interpolation	Xu et al.'s Method	Success	Bicubic Interpolation	Xu et al.'s Method	Success
Flowers	30.38	33.40	9.9%	0.898	0.938	4.5%
Comic	26.06	27.92	7.1%	0.851	0.908	6.7%
Butterfly	27.42	31.19	13.7%	0.915	0.958	4.7%
Skiing	32.00	34.33	7.3%	0.931	0.953	2.4%
Bike	25.66	27.92	8.8%	0.850	0.913	7.4%

[1] Peak Signal-to-Noise Ratio, [2] Structural Similarity Index Measure

In all the experiments of our study, the resolution improvement process is carried out in RGB color space, and measurements are calculated before and after the conversion to the color spaces specified in the tables. Therefore, the effects of different color spaces on the calculations of success values are examined without any effect on the improvement phase. Although converting an image in RGB color space to YCbCr and CIELab color spaces does not affect the image quality, it positively affects the quality assessment results. The metrics used to assess the success of SISR methods are not sufficient for evaluating the effects on different color spaces. There is a need for alternative metrics that can effectively assess the success across various color spaces. Without developing these metrics, examining the impact of color space transformation will not be robust.

The success seems to be high in interpolating and deep learning architectures because the value ranges between the color spaces do not match exactly. The extreme values and the number of possible different values are shown in Table 3.

Table 3. Value ranges of RGB, YCbCr, and CIELab color space axes (Yang et al., 2007)

	RGB[1]			YCbCr[2]			CIELab[3]		
	R	G	B	Y	Cb	Cr	L*	a*	b*
Maximum Value	255	255	255	235	240	240	100	110	110
Minimum Value	0	0	0	16	16	16	0	-110	-110
Number of values	256	256	256	220	225	225	101	221	221
Possible values per color space	16,777,216			11,137,500			4,932,941		

[1] RGB: Red, Green, and Blue, [2] YCbCr: Luminance, Chrominance Blue, and Chrominance Red, [3] CIELab: Commission Internationale de l'Eclairage's standard; L* is for luminance, a* is for green to red, b* is for blue to yellow.

Converting an image from an RGB color space that scales to a wider range of values, such as a YCbCr color space that scales to a narrower range of values, will reduce the variety of color values from 16,581,375 different possible values to 11,137,500. As a result of this decrease, although there is no improvement other than the technique applied in the image quality, the quality seems to increase according to the calculation metrics. The same situation is observed in the CIELab color space, too. This time, while converting from RGB, all possible values in CIELab decrease to 4,932,941.

The impact of color space transformation on performance metrics could similarly be a subject of investigation in other areas of image processing.

Despite these considerations, if a comparison between YCbCr and CIELab color spaces is to be made beyond RGB, YCbCr emerges as computationally efficient due to its linear transformation from RGB and the independent processing of the luminance channel. This makes it ideal for tasks where structural accuracy is prioritized over color fidelity. On the other hand, CIELab's alignment with human perception renders it suitable for applications

requiring high color accuracy, albeit at the cost of increased computational complexity. Consequently, YCbCr is often preferred in real-time applications, whereas CIELab is more suitable for offline processes where perceptual quality is of greater importance.

5. Conclusion

This study explores the intricate relationship between color space transformations and super-resolution techniques, highlighting the balance between quantitative metrics and perceptual quality. While RGB continues to dominate as the standard color space for resolution enhancement, our findings challenge its singular dominance by examining the impact of post-enhancement transformations to any color space with achromatic axis like YCbCr and CIELab. Although these transformations do not inherently enhance visual quality, they significantly influence image quality metrics both pixel-wise and perceptual-based. This discrepancy raises important questions about whether working in different color spaces meaningfully impacts perceived image quality or simply skews numerical evaluations. Future efforts should aim to refine quality assessment frameworks and explore innovative hybrid approaches that maximize both perceptual and computational benefits in super-resolution tasks.

Author Contributions

The percentages of the authors' contributions are presented below. All authors reviewed and approved the final version of the manuscript.

	H.H.	Z.G.A.	Ö.D.
C	70	15	15
D	80	10	10
S	30	35	35
DCP	80	10	10
DAI	70	15	15
L	80	10	10
W	80	10	10
CR	80	10	10
SR	70	15	15

C=Concept, D= design, S= supervision, DCP= data collection and/or processing, DAI= data analysis and/or interpretation, L= literature search, W= writing, CR= critical review, SR= submission and revision.

Conflict of Interest

The authors declared that there is no conflict of interest.

Ethical Consideration

Ethics committee approval was not required for this study because there was no study on animals or humans.

Acknowledgements

This study is a part of the PhD thesis of Hürkal HÜSEM at the Institute of Graduate Studies, Istanbul University-Cerrahpaşa, Istanbul, Türkiye. The source code for this project is available on GitHub at https://github.com/hurkal/sisr-color-space

References

Agustsson E, Timofte R. 2017. Ntire 2017 challenge on single image super-resolution: Dataset and study. In: Proceedings of the IEEE conference on computer vision and pattern recognition workshops, Honolulu, HI, USA, July 21-26, pp: 126–135.

Bevilacqua M, Roumy A, Guillemot C, Alberi-Morel ML. 2012. Low-complexity single-image super-resolution based on nonnegative neighbor embedding. In: Proceedings of the 23rd British Machine Vision Conference (BMVC), Surrey, UK, September 3-7, pp: 1–10.

Bosse S, Maniry D, Müller KR, Wiegand T, Samek W. 2017. Deep neural networks for no-reference and full-reference image quality assessment. IEEE Trans Image Process, 27(1): 206–219.

Burger W, Burge MJ. 2008. Introduction to spectral techniques. In: Principles of Digital Image Processing: Core Algorithms. Springer, London, UK, 1st ed, pp: 313–342.

Candès EJ, Fernandez-Granda C. 2014. Towards a mathematical theory of super-resolution. Commun Pure Appl Math, 67(6): 906–956.

Conde MV, Choi UJ, Burchi M, Timofte R. 2023. Swin2SR: Swinv2 transformer for compressed image super-resolution and restoration. In: Proceedings of the European Conference on Computer Vision (ECCV) Workshops, Tel Aviv, Israel, October 23–27, pp: 669–687.

Ding K, Liu Y, Zou X, Wang S, Ma K. 2021. Locally Adaptive Structure and Texture Similarity for Image Quality Assessment. In: Proceedings of the 29th ACM International Conference on Multimedia, Virtual Event, China, October 20-24, pp: 2483–2491.

Ding K, Ma K, Wang S, Simoncelli EP. 2020. Image quality assessment: Unifying structure and texture similarity. IEEE Trans Pattern Anal Mach Intell, 4(5): 2567–2581.

Dong C, Loy CC, He K, Tang X. 2016. Image Super-Resolution Using Deep Convolutional Networks. IEEE Trans Pattern Anal Mach Intell, 38(2): 295–307.

Dosovitskiy A, Beyer L, Kolesnikov A, Weissenborn D, Zhai X, Unterthiner T. 2020. An image is worth 16x16 words: Transformers for image recognition at scale. ArXiv Prepr ArXiv201011929.

Dosselmann R, Yang XD. 2005. Existing and emerging image quality metrics. In: Canadian Conference on Electrical and Computer Engineering, Saskatoon, SK, Canada, May 1-4, pp: 1906–1913.

Erdemir E, Dragotti P.L, Gündüz D. 2020. Privacy-aware time-series data sharing with deep reinforcement learning. IEEE Trans Inf Forensics Secur, 16: 389–401.

Fadnavis S. 2014. Image interpolation techniques in digital image processing: an overview. Int J Eng Res Appl, 4(10): 70–73.

Getreuer P. 2011. Linear methods for image interpolation. Image Process Line, 1: 238–259.

Gong R, Wang Y, Cai Y, Shao X. 2017. How to deal with color in super resolution reconstruction of images. Opt Express, 25(10): 11144–11156.

Han D. 2013. Comparison of commonly used image interpolation methods. In: Proceedings of the 2nd International Conference on Computer Science and Electronics Engineering, Hangzhou, China, March 22-23, pp: 1556–1559.

Huang JB, Singh A, Ahuja N. 2015. Single image super-resolution from transformed self-exemplars. In: Proceedings of the IEEE conference on computer vision and pattern recognition, Boston, MA, USA, pp: 5197–5206.

John N, Viswanath A, Sowmya V, Soman KP. 2016. Analysis of various color space models on effective single image super resolution. In: Berretti S, Thampi S.M, Srivastava P.R, editors. Intelligent Systems Technologies and Applications. Springer, Cham, Switzerland, 1st ed, pp: 529–540.

Jolicoeur-Martineau A. 2018. The relativistic discriminator: a key element missing from standard GAN. ArXiv Prepr ArXiv180700734.

Keles O, Yilmaz, MA, Tekalp AM, Korkmaz C, Dogan Z. 2021. On the Computation of PSNR for a Set of Images or Video. In: Picture Coding Symposium, Bristol, UK, June 29 - July 2, pp: 1–5.

Ledig C, Theis L, Huszár F, Caballero J, Cunningham A, Acosta A. 2017. Photo-realistic single image super-resolution using a generative adversarial network. In: Proceedings of the IEEE conference on computer vision and pattern recognition, pp: 4681–4690.

Liang J, Cao J, Sun G, Zhang K, Van Gool L, Timofte R. 2021. SwinIR: Image restoration using swin transformer. In: Proceedings of the IEEE/CVF International Conference on Computer Vision, Montreal, BC, Canada, October 11-17, pp: 1833–1844.

Liu Z, Hu H, Lin Y, Yao Z, Xie Z, Wei Y. 2022. Swin transformer v2: Scaling up capacity and resolution. In: Proceedings of the IEEE/CVF conference on computer vision and pattern recognition, New Orleans, LA, USA, June 18-24, pp: 12009–12019.

Ma J, Tang L, Fan F, Huang J, Mei X, Ma Y. 2022. SwinFusion: Cross-domain long-range learning for general image fusion via swin transformer. IEEECAA J Autom Sin, 9(7): 1200–1217.

Martin D, Fowlkes C, Tal D, Malik J. 2001. A database of human segmented natural images and its application to evaluating segmentation algorithms and measuring ecological statistics. In: Proceedings Eighth IEEE International Conference on Computer Vision, Vancouver, BC, Canada, pp: 416–423.

Nilsson J, Akenine Möller T. 2020. Understanding ssim. ArXiv Prepr ArXiv200613846.

Popat K, Picard RW. 1997. Cluster-based probability model and its application to image and texture processing. IEEE Trans Image Process, 6(2): 268–284.

Ronneberger O, Fischer P, Brox T. 2015. U-net: Convolutional networks for biomedical image segmentation. In: Medical Image Computing and Computer-Assisted Intervention, Munich, Germany, October 5-9, pp: 234–241.

Sheikh H.R, Bovik A.C. 2006. Image information and visual quality. IEEE Trans Image Process, 15(2): 430–444.

Su H, Li Y, Xu Y, Fu X, Liu S. 2024. A review of deep-learning-based super-resolution: From methods to applications. Pattern Recognit, 157: 110935.

Vaswani A, Shazeer N, Parmar N, Uszkoreit J, Jones L, Gomez AN. 2017. Attention is all you need. Adv Neural Inf Process Syst, 30.

Wang X, Xie L, Dong C, Shan Y. 2021. Real-esrgan: Training real-world blind super-resolution with pure synthetic data. In: Proceedings of the IEEE/CVF International Conference on Computer Vision, Montreal, BC, Canada, October 11-17, pp: 1905–1914.

Wang X, Yu K, Wu S, Gu J, Liu Y, Dong C. 2018. Esrgan: Enhanced super-resolution generative adversarial networks. In: Proceedings of the European conference on computer vision (ECCV) workshops, Munich, Germany, September 8-14, pp: 0–0.

Wang Y, Liu W, Sun W, Meng X, Yang G, Ren K. 2023. A progressive feature enhancement deep network for large-scale remote sensing image super-resolution. IEEE Trans Geosci Remote Sens, 61(1): 1–13.

Wang Z, Bovik AC, Sheikh HR, Simoncelli EP. 2004. Image quality assessment: from error visibility to structural similarity. IEEE Trans Image Process, 13(4): 600–612.

Wang Z, Chen J, Hoi SCH. 2021. Deep Learning for Image Super-Resolution: A Survey. IEEE Trans Pattern Anal Mach Intell, 43(10): 3365–3387.

Xu Z, Ma Q, Yuan F. 2020. Single color image super-resolution using sparse representation and color constraint. J Syst Eng Electron, 31(2): 266–271.

Xue W, Zhang L, Mou X, Bovik AC. 2013. Gradient magnitude similarity deviation: A highly efficient perceptual image quality index. IEEE Trans Image Process, 23(2): 684–695.

Yang Y, Yuhua P, Zhaoguang L. 2007. A fast algorithm for YCbCr to RGB conversion. IEEE Trans Consum Electron, 53(4): 1490–1493.

Yilmaz İ, Güllü M, Baybura T, Erdoğan AO. 2002. Renk Uzayları ve Renk Dönüşüm Programı (RDP). Afyon Kocatepe Üniversitesi Fen Ve Mühendis Bilim Derg, 2(2): 19–35.

Zeyde R, Elad M, Protter M. 2012. On single image scale-up using sparse-representations. In: Curves and Surfaces: 7th International Conference, Avignon, France, pp: 711–730.

Zhang Lin, Zhang Lei, Mou X, Zhang D. 2011. FSIM: A feature similarity index for image quality assessment. IEEE Trans Image Process, 20(8): 2378–2386.

Zhang R, Isola P, Efros AA, Shechtman E, Wang O. 2018. The unreasonable effectiveness of deep features as a perceptual metric. In: Proceedings of the IEEE conference on computer vision and pattern recognition, Salt Lake City, UT, USA, June 18-23, pp: 586–595.

Black Sea Journal of Engineering and Science
doi: 10.34248/bsengineering.1597989

Open Access Journal
e-ISSN: 2619 – 8991

Araştırma Makalesi (Research Article)
Cilt 8 - Sayı 2: 341-353 / Mart 2025
(Volume 8- Issue 2: 341-353 / March 2025)

UZAKTAN EĞİTİMDEN YÜZ YÜZE EĞİTİME: KTÜ KANUNİ KAMPÜSÜ MEKÂNSAL İMGELERİ

Hare KILIÇASLAN[1]*, Esra BABUL KOÇ[1]

[1]*Karadeniz Technical University, Faculty of Architecture, Department of Architecture, 61080, Trabzon, Türkiye*

Özet: Bu araştırmada, Karadeniz Teknik Üniversitesi Kanuni Kampüsü'nde eğitim gören öğrencilerin pandemi ve deprem felaketleri nedeniyle uzaktan eğitim sürecine geçiş yapmalarının ardından, yüz yüze eğitime geri dönüşleriyle değişen mekânsal imgelerinin incelenmesi hedeflenmektedir. Araştırmanın temel amacı, öğrencilerin zihinlerinde zaman içerisinde değişen imgelerin bilişsel haritalar aracılığıyla temsil edilmesidir. Araştırma, "Öğrencilerin hedef ve tercihleri doğrultusunda deneyimledikleri mekânlarda ve kampüs içi yaya hareketlerinde, uzaktan eğitim ve yüz yüze eğitime bağlı olarak değişkenlik gösteren imgeler nelerdir?" sorusuna yanıt aramaktadır. Bu bağlamda, aynı öğrenci grubuna bir yıl arayla uygulanan bilişsel haritalara odaklanılmıştır. Elde edilen haritaların, Kevin Lynch'in çevrenin algılanmasında ve okunabilmesinde temel unsurlar olan yollar, düğüm noktaları, işaret öğeleri/nirengi noktaları, kenarlar/sınırlar ve bölgelere göre analiz edilmesi yoluyla öğrencilerin mekân algılarındaki değişim ortaya konulmuştur. Ayrıca bilişsel haritalar Gary T. Moore tarafından önerilen sınıflandırma seviyelerine göre kategorize edilerek, süreç içerisinde farklılaşan mekânsal kullanımların bilişsel değişimi irdelenmiştir. Öğrencilerin bilişsel haritaları üzerine yapılan bu araştırma, kampüs deneyimlerinin ve zaman faktörünün bilişsel haritaların oluşumunda önemli rol oynadığını göstermektedir.

Anahtar kelimeler: Mekân algısı, Mekânsal deneyim, Bilişsel harita, KTÜ Kanuni Kampüsü

From Distance Education to Face-to-Face Education: Spatial Images of KTU Kanuni Campus

Abstract: This study aims to investigate the evolving spatial perceptions of students at Karadeniz Technical University's Kanuni Campus as they transition back to face-to-face education following a period of distance learning necessitated by the pandemic and earthquake disasters. The primary objective of the study is to represent the evolving images in students' minds over time through the use of cognitive maps. The research aims to answer the question, "What are the images that change depending on distance education and face-to-face education in the spaces and on-campus pedestrian movements that students experience in line with their goals and preferences?" In this context, the study focused on cognitive maps applied to the same group of students one year apart. The maps were analyzed within the framework of Lynch's city images and categorized according to the classification levels proposed by Moore. The change in students' spatial perception was elucidated through an analysis of maps generated based on the fundamental elements of Kevin Lynch's theory of environmental perception and legibility: paths, nodes, landmarks, edges, and districts. In addition, the cognitive maps were categorized according to the classification levels proposed by Gary T. Moore, and the cognitive change of differentiated spatial uses in the process was examined. This study on students, cognitive maps shows that campus experiences and the factor of time play a significant role in the formation of cognitive maps.

Keywords: Space perception, Spatial experience, Cognitive map, KTU Kanuni Campus

***Sorumlu yazar (Corresponding author):** Karadeniz Technical University, Faculty of Architecture, Department of Architecture, 61080, Trabzon, Türkiye
E mail: hkilicaslan@ktu.edu.tr (H. KILIÇASLAN)
Hare KILIÇASLAN https://orcid.org/0000-0002-6113-7962
Esra BABUL KOÇ https://orcid.org/0000-0003-4664-4656

Gönderi: 09 Aralık 2024 **Received:** December 09, 2024
Kabul: 15 Ocak 2025 **Accepted:** January 15, 2025
Yayınlanma: 15 Mart 2025 **Published:** March 15, 2025

Cite as: Kılıçaslan H, Babul Koç E. 2025. From distance education to face-to-face education: Spatial images of KTU Kanuni Campus. BSJ Eng Sci, 8(2): 341-353.

1. Giriş

Küresel ve yerel değişimler/dönüşümlerden en başta etkilenen alanlardan biri de hiç şüphesiz ki eğitim olmuştur. Eğitimin tüm kademelerinde olduğu gibi üniversiteler de hızla uyum sağlanması gereken süreçlerin ortasında kalmıştır. Eğitim-öğretim ve araştırma süreçlerinin sürdürülebilmesi için Covid-19 pandemisi sırasında adapte olunan uzaktan eğitim, 2024 yılı şubat ayında yaşanan deprem felaketinin ardından yine gündeme gelmiştir. Bu süreçte üniversite öğrencileri, kampüs yaşantısından bir süre uzak kalmışlardır. Kampüs deneyimine verilen bu ara, öğrencilerin kampüs imajlarının zihinlerindeki değişiminin nasıl ve ne yönde olduğu sorusunu gündeme getirmiştir. Demirel'in (2004) de ifade ettiği gibi, mekân fiziksel olarak durağan bir yapıya sahip olsa da mekânı deneyimleyen insanlar mekân içinde hareket ettikçe, birtakım eylemler gerçekleştirdikçe mekânla olan konumsal ve boyutsal ilişkiler değişmektedir. Bu durumun bir sonucu olarak bakış açılarındaki değişkenlik, insanların zihinlerindeki mekâna dair farklı ayrıntıları bir araya getirerek toplu bir mekân izlenimi oluşturur.

Bireyin mekân ile ilişkisini odağına alan bu çalışma, öğrencilerin kampüsle kurdukları ilişkiler ve deneyimler sonucu değişen çevre algısını biliş haritaları aracılığıyla

This work is licensed (CC BY-NC 4.0) under Creative Commons Attribution 4.0 International License

değerlendirmektedir. Biliş haritaları, 20. yüzyılın ortalarından itibaren Kevin Lynch'in öncülüğünde gündelik hayatta edinilen deneyimlerin fiziksel gösteri aracına dönüştürüldüğü bir yöntem olarak kullanılmaktadır. En genel ifadeyle bilişsel haritalamayı, fiziksel çevreye ait başta uzaklık ve konumsal bilgiler olmak üzere her türlü bilginin hatırlanma, depolanma ve organize edilmesine dayanan ilişki örüntüsünün oluşturduğu bir araç olarak tanımlamak mümkündür (Gifford, 1987; Gulliver, 1908). Bilişsel haritalar günlük yaşantıda bilinçli veya bilinçdışı ilişkiler aracılığıyla çevreyle kurulan diyalektikte, mekânsal bilginin konumsal ve olgusal niteliklerinin kodlanma, saklanma, hatırlanma, çözümlenme ve deneyimlenme ağını içeren bir süreci tanımlamaktadır (Downs ve Stea, 1973). Dolayısıyla bu haritalar, mekânsal ve çevresel ilişkilerin olgusal durumlarını ve birbirleriyle ilişkilerini temsil eden zihinsel modellerdir (Billinghurst ve Weghorst, 1995). Rapoport da (1977) temelde mekânsal bir özellik taşıyan bilişsel haritaların, toplumsal veya bireysel ölçekte değerler içeren bilinçli ya da bilinçsiz, gerçeğe yakın ya da değil sübjektif tecrübeler ve değerler içerdiğini belirtmektedir. Bilişsel haritalar, bireylerin mekânsal temsilinin analizine bilgi sağlayan, günlük fiziksel çevredeki nesnelerin veya olguların göreceli konumları hakkında uzun süreli depolanmış bilgi olarak tanımlanmaktadır (Golledge ve Stimson, 1997). Zihinsel imgelere ve kavramlara ilişkin görselleştirmelere yarayan bilişsel haritalar, uzun zaman dilimlerine yayılan bilgilerin temsil edilmesinde araç görevi görmektedir. Biliş, algılama, sezgi ve muhakeme içeren bilişsel haritalama süreçleri, karmaşık bilgilerin düzenlenmesini ve basitleştirilmesini sağlamaktadır (Sammut-Bonnici ve McGee, 2015). Diğer bir deyişle, çevrede bulunan farklı alanların okunmasına ve yorumlanmasına ilişkin analizlerin yapılabileceği, bireyin bilişinin bir ürünüdür (Richter vd., 2012).

Lynch (1960) çevre ile birey arasında kurulan çift yönlü ilişkiyle çevrenin bireye birçok imge sunduğunu, bireyin de bu bilgiyi kendi filtresinden geçirerek anlamlandırdığını ifade etmektedir. Haritaların şekillendirilmesi, gerçekliğe dayanan deneyimlerin kişisel, kültürel ve öznel yargılar aracılığıyla; kullanım, algılama ve değerlendirme sürecinden geçen bir üretim aşamasına dayanmaktadır (Sulster, 2005). Haritaların bilişsel sürecinin tamamlanarak somut olarak ortaya konulabilmesi için bireyin çevresel algılama ve deneyimleme edinimini yaşaması gerekir. Bilişsel bir eylem olan çevre deneyimi bir yandan mekânsal ve dokunsal ilişkileri içerirken diğer yandan da imgelenebilir nitelikler taşır.

Tasarlanmış bir çevre ve kurgulanmış işlevler bağlamında kampüs mekânları, önemli birer deneyim alanıdır. Kampüsün yapılı çevresi, farklı amaçlar için kurgulanan alanların niteliği ve öncelikleri kullanıcıların deneyimlerini şekillendiren mekânları oluşturur (Temple, 2008). Kampüs tasarımları içerdikleri yapı tasarımları, kent mobilyaları ve peyzaj düzenlemeleri gibi tasarım kriterleriyle, kullanıcılara bir yandan farklı bilişsel süreç kazanma imkânı sağlarken diğer yandan da çok sayıda imge sunma potansiyeline sahiptir. Lynch (1960) tarafından öncü bir model olarak kullanılan bilişsel haritalama, kampüs deneyimini keşfeden birçok çalışmaya aracı olmuştur (Gieseking 2013; Gourlay ve Oliver, 2018). Bu durum kampüs mekânlarının zihinsel ve bilişsel haritalama yöntemiyle deneyimleri keşfetmeye odaklanan çalışmaların önünü açmıştır (Cromley ve Cromley, 1986; Herman vd., 1979; McGregor, 2003).

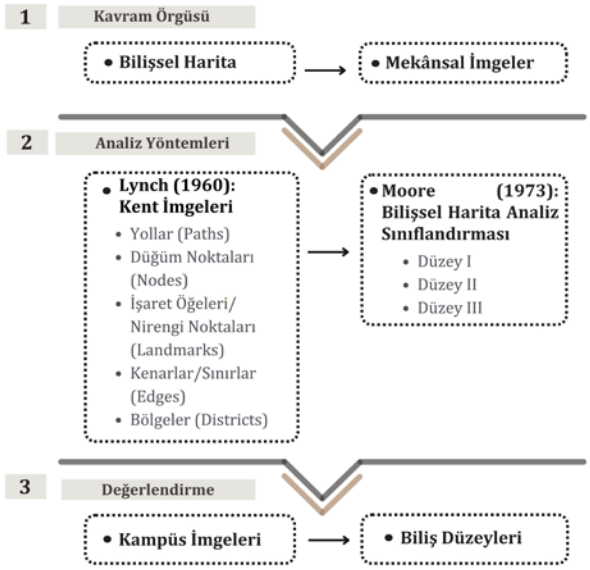
Mekânın birey tarafından algılanmasını bilişsel bir eylem olarak niteleyen Lynch (1960) çevrenin algılanmasında imgenin rolüne dikkat çekerek beş temel unsurdan bahsetmiştir. Çevrenin algılanmasında ve okunabilir alanlar yaratılmasında başat unsurlar aşağıdaki gibidir:

- Yollar (*Paths*): En okunabilir imge olarak hareket eyleminin gerçekleştiği, mekânları/unsurları birbirine bağlayan ve dolaşıma imkân sunan ağlar.
- Düğüm Noktaları (*Nodes*): Birbirinden farklı ulaşım hatlarının kesiştiği stratejik noktalar.
- İşaret Öğeleri/Nirengi Noktaları (*Landmarks*): Mevcut çevreden farklı nitelik taşıyan dikkat çekici referans noktaları.
- Kenarlar/Sınırlar (*Edges*): İki bölge arasında sınır elamanı olarak görev alan, birey tarafından ulaşım ekseni olarak kullanılmayan lineer unsurlar.
- Bölgeler (*Districts*): Belirgin ortak özellikleriyle zihinlerde fiziksel sınırları çizilebilen tanımlı alanlar.

Mekânın algılanmasında ve yaşanmasında duyguların etkisi yadsınamaz bir gerçektir. Farkındalık, bilgi, imaj ve inanışların etkisiyle şekillenen bir süreci kapsayan çevresel biliş, mekânsal bilişi de içinde barındırır (Moore, 1976). Böylelikle çevresel bilişin bir parçası olan mekânsal biliş, düşüncenin tekrar tekrar yapılanarak özümsenen bilginin yansıması olarak karşımıza çıkar. Lynch'in imgeleri, mekânın okunabilirliğini tanımlama da önemli ölçütleri sunarken bilişsel haritaların kullanılarak bireylerin deneyimledikleri çevreyi nasıl algıladıkları, zihinlerinde nasıl kodladıkları, hangi temsil öğelerini ön plana çıkardıkları ve bu bilgileri kâğıda nasıl aktardıkları, bilişsel yetkinliği sözel ve çizgisel olarak haritaların bilişsel düzeyinin analizi mekânsal öğrenme ve anlama açısından önemlidir. Bu konuda Hart ve Moore'un (1973) bilişsel haritalamaların analizinde kullandığı sınıflandırma yöntemi önemli bir değerlendirme aracıdır. Bilişsel haritaların sınıflandırılmasında önerilen üç aşama şunlardır:

- Düzey I (Farklılaşmamış Sağlam Benmerkezci): Benmerkezci bakış açısıyla düzenlenen haritalar, topolojik ve çevresel verilere ait bağlantılı bilgiler taşıyan fiziksel ve konumsal olarak her zaman doğru bilgiler sunmayan göstergeler içerebilir.
- Düzey II (Farklı ve Kısmen Organize): Topolojik ve çevresel veriler doğru işlenirken, kümeler arasındaki ilişki ve bağlantılar kısmen hatalı olabilir.
- Düzey III: Çevresel verilerin en doğru biçimde ilişkilendirilerek alan hakkında okuyucuya en doğru bilgiyi aktaran haritalardır.

Bu araştırmada, kampüsün birebir kullanıcıları olan öğrencilerin kampüs yaşamlarının deneyimsel ve ruhsal hallerine ilişkin değerlendirmeleri, alana dair bilişsel imgelerin ortaya konulması yoluyla sunulmaya çalışılmaktadır. Bu bağlamda araştırmanın temel amacı, içerdiği mekânsal ve sosyal katmanlar ile Karadeniz Teknik Üniversitesi Kanuni Kampüsü'nün uzaktan ve yüz yüze eğitim süreçlerinde öğrenciler tarafından algılanan imgeleri açığa çıkarmaktır. Bu amaca bağlı olarak, öğrencilerin zihinlerinde görselleştirilen bilgilerin bilişsel haritalar yoluyla temsil edilmesi hedeflenmektedir. "Öğrencilerin hedef ve tercihleri doğrultusunda deneyimledikleri mekânlarda/alanlarda ve kampüs içi yaya hareketlerinde, uzaktan eğitim ve yüz yüze eğitime bağlı olarak değişkenlik gösteren imgeler nelerdir?" araştırma sorusundan hareketle, aynı öğrencilerle bir yıl arayla oluşturulan haritalara odaklanılmaktadır. Deneyimlenen mekân, zaman ve nitelikler arasındaki karmaşık ilişkilerin sadeleştirilerek gösterilmesine yarayan bilişsel haritaların ele alındığı bu araştırmanın aşamaları Şekil 1'de sunulmaktadır.



Şekil 1. Araştırmanın aşamaları.

2. Materyal ve Yöntem

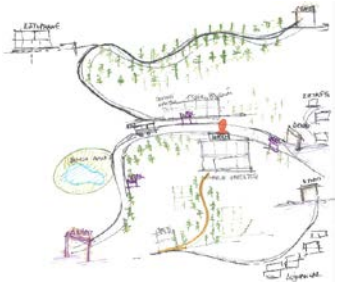
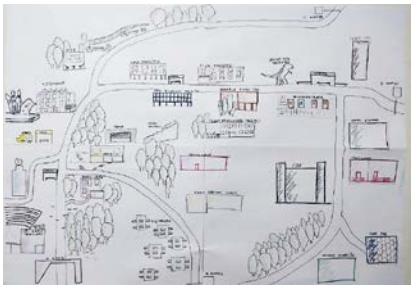
Araştırmanın metodolojisini oluşturan iki aşamalı harita uygulamalarının birinci aşaması uzaktan eğitimin uygulandığı 2022-2023 eğitim öğretim yılı bahar yarıyılında, ikinci aşaması ise yüz yüze eğitim ile sürdürülen 2023-2024 eğitim öğretim yılı bahar yarıyılında gerçekleştirilmiştir. 9'u kadın, 1'i erkek olmak üzere toplam 10 gönüllü öğrenci ile yürütülen uygulamalar, bilişsel haritaların çizilmesi ve haritalara ait raporların yazılmasını içermektedir. Kalem kullanımının serbest bırakıldığı harita çizimlerinde A3 boyutunda beyaz kâğıt, raporların yazılmasında ise A4 boyutunda beyaz kâğıt kullanılmıştır.

Kevin Lynch, Kent İmgesi (2022) adlı kitabında kentsel imgeleri ayırt edici fiziksel özelliklerin dışavurumu olarak belirtmekte; kişilerin yer-yön bulmasında, çevreyi çabuk öğrenmesi ve hatırlamasında, daha hızlı ve kolayca hareket etmesinde ve çevrenin kullanıcılar tarafından benimsenmesinde etkili olduğunu ifade etmektedir. Buradan hareketle bilişsel haritalara ait çizimler ve raporların analiz edilmesi sürecinde Moore (1973) tarafından önerilen sınıflandırma seviyelerinden ve Lynch'in (1960) temel öğelerinden yararlanılmıştır. KTÜ Kampüsü'nün kendisinin bir bölge tanımlıyor olması nedeniyle bu öğelerden biri olan "bölgeler", analiz sürecine dâhil edilmemiş olup, "yollar", "düğüm noktaları", "işaret öğeleri" ve "kenarlar/sınırlar" değerlendirilmiştir.

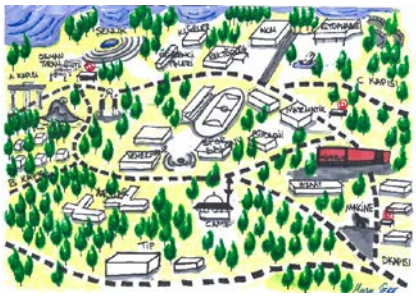
3. Bulgular

Araştırmaya katılan öğrencilerin bilişsel haritaları Lynch'in (1960) tanımladığı kent imgeleri ve Moore'un (1973) sınıflandırma seviyeleri aracılığıyla analiz edilerek Tablo 1'de sunulmaktadır. Bilişsel haritalar sınıflandırma seviyeleri açısından incelendiğinde, dört öğrencinin 2023 yılı haritaları, belleklerinde yer edinen bilgilerin çevre ile kurdukları ilişki, fiziksel ve konumsal verilerin doğruluğu açısından Düzey III olarak nitelendirilmiştir. Bu öğrencilerin 2024 yılı haritalarına bakıldığında iki öğrencinin haritasının düzeyini korurken, bir öğrenciye ait haritanın imgeler arasındaki ilişkinin azalması nedeniyle Düzey II'ye, bir diğer öğrencinin haritasının ise öğeler arasındaki doğru bilginin oldukça zayıflaması nedeniyle Düzey I'e gerilediği tespit edilmiştir. Geri kalan öğrencilerden beşinin ilk haritası Düzey II'de kategorize edilmiştir. Bu öğrencilerden ikisinin 2024 yılı haritalarının düzeyi sabit kalırken, üç öğrencinin haritaları zayıflayan ilişkiler nedeniyle Düzey I'e gerilemiştir. Yalnızca bir öğrencinin 2023 ve 2024 yıllarına ait bilişsel haritaları Düzey I olup aynı seviyede bilgi aktarımı sağlamıştır. Buradan hareketle; 5 öğrencinin her iki yıla ait bilişsel harita düzeyinin değişmediği, diğer 5 öğrencinin ise bir alt düzeye gerilediği görülmektedir. Çizilen ilk haritalara oranla, yinelenen bazı haritalarda algılanan imajların çeşitliliğinin artmasına karşın, mekânsal öğelerin aralarındaki ulaşım ağları zayıflamıştır. Bu durum, kampüse ait algılanan imgelerin, mekânla fiilen ilişki içinde olunmasa da belleklerde yer aldığını göstermektedir.

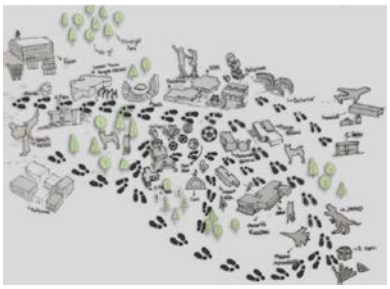
Tablo 1. Bilişsel haritalara ilişkin analizler

	2023	2024
Yollar	A Kapısı-Mimarlık Fakültesi Ana yol-Kütüphane Ana yol-Kafe 5	A Kapısı-D Kapısı Ana yol-Kütüphane Ana yol-C Kapısı D Kapısı-Kırtasiye Mimarlık Fakültesi-Kafe 5 B Kapısı-Kafe 5
Düğüm Noktaları	-	-
İşaret Öğeleri	Açık oturma alanları, şenlik alanı	Şenlik alanı, Akademi Kırtasiye
Kenarlar/Sınırlar	Sıralı ağaçlı yollar	Sıralı ağaçlı yollar
Ayşe Nazlı Peker		
	Düzey I	Düzey I
Yollar	A Kapısı-B Kapısı A Kapısı-C Kapısı A Kapısı-D Kapısı Ana yol-KTU CODE FAB Ana yol-Koru Kafe Ana yol-Kafe 5	D Kapısı-Mimarlık Fakültesi Ana yol-Kütüphane Kütüphane-C Kapısı Ana yol-Kapalı Spor Salonu Ana yol-Spor Sahaları Lojmanlar-B Kapısı
Düğüm Noktaları	Duraklar	Durak, D Kapısı çevresi
İşaret Öğeleri	Atatürk Heykeli, dinozor maketi, seyir terasları, amfi, bankamatikler	Bordo Kırtasiye, A Kapısı yakınındaki heykel, açık oturma alanı, amfi, istinat duvarları, basamaklar, köpekler
Kenarlar/Sınırlar	Sıralı ağaçlı yollar	Hatıra Ormanı
Berna Kayan		
	Düzey II	Düzey I
Yollar	A, B, C, D ve E Kapıları aralarındaki güzergâh Ana yol-B Kapısı Ana yol-Koru Kafe Ana yol-Spor alanları Ana yol-Kafe 5	A Kapısı-B Kapısı A Kapısı-D Kapısı
Düğüm Noktaları	A Kapısı yakınındaki heykel	-
İşaret Öğeleri	Savaş uçağı, dinozor maketi, açık oturma alanları, Kafe 5'in önündeki ağaç, kediler ve köpekler	Köprü, savaş uçağı, dinozor maketi, açık oturma alanları
Kenarlar/Sınırlar	Sıralı ağaçlı yollar	Sıralı ağaçlı yollar
Gamze Nur Bekar		
	Düzey III	Düzey I

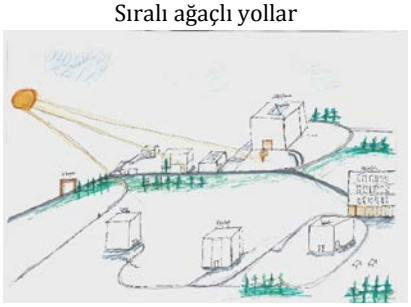
Tablo 1. Bilişsel haritalara ilişkin analizler (devamı)

Yollar	A Kapısı-C Kapısı Ana yol-B Kapısı Ana yol-D Kapısı Ana yol-Koru Otel Ana yol-Şenlik alanı	A Kapısı-C Kapısı Ana yol-Mimarlık Fakültesi Ana yol-B Kapısı Ana yol-Koru Kafe Ana yol-Kafe 5
Düğüm Noktaları	A Kapısı yakınları, Kütüphane önü	Kütüphane önü
İşaret Öğeleri	Açık oturma alanları, bayraklar, bankamatikler	KTÜ Camii, Pati Park, Mimarlık Fakültesi'nin önündeki ağaç
Kenarlar/Sınırlar	Karadeniz Sahil Yolu	-
Mehtap Karataş		
	Düzey III	Düzey II
Yollar	A Kapısı-D Kapısı A Kapısı-Mimarlık Fakültesi D Kapısı-Ev	A Kapısı-D Kapısı A Kapısı-Mimarlık Fakültesi Ana yol-B Kapısı
Düğüm Noktaları	Atatürk Heykeli önü, köprü yakın çevresi	AKM önü, durak, köprü yakın çevresi
İşaret Öğeleri	Atatürk Heykeli, istinat duvarları, köprü, bankamatikler	Açık oturma alanları, dinozor maketi, köprü, bankamatikler
Kenarlar/Sınırlar	Karadeniz, sıralı ağaçlı yollar	Sıralı ağaçlı yollar
Melisa Yalçin		
	Düzey II	Düzey II
Yollar	A Kapısı-B Kapısı A Kapısı-C Kapısı A Kapısı-Makina Mühendisliği Bölümü	A Kapısı-D Kapısı B Kapısı-D Kapısı Ana yol-C Kapısı
Düğüm Noktaları	A, B ve C Kapıları çevresi, Kütüphane önü, köprü yakın çevresi	A ve D Kapıları çevresi
İşaret Öğeleri	Duraklar, amfiler, istinat duvarları	A Kapısı yanındaki şelale, A Kapısı yakınındaki heykel, savaş uçağı, duraklar, seyir terasları
Kenarlar/Sınırlar	Karadeniz Sahil Yolu	Karadeniz
Merve Teke		
	Düzey III	Düzey III

Tablo 1. Bilişsel haritalara ilişkin analizler (devamı)

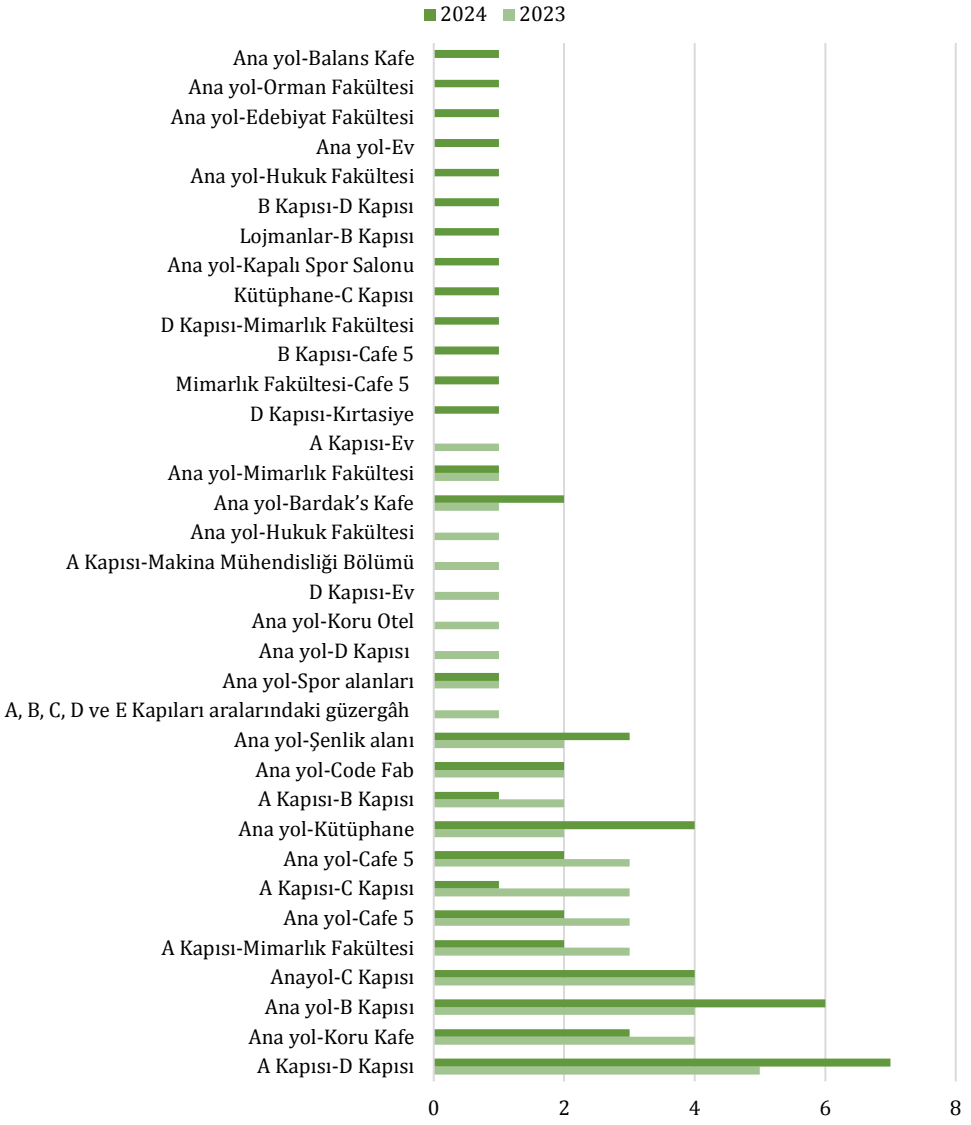
Yollar	A Kapısı-D Kapısı Anayol-C Kapısı	A Kapısı-D Kapısı Ana yol- B Kapısı Ana yol-Kütüphane Anayol-Şenlik alanı
Düğüm Noktaları	Kütüphane önü	Kütüphane önü, Mimarlık Fakültesi yakını
İşaret Öğeleri	Atatürk Heykeli, seyir terasları, savaş uçağı, dinozor maketi, kediler ve köpekler	Mimarlık Fakültesi Binası, Kütüphane, Kafe 5, savaş uçağı
Kenarlar/Sınırlar	-	Kampüs sınırları
Murat Kaya		
	Düzey II	Düzey I
Yollar	A Kapısı-D Kapısı Ana yol-C Kapısı Ana yol-Hukuk Fakültesi Ana yol-Koru Kafe Ana yol-Kafe 5 Ana yol-bardak's Kafe	A Kapısı-D Kapısı Ana yol-B Kapısı Ana yol-C Kapısı Ana yol-Edebiyat Fakültesi Ana yol-Orman Fakültesi Ana yol-Şenlik alanı Ana yol-Balans Kafe Ana yol-Koru Kafe & Kafe 5 Ana yol-bardak's Kafe Ana yol-KTU CODE FAB
Düğüm Noktaları	Kütüphane önü	A Kapısı yakınındaki heykel önü, Kütüphane önü
İşaret Öğeleri	A Kapısı yanındaki şelale, Atatürk Heykeli, açık oturma alanları, duraklar, savaş uçağı, dinozor maketi, amfi, merdivenler, bankamatik	A Kapısı yanındaki şelale, A Kapısı yakınındaki heykel, Atatürk Heykeli, açık oturma alanları, duraklar, savaş uçağı, dinozor maketi, amfiler
Kenarlar/Sınırlar	-	Havalimanı
Neslihan Alemdar		
	Düzey II	Düzey II

Tablo 1. Bilişsel haritalara ilişkin analizler (devamı)

Yollar	A Kapısı-D Kapısı Ana yol-B Kapısı Ana yol-C Kapısı Ana yol-Mimarlık Fakültesi Ana yol-KTU CODE FAB Ana yol-Koru Kafe Ana yol-Şenlik alanı A Kapısı-Ev	A Kapısı-D Kapısı Ana yol-B Kapısı Ana yol-C Kapısı Ana yol-KTU CODE FAB Ana yol-Hukuk Fakültesi Ana yol-Koru Kafe Ana yol-bardak's Kafe Ana yol-Şenlik alanı Ana yol-Ev
Düğüm Noktaları	A Kapısı yakınındaki durak önü, Mimarlık Fakültesi yakını	A Kapısı yakınındaki güvenlik noktası önü, Mimarlık Fakültesi yakını
İşaret Öğeleri	Açık oturma alanları, Balans Kafe, bankamatik	Açık oturma alanları, dinozor maketi, köprü, amfiler, seyir terasları, istinat duvarları, bayraklar, bankamatikler
Kenarlar/Sınırlar	Karadeniz, sıralı ağaçlı yollar	Karadeniz Sahil Yolu, sıralı ağaçlı yollar
Sena İnce		
	Düzey III	Düzey III
Yollar	A Kapısı-Mimarlık Fakültesi Ana yol-Kütüphane Ana yol-B Kapısı güzergâhı Ana yol-C Kapısı güzergâhı	A Kapısı-Mimarlık Fakültesi Ana yol-Kütüphane Ana yol-B Kapısı güzergâhı
Düğüm Noktaları	A Kapısı yakınındaki durak önü, Kütüphane önü	A Kapısı yakınındaki durak önü, Kütüphane önü
İşaret Öğeleri	Açık oturma alanları, A Kapısı yakınındaki heykel, amfi, seyir terasları, bayraklar	Açık oturma alanı, durak, basamaklar
Kenarlar/Sınırlar	Karadeniz, sıralı ağaçlı yollar	Sıralı ağaçlı yollar
S. Dilay Bayraktar		
	Düzey II	Düzey I

3.1. İmgelere İlişkin Değerlendirmeler

Kampüs deneyimlerini imgeye dönüştürerek bilişsel haritalar aracılığıyla yeniden üreten öğrenciler, bir yaya olarak bireysel ve/veya grup yürüyüşleriyle ya da dolmuş, otobüs ve özel araç kullanımıyla kampüsün hemen her noktasına uzanan, bir yandan pratik ortaklığa dayanan bir taraftan da kişiselleşmiş tecrübelerle, kampüsün algılanma biçimlerine yönelik birtakım veriler sunmaktadır. Çalışma kapsamında farklı zaman aralıklarında ve deneyim süreçlerinin sonunda elde edilen haritalarda, bu imgelerin değişimi açıkça görülmektedir. Haritalardan alınan verilerle hazırlanan Şekil 2'ye bakıldığında yollara ait imgelerin sayısı dikkat çekmektedir. 2024 yılına gelindiğinde haritalarda Anayol- Şenlik Alanı, Anayol-Kütüphane, Anayol-C Kapısı, Ana yol-B Kapısı, A Kapısı-D Kapısı güzergâhlarının imgelenmesinde artış yaşanırken, Ana yol-Kafe 5, A Kapısı-C Kapısı, A Kapısı-Mimarlık Fakültesi ve Ana yol-Koru Kafe güzergâhları daha az işlenmiştir. Haritaların bütününde 35 farklı yol ilişkisi tespit edilmiştir.



Şekil 2. Yollara ilişkin imgeler.

Yolların çeşitliliği ve alternatif güzergâhların varlığı öğrencilerin metinlerinde şu ifadelerle aktarılmıştır:

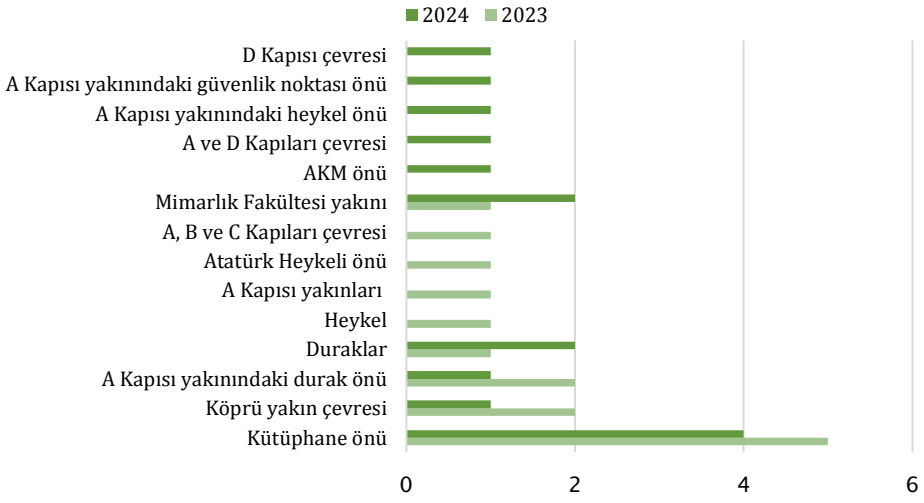
• Sümeyye Dilay Bayraktar (2023): ''Ders çalışma aralarında gezdiğim C kapısına doğru giden yolu ve oradaki patika yolu da ekledim. Bu yolun sakinliği, doğa ve yeşilliği, kuşların sesleri beni rahatlattığından ve burada yürürken kafamı dinlendirdiğinden bu alanları da eskizime işledim.''

• Sena İnce (2023): ''Biliş haritası hazırlarken A kapısının sol tarafında kalan Kongre Merkezi'nin binasından çok giriş yolunun zihnimde yer edindiği söyleyebilirim. Bazen gün batımında yolu tanımlayan elemanların aralarından süzülen güneşi hatırlarken bazen de sabahları gördüğüm bir tekrarı anımsamaktayım.''

• Merve Teke (2023): ''Kampüsümüz, şehir ve buna bağlı olarak şehir içi yollarla ayrılmaz bir bütünlük oluşturmaktadır. Bu sayede evimden kampüse ulaşmak için 3 farklı yol seçebilmekteyim.''

Katılımcıların önemli bir bölümü kampüs ile ilgili deneyimlerini aktarırken yolların varlığına dikkat çekmiştir. Öğrenciler yolları; gündelik hayatlarının bir parçası, varış noktası, hedefe erişim sağlayan olanak, buluşma alanı, geliş ve gidiş rutinlerinin ana hattı, zihinsel aktivitelerin yeri ve kampüsü seyredebilecekleri bir görü noktası olarak nitelendirmişlerdir. Özellikle kampüsün girişlerini tanımlayan kapılar ile ilişkilendirilen yollar, öğrencilerin hafızalarında yer edinen yeme-içme mekânları, sosyal aktivite alanları, eğitim birimleri, ders çalışma alanları gibi farklı işlevlerle imgelendirilmiştir.

Şekil 3'te sunulduğu üzere, haritalarda 14 farklı düğüm noktası yer almaktadır. 2023 ve 2024 yıllarına ait bilişsel haritalar karşılaştırıldığında Kütüphane önü, Mimarlık Fakültesi yakını ve durakların düğüm noktaları olarak ön planda çıktığı görülmektedir.



Şekil 3. Düğüm noktalarına ilişkin imgeler.

Haritalara işlenen bu düğüm noktalarını tanımlayan bazı ifadeler şöyledir:

• Gamze Nur Bekar (2023): ''C kapısından girince; kafamı toplamak için yürüdüğüm yeşil yolu, yolun sonundaki dolmuş durağını ve durakta yolcu toplayan dolmuşçu amcayı, dışarıdan heyecan uyandıran ama içine girince o kadar da ilginç olmayan Harita Mühendisliği binasını, ara sıra tiyatro izlemeye gittiğim Atatürk Kültür Merkezi'ni, ders çalışmanın yanı sıra kapısında sohbet edilen Kütüphane'yi, yanındaki bardak's Kafe'den aldığım kahve ile gün doğumunu izlemeyi çok sevdiğim seyir teraslarını gösterdim.''

• Berna Kayan (2023): ''Koru Tesisleri'nin ardından ağaçlı yoldan yürüyerek oradaki Koru Kafe'ye gidebiliyoruz. Eğer bu kafenin önündeki yolu takip edecek olursak lojmanlara ve oradan da B kapısına ulaşırız. Ancak bu kafenin önündeki ana yolu takip edersek karşı yolda en çok kullandığım otobüs durağını görürüz. Birkaç metre ilerisinde taksi durağı ve karşısında Kafe 5 ve diğer kafeler konumlanıyor.''

• Ayşe Nazlı Peker (2023): ''Benim kampüsteki yolumun sonu Mimarlık Fakültesi'nde biter.''

Bu veriler, öğrencilerin mekânlardaki aktivitelerinin yoğunluğunun ve buna bağlı olarak deneyim sürelerinin artması ile, sözü geçen düğüm noktalarının zaman içerisinde daha fazla öğrencinin biliş haritasında yer edindiğini açığa çıkarmaktadır.

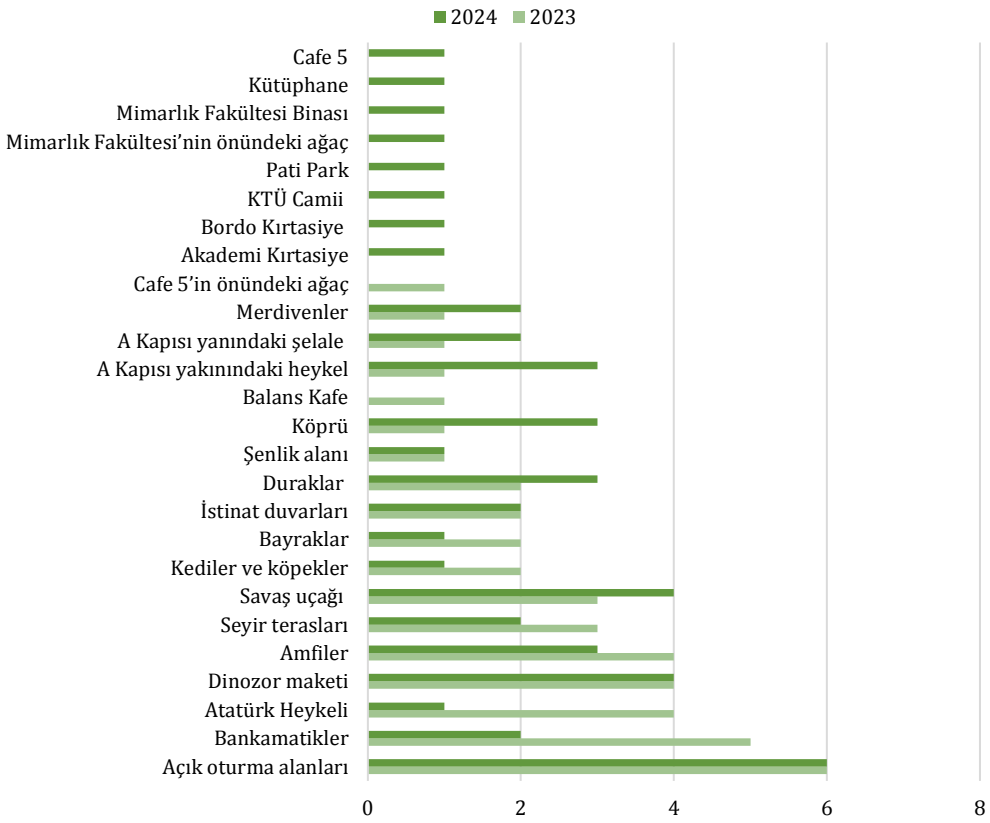
Kampüsün farklı deneyimlere olanak sunan fiziksel çeşitliliği, öğrencilerin bilişsel haritalarında birçok çevresel verinin imgelenmesini sağlamıştır. Haritalardaki imgeler incelendiğinde; 25 farklı işaret öğesi tespit edilmiştir (Şekil 4).

İşaret öğeleri incelendiğinde en belirgin imgenin, öğrencilerin sosyalleşmesine olanak sağlayan açık oturma alanları olduğu belirlenmiştir. Öğrencilerin metinlerinde de sıklıkla bahsedilen bu duruma ilişkin ifadelerden bazıları aşağıdaki gibidir:

• Mehtap Karataş (2023): ''Ormanlık alan ve patika yolların bulunduğu bu yollar, yürürken kuş sesleri ile huzur bulduğum, çokça zaman geçirdiğim, çok sevdiğim arkadaşlarımla pazar kahvaltılarımızı yaptığımız, ders çıkışlarında oturup dinlendiğimiz, sohbet ettiğimiz yerler.''

• Melisa Yalçin (2023): ''Çizerken fark ettim ki en sevdiğim mekânlar sanırım Mimarlık Fakültesi Kantini ve Kütüphane'nin yakınındaki seyir terasları.''

• Ayşe Nazlı Peker (2023): ''Kampüsün ayrılmaz parçası olan yeşil alanlar, kampüs içindeki oturma alanları, benim için bir tür kaçış noktası gibi.''



Şekil 4. İşaret öğelerine ilişkin imgeler.

Öğrencilerin birçoğu tarafından haritalara işaret öğesi olarak işlenen bankamatikler, Atatürk Heykeli, seyir terasları ve amfiler 2024 yılına gelindiğinde azalan bir öneme sahip olmuştur. Buna karşın dinozor maketi, savaş uçağı ve köprü, hem 2023 hem de 2024 yılına ait haritalarda öne çıkan işaret öğeleri arasındadır. Bu işaret öğelerine dikkat çeken bazı öğrencilerin ifadeleri şu şekildedir:

• Gamze Nur Bekar (2024): ''-Üstünden geçenlerin okulu uzuyor- söylentilerine inanmayıp üstünden geçtiğim ve gerçekten de okulumun uzamasına sebep olan köprüyü, kampüsteki hemen herkesin fotoğraf çekildiği dinozoru ve her geçtiğimde dikkatimi çeken uçağı da unutmadım.''

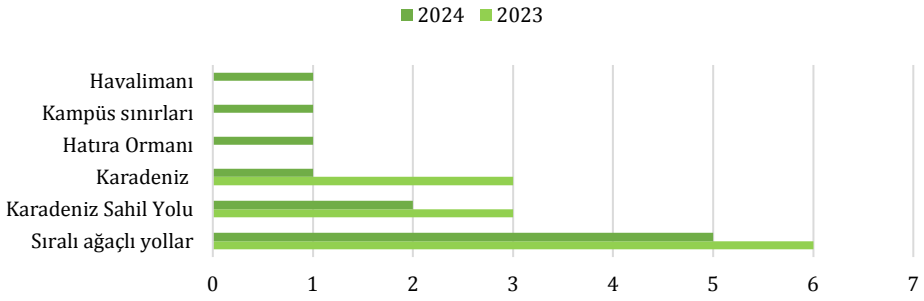
• Sena İnce (2024): ''Jeoloji Fakültesi ağaçların arasında geride kaldığı için, zihnimde daha çok önündeki dinozor şekilleniyor.''

• Neslihan Alemdar (2024): ''Benim için en dikkat çekici öğeler Elektrik-Elektronik Mühendisliği'nin önündeki uçak ve Jeoloji Mühendisliği'nin önündeki dinozordur.''

Çalışma kapsamında analiz edilen kenarlar/sınırlar kapsamında en belirleyici imgeler Şekil 5'te de görüldüğü üzere, sıralı ağaçlı yollar ve Karadeniz Sahil Yolu'dur. Özellikle ağaçlı yolların varlığı öğrencilerin metinlerine şu şekilde yansımıştır:

• Neslihan Alemdar (2023): ''Fakülteyi ilk kazandığımda, deneyimlemek için gittiğimde C kapısını kullanmıştım ve ağaçların arasında bulunan merdivenlerden çıkarken bana hissettirdiği hoşnutluk hala belleğimde bulunuyor.''

• Merve Teke (2023): ''Bu kadar fazla yeşil olması çok hoşuma gidiyor. Bazen kampüsün farklı noktalarında kaç ağaç peş peşe sıralanmış diye sayıyorum. İnşaat Mühendisliği'nin merdivenlerinden çıktığımda her defasında yan yana dikilmiş üç ağacın altından geçmek ve oranın bu simgeselliği çok hoşuma gidiyor. Ya da şenlik alanında kocaman havuzlu, boş bir arazinin ortasında bulunan tek ağaç.''



Şekil 5. Kenarlar/sınırlara ilişkin imgeler.

Biliş haritalarından elde edilen imgeler karşılaştırıldığında, 2023 yılına ait haritalarda yer alan sıralı ağaçlı yollar, Karadeniz Sahil Yolu ve Karadeniz kenar/sınır imgelerinin, 2024 yılına gelindiğinde azaldığı görülmektedir. Buna karşın kampüs sınırları, Havalimanı ve Hatıra Ormanı 2023 yılı haritalarında imge olarak yer almazken 2024 yılındaki haritalarda kendini göstermektedir.

4. Sonuç

'Yer'ler, orada meydana gelen aktiviteler sonucu birer çekim noktası haline gelerek insanları çekerler. İnsanları sosyal birtakım aktivitelere yönlendirirler. Yerler böylece sosyalleşir. 'Yer'in sosyalleşmesi ise, herkesin kullandığı bir alanın iyi olarak anılması ve bu yargının sürekliliğini koruyarak davranışları etkileyip yönlendirmesi olarak düşünülebilir. Bir yerin sosyalleşmesi, o alanda kullanıcılar arasında uzlaşma sonucu oluşmuş değerlerle ve biçimlenmesini belirleyen somut öğelerle tanımlı bir yere dönüşmesi ile gerçekleşir (Çakır, 2015). Yerler ve mekânlar, kullanıcıları ile kurulan etkileşim/iletişim ile zenginleşir. Bu etkileşimde kullanıcı eylemleri büyük rol oynar ve mimaride mekân tanımı eylem ilişkisini kapsar. Dolayısıyla öğrencilerin kampüs ile ilişkisi, çevresel bileşenlerin ilettiği mesajlar ve bunların algılanmasıyla gerçekleşebilmektedir. Buradan hareketle araştırmada, uzaktan eğitim sürecinde çizilen bilişsel haritaların, yüz yüze eğitime geçilmesiyle fiilen artan kampüs deneyimleri üzerinden yeniden oluşturulan bilişsel haritalarındaki olası değişiklikler değerlendirilmiştir.

2023 ve 2024 yıllarına ait bilişsel haritalardaki imgeler, tekrar edilme sıklığı ile ilişkilendirilerek Şekil 6'da verilmiştir. Bu imgelerin kampüs haritası üzerinde görselleştirilmesinde; yollar kırmızı, düğüm noktaları mavi, işaret öğeleri yeşil ve kenarlar/sınırlar sarı renk ile gösterilmiştir.

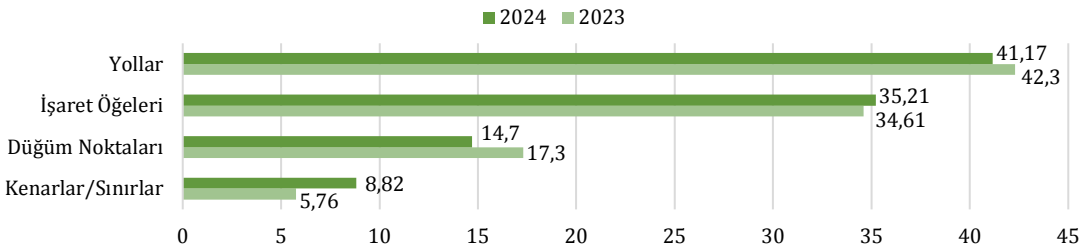


Şekil 6. Bilişsel haritalarda öne çıkan kampüs imgeleri (URL 1).

Öğrencilerin belleklerinde yer edinen yollar arasından, A Kapısı-D Kapısı (2023:5; 2024:7), ana yol-B Kapısı (2023:4; 2024:6), ana yol-C Kapısı (2023:4; 2024:4), ana yol-Kütüphane (2023:2; 2024:4), ana yol-şenlik alanı (2023:2; 2024:3) güzergâhlarının öne çıktığı görülmektedir. Öğrencilerin haritalarında çok sayıda yol öğesine yer vermiş olmaları, kampüs içerisindeki yaya deneyimlerine paralel olarak oluşmuştur. Bu duruma benzer bir görüşle, Herman ve Siegel (1978) de makul ölçüde doğru bir uzamsal temsilin geliştirilmesinde, deneyimlenen alanın belli bir sırayla tekrar tekrar görme deneyiminin önemine ve görmenin de yürüme eylemi kadar aktif olmasına değinmektedir. Kampüs genelinde çeşitli düğüm noktaları belirtilmiş olsa da tekrar edilen alanlar, Kütüphane önü (2023:5; 2024:4) başta olmak üzere duraklar (2023:1; 2024:2) ve Mimarlık Fakültesi yakınları (2023:2; 2024:1) olmuştur. Belleklerde kesişim noktaları tanımlayan ve yol bağlantılarının güçlü olduğu bu alanların, öğrencilerin sıklıkla bulundukları çevrelerde yer alması nedeniyle öne çıktığı düşünülmektedir.

İşaret öğeleri açısından değerlendirildiğinde açık oturma alanları (2023:6; 2024:6), bankamatikler (2023:5; 2024:2), dinozor maketi (2023:4; 2024:4), savaş uçağı (2023:3; 2024:4) ve seyir teraslarının (2023:3; 2024:2) belleklerde güçlü bir biçimde yer edindiği söylenebilmektedir. Bu imgelerin kampüs yaşantısına dair ipuçları taşıdığı ve kampüs ile bütünleştiği anlaşılmaktadır. Bilişsel haritalarda kampüsün kenar/sınır öğeleri olarak işlenen imgeler ise; sıralı ağaçlı yollar (2023:6; 2024:5), Karadeniz Sahil Yolu (2023:3; 2024:2) ve Karadeniz'dir (2023:3; 2024:1). Tekrar edilmemesine karşın, 2024 yılına ait haritalarda 2023 yılına kıyasla daha fazla sayıda kenar/sınır öğesi yer almıştır. Bu durum, öğrencilerin deneyimledikleri mekânların zamanla çoğalmasıyla ve mekânlardaki deneyim süresinin artmasıyla açıklanabilir. Nitekim Herman ve diğerleri (1979) de üniversite öğrencileri tarafından farklı zaman dilimlerinde çizilen bilişsel haritaları değerlendirerek, kampüste sadece üç ay geçiren birinci sınıf öğrencilerinin özellikle işaret öğeleri açısından daha doğru bilişsel haritalar oluşturdukları sonucuna ulaşmışlardır. Haritalardan elde edilen bu bilgiler, öğrencilerin zihinlerinde kalan görüntü sayısının deneyimle birlikte arttığını, ancak detayların silikleşebildiğini göstermektedir.

Öğrencilerin 2023 yılına ait biliş haritaları analiz edildiğinde toplam imge sayısının %42,30'unu yollar, %35,21'ini işaret öğeleri, %14,7'sini düğüm noktaları oluştururken %8,82'sini de kenarlar/sınırlar takip etmektedir (Şekil 7). 2023 yılı haritalarından elde edilen bulgular doğrultusunda, öğrencilerin belleklerindeki kodlamaların ilk adımlarını yolların ve işaret öğelerinin oluşturduğunu söylemek mümkündür.



Şekil 7. Kampüs imgelerinin yüzdelik değer değişimleri.

Yüz yüze eğitime dönülmesi ile öğrencilerin kampüs deneyimlerinde artış yaşanmış olmasına rağmen imgelerde değişen oranlar dikkat çekicidir. 2024 yılında çizilen haritaların toplam öğe sayısının yüzdelik oranları incelediğinde; 2023 yılına kıyasla yollar (%1,13) ve düğüm noktalarında (%2,6) azalma olduğu görülmektedir. Bu durumun aksine, 2024 yılına gelindiğinde işaret öğeleri (%0,6) ve kenarlar/sınırlar (%3,06) imgelerinde artış olduğu tespit edilmiştir.

Öğrencilerin kampüste daha fazla zaman geçirme imkânı bulmalarına rağmen haritalarındaki bilgi, konum ve detaylara ilişkin verilerinin artmayıp benzer düzeyde kaldığı veya azaldığı gözlemlenmektedir. Downs ve Stea'nın (1973) da benzer görüşü ışığında, öğrencilerin 2024 yılında kampüste daha fazla vakit geçirmiş olmalarının ayrıntıları sıradanlaştırarak biliş haritalarında daha az detaya yer vermelerine neden olmuş olabileceği düşünülmektedir. Boulding (1956) de zaman içerisinde edinilen mekânsal bilginin o mekânı etkin bir biçimde kullanmak için gerekli olduğunu, ancak depolanan bilginin bilişsel harita üzerinde herhangi bir etkisi olmayacağını ileri sürmektedir. Buradan hareketle öğrencilerin kampüs deneyimlerinin tekrarlanması, artması ve/veya yenilenmesine rağmen çevresel bilginin zaman içerisinde zaman aşımına uğrayarak unutulduğunu söylemek mümkündür. Bu durum bazı öğrencilerin biliş haritalarını açıkladıkları metinlerde de dile getirilmiştir:

• Murat Kaya (2024): "Uzaktan eğitim dönemince kampüsten bir hayli uzak kalmam ve çok az etkileşimde bulunmam önceki bellek verilerinin de yavaş yavaş silindiğini anlamamı sağladı."

• Merve Teke (2024): "İlk bilişsel haritamda gözlem şeklim daha çok bulunduğum konumu inceleme ve nokta detaylarını yakalamak üzerine kuruluydu. Ancak ikinci bilişsel haritamda bu nokta detaylarına hâkim olduğumdan dolayı artık ilgimin daha geniş açıyla incelemek üzerine kurulu olduğunu düşünüyorum. Kampüsün küçük detaylarına hâkim olduğum için artık ilgimin o noktalara kaymadığı, kampüsü bir bütün haliyle gözlemleyerek incelediğimi ve detayların gizlendiğini söyleyebilirim."

• Neslihan Alemdar (2024): "Uzaktan eğitimden sonra çoğu fakülte binasının içine girmediğimi fark ettiğim için gezmeye başladım, içlerine girdim ve fotoğraf çekme şansı buldum. Fotoğrafladığım yerler aklımda daha çok yer edindi ve oraların detayına inebildim, ancak bu durum Şenlik Alanı'ndaki birimler için geçerli değil. Birkaç kere B Kapısı'nı kullandım ve oraya giderken lojmanların içinde kaybolmuştum. Sadece yapıların eski ve küçük balkonlu olması dikkatimi çekmişti. Bunların tam konumlarını ve kaç tane olduklarını bilmiyorum."

• Sena İnce (2024): "Pandemi ve deprem sürecinde verilen aralar nedeniyle kampüs ve çevresiyle tam bir etkileşim halinde olamadığımız dönemler geçirdik. Bu süreçte ana kullanım güzergâhının belleğimde daha çok yer edindiğini düşünüyorum. Sonrası sürece baktığımda zamanımın çoğunu kampüste geçiren biri olarak kendime farklı deneyim rotaları oluşturmaya çalıştığım ve daha çok ormanlık alanlara kaçtığımı ifade edebilirim. B kapısına giden güzergâhı çok fazla kullanmamaktayım. Önceki deneyimlerimden kalanlar zihnimde silik bir şekilde varlığını sürdürmektedir."

Öğrencilerin ifadeleri, bilişsel haritalarda deneyim ve zaman faktörünün önemli etkileri olduğunu ortaya koymaktadır. Bazı öğrenciler kampüste en çok vakit geçirdiği mekânlara yer verdiğini ve öncekilere ilişkin bellek verilerinin yavaş yavaş silindiğini belirtmiştir. Benzer şekilde, yüz yüze eğitime dönüldüğünde kampüsü tekrar inceleme fırsatı bulan öğrencilerin daha öncesinde bazı yerleri göz ardı ettikleri ve vakit geçirmedikleri alanlar olduğunu fark ettikleri belirlenmiştir. Sonuç olarak, doğa ile iç içe olan KTÜ Kanuni Kampüsü'nün eğitim binalarının yanı sıra sosyal mekânları ile öğrencilerin belleklerinde bir kimlik meydana getirmiş olduğu söylenebilir. Bu araştırma, çevresel bilginin zamanla unutulması ve deneyimlerin yenilenmesi, bilişsel haritaların dinamik bir süreç olduğunu ortaya koymaktadır. Öğrencilerin haritalarındaki bilgiler, konumlar, bağlantılar ve detaylara ilişkin verilerin zamanla değişmesi, mekânsal bilgilerin kullanım sıklığına bağlı olduğundan, haritaların zaman içerisinde güncellenmesi gerekliliği açıktır.

Katkı Oranı Beyanı

Yazarların katkı yüzdeleri aşağıda verilmiştir. Yazarlar makaleyi incelemiş ve onaylamıştır.

	H.K.	E.B.K.
K	50	50
T	50	50
Y	50	50
VTI	50	50
VAY	50	50
KT	50	50
YZ	50	50
KI	50	50
GR	50	50
PY	50	50

K= kavram, T= tasarım, Y= yönetim, VTI= veri toplama ve/veya işleme, VAY= veri analizi ve/veya yorumlama, KT= kaynak tarama, YZ= Yazım, KI= kritik inceleme, GR= gönderim ve revizyon, PY= proje yönetimi.

Çatışma Beyanı

Yazarlar bu çalışmada hiçbir çıkar ilişkisi olmadığını beyan etmektedirler.

Etik Onay Beyanı

Bu araştırma Karadeniz Teknik Üniversitesi Fen ve Mühendislik Bilimleri Etik Kurulu tarafından onay alınarak gerçekleştirilmiştir (onay tarihi: 27 Kasım 2024, onay numarası: E-26014373-050.06.03-590944).

Kaynaklar

Billinghurst M, Weghorst S. 1995. The use of sketch maps to measure cognitive maps of virtual environments. In: Proceedings of the Virtual Reality Annual International Symposium (VRAIS'95), March 11-15, North Carolina, USA: pp: 40-47.

Boulding KE. 1956. The image: Knowledge in life and society. University of Michigan Press, Michigan, USA, 47th ed, pp: 64-81.

Cromley RG, Cromley EK. 1986. Cognitive maps of campus: Student views of spatial arrangement. J Geography, 85(2): 67-71.

Çakır H. 2015. Analysis of the relationship between spatial memory and interiors in historical buildings. MSc thesis, Beykent University, Institute of Graduate Studies, Istanbul, Türkiye, pp: 12.

Demirel E. 2004. Mekân kurgusu-boşluğun mimarisi. Mimarlık Derg, 315: 42-46.

Downs RM, Stea D. 1973. Cognitive maps and spatial behavior: Process and products. In: Downs RM, Stea D, editors. Image and Environment, Chicago, USA, pp: 8-26.

Gieseking JJ. 2013. Where we go from here: The mental sketch mapping method and its analytic components. Qualit Inq, 19(9): 712-724.

Gifford R. 1987. Environmental psychology: Principles and practice. Massachusetts, USA, pp: 34-37.

Golledge RG, Stimson RJ. 1997. Spatial behavior: A geographic perspective. The Guilford Press, New York, USA, pp: 31-32.

Gourlay L, Oliver M. 2018. Student engagement in the digital university: Sociomaterial assemblages. Routledge, London. pp: 14-27.

Gulliver FP. 1908. Orientation of maps. J Geography, 7: 55-58.

Hart RA, Moore G. 1973. The development of spatial cognition: A review. In: Downs RM, Stea D, editors. Image and Environment. Chicago, USA, pp: 246-288.

Herman JF, Siegel AW. 1978. The development of cognitive mapping of the large-scale environment. J Experiment Child Psychol, 26: 389-406.

Herman JF, Kail RV, Siegel AW. 1979. Cognitive maps of a college campus: A new look at freshman orientation. Bullet Psychon Soc, 13(3): 183-186.

Lynch K. 1960. Image of the city. The MIT Press, London, UK, pp. 6-90.

Lynch K. 2022. Kent imgesi. Is Bankası Kültür Yayınları, Istanbul, Türkiye, 16th ed, pp: 16-53.

McGregor J. 2003. Spatiality and teacher workplace cultures: The Department as Nexus. In: Edwards R, Usher R, editors. Space, curriculum and learning. Information Age Publishing, New York, USA, pp: 43-60.

Moore GT. 1973. Developmental differences in environmental cognition. In: Preiser, W, editor. Environmental design research. Dowden, Hutchinson & Ross, Stroudsburg, USA, pp: 232-239.

Moore GT. 1976. Theory and research on the development of environmental knowing. In: Moore, GT, Golledge RG, editors. Environmental knowing: Theories, research, and methods. Van Nostrand Reinhold, New York, USA, pp: 138-164.

Rapoport A. 1977. Human aspects of urban form: Towards a man-environment approach to urban form and design. Pergamon Press, New York, USA, pp: 108-174.

Richter D, Marin FADG, Decanini MMS. 2012. The sketch maps as a language to analyze geographic reasoning. Proced Soc Behav Sci, 46: 5183-5186.

Sammut-Bonnici T, McGee J. 2015. Cognitive map. Wiley, Encyclopedia of Management, London, UK, pp: 1-3.

Sulsters WA. 2005. Mental mapping, viewing the urban landscapes of the mind. In: International conference "Doing, thinking, feeling home: The mental geography of residential environments", October 14-15, Delft, Netherlands, pp: 1-5.

Temple P. 2008. Learning spaces in higher education: An under-researched topic. London Rev Educ, 6(3): 229-241.

URL 1. https://www.ktu.edu.tr/pum/kampusmimarisi (accessed date: November 7, 2024).

Black Sea Journal of Engineering and Science
doi: 10.34248/bsengineering.1599606

Open Access Journal
e-ISSN: 2619 – 8991

Research Article
Volume 8 - Issue 2: 354-362 / March 2025

EXAMINATION OF DISTANCE BASED REGRESSION METHODS FOR DIFFERENT DATA STRUCTURES IN ANIMAL SCIENCE

Burcu KURNAZ[1]*, Hasan ÖNDER[1]

[1]*Ondokuz Mayıs University, Agricultural Faculty, Department of Animal Science, 55139, Samsun, Türkiye*

Abstract: Distance-based regression is an alternative method for parameter estimation in linear regression models when mixed-type explanatory variables are used. Distance-based regression is similar to classical linear regression, except that explanatory variables are measured by distance measures rather than raw values. In this study, datasets with sample sizes of 10, 25, 50, 100, 250 and 500 produced for Binomial, Normal, t, Chi-square and Poisson distributions of Euclidean, Gower and Manhattan distance measures and real data with discrete and continuous distribution that body weight at sixth months was used as outcome variable, body length and chest depth at sixth months of Saanen kids were used as explanatory variables as continuous data. Milk fat ratio was determined as the response variable, while the number of milking per day and the season of Polish Holstein Friesian cattle were determined as the explanatory variables as discrete data. It was aimed to determine the effect on the data sets (10, 50 and 100 sample sizes) by comparing the results obtained from the Linear Regression method. R packages "dbstats", "cluster" and "tidyverse" were used to perform the analysis. As a result, it has been determined that the use of Manhattan distance in data with Poisson distribution may produce unsuccessful results, especially in small sample sizes (n<50). Although there is no significant difference between Gower and Euclidean distances in different distributions according to sample sizes, it has been determined that the use of Euclidean distance measure in some distributions produces results that cause fluctuation. However, it has been understood that the Gower distance can be recommended as a more suitable choice since it has a more stable structure. For the applicability of the Least Square Estimation method, it may be recommended to use Distance Based Regression methods in cases where the necessary assumptions mentioned in this study cannot be met.

Keywords: Distance measures, Package dbstats, Regression, R software

***Sorumlu yazar (Corresponding author):** Ondokuz Mayıs University, Agricultural Faculty, Department of Animal Science, 55139, Samsun, Türkiye
E mail: burcu2039@hotmail.com (B. KURNAZ)
Burcu KURNAZ https://orcid.org/0000-0001-5613-6992
Hasan ÖNDER https://orcid.org/0000-0002-8404-8700

Received: December 11, 2024
Accepted: January 16, 2025
Published: March 15, 2025

Cite as: Kurnaz B, Önder H. 2025. Examination of distance based regression methods for different data structures in animal science. BSJ Eng Sci, 8(2): 354-362.

1. Introduction

In any relationship analysis, the goal is to obtain an accurate and reliable prediction equation using the available data. This is one of the most important and common questions about whether there is a statistical relationship between a response variable (Y) and the explanatory variable(s) (X_i). One option to answer this question is to use regression analysis to model its relationship. There are several types of regression analysis. The type of regression model depends on the shape of the distribution of the response variable (Y) (Arı and Önder, 2013; Kurnaz and Önder, 2021; Kurnaz et al., 2021).

Linear regression analysis is a method of creating a model that predicts the desired response variable based on the variable(s) that can be detected more easily, at lower cost, or earlier than the variable to be determined. Simple linear regression analysis explains the linear relationship between the response variable and a single explanatory variable. If a linear relationship between a single response variable and more than one explanatory variable is desired, the relationship is examined by multiple linear regression analysis (Weisberg, 2005; Okur, 2009; Alpar, 2010). In order for the parameter estimations of the regression model, which will be obtained as a result of both simple and multiple linear regression analysis, to be reliable, some assumptions about the model must be provided. In order to use the regression equation obtained in the simple linear regression analysis for estimation; The error terms ($\epsilon_i = Y_i - \hat{Y}$) show normal distribution due to chance, the mean of the expected value of the errors is 0 and the variance is homogeneous and equal to σ^2, the errors are independent [Cov(ϵ_i, ϵ_j)]=0, with error terms it is necessary to provide some assumptions such as the absence of correlation between the explanatory variable(s) (Alma and Vupa, 2008). In multiple linear regression, in addition to the assumptions in simple linear regression, the assumption that the explanatory variables are independent from each other should also be provided (Vural, 2007). This assumption, which can also be explained as the condition that the simple linear correlation coefficients between the explanatory variables are zero or very close to zero, is expressed as

This work is licensed (CC BY-NC 4.0) under Creative Commons Attribution 4.0 International License

the absence of "multicolinearity" in statistics (Orhunbilge, 2017). In case of multiple connections, Least Squares estimation method loses its power (Vural, 2007). For the biological researches, some discrete or count variables such as sex, genotype, level of crossbreed (F1, G1, etc.) used as explanatory variables that break the assumptions of linear regression. In cases where these assumptions cannot be met, it is recommended to change the parameter estimation methods (Arı and Önder, 2013).

One of the few models developed as a solution for the above-mentioned situation in parameter estimation methods is Distance Based Regression methods. The purpose of these methods is to correctly address problems with non-true value estimators, including categorical or real-valued and categorical explanatory variables (Arenas and Cuadras, 2002). In statistics and data analysis, the geometric concept of distance between individuals or populations has been applied in fields such as anthropology, biology, genetics, psychology, linguistics, and others. The concept of distance is a useful tool for hypothesis testing and parameter estimation among other applications. In addition, the concept of distance is a basic tool in some statistical techniques such as fitness analysis or multidimensional scaling (Cuadras, 1988). Various multivariate approaches can evaluate relationships in connectivity (Varoquaux and Craddock, 2013), some factors have led researchers to examine multivariate distance matrix regression (MMR) (Anderson, 2001; McArdle and Anderson, 2001; Schork et al., 2008; Shehzad et al., 2014). These include:

• Ability to examine more than one explanatory variable at a time (i.e. covariates can be included),

• Applicability for categorical and/or continuous variables,

• Ease of interpretability due to the regression-like analytical structure.

Recently, the distance-based regression model has been successfully applied in many fields. In genomics, Xu et al. (2015) sequenced genes according to clusters associated with a distance-based regression model in the presence of a driver mutation and selected the important gene. In neuroscience, Shehzad et al. (2014) identified voxels (units of volume in body parts in images from computed tomography) associated with brain phenotypes with a distance-based regression model. In human microbiome research, Chen et al. (2012) determined the factors affecting the composition of the microbiome with a regression-based approach. In all these applications, the statistical significance derived from the distance-based regression model of the pseudo F test was calculated numerically with the permutation procedure, which proved to be superior for this purpose (Li et al., 2019).

In this study, datasets with sample sizes of 10, 25, 50, 100, 250 and 500 produced belonging to Binomial, Normal, t, Chi-square and Poisson distributions of Euclidean, Gower and Manhattan distance measures and real datasets showing discrete and continuous distribution (10, 50 and 100 sample sizes) were examined. It is aimed to determine the effect of linear regression by comparing the results obtained from the linear regression method.

2. Materials an Methods

In this study, data sets consisting of Binomial, Poisson, Chi-Square, Normal, t distributions and linear regression (LR) (no distance measure) with sample sizes of 10, 25, 50, 100, 250 and 500 were analyzed. Analyzes were performed using the R software version 4.2.2. 10000 repetitions were used in the simulation study. The continuous data used in the study belong to the Saanen kids used in a study by Önder and Abacı (2015). While body weight at 6 months was used as outcome variable, body length and chest depth at 6 months were used as explanatory variables. The discrete data used in the study were previously reported by Aerts et al. (2022) belong to the Polish Holstein Friesian cattle used in the study. In this example, milk fat ratio was determined as the response variable, while the number of milking per day and the season were determined as the explanatory variables. Mean, standard deviation and error calculations of AIC, BIC, GCV values were used in the evaluation of the obtained results.

Generally a linear regression model; It is defined as $Y = X\beta + \varepsilon$. Here; Y; (nx1) dimensional response variable vector, X; (nxp) dimensional known coefficient matrix (design matrix), β; (nx1) dimensional unknown parameter vector (vector of coefficients), ε; It is an (nx1) dimensional residuals (error) vector, with a mean of zero ($E(\varepsilon)=0$) and a constant variance ($var(\varepsilon)=\sigma^2 I$) (Atkinson and Riani, 2000).

Least Square estimator (LSE) of a linear regression model (equation 1) can be defined as (Anon, 2023a);

$$\hat{\beta}=(X'X)^{-1}X'Y \quad (1)$$

here, X is n×k dimensional explanatory variable data matrix (design matrix), $\hat{\beta}$ is k×1 dimensional vector of coefficients and Y is n×1 dimensional vector of dependent variable observations.

Matrix representation of General Sum of Squares (GSS) in linear regression model; GSS= Y'Y, matrix representation of Regression Sum of Squares (RSS); RSS=$\hat{\beta}'X'Y$, mean of Squares of Error (ESS) is expressed as ESS= GSS-RSS.

The Distance Based Regression model involves multiple regression of a response matrix over any number of explanatory matrices; wherein each matrix contains distances or similarities (in terms of ecological, spatial or other attributes) between all binary combinations of n objects (sample units); Statistical significance tests are performed by permutation. The method shows flexibility in terms of the types of data that can be analyzed (numbers, absent, continuous, categorical) and the shapes of the response curves (Lichstein, 2007).

For a selection of reference input points $R=\{m_k\}_{k=1}^{K}$ with $R\subseteq X$ and corresponding outputs $T=\{t_k\}_{k=1}^{K}$ with $T\subseteq Y$,

define $D_x \epsilon \mathbb{R}^{N\times K}$ in such a way that its kth column contains the distances $d(x_i, m_k)$ between the i= 1,...,N input points x_i and the kth reference point m_k. Analogously, define $\Delta_y \epsilon \mathbb{R}^{N\times K}$ in such a way that its kth column contains the distances $\delta(y_i, t_k)$ between the N output points y_i and the output $\boldsymbol{t}_k$ of the kth reference point. The mapping g between the input distance matrix Dx and the corresponding output distance matrix Δy can be reconstructed using the multiresponse regression model (equation 2).

$$\Delta_y = g(D_x) + E. \quad (2)$$

The columns of the matrix Dx correspond to the K input vectors and the columns of the matrix Δy correspond to the K response vectors, the N rows correspond to the observations. The columns of the $N \times K$ matrix E correspond to the K residuals. Assuming that mapping g between input and output distance matrices has a linear structure for each response, the regression model has the form (equation 3).

$$\Delta_y = D_x B + E \quad (3)$$

The columns of the $K \times K$ regression matrix B correspond to the coefficients for the K responses. The matrix B can be estimated from data through a minimization of the multivariate residual sum of squares as loss function (equation 4):

$$RSS(B) = tr((\Delta_y - D_x B)' (\Delta_y - D_x B)) \quad (4)$$

Under the normal conditions where the number of equations in equation 3 is larger than the number of unknowns, the problem is overdetermined and, usually, with no solution. This corresponds to the case where the number of selected reference points is smaller than the number of available points (i.e. $K<N$). In this case, we must rely on the approximate solution provided by the usual least squares estimate of B (equation 5),

$$\hat{B} = (D_x' D_x)^{-1} D_x' \Delta_y. \quad (5)$$

The problem is uniquely determined if he number of equations equals the number of unknowns (i.e. K=N because all the learning points are also reference points) in equation 3. It has a single solution if the matrix Dx is full-rank (equation 6). So,

$$\hat{B} = D_x^{-1} \Delta_y. \quad (6)$$

Clearly less interesting is the case where in equation 3 the number of equations is smaller than the number of unknowns (i.e. for K>N, corresponding to the situation where, after selecting the reference points, only a smaller number of learning points is used). This case usually leads to an underdetermined problem with infinitely many solutions (de Souza et al., 2015).

The sum of squares associated with any term in any linear model can be calculated directly from a distance matrix. The reason for this is that for any centralized data matrix $Y_{(n\times p)}$ (for p variables and n samples), it can be calculated with the inner product matrix Y'Y used in classical multivariate statistics, as well as with the outer product matrix YY'. In addition, an outer product matrix can be obtained from any (n×n) distance matrix (Gower, 1966), thus allowing the analysis to be based on a chosen distance measure, including semimetric measures such as Bray-Curtis.

Let $X_{(n\times m)}$ be a model (i.e. design or regression) matrix with m number of parameters. For classical multivariate statistics (pxp), the total sum of squares is obtained by breaking down the inner product matrix Y'Y. The total sum of squares (SST) is the trace or sum of the diagonal elements in this matrix (sum of squares for each variable), which we will symbolize by tr(Y'Y). The fragmentation process can be done according to the linear model $Y = X\beta + \epsilon$. Here β denotes the parameters matrix in the model and ϵ denotes the error matrix. The least squares solution for β is $\beta = (X'X)^{-1}X'Y$. The prediction values matrix can be written as $\hat{Y} = XB = HY$ where; H is the idempotent prediction (hat) matrix and can be represented as $X(X'X)^{-1}X'$. The error (residuals) matrix can be represented as $R = Y - \hat{Y} = (I-H)Y$. The pseduo F statistic, which is a statistic applied to test the hypothesis of whether there is an effect of the model parameters, the regression sum of squares tr($\hat{Y}'\hat{Y}$) and the error sum of squares tr(R'R), is calculated as follows (equation 7):

$$F = \frac{tr(\hat{Y}'\hat{Y})/(m-1)}{tr(R'R)/(n-m)}. \quad (7)$$

In case of a single variable, the pseudo F test is calculated the same as the Fisher F test. In the case of non-parametric testing, the probability of Type I error is P=P(F*>=F) where F* is the value calculated by permutation of the unit. The degrees of freedom (m-1) and (n-m) are not required for the permutation test and are taken as constants (Anderson, 2001).

Once a similarity matrix is calculated, it is subjected to a regression analysis that tests hypotheses about this matrix. Whether there is a change in the level of similarity exhibited by pairs of individuals reflected in that matrix can be explained through the characteristics that these individuals have with others (e.g. a certain phenotype or a quantitative phenotype with higher or lower values of a certain feature) (Wessel and Schork, 2006).

2.1. Euclidean Distance Measure

Euclidean distance is the most commonly used distance measure to measure the similarity between two units and is based on the length of a straight line to be drawn between two units (Ünlükaplan, 2008). Using the Euclidean distance measure, the distance between two units is as follows: n is the number of units and p is the number of variables; i,j = 1,2,3……n , i. and j. distance of unit from each other can be calculated as (equation 8):

$$(d_{i,j}) = \sqrt{(x_{i1} - x_{j1})^2 + (x_{i2} - x_{j2})^2 + \cdots + (x_{ip} - x_{jp})^2}. \quad (8)$$

This method has been proven to be compatible with the

classical linear regression model when the Euclidean distance measure is used (Arenas and Cuadras, 2002).

2.2. Manhattan Distance Measure

It is the sum of the distances between objects according to their dimensions. In measuring the distance between two objects in two-dimensional space, the hypotenuse of the triangle shown inside shows the Euclidean distance. The sum of the lengths of the sides of this triangle outside the hypotenuse gives the distance to Manhattan City Block. It is recommended to be used mostly for variables with discrete quantitative data. It is calculated as follows (equation 9) (Alpar, 2013):

$$d_{i,j} = \sum_{k=1}^{p} |x_{ik} - x_{jk}| \quad (9)$$

Manhattan City Block distance is a distance measure that is less sensitive to outliers (Timm, 2002).

2.3. Gower Distance Measure

The most basic feature of Gower distance is that it can be used in data sets that contain both categorical and continuous data. Gower distance is calculated using standardized data. Gower distance is calculated with a separate formula only when continuous data is used. The distance used for a data set containing both categorical and continuous data is called the Gower general similarity measure (URL2). Gower expressed the general similarity measure for categorical variables in the form (equation 10):

$$S_{ij} = \frac{\sum_{k=1}^{p} W_{ijk} S_{ijk}}{\sum_{k=1}^{p} W_{ijk}} \quad (10)$$

here S_{ijk}, k. according to variable value i. and j. It is a measure of similarity between observations. W_{ijk} is i. and j. observation k. When comparing by variable, it takes the value 0 if there is no variable value, and 1 in other cases. For continuous variables in the data, Gower (1971) defined the similarity measure as (equation 11):

$$S_{ij} = 1 - \frac{|x_{ik} - x_{jk}|}{R_k} \quad (11)$$

here R_k is defined as the range of change of k. variable values of i. and j. observations (Servi, 2009).

2.4. Comparison Criteria

Akaike Information Criterion (AIC) can be called an indicator of the goodness of fit of any estimated statistical model. Akaike Information Criteria are asymptotically equivalent to cross-validation (URL3). It can be calculated with the equation (12):

$$AIC = -2\log(L) + 2k. \quad (12)$$

here, k is the number of parameters including the constant term, n is the number of observations, and L is likelihood (Ucal, 2006).

The Bayesian information criterion (BIC) is based in part on the likelihood function and is closely related to the Akaike information criterion (AIC). When fitting models, it is possible to increase the maximum likelihood by adding parameters, but doing so can lead to overfitting. Both BIC and AIC try to solve this problem by introducing a penalty term for the number of parameters in the model; The penalty term is larger in BIC than AIC for sample sizes greater than 7 (McQuarrie and Tsai, 1998) and can be calculated as shown below (equation 13):

$$BIC = -2\log(L) + k\log(n) \quad (13)$$

BIC differs from AIC in that the second part on the right-hand side of the equation depends on the sample size. However, despite the superficial similarity between AIC and BIC, it was later determined that they differ within the Bayesian structure (Raftery, 1995; Wasserman, 2000).

The Generalized Cross Validitation (GCV) criterion developed by Craven and Wahba in 1979 is one of the criteria for selecting the most appropriate model (Adıgüzel, 2021). The GCV criterion is based on the minimization of errors and also takes into account the complexity of the model (equation 14) (Yıldız, 2022).

$$GCV(M) = \frac{1}{N}\sum_{i=1}^{N} \frac{[y_i - f_M(x_i)]^2}{\left[1 - \frac{C(M)}{N}\right]^2} \quad (14)$$

In the equation, C(M) is the function that penalizes the model complexity for valid basis functions, y_i is the observation values of the dependent variable and $f_M(x_i)$ is the prediction values, and N is the number of observations (Chen et al., 2012).

All statistical evaluation was performed using R software (R Core Team, 2022). The sample code sequence used in the analysis is given below;

```
library("dbstats")
library("cluster")
library(tidyverse)
simulnumber=10000
sampsize=25
results=matrix(nrow= simulnumber, ncol=10)
for(i in 1: simulnumber) {
        Y=rnorm(sampsize,0,1)
        X1=rchisq(sampsize,5)
        X2=rchisq(sampsize,5)
        Model1 <- dbglm(formula = Y ~ X1 + X2, family
= gaussian(), method = "GCV", full.search = TRUE, metric
= "euclidean", weights = NULL, range.eff.rank = c(1, 2))
        Model2 <- dbglm(formula = Y ~ X1 + X2, family
= gaussian(), method = "GCV", full.search = TRUE, metric
= "gower", weights = NULL, range.eff.rank = c(1, 2))
        Model3 <- dbglm(formula = Y ~ X1 + X2, family
= gaussian(), method = "GCV", full.search = TRUE, metric
= "manhattan", weights = NULL, range.eff.rank = c(1, 2))
        glm1 <- glm(Y ~ X1 + X2, family = gaussian())
 results[i,1]=summary(Model1$aic.model)[4][1]
 results[i,2]=summary(Model1$bic.model)[4][1]
 results[i,3]=summary(Model1$gcv.model)[4][1]
 results[i,4]=summary(Model2$aic.model)[4][1]
 results[i,5]=summary(Model2$bic.model)[4][1]
 results[i,6]=summary(Model2$gcv.model)[4][1]
```

```
 results[i,7]=summary(Model3$aic.model)[4][1]
 results[i,8]=summary(Model3$bic.model)[4][1]
 results[i,9]=summary(Model3$gcv.model)[4][1]
 results[i,10]=summary(glm1$aic)[4][1]
}
sink("D:/result_matrix.txt")
results
sink()
```

3. Results and Discussion

In order to examine the effects of distributions and distance measures on AIC, BIC and GCV, analyzes were made according to the factorial experimental design and the sample size was used as a covariate. Since the distribution × distance interaction was found to be insignificant (P>0.05), only main effects are presented. The sample size used as a covariate was determined to be statistically significant as expected (P<0.01), therefore marginal means and standard error values are given in the tables. According to the findings, it was determined that the distribution had a statistically significant effect on AIC, BIC and GCV (P<0.01), while distance measures had an effect only on the AIC value (P<0.01) as seen in table 1 and 2.

Although the lowest AIC value is obtained from data with normal distribution, there is no difference in terms of AIC value between the results obtained from Normal, Binomial and t distribution. The highest AIC values were obtained from data with Poisson distribution and a significant difference was determined between them and other distributions. It was determined that the AIC values obtained from the Chi-Square distribution were different from the AIC values obtained from the Normal and Poisson distributions, but there was no difference in terms of AIC values between the results obtained from the Binomial and t distribution. When the effect of distribution on BIC values was evaluated, it was determined that the BIC values obtained only from the Poisson distribution were significantly higher than those obtained from other distributions. It was observed that the BIC values obtained from other distributions were similar. When the effect of distributions on GCV values was evaluated, it was understood that the results obtained were similar to the effect on AIC (Table 1).

It is understood that the difference in the AIC value arises from the values obtained from the linear regression least squares method and that there is no difference between the Euclidean, Gower and Manhattan distance measures (Table 2). Boj et al. (2002) mentioned that using distance measures when the existence of non-normal variables were more reliable than classic linear regression, which supports our results.

For the combination of distribution × distance measure, AIC, BIC and GCV measurements are evaluated together and the hierarchical clustering dendrogram drawn using the Ward method and Square Euclidean distance is given in figure 1.

According to the results obtained, it was determined that a total of 20 combinations could be examined in five clusters. According to this; All distance measures and the LSE solution used in the t distribution form a separate cluster (cluster 1), All distance measures and the LSE solution used in the binomial distribution form a separate cluster (cluster 2), Manhattan and the LSE solution in the normal distribution and Euclidean distance in the Poisson distribution form a separate cluster. It was determined that Manhattan, Gower and LSE solutions formed a separate cluster in the Poison distribution (cluster 4), and all methods in the Chi-square distribution and Euclidean and Gower solutions in the normal distribution formed the last cluster (cluster 6).

Table 1. Effects of distributions on AIC, BIC and GCV

Distributions	AIC	BIC	GCV
Binom	156.841 ± 0.027^{bc}	159.956 ± 0.031^{b}	0.984 ± 0.001^{b}
Chi-Square	156.870 ± 0.027^{b}	159.978 ± 0.031^{b}	0.981 ± 0.001^{bc}
Normal	156.763 ± 0.027^{c}	159.876 ± 0.031^{b}	0.979 ± 0.001^{c}
Poisson	157.002 ± 0.029^{a}	160.421 ± 0.034^{a}	0.989 ± 0.001^{a}
t	156.812 ± 0.027^{bc}	159.915 ± 0.031^{b}	0.983 ± 0.001^{bc}
P	<0.001	<0.001	<0.001

The co-variate, sample size, was determined as 54.3092; ^{a,b}= different letters in the same column indicate statistical difference (P<0.05).

Table 2. Effects of distance measures on AIC, BIC and GCV

Distances measure	AIC	BIC	GCV
Euclidean	156.557 ± 0.024^{b}	160.025 ± 0.025	0.983 ± 0.001
Gower	156.555 ± 0.024^{b}	160.022 ± 0.025	0.983 ± 0.001
Manhattan	156.576 ± 0.024^{b}	160.040 ± 0.025	0.984 ± 0.001
LR	157.743 ± 0.024^{a}		
P	<0.001	0.862	0.402

The co-variate, sample size, was determined as 54.3092; ^{a,b}= different letters in the same column indicate statistical difference (P<0.05).

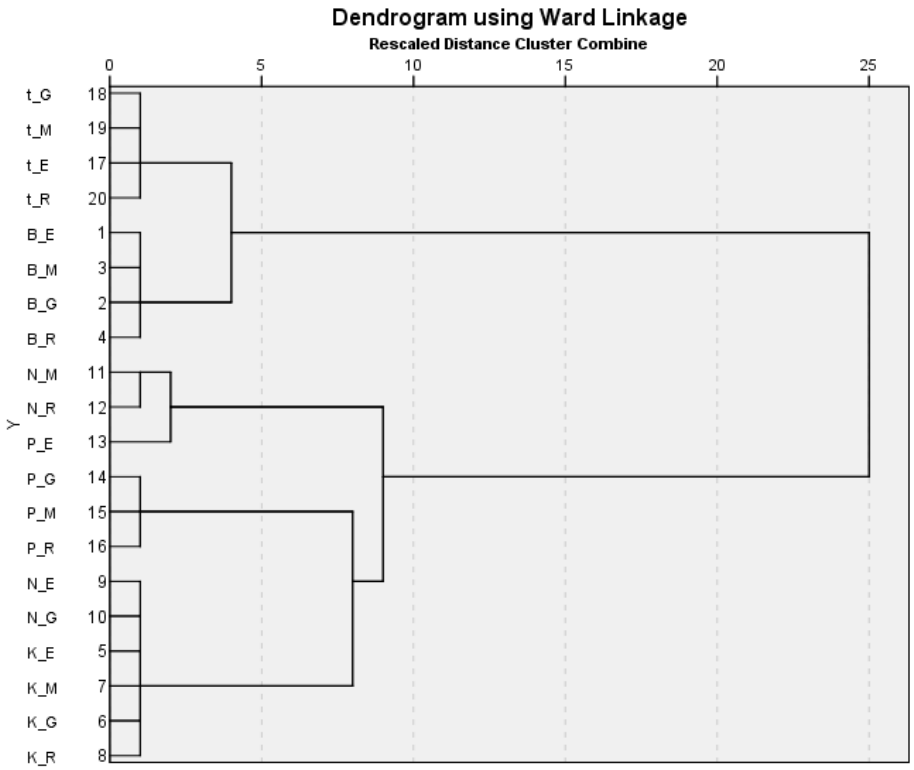


Figure 1. Hierarchical clustering dendrogram drawn by evaluating AIC, BIC and GCV measurements together for the distribution x distance measure combination. X_X: the first letter indicates the distribution and the second letter indicates distance measure.

It is understood that the first two clusters are farther from the other clusters. It has been determined that binomial and t distributions form unique clusters, but other distributions form mixed clusters. When the last three clusters are examined; it is understood that normal distribution can be evaluated with different solutions of both Poisson and Chi-square distribution, but Chi-square and Poison distributions are not in the same cluster. This interpretation was supported by the study of Zapala and Schork (2012) that they mentioned the choice of an appropriate distance measure may be problematic, although our experience suggests that different distance measures provide roughly the same inferences.

3.1. Real Data Results

The effects of distance measures on the real data structure of continuous and discrete distribution for sample sizes of 10, 50 and 100 are given in table 3 and 4.

According to the findings obtained as a result of the analysis, it was determined that the LSE method produced higher AIC values than distance measurements for n = 10. It is understood that Euclidean and Gower have the same and lowest information criterion values among distance measures. Li et al. (2019) supports our results that distance-based regression with Euclidean distance was more reliable than linear regression for embryonic imprint data with the sample size of 24. Also Kim et al. (2001) mentioned that using Cook distance in local polynomial regression was more robust than standard approaches. It was observed that when the sample size was n=50, the AIC value obtained from the LSE method produced the lowest value closest to the Euclidean measure. For continuous distribution, it is seen that the Gower distance measure has the largest AIC value for the sample size n = 50. It was determined that the smallest AIC value for the sample size n=100 was the value obtained from linear regression. It is understood that the AIC value closest to this value belongs to the Euclidean distance measure. According to the results obtained, it was determined that the LSE estimation method did not produce reliable results according to the selection criteria obtained from distance-based regression in continuously distributed real data with a small sample size. It is understood that when the sample size increases, there is no significant difference with Euclidean, which is the distance measure for continuous data, when the assumptions of linear regression methods are met. It was observed that the Gower distance measure had the smallest BIC value for the sample size n = 50. Lichstein (2007) argued with supporting our results that use of Bray-Curtis distances was superior to linear regression.

In data sets belonging to discrete distribution, the AIC values for sample size n = 10 were obtained from the Euclidean distance measure that produced the smallest value. It has been observed that the LSE method has the highest Akaike Information Criterion value. When we look at the BIC values, it is understood that the Euclidean distance measure produced the smallest value. It was determined that there was no difference between the GCV values obtained from all distance measurements.

Table 3. Effect of distance measurements on continuous data

Criteria	Distance measure	n=10	n=50	n=100
AIC	Euclidean	41.72	208.47	338.74
	Gower	41.72	209.33	340.35
	Manhattan	41.77	208.77	340.10
	LR	43.44	208.50	338.70
BIC	Euclidean	42.32	214.21	345.96
	Gower	42.32	213.16	347.57
	Manhattan	42.38	214.50	347.32
GCV	Euclidean	2.57	3.50	3.47
	Gower	2.57	3.56	3.54
	Manhattan	2.59	3.52	3.53

Table 4. Effect of distance measurements on discrete data

Criteria	Distance measures	n=10	n=50	n=100
AIC	Euclidean	20.31	48.03	147.00
	Gower	20.44	48.11	146.63
	Manhattan	20.38	50.21	147.77
	EKK	22.27	48.41	148.60
BIC	Euclidean	21.10	51.81	152.21
	Gower	21.24	51.89	151.84
	Manhattan	21.18	53.99	152.98
GCV	Euclidean	0.26	0.14	0.24
	Gower	0.26	0.14	0.24
	Manhattan	0.26	0.15	0.25

It was determined that the Manhattan distance measure produced the highest AIC value when the sample size was n=50. It was observed that the criterion value obtained from linear regression was close to the Euclidean measure, which has the smallest criterion value. This may be because the assumptions for linear regression were met. It has been determined that the Gower distance measure, which produces reliable results in discrete data, produces the smallest AIC value for the sample size n=100 for discrete distribution. While BIC values were determined to be the Euclidean distance measure that produced the smallest information criterion for sample sizes of 10 and 50, it was determined that the Gower distance measure had the smallest value when the sample size was 100. It appears that there is no significant difference in GCV values for all sample sizes. Kurnaz and Önder (2021) supports our results that they mentioned the comparison of Euclid, Manhattan and Gower distance measures within the scope of distance based regression can give more reliable results especially existence of discrete explanatory variables. Cuadras and Arenas (1990) mentioned the use of Gower distance for mixed explanatory variables (discrete and continuous) to predict normal response variable was more powerful than linear regression, which supports our results. Ferreira Barreto et al. (2020) found that distance-based estimation for fNIRS signals and behavioral data was successful. Haron et al. (2019) also mentioned that distance-based regression is a good alternative method for estimating the unknown parameters in regression modeling when dealing with mixed-type of exploratory variables.

4. Conclusion

When the effect of Distance Based Regression methods on distributions is evaluated, it is seen that the lowest information criteria value is in the data set consisting of explanatory variables with a normal distribution structure, which is a theoretical expectation. Considering the AIC, BIC and GCV values obtained from distance measures, it can be recommended to use this distance measure for model selection since the Gower distance measure has the lowest information criteria values compared to other distance measures.

When the findings are evaluated, it can be said that using Manhattan distance in data with Poisson distribution, especially in small sample sizes (n<50), may produce unsuccessful results. Although there is no significant difference between Gower and Euclidean distances in different distributions depending on sample sizes, it has been determined that the use of Euclidean distance measure in some distributions produces results that cause fluctuations. However, the Gower distance can be suggested as a more appropriate choice because it has a more stable structure. This may be because the Gower distance is calculated using standardized data.

When the information criteria values in model selection were examined, it was determined that the method that produced the highest AIC value for all distributions and sample sizes of the data sets was the LSE estimation method for linear regression. When information criteria values are evaluated for model selection, choosing the model that produces the smallest value increases the prediction success. Therefore, it can be said that the model obtained from linear regression analysis methods will not be reliable. In cases where the necessary assumptions mentioned in this study cannot be met for

the applicability of the LSE estimation method, it may be recommended to use Distance Based Regression methods.

It is considered that in future studies, evaluating other distance measures such as Bray-Curtis, Orloci's Chord, Chi-square, Canberra and Hellinger and/or examining combinations of explanatory variables with different distributions may be useful for the subject.

Author Contributions

The percentages of the authors' contributions are presented below. All authors reviewed and approved the final version of the manuscript.

	B.K.	H.Ö.
C	50	50
D	100	
S		100
DCP	80	20
DAI	90	10
L	100	
W	80	20
CR	90	10
SR	100	

C=Concept, D= design, S= supervision, DCP= data collection and/or processing, DAI= data analysis and/or interpretation, L= literature search, W= writing, CR= critical review, SR= submission and revision.

Conflict of Interest

The authors declared that there is no financial/commercial conflict of interest.

Ethical Consideration

Ethics committee approval was not required for this study because of there was no study on animals or humans.

Acknowledgements

This study is short summary of MSc thesis of first author under the supervision of the second author.

Data Availability

To obtain the data, please contact the corresponding author.

References

Adıgüzel MB. 2021. Çok değişkenli uyarlanabilir regresyon eğrilerinde alternatif bilgi kriterleri ile model seçimi. PhD Thesis, Ondokuz Mayıs University, Graduate Shool of Education, Department of Statistics, Samsun, Türkiye, pp: 86.

Aerts J, Sitkowska B, Piwczyński D, Kolenda M, Önder H. 2022. The optimal level of factors for high daily milk yield in automatic milking system. Livestock Sci, 264: 105035.

Alma ÖG, Vupa Ö. 2008. Regresyon analizinde kullanılan en küçük kareler ve en küçük medyan kareler yöntemlerinin karşılaştırılması. SDÜ Fen Ede Fak Fen Derg, 3(2): 2019-229.

Alpar R. 2010. Basit doğrusal regresyon çözümlemesi: Spor, sağlık ve eğitim bilimlerinden örneklerle uygulamalı istatistik ve geçerlik-güvenirlik. Detay Yayıncılık, Ankara, Türkiye, pp: 672.

Alpar R. 2013. Uygulamalı çok değişkenli istatistiksel yöntemler. Detay Yayıncılık, Ankara, Türkiye, pp: 853.

Anderson MJ. 2001. A new method for non-parametric multivariate analysis of variance. Austral Ecol, 26: 32-46.

Anonymous. 2011. Kümeleme analizinde kullanılan bazı farklılık ve benzerlik ölçülerinin incelenmesi. URL: http://emredunder.blogspot.com/2011/06/kumeleme-analizinde-kullanlan-baz.html (accessed date: June18, 2023).

Anonymous. 2023a. Ankara Üniversitesi açık ders. URL: https://acikders.ankara.edu.tr/pluginfile.php/130799/mod_resource/content/0/6-%20Matris.pdf (accessed date: May 12, 2023).

Anonymous. 2023b. Model ve dağılım seçme URL: https://avys.omu.edu.tr/storage/app/public/kamilal/108861/HPTZ.HF10.pdf (accessed date: May 16, 2023).

Arenas C, Cuadras M. 2002. Recent statistical methods based on distances. Contrib Sci, 2(2): 183-191.

Arı A, Önder H. 2013. Farklı veri yapılarında kullanılabilecek regresyon yöntemleri. Anadolu Tar Bil Derg, 28(3): 168-174.

Atkinson AC, Riani M. 2000. Robust diagnostic regression analysis. Springer, New York, US, pp: 328.

Boj E, Claramunt MM, Fortiana J, Vidiella A. 2002. The use of distance-based regression and generalized linear models in the rate making process: An empirical study. Universitat de Barcelona. Institut de Matemàtica [IMUB], Barcelona, Spain, pp: 47.

Chen J, Bittinger K, Charlson ES, Hoffmann C, Lewis J, Wu GD, Li H. 2012. Associating microbiome composition with environmental covariates using generalized UniFrac distances. Bioinf, 28(16): 2106-2113.

Cuadras CM, Arenas C. 1990. A distance based regression model for prediction with mixed data. Commun Stat A. Theory Methods, 19: 2261-2279.

Cuadras CM. 1988 Statistical distances. Estadística Española, 30: 295-378.

de Souza Jr AH, Corona F, Barreto GA, Miche Y, Lendase A. 2015. Minimal learning machine: A novel supervised distance-based approach for regression and classification. Neurocomputing, 164: 34-44.

Ferreira Barreto CDS, Zimeo Morais GA, Vanzella P, Sato JR. 2020. Combining the intersubject correlation analysis and the multivariate distance matrix regression to evaluate associations between fNIRS signals and behavioral data from ecological experiments. Experl Brain Res, 238: 2399-2408. https://doi: 10.1007/s00221-020-05895-8

Gower JC. 1966. Some distance properties of latent root and vector methods used in multivariate analysis. Biometrika, 53(3-4): 325-338.

Gower JC. 1971. A general coefficient of similarity and some of its properties. Biometrics, 1971: 857-871.

Haron NH, Ahad NA, Mahat NI. 2019. Distance-based regression for non-normal data. The 4th Innovation and Analytics Conference & Exhibition (IACE 2019), March 21-28, Kedah, Malaysia. https://doi.org/10.1063/1.5121118

Kim C, Lee Y, Park BU. 2001. Cook's distance in local polynomial regression. Stat Probab Lett, 54: 33-40.

Kurnaz B, Önder H, Piwczynski D, Kolenda M, Sitkowska B. 2021. Determination of the best model to predict milk dry matter in high milk yielding dairy cattle. Acta Sci Pol Zootechnica, 20(3): 41-44. https://doi: 10.21005/asp.2021.20.3.05

Kurnaz B, Önder H. 2021. Distance based regression models. II. International Applied Statistics Conference (UYIK-2021), June 29- July 2, Tokat, Türkiye, pp: 120-126.

Li J, Zhang W, Zhang S, Li Q. 2019. A theoretic study of a

distance-based regression model. Sci China Math, 62: 979-998.

Lichstein JW. 2007. Multiple regression on distance matrices: a multivariate spatial analysis tool. Plant Ecol, 188: 117-131.

McArdle BH, Anderson MJ. 2001. Fitting multivariate models to community data: a comment on distance-based redundancy analysis. Ecology, 82(1): 290-297.

McQuarrie AD, Tsai CL. 1998. Regression and time series model selection. World Scientific Publication Co Pte. Ltd., London, UK, pp:45

Okur S. 2009. Parametrik ve parametrik olmayan doğrusal regresyon analiz yöntemlerinin karşılaştırılmalı olarak incelenmesi. MSc Thesis, Çukurova University, Institute of Science, Department of Animal Science, Adana, Türkiye, pp: 62.

Orhunbilge N. 2017. Uygulamalı regresyon ve korelasyon analizi. Nobel Yayıncılık, Ankara, Türkiye, pp: 394.

Önder H, Abacı SH. 2015. Path analysis for body measurements on body weight of Saanen kids. Kafkas Üniv Vet Fak Derg, 21(3): 351-354.

R Core Team. R: A language and environment for statistical computing. R Foundation for Statistical Computing, Vienna, Austria. 2022, URL: https://www.R-project.org/.

Raftery AE. 1995. Bayesian model selection in social research. Sociol Methodol, 25: 111-163.

Schork NJ, Wessel J, Malo N. 2008. DNA sequence-based phenotypic association analysis. Adv Genet, 60: 195-217.

Servi T. 2009. Çok değişkenli karma dağılım modeline dayalı kümeleme analizi. PhD Thesis, Çukurova University, Institute of Science, Department of Statistics, Adana, Türkiye, pp: 266.

Shehzad Z, Kelly C, Reiss PT, Craddock RC, Emerson JW, McMahon K, Milham MP. 2014. A multivariate distance-based analytic framework for connectome-wide association studies. Neuroimage, 93: 74-94.

Timm NH. 2002. Applied Multivariate Analysis. Splinger-Verlag, New York, US, pp: 718.

Ucal MŞ. 2006. Ekonometrik Model seçim kriterleri üzerine kisa bir inceleme. CÜ İİBF Derg, 7(2): 41-57.

URL1: https://acikders.ankara.edu.tr/pluginfile.php/130799/mod_resource/content/0/6-%20Matris.pdf (accessed date: May 12, 2023).

URL2: http://emredunder.blogspot.com/2011/06/kumeleme-analizinde-kullanlan-baz.html (accessed date: June18, 2023).

URL3: https://avys.omu.edu.tr/storage/app/public/kamilal/108861/HPTZ.HF10.pdf (accessed date: May 16, 2023).

Ünlükaplan Y. 2008. Çok değişkenli istatistiksel yöntemlerin peyzaj ekolojisi araştırmalarında kullanımı. PhD Thesis, Çukurova University, Institute of Science, Department of Statistics, Adana, Türkiye, pp: 156.

Varoquaux G, Craddock RC. 2013. Learning and comparing functional connectomes across subjects. NeuroImage, 80: 405-415.

Vural A. 2007. Aykırı değerlerin regresyon modellerine etkileri ve sağlam kestiriciler. MSc Thesis, Marmara University, Institute of Social Sciecnes, Department of Econometry, İstanbul, Türkiye, pp: 73.

Wasserman L. 2000. Bayesian model selection and model averaging. J Math Psychol, 44(1): 92-107.

Weisberg S. 2005. Applied linear regression. John Wiley & Sons, New Jersey, US, pp: 340.

Wessel J, Schork NJ. 2006. Generalized genomic distance-based regression methodology for multilocus association analysis. Amer J Human Genet, 79(5): 792-806.

Xu Y, Guo X, Sun J, Zhao Z. 2015. Snowball: resampling combined with distance-based regression to discover transcriptional consequences of a driver mutation. Bioinformatics, 31(1): 84-93.

Yıldız M. 2022. Dolar ve Euro kurları üzerinde etkili faktörlerin iki bağımlı değişkenli MARS modeli ile belirlenmesi. Kastamonu Üniv İİBF Derg, 24(1): 6-29.

Zapala MA, Schork NJ. 2012. Statistical properties of multivariate distance matrix regression for high-dimensional data analysis. Front Genet, 3: 190. https/doi.org/10.3389/fgene.2012.00190

Black Sea Journal of Engineering and Science
doi: 10.34248/bsengineering.1596008

Open Access Journal
e-ISSN: 2619 – 8991

Research Article
Volume 8 - Issue 2: 363-370 / March 2025

A COMPARATIVE ASSESSMENT ON THE NOVEL LONG-TERM REAL-TIME SINGLE OBJECT TRACKING TECHNIQUES USING YOLO-NAS AND YOLO11

Cevahir PARLAK[1]*

[1]*Fenerbahçe University, Faculty of Engineering, Department of Computer Engineering, 34758, İstanbul, Türkiye*

Abstract: This study sheds light on the daunting task of single-object tracking using state-of-the-art BoT-SORT, DeepSORT, SORT, and ByteTrack tracking algorithms with YOLO-NAS and YOLO11 object detectors. Object tracking is a step further of object detection and tries to detect the movement of objects in video files and it has enormous range of real-world application fields. Object tracking also assigns unique identifiers to each tracked object and tries to maintain the identity throughout the entire sequence. Current models can achieve great success in object tracking, however there are still too many obstacles and challenges lying ahead to resolve. YOLO-NAS and YOLO11 are the latest and most used object detection models. YOLO can be combined with different tracking methods such as ByteTrack, BoT-SORT, SORT, and DeepSORT for object tracking. The advantage of YOLO is its extremely fast implementation compared to the other methods. When accompanied by specialized tracking algorithms, YOLO achieves the best scores in object tracking. This study focuses on the implementation of YOLO-NAS and YOLO11 in tracking and results demonstrate that YOLO11 is more accurate and stable with BoT-SORT, however, it is faster using ByteTrack method.

Keywords: Single-Object tracking, YOLO, BoT-SORT, ByteTrack, SORT, DeepSORT

***Corresponding author:** Fenerbahçe University, Faculty of Engineering, Department of Computer Engineering, 34758, İstanbul, Türkiye
E mail: cevahir.parlak@fbu.edu.tr (C. PARLAK)
Cevahir PARLAK https://orcid.org/0000-0002-5500-7379

Received: December 04, 2024
Accepted: January 17, 2025
Published: March 15, 2025

Cite as: Parlak C. 2025. A comparative assessment on the novel long-term real-time single object tracking techniques using YOLO-NAS and YOLO11. BSJ Eng Sci, 8(2): 363-370.

1. Introduction

Object tracking is a very formidable, energetic, and vitally important computer vision field which combines the detection of an object and pursuing its traces across multiple video frames. Broadly speaking, SOT (stands for Single-Object Tracking) together with Multi-Object Tracking (abbreviated as MOT) constitute two major branches of object tracking. SOT technology deals with single objects even if there can be other objects in the environment. MOT tries to detect all different objects, assigns unique identities to each of them, and furthermore tracks them by their identities across the entire sequence. Object tracking harbors two main ideas: Detection of certain objects and Tracking of the Detected Objects with their unique identities. In the first stage of object tracking a detection algorithm is used to identify specified objects and in the second phase, specified objects are pursued by another algorithm using their unique identities. Object tracking becomes increasingly popular and finds a broad range of application areas such as traffic surveillance, security, robotics, sports analytics, automatic driving assistance systems, and medical diagnosis.

Many methods and algorithms have been put forward to advance object tracking in computer vision. Tracking can be done using Kalman filters, Meanshift (Fukunaga and Hostetler, 1975), deep learning-based methods, and particle filters. Optical flow (Black and Anandan, 1993) and Kalman filters are the most popular methods of object tracking. Optical flow tracks the movement of pixels whereas Kalman filter pursues the movement of specified object. Boosting (Grabner et al., 2006) is an Adaboost-based (Freund and Schapire, 1996) old algorithm and quite slow, susceptible to noise and obstacles, and does not stop when the object is lost. Boosting can be used in simple and low-resource cases. Multiple Instance Learning (MIL) (Babenko et al., 2009) method runs on the positive and negative samples and noise-robust, however cannot stop when object is lost. Kernelized Correlation Filters (KCF) (Henriques et al., 2014) is a Boosting and MIL combined method. It is fast, it can stop tracking when the object is lost, however it is difficult to restart the tracking. Tracking, Learning, Detection (TLD) (Kalal et al., 2012) splits tracking operation into tracking, learning, and detecting phases. It is good at object scaling and overlapping, however, it has rather unpredictable behavior and confuses the similar objects instead of the intended object. MedianFlow (Kalal et al., 2010) uses Lucas-Kanade algorithm by tracking the object in forward and backward time directions to calculate the errors of these paths. Median-flow is vulnerable to high-speed objects. Generic Object Tracking

This work is licensed (CC BY-NC 4.0) under Creative Commons Attribution 4.0 International License

Using Regression Networks (GoTurn) (Held et al, 2016) uses convolutional neural networks. The previous and current frames are used as the network input and current location of the object is predicted. It is noise-robust, but accuracy may depend on the dataset it was trained on and therefore prone to overfitting. It may lose the object and track another one at high-speed tracking applications. Minimum Output Sum of Squared Error (MOSSE) (Bolme et al., 2010) tracker uses adaptive correlations of Fourier transformation. It is useful in high-speed tracking but may continue tracking even if the object is totally lost from the screen. Channel and Spatial Reliability Tracker (CSRT) (Lukežič et al., 2017) leverages spatial reliability maps to obtain a wider area for its search and can pursue non-rectangular-shaped objects. It uses Colornames and HOG attributes which derive the oriented gradients and obtain their histograms by (Dalal and Triggs, 2005). It can achieve higher accuracy, but it is slow and also it can produce unexpected results if the object disappears from the frame. Meanshift and CamShift (Continuously Adaptive Meanshift) (Bradski, 1998) are based on the same methods which use color histograms. Meanshift cannot evaluate rotations, translations, and scales whereas CAMShift can. Optical flow tracks pixel movements in time using a vector field. It is based on spatial smoothness and constancy brightness. It can be implemented using Shi-Tomasi, Lucas-Kanade-Tomasi (sparse) or Fanerbäck (dense) methods. Siamese networks (Bertinetto et al, 2016) have two identical networks to unearth the relevant features of objects to pinpoint the location and appearance of the objects. These feature vectors are compared using some distance methods such as cosine or Euclidean distances. After determining the objects in the first frame, extracted features are used to find the best likely matches in the next frames. Siamese networks need only a single image to track an image enabling fast online learning. They can be robust against translation and occlusion or other light changes. They are also fast enough to be used in real-time tracking. StrongSORT (Du et al., 2023) is proposed to resolve the missing detection and missing association problems of previous tracking methods. StrongSORT also incorporates Gaussian-smoothed interpolation (GSI) and appearance-free link algorithms to alleviate the missing detection problem and to balance the speed-accuracy trade-off. MCITrack (Kang et al., 2024) uses a mamba layer and cross-attention layer as principal components to further exploit the contextual information inside the video streams. Experiments on the LASOT dataset demonstrated strong performance and achieved 76.6% AUC. Another newly introduced tracking algorithm called LoRAT (Lin et al., 2025) facilitates a large ViT (Vision Transformer) which decomposes positional embeddings as shared spatial embeddings and independent embeddings. LoRAT is highly inspired by the success of PEFT (Parameter-Efficient Fine-Tuning) in the transformers and adapts it with a special multilayer perceptron architecture. Thus, obtains less computational complexity while boosting performance. Other newly introduced methods are Simple Online and Realtime Tracking also known as SORT (Bewley et al., 2016), Simple Online and Realtime Tracking with a Deep Association Metric also referred to as DeepSORT (Wojke et al., 2017), ByteTrack (Zhang et al., 2022), and Bag of Tricks for SORT aka BoT-SORT (Aharon et al., 2022) are evaluated in this paper and discussed in the next section.

There are numerous issues that need to be overcome in object tracking including object reidentification, occlusion, and interlacing handling. Object reidentification is the process of reidentifying the object after it disappeared for a while and assigning the same identity to the object. Occlusion handling involves tracking while the object is covered by other objects partially or completely. Interlacing occurs when different objects are identified inside the same bounding box intertwined with one another or distinct parts of the same object are identified as different objects. Fast moving objects, dynamic ambience (complex background, light changes etc.), and detection of similar objects are other difficulties in object tracking applications.

Deep learning techniques and object detection is investigated by Tan et al (Tan et al., 2021). A comprehensive review of object tracking techniques, datasets, and metrics can be found in (Kadam et al., 2024). Soleimanitaleb and Keyvanrad (Soleimanitaleb and Keyvanrad, 2022) surveyed the single object tracking methods, metrics, and datasets.

Şimşek and Tekbaş (Şimşek and Tekbaş, 2024) proposed a YOLO8-based DeepSORT approach utilizing heatmaps to efficiently and adaptively analyze the in-store behaviors of customers. Instead of tracking the full bounding boxes of customers they used only the bounding boxes of feet of customers. Their study achieved 89.16% F1-score.

Havuç et al. (Havuç et al., 2021) proposed a YOLO-based ping-pong playing robotic arm tracking the ping-pong ball. They created their own table-tennis dataset by recording their tennis matches and obtaining videos from YouTube. They included 21000 images in their datasets. They used a specialized camera hardware to detect the fast-moving ping-pong balls. They trained their model with 80% of the data and 20% is used as test data. In their experiments, they used YOLO-tiny model for fast implementation of detecting the fast-moving ball. They showed that YOLO-tiny can successfully track the ping-pong ball and respond accurately to the ball movements.

Atalı and Eyüboğlu (Atalı and Eyüboğlu, 2022) studied tracking on the colorful circular objects with varying diameters using CIE (Commission Internationale de l'éclairage) color format by a mobile robot and compare the results with the HSV color mode. A robot with a constant speed pursuing the detected object from a certain distance using ROS (Robot Operating System) system. They concluded that CIE color provides better

results from the noisy images compared to HSV (Hue Saturation Value) color coding system, but HSV is better in response time and image capturing.

2. Materials and Methods

This section summarizes the single object dataset of this study, YOLO11, YOLO-NAS, SORT, DeepSORT, ByteTrack, and BoT-SORT methods. YOLO11 and YOLO-NAS are used for detection part whereas SORT, DeepSORT, ByteTrack, and BoT-SORT are used for tracking the detected objects and assigning unique identities.

2.1. LASOT Dataset

There are too many datasets related to object tracking and, in this study, 3 different image sequences are used from the freely available Large-Scale Single Object Tracking image dataset by Fan and others (LASOT) (Fan et al., 2020). LASOT is an image dataset intended for long-term single object detection and tracking; however, some of the images contain many other objects. The difference in single object datasets is that the camera mostly focuses on a specified target object making it easier to detect. LASOT contains 1550 image sequences with 85 categories and more than 3.87 million frames and various object types including ground-truth bounding-box, visual, and lingual information. In this study, cat, car, and airplane images are selected. The videos that were used in this study almost always contain single objects. The Cat video has 2651 frames, the Car video has 3401 frames, and the Airplane video contains 1567 frames totaling 7619 frames combined. The resolutions are $640x360$, $480x360$, and $1280x720$ for the Car, the Cat, and the Airplane videos, respectively. All videos of this study have been recorded with 25 frame per second video speed. Another newly introduced and more comprehensive dataset is the SOTVerse (Hu et al., 2024) dataset which can be used for more advanced tracking tasks. LASOT is primarily designed for long-term tracking whereas SOTVerse is designed for short-term tracking, however, SOTVerse is gradually removing some of its short-term and single camera constraints.

2.2. YOLO11

Currently, YOLO11 (Jocher and Qiu, 2024) is the latest YOLO product for object detection and tracking. It is fast, efficient, and accurate compared to the previous YOLO versions. YOLO11 comes with novel training methods model architecture to enable different machine vision tasks such as object detection, instance segmentation, pose/keypoint estimation, oriented bounding box object detection (OBB), multithreaded tracking and as well as object classification. It introduces many different models such as nano, small, medium, large, and xlarge models. It has enhanced, stronger neck and backbone design to improve the feature extraction stages. Its architectural design is optimized for training processes to achieve faster implementations. It can reach higher accuracies with smaller number of parameters and less complex structures. YOLO11 also is adaptable to different environments and cloud platforms.

2.3. YOLO-NAS

YOLO-NAS (Neural Architecture Search) (Aharon et al., 2021) is another groundbreaking YOLO model for object detection. YOLO-NAS facilitates AutoNAC (Automated Neural Architecture Construction) to resolve the limitations of older YOLO models. YOLO-NAS uses selective quantization and quantization-aware blocks. AutoNAC is an advanced model optimization technology to obtain the best trade-off between latency, memory consumption, throughput, and accuracy on a specific hardware. It delivers small, medium, and large models. YOLO models may have problems when dealing with small objects or objects that are too close to each other, however, this is no concern for our study since we deal with single object tracking. Contrary to R-CNN family, YOLO is a one-stage detector which allows it to process images faster and also has a very good tradeoff between speed and accuracy which make it very popular and suitable for real-time object detection and tracking applications.

2.4. SORT Tracking Algorithm

SORT algorithm uses Kalman filters for real-time object tracking. İt is quite fast and easy to implement. SORT needs an object detection algorithm such as YOLO or faster R-CNN, uses Kalman filter for object movement estimation, and applies Hungarian Algorithm to associate the objects with the previous frames. SORT has difficulties with occlusions and does not take the visual features of objects while tracking.

2.5. DeepSORT Tracking Algorithm

DeepSORT is an improved version of SORT method to overcome its limitations. DeepSORT uses a deep learning based Reidentification algorithm by evaluating the visual features of tracked objects. DeepSORT algorithm creates a feature vector containing visual features of objects which are extracted with a deep learning model. DeepSORT includes this information with the tracking algorithm to compare them to the objects in the next frames. DeepSORT performs better in occlusion cases and can reidentify objects even after they disappear from the scene, or they are occluded. However, it is costlier than SORT and slower.

2.6. ByteTrack Tracking Algorithm

ByteTrack tracks both the objects with high and low confidence scores. ByteTrack does not ignore low confidence scores instead it evaluates them temporarily making it more powerful for occlusions and dense scenes. ByteTrack unifies the objects with low confidence scores to improve the tracking predictions.

2.7. BoT-SORT Tracking Algorithm

BoT-SORT tries to improve the capabilities of SORT by adding visual-matching techniques. It employs deep learning-based techniques to obtain and uncover the visual features of objects. It adds to the ability to work with the low confidence scores borrowed from ByteTrack algorithm. It uses an advanced Re-Identification method. It is very strong in dense and dynamic fast-moving scenes and also more stable than ByteTrack. BoT-SORT also

includes CMC (Camera Motion Compensation) method to compensate for possible camera movements.

As summary, SORT is most suitable for real-time fast applications, DeepSORT and BoT-SORT is used for occlusions and reidentifications for high precision task, ByteTrack is suitable for high and low confidence tasks and fast implementations.

Another difficult and intriguing aspect of object tracking is the performance evaluation of trackers. Various elements and factors need to be taken into consideration to precisely assess the performance of tracking methods including detection confidence scores, missing objects etc. Single object detection metrics are precision, accuracy, Center Location Error, robustness for occlusion and reidentification. For multi object detection, Multi Object Tracking Accuracy (MOTA), Fragmentation (Frag), False Positives, Higher Order Tracking Accuracy (HOTA), False Negatives, Track Completeness (TC), and Multi Object Tracking Precision (MOTP) metrics can be recruited. Frame per second (FPS), latency, Identity Switches (IDS), and accuracy vs speed trade-off are metrics for both single and multi-object tracking.

In this study, 4 different experiments are conducted using YOLO-NAS and YOLO11. YOLO-NAS is used together with SORT and DeepSORT, on the other hand, YOLO11 is used with BoT-SORT and ByteTrack algorithms. For all experiments, the minimum confidence score is set to 0.35, minimum IoU (Intersection of Union) threshold is fixed at 0.5. This study also compares the speed of the trackers. Experiments used YOLO-NAS-medium and YOLO11-medium models pretrained in the COCO (Lin et al., 2014) complex and diverse image dataset with Python 3.10 (Rossum, 2007) and Torch 2.5.0 (Paszke et al., 2019) environment. COCO is a diverse and extensive image dataset contrived for object classification, segmentation, instance segmentation, object tracking, oriented bounding box tracking applications. COCO contains 330,000 mostly annotated pictures, 1.5 million sample objects, 80 different classes, and 250,000 people key points.

3. Results and Discussions

In this part of this manuscript, the outputs of experiments are delineated and presented. The evaluations of the models are run according to the FPS and IDS (identity switches) metrics. Speed is an important key facet in object detection and tracking, particularly for real-time online implementations of the applications. Actually, defining a perfect metric for tracking is an extremely complicated and intimidating issue due to the variety and diversity of the applications. For instance, speed is usually evaluated by frames processed in a second, however, frames in a video sequence can be vastly different from one another. Some frames may have lots of different objects whereas some of them may contain single or no objects to detect at all. In this study, experimentations are done with single object frames, therefore, FPS is a suitable metric for speed evaluations. FPS and IDS are defined as follows (equations 1 and 2):

$$FPS = \frac{FC}{T} \tag{1}$$

$$IDS = \#\{id | id_{k+1} \neq id_k, k = 1, 2, 3, \dots, \mathrm{FC}\} \tag{2}$$

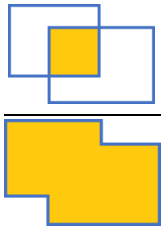
where FC denotes and indicates the total number of frames and T represents total elapsed time for tracking.

The total number of frames term points to the frame images available in the video sequence. Total time is the time spent on tracking and also includes the time spent on detection.

IDS denotes the number of times the algorithm assigns a new tracking identity to the tracked object. Note that tracking identity is different than the class identity. A perfect tracker should follow the same object throughout the entire sequence with the same tracking identity number and object class identity number. Tracking identity may change when objects are lost and then they reappear or are occluded or are covered by some other objects partially or completely. In these cases, trackers need to assign a new identity to the same objects assuming it is a new object. This study also includes incorrect class detections to evaluate the algorithms because as stated earlier on this text, tracking is composed of detection and then tracking. In some cases, the detection algorithm may fail but the tracking algorithm can correctly track the object bounding box as depicted in Figure 1 a and b. In our experiments, this happens mostly in the Cat video. In Figure 1 a, the tracking employing YOLO-NAS and DeepSORT is shown and in Figure 1 b, the tracking employing YOLO11 and BoT-SORT is depicted. As can be seen BoT-SORT is able to maintain the same identity for the tracked cat while DeepSORT needs to assign a new identity. Detectors are confusing the cat with dog most of the time, however, trackers can still be able to track the related bounding box correctly with the same tracking identity. In the Cat video, however, there is great confusion between cat and dog classes. In the Airplane video, the airplane class sometimes is seen as bird, kite, or even person class as illustrated in Figure 2 a and b.

Another important metric is the confidence score which is highly related to precision for the evaluation of tracking methods. Confidence score is the detection correctness probability of the object. The scores are evaluated at different Intersection of Union (IoU) thresholds (e.g., 0.5, 0.6, …, 0.9, 0.95) which means that the label will be evaluated if and only if the confidence of detected object is over the required threshold value. IoU metric is governed by the formula (equation 3):

$$IoU = \frac{Area\ of\ Overlap}{Area\ of\ Union} = \frac{}{} \quad (3)$$



The Confidence Score denotes the average precision for all given thresholds as follows (equation 4):

$$Conf = mean\ Precision = \frac{1}{\#thresholds}\sum_{t}\frac{tp}{tp+fp+fn} \quad (4)$$

YOLO models provide two types of confidence score as outputs. The first one is the box confidence and typically relates to the probability of how certain an object inside a bounding box is the interested class and it is multiplied by IoU as denoted by the following formula (equation 5):

$$Conf_{box} = P(object) \times IoU \quad (5)$$

The second YOLO confidence score is the class confidence score which expresses the probability of how certain the detected object belongs to a certain class. This computation multiplies the conditional probability of the particular class with IoU and objectness score (the probability that there is an object inside the box) and the final confidence score is defined as below (equation 6) (Redmon, 2016; Kim and Cho, 2021):

$$Conf_{class_i} = P(class_i) \times IoU \quad (6)$$

In this study, confidence scores are also included to further evaluate the tracking processes. Because detectors can detect incorrect classes with extraordinarily strong confidence scores. As seen in Figure 2, the cat can be detected as dog, bird, or even cow with strong confidences. Airplane can be detected as kite, bird, or even person with strong prediction scores. Therefore, high confidence scores do not mean correct detections and tracking. Particularly in the Cat video, detectors give remarkably high confidence scores to the dog class incorrectly. The Car video is an amazingly easy task for detectors and trackers. In the Car video, there is no class confusion, and the car is detected and tracked nearly perfectly with the exact box boundaries throughout the entire video as shown in Figure 3. There are some frames with no detection and tracking at all as depicted in Figure 4. One of the major intriguing obstacles of object detection and tracking techniques is the interlacing of the objects inside one another as illustrated in Figure 5. Detectors and trackers can intertwine different objects inside the same area, or some part of the same object can be detected as another new object.

The Car video results are presented in Table 1 and as stated, the car video is the easiest task for all trackers. Trackers can track the car from start to end of the video without any error either on tracking identity or on class identity. On the other hand, The Cat video is the hardest challenge for all detectors and trackers as pointed by the results in Table 2. In the Cat video, there are too many incorrect class predictions, particularly between cat and dog classes. SORT and DeepSORT incur many IDS changes whereas BoT-SORT and ByteTrack have no or very little IDS changes. Finally, in Table 3, the results of the Airplane video are tabulated. This video is in-between the Cat video and the Car video in terms of difficulty level. The number of incorrect class detections and IDS are fairly lower than the Cat video.

When we investigate these tables, we can conclude that in terms of tracking accuracy and precision BoT-SORT is the winner with 0 IDS value for all experiments. But speed is the factor where ByteTrack shines. DeepSORT and SORT are significantly weak compared to BoT-SORT and ByteTrack in FPS and exclusively in IDS measures. As seen from the following Tables, YOLO11 performs better and faster tracking than YOLO-NAS, however, YOLO-NAS obtains higher confidence scores in detection part of the tracking. Note that confidence score is averaged over all frames for the object interested. As can be seen from these tables, the Car video has the highest confidence score, lowest IDS, and zero incorrect class assignments. We should also note that both YOLO-NAS and YOLO11 are pre-trained on COCO dataset with 80 classes.

4. Conclusions and Future Works

This manuscript evaluates the performance of YOLO-NAS with SORT and DeepSORT tracking, and YOLO11 with BoT-SORT and ByteTrack methods in long-term, real-time, single-object tracking experiments. Results show that object tracking can achieve outstanding jobs, however, there are too many obstacles that need to be overcome. ByteTrack outperforms all others in speed whereas BoT-SORT shows its strength in IDS measure. In the Car video, all tracking algorithms exhibit near-perfect detection and tracking without losing the tracking identity and maintaining very high confidence scores all the way through the video. In terms of number of incorrect classes, on the Cat video, detection of YOLO-NAS is more accurate than YOLO11, on the Airplane video, YOLO11 detects better than YOLO-NAS. However, YOLO-NAS provides better confidence scores in all videos compared to YOLO11. In all experiments, BoT-SORT and ByteTrack outperform SORT and DeepSORT both in IDS and FPS metrics, BoT-SORT and ByteTrack demonstrate equally similar performances. ByteTrack is faster than BoT-SORT, however BoT-SORT is more precise and accurate than ByteTrack in maintaining IDS metric. In the future works, more advanced tracking methods such as MCITrack and LoRAT which include Vision Transformers for object detection can be evaluated in larger datasets and different tracking modalities.

Table 1. Experimental results of object tracking algorithms in the Car video

	#Incorrect Classes	FPS	IDS	Confidence
YOLO11+BoT-SORT	0	4.51	0	93.37
YOLO11+ByteTrack	0	6.22	0	93.37
YOLO-NAS+DeepSORT	0	0.89	0	97.52
YOLO-NAS+SORT	0	0.94	0	97.52

Table 2. Experimental results of object tracking algorithms in the Cat video

	#Incorrect Classes	FPS	IDS	Confidence
YOLO11+BoT-SORT	1318	4.90	0	64.84
YOLO11+ByteTrack	1320	6.38	2	64.86
YOLO-NAS+DeepSORT	906	0.98	14	69.28
YOLO-NAS+SORT	946	0.98	81	69.28

Table 3. Experimental results of object tracking algorithms in the Airplane video

	#Incorrect Classes	FPS	IDS	Confidence
YOLO11+BoT-SORT	152	4.82	0	78.35
YOLO11+ByteTrack	151	5.88	3	78.35
YOLO-NAS+DeepSORT	195	0.95	3	86.37
YOLO-NAS+SORT	195	0.94	6	86.37



Figure 1. In a) YOLO-NAS and DeepSORT, in b) YOLO11 and BoT-SORT on the Cat video. DeepSORT assigns a new id to the cat when a class change occurs. BoT-SORT can maintain the same id even if an incorrect class detection occurs.



Figure 2. In a) YOLO-NAS and DeepSORT, in b) YOLO11 and BoT-SORT on the Cat video and the Airplane video. The bounding box calculations are remarkably successful and accurate, the tracking is also quite good, however there are too many incorrect class detections both in YOLO-NAS and YOLO11.



Figure 3. The Car video is the easiest challenge for all detectors and trackers. The car is always detected and tracked perfectly by all algorithms. It is detected as car with very strong confidence scores, and it never loses its tracking identity throughout the entire video.



Figure 4. Object detectors and trackers sometimes fail to produce an output even though the object is quite clear on the scene.

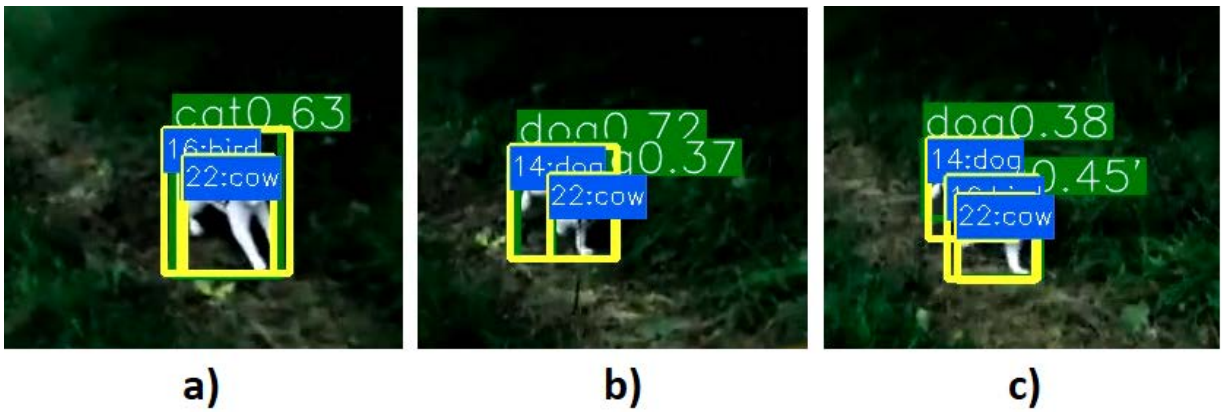


Figure 5. Interlacing different objects is one of the major problems in object detection and tracking. In a) a cow inside a bird, in b) a cow inside a dog, in c) a cow inside a bird inside a dog (YOLO-NAS+DeepSORT)

Author Contributions

The percentages of the author' contributions are presented below. The author reviewed and approved the final version of the manuscript.

	C.P.
C	100
D	100
S	100
DCP	100
DAI	100
L	100
W	100
CR	100
SR	100
PM	100
FA	100

C=Concept, D= design, S= supervision, DCP= data collection and/or processing, DAI= data analysis and/or interpretation, L= literature search, W= writing, CR= critical review, SR= submission and revision, PM= project management, FA= funding acquisition.

Conflict of Interest

The author declares that there is no conflict of interest in this study.

Ethical Consideration

Ethics committee approval was not required for this study because there was no study on animals or humans.

Acknowledgements

There is no financial support for this article.

References

Aharon N, Orfaig R, Bobrovsky BZ. 2022. BoT-SORT: Robust associations multi-pedestrian tracking. arXiv, 2206: 14651.

Aharon S, Dupont L, Masad O, Yurkova K, Fridman L, Lkdci, Khvedchenya E, Rubin R, Bagrov N, Tymchenko B, Keren T, Zhilko A, Deci E. 2021. Supergradients. Github Repository, URL: https://github.com/Deci-AI/super-gradients (accessed date: December 4, 2024).

Atalı G, Eyüboğlu M. 2022. A study on object detection and tracking of a mobile robot using CIE L*a*b* color space. Düzce Uni J Sci Technol, 10(5): 77-90.

Babenko B, Yang MH, Belongie S. 2009. Visual tracking with online multiple instance learning. In: Proceedings of 2009 IEEE Conference on Computer Vision and Pattern Recognition,

June 20-25, Miami FL, USA, p: 983-990.

Bertinetto L, Valmadre J, Henriques JF, Vedaldi A, Torr PHS. 2016. Fully-Convolutional Siamese networks for object tracking. In: Proceedings of Computer Vision–ECCV 2016 Workshops: Proceedings, Springer International Publishing Part II 14, October 8-10 and 15-16, Amsterdam, the Netherlands, p: 850-865.

Bewley A, Ge Z, Ott L, Ramos F, Upcroft B. 2016. Simple online and realtime tracking. In: Proceedings of 2016 IEEE International Conference on Image Processing (ICIP), September 20-25, Phoenix AZ, USA, p: 3464-3468.

Black MJ, Anandan P. 1993. A framework for the robust estimation of optical flow. In: Proceedings of 1993 4th International Conference on Computer Vision, May 11-14, Berlin, Germany, p: 231-236.

Bolme DS, Beveridge JR, Draper BA, Lui YM. 2010. Visual object tracking using adaptive correlation filters. In: Proceedings of 2010 IEEE Computer Society Conference on Computer Vision and Pattern Recognition, June 13-18, San Francisco CA, USA, p: 2544-2550.

Bradski GR. 1998. Computer vision face tracking for use in a perceptual user interface. Intel Technol J, 2.

Dalal N, Triggs B. 2005. Histograms of oriented gradients for human detection. In: Proceedings of 2005 IEEE Computer Society Conference on Computer Vision and Pattern Recognition (CVPR'05) 1, June 20-25, San Diego CA, USA, p: 886-893.

Du Y, Zhao Z, Song Y, Zhao Y, Su F, Gong T, Meng H. 2023. Strongsort: Make deepsort great again. IEEE Trans Multimedia, 25: 8725-8737.

Fan H, Bai H, Lin L, Yang F, Chu P, Deng G, Ling H. 2020. LaSOT: A high-quality large-scale single object tracking benchmark. Int J Comput Vis, 129: 439-461.

Freund Y, Schapire RE. 1996. Experiments with a new boosting algorithm. In: Proceedings of 13th International Conference on Machine Learning, July 3-6, Bari, Italy, p: 148-156.

Fukunaga K, Hostetler LD. 1975. The Estimation of the gradient of a density function, with applications in pattern-recognition. IERE Trans Inf Theory, 21(1): 32-40.

Grabner H, Grabner M, Bischof H. 2006. Real-time tracking via on-line boosting. In: Proceedings of the British Machine Vision Conference 2006, British Machine Vision Association BMVA, September 4-7, Edinburg, UK, p: 47–56.

Havuç E, Alpak Ş, Çakırel G, Baran MK. 2021. Ping-pong ball tracking through deep learning, Eur J Sci Technol, 27: 629-635.

Held D, Thrun S, Savarese S. 2016. Learning to track at 100 fps with deep regression networks. In: Proceedings of Computer Vision–ECCV 2016: 14th European Conference Part I 14 Springer International Publishing, October 11–14, Amsterdam, the Netherlands, p: 749-765.

Henriques JF, Caseiro R, Martins P, Batista J. 2014. High-speed tracking with kernelized correlation filters. IEEE Trans Pattern Anal Mach Intell, 37(3): 583-596.

Hu S, Zhao X, Huang K. 2024. SOTVerse: A user-defined task space of single object tracking. Int J Comput Vis, 132(3): 872-930.

Jocher G, Qiu J. 2024. Ultralytics YOLO11. URL: https://github.com/ultralytics/ultralytics, (accessed date: December 4, 2024).5

Kadam P, Fang G, Zou JJ. 2024. Object tracking using computer vision: A review. Comput, 13(6): 136.

Kalal Z, Mikolajczyk K, Matas J. 2010. Forward-backward error: Automatic detection of tracking failures. In: Proceedings of 2010 20th International Conference on Pattern Recognition, August 23–26, Istanbul, Türkiye, p: 2756-2759.

Kalal Z, Mikolajczyk K, Matas J. 2012. Tracking-learning-detection. IEEE Trans Pattern Anal Mach Intell, 34(7): 1409-1422.

Kang, B., Chen, X., Lai, S., Liu, Y., Liu, Y., & Wang, D. 2024. Exploring enhanced contextual information for video-level object tracking. arXiv preprint arXiv:2412.11023.

Kim J, Cho J. 2021. A set of single YOLO modalities to detect occluded entities via viewpoint conversion. Appl Sci, 11(13): 6016.

Lin L, Fan H, Zhang Z, Wang Y, Xu Y, Ling H. 2025. Tracking meets LoRA: Faster training, larger model, stronger performance. In: Proceedings of European Conference on Computer Vision, Jan 15-16, London, UK, Springer, Cham, p: 300-318.

Lin TY, Maire M, Belongie S, Hays J, Perona P, Ramanan D, Dollár P, Zitnick CL. 2014. Microsoft COCO: Common objects in context. In: Proceedings of Computer Vision–ECCV 2014: 13th European Conference, Proceedings, Part V 13, Springer International Publishing, September 6-12, Zurich, Switzerland, p: 740-755.

Lukezic A, Vojir T, Cehovin ZL, Matas J, Kristan M. 2017. Discriminative correlation filter with channel and spatial reliability. In: Proceedings of the IEEE Conference on Computer Vision and Pattern Recognition, July 21-26, Honolulu HI, USA, p: 6309-6318.

Paszke A, Gross S, Massa F, Lerer A, Bradbury J, Chanan G, Killeen T, Lin Z, Gimelshein N, Antiga L, Desmaison A, Kopf A, Yang E, DeVito Z, Raison M, Tejani A, Chilamkurthy S, Steiner B, Fang L, Bai J, Chintala S. 2019. PyTorch: An imperative style, high-performance deep learning library. In: Proceedings of Advances in Neural Information Processing Systems 32, December 8-14, Vancouver, Canada, p: 8026–8037.

Redmon J. 2016. You Only Look Once: Unified, real-time object detection. In: Proceedings of the IEEE Conference on Computer Vision and Pattern Recognition, June 27-30, Las Vegas NV, USA, p: 779-788.

Rossum GV. 2007. Python programming language. In: Proceedings of USENIX Annual Technical Conference 41:1, June 17-22, Santa Clara CA, USA, p: 1-36.

Soleimanitaleb Z, Keyvanrad MA. 2022. Single object tracking: A survey of methods, datasets, and evaluation metrics. arXiv preprint arXiv:2201.13066.

Şimşek M, Tekbaş MK. 2024. Heatmap creation with YOLO-Deep SORT system customized for in-store customer behavior analysis. Commun Fac Sci Univ Ank Series A2-A3 Phys Sci and Eng, 66(1): 118-131.

Tan FG, Yüksel AS, Aydemir E, Ersoy M. 2021. A review on object detection and tracking with deep learning techniques. Eur J Sci Technol, 25: 159-171.

Wojke N, Bewley A, Paulus D. 2017. Simple online and realtime tracking with a deep association metric. In: Proceedings of 2017 IEEE International Conference on Image Processing (ICIP), September 17-20, Beijing, China, pp: 3645-3649.

Zhang Y, Sun P, Jiang Y, Yu D, Weng F, Yuan Z, Luo P, Liu W, Wang X. 2022. Bytetrack: Multi-object tracking by associating every detection box. In: Proceedings of European Conference on Computer Vision, Cham: Springer Nature Switzerland, October 23–27, Tel Aviv, Israel, p: 1-21.

Black Sea Journal of Engineering and Science
doi: 10.34248/bsengineering.1583610

Open Access Journal
e-ISSN: 2619 - 8991

Research Article
Volume 8 - Issue 2: 371-380 / March 2025

CLASSIFICATION OF VIBRATION DATA FROM BROWNFIELD MILLING MACHINES USING MACHINE LEARNING

Rasim ÇEKİK[1], Abdullah TURAN[2]*

[1]*Sirnak University, Faculty of Engineering, Department of Computer Engineering, 73000, Sirnak, Turkey*
[2]*Sirnak University, Sırnak Vocational School, Department of Mechanical and Metal Technology, 73000, Sirnak, Turkey*

Abstract: This study aims to classify vibration data obtained from old CNC milling (brownfield) machines used in industrial production processes with machine learning algorithms. The analysis of data obtained from such machines is of critical importance in order to increase the efficiency of old production machines and optimize production processes. In the study, vibration data collected from three different CNC machines under real production conditions for two years were used. The collected data were analyzed with various machine learning algorithms, especially overfitting prevention techniques, and the performances of these algorithms were compared. The results showed that the proposed machine learning methods can classify the information obtained from vibration data with high accuracy rates. The algorithms used provided an effective solution for early detection of tool wear, operational errors and other production problems caused by vibration, thus enabling more efficient management of production processes. The study presents an innovative method for modernizing old machines in particular within the framework of Industry 4.0, and provides important practical contributions in terms of improving industrial processes, optimizing maintenance processes and increasing overall efficiency.

Keywords: CNC machines, Vibration, Machine learning, Extreme learning, Classification

***Corresponding author:** *Sirnak University, Sırnak Vocational School, Department of Mechanical and Metal Technology, 73000, Sirnak, Turkey*
E mail: abdullahturan@sirnak.edu.tr (A. TURAN)
Rasim ÇEKİK https://orcid.org/0000-0002-7820-413X
Abdullah TURAN https://orcid.org/0000-0002-0174-2490

Received: November 12, 2024
Accepted: January 20, 2025
Published: March 15, 2025

Cite as: Çekik R, Turan A, 2025. Classification of vibration data from brownfield milling machines using machine learning. BSJ Eng Sci, 8(2): 371-380.

1. Introduction

In production technologies, the longevity and durability of industrial equipment is one of the most important elements in terms of the sustainability of production processes. However, these equipment's need to be modernized over time in order to meet modern production requirements. The rise of Industry 4.0 has brought about significant transformations in production technologies. In particular, the modernization of old (brownfield) production machines allows these machines to be transformed into more efficient and intelligent systems and provide a competitive advantage. These machines, which were not initially integrated with modern digital technologies such as the Internet of Things (IoT) and big data analysis, can be transformed into systems that can provide real-time data by adding sensors and data collection systems (Quatrano et al., 2017). The analysis of this data is of critical importance in terms of optimizing production processes, detecting faults in advance and improving overall production quality. One of the most notable examples of these machines, Computer Numerical Control (CNC) machines, holds a significant place in production processes (Lins et al., 2017). CNC machines are among the most reliable and long-lasting elements of production technologies and play a fundamental role in industrial production. However, due to their high-speed production capacities and complex operational structures, the vibrations that occur in these machines can negatively affect production processes by causing various problems such as tool wear and operational errors (Nath, 2020). Vibrations, especially observed in milling machines, can be associated with problems such as tool breakage, chip jamming and faulty tool clamping. Therefore, effective monitoring and analysis of vibration data is of great importance in terms of improving production quality and preventing possible failures. Early detection and prevention of such problems is possible with the application of process monitoring systems and machine learning algorithms.

This study aims to classify vibration data collected from brownfield CNC milling machines. Vibration data recorded under various operating conditions will be analyzed using overfitting techniques to address the complexity and imbalances in the dataset. Overfitting methods are known to be effective tools to overcome class imbalances, data drifts, and other difficulties, especially in large and complex datasets. In this study, different machine learning algorithms were compared and the methods that will provide the most effective classification of vibration data were evaluated. The main objective of the study is to develop robust and generalizable classification models based on this dataset and to offer practical solution suggestions that can contribute to the optimization of

This work is licensed (CC BY-NC 4.0) under Creative Commons Attribution 4.0 International License

industrial processes. Correct classification of vibration data is critical for the early detection of tool wear, operational errors, and other production problems. Therefore, this study constitutes an important step for the improvement of industrial production processes and increasing machine efficiency.

2. Materials and Methods

2.1. Data Acquisition System

Vibration data collected from three different CNC machines over a period of two years were used for analysis. These data were obtained under real production conditions and reflect long-term and various operational situations. The data used in this study consists of vibration data obtained from CNC machining centers through an experimental setup designed by Tnani et al., (2022). Thani and his team meticulously planned and implemented the data collection process for the classification of vibration data. In order to obtain results as close as possible to industrial production conditions, the data was collected in real time from four-axis horizontal CNC machining machines used in different operations. As shown in Figure 1, acceleration data was recorded with the help of Bosch CISS sensors (Anon, 2020) while the machines were machining aluminum work pieces. The sensors were placed in the background of the machines, protected from the harsh conditions of the processing environment, especially from environmental factors such as coolants and chips (Hesser and Markert, 2019; Hui et al., 2019; Lu et al, 2019; Wszołek et al., 2020). This method provides an approach that facilitates the integration of the sensors into existing brownfield machines while ensuring reliable data collection without being adversely affected by environmental factors. This meticulous data collection process contributed to obtaining more reliable classification results and increasing the efficiency of machine learning algorithms.

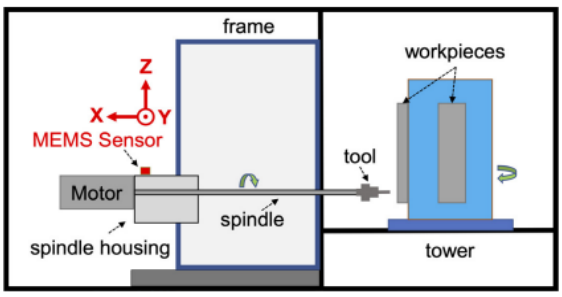


Figure 1. Schematic sketch of the experimental setup:4-axis machining center with mounted sensor (Tnani et al., 2022).

During the data collection process, acceleration data was recorded at a sampling rate of 2 kHz using low-cost three-axis Bosch CISS sensors. This sampling rate was determined to be the minimum rate required to reliably detect machine anomalies. The analysis conducted by Thani and his team revealed that the most critical frequency ranges in the machining process were between 75 Hz and 1 kHz, which are low integer multiples of the spindle speed. Data collected in this critical frequency range generated an average of 4.14 GB of data per day across the three axes. However, such large data volumes create significant challenges in on-site storage and processing processes. Therefore, an intelligent data mining system was developed to collect, store, analyze and process the data (Tnani et al., 2022). As shown in Figure 2, this system enables the efficient management of high-volume data and allows the optimization of data analysis processes. The development of the system is an important step towards overcoming the difficulties encountered in processing and analyzing large data sets.

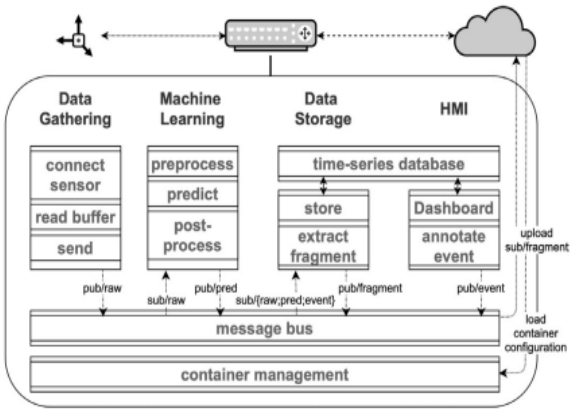


Figure 2: Concept and interaction of containers in the edge stack (Tnani et al., 2022).

The edge stack, shown in Figure 2, defines the various modules operating in the production line and the management of these modules by the cloud infrastructure. The Message Queuing Telemetry Transport (MQTT) protocol is used as a standard interface to communicate between local applications. The data collection system initiates the data flow by connecting to the accelerometer sensors, and this flow is published on the messaging bus. The machine learning (ML) module supports the quality control process for anomaly detection by subscribing to this data flow.

While the data segments are stored in the edge time series database, the quality control process is subject to delayed annotations. The dashboard serves to visualize the machine learning labels and manual annotations. The data segments verified by domain experts are uploaded to the cloud environment, which strengthens the collaboration between data science experts and domain experts and supports the updating of ML modules. This architecture provides a modern solution for more effective monitoring and optimization of production processes.

2.2. Extreme Learning Machines (ELM)

Extreme learning algorithms stand out as powerful machine learning methods that have faster learning capacity and lower error rates compared to traditional artificial neural networks. The advantages of these algorithms can be listed as follows (Huang et al., 2006):

1. Traditional artificial neural networks have a slower learning process due to the presence of feedback loops.
2. The use of techniques such as derivative-based methods and swarm optimization can negatively affect the learning speed and slow down the process.
3. In extreme learning algorithms, the weights between the input and hidden layers are randomly assigned, while the weights between the hidden layer and the output layer are calculated using the least squares method. This approach provides a faster and more effective learning process by ensuring that the model is optimized with minimum error.

These features make extreme learning algorithms advantageous, especially in terms of analyzing and classifying large and complex data sets.

Developed by Huang et al. (2006), Extreme Learning Machines (ELM) are machine learning algorithms that stand out with their fast-learning capacity and low error rates. Unlike traditional artificial neural networks, the fact that they do not contain a feedback loop enables a more effective and faster learning process. In ELM algorithms, the weights between the hidden layer and the output layer are optimized by the least squares method, and thus the model reaches the lowest level in terms of root mean square error (RMSE).

The number of neurons in the hidden layer plays a critical role in the success of the model. Using too many neurons leads to overfitting, while an insufficient number of neurons can negatively affect the learning performance of the model. ELM was developed to ensure that single-layer feedforward artificial neural networks can be trained quickly and efficiently. This algorithm offers faster learning with fewer parameters, and the weights of the neurons in the hidden layer are randomly assigned. These weights remain constant throughout the training process, which simplifies the computational process and increases the speed of the model.

Fixed weights in the hidden layer allow the weights in the output layer to be calculated analytically, which provides high accuracy rates in regression and classification problems (Huang and Chen, 2007; Huang et al., 2014; Zhu at al., 2015; Xiao et al., 2017). The general structure of ELM is presented in Figure 3.

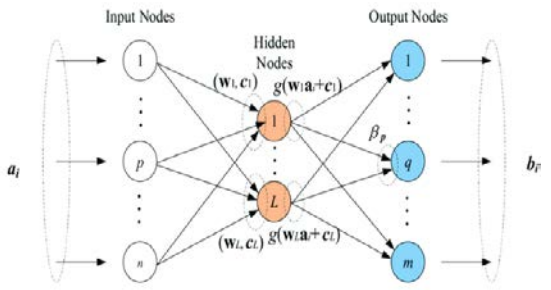


Figure 3: The schematic diagram of ELM.

The mathematical model of ELM is expressed by the input and output training samples $(x_i, y_i) \in \mathbb{R}^n \times \mathbb{R}^m, (i = 1,2, \dots, N)$. Here $\widehat{N}$, represents the number of hidden neurons and g represents the activation function. This approach allows ELM to give successful results in terms of speed and accuracy and is formulated as follows equation 1.

$$\sum_{i=1}^{\widehat{N}} \varphi_i g(w_i x_j + b_i) = \Upsilon_j \quad (1)$$

Here Υ_j, j indicates the jth output value and N is the training data number. $w_i \in \mathbb{R}^n$ indicates the weight vector and b_i bias values. In addition, $\varphi_i = [\varphi_{i1}, \varphi_{i2}, \dots, \varphi_{im}]^T$ represents the parameter vector between the hidden node and the output nodes, while $w_i = [w_{i1}, w_{i2}, \dots, w_{in}]^T$ are the randomly generated learning parameters between the input and hidden layers. The mathematical model of Single hidden layer feedforward neural networks (SLFN) approaching zero error is expressed as follows equation 1 and 2.

$$\sum_{j=1}^{\widehat{N}} |\Upsilon_i - t_j| = 0. \quad (2)$$

$$\sum_{i=1}^{\widehat{N}} \varphi_i g(w_i x_j + b_i) = \mathrm{t}_j, j = 1,2 \dots N \quad (3)$$

This equation is explained as follows equation 4.

$$H\alpha = T \quad (4)$$

The left side of the equation Hα is expressed as f(x) = h(x)α where equation 5 and 6,

$$H = \begin{bmatrix} g(w_1 x_1 + b_1) & \cdots & g(w_{\widehat{N}} x_1 + b_{\widehat{N}}) \\ \vdots & \ddots & \vdots \\ g(w_1 x_N + b_1) & \cdots & g(w_{\widehat{N}} x_N + b_{\widehat{N}}) \end{bmatrix}_{N x \widehat{N}} \quad (5)$$

$$\alpha = \begin{bmatrix} \alpha_1^T \\ \vdots \\ \alpha_{\widehat{N}}^T \end{bmatrix} \quad \text{ve} \quad T = \begin{bmatrix} t_1^T \\ \vdots \\ t_N^T \end{bmatrix} \quad (6)$$

H represents the output matrix of the hidden layer. In ELM, the weights in the output layer are calculated analytically, where the parameters w_j and b_j are randomly assigned. In order to find the parameters w_j and b_j, the linear equation system given in equation 4 needs to be solved. Thus, the vector α forms the solution set of the linear equation 7.

$$\hat{\alpha} = H^{\dagger} T \quad (7)$$

In equation 7, $H^{\dagger}$ is the Moore-Penrose inverse of H. In fact, it denotes the updated output parameters $\hat{\alpha}$ vector in the ELM structure. As a result, obtaining the output weights $\hat{\alpha}$ using ELM can be divided into three steps.

Step 1. Choose random numerical values between 0 and 1 to set the input weights a_{ij} and the hidden layer bias b_j.

Step 2. Calculate the output matrix H.

Step 3. Calculate the output weights V equation 8:

$$V = H\dagger Y \quad (8)$$

where $H\dagger$ represents the generalized inverse matrix of the output matrix H.

2.3. Other Methods

ELM have attracted the attention of researchers due to their wide application area and extensive studies have been conducted on them. There are various versions of ELM developed to optimize its use in different problem areas. In this section of this study, brief information about the methods used is presented. The basic structure and implementation of the ELM algorithm will be discussed in detail, and the improved ELM approaches in the existing literature will also be discussed. Thus, it is aimed to provide a comprehensive understanding of the performance and suitability of the methods used.

2.3.1. Multiple Hidden Layers Extreme Learning Machine (MELM)

MELM is an algorithm proposed by Xiao et al. (2017), which uses a network with three hidden layers within the ELM structure. The MELM structure contains three hidden layers, each of which performs calculations related to weight matrices and activation functions. The basic steps of the algorithm include transmitting training data through the network, updating the weight and bias values for each layer, and calculating the output in the last layer. The performance of the MELM algorithm has been tested using different activation functions in regression and classification problems. The algorithm has a repeating calculation cycle depending on the number of hidden layers, and this cycle includes recalculating the formulas for each hidden layer. Thus, the calculations performed in each layer allow the network to learn more complex structures and produce more accurate results. In summary, the MELM algorithm expands the structure of the ELM with more hidden layers, and provides higher accuracy output by optimizing the parameters in each layer.

2.3.2. Constrained ELM (CELM)

CELM is a model developed by Zhu et al., (2014) to provide more effective classification performance while preserving the simplicity of ELM. The parameters in the hidden layer of traditional ELM are usually determined completely randomly; however, this randomness can lead to the parameters not being able to adequately represent the distinctive features of the data. As a result, a large number of hidden nodes must be used for the model to achieve the desired generalization performance. However, the use of too many hidden nodes can lead to increased processing time, more computational resources, and overfitting. Overfitting refers to the situation where the model loses its generalization ability as a result of excessive adaptation to the training data. The CELM is an approach developed to find solutions to these problems. In this model, it is suggested that the weight vectors in the hidden layer are selected from the difference vectors of the examples between classes instead of random values (Zhu et al., 2015). This approach allows the model to create more distinctive hidden nodes and therefore to have a more efficient classification structure. Thus, while preserving the simple structure and fast learning ability of ELM, a more effective classification performance is achieved without the need for excessive number of nodes.

2.3.3. Sample Extreme Learning Machine (SELM)

SELM is an algorithm that determines the weights from the input layer to the hidden layer using randomly selected sample vectors from the training set. These vectors are normalized and assigned as weights, and the bias values of SELM are obtained from a random uniform distribution as in ELM. SELM has the ability to cope with nonlinear situations by using polynomial kernel functions, which exhibits a similar approach to kernel-based methods. In this model, the sigmoid activation function helps linear classification by expanding the data mapped with the kernel. The main feature of SELM is that it restricts the hidden layer weights in the direction of the sample vectors instead of randomly determining them. This restriction allows the model to learn more effectively and increase its overall classification performance. Thus, SELM overcomes the limitations of traditional ELM and offers better generalization ability and performance.

As a result, the CELM approach aims to eliminate the performance limitations of traditional ELM and provide a more efficient, computationally optimized and high generalization capacity model. In particular, the use of difference vectors of inter-class examples allows the model to better capture distinguishing features.

2.3.4. The Constrained Sum Extreme Learning Machine (CSELM)

CSELM is an algorithm that generates weights from the input layer to the hidden layer using the sums of within-class sample vectors (Zhu et al., 2015). CSELM first selects two random sample vectors from the same class and obtains a new vector by summing these vectors. Then, the obtained total vector is normalized and this normalized sum is assigned as the weights of the hidden layer.

The bias values used in CSELM are randomly generated from a uniform distribution, as in ELM. Total vectors are created by taking inspiration from difference vectors between classes and at the same time, they have the potential to reduce the effect of noise samples in CSELM by being considered as derivative samples. The basic principle of CSELM is to restrict the input connection weights of hidden neurons in accordance with the directions of the derivative and robust sample vectors. In this context, random weights are selected from a set consisting of the sums of within-class sample vectors. This approach allows the model to learn more discriminative features and increase the overall classification performance.

2.3.5. Deep Extreme Learning Machine (DELM)

DELM was developed to benefit from the advantages of ELM method such as fast computational ability, real-time estimation ability and simplicity of network structure (Zhang et al., 2023). Although ELM is a successful method in terms of generalization performance, it leads to disadvantages such as the limited representation learning capacity of traditional ELM and the inability to fully learn deep structures and hidden relationships in more complex

data sets. In order to overcome these limitations and obtain more effective results, DELM model was designed. DELM aims to show better performance on complex data sets by increasing the ability to learn deep features in data thanks to its multi-layered structure. This approach provides both more flexibility in representation learning and allows deeper relationships to be discovered. Therefore, DELM offers a suitable solution for more complex applications by expanding the potential of ELM.

3. Experimental Studies

3.1. Data Definition

The data were collected at regular intervals from three different CNC machines (M01, M02, and M03) located in a specific production facility between October 2018 and August 2021 (Tnani et al., 2022). The time frame of this dataset is labeled in the "Month Year" format, with each label representing the six-month period before it. For example, the label "Aug 2019" represents the time period between February 2019 and August 2019.

CNC machines perform various operations on aluminum parts using different tools to process a specific design. The variety of parts produced by the machines and the variability of their process flows over time are important factors to consider. The aim of the research was to examine the variability between machines and overtime, and for this purpose, the dataset was created with 15 different tool operations. These operations are applied on three different CNC machines at various time periods. Table 1 provides an overview of the characteristics of these different operations.

One of the common challenges encountered in industrial datasets, especially in process monitoring tasks, is a significant OK/NOK imbalance. Figure 4 shows the imbalance ratio between OK and NOK instances in the studied dataset as 816:35. In real production processes, the number of OK instances is considerably higher. In order to reduce the effects of this imbalance, a sample dataset was created by selecting a reasonable number of OK transactions from various time periods. This approach constitutes an important step towards reducing the class imbalance.

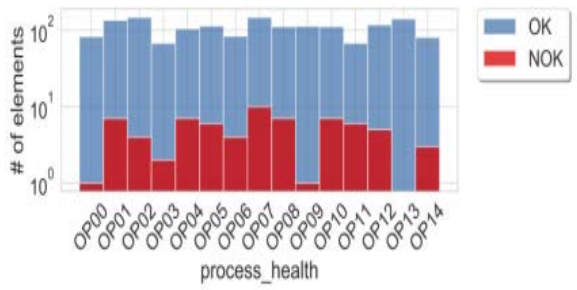


Figure 4. Class distribution per process operation (Tnani et al., 2022).

Table 1. Tools operations collected from M01, M02 and M03 (Tnani et al., 2022)

Tool operation	Description	Speed (Hz)	Feed (mm s^{-1})	Duration (s)
OP00	Step drill	250	≈100	≈132
OP01	Step drill	250	≈100	≈29
OP02	Drill	200	≈50	≈42
OP03	Step drill	250	≈330	≈77
OP04	Step drill	250	≈100	≈64
OP05	Step drill	200	≈50	≈18
OP06	Step drill	250	≈50	≈91
OP07	Step drill	200	≈50	≈24
OP08	Step drill	250	≈50	≈37
OP09	Straight flute	250	≈50	≈102
OP10	Step drill	250	≈50	≈45
OP11	Step drill	250	≈50	≈59
OP12	Step drill	250	≈50	≈46
OP13	T-slot cutter	75	≈25	≈32
OP14	Step drill	250	≈100	≈34

An example is presented in Figure 5, where a comparison is made between OP07 and OP08 in the time and frequency domains. This analysis reveals that the effect of OP07 is more pronounced and severe than that of OP08, and that there is a clear separation between the two processes in the time and frequency domains. However, a common phenomenon observed is the tendency for the abnormality to be detected at integer multiples of the spindle speed. In the case of OP07, it is observed that the frequency characteristics in the 200 Hz and 400 Hz regions are of significantly higher amplitude than in the healthy process. This indicates the presence of an abnormal situation in the relevant processes.

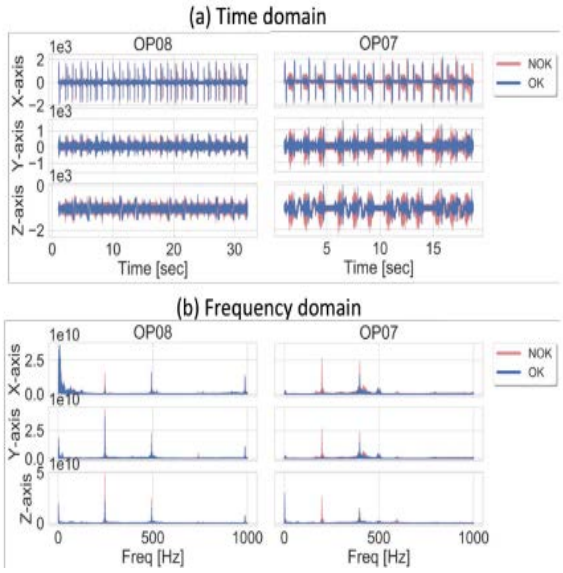


Figure 5. Comparison of 2 different tool operation: OP07, OP08 (Tnani et al., 2022).

In order to obtain fast processing and non-invasive solutions, time series signals are usually segmented into fixed-length (WS) windows. This technique is widely used

as a data augmentation method, especially for NOK data. However, the disadvantage of segmenting NOK data is that the labeling of small segments may not be equivalent to the full processing. This situation is clearly observed in the first and last samples where anomalies have not yet been detected. In the data labeling process, the beginning and the last segments of OP from NOK samples are shortened. However, this problem can also occur in the middle of the process due to rapid position changes. This situation is clearly seen in Figure 6, where a small segment taken from the middle of OP08 is observed to show that OK and NOK classes match exactly.

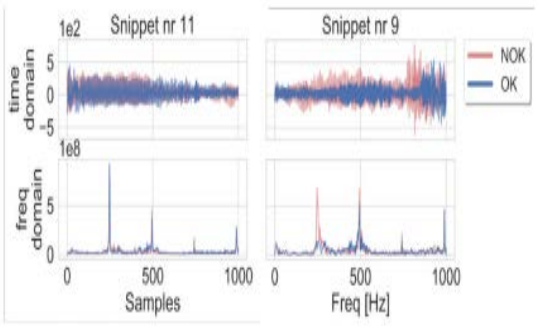


Figure 6. Data segmentation causing faulty labels (Tnani et al., 2022).

To address this issue, a reasonable selection criterion of WS should be determined. The CNC machining dataset provides examples and classes with the necessary diversity and separation levels that allow the research community to systematically work on solutions and examine the robustness of data-driven methods to industrial challenges. In this context, the selection of an appropriate WS is critical to the effective use of the dataset and to increase the reliability of the results.

3.2. Data Partitioning

With the publication of this dataset, research on ML models and learning techniques for noisy time series data is encouraged. In order to realistically evaluate the performance in real-world challenges, three strategies are proposed for partitioning the CNC machining dataset.

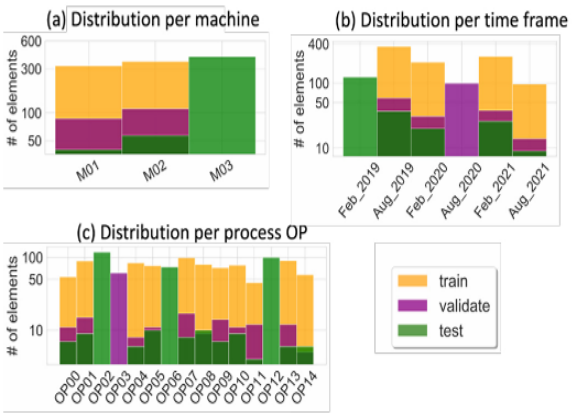


Figure 7. There are strategies for dataset partitioning (Tnani et al., 2022).

As shown in Figure 7a, a machine-based partitioning evaluates the ability to perform on a new machine outside of the training set. Figure 7b demonstrates a time-based partitioning approach where certain time intervals are stored only for validation and testing to address data drift over time. These strategies aim to increase the effectiveness of ML models in industrial applications (Tnani et al., 2022).

4. Experimental Results

At this stage of this study, various experimental analyses were performed. In the experiments, in order to examine the effect of neuron numbers on classification performance, 100, 200, 400, 600, 800, 1000, 1300 and 1500 neuron numbers were randomly determined. Using these determined neuron numbers, the performances of ELM, CELM, CSELM, DELM, MELM and SELM algorithms were evaluated under different activation functions.

These analyses aim to comprehensively examine how each algorithm affects the classification accuracy depending on the number of neurons and the activation function used. Based on the experimental results, the differences between the performance and accuracy percentages of each algorithm with the determined neuron numbers were revealed. In this context, the effects of both the algorithms and the neuron numbers on the classification accuracy were evaluated comparatively.

The obtained findings are presented in (Figure 1-5), and in these graphs, the results obtained by each algorithm with different activation functions depending on the number of neurons are shown in detail. The analyses highlight which methods provide more effective results by revealing the overall success of the algorithms, changes in accuracy percentages, and stability features. This study provides important data to understand the effects of the number of neurons and activation functions on the performance of machine learning-based classification algorithms.

When Figure 8 is examined, it is observed that the ELM algorithm has the lowest accuracy rate compared to other methods. Although it is seen that the general accuracy increases with the increase in the number of neurons, there is a significant performance decrease especially around 400 neurons. The ELM algorithm exhibited a continuous loss of accuracy in the number of neurons between 100 and 400, which led to significant fluctuations in classification success.

On the other hand, the CELM, CSELM, DELM, MELM and SELM algorithms exhibited quite consistent and constant accuracy rates regardless of the number of neurons. It is observed that the accuracy rates of these algorithms are fixed at around 95%, thus indicating that this performance provides more stable results regardless of the number of neurons. This situation reveals that these algorithms are more robust by maintaining their classification accuracy in a wider range of neurons.

In addition, it was determined that the MELM algorithm gave slightly better results compared to other methods for

the sigmoid activation function. This superiority becomes especially evident in the number of neurons between 400 and 1300; MELM managed to increase the classification accuracy slightly in this range of neuron numbers. Finally, it is noteworthy that CSELM and SELM algorithms give quite stable and consistent results across all neuron numbers. These findings contribute to a better understanding of the relationships between neuron numbers and algorithm performance and emphasize the importance of choosing the right algorithm in machine learning-based classification processes.

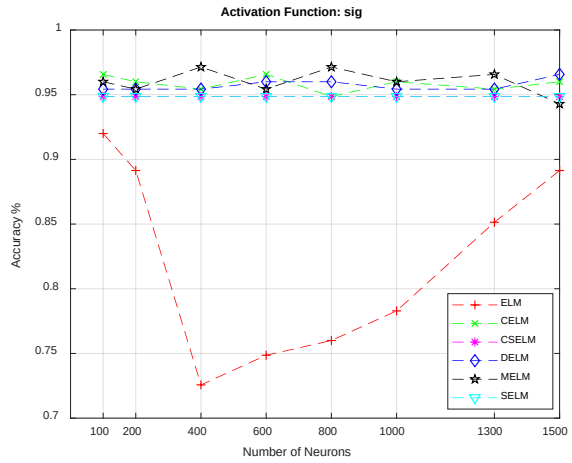


Figure 8. Success of methods with different neuron numbers for sigmoid function

Figure 9 shows the comparison of the accuracy rates of the ELM, CELM, CSELM, DELM, MELM and SELM algorithms with different neuron numbers (100, 200, 400, 600, 800, 1000, 1300, 1500) according to the hardlim activation function. When the graph is examined, significant fluctuations are observed in the accuracy rate of the ELM algorithm. While a peak is observed around 100 neurons, a significant decrease is experienced around 600 neurons. Later, it is seen that the accuracy increases again around 800 neurons, but it generally exhibits a more unstable performance compared to the other algorithms.

Although the CELM algorithm exhibits a relatively more stable performance, it is noteworthy that it experiences a decrease around 400 neurons and then fluctuations up to the 800 neuron level. At the 1000 and 1300 neuron levels, the performance is more stable. The CSELM algorithm is one of the algorithms that exhibit the most stable performance in the graph; It has given relatively stable results with an accuracy of around 94-95% in all neuron numbers. It is less sensitive to changes in the number of neurons compared to other algorithms.

DELM algorithm has exhibited significant fluctuations in accuracy rate. While it is observed that the accuracy increases around 400 and 1500 neurons, there are significant decreases around 800 and 1300 neurons. This situation shows the sensitivity of DELM algorithm to the number of neurons. MELM has achieved relatively good results compared to other algorithms; It has reached the highest accuracy rate by peaking around 400 neurons, while it has experienced a sudden decrease around 600 neurons and significant fluctuations in accuracy have been observed.

SELM is one of the algorithms with the most stable performance and provides stable results without changing accuracy rates in the range of 94-95%. It can be said that it is the algorithm that is least affected by changes in the number of neurons. In general, ELM and DELM algorithms have exhibited a more sensitive and fluctuating accuracy performance to the number of neurons. Performance decreases are especially noticeable around 400 and 600 neurons. CSELM and SELM, on the other hand, were not affected much by changes in the number of neurons and gave more stable results. MELM was one of the algorithms that achieved the best accuracy rate, peaking around 400 neurons, but it experienced fluctuations in other neuron numbers. Figure 9 clearly shows the effect of the number of neurons on the accuracy of the algorithms and shows that CSELM and SELM generally provide more stable results.

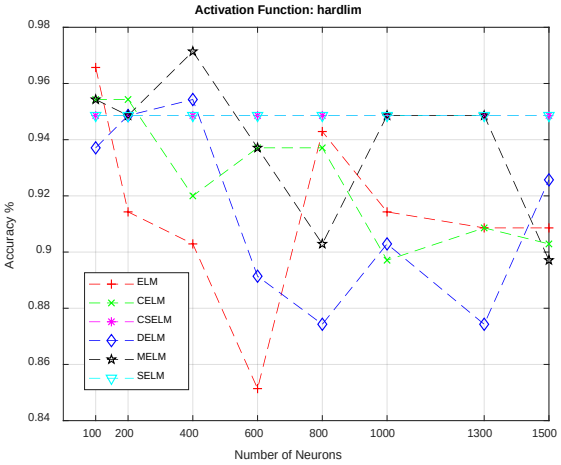


Figure 9. Success of methods with different neuron numbers for the hardlim function.

Figure 10 compares the accuracy performances of the determined machine learning algorithms according to the sin activation function depending on the number of neurons. When the graph is examined, it is observed that the ELM algorithm exhibits a significantly lower accuracy percentage compared to the other algorithms. Although the accuracy rate starts with 100 neurons and increases to 75% around 600 neurons, there is a significant decrease starting from 800 neurons and the accuracy rate drops below 70%. However, an increase in the accuracy rate is observed again around 1500 neurons. There is a serious imbalance in the overall performance of the ELM algorithm, and the accuracy rate fluctuates significantly depending on the number of neurons.

On the other hand, the CELM, CSELM, DELM, MELM and SELM algorithms exhibit a much higher and more stable accuracy rate compared to ELM. The accuracy rates of these algorithms are above 95% and show very little

fluctuation depending on the number of neurons. CELM and SELM stand out as the most stable algorithms with a constant 95% accuracy rate across all neuron numbers. In particular, SELM is the algorithm that is least affected by changes in the number of neurons. Although MELM shows a slight increase around 400 neurons, it generally shows a performance close to 95% accuracy. DELM, on the other hand, shows a more fluctuating performance compared to other algorithms; especially between 600 and 1000 neurons, its accuracy decreases. However, its overall accuracy remains in the range of 94-96%.

Figure 10 shows that the accuracy performance of the ELM algorithm is significantly lower and unstable compared to other algorithms. CELM, CSELM, DELM, MELM and SELM algorithms have higher and more stable accuracy rates and provide more reliable results regardless of the number of neurons. In particular, the constant high accuracy rates of the SELM and CELM algorithms show that these algorithms are minimally affected by changes in the number of neurons. These findings allow a better understanding of the performance of different neuron numbers and algorithms and emphasize the importance of choosing the right algorithm in machine learning applications.

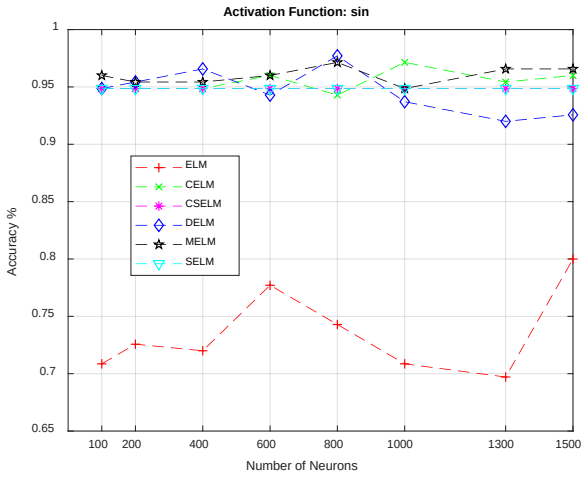


Figure 10. Success of methods for different neuron numbers for the sin function.

Figure 11 compares the performance of the determined overfitting machine algorithms with different neuron numbers. The results obtained show that SELM, MELM and CSELM algorithms achieve consistent and high accuracy rates above 95% regardless of the number of neurons. This situation reveals that these algorithms can produce more stable results without being affected by changes in the number of neurons and are more resistant to overfitting.

On the other hand, the ELM algorithm exhibits significantly lower accuracy rates and fluctuations are observed in its performance depending on the increase in the number of neurons. It is especially noteworthy that there are serious decreases in the accuracy of ELM at the number of 1000 neurons. This situation shows that the generalization ability of the ELM algorithm is limited and it becomes more prone to overlearning (overfitting). In addition, although there is an improvement in the accuracy rates of ELM when the number of neurons exceeds a certain limit, this improvement does not continue consistently.

Generally, Figure 11 shows that there is an increase in the performance of the algorithms with the increase in the number of neurons, but after a certain point, this increase slows down or stops completely due to over-learning. While algorithms such as SELM, MELM and CSELM show more consistent and high performance in wide neuron ranges, the ELM algorithm requires more optimization and careful tuning to reach high accuracy rates. Moreover, it is understood that SELM and MELM algorithms show superior performance in this dataset, while ELM is not as effective as these algorithms and its performance needs to be optimized more carefully. This situation emphasizes once again the importance of making adjustments appropriate to the structure of the algorithm and the characteristics of the dataset in model selection.

In conclusion, these findings show the importance of robustness against over-learning in addition to understanding the effects of algorithms and the number of neurons on performance in machine learning applications. In this context, it is necessary to select appropriate models and tunings to obtain more robust and stable results.

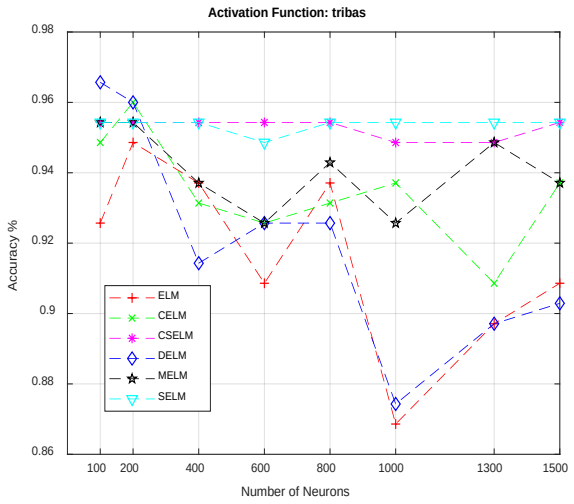


Figure 11. Success of methods with different neuron numbers for the tribas function.

Figure 12 compares the performances of various methods for the Radbas activation function. The findings show that the SELM method generally achieved the highest accuracy rates and exhibited stable and high performance together with CSELM. Although the MELM method showed a decrease up to the number of neurons 400, an increase in its performance was observed with increasing neuron numbers from this point onwards and reached the highest performance at 1500 neurons. The CELM method also exhibited a similar trend, showing the lowest performance at 1000 neurons and reaching the highest value at 1500

neurons.

The DELM method experienced a decrease in performance with increasing neuron numbers, but reached the highest performance level at 1500 neurons. The ELM method exhibited an unstable performance at different neuron numbers; it is especially noteworthy that there was a significant performance decrease at the number of 1500 neurons, unlike the other methods.

As a result, the SELM and CSELM methods stand out with their high and stable performance for the Radbas function. MELM and CELM methods also showed significant performance increases after a certain number of neurons. However, the responses of ELM and DELM methods to increasing number of neurons are fluctuating, and especially the serious performance decrease experienced by ELM at 1500 neurons shows that this method does not provide a stable solution in the Radbas function. These findings provide an important perspective in understanding and optimizing the performance changes of machine learning algorithms depending on the number of neurons.

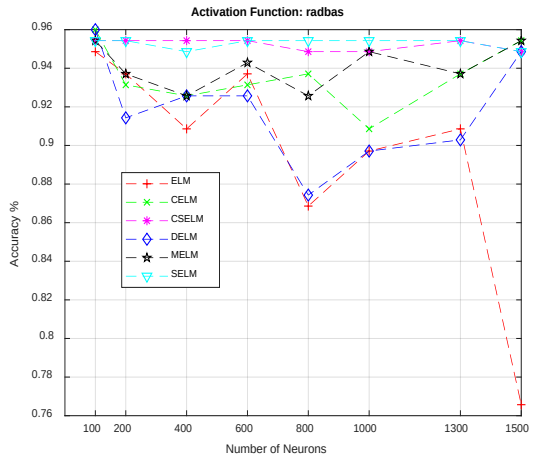


Figure 12. Success of methods with different neuron numbers for the radbas function.

5. Conclusion

This study focuses on the analysis of vibration data obtained from old (brownfield) CNC milling machines using machine learning methods. Data collected from three different CNC machines under real production conditions for two years were classified using various machine learning algorithms. This process aims to optimize production processes and increase the efficiency of old machines. The results obtained provide important findings for the early detection and prevention of problems that occur in production processes, especially tool wear, operational errors and mechanical failures.

Comparisons made on various machine learning algorithms have shown that these algorithms can successfully classify vibration data collected from CNC machines. In particular, it was observed that CSELM and SELM algorithms provided more stable and consistent results. MELM algorithm reached the highest accuracy rates at certain neuron numbers; this situation proves that these algorithms offer reliable classification methods in production processes. Unbalanced data distributions, which are commonly encountered in industrial data sets, were also observed in this study. Although the number of successful (OK) operations was significantly higher than the number of unsuccessful (NOK) operations, the classification accuracy was increased thanks to the applied extreme learning techniques and balancing methods. This is a critical stage for machine learning algorithms to obtain accurate results when working with class-imbalanced data sets.

This study offers a solution for the modernization of old CNC machines with Industry 4.0 technologies. Analysis of data obtained from machines using sensors and data acquisition systems stands out as an important tool for monitoring machine performance and early detection of faults. In this way, it is possible to minimize production interruptions and costly faults. In addition, this approach can increase production efficiency and extend machine life by integrating old machines with digital technologies.

Frequency analyses of vibration data have enabled the detection of anomalies occurring in certain frequency ranges, and anomalies at certain frequencies depending on the spindle speed have enabled early detection of tool wear and mechanical errors. Such frequency-based analyses are of critical importance in precision manufacturing processes. In addition, the study makes significant contributions to the digital transformation of old CNC machines within the scope of Industry 4.0. Many industrial organizations working with old machines can increase their efficiency and reduce maintenance costs through such analysis methods. In particular, applicable strategies are presented to increase the competitiveness of small and medium-sized enterprises (SMEs) in Turkey. In addition, these analysis methods can be adapted to other machine types and have a wide range of applications.

The results obtained in this study have demonstrated the applicability of machine learning models based on the analysis of vibration data in industrial production. However, future studies should be tested on larger data sets and different industrial machines to increase the generalizability of these results. It is recommended to use more advanced sensor systems and machine learning models for real-time data analysis and anomaly detection. In addition, the application of more complex algorithms such as deep learning can provide higher accuracy rates, especially in large data sets.

As a result, this study provides an important roadmap for the modernization and efficiency of old CNC machines. The analysis of vibration data enables early detection of machine failures and enables the optimization of production processes. The adoption of such technologies by industrial facilities will contribute to the formation of a more sustainable and competitive production environment in the future.

Author Contributions

The contribution percentages of the authors' are given below. The authors have reviewed and approved the article.

	R.C.	A.T.
C	60	40
D	60	40
M	40	60
DCP	30	70
DAI	70	30
LR	50	50
W	80	20
LR	40	60
SR	20	80

C= concept, D= design, M= management, DCP= data collection and/or processing, DAI= data analysis and/or interpretation, LR= literature review, W= writing, LR= critical review, SR= submission and revision.

Conflict Statement

The authors declare that they have no conflict of interest in this study.

Ethical Approval Statement

Ethics committee approval was not required for this study because of there was no study on animals or humans.

References

Anonymous. 2020. Retrieved from bosch connected devices and solutions GmbH. URL: https://www.bosch-connectivity.com/%0Amedia/downloads/ciss/ciss_datasheet.pdf (accessed date: 23 September 2024).

Hesser DF, Markert B. 2019. Tool wear monitoring of a retrofitted CNC milling machine using artificial neural networks. Manuf Lett, 19: 1-4.

Huang G, Song S, Gupta JND, Wu C. 2014. Semi-supervised and unsupervised extreme learning machines. IEEE Trans Cybern, 44(12): 2405-2417.

Huang GB, Chen L. 2007. Convex incremental extreme learning machine. Neurocomputing, 70(16-18): 3056-3062.

Huang GB, Chen L, Siew, CK, 2006. Universal approximation using incremental constructive feedforward networks with random hidden nodes. IEEE Trans Neural Networks, 17(4): 879-892.

Hui Y, Mei X, Jiang G, Tao T, Pei C, Ma Z, 2019. Milling tool wear state recognition by vibration signal using a stacked generalization ensemble model. Shock Vib, 1: 7386523.

Lins RG, Guerreiro B, Schmitt R, Sun J, Corazzim M, Silva F. R, 2017. A novel methodology for retrofitting CNC machines based on the context of industry 4.0. 2017 IEEE Int Syst Eng Symp (ISSE), 1-6.

Lu Z, Wang M, Dai W. 2019. Machined surface quality monitoring using a wireless sensory tool holder in the machining process. Sensors, 19(8): 1847.

Nath C, 2020. Integrated tool condition monitoring systems and their applications: a comprehensive review. Procedia Manuf, 48: 852-863.

Quatrano A, De Simone MC, Rivera ZB, Guida D. 2017. Development and implementation of a control system for a retrofitted CNC machine by using Arduino. FME Trans, 45(4).

Tnani MA, Feil M, Diepold K. 2022. Smart data collection system for brownfield CNC milling machines: A new benchmark dataset for data-driven machine monitoring. Procedia CIRP, 107: 131-136.

Wszołek G, Czop P, Słoniewski J, Dogrusoz H. 2020. Vibration monitoring of CNC machinery using MEMS sensors. J Vibroeng, 22(3): 735-750.

Xiao D, Li B, Mao Y. 2017. A multiple hidden layers extreme learning machine method and its application. Math Probl Eng, 1: 4670187.

Zhang X, Dong S, Shen Q, Zhou J, Min J. 2023. Deep extreme learning machine with knowledge augmentation for EEG seizure signal recognition. Front Neuroinf, 17: 1205529.

Zhu W, Miao J, Qing L. 2014. Constrained extreme learning machine: a novel highly discriminative random feedforward neural network. Int Joint Conf Neural Networks (IJCNN), 800-807.

Zhu W, Miao J, Qing L, 2015. Constrained extreme learning machines: A study on classification cases. ArXiv Preprint ArXiv:1501.06115.

Black Sea Journal of Engineering and Science
doi: 10.34248/bsengineering.1601734

Open Access Journal
e-ISSN: 2619 – 8991

Research Article
Volume 2 - Issue 2: 381-390 / March 2025

ENHANCED THERMAL, MECHANICAL, AND ELECTRICAL PROPERTIES OF EPOXY COMPOSITES REINFORCED WITH CDS/MWCNT NANOHYBRIDS SYNTHESIZED VIA HYDROTHERMAL METHOD

Hakan ŞAHAL[1]*, Ercan AYDOĞMUŞ[2]

[1]*Munzur University, Institute of Graduate Education, Department of Strategic Raw Materials and Advanced Technology Applications, Tunceli, Türkiye*
[2]*Fırat University, Faculty of Engineering, Department of Chemical Engineering, Elazığ, Türkiye*

Abstract: In this research, the effects of incorporating a hybrid nanocomposite consisting of cadmium sulfide (CdS) nanoparticles and multi-walled carbon nanotubes (MWCNTs) synthesized by hydrothermal method into an epoxy resin system on the bulk density, Shore D hardness, thermal conductivity coefficient, thermal stability, and dielectric properties have been investigated. In addition, the structural and physical properties of these nanocomposites aimed to determine their potential applications as lightweight and thermal insulation materials. The study included synthesizing CdS/MWCNT nanohybrid structures using $CdCl_2 \cdot H_2O$ and $Na_2S_2O_3 \cdot 5H_2O$ precursors under specific time and concentration parameters. Then, these nanohybrids were integrated into the epoxy matrix to form innovative composite materials. The prepared composite samples were characterized using various methods to evaluate their mechanical, thermal, structural, and electrical properties. Techniques such as tensile tests, Shore D hardness measurements, microscopy, Fourier transform infrared spectroscopy (FT-IR), thermal conductivity, and dielectric measurements were used. The findings revealed that incorporating certain amounts of CdS/MWCNT nanohybrids significantly affected the density, hardness, thermal conductivity, mechanical strength, and dielectric properties of epoxy composites. In particular, the high surface area and effective distribution of CdS/MWCNT nanohybrid increased the mechanical strength and improved the thermal and electrical conductivities. The bulk density measured as 1133.5 kg/m^3 in the first experimental group reached 1145.1 kg/m^3, showing a steady increase until the 5th group. Shore D hardness measurements, which were initially measured as 77.6, increased to 79.8 in the last experimental group with the addition of nanohybrid structures. The thermal conductivity measured as 0.112 W/m·K in the first experimental group reached 0.136 W/m·K in the last group. Dielectric measurements showed that the dielectric coefficient increased from 3.86 in the initial sample to 5.67 in the nanoparticle-reinforced epoxy composites, indicating that the additive significantly improved the electrical properties, leading to a higher dielectric constant and enhanced energy storage potential. Microscopy images confirmed the homogeneous distribution of the nanohybrid within the epoxy matrix and strong interfacial interactions. FT-IR analysis confirmed the chemical bonds present in the hybrid composite structure. These results highlight the significant potential of incorporating CdS/MWCNT nanohybrid structures into epoxy composites to develop functional materials with advanced technological applications. This comprehensive study provides valuable insights into nanocomposite technology and highlights the promising role of CdS and MWCNT-based hybrid systems in future material designs.

Keywords: Cadmium sulfide, MWCNT, Hydrothermal method, Thermal Conductivity, Dielectric constant, Hybrid nanocomposite

***Corresponding author:** Munzur University, Institute of Graduate Education, Department of Strategic Raw Materials and Advanced Technology Applications, Tunceli, Türkiye
E mail: hakansahal@munzur.edu.tr (H. ŞAHAL)
Hakan ŞAHAL https://orcid.org/0000-0001-8714-1735
Ercan AYDOĞMUŞ https://orcid.org/0000-0002-1643-2487

Received: December 15, 2024
Accepted: January 22, 2025
Published: March 15, 2024

Cite as: Şahal H, Aydoğmuş E. 2025. Enhanced thermal, mechanical, and electrical properties of epoxy composites reinforced with cds/mwcnt nanohybrids synthesized via hydrothermal method. BSJ Eng Sci, 8(2): 381-390.

1. Introduction

Since the desired qualities of nanoparticles vary depending on the field in which they are generated, many manufacturing techniques have been developed. Several factors, including the synthesis techniques used, the precursor concentration, the reaction environment, temperature, pressure, reaction time, and stabilizing agents, affect the degree of production at the nanoscale. Variations in a product's nanosize often result in significant changes to the composition's properties. Nanoparticles, both single and aggregate, find use in solar systems (Bastianini et al., 2024), thermoelectricity (Hussain et al., 2024), catalysis (Shaban et al., 2024), and health diagnostics (Ndlovu et al., 2024; Stiufiuc et al., 2024; Manoharan et al., 2024; Abid et al., 2024). It is used in many different industries, including the pharmaceutical (Bharmal et al., 2024), solar cell manufacturing (Holmes et al., 2024), and other industries (Solomon et al., 2024; Majeed et al., 2024; Jan et al., 2024).

The variations in their electrical, optical, magnetic, and catalytic properties can be attributed to the fact that

This work is licensed (CC BY-NC 4.0) under Creative Commons Attribution 4.0 International License

many nanoparticles differ from their macroscopic counterparts with the same composition in terms of size, shape, surface chemistries, and quantum effects (Ozcan and Meral, 2024). To produce nanoparticles with precise morphologies, sizes, forms, and surface chemistries, control over the synthesis process is required (Eikey, 2024). This is a difficult, demanding, and drawn-out procedure. Because it usually calls for many chemicals and dependent experimental parameters including reagent concentrations, reaction periods, temperatures, and mixing efficiency, the precise synthesis of nanoparticles is difficult. Completing the synthesis successfully also depends on the order in which the chemicals are added to the reaction mixture. To ascertain the exact amount that each experimental variable contributes to the outcome, experience, intuition, and trial and error are usually combined. This makes it difficult and time-consuming to determine the ideal recipe and reaction conditions. As a result, more precise and effective techniques are needed for the synthesis of nanoparticles with specific characteristics (Nanda and Yi, 2024).

Epoxy resins are exceptionally durable, versatile, and customizable synthetic polymer materials. Because of their chemical resistance, adhesive strength, and mechanical strength, these materials are widely used in a variety of industries (Singla and Chawla, 2010; Wang et al., 2011; Hsissou et al., 2019). Epoxy resin and hardener are the two main ingredients of epoxy resins. When these two ingredients are combined, a chemical reaction takes place that causes the resin to cross-link and solidify (Unnikrishnan and Thachil, 2008). Epoxy resins are very resistant to impacts, abrasion, acids, bases, oils, and solvents after curing (Anwar and Li, 2024). They are therefore usually chosen in the aircraft sector (Xavier, 2024), floor coatings (Ruf et al., 2024), tank coatings (Dong et al., 2024), pipelines (Samardžija et al., 2024), and industrial coatings (Yu et al., 2022). Nevertheless, because of their waterproof and moisture-resistant qualities, epoxy resins are widely used in marine (Şomoghi et al., 2024) and other areas that come into contact with water, as well as in strengthening structures (Brandtner-Hafner, 2024), improving the properties of concrete (Ahn et al., 2024), installing floor coverings (Al-kawaz et al., 2024), and bonding different materials like metal, wood, and glass. Because of their electrical insulating qualities, they are also employed to cover circuit boards and safeguard electrical components (Tian et al., 2024; He et al., 2024).

Because of their energy band structures, metal sulfides including zinc sulfide (ZnS), copper sulfide (CuS), lead sulfide (PbS), and cadmium sulfide (CdS) offer a compromise between electrical insulation and conductivity. They become a technical system that can be employed in sensors (Karikalan et al., 2017), photodetectors (Duan et al., 2024), and electronic gadgets (Karikalan et al., 2017; Fang et al., 2020). Because of its narrow band gap, lead sulfide (PbS) is used in infrared sensors and photodetectors (Halge et al., 2020), and zinc sulfide (ZnS) is used in optoelectronic applications (Vijai Anand, 2021), because it can be made conductive under certain conditions despite showing insulating properties, and copper sulfide (CuS) is used as materials that absorb electromagnetic waves (Han et al., 2024). The primary factor influencing the electrical characteristics of metal sulfide nanoparticles is their band gap, or quantum size effect, which varies with particle size. For instance, reducing the particle size in semiconductors like zinc sulfide (ZnS) and cadmium sulfide (CdS) increases the band gap, altering the material's electrical characteristics (Heiba et al., 2020). The characteristics of light transmission and absorption are likewise impacted by this attribute. Smaller nanoparticles may differ in their electrical conductivity characteristics due to their greater band gap.

Thanks to its special optical, electrical, and chemical characteristics, nanocadmium sulfide is a semiconductor material with a wide range of uses (Heiba et al., 2024; Azab et al., 2024). With a straight band gap of 2.42 eV at 300 K, CdS has a variety of beneficial chemical and physical characteristics. This results in appropriate and potential uses of CdS in several devices related to contemporary needs, such as solar cells, photochemical devices, sensor devices, detector devices, optoelectronic devices, luminescence devices, and many more (Erra et al., 2007). Numerous methods for creating CdS nanoparticles have been published during the last few decades (Chatterjee and Patra, 2001). The potential to develop novel experimental techniques facilitates the production of nanoparticles with a restricted size and shape distribution at an extremely cheap cost. In recent years, scientists have engaged themselves in the creation of high-quality CdS nano-particles and the investigation of their many qualities (Dabhane et al., 2021). Semiconducting metal sulfides such as cadmium sulfide (CuS) increase the electrical conductivity of epoxy composites, enabling their use in electronic applications (Rahimi-Ahar and Ahar, 2024). Such composites can be used in applications such as electronic circuits (Panda et al., 2021), antistatic materials (Yudaev et al., 2023), and electromagnetic shielding (Bheema et al., 2024).

Researchers investigated the feasibility of incorporating MWCNT/CdS nanohybrid structures as additives into epoxy composites. In the literature, it has not yet been fully addressed how various variables during the synthesis of metal sulfides do not change the overall properties of the composite. In this case, further research is required to create CdS/MWCNT doped composite components fabricated under different conditions. The main objective of this study was to better study the strength, heat resistance, and dielectric properties of doped nanocomposite materials and also the potential of CdS/MWCNTs as reinforcements for composite properties under various manufacturing process conditions. This was achieved by looking at potential applications, evaluating their strength, and investigating

processing methods for these methods. The study also seeks to pinpoint the difficulties faced and offer perspectives on the subject of materials science attained through environmentally friendly synthesis.

2. Materials and Methods

All chemicals used for the synthesis and characterization of the nanocomposite were supplied and used directly from Merck ($CdCl_2 \cdot H_2O$), Zag Chemical ($Na_2S_2O_3 \cdot 5H_2O$), Nanography (MWCNT), and Polisan (epoxy resin). The epoxy resin used here is a solvent-free, two-component reaction-curing epoxy resin. Nanoparticle synthesis components are used without any additional processing, such as drying. Epoxy resins are directly cured at room temperature without the use of any additional materials.

2.1. Production of CdS Nanoparticles

In this study, cadmium sulfide nanoparticles were synthesized using an environmentally friendly hydrothermal process, a green synthesis technique. $CdCl_2 \cdot H_2O$ and $Na_2S_2O_3 \cdot 5H_2O$ were used as precursor chemicals. The specified amounts of $CdCl_2 \cdot H_2O$ were taken into a beaker and dissolved in 50 mL of pure water. $Na_2S_2O_3 \cdot 5H_2O$ was dissolved in 30 mL of pure water in another beaker. $Na_2S_2O_3 \cdot 5H_2O$ precursor solution was added dropwise to $CdCl_2 \cdot H_2O$ precursor solution in an ultrasonic bath environment at room temperature for 20 min. At the end of the period, the mixture obtained was transferred to a 100 mL hydrothermal reaction vessel made of Teflon to complete the nanoparticle formation process. At the end of the period, the obtained nanoparticles were centrifuged at 4000 rpm to remove the liquid part. The obtained nanoparticles were washed with distilled water three times, then the precipitate was collected and dried in a 105 °C oven. Finally, they were manually crushed in a mortar and dried again to obtain cadmium sulfide nanoparticles (CuS-NPs) in the form of powder samples. Table 1 shows the concentration and time programming for nanoparticle synthesis.

Table 1. Concentration and time scheduling scheme for CdS-NPs

Sample No	Conc. of $CdCl_2$ (mM)	Conc. of $Na_2S_2O_3$ (mM)	Time (h)
1st	57.5	115	21
2nd	137.5	275	15
3rd	217.5	435	9
4th	250.0	500	15

2.2. Production of CdS/MWCNT Hybrid Nanocomposite

For each hybrid nanocomposites, the same amount of CdS-NP and MWCNT were 0.25 wt.% for the composite 1, 0.50 wt.% for the composite 2, 0.75 wt.% for the composite 3, and 1 wt.% for the composite 4 of epoxy resin. The indicated amounts were taken into a beaker and 10 mL of ethanol was added. This mixture was sonicated in an ultrasonic bath for 30 min. At the end of the period, the obtained hybrid nanocomposites were centrifuged at 4000 rpm to remove the liquid part. The obtained hybrid nanocomposites were dried in an oven at 60 °C. Finally, the CdS/MWCNT nanocomposites were manually pounded in a mortar and dried again to obtain the powder sample form.

2.3. Production of CdS/MWCNT/epoxy Resin Nanocomposite

This production was carried out in two stages. In the first stage, the epoxy primary component (A) and the CdS/MWCNT hybrid nanocomposite component were combined in a beaker. It was mixed with a mechanical mixer at 500 rpm for 30 min to ensure homogenization. This pretreatment was performed to homogeneously distribute the nanomaterial before the reaction of the epoxy components began. In the second stage, the hardener component (B) was added to the medium and mixed at the same speed for another 15 min. When the time was up, the composite paste was immediately transferred to the silicone molds. It was left to cure at room conditions for one day. Commercial epoxy resin consists of approximately 5/8 primary component and 3/8 hardener component by mass.

The numbering of the produced epoxy composites was made by considering the studies in Table 1. Experiment 1 (pure epoxy resin-based polymer), Experiment 2 (1st sample reinforced composite), Experiment 3(2nd sample reinforced composite), Experiment 4 (3rd sample reinforced composite), and Experiment 5(4th sample reinforced composite) are expressed.

3. Results and Discussion

In Figure 1, the bulk density values (kg/m^3) of the composites belonging to different experimental groups are given and the results show that the bulk density increases regularly with the increase in the amount of CdS/MWCNT hybrid nanostructure added to the composite structure. The bulk density measured as 1133.5 kg/m^3 in the first experiment (1st group) showed a steady increase until the 5th group reached 1145.1 kg/m^3. This increase reveals that the hybrid nanostructures are homogeneously distributed in the epoxy matrix and the nanocomposite gains a more compact and dense structure. The high density of the nanohybrids and the increase in the bonding surfaces in the epoxy resin matrix play a key role in the increase in density. The significant increase seen especially in the 4th and 5th groups indicates that the added nanostructure amount provides an effective interface

interaction with the matrix, fills the voids, and improves the microstructural integrity. These findings show that optimizing the amount of nanostructures can also make positive contributions to other properties of composites such as mechanical strength and thermal conductivity (Aydoğmuş et al., 2022).

Figure 2 shows the Shore D hardness values of epoxy-based composites belonging to different experimental groups. It is seen from the graph that the hardness values increase regularly with the increase in the amount of CdS/MWCNT nanostructure in the hybrid nanocomposite. The Shore D hardness value, which was initially measured as 77.6, increased to 79.8 in the 5th experimental group. This increase can be associated with the homogeneous distribution of nanohybrids in the epoxy matrix and the increase in the mechanical strength of the composite by providing a strong interface interaction with the matrix. Nanohybrids increased the compactness of the material and improved the load-carrying capacity by filling the micro-voids in the composite structure. These findings show that optimizing the amount of nanostructures provides positive contributions to the mechanical performance of the composite (Dağ et al., 2023).

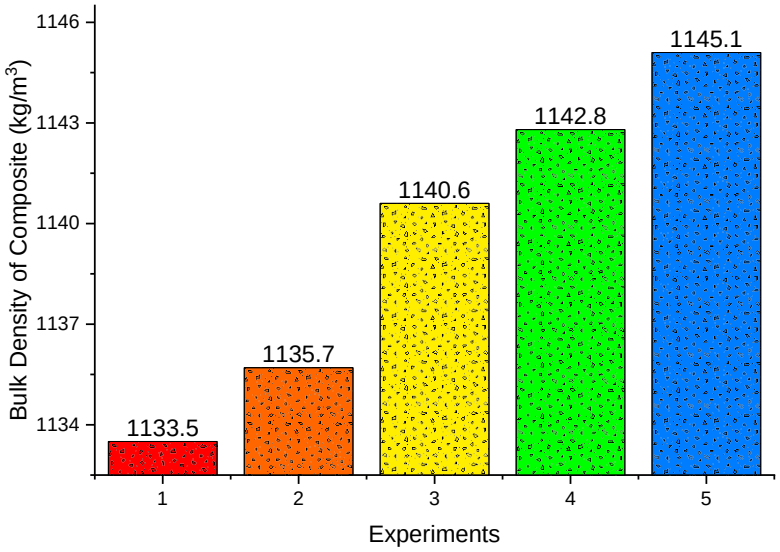


Figure 1. Bulk densities of the obtained epoxy-based composites.

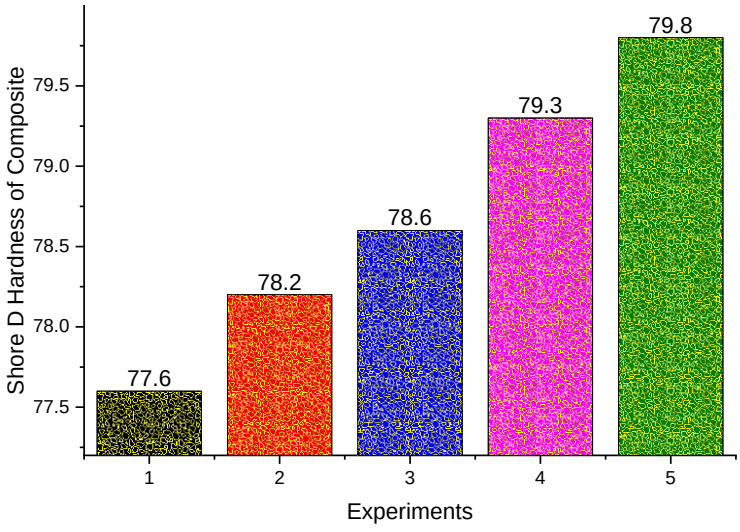


Figure 2. Shore D hardness of the produced composites.

Figure 3 shows the thermal conductivity coefficients of the composites in different experimental groups. It is observed from the graph that the thermal conductivity values increase significantly with the increase in the amount of CdS/MWCNT nanohybrid. The thermal conductivity measured as 0.112 W/m·K in the first experimental group reached 0.136 W/m·K in the 5th group. This increase is related to the high thermal conductivity capacity of the nanohybrids and their homogeneous distribution in the epoxy matrix. The nanohybrids increased the heat conduction in the matrix by acting as a bridge during heat transfer. In addition, the decrease in the thermal barriers in the matrix with the increase in the interfacial area of the nanostructures

strengthened the thermal performance of the composite. These results show that hybrid nanocomposites are a potential candidate in applications requiring high thermal conductivity (Buran et al., 2023).

Figure 4 shows the dielectric coefficients of the epoxy composites without additives and nanoparticle-reinforced. It is understood that the dielectric coefficient of the epoxy matrix-based composite increases with the addition of nanoparticles. As seen in the figure, the dielectric coefficient of the pure epoxy-based polymer without additives is 3.86, while it increases to 5.67 in the epoxy composites with nanoparticle reinforcement. Accordingly, an increase in electrical conductivity is observed depending on the amount of additives, which can increase dielectric losses. The change in the dielectric coefficient exhibits a complex relationship depending on the amount of additives, frequency range, and the internal structure of the composite. The dielectric coefficient of pure epoxy-based polymer without additives is 3.86 (Torğut and Gürler, 2024).

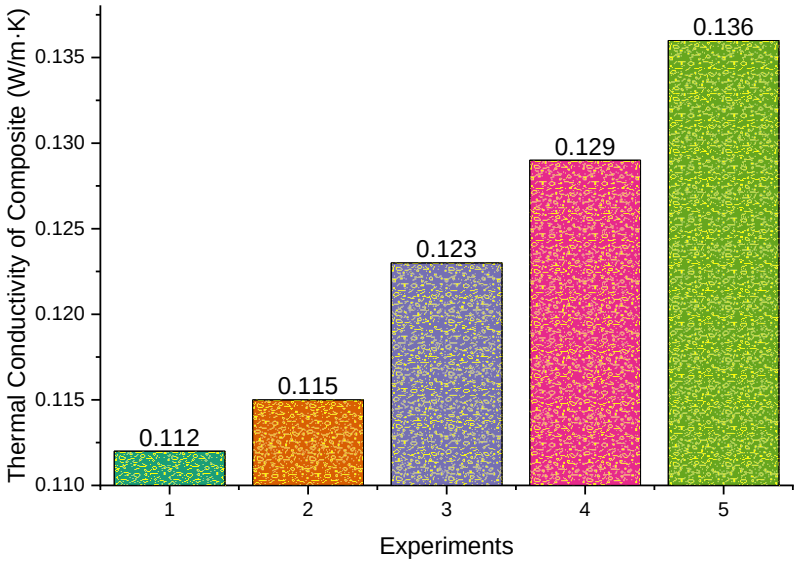


Figure 3. Thermal conductivity coefficients of epoxy-based composites.

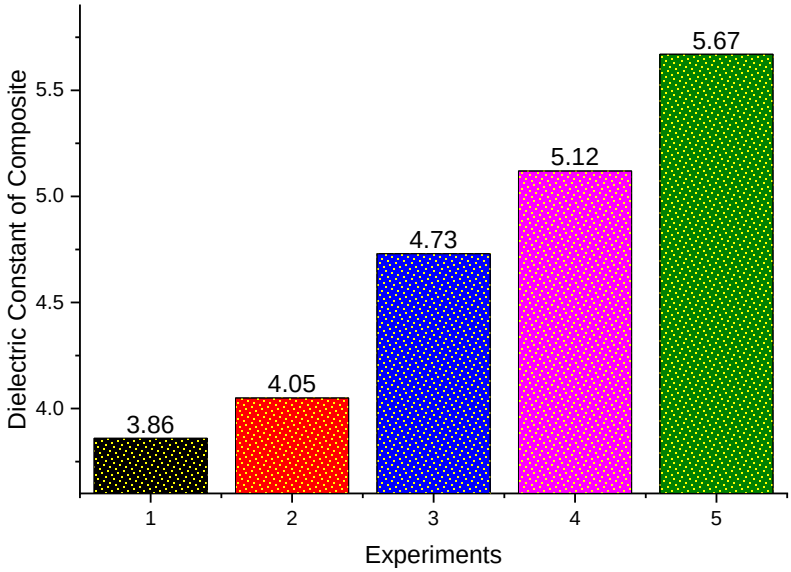


Figure 4. Dielectric coefficients of the samples produced in the experiments.

Figure 5 and Figure 6 show the tensile stress and strain (%) values as a result of the tensile test. As the tensile stress values of the samples increase, the strain rates decrease. When the experimental studies are evaluated, the elastic behavior decreases as the mechanical strength of the composites increases.

FT-IR spectra provide important information to evaluate the chemical bond structures and interactions between the components of epoxy resin-based CdS/MWCNT hybrid nanocomposite. In the pure epoxy resin spectrum, a broad peak around 3400 cm^{-1} generally indicates hydroxyl groups (O–H), while peaks belonging to C–H stretching vibrations are observed in the range of 2920-2850 cm^{-1}. In addition, the characteristic peaks of epoxy are C–O–C asymmetric and symmetric stretching vibrations in the range of 1250-1050 cm^{-1} and vibrations

confirming the presence of an epoxy ring at a wavelength of approximately 910 cm^{-1}. The preservation of the characteristic peaks of the epoxy matrix in FT-IR spectra indicates that the nanohybrid does not cause structural changes by reacting with epoxy but instead forms interfacial interactions such as physical or hydrogen bonds. However, the decrease or disappearance of the epoxy ring peak around 910 cm^{-1} indicates that the epoxy cross-links with the hardener. The decrease or disappearance of the O–H broad peak around 3400 cm^{-1} with the inclusion of CdS/MWCNT may indicate that the free hydroxyl groups on the surface interact with the epoxy matrix and contribute to the formation of a hydrophobic structure. This indicates that the nanohybrid provides a homogeneous distribution and the binding areas within the matrix increase. In addition, characteristic vibrations belonging to metal-sulfur (Cd–S) bonds can be observed in the FT-IR spectra of the CdS/MWCNT nanohybrid (400-600 cm^{-1}). These peaks confirm that the nanohybrid is successfully dispersed in the epoxy matrix and integrated into the material structure. In addition, the increases in the intensity of the C–O–C and C–H peaks with the addition of the nanohybrid support that the nanohybrids reinforce the epoxy matrix. Overall, FT-IR results reveal that the hybrid structure is homogeneously distributed within the epoxy matrix and the observed improvements in physical properties are due to effective interfacial interactions through chemical bonds (Lu et al., 2024; Qin et al., 2024).

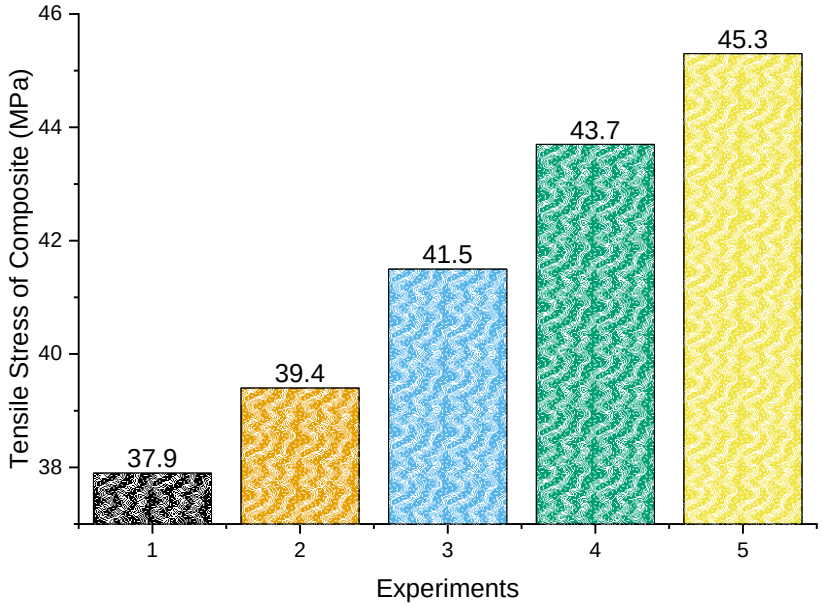


Figure 5. Tensile strength values of the obtained composite samples.

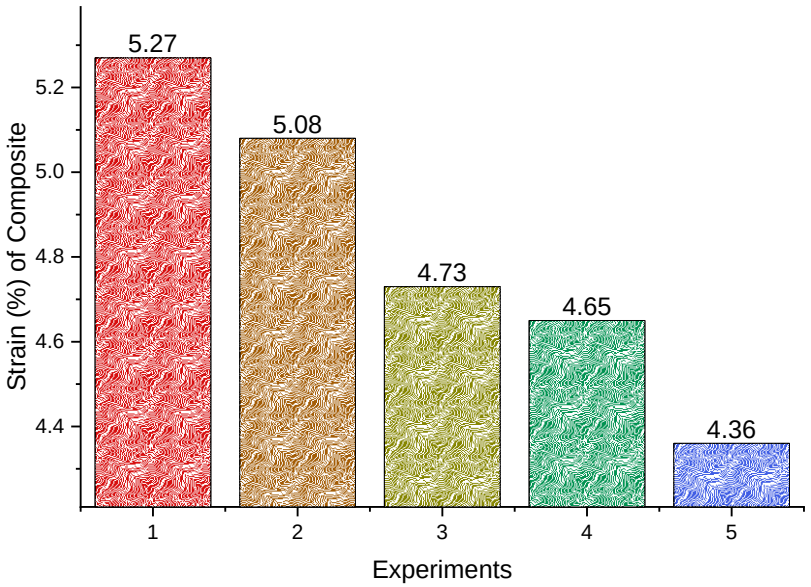


Figure 6. Tensile strain (%) values of samples obtained in experimental studies.

Figure 7 shows the FTIR spectra of the CdS/MWCNT/Epoxy nanocomposite containing CdS-NPs produced by hydrothermal technique immobilized in epoxy resin. In FTIR spectra, it is expressed as pure epoxy resin (Experiment 1), 1st composite (Experiment 2), 2nd composite (Experiment 3), 3rd composite (Experiment 4), and 4th composite (Experiment 5). According to the FTIR spectrum results, there is no chemical bond between the nanocomposite additive and the epoxy resin, but there is a physical interaction. The absence of any shift in the characteristic spectrum peaks supports the idea of physical interaction.

In the microscope images shown in Figure 8, the light-colored sample (left side) is the pure epoxy-based composite. The darker image (right side) is the product of Experimental 3.

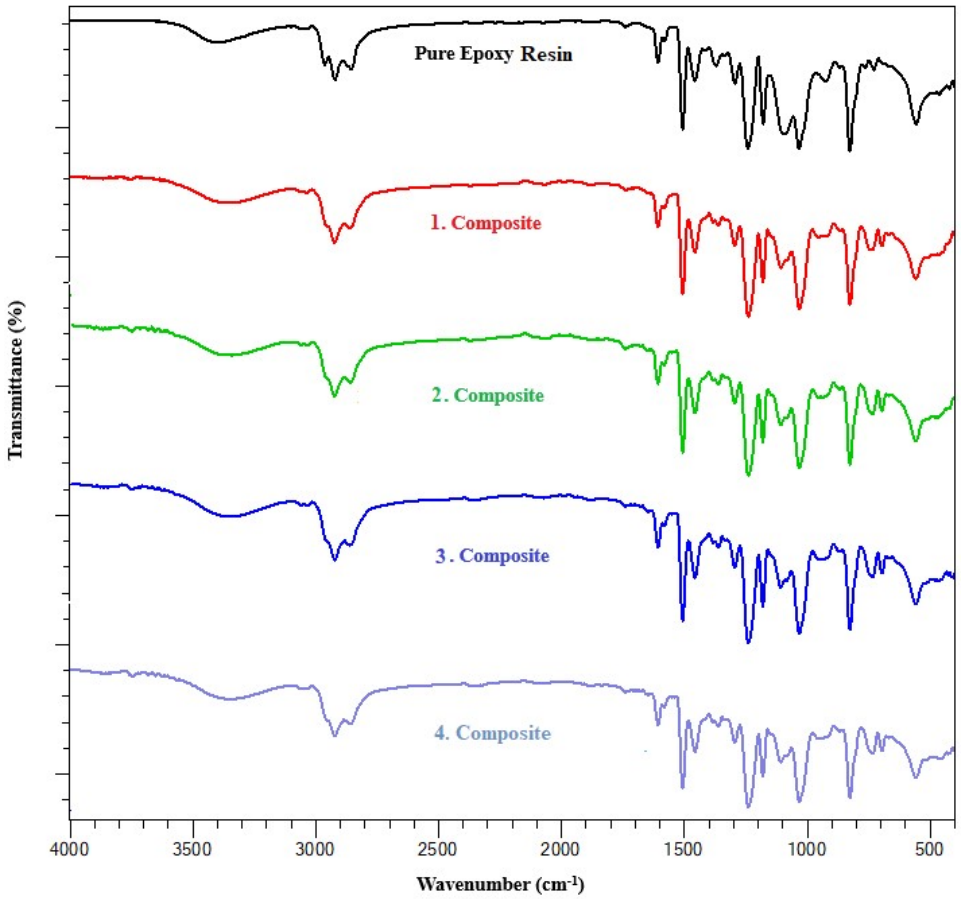


Figure 7. FTIR spectra of the pure polymer and CdS/MWCNT/epoxy nanocomposites.

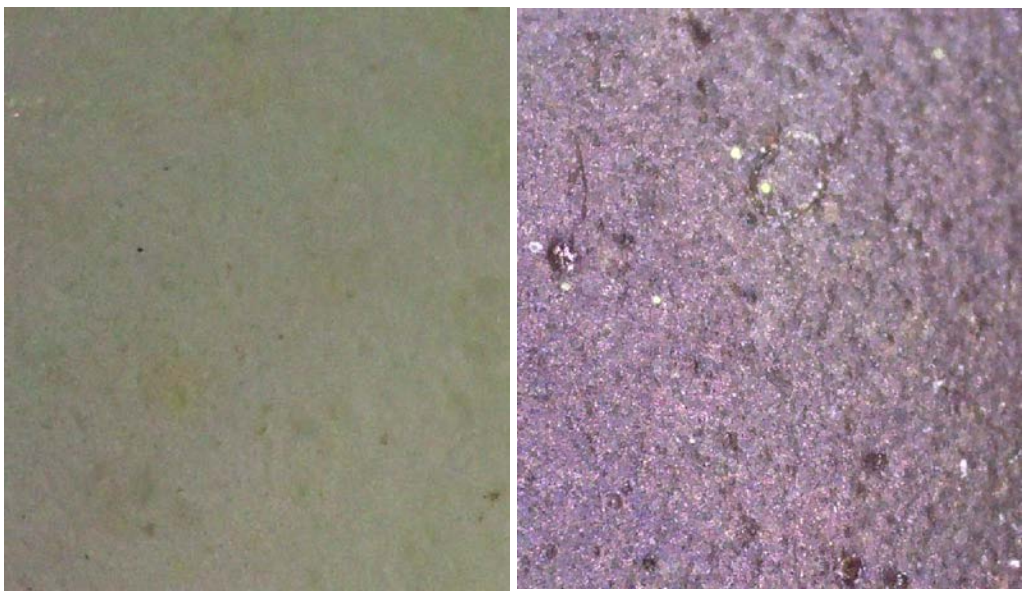


Figure 8. Microscope images of first experiment (left image) and third experiment (right image) samples.

4. Conclusion

This study comprehensively investigated the incorporation of CdS/MWCNT nanohybrids synthesized via hydrothermal methods into epoxy resin composites, focusing on their mechanical, thermal, structural, and electrical properties. The results revealed significant enhancements in key properties due to the synergistic effects of the hybrid nanostructures.

The incorporation of CdS/MWCNT nanohybrids increased the bulk density, Shore D hardness, thermal conductivity, and dielectric coefficient of the composites. These improvements were attributed to the homogeneous distribution of nanohybrids in the epoxy matrix and the strong interfacial interactions between the components. The nanohybrids filled micro-voids within the composite structure, enhancing its compactness, thermal performance, and mechanical strength. Thermal conductivity values showed a noticeable increase from 0.112 W/m·K to 0.136 W/m·K, highlighting the ability of the nanohybrids to act as efficient thermal bridges. Similarly, the dielectric coefficient rose significantly from 3.86 to 5.67, demonstrating the potential of the nanocomposites in energy storage and other dielectric applications. Microscopic analysis confirmed the effective dispersion and interfacial integration of the hybrid structures, while FT-IR analysis supported the presence of strong physical interactions, contributing to the observed property enhancements. These findings underscore the potential of CdS/MWCNT hybrid nanocomposites for advanced technological applications, particularly in fields requiring lightweight materials with high thermal conductivity, dielectric properties, and mechanical strength. Future research should explore further optimization of the hybrid structure and its application in diverse industrial sectors such as electronics, energy, and aerospace. The results provide a solid foundation for developing multifunctional materials leveraging hybrid nanostructures.

Author Contributions

The percentages of the authors' contributions are presented below. All authors reviewed and approved the final version of the manuscript.

	H.Ş.	E.A.
C	60	40
D	50	50
S	50	50
DCP	40	60
DAI	40	60
L	60	40
W	50	50
CR	50	50
SR	60	40
PM	60	40

C=Concept, D= design, S= supervision, DCP= data collection and/or processing, DAI= data analysis and/or interpretation, L= literature search, W= writing, CR= critical review, SR= submission and revision, PM= project management.

Conflict of Interest

The authors declared that there is no conflict of interest.

Ethical Consideration

Ethics committee approval was not required for this study because there was no study on animals or humans.

References

Abid J, Khalil FMA, Saeed S, Khan SU, Iqbal I, Anthony S. 2024. Nano revolution in cardiovascular health: Nanoparticles (NPs) as Tiny titans for diagnosis and therapeutics. Curr Probl Cardiol, 49(5): 102466.

Ahn E, Kim C, Choi H, Shin M. 2024. Assessment of crack repairing in concrete using air-coupled surface-wave technique: Experimental and numerical investigations. Constr Build Mater, 441: 137552.

Al-kawaz AE, Al-Mutairi NH, Alobad ZKM. 2024. Tribological behavior of epoxy/nano-clay nanocomposites used as a floor coating. J Adhes Sci Technol, 38(23): 4299-4315.

Anwar S, Li X. 2024. A review of high-quality epoxy resins for corrosion-resistant applications. J Coatings Technol Res, 21: 461-480.

Aydoğmuş E, Dağ M, Yalçın ZG, Arslanoğlu H. 2022. Synthesis and characterization of EPS reinforced modified castor oil-based epoxy biocomposite. J Building Engin, 47: 103897.

Azab AA, Ibrahim RS, Seoudi R. 2024. Investigating the effects of Mn content on the morphology and dielectric properties of CdS nanoparticles. Appl Phys A, 130: 294.

Bastianini F, Hidalgo, AIC, Hook DZ, Smith JA, Cumming D, Dunbar A. 2024. Using Ag nanoparticles in the electron transport layer of perovskite solar cells to improve efficiency. Sol Energy, 268: 112318.

Bharmal KJ, Parlikar UR, Sarkar J. 2024. Biological synthesis of nanoparticles from fungal endophytes and their application in pharmaceutical industries. Springer International Publishing, London, UK, pp: 99-128.

Bheema RK, Gopu J, Kumar AP, Etika KC. 2024. BST@ Copper Nanowire/Epoxy composites with excellent microwave absorption in the X-band. Chem Eng J, 496: 153760.

Brandtner-Hafner M. 2024. Evaluating the bonding effectiveness of CFRP patches in strengthening concrete structures. Constr Build Mater, 436: 136966.

Buran A, Durğun ME, Aydoğmuş E, Arslanoğlu H. 2023. Determination of thermophysical properties of Ficus elastica leaves reinforced epoxy composite. Firat Univ J Exp Comp Eng, 2: 12-22.

Chatterjee M, Patra A. 2001. Cadmium sulfide aggregates through reverse micelles. J Am Ceram Soc, 84: 1439-1444.

Dabhane H, Ghotekar S, Tambade P, Pansambal S, Murthy HA, Oza R, Medhane V. 2021. A review on environmentally benevolent synthesis of CdS nanoparticle and their applications. Environ Chem Ecotoxicol, 3: 209-219.

Dağ M, Aydoğmuş E, Yalçin ZG, Arslanoğlu, H. 2023. Diatomite reinforced modified safflower oil-based epoxy biocomposite production: Optimization with RSM and assessment of outcomes by ANN. Mater Today Commun, 35: 106327.

Dong H, Qiao Y, Yang K, Zhen Y, Tan W, Cheng Q, Wang Y. 2024. Epoxy resin coatings doped with layered double hydroxide for enhanced anti-permeation performance. Appl Clay Sci, 258: 107505.

Duan Y, Yang B, Ma Y, Gao C, Li S, Yang L, Li Z. 2024. Copper-based polynary chalcogenide thin film photodetectors for infrared photodetection and light communication. ACS Appl Electron Mater, 6: 5734-5744.

Eikey EA. 2024. Understanding and leveraging atom arrangement in materials: synthetic control and computational theory development. PhD thesis, University of Pittsburgh, Pittsburgh, USA, pp: 165.

Erra S, Shivakumar C, Zhao H, Barri K, Morel DL, Ferekides CS. 2007. An effective method of Cu incorporation in CdTe solar cells for improved stability. Thin Solid Films, 515: 5833-5836.

Fang R, Xu J, Wang DW. 2020. Covalent fixing of sulfur in metal–sulfur batteries. Energy Environ Sci, 13: 432-471.

Halge DI, Narwade VN, Khanzode PM, Dadge JW, Rana AS, Bogle KA. 2020, May. Spray coated nano-crystalline lead sulfide thin film for photo-detector application. AIP Publishing, New Delhi,India, pp: 162.

Han M, Lan D, Zhang Z, Zhao Y, Zou J, Gao Z, Jia Z. 2024. Micro-sized hexapod-like CuS/Cu9S5 hybrid with broadband electromagnetic wave absorption. J Mater Sci Technol, 214: 302-312.

He Y, Yang S, Tian P, Zhang J. 2024. Photo-cross-linked acrylate resins enabled by tuning various flexible diamine-extended species for high-performance printed circuit board coatings. ACS Appl Polym Mater, 6: 9771-9783.

Heiba ZK, El-Naggar AM, Kamal AM, Mohamed MB. 2024. Structural, linear/nonlinear optical, and electrical characteristics of polyvinyl chloride doped with non-stoichiometric nano cadmium sulfide. Opt Quantum Electron, 56: 356.

Heiba ZK, Mohamed MB, Farag NM, El-Naggar AM, Albassam AA. 2020. Cu-substituted sulfur in nano-ZnS: structural, optical and electronic properties study. J Mater Sci: Mater Electron, 31: 12696-12707.

Holmes A, Laval H, Guizzardi M, Maruzzo V, Folpini G, Barbero N, Bousquet A. 2024. Water-based solar cells over 10% efficiency: designing soft nanoparticles for improved processability. Environ Sci, 17: 1107-1116.

Hsissou R, Bekhta A, Khudhair M, Berradi M, El-Aouni N, Elharfi A. 2019. Review on epoxy polymers composites with improved properties. J Chem Technol Metall, 54: 1128–1136.

Hussain W, Algarni S, Rasool G, Shahzad H, Abbas, M, Alqahtani T, Irshad K. 2024. Advances in nanoparticle-enhanced thermoelectric materials from synthesis to energy harvesting: A review. ACS omega, 9: 11081-11109.

Jan HA, Saqib NU, Aamir A, Haleem, MA. 2024. Aleurites moluccana as a potential non-edible feedstock for industrial-scale biodiesel synthesis using homemade zinc oxide nanoparticles as a catalyst. Waste Biomass Valori, 15: 1081-1095.

Karikalan N, Karthik R, Chen SM, Karuppiah C, Elangovan A. 2017. Sonochemical synthesis of sulfur doped reduced graphene oxide supported CuS nanoparticles for the non-enzymatic glucose sensor applications. Sci Rep, 7: 2494.

Lu LI, Xian-ming ZHANG, Li-jie ZHOU. 2024. Study on curing mechanism of epoxy resin/multi-walled carbon nanotubes composites based on 2d correlation infrared spectroscopy. Plastics Sci Technol, 52: 2.

Majeed H, Iftikhar T, Nadeem MA, Nazir, MA. 2024. Green synthesis of Eucalyptus globulus zinc nanoparticles and its use in antimicrobial insect repellent paint formulation in bulk industrial production. Heliyon, 10(2).

Manoharan D, Wang LC, Chen YC, Li WP, Yeh CS. 2024. Catalytic nanoparticles in biomedical applications: exploiting advanced nanozymes for therapeutics and diagnostics. Adv Healthc Mater, 13(22): 2400746.

Nanda SS, Yi DK. 2024. Recent advances in synergistic effect of nanoparticles and its biomedical application. Int J Mol Sci, 25: 3266.

Ndlovu NL, Mdlalose WB, Ntsendwana B, Moyo T. 2024. Evaluation of advanced nanomaterials for cancer diagnosis and treatment. Pharmaceutics, 16: 473.

Ozcan A, Meral H. 2024. Introduction to fundamentals of nanoparticle synthesis, characterization, and properties. In Nanotechnology for Abiotic Stress Tolerance and Management in Crop Plants. Academic Press, London, UK, pp: 41-60.

Panda R, Pant KK, Bhaskar T, Naik SN. 2021. Dissolution of brominated epoxy resin for environment friendly recovery of copper as cupric oxide nanoparticles from waste printed circuit boards using ammonium chloride roasting. J Cleaner Prod, 291: 125928.

Qin Q, Wu C, Wang Y, Chen J, Chen H, Guo W, ... & Zhang Y. 2024. Study of electrical properties of graphene/epoxy resin composites induced by external electric field. J Polym Res, 31: 43.

Rahimi-Ahar Z, Ahar LR. 2024. Thermal, optical, mechanical, dielectric, and electrical properties of nanocomposites. Eur Polym J, 2024: 113337.

Ruf M, Sims S, Hillebrand G, Schneider JP. 2024. Microwave-based removal of polyurethane and epoxy floor coatings. Prog Org Coat, 189: 108345.

Samardžija M, Stojanović I, Kurtela M, Alar V. 2024. Influence of aluminum nanoparticles in epoxy resin and epoxy coating for anticorrosion and antibacterial protection in pipeline industry. J Appl Polym Sci, 141: e55002.

Shaban SM, Taha AA, Elged AH, Taha ST, Sabet VM, Kim DH, Moustafa AH. 2024. Insights on Gemini cationic surfactants influence AgNPs synthesis: Controlling catalytic and antimicrobial activity. J Mol Liq, 397: 124071.

Singla M, Chawla V. 2010. Mechanical properties of epoxy resin – fly ash composite. J Miner Mater Charact. Eng, 9: 199–210.

Solomon NO, Kanchan S, Kesheri M. 2024. Nanoparticles as detoxifiers for industrial wastewater. Water Air Soil Pollut, 235: 214.

Şomoghi R, Mihai S, Teodorescu GM, Vuluga Z, Gabor AR, Nicolae CA, Stănciulescu CM. 2024. Influence of HNT-ZnO nanofillers on the performance of epoxy resin composites for marine applications. Coatings, 14: 532.

Stiufiuc GF, Stiufiuc RI. 2024. Magnetic nanoparticles: synthesis, characterization, and their use in biomedical field. Appl Sci, 14: 1623.

Tian P, Yang S, He Y, Liu W, Zhang J. 2024. High-performance naphthalene-based photocurable epoxy resin for advanced printed circuit boards coatings by optimizing fluorodiamine-mediator extension chemistry. Polymer, 308: 127421.

Torğut G, Gürler N. 2024. Enhanced impedance, electrical conductivity, dielectric properties for colloidal starch-g-poly (methyl methacrylate) supported with semiconductor cadmium sulfide. Polym Bull, 81: 8883-8900.

Unnikrishnan KP, Thachil ET. 2008. Studies on the modification of commercial epoxy resin using cardanol-based phenolic resins. J Elastomers Plast, 40: 271–286.

Vijai Anand K. 2021. Improved structural, optical and photoluminescence properties of EDTA capped zinc sulfide nanoparticles for optoelectronic applications. J Cluster Sci, 32: 155-161.

Wang RM, Zheng SR, Zheng YG. 2011. Polymer matrix composites and technology. Elsevier, London, UK, pp: 124.

Xavier JR. 2024. Innovative Nanocomposite coating for aluminum alloy in the aircraft manufacturing industry with increased mechanical strength, flame retardancy, and corrosion resistance. Chem Select, 9: e202402056.

Yu Z, Yan Z, Zhang F, Wang J, Shao Q, Murugadoss V, Guo Z. 2022. Waterborne acrylic resin co-modified by itaconic acid and γ-methacryloxypropyl triisopropoxidesilane for improved mechanical properties, thermal stability, and corrosion resistance. Prog Org Coat, 168: 106875.

Yudaev PA, Tamboura B, Chistyakov EM. 2023. Antistatic polymer materials. Nanotech Construct Sci Internet J, 15(2): 139-152.

Black Sea Journal of Engineering and Science
doi: 10.34248/bsengineering.1600965

Open Access Journal
e-ISSN: 2619 – 8991

Research Article
Volume 8 - Issue 2: 391-397 / March 2025

DITTRICHIA VISCOSA METHANOL EXTRACT-CONTAINING NANOEMULSION AND NANOEMULSION-BASED GEL FORMULATIONS: PREPARATION AND *IN VITRO* CHARACTERIZATION STUDIES

Farnaz SHARIFLOO[1], Afife Busra UGUR KAPLAN[2], Yasar Furkan KILINBOZ[3], Meltem CETIN[2*]

[1]*Atatürk University, Faculty of Pharmacy, 25240, Erzurum, Türkiye*
[2]*Atatürk University, Faculty of Pharmacy, Department of Pharmaceutical Technology, 25240, Erzurum, Türkiye*
[3]*Ondokuz Mayıs University, Faculty of Pharmacy, Department of Pharmaceutical Technology, 55270, Samsun, Türkiye*

Abstract: *Dittrichia viscosa* (L.) Greuter (Dv) has antimicrobial, analgesic, antioxidant, anti-inflammatory, cytotoxic, and wound-healing properties. We aimed to prepare the methanol extract (Dv-Me) of the aerial parts of Dv and to determine its antioxidant capacity by FRAP, CUPRAC, and DPPH methods. In addition, we prepared nanoemulsion (NE) and NE-based gel (NEG) formulations containing Dv-Me for topical application to the skin for wound healing and characterized these formulations *in vitro*. The antioxidant capacity of Dv-Me was determined by CUPRAC, FRAP, and DPPH methods. Then, NE formulations with/without extract (B-NE and Dv-Me-NE) were developed and *in vitro* characterized [morphological analysis; centrifuge test; viscosity and pH measurements; FT-IR analysis; the determination of zeta potential, droplet size and polydispersity index (PDI)]. Besides, B-NEG and Dv-Me-NEG were prepared and *in vitro* characterized [FT-IR analysis; viscosity and pH measurements]. The droplet size and zeta potential values of NE formulations were smaller than 185 nm and around -30 mV, respectively. PDI values were found to be less than 0.3. The pH values of Dv-Me-NE and Dv-Me-NEG were found to be 5.13±0.01 and 5.87±0.02, respectively. The NE and NEG formulations showed Newtonian and pseudoplastic behaviors, respectively. As a result, Dv-Me-NEG exhibits the desired pseudoplastic behavior for topical application to the skin.

Keywords: *Dittrichia viscosa*, *In vitro* studies, Methanol extract, Nanoemulsion, Nanoemulsion-based gel

***Corresponding author:** Atatürk University, Faculty of Pharmacy, Department of Pharmaceutical Technology, 25240, Erzurum, Türkiye
E mail: melcetin@atauni.edu.tr (M. CETIN)
Farnaz SHARIFLOO https://orcid.org/0009-0000-7669-5847
Afife Busra UGUR KAPLAN https://orcid.org/0000-0003-2222-8789
Yasar Furkan KILINBOZ https://orcid.org/0000-0002-9646-4197
Meltem CETIN https://orcid.org/0000-0003-4009-2432

Received: December 13, 2024
Accepted: January 27, 2025
Published: March 15, 2025

Cite as: Sharifloo F, Ugur Kaplan AB, Kilinboz YF, Cetin M. 2025. *Dittrichia viscosa* methanol extract-containing nanoemulsion and nanoemulsion-based gel formulations: Preparation and *in vitro* characterization studies. BSJ Eng Sci, 8(2): 391-397.

1. Introduction

Dittrichia viscosa (L.) Greuter (Dv; former name: "*Inula viscosa* (L.) Aiton"), known in Turkey as 'kanser otu' or 'yapışkan andız otu', belongs to the Asteraceae family and is an herbaceous perennial plant (Brahmi-Chendouh et al., 2019; Canli Taşar, 2020; Seca et al., 2014). It is widespread on the slopes of the coastal regions of the Mediterranean (Brahmi-Chendouh et al., 2019). It has been used traditionally to treat various diseases/conditions, such as bronchitis, rheumatic pain, tuberculosis, infertility, and cancer. It also has wound-healing activity (Danino et al., 2009; Mrid et al., 2022). Dv contains various compounds, such as essential oils, sesquiterpenes, triterpenoids, lactones, flavonoids, sesquiterpene acids, and guaianolides. Therefore, it has several biological properties such as antipyretic, anti-inflammatory, antimicrobial, antidiabetic, antioxidant, and anti-scabies (Brahmi-Chendouh et al., 2019; Mrid et al., 2022; Rechek et al., 2023; Seca et al., 2014).

Excessive levels of reactive oxygen species (ROS) cause an imbalance between antioxidant defense mechanisms and cellular production of free radicals (oxidants), an increase in the inflammatory response, and wound repair inhibition. Therefore, antioxidants are significant in eliminating ROS damage during wound healing. In this sense, plant extracts containing antioxidant compounds are gaining increasing importance (Rhimi et al., 2019).

Dv has been used in Jordan and Palestine for its wound-healing effect (Khalil et al., 2007). In an in vivo study, the wound-healing effect of the aqueous extract of the aerial parts of Dv (formulated in Pluronic F127) was demonstrated by histological evaluation. They emphasized that the wound-healing effect of the extract could be due to its anti-inflammatory activity (Khalil et al., 2007). In another study, an ointment formulation was prepared containing the ethanolic extract of leaves of Dv (2.5% and 5%; w/w). They evaluated the wound healing activities of these formulations in an excision wound model in mice by applying it daily for 12 days after wound formation. They observed full re-epithelialization

This work is licensed (CC BY-NC 4.0) under Creative Commons Attribution 4.0 International License

and complete healing in the group treated with the 5% extract-containing ointment on day 12. They reported that antioxidants such as polyphenolic compounds support wound healing (Rhimi et al., 2019).

Nanoemulsions (NEs), which are also known as mini-emulsions and submicron emulsions, consist of an oil phase, aqueous phase, and emulsifier/s, have a generally accepted droplet size range of 20-200 nm and have long-term physical stability. NEs' droplet sizes affect their rheological properties and stability as well as active compounds' absorption/penetration (Mushtaq et al., 2023; Preeti et al., 2023). NEs, which exhibit low retention time and spreadability due to their low viscosity, are converted into an NE-based gel (NEG) using a suitable gelling agent (such as sodium carboxymethylcellulose, chitosan, Carbopol), thus making them easily applicable topically to the skin (Donthi et al., 2023). NE-based gel formulations are widely prepared for topical application for wound healing (Algahtani et al., 2021a; Morsy et al., 2019).

It was aimed to prepare the methanol extract of the aerial parts of Dv (Dv-Me) and to determine its antioxidant capacity by "cupric reducing antioxidant capacity" (CUPRAC), "ferric reducing antioxidant power" (FRAP), and "DPPH radical scavenging" assays. We also aimed to prepare and *in vitro* characterize Dv-Me-containing NE and NEG formulations for wound healing.

2. Materials and Methods

2.1. Materials

Isopropyl myristate, Lipoid S100, Labrafac PG, Kolliphor RH 40, and Protasan UP G213 were obtained from Sigma-Aldrich (Switzerland), Lipoid GmbH (Germany), Gattefossé (France), Sigma (USA), and Novamatrix (Norway), respectively. Methanol, $CuCl_2.2H_2O$, tripyridyltriazine (TPTZ), diphenylpicrylhydrazyl (DPPH), neocuproine (Nc), $FeCl_3$, and ammonium acetate were obtained from J.T. Baker (Norway), Merck Millipore (Germany), and Sigma-Aldrich (USA), respectively.

2.2. Methods

2.2.1. Preparation of Dv-Me and determination of antioxidant capacity

The dried Dv aerial parts were pulverized using a laboratory blender. Then, we added 250 mL of methanol to 10 g of powder and mixed it on a magnetic stirrer (600 rpm; at room temperature; 24 h). After the filtration, methanol was removed by a rotary evaporator (40 °C, 90 rpm). Dv-Me was stored in airtight containers at 2-8 °C, protected from light.

FRAP, DPPH radical scavenging activity, and CUPRAC assays were used to determine antioxidant capacity of Dv-Me. For the FRAP assay, the FRAP reagent was prepared freshly [0.3 N acetate buffer (pH 3.6), 20 mM $FeCl_3$ solution and 10 mM TPTZ solution (in 40 mM HCl); 10:1:1 (v/v/v)] (Spiegel et al., 2020). Then, 200 µL of FRAP reagent and 10 µL of sample (Trolox standard solution or Dv-Me) were added into the wells of the 96-well plate. After 30 min incubation (protected from light; room temperature), we read the absorbance at 593 nm (Benzie and Strain, 1996; Büyüktuncel, 2013; Spiegel et al., 2020).

For the CUPRAC assay, 10 mM $CuCl_2.2H_2O$ solution, 7.5 mM Nc solution, and ammonium acetate (pH 7.0) buffer were prepared (Apak et al., 2006). Then, $CuCl_2.2H_2O$ solution (60 µL), Nc solution (60 µL), acetate buffer (60 µL), and the sample (Trolox standard solution or Dv-Me) (66 µL) was added into each well of 96-well plates, respectively. After incubation (30 min; room temperature; protected from light), we read the absorbance at 450 nm.

For the DPPH radical scavenging assay, we added 210 µL of the sample (Trolox standard solution or Dv-Me) and 70 µL of freshly prepared DPPH solution into each well of 96-well plates. After 30 min incubation (protected from light; room temperature), the absorbance was read at 515 nm (Mekky et al., 2017). Then, we calculated the percent DPPH inhibition (Salar et al., 2015).

2.2.2. NE and NEG formulations' preparation

We prepared a mixture of Lipoid S100 (2%) and isopropyl myristate (8%) in a hot water bath (70 °C). Then, we mixed it on a magnetic stirrer (600 rpm) until it reached room temperature. We added Dv-Me (10 mg) in Labrafac PG (2%) to the oil phase and mixed on a magnetic stirrer (5 min; 600 rpm). After adding the aqueous phase consisting of Kolliphor RH 40 and ultrapure water to the oil phase under magnetic stirring (600 rpm), high-speed mixing for 7 min (Ultraturrax; 27500 rpm) and ultrasonication for 14 min (55% power) were applied to reduce the droplet size of the obtained emulsion and prepare the Dv-Me-NE formulation, respectively.

The blank NE (B-NE) formulation was prepared using the same procedure without adding Dv-Me.

To prepare NEG formulations (B-NEG or Dv-Me-NEG), Protasan UP G213 (1%) was added to the B-NE or Dv-Me-NE formulations and mixed overnight on a magnetic stirrer (600 rpm).

2.2.3. NE and NEG formulations' characterization

First, NE formulation (5 g) was centrifuged (15 min; 3500 rpm) to assess whether phase separation occurred. Then, we used the Zetasizer Nano ZSP ("Malvern Instruments Ltd., UK") to determine the zeta potential, droplet size, and PDI values of NE formulations (100-fold diluted). pH and viscosity measurements of NE and NEG formulations were carried out at room temperature with a pH meter ("Thermo Scientific, Orion 3 StarTM, USA") and a Brookfield viscometer (RV DV2T; USA), respectively. In addition, FT-IR spectra of Dv-Me, B-NE, B-NEG, Dv-Me-NE, and Dv-Me-NEG were taken in the range of 4000-400 cm^{-1}. The TEM image of NE formulation containing Dv-Me (Dv-Me-NE) was also obtained ("Hitachi HighTech HT7700, Japan").

2.3. Statistical Analysis

The "Independent t-test" ("SPSS Statistics Version 22.0 software; SPSS Inc., USA") was used to compare the obtained results. The results are shown as

mean±standard deviation (SD) ($p<0.05$: statistically significant).

3. Results and Discussion

With the increase in chronic diseases such as peripheral vascular diseases and diabetes in the world, the frequency of acute or chronic wounds has also increased. Topical drug application provides significant advantages in wound treatment. The topical application of active ingredients for wound healing offers direct access to affected areas. NE-based gel formulation has attracted considerable attention in recent years as an effective delivery system that can facilitate the topical application of active compounds and improve the therapeutic efficacy of these compounds in wound healing (Ahmad et al., 2019; Algahtani et al., 2021b).

Dv has antimicrobial, analgesic, antioxidant, anti-inflammatory, cytotoxic, and wound healing properties. Mssillou et al. (2022) showed that the hydroalcoholic extract of Dv achieved nearly complete wound healing on the 21st day in burn-wounded rats.

In light of this information, NE and NE-based gel formulations containing Dv-Me for wound healing were prepared and characterized *in vitro* in our study. First, the methanol extract of Dv was prepared and its total antioxidant capacity was evaluated using FRAP, CUPRAC and DPPH assays. Trolox solution in methanol was used as a standard for all three assays. We presented the obtained Trolox standard curves and equations (in the concentration range of 1-10 µg/mL for DPPH assay and 1-100 µg/mL for FRAP and CUPRAC assays) in Figure 1. Table 1 shows the total antioxidant capacity values of Dv-Me.

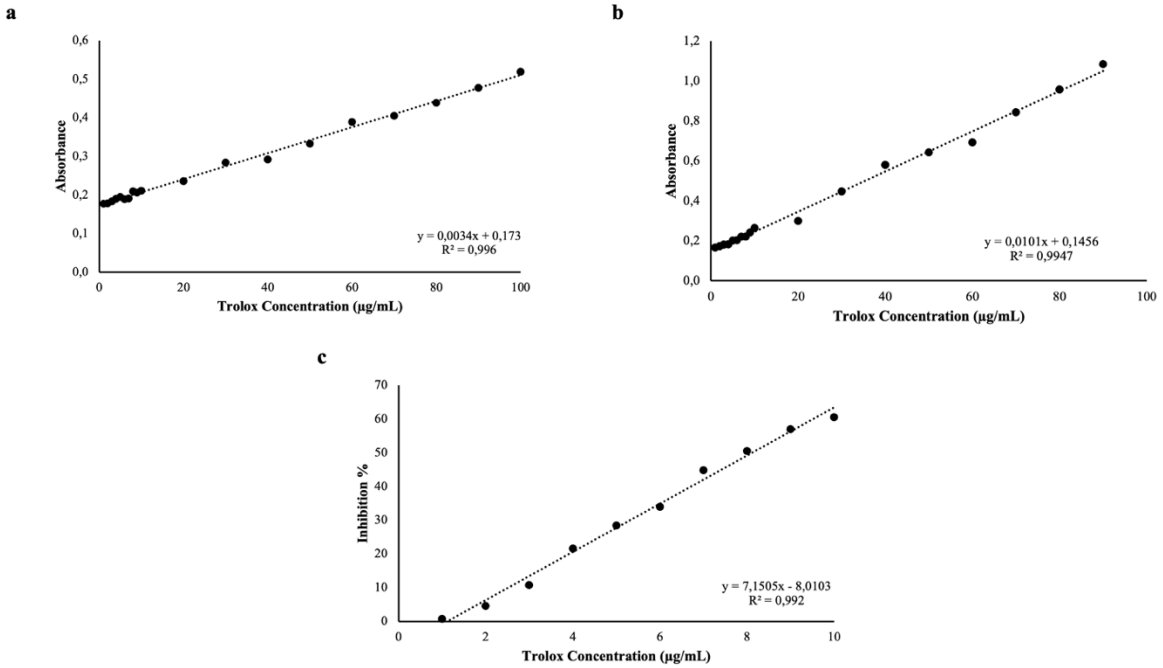


Figure 1. Trolox standard curves and equations for FRAP (a), CUPRAC (b) and DPPH (c) assays.

Table 1. Dv-Me's total antioxidant capacity values (Mean±SD; n=3)

Dv-Me (500 µg/mL)	Trolox-equivalent antioxidant capacity (µg/mL)		
	FRAP	CUPRAC	DPPH
	51.58±0.32	72.22±2.17	42.65±0.36

SD= standard deviation

Then, we prepared the NE formulation containing Dv-Me and first evaluated whether there was phase separation in the NE formulations after centrifugation. There was no phase separation in the prepared NE formulations after centrifugation. The zeta potential, droplet size and PDI values are significant parameters for the physical stability of NE formulations. In addition, the increased surface area (due to nano-sized droplets) also affects the skin penetration of active compounds (Ashaolu, 2021; Solans et al., 2005; Ugur Kaplan et al., 2019). Thus, we determined these parameters. The droplet sizes of the NE formulations (B-NE and Dv-Me-NE) were smaller than 185 nm (Table 2). The droplet sizes of B-NE and Dv-Me-NE formulations were statistically different ($p<0.05$). An increase in the droplet size of NEs occurred depending on the presence of the extract. Additionally, the PDI values found for B-NE and Dv-Me-NE formulations were smaller than 0.3 (Table 2), indicating the droplet size distribution of NE formulations was in an acceptable narrow range ("Ugur Kaplan et al., 2019"). The zeta potential values of the NE formulations were around -30 mV (Table 2). There was a decrease in the zeta potential value of NE formulation in the presence of Dv-Me. The zeta potential values of B-NE and Dv-Me-NE formulations were

statistically different ($p<0.05$). The absolute zeta potential values of 30 mV and above provide good physical stability for emulsions (Mahamat Nor et al., 2017). The TEM image of the Dv-Me-NE formulation (Figure 2) showed that nano-sized and approximately spherical droplets were obtained.

Table 2. The zeta potential, droplet size, and PDI values determined for the NE formulations (Mean±SD; n=9)

Formulation	Droplet Size (nm)	PDI	Zeta Potential (mV)
B-NE	145.08±9.01	0.238±0.044	-32.10±1.36
Dv-Me-NE	182.12±8.04	0.258±0.038	-28.46±1.69

SD= standard deviation

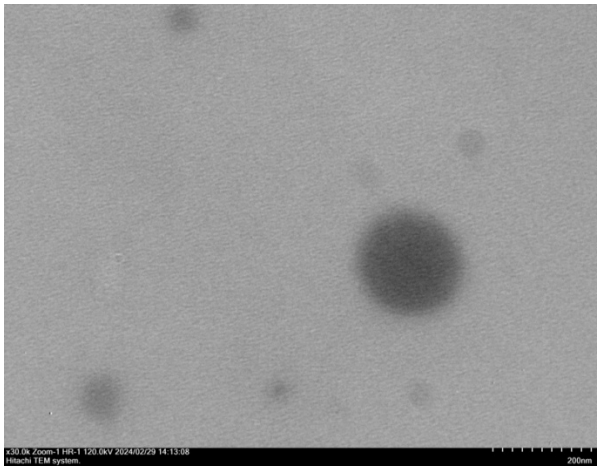


Figure 2. The TEM image of NE formulation containing Dv-Me (Dv-Me-NE).

The pH of human skin is typically acidic, but it can range from 4.0 to 7.0 (Lambers et al., 2006). The formulations with very low or very high pH values cause skin irritation. In our study, Table 3 shows that the pH values of NE and NE-based gel formulations were ranged from 5.13 to 6.10. The pH values of B-NE and Dv-Me-NE or B-NEG and Dv-Me-NEG formulations were statistically different ($p<0.05$). There was a slight decrease in the pH values of the formulations in the presence of the extract (Dv-Me). As a result, the pH values of NE and NEG formulations containing Dv-Me are suitable for topical application to the skin.

Table 3. The NE and NEG formulations' pH values (Mean±SD; n=3)

Formulation	pH
B-NE	5.24±0.02
Dv-Me-NE	5.13±0.01
B-NEG	6.10±0.02
Dv-Me-NEG	5.87±0.02

SD= standard deviation

FT-IR spectra of Dv-Me, NE, and NEG formulations are presented in Figures 3a and 3b. In the FT-IR spectrum of Dv-Me, there was a broad band associated with O-H groups at around 3200-3300 cm^{-1}. In addition, we observed C-H stretching vibration at 2923 cm^{-1}, C–O stretching vibration at 1155 cm^{-1}, C–H bending vibration at 1469 cm^{-1}, C=O and C=C stretching vibrations at 1692 cm^{-1} and 1623 cm^{-1}, respectively (Figures 3a and 3b). These results are consistent with the literature (Kebir et al., 2015; Kouache et al., 2022). The B-NE and Dv-Me-NE formulations and the B-NEG and Dv-Me-NEG formulations have similar spectra. The peaks belonging to Dv-Me were not observed in the FT-IR spectra of NE and NEG formulations containing the extract.

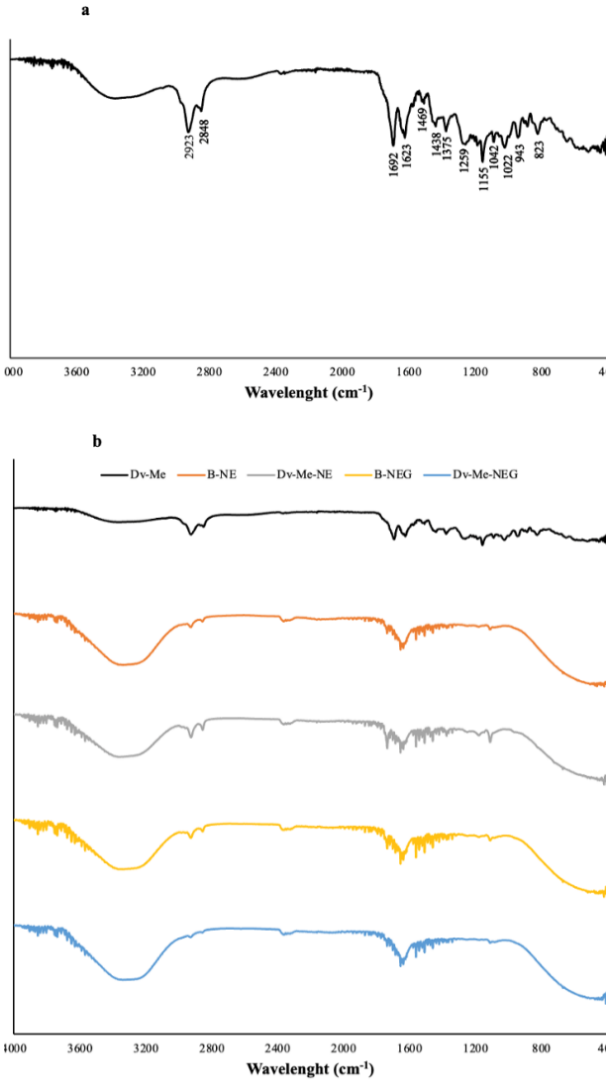


Figure 3. FT-IR spectra of Dv-Me (a and b), NE and NEG formulations (b).

The viscosity of NEs is a function of the components in the formulation (oil, water, and surfactant) and their concentrations (Lovelyn and Attama, 2011). The viscosity and "n" (flow behavior index) values determined for NE and NEG formulations are given in Table 4. The rheograms of these formulations are shown in Figures 4a and 4b. The B-NE and Dv-Me-NE

formulations' viscosity values were 2.56 cP and 2.79 cP, respectively. A slight increase in viscosity of the formulation was observed in the presence of the extract ($p<0.05$, Table 4). To overcome the obstacles of low viscosity and spreadability of NE, NE-based gel formulations are widely prepared. The viscosity values of B-NEG and Dv-Me-NEG formulations were 72.31 cP and 75.31 cP, respectively ($p>0.05$, Table 4). In addition, while the "n" value was around 1 for NE formulations, it was less than 1 for NEG formulations. n=1 represents Newtonian behavior; n<1 represents pseudoplastic flow behavior (Teixeira et al., 2017). As a result, the NE-based gel formulations have suitable rheological properties for topical application.

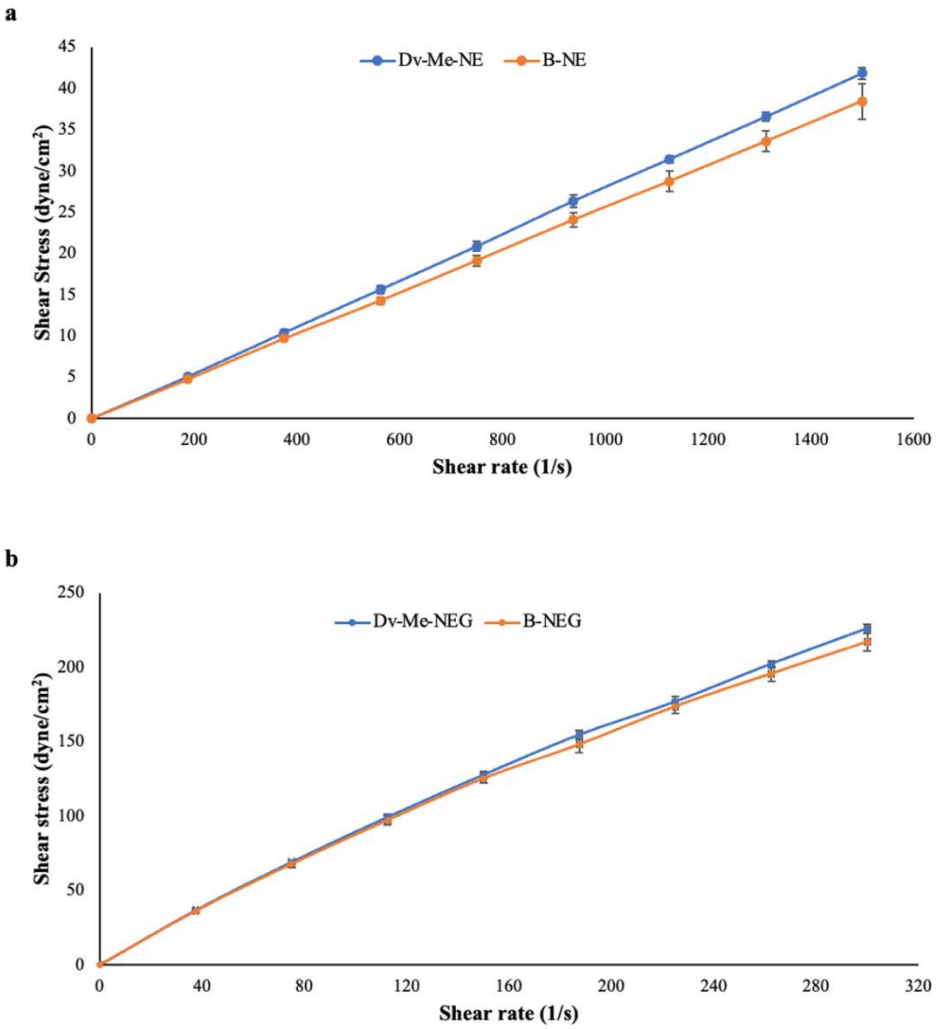


Figure 4. The rheograms of the NE formulations (a) and the NEG formulations (b) (Mean±SD; n=3).

Table 4. The viscosity and "n" values of NE and NEG formulations (Mean±SD; n=3)

Formulation	Shear rate (s^{-1})	Viscosity (cP)	n
B-NE	1500	2.56±0.03	1.003
Dv-Me-NE		2.79±0.09	1.013
B-NEG	300	72.31±1.98	0.860
Dv-Me-NEG		75.31±0.99	0.872

SD= standard deviation

4. Conclusion

In our study, Dv-Me-containing NE and NEG formulations were prepared for topical use for wound healing, and *in vitro* characterization studies were performed. The prepared NEG formulations containing Dv-Me had suitable pH and rheological properties (pseudoplastic behavior) for topical application to the skin.

Author Contributions

The percentages of the authors' contributions are presented below. All authors reviewed and approved the final version of the manuscript.

	F.S.	A.B.U.K.	Y.F.K.	M.C.
C	-	-	-	100
D	-	50	-	50
S	-	-	-	100
DCP	25	25	25	25
DAI	-	50	-	50
L	25	25	25	25
W	10	20	10	60
CR	-	40	-	60
SR	-	50	-	50
PM	-	-	-	100
FA	-	50	-	50

C=Concept, D= design, S= supervision, DCP= data collection and/or processing, DAI= data analysis and/or interpretation, L= literature search, W= writing, CR= critical review, SR= submission and revision, PM= project management, FA= funding acquisition.

Conflict of Interest

The authors declared that there is no conflict of interest.

Ethical Consideration

Ethics committee approval was not required for this study because of there was no study on animals or humans.

References

Ahmad N, Ahmad R, Al-Qudaihi A, Alaseel SE, Fita IZ, Khalid MS, Pottoo FH. 2019. Preparation of a novel curcumin nanoemulsion by ultrasonication and its comparative effects in wound healing and the treatment of inflammation. RSC Adv, 9(35): 20192–20206.

Algahtani MS, Ahmad MZ, Nourein IH, Albarqi HA, Alyami HS, Alyami MH, Algahtani AA, Alasiri A, Algahtani TS, Mohammed AA, Ahmad J. 2021a. Preparation and characterization of curcumin nanoemulgel utilizing ultrasonication technique for wound healing: in vitro, ex vivo, and in vivo evaluation. Gels, 7(4): 213.

Algahtani MS, Ahmad MZ, Shaikh IA, Abdel-Wahab BA, Nourein IH, Ahmad J. 2021b. Thymoquinone loaded topical nanoemulgel for wound healing: formulation design and in vivo evaluation. Molecules, 26(13): 3863.

Apak R, Güçlü K, Ozyürek M, Esin Karademir S, Erçağ E. 2006. The cupric ion reducing antioxidant capacity and polyphenolic content of some herbal teas. Int J Food Sci Nutr, 57(5–6): 292–304.

Ashaolu TJ. 2021. Nanoemulsions for health, food, and cosmetics: a review. Environ. Chem. Lett. 19(4): 3381–3395.

Benzie IFF, Strain JJ. 1996. The ferric reducing ability of plasma (FRAP) as a measure of "antioxidant power": the FRAP assay. Anal Biochem, 239(1): 70–76.

Brahmi-Chendouh N, Piccolella S, Crescente G, Pacifico F, Boulekbache L, Hamri-Zeghichi S, Akkal S, Madani K, Pacifico S. 2019. A nutraceutical extract from Inula viscosa leaves: UHPLC-HR-MS/MS based polyphenol profile, and antioxidant and cytotoxic activities. J Food Drug Anal, 27(3): 692–702.

Büyüktuncel E. 2013. Toplam fenolik içerik ve antioksidan kapasite tayininde kullanılan başlıca spektrofotometrik yöntemler. Marmara Pharm J, 17(2): 93–103.

Canli Taşar Ö. 2020. Inulinase production capability of a promising medicinal plant: Inula viscosa. Commagene J Biol, 4(1): 67-73.

Danino O, Gottlieb HE, Grossman S, Bergman M. 2009. Antioxidant activity of 1,3-dicaffeoylquinic acid isolated from Inula viscosa. Food Res Int, 42(9): 1273–1280.

Donthi MR, Munnangi SR, Krishna KV, Saha RN, Singhvi G, Dubey SK. 2023. Nanoemulgel: a novel nano carrier as a tool for topical drug delivery. Pharmaceutics, 15(1): 164.

Kebir M, Trari M, Maachi R, Nasrallah N, Amrane A. 2015. Valorization of Inula viscosa waste extraction, modeling of isotherm, and kinetic for the tartrazine dye adsorption. Desalin Water Treat, 54(10): 2806–2816.

Khalil EA, Afifi FU, Al-Hussaini M. 2007. Evaluation of the wound healing effect of some Jordanian traditional medicinal plants formulated in Pluronic F127 using mice (Mus musculus). J. Ethnopharmacol, 109(1): 104–112.

Kouache A, Khelifa A, Boutoumi H, Moulay S, Feghoul A, Idir B, Aoudj S. 2022. Experimental and theoretical studies of Inula viscosa extract as a novel eco-friendly corrosion inhibitor for carbon steel in 1 M HCl. J Adhes Sci Technol, 36(9): 988–1016.

Lambers H, Piessens S, Bloem A, Pronk H, Finkel P. 2006. Natural skin surface pH is on average below 5, which is beneficial for its resident flora. Int J Cosmet Sci, 28(5): 359–370.

Lovelyn C, Attama AA. 2011. Current state of nanoemulsions in drug delivery. J Biomater Nanobiotechnol, 2: 626–639.

Mahamat Nor SB, Woi PM, Ng SH. 2017. Characterisation of ionic liquids nanoemulsion loaded with piroxicam for drug delivery system. J Mol Liq, 234: 30–39.

Mekky H, Sohafy SE, El-khair RA, Hawiet AE. 2017. Total polyphenolic content and antioxidant activity of Silybum marianum cultures grown on different growth regulators. Int J Pharm Pharm Sci, 9(4): 44–47.

Morsy MA, Abdel-Latif RG, Nair AB, Venugopala KN, Ahmed AF, Elsewedy HS, Shehata TM. 2019. Preparation and evaluation of atorvastatin-loaded nanoemulgel on wound-healing efficacy. Pharmaceutics, 11(11): 609.

Mrid RB, Bouchmaa N, Kabach I, Zouaoui Z, Chtibi H, Maadoudi, ME, Kounnoun A, Cacciola F, Majdoub YOE, Mondello L, Zyad A, Nhiri M. 2022. Dittrichia viscosa L. leaves: a valuable source of bioactive compounds with multiple pharmacological effects. Molecules, 27(7): 2108.

Mssillou I, Agour A, Slighoua M, Chebaibi M, Amrati FE, Alshawwa SZ, Kamaly OA, El Moussaoui A, Lyoussi B, Derwich E. 2022. Ointment-based combination of Dittrichia viscosa L. and Marrubium vulgare L. accelerate burn wound healing. Pharmaceuticals, 15(3): 289.

Mushtaq A, Mohd Wani S, Malik AR, Gull A, Ramniwas S, Ahmad Nayik G, Ercisli S, Alina Marc R, Ullah R, Bari A. 2023. Recent insights into nanoemulsions: their preparation, properties and applications. Food Chem X, 18: 100684.

Preeti, Sambhakar S, Malik R, Bhatia S, Al Harrasi A, Rani C Saharan S, Kumar S, Geeta, Sehrawat R. 2023. Nanoemulsion: an emerging novel technology for improving the bioavailability of drugs. Scientifica, 2023: 6640103.

Rechek H, Haouat A, Hamaidia K, Pinto DCGA, Boudiar T, Válega MSGA, Pereira DM, Pereira RB, Silva AMS. 2023. Inula viscosa (L.) Aiton ethanolic extract inhibits the growth of human AGS

and A549 cancer cell lines. Chem Biodivers, 20(3): e202200890.

Rhimi W, Hlel R, Ben Salem I, Boulila A, Rejeb A, Saidi M. 2019. Dittrichia viscosa L. ethanolic extract based ointment with antiradical, antioxidant, and healing wound activities. BioMed Res Int, 2019: 4081253.

Salar RK, Sharma P, Purewal SS. 2015. In vitro antioxidant and free radical scavenging activities of stem extract of Euphorbia trigona Miller. CELLMED, 5(2): e14.

Seca AML, Grigore A, Pinto DCGA, Silva AMS. 2014. The genus Inula and their metabolites: from ethnopharmacological to medicinal uses. J Ethnopharmacol, 154(2): 286–310.

Solans C, Izquierdo P, Nolla J, Azemar N, Garcia-Celma M. 2005. Nano-emulsions. Curr Opin Colloid Interface Sci, 10: 102–110.

Spiegel M, Kapusta K, Kołodziejczyk W, Saloni J, Żbikowska B, Hill GA, Sroka Z. 2020. Antioxidant activity of selected phenolic acids-ferric reducing antioxidant power assay and QSAR analysis of the structural features. Molecules, 25(13): 3088.

Teixeira MC, Severino P, Andreani T, Boonme P, Santini A, Silva AM, Souto EB. 2017. d-α-tocopherol nanoemulsions: size properties, rheological behavior, surface tension, osmolarity and cytotoxicity. Saudi Pharm J, 25(2): 231–235.

Ugur Kaplan AB, Cetin M, Orgul D, Taghizadehghalehjoughi A, Hacımuftuoglu A, Hekimoglu S. 2019. Formulation and in vitro evaluation of topical nanoemulsion and nanoemulsion-based gels containing daidzein. J Drug Deliv Sci Technol, 52: 189–203.

Black Sea Journal of Engineering and Science
doi: 10.34248/bsengineering.1594171

Open Access Journal
e-ISSN: 2619 – 8991

Research Article
Volume 8 - Issue 2: 398-404 / March 2025

EFFECT OF DIFFERENT SUBSTRATES ON H_2S AND N_2 PRODUCTION IN BIOGAS PRODUCTION

Cevat FİLİKCİ[1]*, Tamer MARAKOĞLU[2]

[1]*Kırşehir Ahi Evran University, Çiçekdağı Vocational School, Department of Plant and Animal Production, 40700, Kırşehir, Türkiye*
[2]*Selçuk University, Faculty of Agriculture, Department of Agricultural Machinery and Technologies Engineering, 42130, Konya, Türkiye*

Abstract: The aim of this study is to determine the hydrogen sulfide (H_2S) and nitrogen (N_2) ratio of biogas produced from various combinations of cattle waste (CW), three different Switchgrass (SG) (*Panicum virgatum* L.) plant varieties (Kanlow (SG1), Shawne (SG2), Alamo (SG3) and sugar beet (*Beta Vulgaris* L.) leaves (BL). In the study, a laboratory-scale biomethane application setup was established to determine the biogas potential. Within the scope of the research, a trial design was created as 1st application group, 2nd application group and 3rd application group. In the established application setup, biogas measurements were recorded in a computer environment for 16 days, 30 days and 43 days, considering the end of biogas production of the materials. During the measurements, temperature and pH values were checked at certain periods and mixing was done by shaking by hand every day. Applications were carried out considering 10% dry matter ratio. Methane (CH_4) in biogas is a valuable energy source, other components constitute a major obstacle to the commercial use of biogas. The variable composition is due to the various materials that can be used for the production of biogas. In the study, the effect of H_2S and N_2 ratios of biogas obtained from mixtures of different materials at different ratios on biogas production was investigated. As a result of the measurements made, the biogas components of each mixture were measured using a gas analyzer. H_2S and N_2 ratios obtained from different substrates were determined. The highest H_2S ratio was measured from cattle waste with 12 ppm, and the highest N_2 ratio was measured in the CW-SG3 mixture with 32.1%.

Keywords: Hydrogen sulfide, Nitrogen, Renewable energy, Biogas, Biomass

***Corresponding author:** Kırşehir Ahi Evran University, Çiçekdağı Vocational School, Department of Plant and Animal Production, 40700, Kırşehir, Türkiye
E mail: cevat.filikci@ahievran.edu.tr (C. FİLİKCİ).
Cevat FİLİKCİ https://orcid.org/0000-0002-4169-8412
Tamer MARAKOĞLU https://orcid.org/0000-0002-2824-116X

Received: November 30, 2024
Accepted: January 06, 2025
Published: March 15, 2025

Cite as: Filikci C, Marakoğlu T. 2025. Effect of different substrates on H_2S and N_2 production in biogas production. BSJ Eng Sci, 8(2): 398-404.

1. Introduction

Energy can be defined as the ability of an object or system to do work. The main types of energy are chemical energy, heat energy, electrical energy and mechanical energy. These energies can be converted into each other with energy conversion systems. However, they become capable of doing work. The current source of energy in the world is solar energy. Most renewable energy sources get their energy directly or indirectly from the sun. For this reason, these resources are not exhausted because they are constantly renewed.

Biogas, whose production has increased rapidly in the world and in our country in recent years, has been the most remarkable among these energy sources, especially the fact that its production is easy and cheap and that it can provide the energy needed in many areas such as fuel, heating, lighting, etc. has caused the studies on biogas to gain momentum. In addition, the fact that the raw material left over from biogas production can be used in an area such as greenhouse cultivation is another advantage (Khalil et al., 2019).

Anaerobic bacteria produce biogas, a high-calorie gas produced by the decomposition of plant waste, animal feces and agricultural wastewater in special organic-loaded hermetic containers. In other words, biogas is a colorless and flammable gas mixture produced by the decomposition of organic materials such as plant and animal wastes in the absence of oxygen, containing 40-75% methane, 20-50% CO_2 and a small amount of H_2S and very little hydrogen, water vapor, ammonia, carbon monoxide and nitrogen (Filikci, 2024).

In the acid-forming step, acetogenic bacteria convert soluble organic matter into polycarbonate volatile fatty acids (acetic acid, butyric acid, propionic acid, valenic acid); carbohydrates into ethanol, H_2 and CO_2 and; amino acids, succinic acid and H_2; fatty acids into acetate and H_2. In the third step, biogas is produced with organic acids, H_2 and acetate with the help of methane-forming microorganisms. In this step, 70% of the methane produced comes from decarboxylation of acetate and the rest from CO_2 reduction reactions of methane bacteria using hydrogen. The stages of biogas formation are given in Figure 1 (Anonymous, 2023a).

This work is licensed (CC BY-NC 4.0) under Creative Commons Attribution 4.0 International License

Table 1. Composition Ratios of biogas

Biogas Component	Chemical Formula	Ratio (%)
Methane	CH_4	40-75
Carbon dioxide	CO_2	20-50
Water Vapor	H_2O	0.10
Nitrogen	N_2	0-2
Oxygen	O_2	0-0.5
Hydrogen	H_2	0-1
Ammonia	NH_3	0-0.5

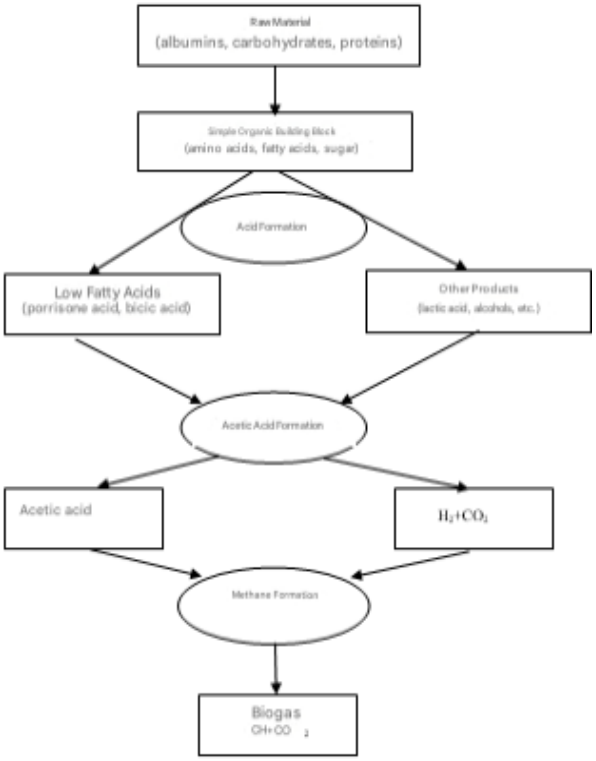


Figure 1. Biogas ProductionStages(Anonymous, 2023a).

Metogenic and anaerobic bacteria use carbon (C) atoms for energy and nitrogen (N) atoms are essential components for bacterial growth and reproduction. The C/N ratio cannot be more than 23 and less than 10. If it is less than 10, ammonia formation occurs in the reactor and this formation negatively affects biogas production. If it is more than 23%, volatile fatty acids are formed and slow down biogas production by showing an inhibitory effect(Anonymous, 2023b).

If C/N is not in equilibrium (suitable), this ratio can be reduced or increased by using gypsum or urea in certain amount(Buğutekin, 2007). If substrates with very low C:N ratio are used, ammonia production increases and methane production is prevented. If substrates with too high C:N ratio are used, protein formation is negatively de due to nitrogen deficiency and the growth and reproduction rate of microorganisms slows down (Deublein andSteinhauser, 2008). Co-fermentation method is mostly used to ensure nutrient balance in anaerobic process. In the co-fermentation method, anaerobic fermentation is realized by using different waste types together. Thus, problems that may arise due to the use of a single type of substrate are prevented (Karlsson et al., 2014).

Methane-producing bacteria constitute the most sensitive group to toxicity in anaerobic digestion, but they are to some extent resistant to many toxic substances and have the ability to acclimatize against them. Many waste contents are toxic to the digestive system. Ammonia has a positive effect on the system in the concentration range 200-1000 $mg.L^{-1}$, while exceeding a concentration of 3000 $mg.L^{-1}$has an inhibitory effect. Similarly, many cations (sodium, potassium, calcium, magnesium, etc.) have a positive effect on the system at low concentrations, while inhibition can occur if concentrations increase (Allegue et al., 2012).

Carbon dioxide (CO_2) is a gas that reduces the consumption of biogas and reduces its calorific value, but it is not as harmful and destructive as H_2S and N_2. Hydrogen sulfur and nitrogen causes environmental pollution and causes deterioration of metallic engine parts, siphons, blowers, gas capacity tanks, valves and shortens the life of the energy (Huertas et al., 2011). The presence of these gases is the limit of the heat energy produced by the combustion of methane. For a better quality methane, biogas should be purified from these gases using biogas purification techniques. (Allegue et al., 2012).

In this study, different mixtures were determined and biogas was produced. As a result of the measurements, the biogas components of each mixture were measured using the optima gas analyzer device. H_2S and N_2 ratios obtained from different substrates were determined. The effect of these ratios on biogas production was analyzed.

2. Materials and Methods

Two different agricultural wastes (beet leaves and switchgrass) and cattle waste were used in the study. The reason for this is that switchgrass is selected as a sample plant among 37 plants in the United States, where its production is the highest, due to its value as a feed source and its strong bio-energy capacity. It is a plant that is encouraged for production for energy and animal feed purposes due to its high net energy production per unit area, low cultivation costs, low ash content, high water utilization rate, developed adaptation ability, easy application of seed production in all lands and sufficient carbon storage in the soil (Samson and Omielan, 1992; Sanderson et al., 1996). However, the reason why sugar beet leaves are preferred is that the production area in our region (Konya, Aksaray) is large and to determine the ways to convert this green biomass into energy. The study was carried out in three different application groups. In the 1st experimental group, biogas production was realized separately from all materials. In the 2nd experimental group, cattle waste was kept constant at a

rate of 50% and mixtures were formed as 1:2 / 1:2 with other materials and biogas production was realized. The 3rd experimental group was prepared by selecting the switchgrass plant variety with the highest biogas yield in the 2nd experimental group. In the 3rd experimental group, the amount of cattle waste was kept constant at 50% and the other materials (switchgrass and beet leaves) were mixed at different ratios and biogas production was realized. The experimental design is given in Table 2.

Table 2. Experimental design

1st experimental	2nd experimental	3rd Experimental
CW	CW-SG1	CW(%50)- SG(%25) -BL(%25)
SG1 (Kanlow)	CW-SG2	CW(%50)- SG(%30) -BL(%20)
SG2 (Shawne)	CW-SG3	CW(%50)- SG(%20) -BL(%30)
SG3 (Alamo)	CW-BL	
BL		

2.1. Determination of Biomethane Potential (BMP)

In the applications, 1000 ml volume glass jar bottles were used as reactors in determining the biomethane potential (Figure 2). The application setup was set up in an isolated area to protect it from sunlight. The reactors were operated in mesophilic (37±° C) conditions. JSR - JSIB-22T Series / circulating water bath device and BW-10H heating bath (11.5l) device were used to keep the temperature constant. In order to measure the amount of biogas produced in the reactors, 2 glass jars operating according to the water displacement principle were connected to each other with pneumatic sealing elements. The first glass jar connected to the reactor was filled to the brim with water acidified with sulfuric acid (H_2SO_4) (pH<2) and closed (Durgut, 2020). The volume determination was made by drawing on the glass jars from the Solidworks program on the PC and the volumes corresponding to each mm length were determined and added to the glass jars in order to make the readings. In order to measure the gas content of the gas between the reactor and the glass jar filled with acidified water, a valve was added to the connection line between the two glass jars. At the end of the applications, the gas storage balloon collected by means of the valve was taken and the gas content was determined. As a result of the applications, measurements were made with the help of scales added to the glass jars filled with water in order to determine the amount of biogas released and recorded in the computer environment. With the termination of the gas output, the gases collected in the balloons by means of the valve were stored and the biogas contents were measured with the help of a measuring device.

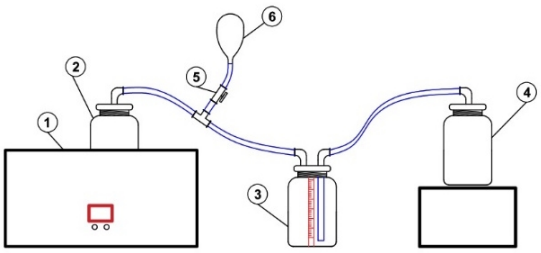


Figure 2. Experimental setup (1. Water Bath Device, 2. Reactor (Glass Jar), 3. Acidified Water (Gas Outlet), 4. Water Inlet, 5. Gas Sampling Valve, 6. Gas Storage Flask).

2.2. Determination of Mixing Ratios Used in Experiments

One of the desired reactor conditions for the best use of bacterial groups performing fermentation in an anaerobic environment in terms of producing biogas and methane content is the dry matter level of the feed materials used (Nagamani andRamasamy, 1999; Von Mitzlaff, 1988). Biogas production is best when the total dry matter ratio of the feed materials is between 6-13% (Šarapatka, 1993). Different mixing ratios were determined by optimizing the three different switchgrass varieties and beet leaf samples with the cattle waste kept constant.

2.3. Basic Characterization Analysis Values

Dry Matter, Raw Ash and Organic Matter analyses were carried out in the laboratory of the Soil Science and Plant Nutrition Department within the Faculty of Agriculture of Konya Selçuk University.

3. Results and Discussion

3.1. Basic Characterization Analysis Values

Basic characterization analyses were carried out to determine the amounts of energy plant switchgrass, sugar beet leaves and cattle waste to be added to the application mechanism established for the Determination of Biomethane Potential and to provide the desired amount of solid matter in the reactor (Table 3).

3.2. Amounts of Biogas Obtained From the Experiments

In the experimental setup, biogas measurements were carried out after 30 days in Experiment 1, 16 days in Experiment 2 and 43 days in Experiment 3, after the biogas production of the materials ended. Biogas production values are given in Table 4.

In the application, the highest daily biogas yield values were obtained as of the 11th day. It was measured as 242 mL.gDM^{-1} in CW, 180.2 mL.gDM^{-1} in SG1 (Kanlow), 119.2 mL.gDM^{-1} in SG2 (Shawne) and 99.4 mL. gDM^{-1} in SG3 (Alamo), respectively (Figure 3). When the biogas yield value was examined, the highest yield value was determined as 3504.07 mL in CW at the end of 30 days. Other total biogas yield values obtained at the end of 30 days were 2148.8 mL.gDM^{-1} , 1971.4 mL.gDM^{-1} , 1058.4 mL.gDM^{-1} and 822.5 mL.gDM^{-1} from BL, SG1(Kanlow), SG2(Shawne), SG3(Alamo) materials, respectively. Liew

et al. (2012) investigated methane production from corn cob, wheat straw, garden waste and leaves by anaerobic fermentation. The highest methane yield (81.2 L .kg DM^{-1}) was obtained from corn cob. This was followed by wheat straw (66.9 L .kg DM^{-1}), leaves (55.4 L .kg DM^{-1}) and garden waste (40.8 L .kg DM^{-1}).

In the application group 2, the highest biogas yield value was determined as 707.82 mL .g DM^{-1}in total from CW-SG1 mixture (Figure 4). Other biogas yield values were determined as 462.7 mL .g $DM^{-1}$from CW-SG mixture, 119 mL .g $DM^{-1}$from CW-SG2 mixture and 198 mL .g $DM^{-1}$from CW-SG3 mixture, respectively. Ahn et al. (2010) investigated the biogas production potential of switchgrass - animal (cattle, poultry and pig) manure mixtures. The maximum methane yield was determined as 337 mL .g DM^{-1}in pig manure, 28 mL .g DM^{-1} in cattle manure and 2 mL .g DM^{-1} in poultry manure.

Table 3. Organic matter (%), dry matter (%) and ash ratio (%) values

Sample Name	Ash (%)	Organic Matter (%)	Sample Weight (gr)	Oven Dry Weight (gr)	Dry Matter (%)
SG-1 (Kanlow)	93.08	6.92	4.6506	4.3286	93.076
SG-2 (Aloma)	93.58	6.42	3.1603	2.9573	93.576
SG-3 (Shelter)	93.70	6.30	3.7667	3.5295	93.702
Beet Leaves	14.29	85.71	20.4167	2.9174	14.289
Cattle Waste	9.88	90.12	14.8338	1.4657	9.880

Table 4. Total biogas yield values of the experiments (mL.gDM-1)

Material	Biogas Yield Values
CW	3504.07
SG1(KANLOW)	1971.4
SG2(SHAWNE)	1058.4
SG3(ALAMO)	822.5
BL	2148.8
CW-SG1	707.82
CW-SG2	119
CW-SG3	198
CW-BL	462.7
CW(%50)- SG(%25)-BL(%25)	151
CW(%50)- SG(%30)-BL(%20)	1913
CW(%50)- SG(%20)-BL(%30)	1997.5

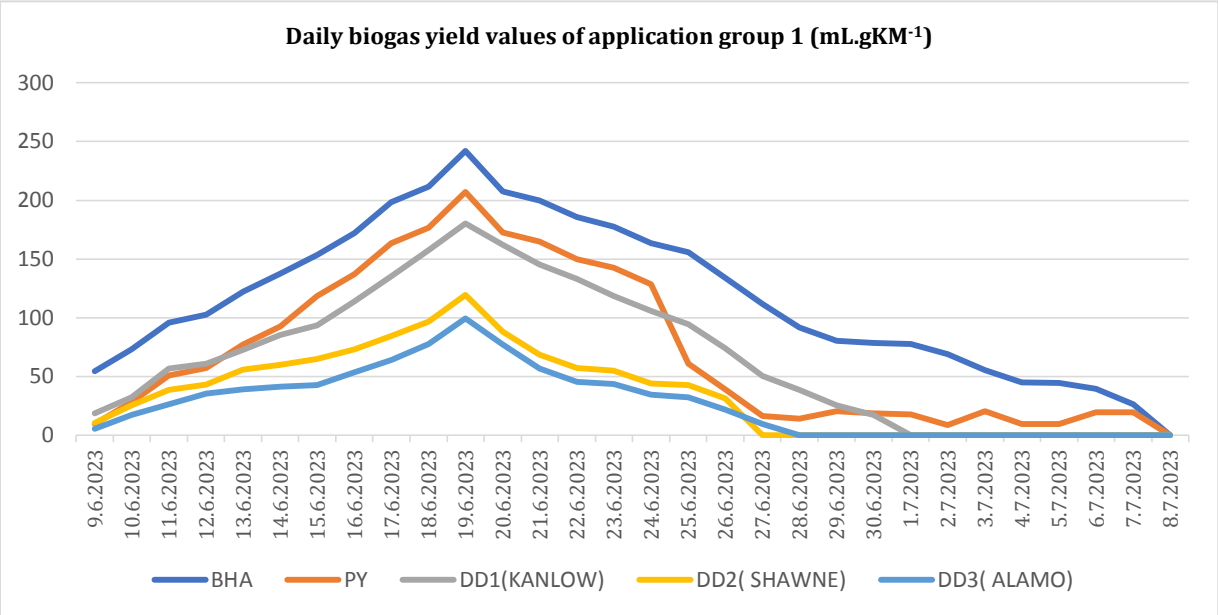


Figure 3. Daily biogas yield values of application group 1 (mL.gKM-1). *BHA=CW, PY=BL, DD=SG.

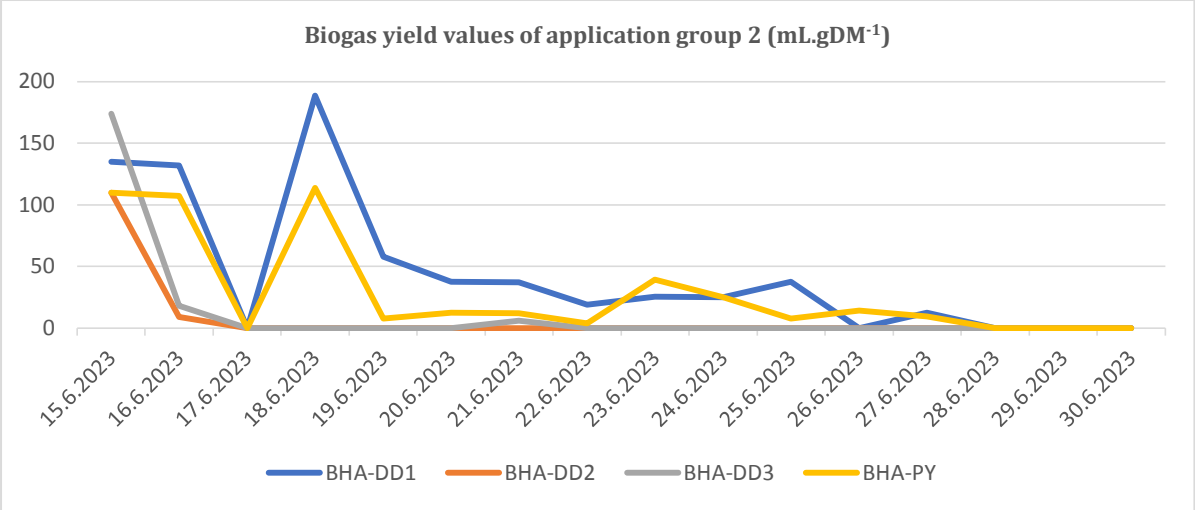


Figure 4. Daily biogas yield values of application group 2 (mL.gKM-1). *BHA=CW, PY=BL, DD=SG.

In the 3rd application group, the highest biogas yield value was determined as 1997.5 mL .g DM^{-1}in total from the mixture of CW(50%)- SG(20%)- BL(30%) (Figure 5). Other biogas yield values in the 3rd application group were determined as 1913 mL .g $DM^{-1}$from the mixture of CW(50%)- SG(30%)- BL(20%) and 119 mL .g $DM^{-1}$from the mixture of CW(50%) - SG(25%)- BL(25%), respectively. In the study conducted by Lehtomäki et al. (2007), anaerobic treatment of mixtures of energy crops and crop wastes with manure in a semi-batch complete mixed reactor was investigated. While the highest methane yield that could be achieved as a result of anaerobic fermentation of cow manure alone was 155 mL .g DM^{-1} , the highest methane yields were found as 268, 229, 213 mL .g DM^{-1}, respectively, with anaerobic fermentation of cow manure with grass, sugar beet and oat straw in certain proportions.

3.3. Biomethane Ratios of Biogas Produced from Experiments

The biomethane components of the biogas produced from the experimental groups were determined and the highest CH_4 (methane) yield was determined as 58.86% in BL (beet leaf) materials and 53.76% in CW-BL mixtures. The methane yields of other mixtures and materials in the experiments varied between 53.22% and 43.12 % (Table 5). In their study, Sheets et al. (2015) also investigated the effect of dry matter ratio in the mixtures with temperature on methane yield from switchgrass. In the reactor operating as solid fermentation in biomethane production, the highest biomethane yield was obtained at 13% and 22% under mesophilic conditions. Ciggin (2016) mixed switchgrass with process sludge in his study. According to the test results, the highest methane yield was found in the mixture with a ratio of 0.4-0.6. In their study, Liew et al. (2012) investigated methane production from corncob, wheat straw, garden waste and leaves by anaerobic fermentation. The highest methane yield was obtained from corncob (81.2 l/kgUKM). This was followed by wheat straw (66.9 L/kgUKM), leaves (55.4 L/kgUKM) and garden waste (40.8 L/kgUKM).

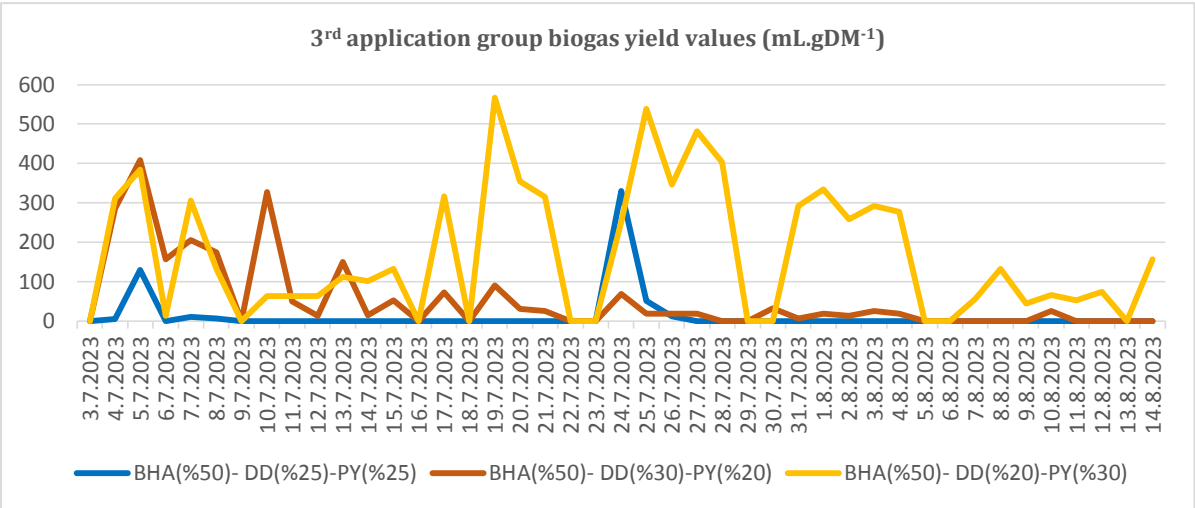


Figure 5. Daily biogas yield values of application group 3 (mL.gKM-1). *BHA=CW, PY=BL, DD=SG. * BHA=CW, PY=BL, DD=SG.

Table 5. Biomethane components of biogas produced from experiments

Material	CH_4 (%)
CW	53.42
SG1(KANLOW)	47.4
SG2(SHAWNE)	46.76
SG3(ALAMO)	43.12
BL	58.86
CW-SG1	49.78
CW-SG2	48.43
CW-SG3	44.86
CW-BL	53.76
CW(%50)- SG(%25)-BL(%25)	51.74
CW(%50)- SG(%30)-BL(%20)	50.86
CW(%50)- SG(%20)-BL(%30)	53.22

3.4. Hydrogen sulfide and Nitrogen Components of Biogas Produced from Experiments

The hydrogen sulfide and nitrogen ratios of the biogas produced from the experimental groups were determined and are given in Table 6. The highest values were reached as 26.18% and 27.79% in the CW-SG1 and CW-SG2 experiments, respectively.

Tablo 6. Hydrogen sulfide and nitrogen components of biogas produced from experiments

Material	H_2S (ppm)	N_2 (%)
CW	12	19.61
SG1(KANLOW)	6	25.25
SG2(SHAWNE)	5	25.17
SG3(ALAMO)	5	26.8
BL	9	24.92
CW-SG1	9	26.18
CW-SG2	8	27.79
CW-SG3	7	32.1
CW-BL	10	20.68
CW(%50)- SG(%25)-BL(%25)	9	23.92
CW(%50)- SG(%30)-BL(%20)	9	24.92
CW(%50)- SG(%20)-BL(%30)	10	21.84

High percentage of CH_4 ratio is important in biogas production. In the study, it was observed that high hydrogen sulphide and nitrogen ratios naturally reduce methane production. Again, the low hydrogen sulphide and nitrogen ratios in our mixtures, especially in the mixtures containing switchgrass, showed that switchgrass has a higher methane production in terms of biogas production.

Ghatak and Mahanta (2016) conducted a Biogas Purification experiment using Chemical Absorption in their study. In this experiment, raw biogas was compressed and stored in air compressor. Compressed biogas is allowed to pass through scrubber by changing the inlet pressure from 1 bar to 5 bar in the range of 1 bar with the help of pressure regulator. The flow rate of inlet biogas is changed from 1 lpm to 5 lpm in 1 lpm steps with the help of rotameter. Raw biogas and purified gas exiting from scrubber are tested for composition analysis with the help of Gas Chromatography (GC). The percentage of raw biogas was found to be 41.5%. It was discovered that the process of using soda lime as absorbent is used where the percentage of carbon dioxide in the outlet gas decreases with the increase in inlet pressure and the percentage of carbon dioxide in the outlet gas increases with the increase in inlet gas flow rate in case of vertical scrubber. Here the minimum carbon dioxide content present in biogas can be reduced up to 1.34% in the off-gas at 5 bar and 1 lpm flow rate of biogas. The biogas was found to be enriched with 97.7% methane.

Song et al. (2020) conducted an experiment of Air Addition as a Stimulation Approach for the Enhancement of in Situ Desulfurization and Methanization of Anaerobic Digestion of Chicken Manure. Biogas produced by anaerobic digestion of chicken manure has a high H_2S level (5000-6000 ppm), which makes biogas plants economically unviable. In their study, they investigated in situ desulfurization by injecting restricted air into the headspace of a digester and the effects on process performance and injection techniques under various oxygen loads (1.4, 2.8, and 4.2 $mL.gVSin^{-1}$). The results showed that a constant oxygen load of 4.2 mL/gVSin removed 99.7% of H_2S (up to 1015 ppm) and simultaneously increased methane output by 6.4 percent.

4. Conclusions

This study evaluated various mixtures for their potential in biogas production. The biogas components of each mixture were analyzed using an Optima gas analyzer. The ratios of hydrogen sulfide (H_2S) and nitrogen (N_2) extracted from different substrates were determined, and their impacts on biogas production were examined. A laboratory-scale setup was created to conduct the biogas production experiments. In this context, three distinct applications were developed, along with a comprehensive experimental framework. Biogas measurements were recorded in a digital environment over periods of 16, 30, and 43 days, focusing on the endpoint of biogas production for the materials used.

Throughout the measurement period, temperature and pH values were periodically monitored, and the mixing process was performed daily through manual shaking. The applications were designed with an emphasis on maintaining a 10% dry matter content.

Biogas production has an important place among sustainable energy sources. However, the quality of biogas can vary depending on the amount of various gases in it. Among the most important of these gases are hydrogen sulfide (H_2S) and nitrogen (N_2). The effects of these two gases on biogas production are very important.

Author Contributions

The percentages of the authors' contributions are presented below. All author reviewed and approved the final version of the manuscript.

	C.F.	T.M.
C	60	40
D	60	40
M	60	40
DCP	60	40
DAI	60	40
LR	60	40
W	60	40
CR	60	40
SR	60	40
PM	60	40
FA	60	40

C= concept, D= design, M= management, DCP= data collection and/or processing, DAI= data analysis and/or interpretation, LR= literature review, W= writing, CR= critical review, SR= submission and revision, PM= project management, FA= funding.

Conflict of Interest

The authors declared that there is no conflict of interest.

Ethical Consideration

Ethics committee approval was not required for this study because of there was no study on animals or humans.

References

Ahn HK, Smith M, Kondrad S, White J. 2010. Evaluation of biogas production potential by dry anaerobic digestion of switchgrass–animal manure mixtures. Applied Biochem Biotech, 160: 965-975.

Allegue LB, Hinge J, Allé K. 2012. Biogas and bio-syngas upgrading. Danish Technol Institut, 2012: 5-97.

Anonymous. 2023a. Biogas formation stages, biogas usage areas. URL: https://bepa.enerji.gov.tr/ (accessed date: September 24, 2023).

Anonymous. 2023b. Some materials used in biogas production. URL: https://bepa.enerji.gov.tr/ (accessed date: September 24, 2023).

Buğutekin A. 2007. Atıklardan biyogaz üretiminin incelenmesi. Ph.D. Thesis, Marmara University, Institute of Science, İstanbul, Türkiye, pp: 157.

Ciggin A. 2016. Anaerobic co-digestion of sewage sludge with switchgrass: Experimental and kinetic evaluation. Energy Sourc Part A: Recov Util Environ, 38 (1): 15-21.

Deublein D, Steinhauser A. 2008. Biogas from waste and renewable resources. Wiley, Weinheim, Germany, 2nd ed, pp: 539.

Durgut FT. 2020. Deneysel amaçlı prototip bir biyogaz reaktörünün imalatı ve farklı biyokütle karışımları ve ortamlarda performansının değerlendirilmesi. Ph.D. Thesis, Tekirdağ Namık Kemal University, Institute of Science, Tekirdağ, Türkiye, pp: 88.

Filikci C. 2024. Bazı bitkisel ve hayvansal atıklar ile dallı darı (Panicum Virgatum L.) karışımlarının biyogaz veriminin incelenmesi. Ph.D. Thesis, Selçuk University, Institute of Science, Konya, Türkiye, pp: 87.

Ghatak MD, Mahanta P. 2016. Biogas purification using chemical absorption. Inter J Engin Technol, 8(3): 1600-1605.

Huertas JI, Giraldo N, Izquierdo S. 2011. Removal of H_2S and CO_2 from Biogas by Amine Absorption. Mass Trans Chem Engin Proces, 307: 133-150.

Karlsson A, Björn Annika S, Shakeri Y, Svensson B. 2014. Improvement of the biogas production process: Explorative project (EP1). Biogas Research Center (BRC) Report: 2, In: Linköping University Electronic Press, Linkoping, Sweden, pp:73

Khalil M, Berawi MA, Heryanto R, Rizalie A. 2019. Waste to energy technology: The potential of sustainable biogas production from animal waste in Indonesia. Renew Sustain Ener Rev, 105: 323-331.

Lehtomäki A, Huttunen S, Rintala J. 2007. Laboratory investigations on co-digestion of energy crops and crop residues with cow manure for methane production: effect of crop to manure ratio. Res Conserv Recycl, 51 (3): 591-609.

Liew LN, Shi J, Li Y. 2012. Methane production from solid-state anaerobic digestion of lignocellulosic biomass. Biomass Bioen, 46: 125-132.

Nagamani B, Ramasamy K. 1999. Biogas production technology: an Indian perspective. Current Sci, 1999: 44-55.

Samson RA, Omielan JA. 1992. Switchgrass: A potential biomass energy crop for ethanol production. The Thirteenth North American Prairie conference, Windsor, Ontario, USA, pp:253-258.

Sanderson MA, Reed R, McLaughlin S, Wullschleger SD, Conger BV, Parrish D, Wolf D, Taliaferro C, Hopkins A, Ocumpaugh W. 1996. Switchgrass as a sustainable bioenergy crop. Bioresour Technol, 56 (1): 83-93.

Šarapatka B. 1993. A study of biogas production during anaerobic fermentation of farmyard manure. Biomass and Bioenergy, 5(5): 387-393.

Sheets JP, Ge X, Li Y. 2015. Effect of limited air exposure and comparative performance between thermophilic and mesophilic solid-state anaerobic digestion of switchgrass. Bioresour Technol, 180:296-303.

Song Y, Mahdy A, Hou Z, Lin M, Stinner W, Qiao W, Dong R. 2020. Air Supplement as a Stimulation Approach for the In Situ Desulfurization and Methanization Enhancement of Anaerobic Digestion of Chicken Manure. Ener Fuels, 34(10): 12606–12615.

Von Mitzlaff, K. 1988. Engines for biogas. Deutsche Zentrum fur Entwicklungstechnologien, Berlin, Germany, pp: 132.

Black Sea Journal of Engineering and Science
doi: 10.34248/bsengineering.1592949

Open Access Journal
e-ISSN: 2619 – 8991

Research Article
Volume 8 - Issue 2: 405-417 / March 2025

UTILIZATION OF WASTE HEAT IN CLOSED BRAYTON CYCLE: A THERMODYNAMIC ANALYSIS WITH VARIOUS WORKING FLUIDS

Gamze SOYTÜRK[1]*

[1]*Isparta University of Applied Sciences, Faculty of Technology, Department of Mechanical Engineering, 32200, Isparta, Turkey*

Abstract: This research investigates the thermodynamic performance of a power generation system employing five working fluids: helium, carbondioxide, nitrogen, argon, and neon. Key parameters like net power generation, exergy destruction, energy and exergy efficiencies, and mass flow rates were evaluated under varying operational conditions. The analysis revealed that carbondioxide consistently outperformed other fluids, achieving the highest net power generation of 450 kW at lower compressor inlet temperatures, and maintaining the lowest exergy destruction of approximately 500 kW. Additionally, carbondioxide exhibited superior energy and exergy efficiencies, with values reaching 31% and 45%, respectively. Nitrogen and argon demonstrated moderate performance, with nitrogen achieving a stable net power generation of around 250 kW and an exergy destruction of approximately 700 kW. Both fluids-maintained energy efficiencies near 17% and exergy efficiencies of approximately 25%, making them suitable for balanced thermodynamic systems. In contrast, neon and helium showed limited performance, with neon recording the lowest net power generation of 170 kW and a relatively high exergy destruction of 770 kW. Helium similarly exhibited reduced efficiencies, with energy efficiency dropping to 13% and exergy efficiency to 19% under varying conditions. Mass flow rate analysis indicated argon required the highest flow, at approximately 9.5 kg/s, while helium maintained the lowest at 1 kg/s, reflecting their respective densities and energy transport capacities. These findings underline the critical role of working fluid selection, with carbondioxide emerging as the optimal choice for systems prioritizing high efficiency and minimal energy losses. The study provides a comprehensive framework for enhancing thermodynamic performance in power generation applications.

Keywords: Waste heat recovery, Power generation systems, Working fluids, Thermodynamic analysis

***Corresponding author:** Isparta University of Applied Sciences, Faculty of Technology, Department of Mechanical Engineering, 32200, Isparta, Turkey
E mail: gamzeyildirim@isparta.edu.tr (G. SOYTÜRK)
Gamze SOYTÜRK https://orcid.org/0000-0001-7191-8765

Received: November 29, 2024
Accepted: January 07, 2025
Published: March 15, 2025

Cite as: Soytürk G. 2025. Utilization of waste heat in closed Brayton cycle: A thermodynamic analysis with various working fluids. BSJ Eng Sci, 8(2): 405-417.

1. Introduction

The need to reduce environmental effects and the growing demand for energy worldwide have made improving power generation systems' efficiency even more important. A critical aspect of this enhancement lies in the selection of appropriate working fluids, which significantly influence the thermodynamic performance of these systems. Closed-cycle gas turbines and Organic Rankine Cycles (ORCs) have emerged as viable technologies for harnessing energy from diverse sources, including waste heat, liquefied natural gas (LNG), and industrial processes. In addition to increasing energy efficiency, these technologies are essential for lowering greenhouse gas emissions and halting climate change.

In addition to being a crucial strategy for advancing the shift to a low-carbon economy and meeting climate targets, industrial waste heat recovery, or WHR, is also a vital step in fostering sustainable growth and protecting the environment. In energy-intensive industries such as iron and steel production, waste heat represents a substantial untapped energy resource. Research has shown that waste heat recovery systems integrated with ORCs can transform low, medium, and high-temperature heat sources into electricity, significantly enhancing energy efficiency and reducing carbon emissions. For instance, the iron and steel industry alone accounts for nearly 5% of global energy consumption, making it a prime candidate for waste heat recovery solutions. Studies have demonstrated that ORCs can efficiently utilize heat sources below 400°C, converting waste energy into usable electricity, thereby reducing reliance on external power grids. A research by Campana et al. (2013) assessed the potential for energy savings and the reduction of CO_2 emissions using ORC systems in conjunction with industrial waste heat recovery. In the most promising industrial sectors of the 27 EU member states, they reported that ORC technology might save 20.000 GWh of energy annually and reduce CO_2 emissions by 7.6 Mt. Chen et al. (2016) investigated the potential of ORCs to generate energy from the surplus heat present at UK industrial sites that participate in the EU ETS. The findings demonstrated that raising the temperature of the available heat source boosts the Carnot efficiency.

This work is licensed (CC BY-NC 4.0) under Creative Commons Attribution 4.0 International License

According to Petr and Raabe (2015), R1234ze(Z) has favourable thermophysical characteristics and may be a viable substitute for R245fa in an ORC system in conjunction with an industrial waste heat recovery system, where the heat source temperature ranges from 183℃ to 224℃ The parametric evaluation of the ORC was carried out by D.K. Kim et al. (2017) utilizing R245fa as the working fluid and a low-grade waste heat below 80 °C. He discovered that at a heat source temperature of 80 °C, the system can produce 411.3W with an efficiency of 3.6%.

Recent advancements in thermodynamic cycle design, such as the incorporation of real gas Brayton cycles, have further expanded the potential for waste heat recovery (Farrukh et al., 2023). By selecting working fluids like nitrogen and carbondioxide, which exhibit favourable critical properties, these systems can maximize energy recovery while minimizing exergy destruction. These innovations are particularly relevant for applications involving cryogenic energy utilization and high-efficiency waste heat recovery (Jafari et al., 2023). In order to attain greater thermal efficiency, Xu and Yu (2014) suggested R245fa and R141b as the ideal working fluids, highlighting the importance of the critical temperature as a determining factor in fluid selection. According to their recommendations, the crucial temperature should be between 30 and 100 K below the waste gas inlet 5 temperature, respectively. Using low-grade waste heat at 85 °C, Zhao et al. (2012) examined the system parameters with various working fluids and concluded that R123 was an efficient working fluid in terms of high thermal efficiency and turbine power production. A new kind of cogeneration system for collecting gas turbine waste heat was proposed by Li et al. (2020). The results demonstrated that the energy efficiency improved by 4.62% to a maximum of 52.53% when the turbine input temperature was 375.4°C. The effects of system parameters (heat storage temperature, temperature difference, and component efficacy) and heat source conditions (flow rate and temperature) were assessed by In their thermodynamic model of a system, Hu et al. (2021) used solar energy, waste heat, and a district heating network. Andreasen et al. (2014) published an approach for selecting the working fluid for an ORC unit that employs low-temperature heat. After the ORC unit was optimized, thirty pure and mixed working fluids were chosen. To recover low-grade waste heat, Yang et al. (2019) suggested a system that combines the absorption refrigeration cycle (ARC) waste heat recovery system with a transcritical CO_2 cycle. According to the findings, the suggested solution performed better at lower ARC refrigeration temperatures. The effectiveness of an ARC system powered by ship waste heat for refrigeration was examined by Salmi et al. (2017). The LiBr-water working pair was more effective than the others, according to the results. Additionally, recovering the waste heat for cooling resulted in a 70% reduction in compressor power consumption. Hajabdollahi et al. (2013) conducted a thermo-economic optimization study that focused on the overall cost and thermal efficiency for diesel waste heat. Their findings indicated that R123 was the best working fluid; R245fa showed comparable results. Mocanu et al. (2024) investigated the reduction of waste heat from the exhaust gas of the internal combustion engine in a series of diesel-electric hybrids buses. They compared the performance of the split-flow supercritical CO_2 recompressions Brayton cycle with the steam Rankine and Organic Rankine cycles by examining the heat recovery and conversion into useful power of the Brayton cycle. Alzuwayer et al. (2024) introduced a cascade system that uses exhaust gases from a marine gas turbine propulsion system as a heat source for the bottom supercritical CO_2 Brayton cycle. The study focused on recompression cycle schemes by analyzing parameters such as CO_2 mass flow rate and the efficiency of low-temperature and high-temperature recuperators to improve the overall system efficiency. Rad et al. (2024) studied the feasibility of utilizing waste heat from refinery exhaust flares by interesting a closed Brayton cycle with an ORC and an absorption cooler. In this research, they analyzed various working fluids including air, helium, oxygen, carbon dioxide, xenon, and nitrogen to improve the system performance through parametric studied and optimization.

Despite these advancements, there remains a critical need for a more comprehensive and systematic comparison of fluids across a broader range of operational conditions to better understand their behaviour and performance. Key factors, such as PR (PR), turbine inlet temperature, and compressor inlet temperature, play pivotal roles in determining the overall efficiency, power output, and thermodynamic effectiveness of power generation systems. Variations in these parameters can significantly influence fluid properties, such as specific heat capacity and thermal conductivity, thereby impacting energy conversion efficiency and exergy destruction. A deeper analysis of how each working fluid responds to these changes is essential for optimizing system design, ensuring robust performance, and tailoring solutions to meet the demands of specific industrial applications and waste heat recovery scenarios. This approach can help bridge existing knowledge gaps and provide a foundation for improving the energy efficiency and sustainability of advanced power generation cycles.

The purpose of this paper is to evaluate and compare the thermodynamic performance of a power generation system utilizing five different working fluids—helium, carbondioxide, nitrogen, argon, and neon—under various operating conditions. By analysing key metrics such as net power generation, exergy destruction, energy and exergy efficiencies, and mass flow rates, the study aims to identify the optimal working fluid for maximizing system efficiency and minimizing energy losses. The originality of this research lies in its comprehensive examination of multiple thermodynamic parameters across a wide range of conditions, offering detailed insights into the performance trade-offs associated with each fluid. Unlike

previous studies, this work integrates the effects of turbine inlet temperature, compressor inlet temperature, and PR into a unified framework, providing a robust comparison of fluid suitability for advanced power generation systems. This approach not only highlights the critical role of fluid selection in improving system efficiency but also contributes valuable data for optimizing the design and operation of thermodynamic cycles.

2. Materials and Methods

2.1. System Description

Figure 1 illustrates a complex thermodynamic cycle, likely representing a combined Brayton and Rankine cycle, which is optimized for efficient energy generation. The system integrates multiple compression and expansion stages, heat exchangers, and a recuperator to enhance thermal efficiency. Starting from the left, ambient air enters the first compressor (C1) and undergoes sequential compression through compressors (C2 and C3), with intercoolers (IC1 and IC2) placed between the stages to reduce the work of compression. After compression, the air flows through a gas cooler (GC) and a recuperator (REC), where waste heat from the cycle is recovered to preheat the working fluid. This preheated air is directed to the combustion chamber, where it mixes with fuel, and the high-temperature flue gases expand through the turbines (T1 and T2), generating mechanical power, which is converted into electricity via a generator. The waste heat from the flue gases is captured in a heat recovery steam generator section, shown as a flue gas heat exchanger, further improving system efficiency by transferring residual heat to other cycle components or processes. The integration of heat exchangers, intercoolers, and the recuperator emphasizes the system's focus on energy recovery and minimization of losses. The flue gases are eventually released after maximizing heat extraction, contributing to overall cycle efficiency. This system demonstrates an advanced thermodynamic design that balances power generation, waste heat recovery, and operational sustainability.

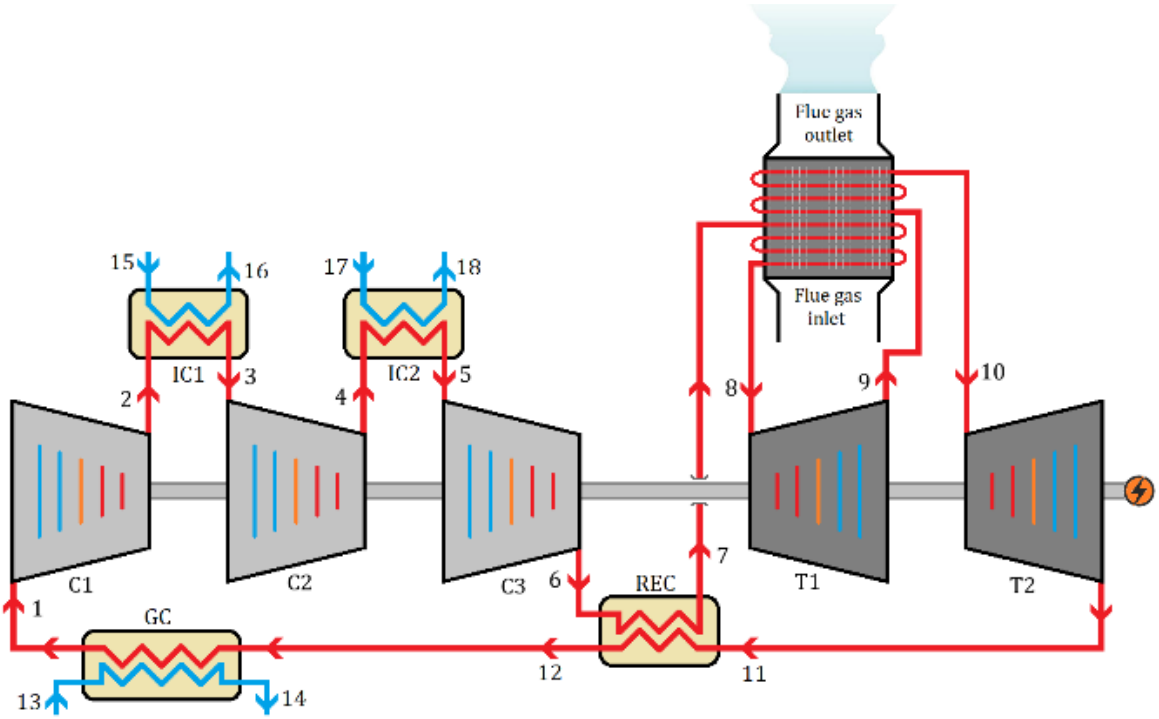


Figure 1. Schematic of a thermodynamic cycle with multi-stage compression, intercooling, recuperation, and dual-stage expansion.

2.2. Working Fluid Selection

The thermodynamic properties of the fluids considered in this research are summarized in the table 1, showcasing key parameters such as molecular mass, critical temperature, and critical pressure. These fluids include nitrogen, air, argon, oxygen, and methane, which are commonly used in various energy and cryogenic systems due to their unique physical characteristics. Nitrogen and air, with relatively low critical temperatures and pressures, are ideal for applications involving low-temperature processes. Argon and oxygen, with higher critical temperatures and pressures, are suitable for systems requiring efficient heat transfer and stable thermodynamic behavior under high-pressure conditions. Methane, characterized by its low molecular mass and moderately high critical temperature, is widely used in energy applications, particularly in power generation and refrigeration cycles. The diverse properties of these fluids allow for their application in a range of thermodynamic cycles, enabling optimized performance for specific operational requirements.

Table 1. Thermodynamic properties of selected working fluids (Angelino and Invernizzi, 2011)

Fluid	Molecular mass (g/mol)	Critical temperature (K)	Critical pressure (bar)
Nitrogen	28.014	126.2	33.98
Air	28.96	132.52	37.66
Argon	39.948	150.86	48.98
Oxygen	31.999	154.58	50.43
Methane	16.043	190.56	45.99

2.3. Thermodynamic Analysis

Establishing the equalities for mass, energy, entropy, and exergy balances is the first stage in thermodynamic evaluation (Arslan and Yılmaz, 2022). Determining characteristics such as the inlet and output power and heat rates, the entropy creation and destruction rates, and providing a summary of the energetic performance of the studied thermodynamic process all require it. This study will explore various modeling methodologies, beginning with the general balance equations of mass and energy and moving on to exergy analysis (Yılmaz et al., 2019). The following primary presumptions form the basis of this study's thermodynamic analysis:

•All system components are chosen to function in both steady-state and steady-flow scenarios; the reference state is taken to be 25°C and 101.325 kPa of pressure.

•Pump and turbine heat losses are not considered.

•When thinking about energy changes, the changes in potential and kinetic energies are neglected.

For a steady-state control volume, the general balance equation of mass is (Cengel and Boles, 2015):

$$\sum \dot{m}_{in} = \sum \dot{m}_{out} \quad (1)$$

The energy balance equation is as follows:

$$\sum \dot{E}_{in} = \sum \dot{E}_{out} \quad (2)$$

The subscripts "*in*" and ""*out*" in equations 1 and 2 indicate the inlet and exit points of the control volume, whereas $\dot{m}$ stands for the mass flow rate and $\dot{E}$ for the energy rate. According to Cengel and Boles, (2015) the energy balance equation is changed by adding heat and work factors to these equations:

$$\dot{Q} + \sum \dot{m}_{in} h_{in} = \dot{W} + \sum \dot{m}_{out} h_{out} \quad (3)$$

$\dot{Q}$ is the heat in the equation above, and $\dot{W}$ is the work.

The exergy balance is calculated as follows to perform a second law analysis of the plant (Dincer and Rosen, 2013):

$$\sum \dot{E}x_{in} = \sum \dot{E}x_{out} + \sum \dot{E}x_{dest} \quad (4)$$

In this case, $\dot{E}x$ denotes the rate of exergy and $\dot{E}x_{dest}$ denotes the rate of exergy destruction. Equation (5) can be written as follows by adding more exergy terms:

$$\dot{E}x_Q - \dot{E}x_W = \sum \dot{m}_{out} e_{out} - \sum \dot{m}_{in} e_{in} + T_0 \dot{S}_{gen} \quad (5)$$

The exergy associated with heat is represented by $\dot{E}x_Q$ in the above equation, the exergy associated with work by $\dot{E}x_W$, and the thermo-physical flow exergy by e. Entropy generation is shown by the equation's last term, $\dot{S}_{gen}$, which has the following definition (Bejan et al., 1996):

$$\dot{E}x_{dest} = T_0 \dot{S}_{gen} \quad (6)$$

The following formulas could be used to calculate the thermo-physical flow exergy and the exergy associated with heat and work (Dincer and Rosen, 2013):

$$\dot{E}x_Q = \dot{Q}\left(\frac{T - T_0}{T}\right) \quad (7)$$

$$\dot{E}x_W = \dot{W} \quad (8)$$

$$e = (h - h_0) - T_0(s - s_0) \quad (9)$$

where *h* stands for the specific enthalpy, *s* for the specific entropy, and the subscript *0* for reference circumstances.

Exergy efficiency is expressed as follows:

$$\eta_{ex} = \frac{\dot{W}_{net}}{\dot{E}x_{\dot{Q},in}} \quad (10)$$

Here $\dot{W}_{net}$ shows for the net power, $\dot{E}x_{\dot{Q},in}$ for exergy of net heat rate.

3. Results

This section presents the findings of a comprehensive thermodynamic analysis performed on a power generation system using five different working fluids: helium, carbondioxide, nitrogen, argon, and neon. The results are analyzed across varying operational conditions, including PR, turbine inlet temperature, and compressor inlet temperature, to evaluate their impact on key performance metrics. These metrics include net power generation, energy and exergy efficiencies, exergy destruction, and mass flow rates. The findings provide valuable insights into the comparative performance of the working fluids, highlighting their suitability for optimizing power generation systems and waste heat recovery processes. Table 2 provides key operational parameters and reference values used in the thermodynamic analysis of the power generation system. These parameters serve as the baseline for evaluating system performance and comparing the working fluids.

Table 2. Operational parameters and reference values for the thermodynamic analysis of the power generation system (Farrukh et al., 2023)

Parameters	Value
Reference temperature	25℃
Reference pressure	101.3 kPa
Total waste heat	1500 kW
Source temperature	650 ℃
Turbine inlet temperature	350 ℃
Compressor inlet temperature	35 ℃
Pressure ratio	3.5
Effectiveness recuperator	0.65
Compressor isentropic efficiency	0.85
Compressor isentropic efficiency	0.88

Figure 2 presents the comparison of net power generation (blue bars) and exergy destruction (orange bars) for

various working fluids: helium, carbondioxide, nitrogen, argon, and neon. The results provide insight into the performance and efficiency of these fluids in the described thermodynamic system. Helium and neon exhibit the lowest levels of net power generation (helium 191.2 kW, neon 185.6 kW), with neon producing even less power than helium. This indicates that neon is less effective as a working fluid in this system configuration. However, both fluids also demonstrate relatively high levels of exergy destruction (helium 751.7 kW, neon 712.8 kW), suggesting significant thermodynamic inefficiencies. Carbondioxide, on the other hand, shows the highest net power generation (437.1 kW) among the fluids, albeit with substantial exergy destruction. This highlights its strong potential for power generation but also points to room for improvement in reducing energy losses. Nitrogen and argon show moderate levels of net power generation compared to carbondioxide, with nitrogen slightly outperforming argon (nitrogen 247.3 kW, argon 231.1 kW). However, both fluids have lower exergy destruction compared to neon and helium, indicating a better balance between power generation and efficiency. Overall, the chart demonstrates the importance of selecting the appropriate working fluid based on system objectives. While carbondioxide excels in power generation, reducing its exergy destruction could further enhance its efficiency. Argon and nitrogen appear to provide a more balanced performance, whereas helium and neon are less suitable for achieving high net power output in this system.

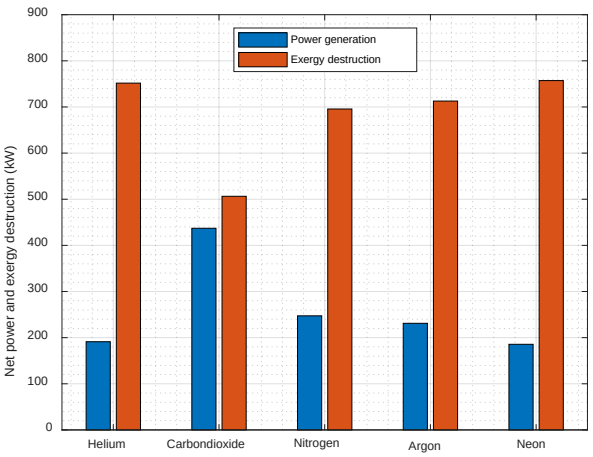


Figure 2. Comparison of net power generation and exergy destruction for different working fluids in the thermodynamic cycle.

Figure 3 displays the energy and exergy efficiencies for helium, carbondioxide, nitrogen, argon, and neon, providing a clear comparison of their performance in the thermodynamic system. The numerical values of these efficiencies, as derived from the chart, offer additional clarity. Carbondioxide stands out with the highest efficiency values, achieving an energy efficiency of 31.22% and an exergy efficiency of 45.75%. This demonstrates its strong potential to effectively convert energy while minimizing irreversibilities in the process. Nitrogen and argon follow with moderate performance, where nitrogen has an energetic efficiency of 17.66% and an exergetic efficiency of 25.88%, and argon shows similar values with an energy efficiency of 16.5% and an exergy efficiency of 24.18%. These results highlight the balanced performance of nitrogen and argon, where a significant portion of energy is effectively utilized at higher thermodynamic quality levels. Helium and neon show considerably lower efficiencies. Helium achieves an energetic efficiency of only 13.66% and an exergetic efficiency of 20%, making it the least efficient working fluid in this system. Neon performs slightly better, with an energy efficiency of 13.26% and an exergy efficiency of 19.43%, but it still falls short compared to carbondioxide, nitrogen, and argon. In summary, carbondioxide clearly emerges as the most efficient fluid in terms of energy and exergy utilization. Nitrogen and argon provide moderate efficiency and could serve as alternatives for systems requiring balanced performance. Helium and neon, however, exhibit poor efficiencies, indicating their limited suitability for high-performance thermodynamic systems. These quantitative findings underline the critical role of fluid selection in achieving optimal system performance.

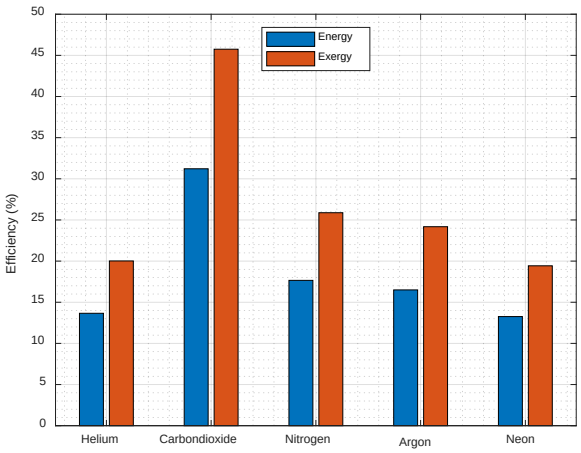


Figure 3. Energy and exergy efficiencies of different working fluids in the thermodynamic system.

Figure 4 illustrates the exergy destruction within various system components for five working fluids: helium, carbondioxide, nitrogen, argon, and neon. Each bar represents the contribution of a specific component—compressors, intercoolers, heat exchangers, gas cooler, recuperator, and turbines—to the general exergy destruction of the plant. Among all working fluids, the heat exchanger labelled HE1 contributes the highest exergy destruction, around 250 kW per fluid. This suggests that HE1 is the primary source of irreversibilities within the system and a critical target for efficiency improvement. Similarly, the gas cooler (GC) and HE2 also show significant exergy destruction, particularly for helium, nitrogen, and neon, emphasizing their substantial impact on system losses. The compressors (C1, C2, C3) and intercoolers (IC1, IC2) exhibit comparatively lower exergy destruction. Among these, C3 shows a slightly higher exergy

destruction for most fluids, especially for carbondioxide and neon, while the other compressors and intercoolers contribute minimally. The turbines (T1, T2) show relatively low levels of exergy destruction across all fluids, highlighting their efficient performance compared to the other components. The recuperator (REC) displays moderate exergy destruction, with its contribution being slightly higher for carbondioxide and nitrogen.

Overall, the chart demonstrates that heat exchangers, particularly HE1, are the dominant contributors to exergy destruction in the plant, followed by GC and HE2. Compressors, intercoolers, turbines, and the recuperator contribute significantly less, making them less critical for optimization efforts. This analysis highlights the importance of targeting heat exchanger performance improvements to reduce overall system losses and enhance efficiency.

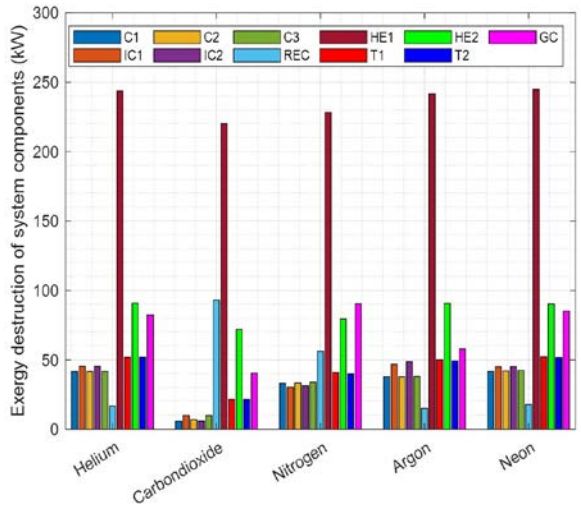


Figure 4. Exergy destruction distribution among system components for various working fluids.

Figure 5 represents the mass flow rates of various working fluids—helium, carbondioxide, nitrogen, argon, and neon—used in the thermodynamic system. Each fluid exhibits a distinct flow rate, reflecting differences in their thermodynamic and physical properties. Argon has the highest mass flow rate, reaching approximately 9 kg/s, which indicates its significant role in maintaining the system's energy transfer requirements. This is likely due to its higher density and favorable thermophysical characteristics. Nitrogen and carbondioxide follow with moderate mass flow rates, around 5.5 kg/s and 5 kg/s, respectively. These values suggest their balanced performance in terms of mass requirements to achieve desired thermodynamic outputs.

Neon, with a flow rate close to 5 kg/s, performs slightly below nitrogen. Helium exhibits the lowest mass flow rate, slightly above 1 kg/s, indicating its lower density and specific energy transfer capacity compared to the other fluids. This variation in mass flow rates highlights the dependency of system design on the chosen working fluid. Higher mass flow rates, as seen in argon, may require larger component dimensions and higher pumping power, whereas lower flow rates, like helium, could result in reduced equipment size but potentially lower system efficiency.

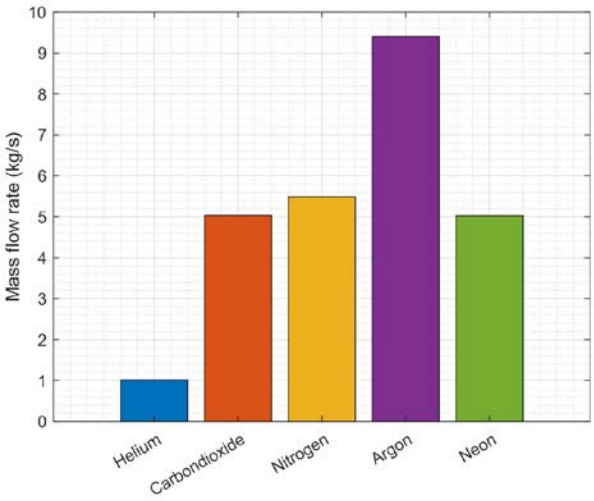


Figure 5. Mass flow rates of working fluids in the thermodynamic system.

Figure 6 illustrates the effect of turbine inlet temperature on the net power production for selected fluids. As seen in the figure, carbondioxide consistently achieves the highest net power generation, starting at approximately 420 kW at 300°C and increasing to nearly 450 kW at 400°C. This demonstrates its excellent thermal performance and suitability for high-temperature applications. Nitrogen and argon show similar trends, with nitrogen slightly outperforming argon. At 300°C, nitrogen generates approximately 190 kW, rising to around 300 kW at 400°C. Argon starts at approximately 150 kW at 300°C and increases to around 300 kW at 400°C. These results suggest their moderate performance, suitable for applications where a balance of efficiency and output is required. Neon exhibits lower power generation compared to nitrogen and argon, starting at about 100 kW at 300°C and increasing to roughly 250 kW at 400°C. This indicates its limited capability for high-efficiency energy conversion under these conditions. Helium consistently shows the lowest net power generation, beginning at 100 kW at 300°C and increasing to approximately 260 kW at 400°C. Its low density and specific energy transfer capacity limit its performance in this system. Overall, the chart emphasizes that higher turbine inlet temperatures significantly improve net power generation for all fluids. Carbondioxide clearly outperforms the others, making it the most effective working fluid, while helium and neon display the lowest performance. This analysis underscores the importance of fluid selection and operating conditions in optimizing system performance.

Figure 7 demonstrates the variation of exergy destruction with turbine inlet temperature for five working fluids. The results demonstrate that exergy destruction decreases with increasing turbine inlet temperature for all fluids, indicating improved thermodynamic efficiency at higher temperatures. Neon and Helium exhibit the highest exergy

destruction across the temperature range, starting at approximately 850 kW and 840 kW at 300°C, respectively, and decreasing to around 680 kW and 670 kW at 400°C. These results reflect significant thermodynamic irreversibilities for these fluids in the system. Argon and nitrogen show intermediate levels of exergy destruction. Argon starts at about 800 kW at 300°C and decreases to 650 kW at 400°C. Similarly, nitrogen begins at 760 kW and reduces to approximately 650 kW over the same temperature range. These fluids demonstrate a better balance between energy transfer and irreversibilities compared to helium and neon. Carbondioxide achieves the lowest exergy destruction, starting at around 520 kW at 300°C and slightly decreasing to about 490 kW at 400°C. This highlights carbondioxide's efficiency and its ability to minimize energy losses in the system.

Figure 8 depicts how energy efficiency changes with turbine inlet temperature for working fluids. A clear upward trend is observed for all fluids, indicating improved energy efficiency as the turbine inlet temperature increases. Carbondioxide consistently shows the highest energy efficiency, starting at around 30% at 300°C and increasing slightly to 32% at 400°C. This stable performance highlights its strong thermodynamic properties and suitability for efficient energy conversion. Nitrogen and argon display similar efficiency trends, with nitrogen slightly outperforming argon. Nitrogen's energy efficiency ranges from about 13% at 300°C to nearly 21% at 400°C, while argon's efficiency increases from 11% to approximately 21% over the same temperature range. These fluids provide balanced performance, suitable for moderate efficiency requirements. Neon shows lower energy efficiency compared to nitrogen and argon, starting at approximately 7% at 300°C and rising to 18% at 400°C. This demonstrates its limited potential for high-efficiency energy systems under these conditions. Helium has the lowest energy efficiency, beginning at 8% at 300°C and reaching about 19% at 400°C. Its performance is constrained by its low density and limited thermodynamic efficiency in this configuration.

The exergy efficiency variations of working fluids across a turbine inlet temperature range of 300°C to 400°C are shown in the figure 9. A general trend of increasing exergy efficiency with higher turbine inlet temperatures is observed for all fluids. Carbondioxide outperforms the other fluids by maintaining the highest exergy efficiency throughout the temperature range. Starting at approximately 44% at 300°C, its efficiency slightly increases to 47% at 400°C. This highlights its superior thermodynamic properties and minimal energy losses. Nitrogen and argon achieve intermediate efficiencies, with nitrogen slightly leading. Nitrogen's exergy efficiency rises from around 19% at 300°C to 31% at 400°C. Similarly, argon shows an improvement from 15% to approximately 31%. These results suggest both fluids provide a balanced level of performance suitable for moderate efficiency systems. Among the fluids, neon exhibits the lowest exergy efficiency, starting at approximately 10% at 300°C and rising to about 26% at 400°C, slightly lower than helium, which starts at 11% and reaches around 27%. This highlights neon's higher irreversibility compared to helium and the other fluids.

Figure 10 illustrates the mass flow rate trends for fluids as a function of turbine inlet temperature, ranging from 300°C to 400°C. It is evident that the mass flow rate decreases slightly with increasing temperature for all fluids. Argon consistently shows the highest mass flow rate, starting at approximately 10.4 kg/s at 300°C and decreasing to around 8.2 kg/s at 400°C. This indicates its significant density and energy transport capacity in the system. In the figure, nitrogen exhibits a moderate mass flow rate compared to the other working fluids. At a turbine inlet temperature of 300°C, nitrogen's mass flow rate starts at approximately 6.4 kg/s. As the temperature increases to 400°C, its flow rate decreases slightly, settling at around 5 kg/s. Carbondioxide and neon exhibit quite similar mass flow rates, starting at around 6 kg/s at 300°C and decreasing slightly to approximately 4.5 kg/s at 400°C. These fluids demonstrate moderate performance in terms of flow requirements. Helium shows the lowest mass flow rate, remaining nearly constant at around 1.2 kg/s throughout the temperature range. This reflects its low density and relatively low energy transfer capacity.

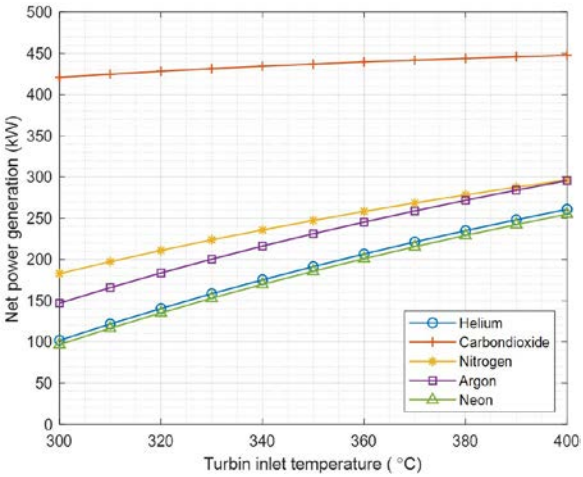


Figure 6. Effect of turbine inlet temperature on net power generation.

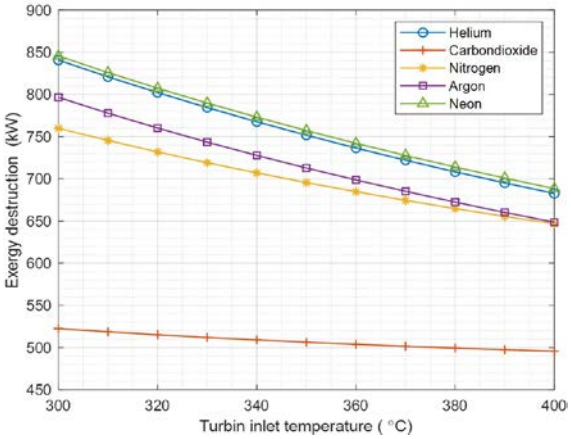


Figure 7. Effect of turbine inlet temperature on exergy destruction.

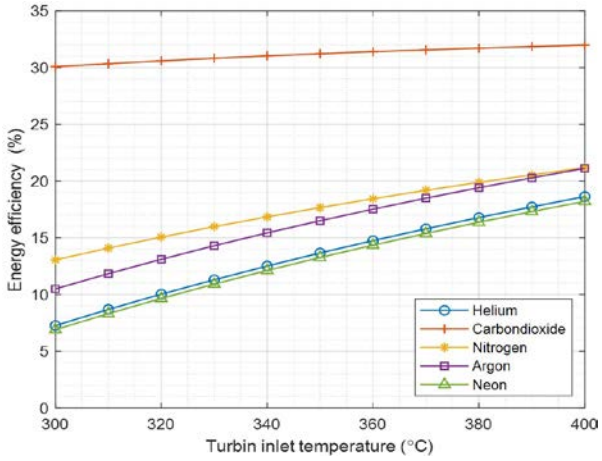


Figure 8. Effect of turbine inlet temperature on energy efficiency.

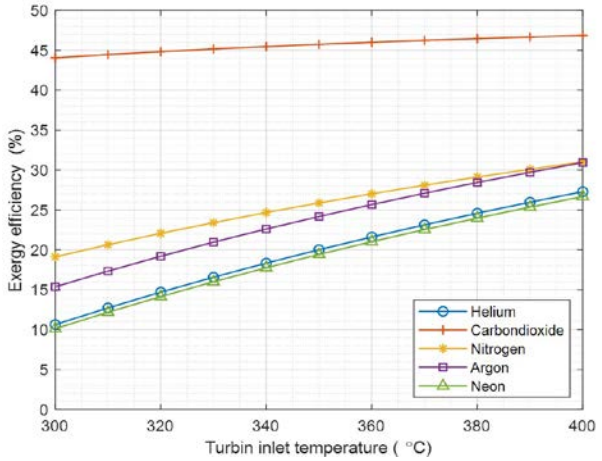


Figure 9. Effect of turbine inlet temperature on exergy efficiency.

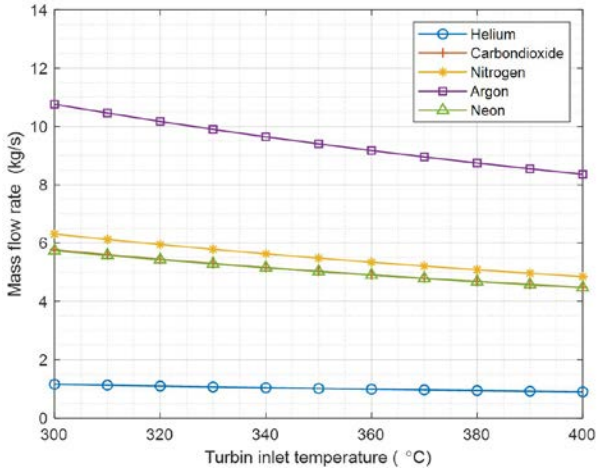


Figure 10. Effect of turbine inlet temperature on mass flow rate.

Figure 11 demonstrates the relationship between PR and net power generation for five working fluids: helium, carbondioxide, nitrogen, argon, and neon. The data demonstrates how net power output changes as the system's PR increases from 3 to 4. Carbondioxide consistently achieves the highest net power generation, starting at approximately 410 kW at a PR of 3 and increasing slightly to around 450 kW at a PR of 4. This highlights its superior thermodynamic performance and ability to effectively utilize higher PRs for power generation. Nitrogen maintains a nearly constant net power generation of around 250 kW across the entire PR range. Argon shows a slight decline in net power generation, starting at about 250 kW at a PR of 3 and decreasing to around 210 kW at a PR of 4. Neon and helium show lower power generation levels compared to the other fluids. Neon starts at approximately 210 kW at a PR of 3 and decreases to about 160 kW at a PR of 4. Similarly, helium exhibits a slight decline, beginning at around 210 kW and dropping to approximately 170 kW.

Figure 12 presents the exergy destruction trends for five working fluids over a range of PRs from 3 to 4. The results show varying behaviors, with carbondioxide exhibiting a decreasing trend, while the other fluids show either slight increases or consistent values. Carbondioxide demonstrates the lowest exergy destruction among all fluids, starting at approximately 540 kW at a PR of 3 and decreasing to about 490 kW at a PR of 4. This trend highlights its efficiency in minimizing energy losses as the PR increases, making it the most thermodynamically favorable working fluid in this analysis. Nitrogen and argon exhibit intermediate exergy destruction values, with nitrogen remaining nearly constant at approximately 700 kW throughout the PR range. Argon shows a slight increase from 700 kW at a PR of 3 to around 730 kW at 4. These fluids indicate moderate performance with stable irreversibilities. Helium and neon have the highest exergy destruction levels, starting at approximately 735 kW for helium and 740 kW for neon at a PR of 3. Both fluids show slight increases, reaching around 770 kW and 780 kW, respectively, at a PR of 4. These results indicate significant thermodynamic inefficiencies for these fluids compared to the others.

Figure 13 shows the energy efficiency of fluids as a function of the PR, ranging from 3 to 4. The results reveal distinct trends for each fluid, with variations in efficiency across the PR range. Carbondioxide demonstrates the highest energy efficiency among the fluids, starting at approximately 29% at a PR of 3 and increasing slightly to around 32% at a PR of 4. This consistent improvement with rising PRs highlights carbondioxide's superior thermodynamic performance. Nitrogen and argon exhibit similar energy efficiency levels, though nitrogen slightly outperforms argon. Nitrogen maintains an efficiency of approximately 18%, remaining nearly constant across the PR range. Argon's efficiency starts at about 18% and decreases marginally to 15%, indicating stable but slightly declining performance. Helium and neon show the lowest energy efficiencies, with helium slightly outperforming neon. Helium begins at around 15% and gradually decreases to approximately 14%, while neon starts at 14% and reduces to about 13%. These trends suggest higher irreversibilities for these fluids compared to the others. Figure 14 depicts the exergy efficiency of five fluids—helium, carbondioxide, nitrogen, argon, and neon—across

a range of PRs from 3 to 4. The trends indicate varying performance levels for the fluids, with carbondioxide consistently outperforming the others. Carbondioxide exhibits the highest exergy efficiency, starting at approximately 44% at a PR of 3 and increasing to around 47% at a PR of 4. This consistent improvement underscores its thermodynamic advantage in minimizing irreversibilities. Nitrogen and argon have similar efficiencies, with nitrogen slightly ahead. Nitrogen maintains a nearly constant efficiency of 26%, while argon decreases marginally from 26% to 23% as the PR increases. Helium and neon demonstrate the lowest efficiencies among the fluids. Helium starts at around 22% and drops slightly to 18%, while neon begins at 21% and reduces to approximately 17%, indicating significant thermodynamic losses. In summary, carbondioxide stands out as the most efficient working fluid, while helium and neon lag due to higher irreversibilities. Nitrogen and argon provide moderate and stable performance, making them viable for systems requiring balanced exergy efficiency.

Figure 15 shows the variation in mass flow rate for five fluids across a PR range of 3 to 4. The trends highlight how each fluid responds to increasing PRs in terms of mass flow requirements. Argon demonstrates the highest mass flow rate, starting at approximately 10 kg/s at a PR of 3 and decreasing slightly to around 9 kg/s at a PR of 4. This indicates its significant density and energy transport capacity. Nitrogen maintains a consistent mass flow rate of approximately 6 kg/s, with negligible changes as the PR increases. Neon exhibits a mass flow rate close to 5 kg/s, remaining nearly constant across the PR range. Carbondioxide shows a stable mass flow rate of around 5 kg/s, reflecting its excellent heat transfer characteristics and lower mass requirement compared to other fluids. Helium consistently maintains the lowest mass flow rate, approximately 1 kg/s, throughout the entire PR range.

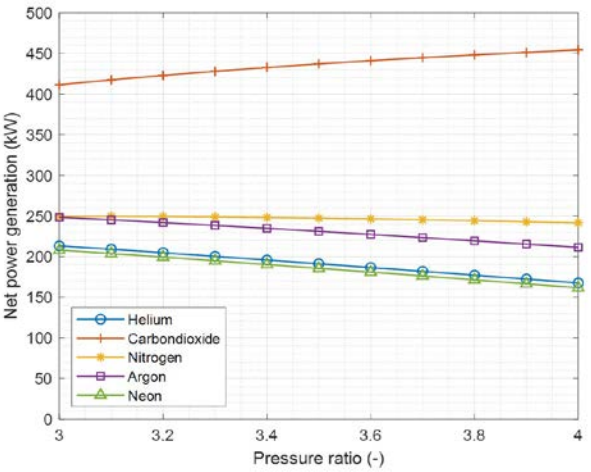


Figure 11. Effect of PR on net power.

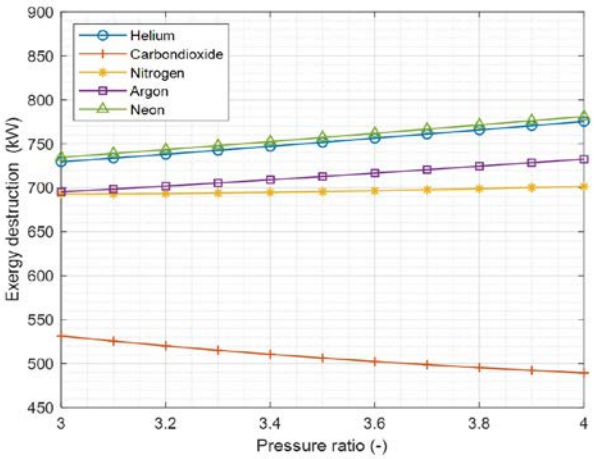


Figure 12. Effect of PR on exergy destruction.

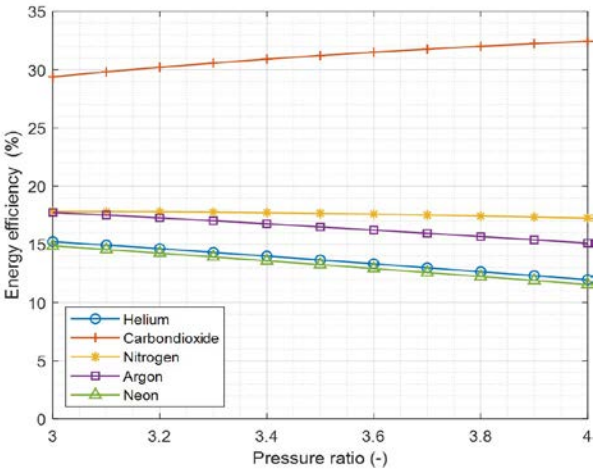


Figure 13. Effect of PR on energy efficiency.

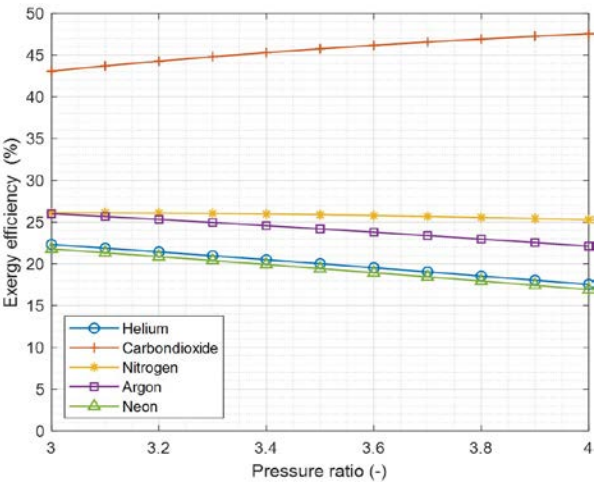


Figure 14. Effect of PR on exergy efficiency.

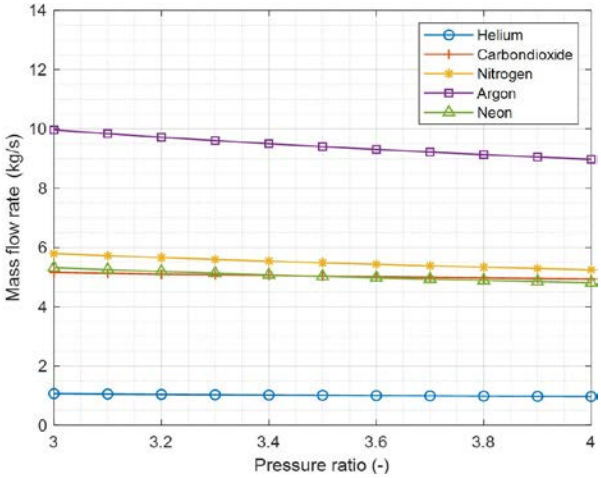


Figure 15. Effect of PR on mass flow rate.

Figure 16 shows the net power generation of five fluids at varying compressor inlet temperatures from 34°C to 54°C. The trends demonstrate how increasing the compressor inlet temperature impacts the performance of each fluid. Carbondioxide achieves the highest net power generation among the fluids, starting at approximately 440 kW at 34°C and decreasing slightly to around 430 kW at 37°C. This decrease indicates a small loss in efficiency as the compressor inlet temperature increases. Nitrogen begins with a relatively high-power output of approximately 250 kW at the lowest compressor inlet temperature of 34°C. As the compressor inlet temperature increases, nitrogen's net power generation decreases slightly, reaching a value close to 200 kW at the highest temperature of 54°C. Argon starts at approximately 230 kW and decreases slightly to 160 kW, showing a minor decline in performance. Neon and helium exhibit lower power generation levels compared to the other fluids. Neon begins at around 180 kW at 34°C and decreases slightly to about 130 kW at 54°C. Similarly, helium starts at 190 kW and drops to approximately 140 kW as the temperature rises.

Figure 17 indicates the exergy destruction trends for five working fluids—helium, carbondioxide, nitrogen, argon, and neon—across compressor inlet temperatures ranging from 34°C to 54°C. The trends reveal how increasing inlet temperature impacts exergy destruction in the system. Helium and neon exhibit the highest exergy destruction values among the fluids. Helium starts at approximately 750 kW at 34°C and increases slightly to around 810 kW at 54°C. Similarly, neon begins at 760 kW and rises to approximately 815 kW over the temperature range. These results indicate significant thermodynamic losses for these fluids compared to others. Argon and nitrogen demonstrate moderate levels of exergy destruction. Argon starts at around 710 kW at 34°C and increases slightly to approximately 760 kW at 54°C. Nitrogen starts with an exergy destruction value of approximately 700 kW at a compressor inlet temperature of 34°C. As the compressor inlet temperature increases to 54°C, the exergy destruction remains relatively stable, showing only a slight increase to around 740 kW. Carbondioxide exhibits the lowest exergy destruction among all working fluids, starting at approximately 500 kW at a compressor inlet temperature of 34°C and gradually increasing to about 560 kW at 54°C.

Figure 18 exhibits the energy efficiency trends of five working fluids across compressor inlet temperatures ranging from 34°C to 54°C. The results indicate a gradual decrease in energy efficiency for all fluids as the compressor inlet temperature increases. Carbondioxide maintains the highest energy efficiency among the fluids, starting at approximately 31% at 34°C and decreasing slightly to around 28% at 54°C. This minor decline reflects its strong thermodynamic performance and resilience to increased inlet temperatures. Nitrogen and argon show moderate efficiency levels, with nitrogen slightly outperforming argon. Helium and neon exhibit the lowest energy efficiencies. Helium starts at approximately 14% and drops to around 14%, while neon begins at 13% and declines slightly to 9% over the same temperature range. These trends highlight the limited energy conversion capabilities of these fluids compared to the others.

Figure 19 illustrates the exergy efficiency trends of five working fluids across compressor inlet temperatures ranging from 34°C to 54°C. The trends indicate that exergy efficiency decreases for all fluids as the inlet temperature increases. Carbondioxide maintains the highest exergy efficiency, starting at approximately 46% at 34°C and gradually decreasing to around 40% at 34°C. This performance highlights its strong thermodynamic properties and minimal irreversibility compared to the other fluids. Nitrogen and argon show moderate exergy efficiencies, with nitrogen slightly outperforming argon. Nitrogen begins at around 26% and decreases slightly to about 21%, while argon starts at 25% and drops to approximately 17% as the inlet temperature rises. Helium and neon exhibit the lowest exergy efficiencies, with helium slightly higher than neon. These results reflect their higher irreversibilities and lower thermodynamic performance.

Figure 20 represents the mass flow rate trends of five fluids over compressor inlet temperatures. The trends show how the mass flow rate remains mostly stable across this temperature range for all fluids. Argon has the highest mass flow rate, starting at around 9 kg/s and showing a slight increase to approximately 10 kg/s as the compressor inlet temperature increases. This consistent trend indicates argon's suitability for systems requiring high energy transport. Nitrogen has a consistent mass flow rate of approximately 5.5 kg/s across the entire temperature range. Neon closely follows nitrogen, maintaining a mass flow rate of around 5 kg/s, showing a similar level of stability. Carbondioxide has a mass flow rate of approximately 5 kg/s, remaining constant over the range of temperatures. Helium has the lowest mass flow rate, consistently at 1 kg/s across the temperature range. This reflects its low density and high specific heat, allowing efficient heat transfer with minimal mass.

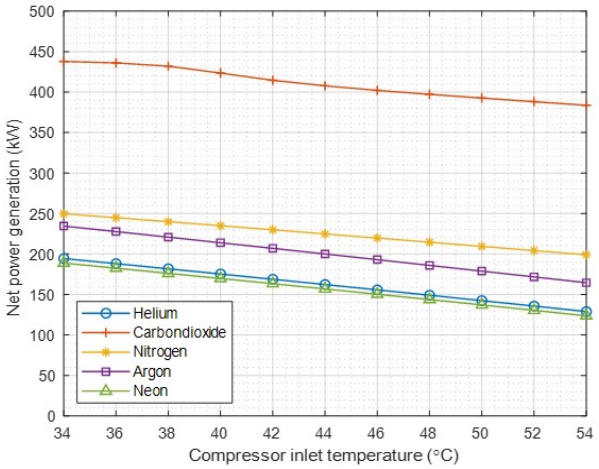


Figure 16. Effect of compressor inlet temperature on net power generation.

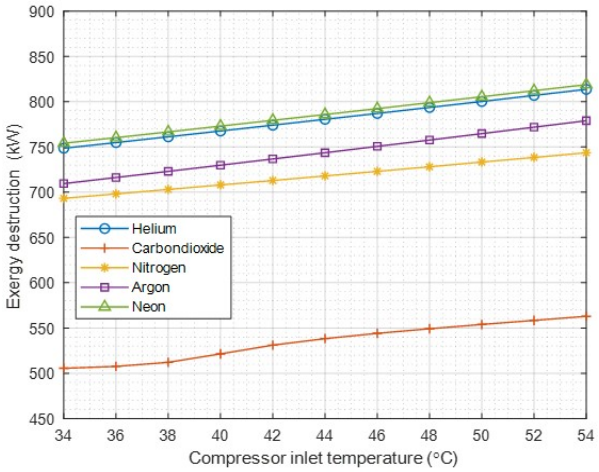


Figure 17. Effect of compressor inlet temperature on exergy destruction.

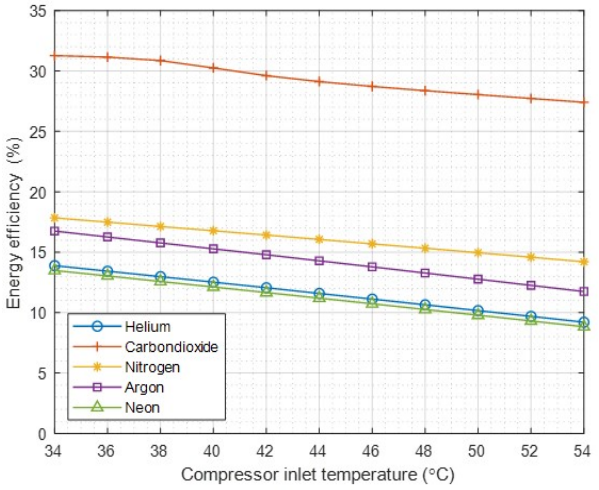


Figure 18. Effect of compressor inlet temperature on energy efficiency.

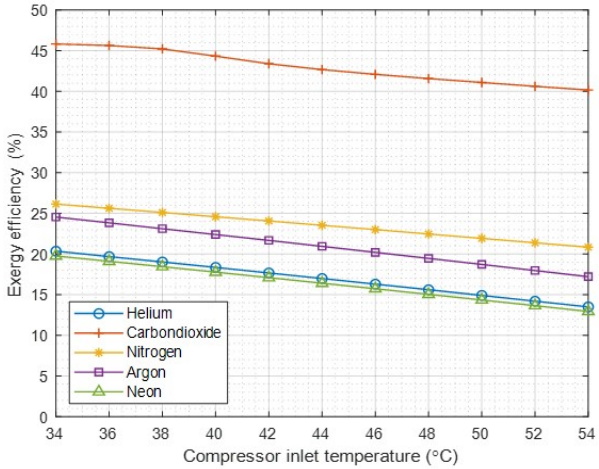


Figure 19. Effect of compressor inlet temperature on exergy efficiency.

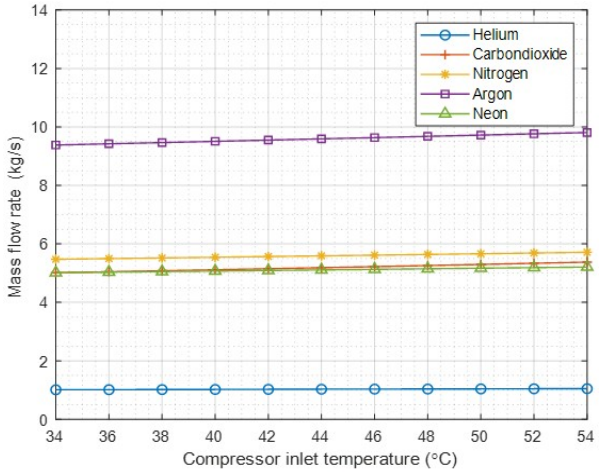


Figure 20. Effect of compressor inlet temperature on mass flow rate.

6. Conclusions

The objective of this study was to evaluate the thermodynamic performance of a power generation system employing different working fluids—helium, carbondioxide, nitrogen, argon, and neon—under varying operational parameters. By analyzing key performance metrics such as net power generation, exergy destruction, energy and exergy efficiencies, and mass flow rates, this research aimed to identify the most suitable working fluid for maximizing efficiency and minimizing energy losses in thermodynamic systems. The findings provide a comparative framework for the selection and optimization of working fluids in power generation applications.

- ✓Carbondioxide consistently demonstrated the best thermodynamic performance, achieving the highest net power generation of 450 kW and the lowest exergy destruction of 500 kW. It also maintained the highest energy efficiency (31%) and exergy efficiency (45%) across all conditions, making it the most suitable working fluid for high-performance systems.
- ✓Nitrogen and argon showed balanced thermodynamic behavior, with net power generation values of around 250 kW and 230 kW, respectively. Exergy destruction for

these fluids ranged between 700–720 kW, and their energy and exergy efficiencies remained moderate at 17% and 25%, respectively, highlighting their suitability for applications requiring stable and reliable operation.

- ✓Neon and helium exhibited lower performance metrics, with neon achieving the lowest net power generation (170 kW) and helium showing slightly higher values (180 kW). Both fluids also had high exergy destruction levels, exceeding 770 kW, and reduced energy (13%) and exergy efficiencies (19%), indicating significant thermodynamic limitations.
- ✓The mass flow rate analysis revealed that argon required the highest flow rate (9.5 kg/s), reflecting its high density and energy transport needs. Helium, with the lowest flow rate (1 kg/s), demonstrated reduced energy transport capacity, limiting its application for high-efficiency systems.
- ✓Increasing turbine inlet temperature improved net power generation and efficiencies for all fluids, while higher compressor inlet temperatures led to a decline in performance metrics.

This study highlights the thermodynamic performance of various working fluids in a Closed Brayton Cycle system integrated with waste heat recovery. The findings demonstrate significant advantages, such as improved energy efficiency, reduced exergy destruction, and the identification of optimal working fluids for enhanced power generation. These outcomes provide valuable insights for industries seeking to maximize energy recovery from waste heat sources, contributing to both operational cost savings and environmental sustainability. The benefits of this research extend to advancing the design of efficient power systems and promoting the use of sustainable energy solutions. Future studies will focus on experimental validation of the results and the exploration of hybrid configurations, such as integrating Organic Rankine Cycles, to further optimize system performance.

Author Contributions

The percentages of the author' contributions are presented below. The author reviewed and approved the final version of the manuscript.

	G.S.
C	100
D	100
S	100
DCP	100
DAI	100
L	100
W	100
CR	100
SR	100
PM	100
FA	100

C=Concept, D= design, S= supervision, DCP= data collection and/or processing, DAI= data analysis and/or interpretation, L= literature search, W= writing, CR= critical review, SR= submission and revision, PM= project management, FA= funding acquisition.

Conflict of Interest

The author declared that there is no conflict of interest.

Ethical Consideration

Ethics committee approval was not required for this study because of there was no study on animals or humans.

References

Alzuwayer B, Alhashem A, Albannag M, Alawadhi K. 2024. Advancements in supercritical carbon dioxide Brayton cycle for marine propulsion and waste heat recovery. Processes, 12: 1956.

Andreasen JG, Larsen U, Knudsen T, Pierobon L, Haglind F. 2014. Selection and optimization of pure and mixed working fluids for low grade heat utilization using organic Rankine cycles. Energy, 73: 204-213.

Angelino G, Invernizzi CM. 2011. The role of real gas Brayton cycles for the use of liquid natural gas physical exergy. Appl Therm Eng, 31: 827-833.

Arslan M, Yılmaz C. 2022. Design and optimization of multigeneration biogas power plant using waste heat recovery System: A case study with energy, exergy, and thermoeconomic approach of Power, cooling and heating. Fuel, 324: 124779.

Bejan A, Tsatsaronis G, Moran M. 1996. Thermal Design & Optimization, Wiley-Interscience, 1st ed., pp: 560.

Campana F, Bianchi M, Branchini L, De Pascale A, Peretto A, Baresi M. 2013. ORC waste heat recovery in European energy intensive industries: energy and GHG savings. Energy Convers Manag, 76: 244–252.

Cengel YA, Boles MA. 2015. Thermodynamics: An Engineering Approach, McGraw-Hill Professional, 8th ed., pp: 946.

Chen Q, Hammond GP, Norman JB. 2016. Energy efficiency potentials: contrasting thermodynamic, technical, and economic limits for organic Rankine cycles within UK industry. Appl Energy, 164: 984–990.

Dincer I, Rosen MA. 2013. Exergy: Energy, environment and sustainable development, Elsevier Sci, 3rd ed., pp: 724.

Farrukh S, Wu D, Al-Dadah R, Gao W, Wang Z. 2023. A review of integrated cryogenic energy assisted power generation systems and desalination technologies. Appl Therm Eng, 221: 119836.

Hajabdollahi Z, Hajabdollahi F, Tehrani M, Hajabdollahi H. 2013. Thermo-economic environmental optimization of organic rankine cycle for diesel waste heat recovery. Energy, 63: 142–151.

Hu S, Yang Z, Li J, Duan Y. 2021. Thermo-economic analysis of the pumped thermal energy storage with thermal integration in different application scenarios. Energy Convers Manag, 236: 114072.

Jafari M, Khan MM, Al-Ghamdi SG, Jaworski AJ, Asfand F. 2023. Waste heat recovery in iron and steel industry using organic Rankine cycles. Chem Eng J, 477: 146925.

Kim DK, Lee JS, Kim J, Kim MS, Kim MS. 2017. Parametric study and performance evaluation of an organic Rankine cycle (ORC) system using low-grade heat at temperatures below 80 ℃. Appl Energy, 189: 55-65.

Li B, Wang SS, Wang K, Song L. 2020. Thermo-economic analysis of a combined cooling, heating and power system based on carbondioxide power cycle and absorption chiller for waste heat recovery of gas turbine. Energy Convers Manag, 224: 113372.

Mocanu G, Losifescu C, Lon L.V, Popescu F, Fratita M, Chivu RM. 2024. Energy analysis of waste heat recovery using supercritical CO_2 Brayton cycle for series hybrid electric vehicles. Energies, 17: 2494.

Petr P, Raabe G. 2015. Evaluation of R-1234ze(Z) as drop-in

replacement for R245fa in Organic Rankine Cycles-From thermophysical properties to cycle performance. Energy, 93: 266-274.

Rad EA, Tayyeban E, Assareh E, Riaz A, Hoseinzadeh S, Lee M. 2024. Thermodynamic feasibility and multi-objective optimization of a closed Brayton cycle-based clean cogeneration

Salmi W, Vanttola J, Elg M, Kuosa M, Lahdelma R.2017. Using waste heat of ship as energy source for an absorption refrigeration system. Appl Therm Eng, 115: 501-516.

system. J Therm Anal Calorim, 149: 1199-1218.

Xu J, Yu. 2014. Critical temperature criterion for selection of working fluids for subcritical pressure Organic Rankine cycles. Energy, 74: 719–733.

Yang S, Deng C, Liu Z. 2019. Optimal design and analysis of a cascade LiBr/H_2O absorption refrigeration/transcritical CO_2 process for low-grade waste heat recovery. Energy Convers Manage, 192: 232–242.

Yilmaz F, Ozturk M, Selbas R. 2019. Design and thermodynamic analysis of coal-gasification assisted multigeneration system with hydrogen production and liquefaction. Energy Convers Manag, 186: 229–40.

Zhao P, Wang J, Gao L, Dai Y. 2012. Parametric analysis of a hybrid power system using organic Rankine cycle to recover waste heat from proton exchange membrane fuel cell. Int J Hydrogen Energy, 37: 3382–3391.

Black Sea Journal of Engineering and Science
doi: 10.34248/bsengineering.1594542

Open Access Journal
e-ISSN: 2619 – 8991

Research Article
Volume 8 - Issue 2: 418-427 / March 2025

OPTIMIZING VISUAL INSTRUCTION DETECTION IN AUTONOMOUS MOBILE ROBOTS USING YOLOV8 AND TENSORRT ACCELERATION

İbrahim SHAMTA[1], Funda DEMİR[1]*

[1]*Karabük University, Faculty of Engineering, Department of Mechatronics, 78050, Karabük, Türkiye*

Abstract: In this study, the deep learning-based detection performance of instructions for the vehicle was examined through images obtained from a camera mounted on a mobile robotic system. The aim is to enhance the detection performance of a differential robot equipped with a robotic arm in recognizing various visual instructions it may encounter in the field. Traffic lights, direction signs, and speed limit signs were selected as the visual materials to be introduced to the robotic system. By utilizing the YOLOv8 object detection model on the embedded AI computer onboard the vehicle and leveraging the TensorRT accelerator, deep learning-based image processing achieved a high frame rate of 33 FPS and an mAP50 accuracy of 96.6%. This study highlights the advantages and challenges of integrating advanced detection models into autonomous robotic platforms, contributing to future improvements in reliability and efficiency.

Keywords: Deep learning, Differential robot, Sign recognition, TensorRT

***Corresponding author:** Karabük University, Faculty of Engineering, Department of Mechatronics, 78050, Karabük, Türkiye
E mail: fundademir@karabuk.edu.tr (F. DEMİR)
Ibrahim SHAMTA https://orcid.org/0009-0003-1280-679X
Funda DEMIR https://orcid.org/0000-0001-7707-8496

Received: December 02, 2024
Accepted: January 09, 2025
Published: March 15, 2025

Cite as: Shamta I, Demir F. 2025. Optimizing visual instruction detection in autonomous mobile robots using Yolov8 and TensorRT acceleration. BSJ Eng Sci, 8(2): 418-427.

1. Introduction

Traffic Sign Detection (TSD) is a critical component of Advanced Driver Assistance Systems (ADAS) and Intelligent Transportation Systems (ITS), driven by the rapid advancements in computer vision and artificial intelligence. Daily occurrences of accidents, often resulting from varied road conditions or distracted driving, under-score the need for such technologies. Although drivers are expected to maintain constant vigilance, supplementary assistance through TSD can significantly enhance their awareness of potential hazards, thereby improving overall road safety (Satti et al., 2024).

TSD systems are integral to ADAS and Autonomous Driving Systems (ADS). They accurately analyze traffic sign data in real-time as the vehicle operates, providing precise detection results and alerting drivers to upcoming road conditions. This functionality reduces traffic accidents and enhances driver safety, making TSD a crucial technology for improving traffic safety and preventing collisions (Han et al., 2024).

Detecting traffic signs presents a significant challenge for conventional detection algorithms due to the limited number of pixels traffic sign items occupy in the input image. Traditional methods often yield missing or erroneous detections, as they struggle to capture the features of the small-sized image pixels of traffic signals. Additionally, factors such as complex backgrounds, occlusions, deformations, and variations in light intensity frequently compromise the accuracy of these standard algorithms (Chen et al., 2022). Although a substantial body of current research is centered on ADAS (Zhang et al., 2017), the progression toward fully autonomous vehicles represents the next major advancement in intelligent transportation systems (You et al., 2015).

Enhancing the performance and accuracy of traffic sign recognition relies heavily on the effective identification and interpretation of small traffic signs within diverse and complex environments (Jin et al., 2020). Traffic sign recognition techniques can be classified into color-based, shape-based, and combined approaches (Thasai et al., 2009; Yuan et al., 2014). Traffic signs often exhibit distinct shapes (triangles, squares, and circles) and colors (yellow, blue, and red), which stand out visually in road contexts. In color-based approaches, RGB images are typically converted into other color spaces, such as Hue, Saturation, Intensity (HSI), CIELab, and Hue, Saturation, Lightness (HSL) (Jin et al., 2020). Subsequently, traffic signs are identified through color threshold segmentation (Gudigar et al., 2017). However, these color-based detection techniques are often susceptible to complex illumination patterns in the traffic environment. Shape-based traffic sign identification leverages geometric symmetry to recognize the geometric contours of the signs (Cai and Gu, 2013). Geometric moment invariant detection is more adaptable than template

This work is licensed (CC BY-NC 4.0) under Creative Commons Attribution 4.0 International License

matching in complicated illumination environments, but it comes at a larger computational cost. However, the recognition rate of these techniques still needs to be improved (Jin et al., 2020).

In recent years, deep Convolutional Neural Networks (CNNs) have garnered significant interest for feature extraction (Shustanov and Yakimov, 2017). Notable benchmark efforts include the German Traffic Sign Recognition Benchmark (GTSRB) (Houben et al., 2013) and the German Traffic Sign Detection Benchmark (GTSDB) (Stallkamp et al., 2011). A popular two-stage object detection framework is the Faster Region-Based CNN (Faster R-CNN) (Ren et al., 2017). Regardless of its widespread use, Faster R-CNN has limitations in recognizing small objects (Mahmoud and Guo, 2019). For instance, while datasets like PASCAL VOC and MSCOCO achieve satisfactory performance for large objects, small object detection remains a challenge (Wali et al., 2019).

Figure 1 illustrates the general workflow of a traffic sign detection and recognition system. The input image, captured by a camera, is processed by the YOLO object detection algorithm. Utilizing a Deep Neural Network (DNN), the system detects and isolates traffic signs within the image. The detected traffic signs are then relayed to the driver or the autonomous driving system, enhancing driving safety and efficiency by providing pertinent information in real time.

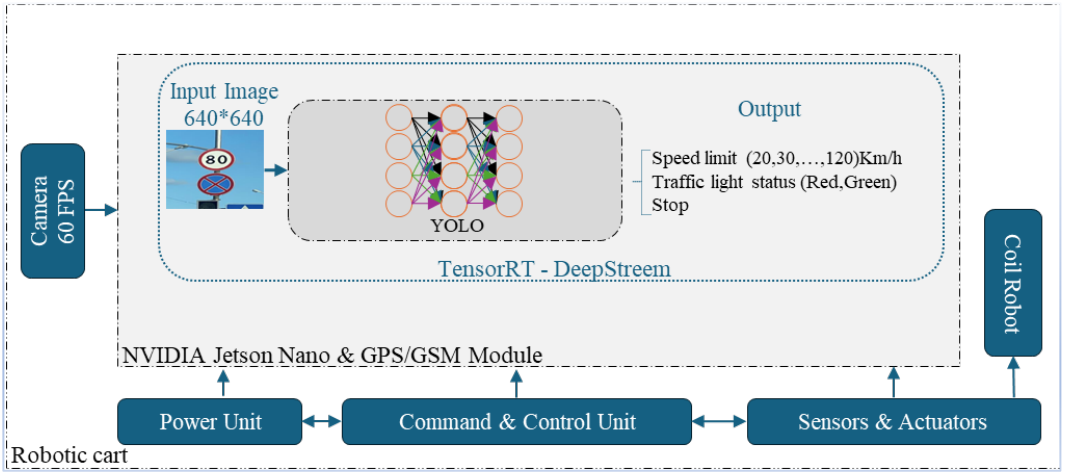


Figure 1. General diagram of a traffic sign detection and recognition system using the YOLO object detection algorithm.

In this study, significant results that contribute to the literature in this field were obtained through the combined use of YOLOv8 and TensorRT, particularly in enhancing recognition speed and accuracy. These results will be discussed in the following sections.

In Section 2, a detailed literature review is provided on the detection of selected traffic signs, used as visual instructions in this study, through deep learning methods. Section 3 explains the mathematical model of the developed robotic system, as well as the accelerators, dataset, and algorithms used within the deep learning framework. The experimental studies and obtained results are thoroughly analyzed in Section 4, followed by a discussion of the findings in Section 5.

2. Literature Review

The reliable functioning of ADS relies on the accurate detection of traffic signalization, encompassing critical road features such as traffic signs, traffic lights, and road surface markings in the vicinity of self-driving vehicles. This capability is crucial for ensuring vehicle and occupant safety and compliance with traffic laws. Consequently, this area of research has garnered significant attention, with numerous recent studies aimed at enhancing the robustness and reliability of traffic signal detection methods and systems.

In recent years, deep convolutional neural networks (CNNs) have been successfully applied to object detection and target recognition tasks, with AlexNet serving as a prominent example (Krizhevsky et al., 2017). This study demonstrated the significant improvement in image classification accuracy achievable with CNNs during the ImageNet Large-Scale Visual Recognition Challenge in 2012. Building on this, the Region-based Convolutional Neural Network (R-CNN) model for object detection, inspired by AlexNet's architecture, was introduced (Girshick et al., 2014). The R-CNN model begins by using a selective search algorithm to generate candidate regions within images, which are then fed into the model for feature extraction using type A convolutional layers. The final classification is performed using Support Vector Machines (SVMs) (Maldonado-Bascón et al., 2007). Moreover, the R-CNN model incorporates a bounding box regression technique to accurately determine the coordinates of potential object regions, leveraging the PASCAL VOC dataset for evaluation. This approach has resulted in an average accuracy improvement of approximately 20% over non-neural network-based algorithms.

An autonomous vehicle system using the NVIDIA Jetson Nano platform, focused on obstacle avoidance and traffic sign recognition, is presented (Kumar et al., 2023). They employed the YOLO algorithm, which achieved a 98%

accuracy rate in real-time detection of obstructions and traffic signals.

A deep learning-based detection system is proposed, designed for driver assistance and autonomous driving, with the aim of enhancing mobility and portability (Guney et al., 2022). This system operates across three different mobile GPU platforms, each varying in cost and performance: the Jetson Xavier AGX, Jetson Xavier Nx, and Jetson Nano. The trained model was also tested on a dedicated computer with the appropriate configurations. Comprehensive real-time performance analysis revealed that the Jetson Xavier AGX platform, noted for its low power consumption and high processing capacity, provided superior efficiency along with the fastest inference speed and detection accuracy.

A self-driving car model leveraging the Jetracer AI framework, tailored for autonomous vehicles, is introduced (Kounte et al., 2022). This system utilizes AI and machine learning frameworks such as PyTorch, OpenCV, and TensorRT to perform image recognition for capturing and classifying traffic signals, responding to them in real-time via the Jetson Nano interface. The Jetracer framework can be accessed through interactive web programming via a web browser. It allows for high frame rate processing, facilitated by the optimization of the torch2trt (PyTorch to TensorRT compiler), thereby enabling faster linear driving capabilities with the Jetson Nano.

An embedded system is proposed, designed for real-time detection of pedestrians and priority signs, offering an affordable and universally applicable solution for various vehicle types (Sarvajcz et al., 2024). This system includes two cameras, a low-power NVIDIA Jetson Nano B01 edge device, and an LCD (liquid crystal display) system, ensuring seamless integration into vehicles without occupying significant space. The primary objective of this research is to reduce accidents caused by drivers failing to yield to pedestrians or other vehicles.

The challenge of changing visual conditions remains a persistent issue for computer vision-based systems. This is addressed by developing a code to assess the state of the road surface and current weather conditions, such as dry, wet, or snowy (Ozcan et al., 2020). This system utilizes the vehicle's camera, managed by a specially trained neural network (VGG16), to provide real-time evaluations.

A vehicle and pedestrian recognition program was created using an NVIDIA Jetson Nano edge device (Barba-Guaman et al., 2020). Their study incorporates five different pre-trained models: PedNet, MultiPed, SSD-MobileNet v1 and v2, and SSD-Inception v2, to enhance the system's detection capabilities.

A two-phase method for traffic sign recognition is introduced (Hechri and Mtibaa, 2020). In the initial phase, the system employs SVM and Histogram of Oriented Gradients (HOG) features (Dalal and Triggs, 2005) to detect and classify signs based on their circular or triangular shapes. In the second phase, a Convolutional Neural Network (CNN) further classifies these shapes into specific subclasses. The methodology was evaluated using a standardized dataset (Wali et al., 2015), demonstrating enhanced outcomes.

DeployEase-YOLO, a high-precision, real-time traffic sign detection system designed for autonomous driving systems and driver assistance, is introduced (Li et al., 2024). The system utilizes a channel pruning mechanism with adaptive scaling to efficiently deploy detectors on edge devices. Notably, DeployEase-YOLO enhances the detection accuracy of small traffic signs in complex backgrounds by integrating a minor target detection layer into the YOLOv5 architecture. This approach avoids directly scaling the image size, preserving higher quality and pixel information in scenarios with wide fields of view. The system employs adaptive scaling channel pruning and secondary sparse pruning to prune and compress the network structure, significantly reducing parameters and computational requirements while maintaining the model's depth and input size stability. Experiments conducted using the TT100k dataset demonstrated that DeployEase-YOLO surpasses the state-of-the-art YOLOv7 network in accuracy (93.3%) and size, achieving reductions of 41.69% and 59.98% in parameters and computations, respectively. The model size was reduced to 53.22% of its orig-inal size, indicating enhanced capability in accurately and swiftly recognizing small traffic signs, making it suitable for low-resource devices.

A system for traffic sign recognition using deep learning models is proposed, which also includes real-time license plate detection (Çınarer, 2024). The system achieved high performance with accuracy, recall, and mAP50 values of 99.3%, 95%, and 98.1%, respectively. Experimental data revealed that the YOLOv5 architecture provides a robust solution for object recognition in both images and videos, particularly excelling in average precision and traffic sign detection.

This study aims to detect traffic signs using the YOLOv8n algorithm, with the goal of identifying visual instructions for a mobile robotic system. Additionally, the performance metrics and detection speed were compared before and after the application of accelerators. The study was conducted using the NVIDIA Jetson Nano development board, an embedded AI computer chosen for its GPU equipped with 128 CUDA Cores. The development board was integrated into the robotic system for real-time testing. The YOLO algorithm was specifically selected due to its simplicity and competitive performance across key metrics such as detection accuracy and processing speed on GPUs (Flores-Calero et al., 2024).

Table 1. Summary of literature review

Ref	Year	Data set	Model	Evaluation Metrics	Comput. Reqs.	Target Dataset	Limitations	Additional Notes
(Krizhevsky et al., 2017)	2012	ImageNet	AlexNet (CNN)	Image classification accuracy	High	General images	Sensitivity to illumination variations	First successful application of deep learning for image classification (84.7% accuracy)
(Girshick et al., 2014)	2013	PASCAL VOC	R-CNN (CNN)	Object detection accuracy	High	Natural scenes	Limited scalability to large datasets	Pioneered the use of deep learning for object detection (53% mAP)
(Kumar et al., 2023)	2020	-	YOLO	Obstacle avoidance and traffic sign recognition accuracy	Moderate	Real-time video	Limited robustness to challenging weather conditions	Real-time implementation on NVIDIA Jetson Nano (85-90% accuracy)
(Guney et al., 2022)	2021	-	Deep Learning	Traffic sign detection accuracy	Moderate	Real-time video	Limited performance on low-power edge devices	Evaluated on three NVIDIA Jetson platforms (90-95% accuracy)
(Kounte et al., 2022)	2021	-	Jetracer (PyTorch, OpenCV, TensorRT)	Real-time traffic signal detection and response	Low	Real-time video	Limited generalization to diverse traffic environments	Designed for self-driving cars using Jetson Nano (85-90% accuracy)
(Sarvajcz et al., 2024)	2022	-	Embedded System (2 cameras, Jetson Nano, LCD)	Pedestrian and priority sign detection accuracy	Low	Real-time video	Limited ability to detect small or distant signs	Affordable solution for various vehicles (85-90% accuracy)
(Ozcan et al., 2020)	2019	Car camera	VGG16 (CNN)	Road surface and weather condition evaluation accuracy	Moderate	Real-time video	Limited ability to handle complex weather conditions	Developed for autonomous driving applications (70-80% accuracy)
(Barba-Guaman et al., 2020)	2020	-	PedNet, MultiPed, SSD-MobileNet v1/v2, SSD-Inception v2	Vehicle and Pedestrian recognition accuracy	Moderate	Real-time video	Limited performance on cluttered scenes	Evaluated on NVIDIA Jetson Nano (80-90% accuracy)
(Hechri and Mtibaa, 2020)	2019	German Traffic Sign Dataset	SVM + HOG, CNN	Traffic sign classification accuracy	High	Static images	Limited robustness to occlusions and degraded signs	Two-phase approach for improved accuracy (95-97% accuracy)
(Li et al., 2024)	2023	TT100k	DeployEase-YOLO YOLOv5	Traffic sign Detection accuracy	High	Real-time video	Limited generalizability to unseen sign types	Optimized for edge devices with reduced model size (90-95% accuracy)
(Çınarer, 2024)	2022	-	YOLOv5	Traffic-sign recognition accuracy	High	Real-time video	Limited performance in low-light conditions	Demonstrated high accuracy and speed on various datasets (90-95% accuracy)

3. Materials and Methods

This study employs the YOLOv8n model to identify traffic signals as visual instructions on a mobile robotic system. The rationale for selecting a differential robot equipped with a robotic arm lies in its potential for further enhancement and adaptation with military or civilian equipment. Moreover, deep learning algorithms are utilized to process images captured by a camera connected to the embedded artificial intelligence computer installed on the vehicle. Deep learning algorithms serve as powerful tools for image processing tasks, such as object detection. However, these algorithms are often computationally complex, making them challenging to execute on devices with limited capacity. To address this issue, the precision of the model's floating-point (FP) representation can be reduced, thereby enhancing processing efficiency without significantly compromising detection accuracy

(Terakura et al., 2024).

In the study, the precision of the FP representation of the chosen deep learning model was reduced to IN8 using TensorRT to enhance performance on Jetson Nano. Figure 2 illustrates the system diagram, which includes the following steps:

•Check Cycle Status: The operational cycle status of the system is checked. If the cycle is running, continue with the following steps.

•Image acquisition: An image of the surrounding environment is captured using a camera mounted on the robot.

•Model: YOLO2TRT model is applied to the detected image for traffic sign detection.

•Check for traffic signal: Checks if there is a traffic signal detected in the image. If no signal is detected, return to step 2.

•Repeatability check: To ensure the validity of the detection, the repeatability of the signal detection within a period of less than 0.5 seconds is checked. If the signal is detected repeatedly, proceed with the following steps.

•Data acquisition: Data related to the detected traffic signal is collected, such as the type of signal, its location, and any other relevant information.

•Data display: The detected data is displayed on a screen.

•Data storage: The detected data is stored in a database for future use.

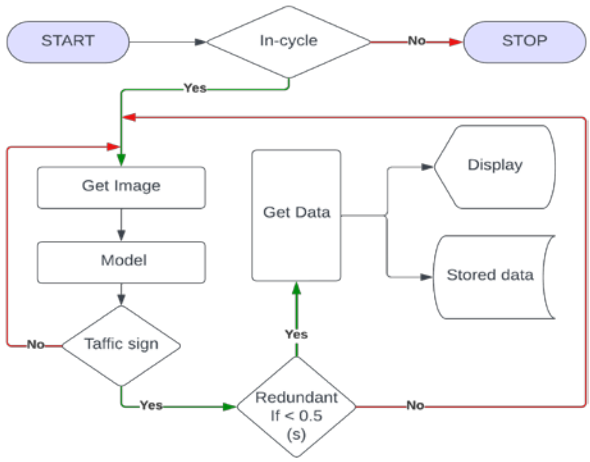


Figure 2. System diagram.

3.1. Mathematical Model of Differential Two-Wheel Mobile

The robot's position in the global coordinate system (GCS) is determined by the x and y coordinates of its local coordinate system (LCS) origin, along with a rotation angle that defines its orientation by an angle φ. The kinematic model for the two-wheeled mobile robot, which features differentially controlled motors, is based on the origin of LCS (OLCS). This point is usually located at the midpoint of the axis of rotation between the wheels, as shown in Figure 3. The distance from the OLCS to the wheel mounts is $2l$, and both wheels share the same radius, denoted by ρ.

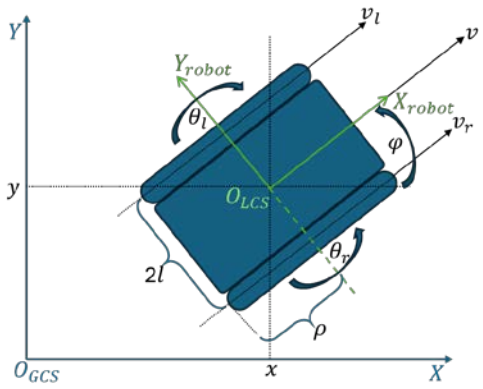


Figure 3. Mobil robot in 2D plane.

The robot's velocity is the average of the velocities of the individual wheels and is given by:

$$v = \frac{v_r + v_l}{2} \tag{1}$$

In equation 1, v_r and v_l denote the linear velocities of the right and left wheels, respectively. The kinematic equations for the differential drive robot in the world frame, given the specified constraints (Hassan et al., 2024), are as follows. Equation 2 represents the motion of a two-wheel differential drive mobile robot (DDMR).

$$v_r = \rho\, \omega_r, v_l = \rho\, \omega_l \tag{2}$$

where:

- ω_r: Angular velocity of the right driving wheel (rads/s).
- ω_l: Angular velocity of the left driving wheel (rads/s).

The robot's dynamic function is defined as:

$$\dot{x} = v\cos(\varphi), \dot{y} = v\sin(\varphi), \dot{\varphi} = \omega = \frac{v_r - v_l}{2l} \tag{3}$$

The previous equations can be expressed in matrix form. The simplified kinematic model of the differential drive mobile robot, used for designing the robot, is represented by equation 4 $R(\varphi)$ in the GCS as:

$$R(\varphi)_{GCS} = \begin{bmatrix} \dot{x} \\ \dot{y} \\ \dot{\varphi} \end{bmatrix} = \begin{bmatrix} \cos(\varphi) & 0 \\ \sin(\varphi) & 0 \\ 0 & 1 \end{bmatrix} \begin{bmatrix} v \\ \omega \end{bmatrix} \tag{4}$$

By transforming these velocities components into rotational velocities (□□, □□), the above model can be improved to:

$$v = \rho \frac{(\omega_r + \omega_l)}{2}, \omega = \rho \frac{\omega_r - \omega_l}{2l} \tag{5}$$

$$\begin{bmatrix} v \\ \omega \end{bmatrix} = \begin{bmatrix} \frac{\rho}{2} & \frac{\rho}{2} \\ \frac{\rho}{2l} & \frac{-\rho}{2l} \end{bmatrix} \begin{bmatrix} \omega_r \\ \omega_l \end{bmatrix} \tag{6}$$

Equation 6 is substituted into equation 4 to derive a more detailed kinematic model, as shown in equation 7.

$$R(\varphi)_{GCS} = \begin{bmatrix} \dot{x} \\ \dot{y} \\ \dot{\varphi} \end{bmatrix} = \begin{bmatrix} \frac{\rho}{2}\cos(\varphi) & \frac{\rho}{2}\cos(\varphi) \\ \frac{\rho}{2}\sin(\varphi) & \frac{\rho}{2}\sin(\varphi) \\ \frac{\rho}{2l} & -\frac{\rho}{2l} \end{bmatrix} \begin{bmatrix} \omega_r \\ \omega_l \end{bmatrix} \tag{7}$$

The robot's velocity is the sum of its two speeds, v_r and v_l. Additionally, the relationship between the robot's angular speed, v_r and v_l, and the separation between the two wheels is given by equation 8.

$$v = \frac{(v_r + v_l)}{2}, \dot{\varphi} = \frac{(v_r - v_l)}{2l} \quad (8)$$

By substituting equation 1 into equation 8, we obtain equation 9, which explains the relationship between each wheel's angular velocity and the robot's linear and angular velocity.

$$v = \rho\frac{(\omega_r + \omega_l)}{2}, \dot{\varphi} = \rho\frac{(\omega_r - \omega_l)}{2l} \quad (9)$$

3.2. Accelerators

The current trend in AI development heavily depends on large models and vast datasets, leading to a significant demand for high computing power in advanced AI solutions. Consequently, future research in Reinforcement Learning-based Energy Management Systems (RL-EMS) will likely encounter challenges related to AI deployment. Effective deployment on individual vehicles will require specific deployment architecture tools. The following three primary tools are commonly used for deploying AI solutions: Open Visual Inference and Neural Network Optimization (OpenVino) for CPU devices, TensorRT for GPU devices, and MediaPipe for edge devices (Jooshin et al., 2024; Lin et al., 2024) .

3.2.1. ONNX

ONNX (Open Neural Network Exchange) is an open standard format for machine learning and deep learning models. It enables the conversion of models from various frameworks, such as TensorFlow, PyTorch, MATLAB, Caffe, and Keras, into a single unified format. ONNX provides a common set of operators, building blocks for deep learning, and a standardized file format. It defines a computation graph and includes built-in operators, where the ONNX nodes, which may have multiple inputs or outputs, form an acyclic graph.

After training a network using any framework, the batch size and precision—such as FP32, FP16, or INT8—are set. The trained model is then processed by the TensorRT optimizer, which generates an optimized runtime referred to as a plan. This plan is stored in a .plan file, a serialized format of the TensorRT engine. To run inference, the plan file must be deserialized using the TensorRT runtime (Lai and Morris, 2019).

To optimize models created in various frameworks, the process involves converting the models to the ONNX format and using the ONNX parser in TensorRT to parse the model and build the TensorRT engine. Figure 4 illustrates the high-level workflow for ONNX model optimization (Lai and Morris, 2019).

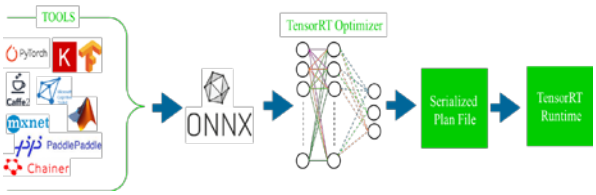


Figure 4. ONNX workflow.

3.2.2. TensorRT

NVIDIA TensorRT is a Software Development Kit (SDK) designed for deep learning inference, supporting both C++ and Python languages. It offers APIs and parsers to import trained models from all major deep learning frameworks, subsequently generating optimized runtime engines suitable for deployment in data centers, as well as automotive and embedded environments. Deep learning is utilized across various applications, including natural language processing, recommender systems, and image and video analysis. As the adoption of deep learning in production grows, the increasing complexity and size of models have heightened demands for accuracy and performance. In safety-critical applications, such as those in the automotive sector, strict requirements for throughput and latency are crucial. Similar demands are present in consumer applications like recommendation systems.

TensorRT is specifically designed to facilitate the deployment of deep learning models for such use cases. It supports all major frameworks, enabling the processing of large datasets with low latency through advanced optimizations, reduced precision, and efficient memory usage.

The deployment process with TensorRT begins by importing the model, which involves loading it from a saved file on disk and converting it into a TensorRT network from its original framework or format. ONNX (Open Neural Network Exchange) serves as a standard for representing deep learning models, facilitating their transfer between different frameworks, including Caffe2, Chainer, CNTK, PaddlePaddle, PyTorch, and MXNet. After conversion, an optimized TensorRT engine is built based on the input model, the target GPU platform, and specified configuration parameters. The final step involves feeding input data to the TensorRT engine to perform inference. Figure 5 illustrates the workflow of converting a trained model into a TensorRT engine (Jeong et al., 2022; Lai and Morris, 2019).

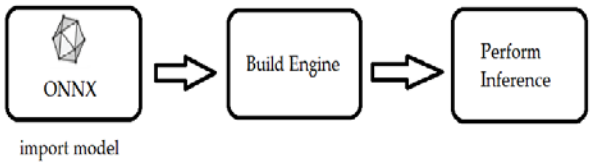


Figure 5. Illustrating work process of trained model into TensorRT.

3.3. Traffic Signs Dataset

The purpose of traffic lights is to warn, inform, arrange or regulate the behavior of users in certain road or traffic conditions. This is why knowing the meaning of traffic lights is essential before you start driving, in this way we will avoid causing accidents due to our fault and car accidents that could have been avoided.

Figure 6 shows the details of the dataset used in this work, which contains 15 categories: two categories for red and green traffic lights, one for stop signs, and the remaining for speed limits. The dataset consists of 4,969 images, divided as follows: 71% for training, 16% for validation, and 13% for testing.

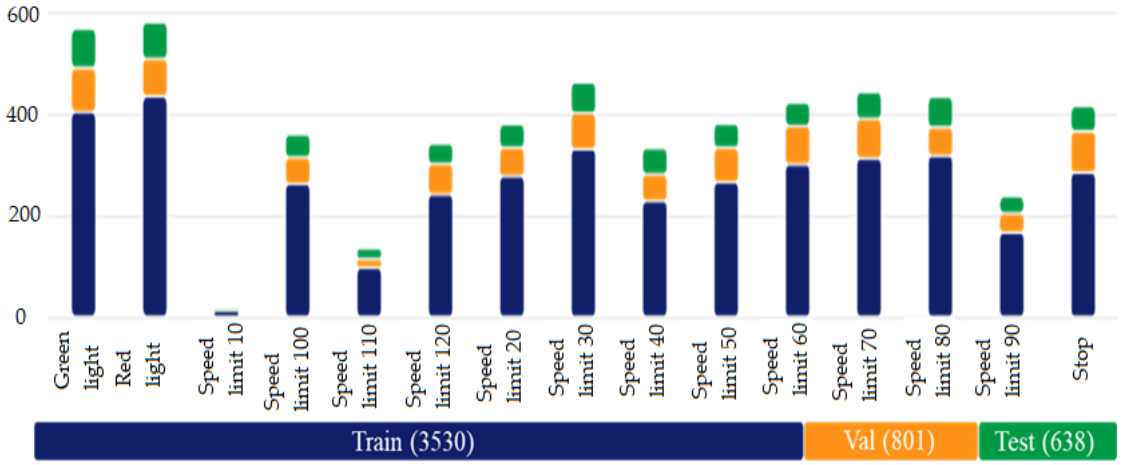


Figure 6. Details of the dataset.

3.4. YOLO Object Detection Algorithm

YOLO algorithm is a state-of-the-art technology developed by Ultralytics for DNN-based object detection / classification, with a major focus on performing real-time tasks without loss of detection accuracy (Terven et al., 2023). YOLO seeks to discover and identify items in real-time inside an image or video stream. By approaching object identification as a single regression issue, YOLO adopts a different strategy from standard approaches, which rely on intricate pipelines and many runs. The input picture is divided into a grid by this method, which then forecasts bounding boxes and class probabilities for items inside each grid cell. It is very quick and efficient since it predicts both the class labels and the bounding boxes that correspond to them at the same time. Because of its remarkable real-time performance, YOLO is renowned for processing photos and movies quickly (Shamta and Demir, 2024).

Table 3 shows a comparison between the performance measurement, Mean Average Precision (mAP) and the number of frames processed for both YOLOv8 and YOLOv5 under the same comparison conditions.

Table 3. A comparison between the performance measurement, (mAP%) and the number of frames processed for YOLOv8 and YOLOv5

Ref	Model	Dataset	Image size (pixels)	Batch size	Device (GPU)	Metrics (mAP@50)	FPS
Terven et al., 2023	YOLOv8	2017 MS COCO	640	32	NVIDIA V100	53.9 %	280
Shamta and Demir, 2024	YOLOv5	2017 MS COCO	640	32	NVIDIA V100	50.7 %	200

4. Experimental Results

The image of the differential robot utilized in this study, equipped with a robotic arm and an NVIDIA Jetson Nano artificial intelligence computer with a camera, is presented in Figure 7. The primary aim of this system is to enable a robotic system, which is open to further hardware development, to perceive visual instructions through deep learning methods. The visual instructions employed include traffic signs such as traffic lights, directional signs, stop signs, and speed limits ranging from 10 to 120 km/h. The YOLOv8 object detection model was used for the detection of these instructions.

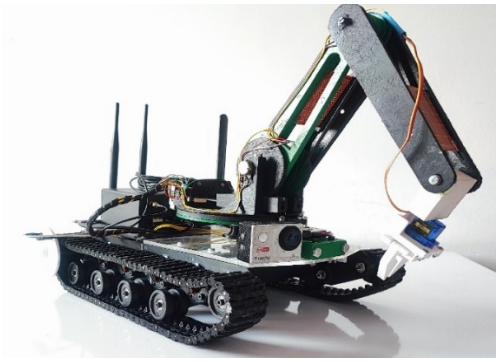


Figure 7. Robotic vehicle.

The training results of the YOLOv8 model demonstrated an overall mAP50 of 96.9%. The performance across the 15 different classes exhibited some variations. Specifically, the mAP50 for the stop sign class was 99.4%, the red traffic light class was 84.6%, and the green traffic light class was 89.3%. For speed limits, the mAP50 values were as follows: 20 km/h at 98.7%, 30 km/h at 99.3%, 40 km/h at 99.2%, 50 km/h at 97.2%, 60 km/h at 97.5%, 70 km/h at 98.7%, 80 km/h at 99.1%, 90 km/h at 98.2%, 100 km/h at 99.2%, 110 km/h at 97.4%, and 120 km/h at 99.4%, as illustrated in Figure 8. The discrepancies observed in the green and red traffic light classes can be attributed to several factors, including the number of images in the dataset, the quality of the captured images, and the presence of noise.

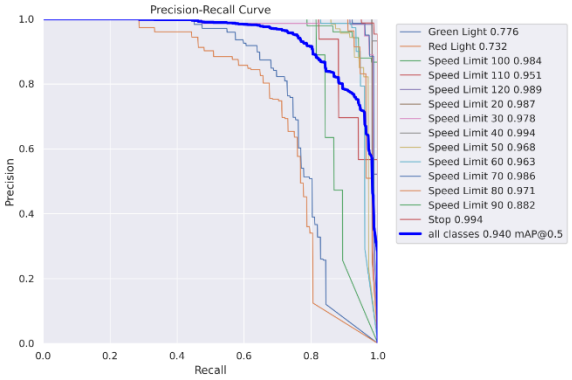


Figure 8. PR curve.

The training process exhibited smooth progression in the training curves for both precision and recall, as well as in the box losses and classification losses during both training and testing phases, as illustrated in Figure 9.

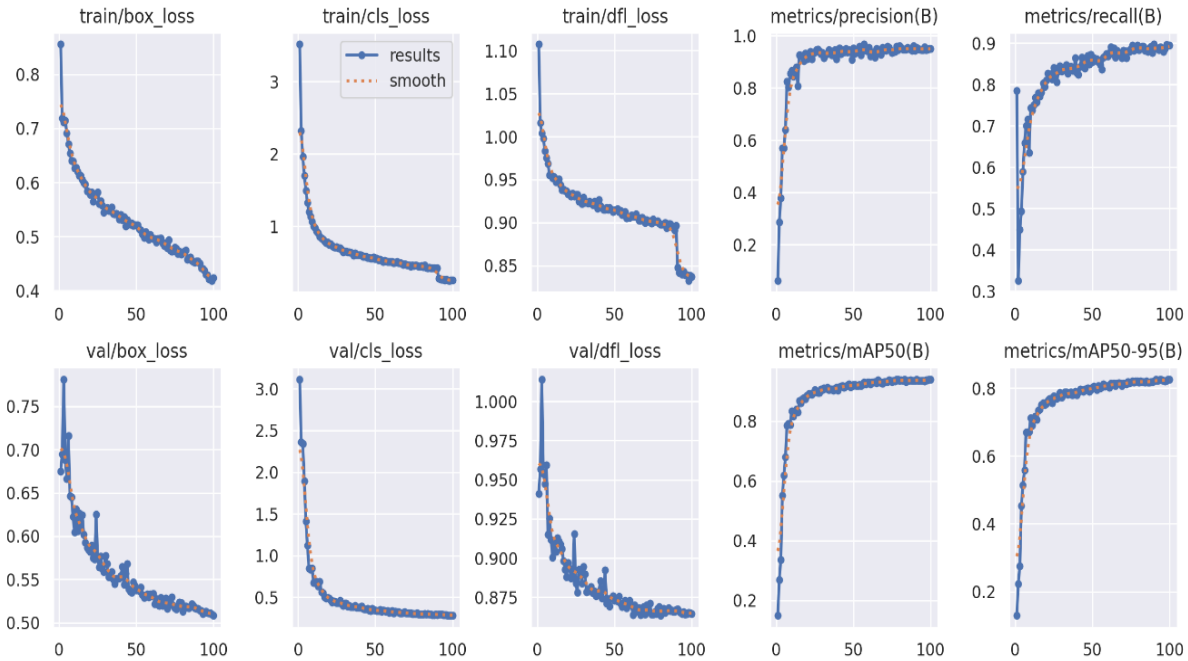


Figure 9. Training process.

In these applications, ensuring the model's accuracy and smooth operation is not sufficient; it is also imperative to consider the computational cost. This is because the computational cost of deploying the models is closely linked to the FPS capability of the camera. To address this, one of Nvidia's accelerators, TensorRT, was employed to optimize the model by reducing its weights, as detailed in Table 4.

Table 4. Results before and after the model acceleration

Model	Image size	FPS
Torch	480x640	14 FPS
TensorRT	640x640	33 FPS

In this study, the employed model demonstrated robustness by achieving a frame rate of 33 FPS with the TensorRT accelerator and an accuracy of 96.6% mAP50 using the YOLOv8 model. However, it exhibited some limitations in terms of high reliability for this type of application. Additional factors include the relative size of Jetson Nano compared to the robot and the accuracy of the camera at various speeds. Jetson Nano's physical dimensions and processing capabilities can pose integration challenges, particularly in maintaining balance and stability of the robot. Moreover, the camera's accuracy can be influenced by motion blur at higher speeds, lighting conditions, and other environmental factors, potentially impacting the model's performance. These constraints highlight the need for ongoing refinement and optimization. Figure 10 illustrates real-time test image from the model using TensorRT.



Figure 10. Real-Time test image of the accelerated model with TensorRT.

5. Conclusions

This study addresses the detection of visual instructions by a deep learning model in a mobile robotic system equipped with an embedded AI computer. A system comprising a differential robot equipped with a robotic arm, Jetson Nano, and a camera was developed to detect traffic signs as visual instructions using the YOLOv8 object detection deep learning model. The preference for a mobile robotic system over a standard electric vehicle is due to its ability to be easily modified with new hardware and adaptable to new instruction structures based on varying needs. The employed model demonstrated a high overall mAP50 accuracy of 96.9%, with individual class accuracy varying across different traffic signs. The integration of TensorRT accelerated the model, achieving 33 FPS while maintaining a mAP50 accuracy of 96.6%. As evident from the results obtained in this research, a foundational framework is provided for developing more reliable and efficient visual instruction recognition systems in autonomous robotic platforms.

Despite these promising results, challenges remain in achieving high reliability for real-world applications. Factors such as the physical size of the on-board AI computer, camera accuracy at various speeds, and environmental conditions impact overall performance. Future studies are planned to focus on improving the model's reliability and robustness. This may include optimizing hardware-software integration, improving image quality under varying conditions, and integrating additional sensors to address the limitations of the current camera system. Continuous development and testing will be crucial to ensure the high reliability required for real-world applications. It is evident that optimizing hardware-software integration, improving image quality, and enhancing overall system reliability will lead to increased performance.

Author Contributions

The percentages of the author's contributions are presented below. All authors reviewed and approved the final version of the manuscript.

	I.S.	F.D.
C	50	50
D	50	50
S	50	50
DCP	50	50
DAI	50	50
L	50	50
W	50	50
CR	50	50
SR	50	50
PM	50	50
FA	50	50

C=Concept, D= design, S= supervision, DCP= data collection and/or processing, DAI= data analysis and/or interpretation, L= literature search, W= writing, CR= critical review, SR= submission and revision, PM= project management, FA= funding acquisition.

Conflict of Interest

The authors declared that there is no conflict of interest.

Ethical Consideration

Ethics committee approval was not required for this study because of there was no study on animals or humans.

References

Barba-Guaman L, Eugenio Naranjo J, Ortiz A. 2020. Deep learning framework for vehicle and pedestrian detection in rural roads on an embedded GPU. Electronics, *9*(4): 589.

Cai ZX, Gu MQ. 2013. Traffic sign recognition algorithm based on shape signature and dual-tree complex wavelet transform. J Cent South Univ, 20(2): 433–439.

Chen J, Jia K, Chen W, Lv Z, Zhang R. 2022. A real-time and high-precision method for small traffic-signs recognition. Neural Comput Appl, 34(3): 2233–2245.

Çınarer G. 2024. Deep learning based traffic sign recognition using YOLO algorithm. Düzce Univ. J Sci Tech, 12(1): 219–229.

Dalal N, Triggs B. 2005. Histograms of oriented gradients for human detection. Soc Conf Comput Vision Pattern Recog (CVPR'05), San Diego, CA, USA, 1: 886–893.

Flores-Calero M, Astudillo CA, Guevara D, Maza J, Lita BS, Defaz B, Ante JS, Zabala-Blanco D, Armingol Moreno JM. 2024. Traffic sign detection and recognition using YOLO object detection algorithm: A Systematic Rev. Mathematics, 12(2): 1–31.

Girshick R, Donahue J, Darrell T, Jitendra M. 2014. Rich feature hierarchies for accurate object detection and semantic segmentation. IEEE Conf Comput Vision Pattern Recog., 580–587.

Gudigar A, Chokkadi S, Raghavendra U, Acharya UR. 2017. Multiple thresholding and subspace based approach for detection and recognition of traffic sign. Mult Tools Appl, 76(5), 6973–6991.

Guney E, Bayilmis C, Cakan B. 2022. An implementation of real-time traffic signs and road objects detection based on mobile

GPU platforms. IEEE Access, 10: 86191–86203.

Han Y, Wang F, Wang W, Li X, Zhang J. 2024. YOLO-SG: Small traffic signs detection method in complex scene. J Supercomp, 80(2): 2025–2046.

Hassan IA, Abed IA, Al-Hussaibi WA. 2024. Path planning and trajectory tracking control for two-wheel mobile robot. J Robot Cont (JRC), 5(1): 1–15.

Hechri A, Mtibaa A. 2020. Two-stage traffic sign detection and recognition based on SVM and convolutional neural networks. IET Image Process, 14(5): 939–946.

Houben S, Stallkamp J, Salmen J, Schlipsing M, Igel C. 2013. Detection of traffic signs in real-world images: The German traffic sign detection benchmark. Int Joint Conf Neural Networks, Dallas, TX, USA, pp: 1–8.

Jeong EJ, Kim J, Tan S, Lee J, Ha S. 2022. Deep learning inference parallelization on heterogeneous processors with TensorRT. IEEE Embed Syst Lett, 14(1): 15–18.

Jin Y, Fu Y, Wang W, Guo J, Ren C, Xiang X. 2020. Multi-feature fusion and enhancement single shot detector for traffic sign recognition. IEEE Access, 8: 38931–38940.

Jooshin HK, Nangir M, Seyedarabi H. 2024. Inception-YOLO: Computational cost and accuracy improvement of the YOLOv5 model based on employing modified CSP, SPPF, inception modules. IET Image Process, 18(8): 1985–1999.

Kounte MR, Shri CvA., Harshvardhan V, Kumari A, Dhruv S. 2022. Design and development of autonomous driving car using nvidiajetson nano developer kit. 8-9 Oct. 2022, 4th Int Conf Cybernetics, Cognition and Machine Learning Appl (ICCCMLA), Goa, India, pp: 486–489.

Krizhevsky A, Sutskever I, Hinton GE. 2017. ImageNet classification with deep convolutional neural networks. Commun ACM, 60(6): 84–90.

Kumar BA, Majji M, Marni HJ, Ateeq M, Koduru S, Maddi SM 2023. A deep transfer learning approach for enhanced traffic sign recognition in autonomous vehicles with NVIDIA jetson nano. Int. Conf Sustain. Emerg Innov Eng Technol (ICSEIET), Ghaziabad, India, pp: 692–698.

Lai G, Morris T. 2019. TensorRT inference with TensorFlow. GPU Tech Conf, pp: 75.

Li Y, Zhang Z, Yuan C, Hu J. 2024. Easily deployable real-time detection method for small traffic signs. J Intell Fuzzy Syst, 46: 8411–8424.

Lin Y, Chu L, Hu J, Hou Z, Li J, Jiang J, Zhang Y. 2024. Progress and summary of reinforcement learning on energy management of MPS-EV. Heliyon, 10(1): e23014.

Mahmoud MAB, Guo P. 2019. A novel method for traffic sign recognition based on DCGAN and MLP with PILAE algorithm. IEEE Access, 7: 74602–74611.

Maldonado-Bascón S, Lafuente-Arroyo S, Gil-Jiménez P, Gómez-Moreno H, López-Ferreras F. 2007. Road-sign detection and recognition based on support vector machines. IEEE Trans Intell Transp Syst, 8(2): 264–278.

Ozcan K, Sharma A, Knickerbocker S, Merickel J, Hawkins N, Rizzo M. 2020. Road weather condition estimation using fixed and mobile based cameras. Advances in Comput. Vision: Proc. of the 2019 Comput. Vision Conf (CVC), 1 (1): 192–204.

Ren S, He K, Girshick R, Sun J. 2017. Faster R-CNN: towards real-time object detection with region proposal networks. IEEE Trans Pattern Anal Mach Intell, 39(6): 1137–1149.

Sarvajcz K, Ari L, Menyhart J. 2024. AI on the road: NVIDIA jetson nano-powered computer vision-based system for real-time pedestrian and priority sign detection. Appl Sci, 14(4): 1440.

Satti SK, Rajareddy GNV, Mishra K, Gandomi AH. 2024. Potholes and traffic signs detection by classifier with vision transformers. Sci Rep, 14(1): 1–18.

Shamta I, Demir BE. 2024. Development of a deep learning-based surveillance system for forest fire detection and monitoring using UAV. PLoS ONE, 19(3): e0299058.

Shustanov A, Yakimov P. 2017. CNN design for real-time traffic sign recognition. Procedia Eng, 201: 718–725.

Stallkamp J, Schlipsing M, Salmen J, Igel C. 2011. The German traffic sign recognition benchmark: A multi-class classification competition. 31 July - 05 August 2011, Int. Joint Conf Neural Networks, San Jose, CA, USA, pp: 1453–1460.

Terakura K, Chang Q, Miyazaki J. 2024. Acceleration of neural network inference for embedded gpu systems. Int Conf Big Data Smart Comput, Bangkok, Thailand, pp: 361–362.

Terven J, Córdova-Esparza DM, Romero-González JA. 2023. A comprehensive review of YOLO architectures in computer vision: from YOLOv1 to YOLOv8 and YOLO-NAS. Machine Learn Knowl Extr, 5(4): 1680–1716.

Thasai Y, Kim P, Ynag Z. 2009. Generalized traffic sign detection model for developing a sign inventory. J Comp Civil Eng, 23(5): 266–276.

Wali SB, Abdullah MA, Hannan MA, Hussain A, Samad SA, Ker PJ, Mansor MB. 2019. Vision-based traffic sign detection and recognition systems: Current trends and challenges. Sensors, 19(9): 2093.

Wali SB, Hannan MA, Hussain A, Samad SA. 2015. An automatic traffic sign detection and recognition system based on colour segmentation, shape matching, and svm. Math Probl Eng, 2015(1): 250461.

You F, Zhang R, Lie G, Wang H, Wen H, Xu J. 2015. Trajectory planning and tracking control for autonomous lane change maneuver based on the cooperative vehicle infrastructure system. Expert Syst Appl, 42(14): 5932–5946.

Yuan X, Hao X, Chen H, Wei X. 2014. Robust traffic sign recognition based on color global and local oriented edge magnitude patterns. IEEE Trans Intell Transp Syst, 15(4): 1466–1474.

Zhang RH, He ZC, Wang HW, You F, Li KN. 2017. Study on self-tuning tyre friction control for developing main-servo loop integrated chassis control system. IEEE Access, 5: 6649–6660.

Black Sea Journal of Engineering and Science
doi: 10.34248/bsengineering.1611775

Open Access Journal
e-ISSN: 2619 – 8991

Research Article
Volume 8 - Issue 2: 428-434 / March 2025

APPLYING PERMANOVA FOR MULTIVARIATE ANALYSIS OF VARIANCE IN HEALTH STUDIES

Fahrettin KAYA[1]*

[1]*Kahramanmaraş Sütçü İmam University, Andırın Vocational School, Department of Computer Technologies, 46400, Kahramanmaraş, Türkiye*

Abstract: Health data often do not meet the normality assumption, which limits the applicability of traditional analysis of variance methods. The aim of this study is to propose a methodological framework for analyzing such data by examining PERMANOVA (Permutational Multivariate Analysis of Variance), a method that does not require the normality assumption and is particularly suitable for complex datasets, within the context of maternal health data. In the context of maternal healthcare in Bangladesh, the effects of two independent variables—risk and age factors—on multivariate response variables such as Systolic Blood Pressure (mmHg), Diastolic Blood Pressure (mmHg), Blood Sugar (mmol/L), Body Temperature (Fahrenheit), and Heart Rate (beats per minute) were examined using the PERMANOVA method. The first independent variable represents the risk factor, comprising three different risk levels (low, mid, high), while the second independent variable represents the age factor, divided into four age groups (young, adolescent, middle-aged, menopausal). The dependent variables did not follow a normal distribution, as confirmed by the Anderson-Darling test and Mardia's multivariate normality test. As a result of the PERMANOVA analysis, it was determined that at least two mean differences between the groups of the risk factor and the age factor were statistically significant in terms of the response variables ($P<0.01$). Furthermore, pairwise comparisons of the factor groups revealed that the mean differences between the low, mid, and high levels of the risk factor, as well as the mean differences among the young, adolescent, and middle-aged groups of the age factor, were statistically significant ($P<0.01$). However, the mean difference between the middle-aged and menopausal groups for the age factor was found to be statistically insignificant ($P>0.01$). The PERMANOVA method is recommended for researchers to accurately determine whether the mean differences in factor levels are statistically significant or to identify threshold values of the groups by using multiple response variables simultaneously and performing pairwise comparisons of factor groups.

Keywords: PERMANOVA, Pairwise comparison, ANOVA, Non-parametric analysis, Maternal health

***Corresponding author:** Kahramanmaraş Sütçü İmam University, Andırın Vocational School, Department of Computer Technologies, 46400, Kahramanmaraş, Türkiye
E mail: fkaya@ksu.edu.tr (F. KAYA)
Fahrettin KAYA https://orcid.org/0000-0003-1666-4859

Received: January 02, 2025
Accepted: February 02, 2025
Published: March 15, 2025

Cite as: Kaya F. 2025. Applying PERMANOVA for multivariate analysis of variance in health studies. BSJ Eng Sci, 8(2): 428-434.

1. Introduction

Health is one of the most fundamental aspects of human life, and research in this field generally focuses on the causes, effects, and treatments of diseases. For instance, diabetes can lead to complications such as diabetic neuropathy and nephropathy, and it may also contribute to the development of cardiovascular diseases and other vascular disorders (Sowers et al., 2001). The development of treatment methods to address such complex health problems represents a significant area of research. The effectiveness of these treatment methods across patient groups should also be investigated.

In such studies, statistical methods provide powerful tools for understanding complex relationships. For example, Analysis of Variance (ANOVA) is a frequently used method in health research. ANOVA is a fundamental statistical tool used to examine variance differences in the means of a dependent variable across different groups of an independent variable (Underwood, 1981; Şahin and Koç, 2018). However, ANOVA is limited to analyzing single dependent variables. In cases in which multiple dependent variables are involved, more comprehensive methods, such as multivariate analysis of variance (MANOVA) are often preferred (Tinsley and Brown, 2000; Tabachnick et al., 2013; Koç et al., 2019). Nevertheless, MANOVA methods may encounter difficulties in meeting key assumptions such as multivariate normality and homogeneity.

In this context, Permutational Multivariate Analysis of Variance (PERMANOVA) has emerged as a nonparametric statistical test method for analyzing complex multivariate datasets (Anderson, 2001). Due to its flexibility and versatility, PERMANOVA is widely used in various fields, including biology, ecology, and environmental sciences. The proposed method allows multivariate analysis independent of data distribution. For instance, using this method, Pasin et al. (2016) demonstrated that individuals with Hashimoto's disease exhibit significantly different lipid levels compared with healthy individuals, regardless of sex.

Considering these challenges, this study makes a methodological contribution by applying the

This work is licensed (CC BY-NC 4.0) under Creative Commons Attribution 4.0 International License

nonparametric multivariate analysis technique PERMANOVA to maternal health data. The study examined the association between risk factors and age groups (independent variables) and key health indicators such as systolic and diastolic blood pressure, blood glucose levels, body temperature and heart rate (dependent variables) and analyzed the mean differences between the factor groups in terms of dependent variables. The findings are expected to provide valuable information for maternal health risk assessments and contribute to the widespread use of nonparametric methods in medical research.

2. Materials and Methods

The dataset used in this study was created by collecting data from healthcare centers, transferring it via an IoT smart health device to a web portal, and storing it on a server. The dataset was obtained from a machine learning repository published on the Kaggle platform and includes 1,014 patient records (Ahmed and Kashem, 2020; Togunwa et al., 2023).

The first independent variable in the dataset is the patient risk level. This variable was categorized into three groups: high risk (272 records), medium risk (336 records), or low risk (406 records). The second independent variable is age group. This variable was restructured according to women's fertility status and categorized into four categories. The young age group (under 20 years) had low fertility levels, with 279 records. The adolescent age group (20-34 years) had the highest fertility levels, with 417 records. The middle age group (35-44 years) exhibits declining fertility levels and includes 135 records. The menopausal age group (above 44 years) had low fertility levels and comprised 183 records. The dependent variables examined in this study comprised five key health-related parameters: diastolic blood pressure (DBP, mmHg), body temperature (BT, °F), systolic blood pressure (SBP, mmHg), blood glucose (BG, mmol/L), and heart rate (HR, bpm). The dataset was analyzed to explore the interactions between these factors and independent variables to evaluate health outcomes. The dataset was analyzed using PERMANOVA to explore the interactions between factors and dependent variables.

PERMANOVA analysis is frequently employed in data structures that exhibit MANOVA patterns. Evaluations of differences between groups were conducted via a transformation predicated on ANOVA. A crucial facet of this analysis is transformation. The F value in the ANOVA table was not derived directly from the raw data; instead, it was calculated on the basis of a distance matrix constructed from the distances between pairs of observations. In ANOVA or MANOVA, the original layout of the raw data was grouped by factors, as depicted in Figure 1a. The grouping order is randomly shuffled hundreds of times, rearrangements are executed (permutations are performed), and pseudo-F values are calculated each time over the distance matrices created by these permutations. Concurrently, the F value of the original layout wass recorded in the initial calculation. A permutation test statistic is obtained by comparing the F-value in the original order with the pseudo F-values, and the difference between the groups is scrutinized with this test statistic (Anderson, 2001; 2014). The distances referenced in the study typically were included distance measurements such as Euclidean, City Block, Chi-square, Bray Curtis, Binomial, Jaccard, and others (Oksanen et al., 2022). In this study, the Bray Curtis, Binomial, and Mahalanobis distance measures were favored. The assumption in this analysis does not necessitate uniformity of variance, provided that a balanced experimental design is in place. The observations (rows in the original data matrix) are deemed independent and originate from an identical distribution.

2.1. Data Preparation

The starting point of this analysis was the creation of a distance observation matrix using the raw data matrix. In the raw data matrix, each observation is represented by a row in the original order of the factor groups, and each response variable is represented by a column. This matrix consists of N rows and p columns and is represented as seen in Figure1a (Anderson, 2001).

The matrix of dimensions N x N, comprising distances between row pairs of observations with indices such as i and j, undergoes transformation as depicted in Figure1b. The matrix derived from this transformation is termed the observation distance matrix. Each cell within the matrix cells the distance value between pairs of response variables. This matrix exhibits a symmetrical structure, composed of gray and white regions. The SS_T is computed utilizing the observation distance matrix in Figure1a's grey area.

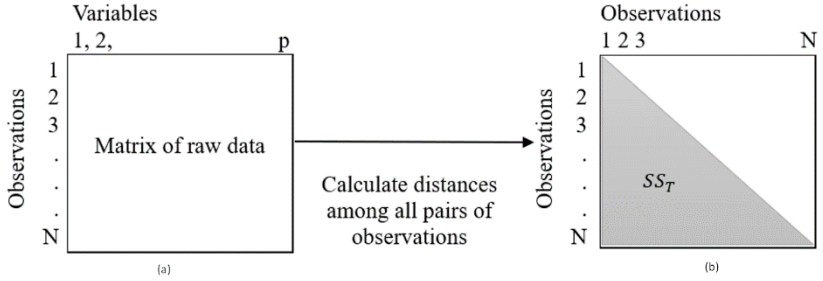


Figure 1. Illustrative representation of the data structure in PERMANOVA analysis.

The distance between the observation rows i and j is denoted by d_{ij}. For instance, the Euclidean distance of three-response variables such as X, Y, Z is calculated by ANOVA by reducing it to a singular distance value as $d_{ij} = \sqrt{(x_i - x_j)^2 + (y_i - y_j)^2 + (z_i - z_j)^2}$. In this scenario, the squares of all distances in the lower-diagonal half of the distance matrix are aggregated (total variance) and divided by the total number of observations N. The sum of the resulting grand total squares is as follows in equation 1:

$$SS_T = \frac{1}{N} \sum_{i=1}^{N-1} \sum_{j=i+1}^{N} d_{ij}^2 \quad (1)$$

2.2. One-Way ANOVA Design

In the instance of a one-way design in the PERMANOVA analysis, in the most elementary scenario, consider a groups in which a factor such as A is examined, and n observations in each group. The total number of observation units N equals an. In this scenario, the exemplar design, which comprises two groups such as single-factor A_2 and A_1, can be depicted as shown in Figure 2a. The summation of the within squares of factor A corresponds to the summation of the distance values d_{ij} in the cells constituting the gray area in Figure 2a. That is, $SS_{W(A)}$ symbolizes the summation of the squared distances between repetitions within the same group and is computed by dividing by n, which represents the number of repetitions of each group. The summation of intragroup squares is expressed as in equation 2:

$$SS_{W(A)} = \frac{1}{n} \sum_{i=1}^{N-1} \sum_{j=i+1}^{N} d_{ij}^2 \, \delta_{ij} \quad (2)$$

here, the value of δ_{ij} is 1 when observation i and observation j are in the same group; otherwise, its value is zero. In addition, the total squares between the groups of factor A are given by in equation 3.

$$SS_A = SS_T - SS_{W(A)} \quad (3)$$

Using these calculations, a one-way analysis of variance table is arranged as shown in Appendix A.

2.3. Two-way ANOVA Design

Consider a two-factorial design scenario with factors A (e.g., Risk Factor) and B (e.g., Age Factor) in the context of statistical analysis. Factor A, the primary factor, comprises 'a' levels or groups, each containing 'n' observations. Similarly, Factor B, the secondary factor, also consists of 'b' distinct levels or groups, each with 'n' observations. The total number of observations, denoted by N, can be mathematically represented as $N = abn$. The distance matrices of observations in a two-factorial design can be depicted as illustrated in Figure 2 (Anderson, 2001).

When the effect of Factor B is disregarded, the within-group sum of squares for Factor A, denoted as $SS_{W(A)}$, is obtained by dividing the sum of squared distances in the cells falling into the grey area in Figure 2a by 'bn', and it is calculated using equation 4.

$$SS_{W(A)} = \frac{1}{bn} \sum_{i=1}^{N-1} \sum_{j=i+1}^{N} d_{ij}^2 \, \delta_{ij}^A \quad (4)$$

here, δ_{ij}^A takes the value of 1 if observation i and observation j are in the same group of factor A; otherwise, it takes the value of zero. In addition, the sum of squares between the groups of Factor A, denoted as SS_A, is obtained by the equation $SS_A = SS_T - SSW(A)$. Similarly, disregarding the effect of Factor A, the within-group sum of squares for Factor B, denoted as $SS_{W(B)}$, is calculated by dividing the sum of squared distances in the cells falling into the grey area in Figure 2b by the number of observations ('an'), and it is calculated using equation 5:

$$SS_{W(B)} = \frac{1}{an} \sum_{i=1}^{N-1} \sum_{j=i+1}^{N} d_{ij}^2 \, \delta_{ij}^B \quad (5)$$

here, δ_{ij}^B takes the value of 1 if observation i and observation j are in the same group of Factor B; otherwise, it takes the value of zero.

In a two-factorial PERMANOVA analysis, the third sum of squares represents the sum of squares of residuals. This total, denoted as S_R, is obtained by dividing the sum of the squared distances in the cells falling into the gray area in Figure 2c by the number of observations "abn". That is, the inter-point distances are calculated for each combination of 'ab' for Factors A and B, as shown in equation 6.

$$SS_R = \frac{1}{abn} \sum_{i=1}^{N-1} \sum_{j=i+1}^{N} d_{ij}^2 \, \delta_{ij}^{AB} \quad (6)$$

here, δ_{ij}^{AB} takes the value of 1 if observation i and observation j are in the same combination of Factors A and B; otherwise, it takes the value of zero. If there is an interaction between the two factors in the design, the sum of squares related to this interaction, denoted as SS_{AB}, is calculated, as shown in equation 7.

$$SS_{AB} = SS_T - SS_A - SS_B - SS_R \quad (7)$$

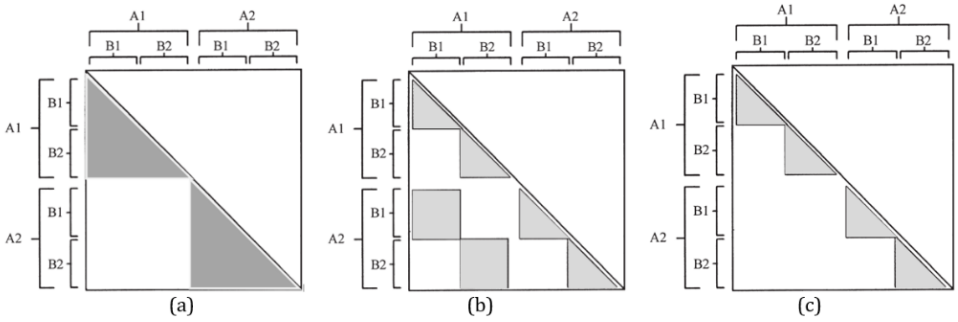


Figure 2. Representation of single or two-factor observation distance matrix shape.

If there is no interaction term in the design, that is, if Factor B is within Factor A, the sum of squares for Factor B within A, denoted as $SS_{B(A)}$, is calculated directly as follows as in equation 8:

$$SS_{B(A)} = SS_T - SS_A - SS_R \quad (8)$$

Following these calculations, the results of the two-way PERMANOVA analysis are organized as shown in Appendix B. In the computation of the table, the 'adonis2' function from the 'vegan' library (Oksanen et al., 2022), which is integrated into the R software, was utilized and coded as follows:

```
library(vegan)
library(readxl)
mydata <- read_excel("C:/Users/…/mydata.xlsx")
mydata<-data.frame(mydata)
mydata$RiskLevel<-as.factor(mydata$RiskLevel)
mydata$AgeGrp<-as.factor(mydata$AgeGrp)
responses = as.matrix(mydata[,3:7])
result <- adonis2(responses ~ RiskLevel*AgeGrp,
          data = mydata, nperm= 999, method="bray")
result
AIC_BIC_value<- calculate_AIC_BIC(result)
AIC_BIC_value
```

In the source code, the dataset in Excel format was assigned to the 'mydata' variable, and the risk and age variables were converted to factors. At the same time, response variables 'SystolicBP', 'DiastolicBP', 'BS', 'BodyTemp', and 'HeartRate' were converted into a matrix and assigned to the 'responses' variable. This transformation was written to obtain the distance observation matrix in Figure1b. In the analysis, a function with arguments 'adonis2(response ~ RiskLevel * AgeGrp, data = data, nperm = 999, method = "bray")' was used. In addition, 999 permutations were performed on the observation distance matrix created using the Bray Curtis, Binomial, and Mahalanobis distance measures.

AIC (Akaike Information Criterion) and BIC (Bayesian Information Criterion) values and R-square (explained variance ratio) were used to select the best model among these three models. Lower AIC and BIC values indicate better model performance, while the R-square value measures the fit of the model to the data (Wikipedia, 2023). Since the Adonis2 function cannot calculate the AIC and BIC values directly, a function called calculate_AIC_BIC was developed to calculate these values. This function takes the result variable, which is the output of the Adonis2 function, as the input and calculates the AIC and BIC values. The calculated AIC and BIC values are assigned to the variable AIC_BIC_value and made ready for use. The details of this function are presented in Appendix C.

When a statistically significant p-value is obtained from the ANOVA analysis, multiple comparison tests are performed to determine from which groups the mean difference between factor groups originates. Paired comparisons of factor groups were made in pairs using the PERMANOVA method. The "RVAideMemoire" library integrated into the R software was used to perform this operation (Hervé ,2022). The "pairwise.perm.manova" function of this library has been coded in R programing as follows:

```
library(RVAideMemoire)
responsesDMatrix<-vegdist(responses, method="bray")
pairwiseAge <-pairwise.perm.manova(
          responsesDMatrix, mydata$AgeGrpp,
           p.method="holm", nperm=999,F=TRUE)
pairwiseAge
pairwiseRisk <-pairwise.perm.manova(
          responsesDMatrix, mydata$RiskLevel,
method="holm", nperm=999,F=TRUE)
pairwiseRisk
```

In the source code, the matrix of response variables calculated using Bray Curtis distance was transferred to the variable 'responsesDmatrix'. The results of the pairwise comparison calculations made for the age factor were assigned to the 'pairwiseAge' variable, and the result of the pairwise comparison calculations made for the risk factor was assigned to the 'pairwiseRisk' variable. The 'pairwise.perm.manova' function was used for both factors, and the arguments were identified as 999 for the number of permutations, Bray Curtis, Binomial, and Mahalanobis for the distance measures, and the Holm method to control for type 1 error. The distributions of the response variables were investigated for compliance with the normality assumption. According to the results of Mardia's multivariate normality test (Korkmaz et al., 2014). It was determined that the SystolicBP, DiastolicBP, BS, BodyTemp, and HeartRate variables do not have a multivariate normal distribution, and this was calculated using the R code as follows:

```
library(MVN)
result <- mvn(responses, mvnTest = "mardia")
print(result)
```

The source code generates both multivariate normality test (Mardia's multivariate normality test) and univariate normality test (Anderson-Darling test) results with the parameter mvnTest = "mardia". The obtained results are assigned to the result variable.

3. Results

Within the scope of this research, the effects of risk and age factors on response variables such as, 'SystolicBP', 'DiastolicBP', 'BS', 'BodyTemp', and 'HeartRate' were examined. The Mardia Skewness and Kurtosis statistics for the multivariate normality test of the response variables were presented, and normality tests were performed separately for each response variable using the Anderson-Darling method. The results are presented in Table 1.

Skewness and kurtosis statistics revealed significant deviations from multivariate normality ($P<0.01$) for all response variables ('SystolicBP', 'DiastolicBP', 'BS', 'BodyTemp', and 'HeartRate').

Table 1. Multivariate and univariate normality test table

		Multivariate	
Test	Statistic	P value	Result
Mardia Skewness	1619.85	<0.001	NO
Mardia Kurtosis	18.55	0	NO
		Univariate	
Variable	F Statistic	P value	Normality
SystolicBP	50.76	<0.001	NO
DiastolicBP	18.38	<0.001	NO
BS	139.50	<0.001	NO
BodyTemp	242.30	<0.001	NO
HeartRate	16.88	<0.001	NO

Table 2. Table of PERMANOVA analysis results

Variable	Df	SumOfSqs	R^2	F	Pr(>F)	AIC	BIC
		Mahalanobis distance					
RiskLevel	2	551.4	0.11	69.78	0.001	4279	4338
AgeGrp	3	337.3	0.07	28.45	0.001		
RiskLevel:AgeGrp	6	216.6	0.04	9.14	0.001		
Residual	1002	3959.6	0.78				
Toplam	1013	5065.0	1				
		Binomial distance					
RiskLevel	2	0.75	0.38	411.33	0.001	-4206	-4147
AgeGrp	3	0.26	0.13	97.056	0.001		
RiskLevel:AgeGrp	6	0.05	0.03	9.58	0.001		
Residual	1002	0.91	0.46				
Toplam	1013	1.98	1				
		Bray Curtis distince					
RiskLevel	2	0.44	0.15	107.77	0.001	-3398	-3339
AgeGrp	3	0.33	0.11	54.24	0.001		
RiskLevel: AgeGrp	6	0.13	0.04	10.27	0.001		
Residuals	1002	2.03	0.70				
Totals	1013	2.91	1				

Df= degree of freedom, R^2= coefficient of determination, AIC= Akaike Information Criterion, BIC= Bayesian Information Criterion.

Indicating they did not follow a normal distribution. Given this non-normality, PERMANOVA, a non-parametric methodology, was employed to analyze the impact of risk level (RiskLevel) and age group (AgeGrp) variables on response variables, as presented in Table 2.

The PERMANOVA analysis, using Mahalanobis, Binomial, and Bray-Curtis distances, revealed a significant impact of both risk and age factors on the response variables ($p < 0.01$). This means there's a significant difference between the means of at least two subgroups within each factor. While higher R-squared values are generally good indicators of model fit and reliability, they can also suggest overfitting, especially when paired with low residuals. In this case, the PERMANOVA analysis with the binomial distance measure showed a residual variance of 46%, meaning that risk and age factors explain 54% of the total variance. Other factors not included in the model likely contribute to the remaining unexplained variance. Additionally, this model has low AIC (-4206) and BIC (-4147) values. Therefore, the binomial distance is preferred for further analysis. The next step involved using PERMANOVA to compare the means of the factor subgroups/levels, as shown in Table 3.

Table 3 reveals statistically significant mean differences between the sublevels of both the risk and age factors, except for the comparison between the middle-aged (35-44) and menopausal (44+) groups ($P>0.05$). This implies that an expectant mother's risk level and age group, except for being middle-aged or menopausal, significantly influence the response variables. Furthermore, while the p-values were similar across all three distance measures, the PERMANOVA analysis with binomial distance exhibited the highest R-squared value, indicative of a stronger relationship between the model's dependent and independent variables.

R version 4.3.1 was used in this study (R Core Team, 2023).

4. Discussion and Conclusion

The health data of pregnant women in Bangladesh were analyzed using the PERMANOVA method to evaluate the effects of maternal risk status and age on response variables. Table 1 reveals that the response variables did not satisfy the assumption of normality.

Table 3. Factor groups' paired mean comparison table

Risk and Age Groups	Bray Curtis		Binomial		Mahalanobis	
	R^2	P	R^2	P	R^2	P
Low risk - Mid risk	0.19	0.003	0.41	0.003	0.13	0.003
Low risk-High risk	0.12	0.003	0.36	0.003	0.09	0.003
Mid risk-High risk	0.03	0.003	0.03	0.003	0.03	0.003
Young age (<20)- Adolescent age (20-34)	0.10	0.006	0.09	0.006	0.05	0.006
Young age (<20)- Middle age (35-44)	0.21	0.006	0.30	0.006	0.09	0.006
Young age (<20)- Menopause (44>)	0.27	0.006	0.34	0.006	0.11	0.006
Adolescent age (20-34)- Middle age (35-44)	0.04	0.006	0.21	0.006	0.04	0.006
Adolescent age (20-34)- Menopause (44>)	0.07	0.006	0.26	0.006	0.06	0.006
Middle age (35-44)- Menopause (44>)	<0.0001	0.698	<0.0001	0.989	<0.0001	0.935

R^2= coefficient of determination, Bray Curtis= Bray Curtis distance, Binomial= Binomial distance, Mahalanobis= Mahalanobis distance.

PERMANOVA utilized distances such as Mahalanobis, Binomial, and Bray-Curtis, enabling the examination of relationships between factor groups from different perspectives. According to the analysis results, the PERMANOVA model based on the binomial distance demonstrated good performance in the multivariate analysis, with a high R-squared value and low AIC and BIC values. Furthermore, the results of this model indicate that age and risk factors have a statistically significant effect on the response variables ($P<0.01$). Ahmed and Kashem (2020) classified risk groups with 97% accuracy using machine learning methods on the same dataset. The accuracy rate provides further evidence of significant differences in response variables across risk groups.

The literature supports the applicability of the PERMANOVA method to various fields. For instance, Nascimento et al. (2019) used this method to identify ecological differences between groups and found significant differences in pairwise comparisons of factor groups.

In this study, age was also converted into a categorical format and categorized into four groups. According to the pairwise comparison results in Table 3, no significant difference was found between the "Middle Age (35-44)" and "Menopause (44+)" groups ($p>0.01$). This finding provides valuable insights for researchers when determining threshold values for age groups.

In conclusion, the PERMANOVA method is a robust and flexible tool for evaluating the effects of factors on response variables in health research, especially when the normality assumption is not met. In addition, this method provides a framework for researchers to determine threshold values for factor groups.

Author Contributions

The authors' contributions are detailed below. The authors have reviewed and approved the final version of the manuscript.

	F.K.
C	100
D	100
S	100
DCP	100
DAI	100
L	100
W	100
CR	100
SR	100
PM	100
FA	100

C=Concept, D= design, S= supervision, DCP= data collection and/or processing, DAI= data analysis and/or interpretation, L= literature search, W= writing, CR= critical review, SR= submission and revision, PM= project management, FA= funding acquisition.

Conflict of Interest

The author declared that there is no conflict of interest.

Ethical Approval/Informed Consent

The datasets used in this study are publicly accessible and can be found at the following link: https://www.kaggle.com/datasets/csafrit2/maternal-health-risk-data

Acknowledgments

We sincerely thank Ahmed and Kashem for making the open-access dataset used in this study available.

References

Ahmed M, Kashem MA. 2020. IoT-based risk level prediction model for maternal health care in the context of Bangladesh. 2nd International Conference on Sustainable Technologies for Industry 4.0 (STI), December 19-20, Dhaka, Bangladesh, pp: 1-6. https://doi.org/10.1109/STI50764.2020.9350320

Anderson MJ. 2001. A new method for non-parametric multivariate analysis of variance. Austral Ecol, 26(1): 32-46. https://doi.org/10.1111/j.1442-9993.2001.01070.pp.x

Anderson MJ. 2014. Permutational multivariate analysis of variance (PERMANOVA). Wiley StatsRef: Statistics Reference Online. https://doi.org/10.1002/9781118445112.stat07841

Hervé M. 2022. RVAideMemoire: Testing and plotting procedures for biostatistics [Computer software]. CRAN. https://CRAN.R-project.org/package=RVAideMemoire

Koç Ş, Çanga Boğa D, Önem AB, Yavuz E, Şahin M. 2019. Monte Carlo simulation study robustness of MANOVA test statistics in Bernoulli and uniform distribution. BSJ Eng Sci, 2(2): 42-51. https://doi.org/10.34248/bsengineering.563330

Korkmaz S, Göksülük D, Zararsiz G. 2014. MVN: An R package for assessing multivariate normality. The R J, 6(2): 151-162. https://doi.org/10.32614/RJ-2014-031

Nascimento FJA, Dahl M, Deyanova D, Lyimo LD, Bik HM, Schuelke T, Bonaglia S. 2019. Above-below surface interactions mediate effects of seagrass disturbance on meiobenthic diversity, nematode and polychaete trophic structure. Commun Biol, 2: 362. https://doi.org/10.1038/s42003-019-0607-z

Oksanen J, Blanchet FG, Friendly M, Kindt R, Legendre P, McGlinn D, Minchin PR, O'Hara RB, Simpson GL, Solymos P, Stevens MHH, Szoecs E, Wagner H. 2022. Vegan: Community ecology package [Computer software]. CRAN. https://CRAN.R-project.org/package=vegan

Pasin O, Ankarali H, Cangür S, Sungur MA. 2016. Nonparametric multivariate analysis of variance and its application in the field of health. J Info Technol, 9(1): 13-20.

R Core Team. 2023. R: A language and environment for statistical computing. R Foundation for Statistical Computing, Vienna, Austria. URL: https://www.R-project.org/

Sowers JR, Epstein M, Frohlich ED. 2001. Diabetes, hypertension, and cardiovascular disease: An update. Hypertension, 37(4): 1053-1059. https://doi.org/10.1161/01.HYP.37.4.1053

Şahin M, Koç Ş. 2018. A Monte Carlo simulation study robustness of MANOVA test statistics in Bernoulli distribution. Süleyman Demirel Univ J Inst Nat App Sci, 22(3): 1125-1131.

Tabachnick BG, Fidell LS, Ullman JB. 2013. Using multivariate statistics. Pearson, London, UK, pp: 983 (6th ed.).

Tinsley HEA, Brown SD. 2000. Multivariate statistics and mathematical modeling. In Handbook of applied multivariate statistics and mathematical modeling. Academic Press, Cambridge, US, pp: 3–36. https://doi.org/10.1016/B978-012691360-6/50002-8

Togunwa TO, Babatunde AO, Abdullah KU. 2023. Deep hybrid model for maternal health risk classification in pregnancy: Synergy of ANN and random forest. Front AI, 6: 1213436. https://doi.org/10.3389/frai.2023.1213436

Underwood AJ. 1981. Techniques of analysis of variance in experimental marine biology and ecology. Oceanog Marine Biol: An Annual Rev, 19(Suppl 1): 513-605.

Wikipedia. 2023. Akaike information criterion. URL: https://en.wikipedia.org/wiki/Akaike_information_criterion https://en.wikipedia.org/wiki/Bayesian_information_criterion (accessed date: September 30, 2023).

Black Sea Journal of Engineering and Science
doi: 10.34248/bsengineering.1606557

Open Access Journal
e-ISSN: 2619 – 8991

Research Article
Volume 2 - Issue 2: 435-443 / March 2025

TUNNELING NANOTUBE (TNT) MEDIATED INTERCELLULAR CROSSTALK AND AUTOPHAGY IN HYPOXIA-INDUCED MESENCHYMAL STEM CELLS

Gizem İLTER AKTAŞ[1], Şeyma KİPEL[2*], Leyla Didem KOZACI[3], Habibe Meltem ÖZGÜNER[2,4]

[1]*Yüksek İhtisas University, Faculty of Medicine, Department of Histology, 06200, Ankara, Türkiye*
[2]*Ankara Yıldırım Beyazıt University, Faculty of Medicine, Department of Histology, 06200, Ankara, Türkiye*
[3]*Ankara Yıldırım Beyazıt University, Faculty of Medicine, Department of Medical Biochemistry, 06200, Ankara, Türkiye*
[4]*Stem Cell Research Laboratory, Ankara City Children's Hospital, 06200, Ankara, Türkiye*

Abstract: Intercellular communication is a critical process and multicellular organisms rely on *communication* networks to coordinate and maintain physiological functions. Tunneling nanotubes (TNTs) defined as a novel cell to cell communication mechanism and characterized by F-actin. TNTs allow the rapid exchange of cellular cargos including organelles, vesicles, molecules etc. Hypoxia plays an essential role in stem cell functions and also a known stimulus of autophagy. Autophagy and Wnt/β-catenin signalling pathways have important roles during essential cellular processes like tissue homeostasis. This study was aimed to investigate the effect of hypoxia on autophagy, Wnt/β-catenin signalling and the formation of TNTs in bone marrow mesenchymal stem cells (BM-MSCs). Western blotting was applied for HIF-1α protein expression. Immunolabeling was applied to investigate LC3B, p62 and β-catenin protein expressions. Immunofluorescence staining was assessed to evaluate TNT formations and HIF-1α protein. HIF-1α protein expression was significantly increased in $CoCl_2$ induced hypoxic BM-MSCs compared to the normoxia. As a result of the immunofluorescence staining, HIF-1α was positively stained in the cell nuclei of hypoxic BM-MSCs. Number and lengths of TNT formations was increased in hypoxic BM-MSCs compared to the normoxia. Also, we showed that hypoxia upregulates LC3B and downregulates p62 expression. In conclusion, our study indicates that TNT-mediated intercellular communication increases under the hypoxia in BM-MSCs and hypoxic microenvironment may be a significant factor for stem cell functions. Our findings may also draw attention to a possible TNT-mediated crosstalk for autophagy and Wnt/β-catenin signalling mechanism between distant cells.

Keywords: Autophagy, Hypoxia, Intercellular communication, Mesenchymal stem cell, Tunneling nanotubes, Wnt signalling.

***Corresponding author:** Ankara Yıldırım Beyazıt University, Faculty of Medicine, Department of Histology, 06200, Ankara, Türkiye
E mail: seymakipel@gmail.com (Şeyma KİPEL)
Gizem İlter AKTAŞ https://orcid.org/0000-0003-3805-8446
Şeyma KİPEL* https://orcid.org/0000-0002-4176-5136
Leyla Didem KOZACI https://orcid.org/0000-0001-5422-1640
Habibe Meltem ÖZGÜNER https://orcid.org/0000-0003-0364-5907

Received: December 26, 2024
Accepted: February 02, 2025
Published: March 15, 2025

Cite as: İlter Aktaş G, Kipel Ş, Kozacı LD, Özgüner HM. 2025. Tunneling nanotube (TNT) mediated intercellular crosstalk and autophagy in hypoxia-induced mesenchymal stem cells. BSJ Eng Sci, 8(2): 435-443.

1. Introduction

Intercellular communication is essential for the maintenance of multicellular organisms. These communications can occur via different mechanisms such as secretion of cytokines, exosomes etc. (Mittelbrunn and Sánchez-Madrid, 2012). In 2004, a novel cell to cell communication mechanism based on the formation of thin membranous channels was reported in the neuron-like PC12 cell line. These unique structures were defined as tunneling nanotubes (TNT) and characterised by F-actin (Rustom et al., 2004). They provide a direct communication way to cells over long distances. TNTs vary in diameter and length in different cell types (Gerdes and Carvalho, 2008; Gurke et al., 2008; Sowinski et al., 2008). These TNT formations allow the rapid transport of cellular cargos including organelles, vesicles, ions and various molecules. They have important communication roles in early development, stem cell functions, regeneration and pathological mechanisms of some diseases (Austefjord et al., 2014; Gerdes et al., 2013; Roehlecke and Schmidt, 2020; Zurzolo, 2021).

Intercellular communication is essential for the maintenance of multicellular organisms. These communications can occur via different mechanisms such as secretion of cytokines, exosomes etc. (Mittelbrunn and Sánchez-Madrid, 2012). In 2004, a novel cell to cell communication mechanism based on the formation of thin membranous channels was reported in the neuron-like PC12 cell line. These unique structures were defined as tunneling nanotubes (TNT) and characterised by F-actin (Rustom et al., 2004). They provide a direct communication way to cells over long distances. TNTs vary in diameter and length in different cell types (Gerdes and Carvalho, 2008; Gurke et al., 2008; Sowinski et al., 2008). These TNT formations allow the rapid transport of cellular cargos including organelles, vesicles, ions and various molecules. They have important communication roles in early development, stem cell functions,

This work is licensed (CC BY-NC 4.0) under Creative Commons Attribution 4.0 International License

regeneration and pathological mechanisms of some diseases (Austefjord et al., 2014; Gerdes et al., 2013; Roehlecke and Schmidt, 2020; Zurzolo, 2021).

Hypoxia is a known stimulus of autophagy (Wu et al., 2014). Autophagy is a cellular homeostatic process and involves degradation of nonfunctional cellular components. Cellular adaptation to environmental conditions are mainly regulated by autophagy and its crosstal with various pathways and one of them is Wnt/β-catenin signaling pathway (Xu et al., 2017). Autophagy and Wnt/β-catenin signaling are the essential pathways which contribute to tumor growth and anticancer therapies. LC3B and p62 are well-known molecules in autophagy mechanism. β-catenin, an essential Wnt signaling protein, are targeted by LC3 for autophagic degradation. β-catenin also acts as a corepressor of the p62, when Wnt signaling is activated. There is a regulatory feedback mechanism coordinating with autophagy, and this mechanism include β-catenin at a key integration point with implications for targeting these pathways for development cancer therapies (Lorzadeh et al., 2021; Petherick et al., 2013; Wu et al., 2014).

Mesenchymal stem cells (MSCs) are sources for cell therapies, immune-modulation and regenerative medicine-based applications (Arthur and Gronthos, 2020; Baker et al., 2015). MSCs are self-renewal, multipotential and highly proliferative cells. They represent a promising cellular strategy in regenerative medicine because of their highly proliferative, self-renewal and multipotential properties (Bornes et al., 2014). The MSC microenvironment is characterized by a low oxygen tension. Since MSCs are quite resistant to oxygen limitations hypoxia is believed to play an essential role in controlling the behavior and function of mesenchymal stem cells (MSCs) (Chen et al., 2019). Despite several studies, the influence of hypoxia on the regulatory mechanisms of MSC functions and other related cellular pathways is still a matter of discussion. In our study, we aimed to mimic the hypoxic microenvironment in order to examine the effects of hypoxia on the formation of tunneling nanotubes in bone marrow mesenchymal stem cells (BM-MSCs) and to investigate the possible relation with autophagy and Wnt/β-catenin signalling.

2. Materials and Methods

2.1. Cell Culture

Bone Marrow-Derived Mesenchymal Stem Cells (BM-MSCs; Cat No: PCS-500-012, *ATCC*) were used for cell culture experimental studies. Cells were cultured in DMEM (Dulbecco's Modified Eagle Medium; Cat No: 11965092, Capricorn), supplemented with 10% fetal bovine serum (FBS; Cat No: 10270106, Gibco) and 1% antibiotics (penicillin/streptomycin; Gibco Penicillin-Streptomycin (10,000 U/mL)) at 37°C and 5% CO_2 in a standard incubator until they reached the required numbers. Inverted microscope (IX70 Olympus) was used for cell culture experiments.

2.2. Hypoxia Mimetic Treatment of BM-MSC

Cobalt chloride ($CoCl_2$) (Cas no: 7791-13-1, Sigma Aldrich) was used to create chemical hypoxia. Equal numbers of BM-MSCs were incubated with $CoCl_2$ (100 μM, final concentration) for 24 h. The optimum concentration for experiments was chosen based on the results from literature (Bhandi et al., 2021; Ciavarella et al., 2016; Liu et al., 2018; Nugraha et al., 2021; Teti et al., 2018; Yoo et al., 2016; Yu et al., 2013). Cell viability was measured using a trypan blue assay after 24 h of incubation with 100 μM concentration of $CoCl_2$ and evaluated with an hemocytometer. To compare hypoxia with normoxic conditions, MSCs were also incubated in $CoCl_2$ free medium for 24 h.

2.3. Western Blotting

The BM-MSCs were cultured with 100 μM $CoCl_2$ for 24 hour and cytosolic content was obtained by using RIPA lysis buffer (with protease inhibitor cocktail). After determining protein concentrations with BCA assay, adequate amount of samples were boiled in sample buffer and loaded to Bis Tris 4–12% gradient gel (Invitrogen) and transferred into a nitrocellulose membrane using a semi-dry transfer system. The membranes were blocked with 3% dry milk in PBS for 1 hour at room temperature and were then incubated with rabbit polyclonal HIF-1α (1:1000, St John's Laboratory), and beta actin (1:1000, Bioss, USA) at 4°C overnight. After washing with PBS Tween, each blot was incubated with secondary anti-rabbit antibody (1:1000, Bioss, USA) at room temperature for 1 hour. After washing, membranes were exposed to Chemiluminescent Substrate (Thermo Fisher Scientific, Monza, Italy) for 2-3 min. After the visualisation, the band densities was evaluated with Image J software programme (National Institutes of Health). Intensities of the protein bands were corrected with equal beta-actin loading.

2.4. Immunolabeling

To evaluate the expression levels of the β-catenin, LC3B and p62, we performed the immunolabeling analysis. Firstly, BM-MSCs were cultured in 6-well culture plates on coverglass. When cells reached ~60% confluency, $CoCl_2$ (100 μM) administered for 24h. At the end of culture period, culture medium was collected and immunolabeling protocol was applied. In summary, cultured cells were fixed with 4% paraformaldehyde (PFA) for 15 minutes at room temperature, washed two times with PBS and blocked with serum Ultra V block (TA-125-UB, Thermo) for 1 hour. After blocking reagent, cells were washed two times with PBS and incubated with primary antibodies; β-catenin (sc7963, 1:100, Santa Cruz Biotechnology), LC3B (ab48394, 1:50, Abcam) and p62/SQSTM1 (H00008878-M01, 1:500, Abnova) at 4°C overnight. After washing, cells were incubated with biotinylated HRP (Cat No: TP-125-BN, Thermo) for 1 hour at room temperature. A streptavidin-peroxidase (Cat No: TS-125-HR, Thermo) was used to identify the antigen–antibody complexes for 30 min at room temperature. Cells were shortly incubated with AEC chromogen (Cat No: TA-125-HA, Thermo) and counterstained with Mayer's

hematoxylin. The light microscope was used to view the samples (Olympus BX43F JAPAN, Olympus DP26 camera JAPAN) and photographed (Photography program: Olympus DP21, JAPAN). The results were evaluated with Image J software for 10 randomly chosen fields. Cytoplasmic expression levels were evaluated as; 0: no expression, 1: low expression, 2: high expression and 3: very high expression. Data were represented as Mean ± Standard Deviation (SD).

2.5. Immunofluorescence Staining

In order to visualize the HIF-1α expression and TNT formations, immunoflorescence staining protocol was applied. After $CoCl_2$ administration, cultured cells were fixed with 4% PFA for 15 minutes, washed two times with PBS, permeabilized with 0.5% Triton X-100 for 15 minutes and washed two times with PBS, blocked with 5% fetal bovine serum for 30 minutes, then incubated with HIF-1α polyclonal antibody at 4°C overnight. After washing, secondary antibody (Texas Red, Abcam) was applied at room temperature for 1 h. Cells were then washed again and incubated with diluted (1:100) Flash Phalloidin™ Green 488 (Cat No: 424201, Biolegend) at the dark for 1 hour. Lastly, the slides were mounted with DAPI mounting medium (ab104139, Abcam) and imaged with Olympus BX53 Fluorescence microscope. TNT formations were assessed at x200 magnification in 10 randomly chosen fields.

2.6. Statistical Analysis

Western blotting and immunolabeling data were evaluated with Image J software (National Institutes of Health). Statistical analysis was done with SPSS Statistics (IBM, version 21.0) and Graphpad Prism (version 7.0). Data was analysed using one-way ANOVA, Mann Whitney-U and Kruskal Wallis tests. All data were represented as mean ± standard deviation (SD) of three independent experiments. The significance levels were defined as P≤0.05 (*), P≤0.01 (**) and P≤0.001 (***).

3. Results

3.1. Cobalt Chloride As a Hypoxia-Mimicking Agent Enhances Hif-1 Alpha Expression in BM-MSCs

In order to examine cytotoxic effect of $CoCl_2$ on BM-MSCs, we first applied Trypan blue staining protocol. We observed that $CoCl_2$ (100 μM) administration for 24h did not affect the cell viability of BM-MSCs, both normoxic and hypoxic cells were 90-92% alive. After the analysis of cell viability, we have continued with same concentration of $CoCl_2$ for hypoxia induction. Expression of HIF-1α is a part of the systemic response to low oxygen levels. Therefore, HIF-1α can act as an effective molecular marker of hypoxia. We performed the western blotting to analyse the expression levels of HIF-1α by BM-MSCs in normoxia and hypoxia. Beta-actin was used for the normalization of HIF-1α protein levels. According to the results of western blotting, HIF-1α protein level was significantly increased in BM-MSCs in hypoxia compared to normoxia (P=0.034, P≤0.05) (Figure 1). In addition to western blotting, our immunofluorescence imaging results also demonstrate that HIF-1α antibody was positively stained in the cell nuclei of hypoxic BM-MSCs (Figure 2).

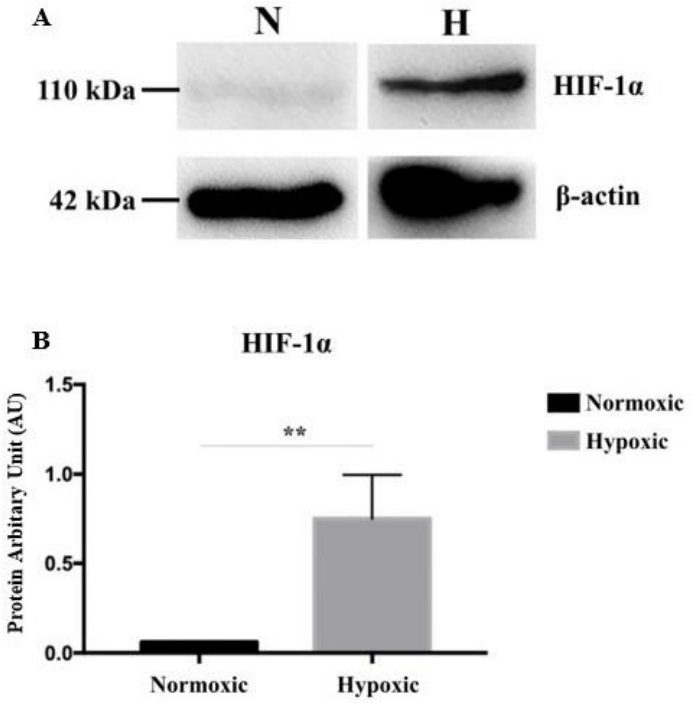


Figure 1. Western blotting analysis of HIF-1α protein for hypoxic and normoxic BM-MSCs (A). The significance level was defined as P≤0.01 (**) (B).

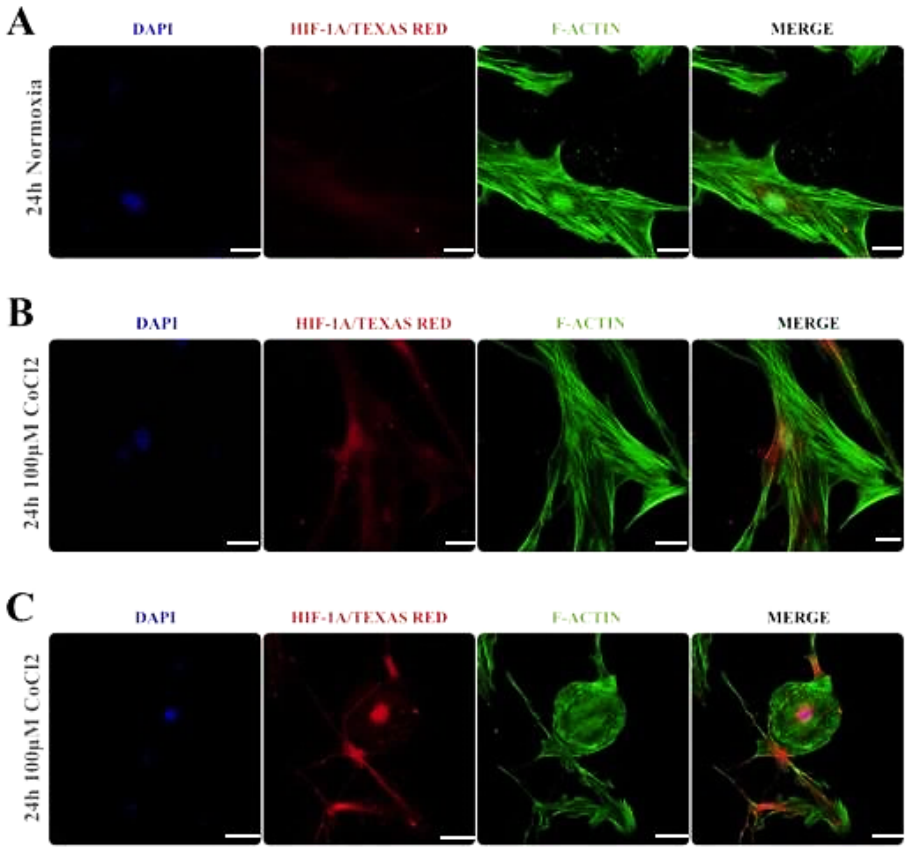


Figure 2. Immunofluorescence imaging of HIF-1α protein (red), F-actin (Phalloidin) (green) and DAPI (blue). (A) 24h normoxic group of BM-MSCs. (B-C) 24h 100μM $CoCl_2$-induced hypoxic group of BM-MSCs. Scale bars: 40 μm.

3.2. Hypoxic Microenvironment Increases the Number and Lengths of TNTs in BM-MSCs

We performed immunoflorescence staining to visualize and analyse TNT formations in BM-MSCs. F-actin containing nanotube structures between BM-MSCs and vesicle-like cargos throughout the TNTs were observed (Figure 3). When TNT formation was assessed we observed that the lengths of TNTs were significantly increased in hypoxic BM-MSCs compared to normoxia (P=0.004, P≤0.05) (shown in the Table 1 and Figure 4A). Also, there were an increased number of TNT formation in hypoxic BM-MSCs compared to the cells in normoxia. However, this finding was not statistically significant (P=0.167, P>0.05) (Figure 4B).

Table 1. Number and lengths of TNT formations for normoxic and hypoxic BM-MSCs

	Groups	Mean ± SD
TNT number	Hypoxic	4.50 ± 2.014
	Normoxic	3.30 ± 1.703
TNT length	Hypoxic	88.923 ± 26.873
	Normoxic	55.942 ± 16.497

SD= standard deviation

3.3. Expression of LC3B Upregulated and p62/SQSTM1 Downregulated in Hypoxia-Induced BM-MSCs

In addition to the evaluating TNT formations, we have also evaluated the expression of autophagy markers in BM-MSCs in normoxia and hypoxia conditions. According to the immunolabeling results, the cytoplasms of hypoxic BM-MSCs were stained positive, intensely. There were also positively stained small granules in their cytoplasms in normoxic BM-MSCs. Our results showed that LC3B protein expression is upregulated in hypoxic BM-MSCs compared to normoxia (P=0.001, P≤0.05) (Figure 5A). Also we have examined the p62 protein expression and our results showed that p62 is downregulated in hypoxic BM-MSCs. There was a few positive cytoplasmic staining in hypoxic BM-MSCs for p62 but it was decreased significantly (P=0.027, P≤0.05). (Figure 5B). Comparison of the expression levels can be seen in Figure 6.

3.4. Hypoxia Can Trigger Wnt/β-catenin Signaling through Increased Cytoplasmic Expression of β-catenin

In order to investigate the effect of hypoxia on the possible relation with Wnt signalling and autophagy, we have also examined the expression of β-catenin with immunolabeling. Our results showed that β-catenin protein expression was increased in hypoxic BM-MSCs. Although there was increased positive cytoplasmic staining in hypoxic BM-MSCs it was not statistically significant (Figure 5C and Figure 6).

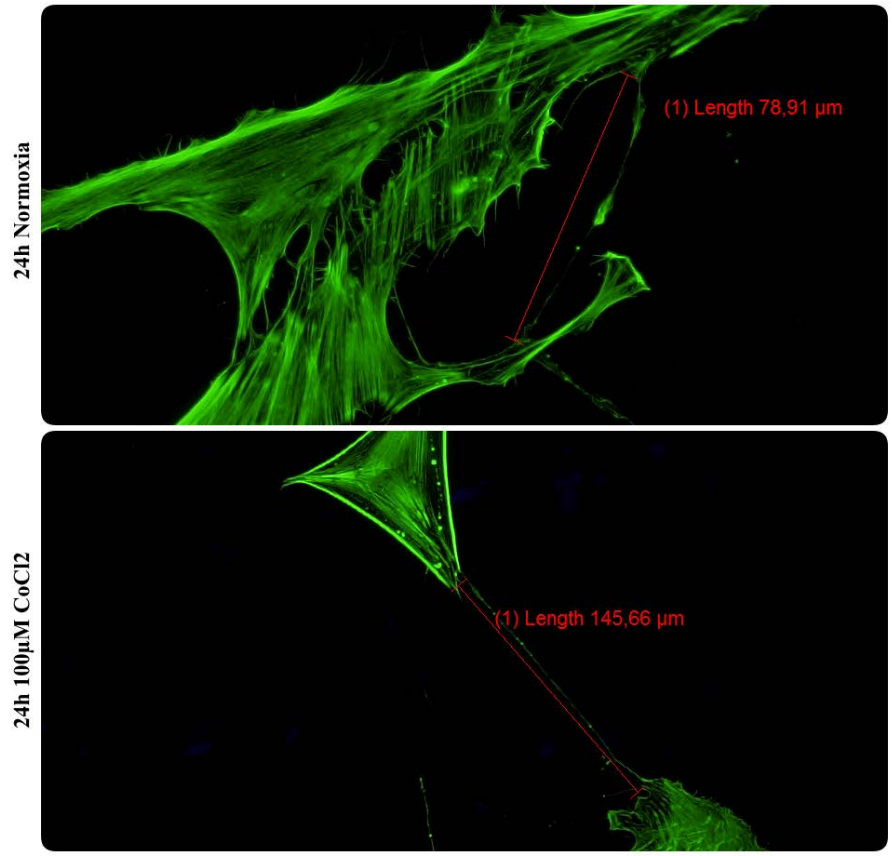


Figure 3. The measurement of TNT lengths in normoxic and hypoxic BM-MSCs. It can be seen there are tubular F-actin containing structures between BM-MSCs and the arrow (→) indicates vesicle-like cargos throughout the TNTs. Scale bars: 100 µm.

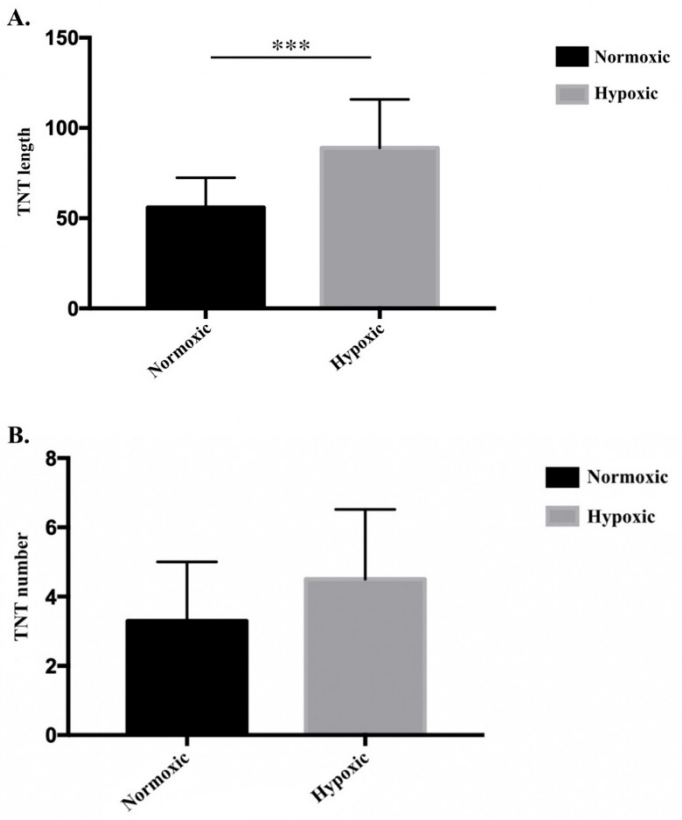


Figure 4. TNT lengths (A) and numbers (B) of normoxic and hypoxic BM-MSCs. (10 random field with x200 magnification and evaluated per cell). The significance level was defined as P≤0.001 (***).

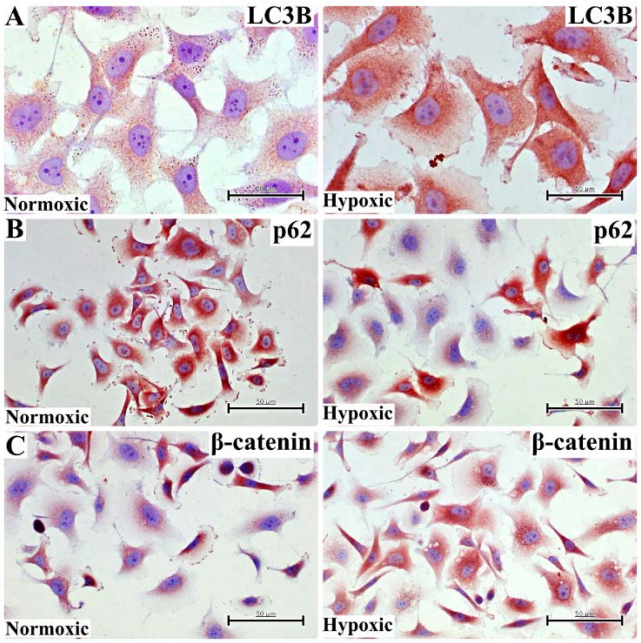


Figure 5. Immunolabeling images for the expressions of LC3B (A), p62 (B) and β-catenin (C) in normoxic and hypoxic BM-MSCs. Scale bars: 50 µm.

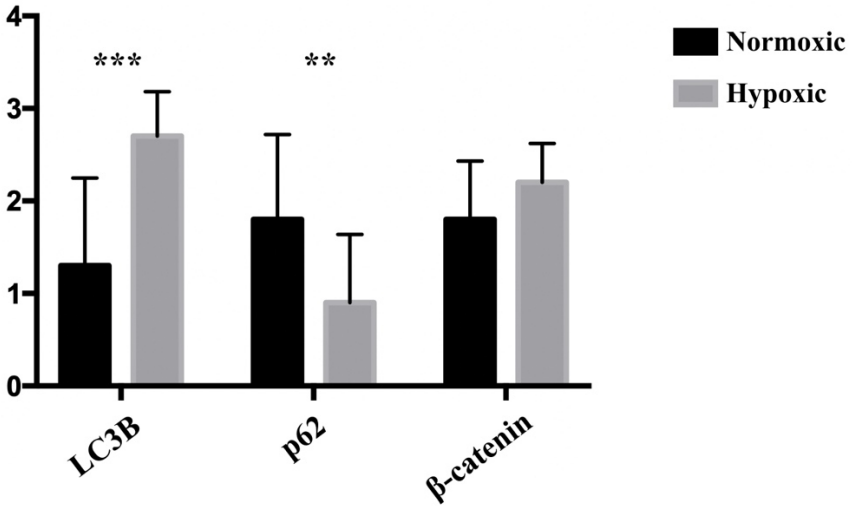


Figure 6. Comparison of expression levels for LC3B, p62 and β-catenin in normoxic and hypoxic BM-MSCs. The significance level was defined as P≤0.01 (**) and P≤0.001 (***).

4. Discussion

Hypoxia is an important microenvironment factor for stem cell behaviour and functions (Buravkova et al., 2012; Gleadle and Ratcliffe, 1998; Liu and Simon, 2004; Simon and Keith, 2008; Di et al., 2021). As previously mentioned, cobalt chloride ($CoCl_2$) is an easier and attractive method in order to induce hypoxia (Laksana et al., 2017). However, studies of the effect of $CoCl_2$ on BM-MSCs are limited and the influence of hypoxia on stem cell behaviour and intercellular communication is still a matter of discussion. This is a unique study to show the effect of $CoCl_2$ induced hypoxia on the formation of tunneling nanotubes (TNTs) in BM-MSCs.

Previous studies have showed that hypoxia induction by $CoCl_2$ increases the HIF-1α protein expression (Ciavarella et al., 2016; Nugraha et al., 2021; Teti et al., 2018; Yoo et al., 2016; Yu et al., 2013). Teti et al showed that the 100 µM concentration of $CoCl_2$ showed the highest cell viability at 24h for mesenchymal stem cells (Teti et al., 2018). Nugraha et al. have also reported that 100µM $CoCl_2$ can enhance significantly HIF-1 α expression of gingival derived mesenchymal stem cells for 24 hours in vitro (Nugraha et al., 2021). Consistent with previous studies, our results of western blotting analysis (Figure 1) and immunofluorescence staining (Figure 2) showed that hypoxia induction by $CoCl_2$ at 100 µM concentration for 24h increased the HIF-1α expression in BM-MSCs in hypoxia compared to normoxia.

In recent years, there has been considerable interest in the transfer of cytoplasmic material and organelles between

cells mediated by different intercellular communication mechanisms. In vitro studies have begun to elucidate the role of TNTs to make easier intercellular trafficking between cells. TNT formations in stem cell-based studies, cancer, as well as in other models of diseases, represent a novel and key topic for understanding how cellular communication takes place in different cell types (Gerdes and Carvalho, 2008; Gurke et al., 2008; Murray and Krasnodembskaya, 2019; Soundara et al., 2020; Roehlecke and Schmidt, 2020; Zurzolo, 2021).

Researchers, studied with SKOV3 and C200 cells, have reported that hypoxia stimulates and increases the number of TNT formations in ovarian cancer cells. They also indicated that cellular stress in the form of hypoxia could induce TNT-mediated intercellular communication (Desir et al., 2016). Another study also showed the TNT formations between K7M2 murine osteosarcoma cells, MC3T3 murine osteoblast cells and MG63 human osteosarcoma cells (Thayanithy et al., 2014). In 2022, Kato et al have studied with MCF-7 breast cancer cells and they showed that the chemotherapy agent 5-fluorouracil (5-FU) induced TNT formation in MCF-7 cells. They have also observed that mitochondrial exchange through TNTs following 5-FU treatment (Kato et al., 2022). Formicola et al identified structural differences of TNT formations by glioblastoma cells, in comparison with astrocytes. They have considered that thicker TNT structures are more effective in transportation of vesicles and organelles. So, their results suggest that tunnelling nanotube formations are potentially useful for drug delivery studies on cancer therapy (Formicola et al., 2019). In 2018, researchers observed and reported the TNT formations in mesenchymal stem cell spheroids as three-dimensional (3D) study (Zhang et al., 2018). Kolba et al reported that tunneling nanotubes (TNTs), which have been identified as a novel mechanism of intercellular crosstalk and mediate transfering cellular vesicles from stroma to leukemic cells (Kolba et al., 2019). Jackson et al have also demonstrated that mitochondrial transfer from MSC to innate immune cells via TNT-like structures (Jackson et al., 2016). In recent years, despite the increasing number of different studies about TNTs on different cell types, there are limited number of studies encountering TNT formations between mesenchymal stem cells (MSCs).

In this study, we have stimulated hypoxia in using $CoCl_2$. Our results showed that $CoCl_2$-induced hypoxia stimulates and enhances the formation of TNTs in BM-MSCs. In addition, the lengths of TNT formations were measured in our study and the result was significantly increased in hypoxic condition compared to normoxia. Overall, our data demonstrates that TNT-mediated intercellular communication increases under the hypoxia in BM-MSCs and hypoxia may be significant microenvironmental factor for stem cell studies. In addition, the increased length of TNTs in BM-MSCs under hypoxic microenvironment may be a target mechanism for the treatment of some hypoxia-related pathological situations such as cancer, metastasis, cardiomyopathy etc.

A key adaptive response to microenvironmental stress like hypoxia is autophagy. Oxidative stress induced by hypoxia may trigger autophagy to remove nonfunctional cellular structures to prevent further damage. In our study, we also investigated the effect of hypoxia on autophagy and Wnt/β-catenin signalling pathway and a possible relation with increased number and length of TNT formations. We showed that the cytoplasmic expression of LC3B, a key molecular component of autophagy mechanism, was upregulated, while p62/SQSTM1 (encoding the autophagy adaptor p62) was downregulated in hypoxic BM-MSCs. These findings were consistent with the previous studies (Jaakkola and Mursiheimo, 2009; Mitani et al., 2015; Monaci et al., 2020). Thus, our results indicate that hypoxia-activated autophagy with increased level of LC3B, accelerates degradation of SQSTM1/p62. In addition, our findings about increased expression of β-catenin in hypoxic group shows that hypoxia can activate the Wnt/β-catenin signalling pathway. This finding may support that β-catenin could also repress p62/SQSTM1 as previously studied (Petherick et al., 2013).

While accumulating data from recent studies reveal their importance for cellular functions, we still have a limited understanding of TNTs. The focus of the future studies must be to elucidate the mechanisms of formation and intercellular cargo transfer via TNTs and also their possible roles in diseases should be investigated. One question that remains to be answered regarding TNTs is whether longer TNTs are functional and allow for more material transfer between donor and recipient cells. Further studies may be conducted to find an answer to this question by lipid dye transfer. Our findings draw attention to a possible TNT-mediated crosstalk for autophagy and Wnt/β-catenin signalling mechanism between distant cells.

5. Conclusion

In conclusion, our study indicates that TNT-mediated intercellular communication increases under the hypoxia in bone marrow mesenchymal stem cells. Thus, hypoxic microenvironment may be a significant factor for stem cell-based regenerative medicine studies. In addition, our results showed that there is a relation between hypoxia-activated autophagy and Wnt/β-catenin signalling pathway. Targeting these pathways to develop stem cell-based therapies could be important for future studies. Also increased numbers and lengths of TNTs under hypoxic microenvironment draws attention to a possible TNT-mediated crosstalk for autophagy and Wnt/β-catenin signalling mechanism between distant cells and it may be a target mechanism for the treatment of some hypoxia-related pathological situations.

Author Contributions

The percentages of the author's contributions are presented below. All authors reviewed and approved the final version of the manuscript.

	G.İ.A.	Ş.K.	L.D.K.	H.M.Ö.
C	25	25	25	25
D	30	30	20	20
S	30	30	20	20
DCP	30	30	20	20
DAI	30	30	20	20
LS	35	35	15	15
W	40	40	10	10
CR	25	25	25	25
SR	10	70	10	10

C= Concept, D= Design, S= Supervision, DCP = Data Collection Processing, DAI= Data Analysis Interpretation, LS= Literature Search, W= Writing, CR= Critical Review, SR= Submission and Revision.

Conflict of Interest

The authors declared that there is no conflict of interest.

Ethical Consideration

Ethics committee approval was not required for this study because of there was no study on animals or humans.

References

Arthur A, Gronthos S. 2020. Clinical application of bone marrow mesenchymal stem/stromal cells to repair skeletal tissue. Inter J Molec Sci, 21(24): 9759.

Austefjord M, Gerdes H, Wang X. 2014. Tunneling nanotubes: Diversity in morphology and structure. Commun Integr Biol 7(1): 1-11.

Baker N, Boyette L, Tuan R. 2015. Characterization of bone marrow-derived mesenchymal stem cells in aging. Bone, 70: 37-47.

Bhandi S, Kahtani A, Mashyakhy M, Alsofi L, Maganur P, Vishwanathaiah S, Testarelli L, Giudice A, Mehta D, Vyas N, Patil V, Raj A, Patil S. 2021. Modulation of the dental pulp stem cell secretory profile by hypoxia induction using cobalt chloride. J Pers Med, 11(4): 247.

Bornes T, Adesida A, Jomha N. 2014. Mesenchymal stem cells in the treatment of traumatic articular cartilage defects: a comprehensive review. Arthritis Res Ther, 16(5): 1-19.

Buravkova L, Andreeva E, Grigoriev A. 2012. The impact of oxygen in physiological regulation of human multipotent mesenchymal cell functions. Fiziol Cheloveka, 38 (4): 121-130.

Chen Y, Zhao Q, Yang X, Yu X, Yu D, Zhao W. 2019. Effects of cobalt chloride on the stem cell marker expression and osteogenic differentiation of stem cells from human exfoliated deciduous teeth. Cell Stress and Chaperones, 24(3): 527-538.

Ciavarella C, Fittipaldi S, Pasquinelli G. 2016. $CoCl_2$ Administration to vascular MSC cultures as an in vitro hypoxic system to study stem cell survival and angiogenesis. Methods Mol Biol, 2016: 309-317.

Desir S, Dickson E, Vogel R, Thayanithy V, Wong P, Teoh, D, Geller M, Steer C, Subramanian S, Lou E. 2016. Tunneling nanotube formation is stimulated by hypoxia in ovarian cancer cells. Oncotarget, 7(28): 43150-43161.

Di Mattia M, Mauro A, Citeroni M, Dufrusine B, Peserico A, Russo V, Berardinelli P, Dainese E, Cimini A, Barboni B. 2021. Insight into hypoxia stemness control. Cells, 10(8): 2161.

Formicola B, D'Aloia A, Dal Magro R, Stucchi S, Rigolio R, Ceriani M, Re F. 2019. Differential exchange of multifunctional liposomes between glioblastoma cells and healthy astrocytes via tunneling nanotubes. Front Bioeng Biotechnol, 7: 403.

Gerdes H, Carvalho R. 2008. Intercellular transfer mediated by tunneling nanotubes. Curr Opin Cell Biol, 20(4): 470-475.

Gerdes H, Rustom A, Wang, X. 2013. Tunneling nanotubes, an emerging intercellular communication route in development. Mech Dev, 130(6-8): 381-387.

Gleadle J, Ratcliffe P. 1998. Hypoxia and the regulation of gene expression. Mol Med Today, 4(3): 122-129.

Gurke S, Barroso J, Gerdes H. 2008. The art of cellular communication: tunneling nanotubes bridge the divide. Histochem Cell Biol, 129(5): 539-550.

Jaakkola P, Mursiheimo, J. 2009. p62 degradation by autophagy: another way for cancer cells to survive under hypoxia. Autophagy, 5(3): 410-412.

Jackson M, Morrison T, Doherty D, McAuley D, Matthay M, Kissenpfennig A, O'Kane C, Krasnodembskaya, A. 2016. Mitochondrial transfer via tunneling nanotubes is an important mechanism by which mesenchymal stem cells enhance macrophage phagocytosis in the in vitro and in vivo models of ARDS. Stem Cells, 34(8): 2210-2223.

Kato K, Nguyen K, Decker W, Silkwood H, Eck S, Hernandez, J, Garcia J, Han, D. 2022. Tunneling nanotube formation promotes survival against 5-fluorouracil in MCF-7 breast cancer cells. FEBS Open Bio, 12(1): 203-210.

Kolba D, Dudka W, Zaręba-Kozioł M, Kominek A, Ronchi P, Turos L, Chroscicki P, Wlodarczyk J, Schwab Y, Klejman A, Cysewski D, Srpan K, Davis D, Piwocka K. 2019. Tunneling nanotube-mediated intercellular vesicle and protein transfer in the stroma- provided imatinib resistance in chronic myeloid leukemia cells. Cell Death Disease, 10(11): 817.

Laksana K, Sooampon S, Pavasant, P, Sriarj, W. 2017. Cobalt chloride enhances the stemness of human dental pulp cells. J Endod, 43(5): 760-765.

Liu L, Simon C. 2004. Regulation of transcription and translation by hypoxia. Cancer Biol Ther, 3(6): 492-497.

Liu L, Yu Q, Fu S, Wang B, Hu K, Wang L, Hu Y, Xu Y, Yu X, Huang H. 2018. CXCR4 antagonist AMD3100 promotes mesenchymal stem cell mobilization in rats preconditioned with the hypoxia-mimicking agent cobalt chloride. Stem Cells Develop, 27(7): 466-478.

Lorzadeh S, Kohan L, Ghavami S, Azarpira N. 2021. Autophagy and the Wnt signaling pathway: A focus on Wnt/β catenin signaling. Biochim Biophys Acta Mol Cell Res, 1868(3): 118926.

Mitani T, Minami M, Harada N, Ashida H, Yamaji R. 2015. Autophagic degradation of the androgen receptor mediated by increased phosphorylation of p62 suppresses apoptosis in hypoxia. Cell Signal, 27(10): 1994-2001.

Mittelbrunn M, Sánchez-Madrid, F. 2012. Intercellular communication: diverse structures for exchange of genetic information. Nat Rev Mol Cell Biol, 13(5): 328-335.

Monaci S, Aldinucci C, Rossi D, Giuntini G, Filippi I, Ulivieri C, Marotta G, Sozzani S, Carraro F, Naldini A. 2020. Hypoxia shapes autophagy in LPS- activated dendritic cells. Front Immunol, 11: 573646.

Murray L, Krasnodembskaya A. 2019. Concise review: intercellular communication via organelle transfer in the biology and therapeutic applications of stem cells. Stem Cells, 37(1): 14-25.

Nugraha A, ,Ihsan I, Dinaryanti A, Hendrianto E, Susilowati H, Prasetyo E, Rantam F. A. 2021. Cobalt (II) chloride in enhancing hypoxia inducible factor-1a expression of gingival derived mesenchymal stem cells in vitro. Res J Pharmcy Technol, 14(5): 2639-2642.

Petherick K, Williams A, Lane J, Ordóñez-Morán P, Huelsken J, Collard T, Smartt H, Batson J, Malik K, Paraskeva C, Greenhough A. 2013. Autolysosomal β-catenin degradation regulates Wnt-autophagy-p62 crosstalk. EMBO J, 32(13): 1903-1916.

Roehlecke C, Schmidt M. 2020. Tunneling nanotubes and tumor microtubes in cancer. Cancers, 12(4): 857.

Rustom A, Saffrich R, Markovic I, Walther P, Gerdes H. 2004. Nanotubular highways for intercellular organelle transport. Science, 303(5660): 1007-1010.

Simon M, Keith B. 2008. The role of oxygen availability in embryonic development and stem cell function. Nat Rev Mol Cell Biol, 9(4): 285-296.

Soundara T, Gugliandolo A, Bramanti P, Mazzon E. 2020. Tunneling nanotubes-mediated protection of mesenchymal stem cells: an update from preclinical studies. Int J Mol Sci, 21(10): 3481.

Sowinski S, Jolly C, Berninghausen O, Purbhoo A, Chauveau A, Köhler K, Oddos S, Eissmann P, Brodsky F, Hopkins C, Onfelt B, Sattentau Q, Davis D. 2008. Membrane nanotubes physically connect T cells over long distances presenting a novel route for HIV-1 transmission. Nat Cell Biol, 10(2): 211-219.

Teti G, Focaroli S, Salvatore V, Mazzotti E, Ingra L, Mazzotti A, Falconi M. 2018. The hypoxia-mimetic agent cobalt chloride differently affects human mesenchymal stem cells in their chondrogenic potential. Stem Cells Int, 13: 3237253.

Thayanithy V, Dickson E, Steer C, Subramanian S, Lou E. 2014. Tumor-stromal cross talk: direct cell-to-cell transfer of oncogenic microRNAs via tunneling nanotubes. Transl Res, 164(5): 359-365.

Wu J, Niu J, Li X, Li Y, Wang X, Lin, J, Zhang F. 2014. Hypoxia induces autophagy of bone marrow-derived mesenchymal stem cells via activation of ERK1/2. Cell Physiol Biochem, 33(5): 1467-1474.

Xu W, Zhou W, Cheng M, Wang J, Liu Z, He S, Luo X, Huang W, Chen T, Yan W, Xiao J. 2017. Hypoxia activates Wnt/β-catenin signaling by regulating the expression of BCL9 in human hepatocellular carcinoma. Sci Rep, 7(1): 40446.

Yoo H, Moon Y, Kim M. 2016. Effects of CoCl2 on multi- lineage differentiation of C3H/10T1/2 mesenchymal stem cells. Korean J Physiol Pharmacol, 20(1): 53.

Yu X, Lu C, Liu H, Rao S, Cai J, Liu S, Kriegel A, Greene A, Liang M, Ding, X. 2013. Hypoxic preconditioning with cobalt of bone marrow mesenchymal stem cells improves cell migration and enhances therapy for treatment of ischemic acute kidney injury. Plos One, 8(5): e62703.

Zhang J, Whitehead J, Liu Y, Yang Q, Leach J, Liu G. 2018. Direct observation of tunneling nanotubes within human mesenchymal stem cell spheroids. J Phys Chem B, 122(43): 9920-9926.

Zurzolo C. 2021. Tunneling nanotubes: Reshaping connectivity. Curr Opin Cell Biol, 71: 139-147.

Black Sea Journal of Engineering and Science
doi: 10.34248/bsengineering.1615656

Open Access Journal
e-ISSN: 2619 – 8991

Araştırma Makalesi (Research Article)
Cilt 8 - Sayı 2: 444-454 / Mart 2025
(Volume 8 - Issue 2: 444-454 / March 2025)

SAHA VERİLERİ IŞIĞINDA BETONARME BİNA DEPREM PERFORMANSININ GÜVENİLİR TAHMİNİ

Abdullah DİLSİZ[1]*, Polat GÜLKAN[2]

[1]*Ankara Yıldırım Beyazıt University, Department of Civil Engineering, 06010, Ankara, Türkiye*
[2]*Başkent University, Department of Civil Engineering, 06790, Ankara, Türkiye*

Özet: Binaların ve özelde betonarme binaların, doğrusal olmayan deprem tepkisinin tahmini bir zorluk olmaya devam etmektedir. Sıradan yapıların sismik talebini ve doğrusal olmayan davranışını makul bir şekilde tahmin edebilmek için farklı hassasiyette pek çok yöntem önerilmiştir. Yöntemlerin tahminleri genellikle Doğrusal Olmayan Tepki Geçmişi Analizi'nin (NRHA) "kesin" sonuçlarıyla karşılaştırılır. Bu çalışmada, NRHA sonuçlarına dayalı olarak yönetmeliklerce belirlenmiş detaylı değerlendirme yöntem tahminleri ve pratik olarak kullanılan bazı ön değerlendirme yöntem tahminleri, güçlü yer hareketlerine maruz kalmış gerçek yapıların performans kayıtlarıyla karşılaştırılmıştır. Hasar görmüş yapılarla ilgili bilgiler Adapazarı'ndan toplanmıştır. Deprem sonrasında binaların gerçek durumunu ve genel hasar durumlarını tarif eden verilerden yararlanılarak, EuroCode-8-3, DBYBHY-2007 ve TBDY-2018 yönetmeliklerinin detaylı değerlendirme yöntemleri, 1999 Marmara Depremi'nin Adapazarı'nda yarattığı etkileri yeniden elde etmek amacıyla uygulanmıştır. Çalışılan binalar için NRHA sonuçlarına göre kullanılan hiçbir hesap yaklaşımının her durumda performansı güvenilir bir şekilde tanımlayabileceğine dair net bir sonuç bulunmamaktadır. Bu nedenle, analiz sonuçlarının hesaplanması ve işlenmesi için harcanan yüksek çaba da göz önüne alındığında, binaların genel sismik performansları ön değerlendirme yöntemleri ile ayrıca değerlendirilmiştir. Ayrıntılı değerlendirme sonuçlarının aksine, incelenen hassas binalar bazı ön değerlendirme yöntemleriyle başarıyla değerlendirilebilmiş ve depremin neden olduğu orta veya ağır hasara göre sınıflandırılabilmiştir. Betonarme binaların sismik davranışına ilişkin testlerden elde edilen bilgiler, sahadan elde edilen daha fazla veriyle desteklenmelidir. Malzeme özelliklerindeki değişimler, geometri, yer hareketi varyasyonları ve diğer birçok parametre nedeniyle saha verileri ile değerlendirme prosedürleri arasındaki tutarsızlıklar göz önüne alındığında, bu yöntemlerin tahmin gücü konusunda daha iyimser olunması gerektiği açıktır.

Anahtar kelimeler: Elastik ötesi davranış, Deprem davranışı, Ön değerlendirme yöntemleri, Detaylı değerlendirme yöntemleri

Reliable Seismic Performance Prediction of RC Buildings in the Light of Field Data

Abstract: The prediction of nonlinear earthquake response of buildings, and specifically reinforced concrete buildings, continues to be a challenge. Many methods with different levels of reliability have been developed to reasonably predict the seismic demand and nonlinear behavior of ordinary structures. The predictions of the methods are usually compared with the "exact" results from Nonlinear Response History Analysis (NRHA). In this study, detailed evaluation method predictions determined by NRHA results and some preliminary predictions used in practice are compared with the observed performance records of real structures subjected to strong ground motions. Information on damaged structures was collected from Adapazarı. Using the data describing the real condition and general damage status of the buildings after the earthquake, detailed evaluation methods of EuroCode-8-3, DBYBHY-2007 and TBDY-2018 regulations were applied to reproduce the effects of the 1999 Marmara Earthquake in Adapazarı. According to the NRHA results for the studied buildings, there is no clear conclusion that any of the procedures can reliably predict the performance at nearly all stages of drift. Therefore, considering the intense labor spent on analyses and processing the results, the general seismic performance of the buildings was also evaluated separately with simplified preliminary assessment methods. In contrast to the detailed assessment results, the response of damaged buildings was successfully reproduced with some preliminary assessment procedures. These were classified as moderate or severe damage caused by the ground shaking. The information obtained from lab tests on the seismic behavior of reinforced concrete buildings should be supported by more data obtained from the field. Considering the inconsistencies between the field data and the assessment procedures due to the changes in material properties, geometry, ground motion variations and many other parameters that are usually unavailable, it is clear that the predictive power of these methods should be viewed with more favorable attention.

Keywords: Nonlinear response, Seismic response, Preliminary assessment procedures, Detailed assessment procedures

***Sorumlu yazar (Corresponding author):** Ankara Yıldırım Beyazıt University, Faculty of Engineering and Natural Sciences, Department of Civil Engineering, 06010, Ankara, Türkiye
E mail: adilsiz@aybu.edu.tr (A. DİLSİZ)
Abdullah DİLSİZ https://orcid.org/0000-0002-1750-9327
Polat GÜLKAN https://orcid.org/0000-0001-7542-7082

Gönderi: 08 Ocak 2025 **Received:** January 08, 2025
Kabul: 11 Şubat 2025 **Accepted:** February 11, 2025
Yayınlanma: 15 Mart 2025 **Published:** March 15, 2025

Cite as: Dilsiz A, Gülkan P. 2025. Reliable seismic performance prediction of RC buildings in the light of field data. BSJ Eng Sci, 8(2): 444-454.

This work is licensed (CC BY-NC 4.0) under Creative Commons Attribution 4.0 International License

1. Giriş

Büyük depremler öncesinde mevcut binaların performans değerlendirmesi ve risk analizlerinin önemi, son Kahramanmaraş Depremleri ile bir kez daha gün yüzüne çıkmış bulunmaktadır. 6 Şubat 2023 tarihinde, Kahramanmaraş ilinin Pazarcık ve Elbistan ilçeleri yakınlarında, yalnızca 9 saat arayla ve 95 km mesafeyle Mw 7.7 ve Mw 7.6 büyüklüğünde iki yıkıcı deprem meydana gelmiştir. Bu depremler birçok çevre ili kapsayan geniş bir alanda büyük yıkıma yol açmış ve çok sayıda bina ağır şekilde hasar görmüş ya da yıkılmıştır. Deprem bölgesinde yaklaşık 700,000 bina çeşitli seviyelerde hasar görürken, bunların yaklaşık 230,000 kadarı ağır hasar görmüş ya da yıkılmıştır (AFAD 2023, Dilsiz vd., 2023, SBB 2023). Bu miktardaki yıkımın sebep olduğu 50,000'i aşan büyük can kaybı ise, tıpkı 1999 Marmara Depremi ve diğer depremlerde olduğu gibi, depremlerin vukuundan önce binaların performans değerlendirilmesinin yapılması zaruretini ortaya koymuş bulunmaktadır.

Mevcut binaların detaylı değerlendirilmesi, bazı ülkelerin deprem yönetmelik ve ilgili kılavuzlarında yer alan yöntemler kullanılarak yapılmaktadır. ABD'de ASCE/SEI-41/06 (ASCE, 2007), Supplement-1 (ASCE, 2008), ve son versiyonu ASCE/SEI-41/23 (ASCE, 2023), Avrupa'da EuroCode-8-3 (EC, 2005) örnek olarak verilebilir. Türkiye'de mevcut bina değerlendirme yöntemi ilk defa Deprem Bölgelerinde Yapılacak Binalar Hakkında Yönetmelik (DBYBHY, 2007)'de yer almış, Türkiye Bina Deprem Yönetmeliği (TBDY, 2018)'de güncellenmiştir. Detaylı değerlendirme yöntemleri binaların "Doğrusal Olmayan Tepki Geçmişi Analizi (Nonlinear Response History Analysis – NRHA)" sonuçları temel alınarak yürütülmektedir. Detaylı performans değerlendirme yöntemleri, bu çalışmanın temelini oluşturan doktora çalışmasında karşılaştırmalı olarak incelenmiştir (Dilsiz, 2013).

Zaman Uzayında Doğrusal Olmayan Tepki Hesabının (NRHA) karmaşıklığı göz önüne alındığında, yapılardaki doğrusal olmayan deprem davranışını belirlemek için onun yerini tutmak üzere başka doğrusal ve doğrusal olmayan analiz yöntemi önerilmiştir. Bunlar arasında, ayrıntılı model ve hesaplamalar gerektirmeyen "ön değerlendirme yöntemleri" ve doğrusal olmayan bina davranışı açısından pratik bir araç olarak "pushover" analizine dayalı Doğrusal Olmayan Statik Prosedürler (NSP) ön plana çıkmıştır. Bu analiz prosedürlerinin temel amacı, belirli bir performans hedefi doğrultusunda uygun bir yapısal tasarım için yeterli bilgi seviyesine ulaşmaktır. Ele alınan meselenin tabiatı icabı varılan sonuçların hepsi elastik sınırın ötesindedir.

NRHA sonuçları, sismik davranış açısından "kesin sonuçlar" olarak kabul edilseler de, NSP'ler ile de doğrusal olmayan davranış makul bir şekilde tahmin edebilir. Bununla birlikte, önerilen tüm doğrusal olmayan analiz prosedürleri, sismik talebin tam olarak tahmin edilmesinde kullanılan yaklaşım ve basitleştirmeler nedeniyle sınırlamalara sahiptir. Ayrıca, beklenen depremin maksimum deformasyon talebinin belirlenmesi de doğrusal olmayan statik analiz probleminin bir başka zorluğudur. Binaların performans değerlendirmesi için NRHA yanında, başlıca şu NSP analiz prosedürleri kullanılagelmiştir: ATC-40 (ATC, 1996), FEMA-356 (ASCE, 2000), FEMA-440 (ATC, 2005) NSP'leri, Eşdeğer SDOF Sisteminin Doğrusal Olmayan Analizi (Fajfar ve Fischinger, 1987), ve Değiştirilmiş Modal Pushover Analizi (MMPA) (Chopra vd., 2004).

Analiz sonuçlarının hesaplanması ve işlenmesi için harcanan yüksek çaba, yapılması gereken kabuller ve bu nedenle yaklaşık sonuçların elde edilebilmesi de göz önünde bulundurularak, binaların genel performansları, ön değerlendirme prosedürleri kullanılarak da değerlendirilebilmektedir. Hassan ve Sözen (1997) ve bunu destekleyen Gülkan ve Sozen (1999), Yakut (2004) ve Özcebe vd. (2004) tarafından önerilen ön değerlendirme prosedürleri literatürde yer alan ve Türkiye bina envanteri için kullanılmış bazı ön değerlendirme yöntemleridir.

Bu çalışma, belirli yer hareketlerinden kaynaklanan yapısal tepkinin araştırılması için NRHA tabanlı detaylı değerlendirme yöntemleri ile ön değerlendirme yöntemlerine odaklanmıştır. Ana amaç, saha gözlemleri temelinde binaların gözlemlenen performansının bu yöntemlerle yapılan tahminlerle karşılaştırılmasıdır. Performans değerlendirme yöntemlerinin bina ölçeğindeki genel performansı, 1999 Marmara Depremi (M7.4) sırasında Adapazarı şehir merkezinde seçilen yapılar için gerçekleştirilen "tersine hesaplamalar" ve bina hasar gözlemleri kullanılarak değerlendirilmiştir. Analizlerde, sahada kaydedilen yer hareketi verisi girdi olarak kullanılmıştır. Bu çalışma, deprem performansını değerlendirmek için geliştirilen yöntemlerin kendilerinin yeterince performans göstermediği sürece, bu yöntemlerin faydasını yeniden değerlendirmeyi gerekli kılmaktadır.

Bu çalışmanın amacı doğrultusunda, Adapazarı şehir merkezinde ve birbirine oldukça yakın olan, orta derecede ve ağır hasar görmüş ikişer bina, Adapazarı Belediyesi arşivlerinden seçilmiştir. Depremde ortaya çıkan genel hasar durumları bilinen binaların, detaylı değerlendirme ve ön değerlendirme yöntemlerine kullanılarak yapılan analiz tahminleriyle karşılaştırmalar yapılmıştır. Bu şekilde, değerlendirme yöntemlerinin genel hasarı uygun şekilde tahmin edip etmedikleri kontrol edilmiştir.

Çalışmada binalar, EuroCode-8-3 (EC, 2005), Deprem Bölgelerinde Yapılacak Binalar Hakkında Yönetmelik (DBYBHY, 2007) ve Türkiye Bina Deprem Yönetmeliği (TBDY, 2018) yönetmeliklerinin ayrıntılı doğrusal olmayan dinamik değerlendirme prosedürleri kullanılarak detaylı bir şekilde incelenmiştir. Bu çalışmada yönetmeliklerin önerdiği doğrusal değerlendirme prosedürleri dikkate alınmamıştır.

Analiz sonuçlarının hesaplanması ve işlenmesi için harcanan çaba göz önünde bulundurularak, binaların genel sismik performansı, Hassan ve Sözen (1997), Yakut

(2004) ve Özcebe vd. (2004) tarafından önerilen ön değerlendirme prosedürleri kullanılarak da değerlendirilmiştir. Tüm sonuçlar karşılaştırmalı olarak sunulmuştur.

2. Binaların Tanımı ve İlgili Hasar

Adapazarı (Sakarya), 17 Ağustos 1999 Marmara Depremi sırasında en çok etkilenen şehirlerden biri olmuştur. Bu nedenle, Dilsiz (2013) tarafından çalışma alanı olarak seçilmiştir. Toplamda on hasarlı bina ayrıntılı şekilde incelenmiştir. Bu makalede, bu binalardan Adapazarı şehir merkezinde yer alan ve orta derecede hasar görmüş iki bina ile ağır hasar görmüş iki bina sunulmaktadır. İncelenen on binadan altısı için yapı malzemelerinin tasarım dayanım değerleri mevcut olup, bu değerlerin tüm binalar için aynı olduğu varsayılmıştır.

Ülkemizdeki betonarme binaların genel özelliklerini temsil etmek amacıyla, düşey ve planda düzensizliklere sahip ve malzeme kalitesi açısından benzer eksiklikleri bulunan binalar seçilmiştir. Bununla birlikte, ele alınan binalar, genel bina envanteri için geçerli olan ortalama malzeme kalitesine sahiptir. Tüm binaların yapısal sistemi betonarme çerçeve sisteminden oluşmaktadır. Adapazarı havzasındaki yüksek yer altı su seviyesi sebebiyle, örnek binalar için zemin seviyesinin altında bir bodrum kat inşa edilmemiştir.

Tablo 1. Seçilen binalar hakkında genel bilgiler

	Bina No	Mahalle	Pafta	Ada	Yapım Yılı	Kat Sayısı	Beton f_{cd} (kg/cm^2)	Çelik f_{yd} (kg/cm^2)	Oturum Alanı (m*m)
Orta	1	Yahyalar	6	72		4			22 * 17
Hasar	2	Tekeler	107	783	1994	5	95	1910	11,5 * 16,5
Ağır	3	Semerciler	54	388	1990	5			11,5 * 9,7
Hasar	4	İstiklal	15	607	1987	5			8,8 * 12,1

Seçilen binalar hakkında genel bilgiler tablo 1'de verilmiştir. Tablo 1'in ikinci sütununda verilen bina kimlik numaraları, yazının geri kalanında seçilen binalar için referans tanımlama numaraları olarak kullanılacaktır.

Adapazarı bölgesindeki malzeme ve inşaat kalitesinin düşük olduğu görülmüştür. Alınan karot numuneleri üzerindeki testlere göre, betonun ortalama basınç dayanımı projelerde kullanılan değerlere göre yüzde 25 daha düşük rapor edilmiştir (Yakut vd., 2006). Beton dayanımı, modelleme ve inşaat eksiklikleri ile mevcut verilerin güvenilirliği gibi sınırlı bilgiler göz önüne alındığında, bu çalışmada betonun basınç dayanımı (f_{cd}) ve donatı çeliğinin çekme dayanımı (f_{yd}) için tasarım değerleri kullanılmıştır. Bu varsayım, bölgedeki malzeme kalitesini dikkate alan çalışmalarla tutarlıdır. Beton ve donatı çeliği için tasarım dayanım değerleri sırasıyla 9,5 MPa ($f_{cd} = f_{ck} / 1,5$) ve 191 MPa ($f_{yd} = f_{yk} / 1,15$) olarak verilmiştir.

Tablo 2. Seçilen binalar hakkında geoteknik bilgiler

	Bina No	Anakaya Derinlik (m)	NEHRP Zemin Sınıfı	DBYBHY Zemin Sınıfı	Faya Uzaklık (km)	PGA (g)	V_S (m/s)	T (s) Hakim Per.	Yeraltı Su Seviyesi (m)	Sıvılaşma Şiddet İndeksi
Orta	1	175	E	Z3	12	<0,21	<263	0,82-1,23	0 – 5	2
Hasar	2	150	E	Z4	13,7	<0,21	<263	<0,82	> 15	0
Ağır	3	175	E	Z3	12	<0,21	263-371	>1,23	0 – 5	2
Hasar	4	175	E	Z4	12,1	<0,21	<263	<0,82	0 – 5	5

İncelenen binalara ait geoteknik veriler, bölge için yapılan Coğrafi Bilgi Sistemi (CBS) çalışmasından ayıklanarak (Dilsiz, 2013) tablo 2'de sunulmuştur. Binaların bulunduğu yerlerdeki ana kaya derinliği 150 m ile 175 m arasında değişmektedir. Bu konumlardaki yumuşak zeminler, NEHRP'ye göre E sınıfı, Deprem Yönetmeliği'ne (DBYBHY, 2007) göre ise Z3 veya Z4 olarak sınıflandırılmıştır. Yumuşak zemin özellikleri nedeniyle bu alanlarda düşük kayma dalgası hızları (Vs) ve uzun hâkim periyot değerleri gözlemlenmiştir. Tablo 2'nin son sütununda yer alan Sıvılaşma Şiddeti İndeksi (LSI) değerlerinin artışı, artan sıvılaşma riskini göstermektedir ve bu değerler 0 ile 10 arasında ölçeklendirilmiştir. Bununla birlikte, bu binalar için herhangi bir zemin kayması rapor edilmediği için sıvılaşma riski orta veya düşük olarak değerlendirilmiştir.

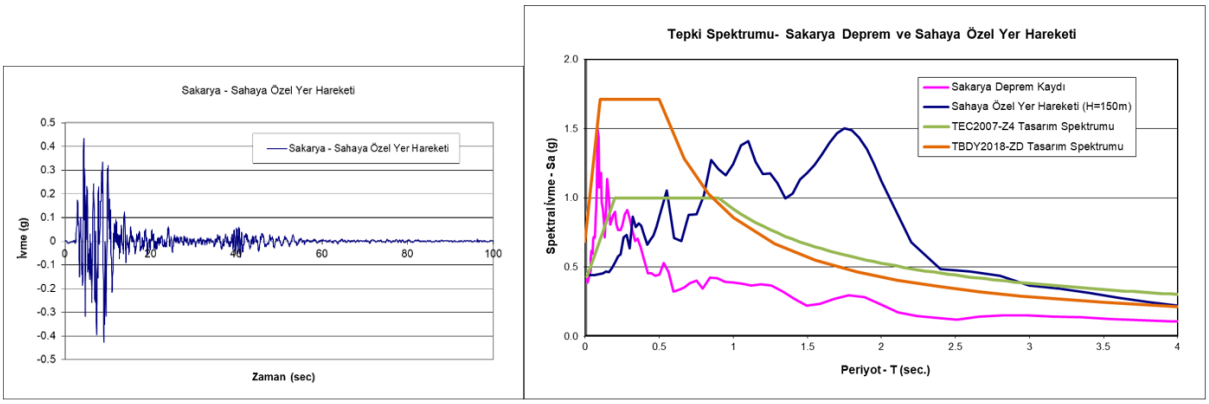
3. Sahaya Özgü Türetilmiş Yer Hareketi

Binaların çok büyük ölçekli bir testi, önceden planlanmamış olsa da 17 Ağustos 1999 tarihinde meydana gelen Marmara Depremi sırasında gerçekleşmiştir. Mw 7,4 büyüklüğündeki deprem, Türkiye'nin Marmara Bölgesi'ni vurmuş, çok sayıda bina hasar görmüş ve on binlerce insan hayatını kaybetmiştir.

Adapazarı şehir merkezine en yakın olan Sakarya istasyonunda, Marmara Depremi'nin ana şokuna ait yatay doğu-batı (kabaca faya paralel) bileşeni ve düşey bileşeni kaydedilmiştir. Yatay doğu-batı bileşeni için maksimum

yer ivmesi (PGA) 0,41g, maksimum yer hızı (PGV) 81 cm/s ve maksimum yer değiştirme 220 cm olarak ölçülmüştür (Sancio vd., 2002). Ancak, depremin kuzey-güney (faya dik) bileşeni, cihaz arızası nedeniyle kaydedilememiştir. Deprem sırasında Sakarya istasyonunun bulunduğu (şehir merkezi) faya daha yakın olan mahallede hasar yoğunluğu düşük olmuştur. Ancak, esas yıkım, fay kırığının yaklaşık 7-8 km kuzeyinde, yumuşak zeminler üzerinde bulunan Adapazarı şehir merkezinde gözlemlenmiştir. Bu bölgede herhangi bir kayıt cihazı ise bulunmamakta idi.

Adapazarı havzasındaki farklı alüvyon tabakalarının derinlikleri için Bakır vd. (2002) tarafından, Sakarya kayıtlarının doğu-batı bileşeni kullanılarak yerel zemin hareketi kaydı geliştirilmiştir. 150 m kalınlığında yumuşak zemin için elde edilmiş olan bu yer hareketi, bu çalışmada değerlendirilen binaların analizinde kullanılmıştır.



Şekil 1. Sahaya özgü türetilmiş yer hareketi ve tepki spektrumu (orijinal kayıt tepki spektrumu ve DBYBHY-2007 (Z4) ve TBDY-2018 (ZD) tasarım spektrumları ile karşılaştırmalı olarak verilmiştir).

Tüm binaların analizlerinde kullanılan türetilmiş yer hareketi kaydı ve yüzde 5 sönüm için karşılık gelen tepki spektrumu şekil 1'de gösterilmiştir. Burada, yer hareketi tepki spektrumu, orijinal yer hareketi tepki spektrumu, DBYBHY-2007 ve TBDY-2018'in tasarım spektrumları ile karşılaştırılmalı olarak verilmiştir. Ayrıca, DBYBHY-2007 için Z4 yerel zemin sınıfı ve TBDY-2018 için de deprem kaydının alındığı Sakarya istasyonunun konumu ile ZD yerel zemin sınıfı kullanılarak tasarım spektrumları elde edilmiştir.

4. Bina Modelleri

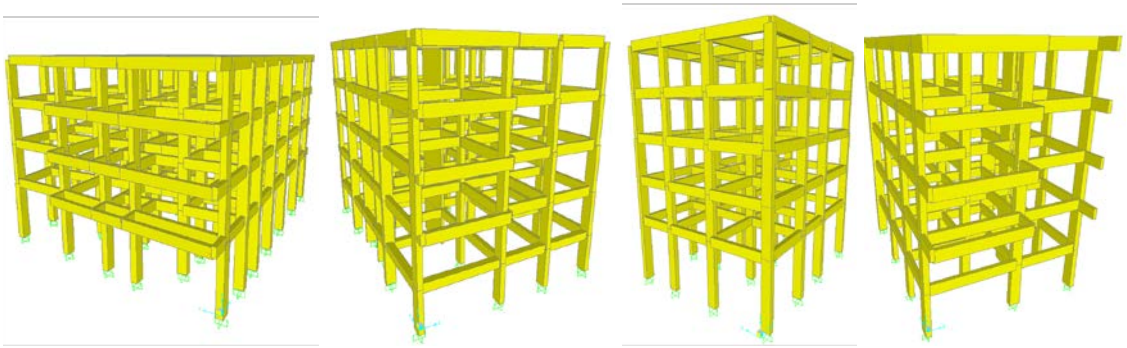
Adapazarı şehir merkezinden seçilen hasarlı binaların bilgisayar modelleri, projeden elde edilen bilgilerin mevcut yapıyı temsil ettiği varsayılarak oluşturulmuştur. Bu varsayım, daha sonra güçlendirilmiş orta derecede hasar görmüş binalar üzerindeki yazar gözlemleriyle uyumludur. Bina planlarının ve düşey boyutlarının yanı sıra yapısal elemanların boyutlarının projelere uygun olduğu gözlemlenmiştir.

Seçilen binaların analitik modelleri, deprem mühendisliği uygulamalarında kullanılan açık kaynak bir yazılım olan OpenSees programı kullanılarak oluşturulmuştur (OpenSees, 2010). Doğrusal olmayan analizler ve yapıların sismik tepkisini simüle etmek için bu yazılım kullanılmıştır.

Kirişler ve kolonlardan (ve varsa perde duvarlardan) oluşan betonarme çerçeve sistemler, OpenSees kütüphanesindeki "uç noktalarında mafsallı kiriş elemanı" (beam with hinges element) kullanılarak modellenebilir. Bu tür elemanlar, elemanı, iki uçta mafsal (konsantre plastiklik) ve ortada doğrusal-elastik bir bölge olacak şekilde üç kısma ayırır. Mafsallar, önceden tanımlanmış bir kesit ataması yapılarak tanımlanır. Her bir mafsalın uzunluğu da belirtilir. Kiriş-mafsallı elemanların modellenmesinde yapısal bileşenlerin doğrusal olmayan kuvvet-deformasyon ilişkilerinin atanması için lif (fiber) kesitler kullanılmıştır. Böylece kirişlerin ve kolonların iki eksenli eğilme davranışı temsil edilmiştir.

Beton ve donatı çeliği için sırasıyla Kent-Scott-Park beton modeli (Kent ve Park, 1971; Scott vd., 1982) Chang ve Mander (1994) tek eksenli çelik modelleri kullanılmıştır.

Doğrusal olmayan analizlerde, yapı elemanlarının yük-deformasyon ilişkisi de doğrusal olmayan modeller ile temsil edilmelidir (ASCE, 2008). Bu çalışmada da yapı elemanları doğrusal olmayan yük-deformasyon ilişkileri kullanılarak modellenmiş ve doğrusal olmayan analizler için çatlamamış kesitler kullanılmıştır.



Şekil 2. Bina modellerinin 3D görünümleri (sırasıyla 1-4 numaralı binalar).

Binaların 3D modellerinde, binalarda pencere veya kapı açıklıkları bulunmayan düzenli ve sürekli duvarların az miktarda olması göz önünde bulundurularak dolgu duvarlar ihmal edilmiştir (Yakut, 2004). Bu modellerle ilgili diğer varsayımlar şunlardır: her bina için kat seviyeleri için rijit diyafram varsayımı uygulanmıştır, kiriş modelleri için güvenli tarafta kalmak amacıyla etkin kanat genişliği dikkate alınmamıştır, P – Δ etkileri göz önüne alınmamıştır ve NRHA için yüzde 5 Rayleigh sönümü kullanılmıştır. Oluşturulan analitik modellerin 3D görünümleri şekil 2'de gösterilmiştir.

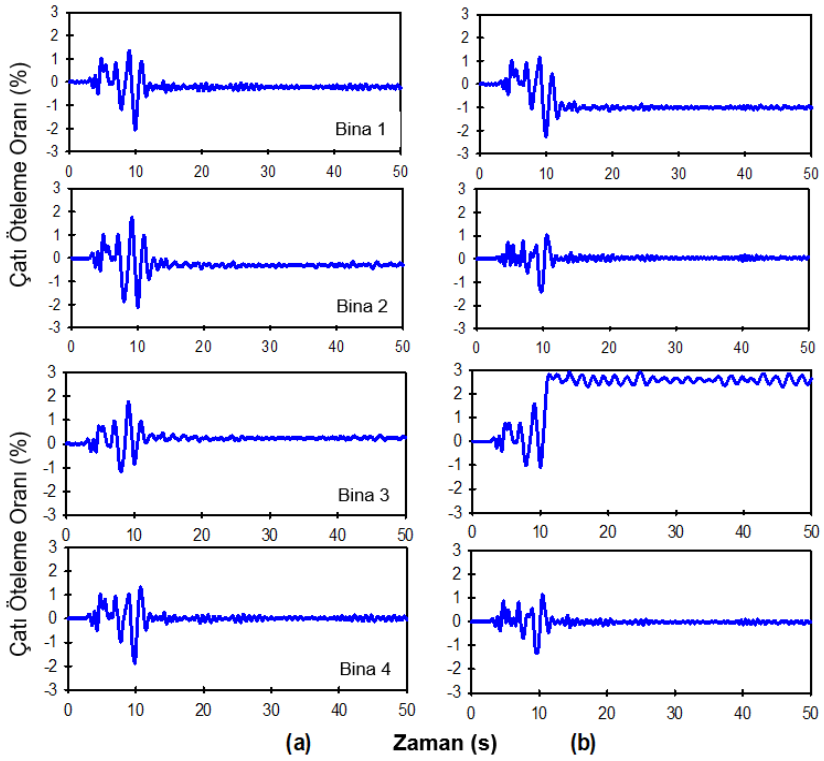
5. Doğrusal Olmayan Tepki Geçmişi Analizi (NRHA) Sonuçları

Bu çalışmada ele alınan her bina için, güçlü yer hareketinin yalnızca bir bileşeni (doğu-batı yönü) mevcut olduğundan, NRHA analizleri binaların plan düzlemindeki her bir ortogonal yönünde ayrı ayrı gerçekleştirilmiştir. Binalar için bina toplam yüksekliğine göre normalleştirilmiş çatı öteleme oranı için zaman geçmişi sonuçları şekil 3'te gösterilmiştir. NRHA sırasında elde edilen (bina ağırlığına göre normalize edilmiş) toplam taban kesme kuvveti ile çatı öteleme oranı arasındaki kuvvet-deformasyon grafikleri şekil 4'te verilmiştir. Her bina için NRHA sırasında hesaplanan maksimum çatı deplasmanı ve toplam taban kesme kuvveti değerleri tablo 3'te sunulmuştur. Tablo 3'te ayrıca, küresel deplasman oranları (maksimum çatı deplasmanının bina toplam yüksekliğine oranı) ve normalleştirilmiş taban kesme kuvveti değerleri (maksimum taban kesme kuvvetinin bina toplam ağırlığına oranı) verilmiştir.

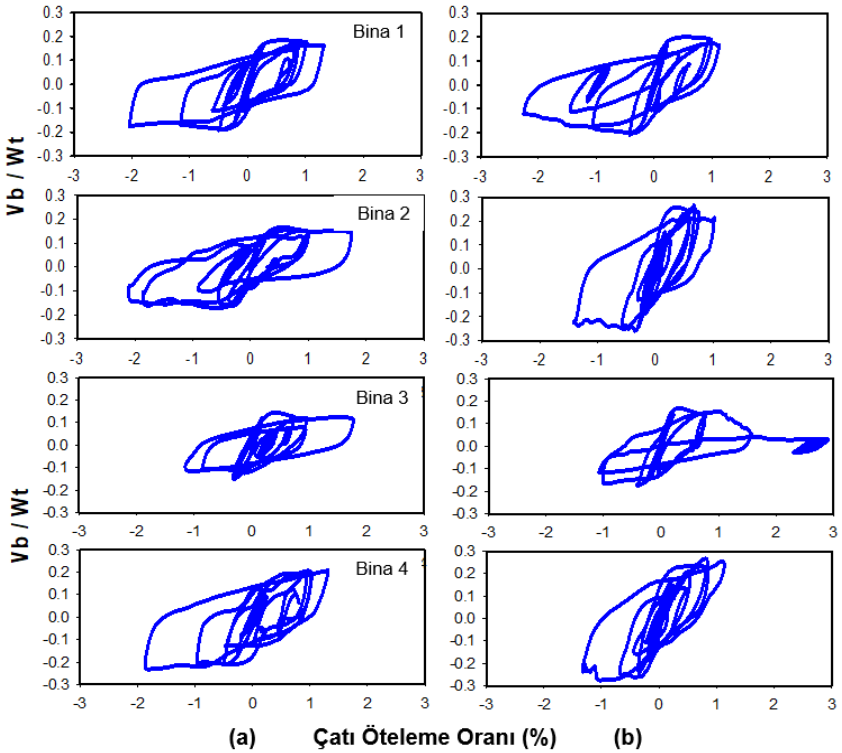
X yönündeki analizlerde, maksimum çatı öteleme oranı Bina 1 için yüzde 2,04 ve Bina 2 için yüzde 2,09 olarak ve elde edilmiştir. Genel olarak, daha büyük yanal çatı öteleme değerleri orta derecede hasar görmüş binalar için elde edilmiştir. Daha büyük çatı öteleme kapasitesine sahip binalar, daha iyi performans göstermiş ve deprem sırasında daha az hasar almıştır.

Tablo 3. Hesaplanan ve normalize edilmiş NRHA sonuçları

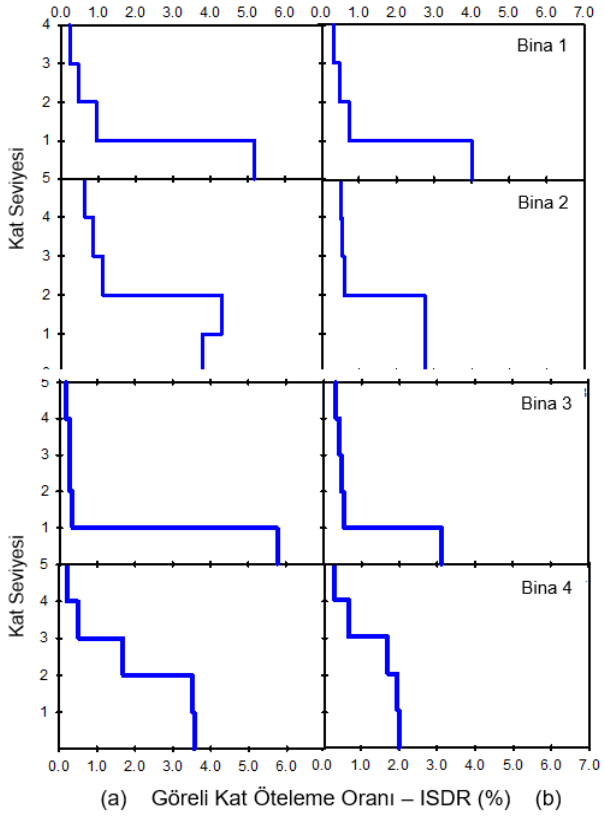
	Bina No	Yön	H_T (m)	W_T (kN)	Δr (m)	Vb (kN)	Çatı Ötelemesi (%)	Vb / W_T
Orta Hasar	1	X	12,4	16566	0,2531	2903,3	2,041	0,175
		Y			0,2040	2452,4	1,645	0,148
	2	X	13,6	11775	0,2848	1608,8	2,094	0,137
		Y			0,1912	2645,1	1,406	0,225
Ağır Hasar	3	X	15,4	7511	0,2723	830,8	1,768	0,111
		Y			0,1780	912,7	1,156	0,122
	4	X	13,5	7082	0,2519	1455,0	1,866	0,205
		Y			0,1782	1600,5	1,320	0,226



Şekil 3. Normalleştirilmiş çatı öteleme oranları, (a) X yönü ve (b) Y yönü.



Şekil 4. Normalleştirilmiş taban kesme kuvveti – çatı ötelenmesi grafikleri, (a) X yönü ve (b) Y yönü.



Şekil 5. Göreli kat ötelenme oranları (NRHA), (a) X yönü ve (b) Y yönü.

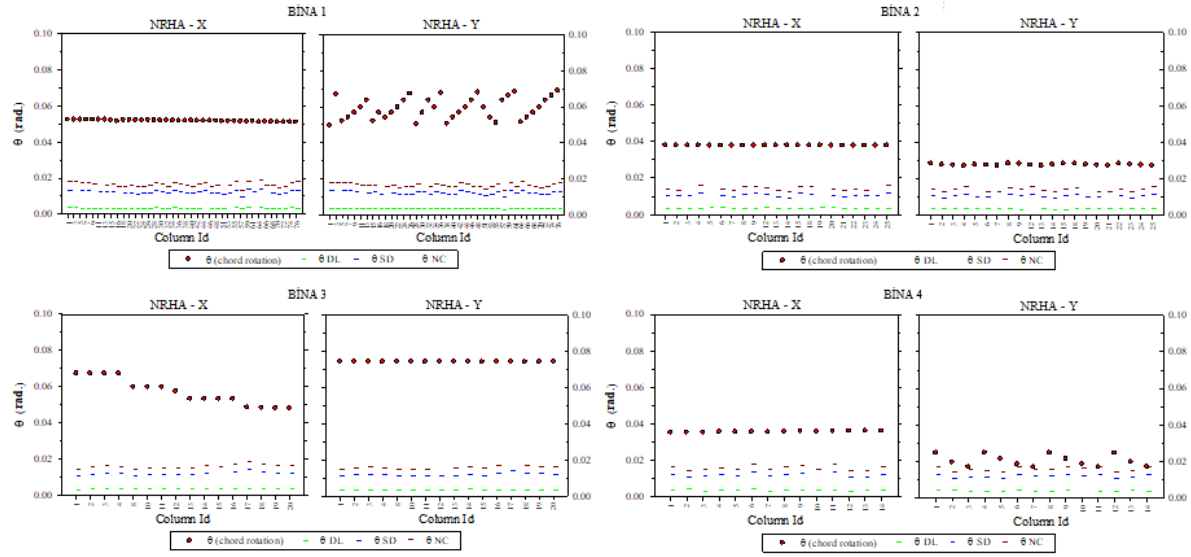
Tablo 3'te de görüldüğü üzere ağır hasar görmüş binaların hiçbiri yüzde 2'nin üzerinde çatı seviyesi öteleme oranına ulaşmamıştır. Küresel çatı öteleme oranları açısından bakıldığında, orta derecede hasar görmüş binaların ağır hasar görmüş binalara kıyasla daha ciddi hasar almış olması beklenir ki bu, gözlemlenen genel hasarla tutarlı değildir.

Her bina için göreli kat ötelenme oranları (interstory drift ratio – ISDR) da incelenmiştir. Binaların yükseklikleri boyunca kat ötelenmesi oranlarının dağılımları şekil 5'te sunulmuştur. X yönünde, Bina 1 ve Bina 3'ün zemin katlarında yüzde 5'in üzerinde maksimum ISDR değerleri elde edilmiştir. Genel olarak, analiz sonuçlarına göre binalarda "yumuşak kat" davranışı gözlemlenmiştir.

6. Binaların Ayrıntılı Değerlendirilmesi

Yukarıda verildiği üzere, NRHA sonuçlarına dayalı olarak yapılan genel değerlendirmenin ardından, binalar ayrıca ASCE/SEI-41/06 (ASCE, 2007) ve Supplement-1 (ASCE, 2008), EuroCode-8-3 (EC, 2005) ve Deprem Bölgelerinde Yapılacak Binalar Hakkında Yönetmelik (DBYBHY, 2007) kapsamında ayrıntılı değerlendirme usulleri kullanılarak kapsamlı bir şekilde incelenmiştir (Dilsiz, 2013). Bu ayrıntılı değerlendirme, özellikle bina ölçeğinde gerçekleştirilen değerlendirme sonuçlarının belirsiz olduğu durumlarda yapısal elemanlar seviyesindeki deprem tepkisini belirlemek için gereklidir. Tüm yönetmeliklerin sonuçları arasında küçük farklılıklar olmakla birlikte, benzer sonuçlar elde edilmiştir. Bu çalışma kapsamında ise yine NRHA sonuçlarına dayalı olarak, EuroCode-8-3 (EC, 2005) ve Deprem Bölgelerinde Yapılacak Binalar Hakkında Yönetmelik (DBYBHY, 2007) yanında, daha sonra güncellenmiş bulunan Türkiye Bina Deprem Yönetmeliği (TBDY, 2018) ile verilen doğrusal olmayan değerlendirme prosedürleri kullanılarak yapılan ayrıntılı değerlendirme sonuçları özetlenmiştir.

Bu kapsamda, binaların tüm kat ve kolonları ayrıntılı yöntemler kullanılarak değerlendirilmiş olmakla birlikte, ayrıntılı değerlendirme sonuçlarının incelenmesiyle belirlenen en kritik kat (zemin kat) için elde edilen sonuçlar aşağıda sunulmuştur. EuroCode-8-3'a göre ayrıntılı değerlendirmede, kritik kattaki kolonların eksen dönmesi (chord rotation – θ) talepleri, NRHA analizleriyle hesaplanmış ve Sınırlı Hasar (Damage Limitation – θ_{DL}), Kontrollü Hasar (Significant Damage – θ_{SD}) ve Göçme Öncesi (Near Collapse – θ_{NC}) hasar durumu sınırları ile karşılaştırmalı olarak şekil 6'da verilmiştir.

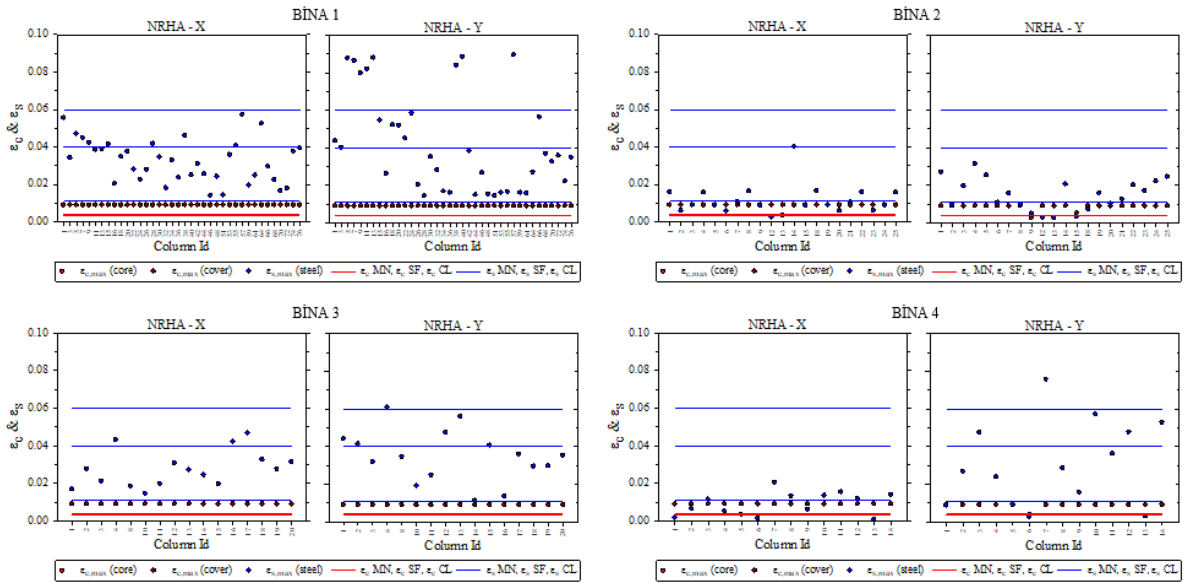


Şekil 6. 1 – 4 numaralı binalar için NRHA ile elde edilen X ve Y yönü eksen dönmesi (θ) sonuçları ile EuroCode-8-3 sınır değerleri karşılaştırması.

Yapısal eleman üzerindeki eksenel kuvvet ve kesme kuvveti seviyelerine, enine donatı oranına ve ayrıca plastik mafsal boyu ve moment kapasitesine bağlı olarak her bir eleman için farklı hasar durumu sınırları grafiklerde gösterilmiştir. Analizlerde hesaplanan θ talebi değerinin θ_{NC} sınırını aşması durumlarında kolon "göçmüş" olarak kabul edilmiştir.

EuroCode-8-3'in ayrıntılı değerlendirme sonuçlarına göre, az sayıdaki bazı kolonlar daha az hasar almış olsa da, orta derecede hasar görmüş binalar veya ağır hasar görmüş binaların tamamı "göçmüş" olarak işaretlenmiştir. Diğer bir deyişle, özellikle orta derecede hasar görmüş binalar için binaların genel hasar durumu ayrıntılı değerlendirme tarafından daha ileri (ağır hasarlı / göçmüş) düzeyde tahmin edilmiştir.

Türk Deprem Yönetmeliklerine (gerek DBYBHY-2007 ve gerekse TBDY-2018) göre mevcut binaların ayrıntılı değerlendirilmesi, beton ve donatı çeliğinde meydana gelen birim şekil değiştirme değerleri esas alınarak yapılmaktadır. DBYBHY-2007'ye göre ayrıntılı değerlendirmede, kritik kattaki kolonlarda beton ve donatı çeliği birim şekil değiştirme (ε_C ve ε_S) talepleri, NRHA analizleriyle hesaplanmış ve Minimum Hasar Sınırı ($\varepsilon_{cu,MN}$ ve $\varepsilon_{s,MN}$), Güvenlik Sınırı ($\varepsilon_{cg,GV}$ ve $\varepsilon_{s,GV}$) ve Göçme Sınırı ($\varepsilon_{cg,GC}$ ve $\varepsilon_{s,GC}$) değerleri ile karşılaştırmalı olarak şekil 7'de verilmiştir. Burada minimum hasar sınırı için beton kesitinin en dış lifindeki birim şekil değiştirme değeri kullanılırken, diğer sınırlar için etriye içindeki bölgenin en dış lifi dikkate alınmaktadır. Bu çalışmada değerlendirmesi yapılan mevcut binalarda sargı etkisinin yetersiz oluşu dikkate alınarak, sınır değerleri sargı etkisini ihmal ederek hesaplanmıştır.



Şekil 7. 1 – 4 numaralı binalar için NRHA ile elde edilen X ve Y yönü beton ve donatı birim şekil değiştirme (ε_C ve ε_S) sonuçları ile DBYBHY-2007 sınır değerleri karşılaştırması.

Tablo 4. DBYBHY-2007 ve TBDY-2018 yönetmeliklerine göre performans düzeylerine göre birim şekil değiştirme sınır değerleri

	DBYBHY 2007		AFAD 2018	
Beton	$(\varepsilon_{cu})_{MN} = 0{,}0035$	Minimum Hasar	$\varepsilon_c^{(SH)} = 0{,}0025$	Sınırlı Hasar
	$(\varepsilon_{cg})_{GV} = 0{,}0035$	Güvenlik	$\varepsilon_c^{(KH)} = 0{,}0026$	Kontrollü Hasar
	$(\varepsilon_{cg})_{GC} = 0{,}004$	Göçme	$\varepsilon_c^{(GÖ)} = 0{,}0035$	Göçmenin Önlenmesi
Çelik	$(\varepsilon_s)_{MN} = 0{,}010$	Minimum Hasar	$\varepsilon_s^{(SH)} = 0{,}0075$	Sınırlı Hasar
	$(\varepsilon_s)_{GV} = 0{,}040$	Güvenlik	$\varepsilon_s^{(KH)} = 0{,}024$	Kontrollü Hasar
	$(\varepsilon_s)_{GC} = 0{,}060$	Göçme	$\varepsilon_s^{(GÖ)} = 0{,}032$	Göçmenin Önlenmesi

DBYBHY-2007'ye göre ayrıntılı değerlendirme sonuçları incelendiğinde, EuroCode-8-3 sonuçlarında olduğu gibi, bazı kolonlarda beton ya da donatı çeliği deformasyonları açısından daha az hasarlı durumlar gözlenmekle birlikte, orta derecede hasar görmüş binalar veya ağır hasar görmüş binaların tamamı "göçmüş" olarak değerlendirilmektedir. Yine, orta derecede hasar görmüş binalar için binaların genel hasar durumu ayrıntılı değerlendirme tarafından daha ileri düzeyde tahmin edilmiştir.

Mevcut binaların değerlendirilmesi yöntemi TBDY-2018'de güncellenmiştir. Bu çalışmada gerek önceki gerekse yeni yönetmeliklerce verilen yöntemler tüm detayları ile verilmemiş olmakla birlikte, iki yönetmeliğin performans seviyeleri için ele aldığı sınır değerleri karşılaştırmalı olarak tablo 4'de özetlenmiştir. TBDY-2018'de performans düzeyleri az hasardan yüksek hasara doğru "sınırlı hasar (SH)", "kontrollü hasar (KH)" ve "göçmenin önlenmesi (GÖ)" düzeyleri olarak verilmektedir. Bu karşılaştırmada, yine binalardaki sargı etkisinin yetersizliği nedeniyle, performans limit değerleri –önceki yönetmeliklerde olduğu gibi– en olumsuz durumları verecek varsayımlar ile sargı etkisini ihmal ederek (sargısız beton) hesaplanmıştır. Burada şu hususa da dikkat çekmek gerekir ki, TBDY-2018'de bu çalışmada değerlendirilen binalarda kullanılmış olan S220 donatı çeliğine yer verilmezken, B420C ve B500C nervürlü donatı çeliğinin kullanılacağı belirtilmiştir. Dolayısıyla performans düzeylerinin sınır değerleri de buna göre hesaplanmaktadır. Bununla beraber, S220 donatı çeliği yeni yönetmelikte kullanılan diğerlerine göre daha sünek bir malzeme olduğundan, yönetmelikte verilen sınır değerlerinin kullanılması, bu çalışmada ele alınan binaların değerlendirilmesinde güvenli tarafta kalınmasını sağlamaktadır.

TBDY-2018 ile verilen hasar sınırlarının DBYBHY-2007'den daha düşük olduğu açıkça görülmektedir. Değerlendirilen binalarda kritik kat kolonlarında NRHA analizleriyle hesaplanmış beton ve donatı çeliği birim şekil değiştirme (ε_C ve ε_S) talepleri, bu sınır değerleri ile karşılaştırıldığında da binaların "göçmüş" olarak belirleneceği aşikârdır. Orta hasarlı ya da ağır hasarlı binaların tamamı için aynı sonuç elde edilmektedir.

Sonuç olarak, bu çalışmamız, incelenen binaların deprem sonrası gerçek hasar durumlarının, özellikle orta derecede hasar görmüş binalar için hem bina düzeyinde ve hem de eleman ölçeğindeki ayrıntılı değerlendirme sonuçlarıyla uyumlu olmadığını ortaya koymuştur.

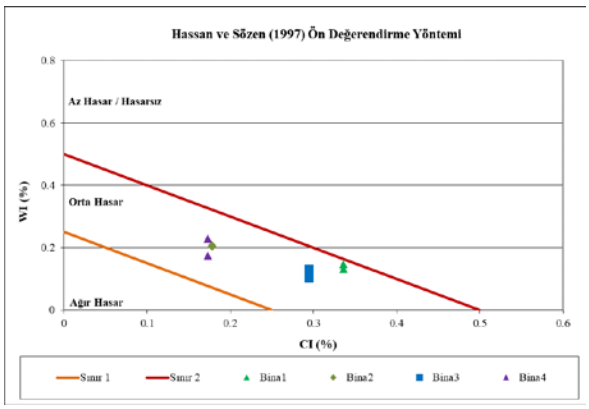
7. Binaların Basit Değerlendirme Yöntemleri ile Değerlendirilmesi

Gerçek hasar durumları elde edilemediği ve hiçbir ayrıntılı değerlendirme prosedürü ile binalar doğru şekilde nitelendirilemediği için, analiz sonuçlarının hesaplanması ve işlenmesi için harcanan yüksek çaba da göz önüne alınarak, binaların genel sismik performansı ön değerlendirme prosedürleri ile değerlendirilmiştir. Ön değerlendirme prosedürlerinin temel amacı, hasar görme riski yüksek olan binaları çabukça tespit etmektir.

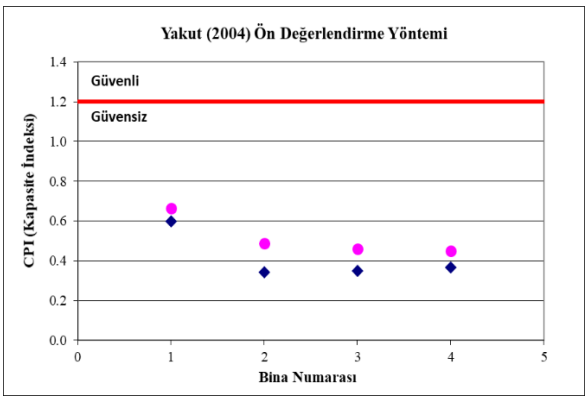
Bu çalışmadaki binalar, Hassan ve Sözen (1997), Yakut (2004) ve Özcebe vd. (2004) tarafından önerilen ön değerlendirme prosedürleri kullanılarak, mevcut yer hareketi etkileri altında olası performanslarını belirlemek amacıyla değerlendirilmiştir. Bu prosedürler ilgili atıflarda mevcut olduğu için burada detaylı olarak açıklanmamış, yalnızca sonuçlar şekil 8, şekil 9 ve tablo 5'te gösterilmiştir.

Tablo 5. Özcebe vd. (2004) ön değerlendirme yöntemi ile performans tahmin sonuçları

Bina	Performans Tahmini
1	Orta düzey deprem riski
2	Orta düzey deprem riski
3	Ağır deprem riski
4	Ağır deprem riski



Şekil 8. Hassan ve Sözen (1997) ön değerlendirme yöntemleri ile performans tahmin sonuçları.



Şekil 9. Yakut (2004) ön değerlendirme yöntemleri ile performans tahmin sonuçları.

Bu ön değerlendirme yöntemleri, büyük bina envanterlerini hızlıca sıralamak için birçok önemli yapısal parametreyi ihmal etse de, incelenen binaların risklilik durumları yeteri düzeyde belirlenebilmiştir. Bu grup içindeki binaların sıralaması başarılı olmuştur, çünkü binalar ağır ve orta derecede hasarlı olarak sınıflandırılabilmiştir. Bu nedenle, özellikle binalarla ilgili güvenilir verilerin eksikliği ve sahadaki beklenen deprem tehlikesi seviyesi durumunda, ön değerlendirmelerin yapılması, incelenen binalar için yeterli olmuştur. Analiz sonuçlarının hesaplanması ve işlenmesi için harcanan yüksek çaba göz önünde bulundurulduğunda, ön değerlendirme prosedürleri pratik bir alternatif olarak görülmektedir.

8. Tartışma ve Sonuçlar

Çalışmamız, Türkiye'deki bina stokuna örnekler üzerinde yönetmeliklerce verilen detayı değerlendirme yöntemlerinin ve riski yapıların hızlı tespitine yönelik ön değerlendirme yöntemlerinin uygulanmasına odaklanmıştır. Riskli bina stokunun belirlenmesinin ehemmiyeti son yıkıcı depremler ve ortaya çıkardığı yıkım ile bir kez daha görülmüştür. Seçilen binalara, ülkemizdeki betonarme bina envanterinin genel yapısal özelliklerini yansıtan değerlendirme prosedürleri uygulanmış ve deprem sırasındaki genel bina performansı değerlendirilmiştir. Binaların bilinen (deprem sonucu gözlenen) genel hasar durumları, NRHA analizlerinden elde edilen tahminlerle karşılaştırılmıştır.

NRHA sonuçlarına dayalı olarak uygulanan ayrıntılı değerlendirme prosedürleri sonuçları irdelendiğinde, kolonlar için değişen hasar seviyeleri tahmin edilmiş olmasına rağmen, incelenen tüm binalar, gerçek deprem hasar durumlarına bakılmaksızın, EuroCode-8-3, DBYBHY-2007 ve TBDY-2018 yönetmeliklerinin ayrıntılı değerlendirme prosedürleriyle "ağır hasarlı" veya "göçmüş" olarak değerlendirilmiştir. Bu nedenle, gerçek hasar durumları doğru tahmin edilememiş ve binalar bu ayrıntılı değerlendirme prosedürleri ile risk durumlarına göre gruplandırılamamıştır. Bu muhafazakâr sonuçların, özellikle yetersiz enine donatı koşulları için, yönetmelik sınırlarının yüksek güvenlik paylarıyla ilişkili olduğu değerlendirilmektedir. Bu yüksek güvenlik aralığı, laboratuvar numunelerindeki detayların, yetersiz inşaat uygulamalarını taklit etmek için kasten kötü yapılmadığı sınırlı araştırmalardan kaynaklanmaktadır.

Çalışmada ele alınan ön değerlendirme yöntemleri ise çok daha sınırlı parametre ile ve çok daha hızlı şekilde daha doğru sonuçların ede edilmesini sağlayabilmişlerdir.

Bugüne kadar geliştirilen değerlendirme prosedürleri, laboratuvar ortamındaki test yapıları için yeterince doğru olabilir. Ancak, gerçek binaların özelliklerindeki değişkenlikler ve sahadaki yer hareketi göz önüne alındığında, bu prosedürlerin saha gözlemleriyle hasar beklentilerinin tutarlılığı çok daha düşüktür. Betonarme binaların sismik davranışı hakkında testlerden elde edilen değerli bilgiler, saha verilerinden elde edilen daha fazla bilgiyle desteklenmelidir. Malzeme özelliklerindeki değişiklikler, geometriler, yer hareketi varyasyonları ve diğer birçok parametre nedeniyle saha verileri ile yönergelerde açıklanan değerlendirme prosedürleri arasındaki tutarsızlıklar göz önüne alındığında, bu yöntemlerin tahmin yetenekleri konusunda daha gerçekçi bir yaklaşıma ihtiyaç olduğu açıktır. Önemli olduğu için altını çizmekte fayda gördüğümüz bir gözlem şudur: Ülkede halen yaygın olarak uygulanmakta olan kentsel dönüşüm programları ve bunların dayandığı hesap yaklaşımları mevcut binaların bulundukları mahallerdeki deprem tehlikesi gerçekleştiği takdirde uğrayacakları hasar konusunda mühendise fikir vermektedir. Kullanılan hesap usulleri ele alınan bina sayılarının çokluğu dikkate alınarak mümkün olduğu kadar pratik çerçeve içinde tutulmaktadır. Bir taraftan bina stokunun barındırdığı can ve mal emniyetini tehdit eden örnekleri doğru şekilde ayıklama ihtiyacı, diğer taraftan ise lüzumsuz yere tehlike arz etmeyen binaları boş yere yıkma kararı vermeme gereği kullanılan hesap araçlarının güvenilir olmasını şart koşmaktadır. Bu amacın sağlanması mutlaka gözlemlere dayalı bilgi dağarcığının geliştirilmesine ihtiyaç göstermektedir. Halen Çevre, Şehircilik ve İklim Değişikliği Bakanlığınca bina değerlendirme firmalarına tavsiye edilen yazılımların fiili gözlemlerle daha güvenilir sonuçlar vermesine yönelik kalibrasyon eylemlerine aralık vermeksizin devam edilmelidir.

Katkı Oranı Beyanı

Yazarların katkı yüzdeleri aşağıda verilmiştir. Yazarlar makaleyi incelemiş ve onaylamıştır.

	A.D.	P.G.
K	40	60
T	50	50
Y	-	-
VTI	80	20
VAY	50	50
KT	60	40
YZ	70	30
KI	30	70
GR	70	30

PY	-	-
FA	-	-

K= kavram, T= tasarım, Y= yönetim, VTI= veri toplama ve/veya işleme, VAY= veri analizi ve/veya yorumlama, KT= kaynak tarama, YZ= yazım, KI= kritik inceleme, GR= gönderim ve revizyon, PY= proje yönetimi, FA= fon alımı.

Çatışma Beyanı

Yazarlar bu çalışmada hiçbir çıkar ilişkisi olmadığını beyan etmektedirler.

Etik Onay Beyanı

Bu araştırmada hayvanlar ve insanlar üzerinde herhangi bir çalışma yapılmadığı için etik kurul onayı alınmamıştır.

Kaynaklar

AFAD 2023. 6 Şubat 2023 Pazarcık (Kahramanmaraş MW 7.7) ve Elbistan (Kahramanmaraş MW 7.6) depremlerine ilişkin ön değerlendirme raporu. Deprem Dairesi Başkanlığı, Ankara, Türkiye, ss: 12.

American Society of Civil Engineers (ASCE). 2000. Prestandard and commentary for the seismic rehabilitation of buildings. FEMA-356, Washington, USA, pp: 518.

American Society of Civil Engineers (ASCE). 2007. Seismic rehabilitation of existing buildings. ASCE/SEI-41/06, Virginia, USA, pp: 426.

American Society of Civil Engineers (ASCE). 2008. Seismic rehabilitation of existing buildings. ASCE/SEI-41/06 Supplement 1, Virginia, USA, pp: 117.

American Society of Civil Engineers (ASCE). 2023. Seismic evaluation and retrofit of existing buildings. ASCE/SEI 41-23, Virginia, USA, pp: 567.

Applied Technology Council (ATC). 1996. Seismic evaluation and retrofit of concrete buildings. Report No. SSC 96-01, ATC-40, Volume 1-2, California, USA, pp: 608.

Applied Technology Council (ATC). 2005. Improvement of nonlinear static seismic analysis procedures. FEMA-440, ATC-55 Project, California, USA, pp: 390.

Bakır BS, Sucuoğlu H, Yılmaz T. 2002. An overview of local site effects and the associated building damage in Adapazarı during the 17 August 1999 İzmit EQ. Bull Seismol Soc Am, 92 (1): 509-526.

Chang G, Mander J. 1994. Seismic energy based fatigue damage analysis of bridge columns: Part I – Evaluation of seismic capacity. NCEER Tech. Rep. 94-0006, NY, USA, pp: 226.

Chopra AK, Goel RK, Chintanapakdee C. 2004. Evaluation of a modified MPA procedure assuming higher modes as elastic to estimate seismic demands, Earthq Spectra, 20(3): 757-778.

Dilsiz A. 2013. Assessment of nonlinear static (pushover) analysis procedures using field experience. PhD. Thesis, Civil Engineering Dept., Middle East Technical University, Ankara, Türkiye, pp: 339.

Dilsiz A, Gunay S, Mosalam K, Miranda E, Arteta C, Sezen H, Fischer E, Hakhamaneshi M, Hassan W, ALhawamdeh B, Andrus S, Archbold J, Arslanturkoglu S, Bektas N, Ceferino L, Cohen J, Duran B, Erazo K, Faraone G, Feinstein T, Gautam R, Gupta A, Haj Ismail S, Jana A, Javadinasab Hormozabad S, Kasalanati A, Kenawy M, Khalil Z, Liou I, Marinkovic M, Martin A, Merino-Pe˜na Y, Mivehchi M, Moya L, P´ajaro Miranda C, Quintero N, Rivera J, Rom˜ao X, Lopez Ruiz MC, Sorosh S, Vargas L, Velani PD, Wibowo H, Xu S, Yilmaz T, Alam M, Holtzer G, Kijewski-Correa T, Robertson I, Roueche D, Safiey A. 2023. StEER: 2023 Mw 7.8 Kahramanmaraş, Türkiye Earthq seq preliminary virtual reconnaissance rep (PVRR). DesignSafe-CI, pp: 144. https://doi.org/10.17603/ds2-7ry2-gv66.

DBYBHY 2007. Deprem bölgelerinde yapılacak binalar hakkında yönetmelik. Bayındırlık ve İskân Bakanlığı, Ankara, Türkiye, 26454.

European Committee for Standardization (EC) 2005. Eurocode 8: Design of structures for earthquake resistance - Part 3: Strengthening and repair of buildings, European Standard, EC-8-3, BS EN 1998–3, Comité Européen de Normalisation, Brussels, Belgium, pp: 81.

Fajfar P, Fischinger M. 1987. Nonlinear seismic analysis of RC buildings: Implications of a case study. European Earthquake Engineering, Bull Earthq Eng, 1: 31-43.

Gülkan P, Sozen MA. 1999. A Procedure for determining seismic vulnerability of building structures. ACI Struct J, 96 (3): 336-342.

Hassan AF, Sözen MA. 1997. Seismic vulnerability assessment of low-rise buildings in regions with infrequent earthquakes. ACI Struct J, 94: 31–39.

Kent DC, Park R. 1971. Flexural members with confined concrete. J Struct Eng (NYNY), New York, 97(7): 1969-1990.

OpenSees 2010. Open system for earthquake engineering simulation. Version 2.2.1, Pacific Earthquake Engineering Research Center, http://opensees.berkeley.edu.

Özcebe G, Yücemen MS, Aydoğan V. 2004. Statistical seismic vulnerability assessment of existing reinforced concrete buildings in turkey on a regional scale. J Earthq Eng, 8 (5): 749-773.

Sancio RB, Bray JD, Stewart JP, Youd TL, Durgunoglu HT, Önalp A, Seed RB, Christensen C, Baturay MB, Karadayılar T. 2002. Correlation between ground failure and soil conditions in Adapazari, Turkey. Soil Dyn Earthq Eng, 22 (9-12): 1093–1102.

SBB (TC Cumhurbaşkanlığı, Strateji ve Bütçe Başkanlığı) 2023. 2023 Kahramanmaraş ve Hatay depremleri raporu. Ankara, Türkiye, pp: 142. URL: https://www.sbb.gov.tr/wp-content/uploads/2023/03/2023-Kahramanmaras-ve-Hatay-Depremleri-Raporu.pdf [erişim tarihi: Aralık 10, 2024]

Scott BD, Park R, Priestley MJN. 1982. Stress-strain behavior of concrete confined by overlapping hoops at low and high strain rates. ACI Struct J, 79 (1): 13-27.

TBDY 2018. Türkiye bina deprem yönetmeliği. Afet ve Acil Durum Yönetimi Başkanlığı (AFAD), Ankara, Türkiye, 30364.

Yakut A. 2004. Preliminary seismic performance assessment procedure for existing RC buildings. Eng Struct, 26 (10): 1447-1461.

Yakut A, Ozcebe G, Yucemen MS. 2006. Seismic vulnerability assessment using regional empirical data. Earthq Eng Struct Dyn, 35: 1187-1202.

Black Sea Journal of Engineering and Science
doi: 10.34248/bsengineering.1613222

Open Access Journal
e-ISSN: 2619 – 8991

Research Article
Volume 8 - Issue 2: 455-461 / March 2025

OPTIMIZATION-BASED PID CONTROLLER DESIGN FOR DC-DC BOOST CONVERTERS IN HYBRID RENEWABLE ENERGY SYSTEMS

Mustafa GÜNEŞ[1], Funda DEMİR[2]*

[1]*Ostim Technical University, Department of Electronics and Automation, 06000 Ankara, Türkiye*
[2]*Karabük University, Faculty of Engineering, Department of Mechatronics Engineering, 78050 Karabük, Türkiye*

Abstract: The increasing awareness of the need for renewable and clean energy sources has become a significant agenda item, especially as global energy demand continues to rise. Studies on renewable energy systems, which provide healthier conditions for current and future generations while meeting energy demand, are becoming increasingly widespread both locally and globally. Hybrid energy systems, formed by combining multiple energy sources, have recently introduced innovative solutions for the integration and management of various energy types. However, the voltage levels obtained from these systems are often low, making it necessary to boost the voltage for storage and household use.To address this, DC-DC boost converters are used to increase the voltage generated by solar panels, wind turbines, or hybrid energy systems. PID (Proportional-Integral-Derivative) controllers are typically required for converter control. However, conventional constant-gain PID controllers and classical PID tuning methods are often ineffective, as they rely on mathematical formulations or experimental system response analyses. To overcome this challenge, meta-heuristic optimization algorithms provide a viable alternative, offering a more stable and faster system response. In this study, a hybrid energy system consisting of a Proton Exchange Membrane (PEM) fuel cell, PV panel, and wind turbine was modeled in the Matlab/Simulink environment. A DC-DC boost converter was designed to elevate the system's output voltage to the desired reference level, enhancing system stability. Three different optimization methods—Particle Swarm Optimization (PSO), Grey Wolf Optimization (GWO), and Artificial Bee Colony (ABC) algorithms—were employed to adjust the parameters of the PID controller used for converter control. The PID coefficients obtained through these optimization algorithms are presented and compared. The performance of the tuned PID controller was evaluated through system response analysis under variable load conditions and by calculating the Root Mean Square Error (RMSE) between the output voltage and the specified reference value. Additionally, the controller performance was analyzed based on overshoot, settling time, and rise time values as shown in the resulting graphs.

Keywords: Renewable energy, Proton exchange membrane, DC-DC boost convertor, Partial swarm optimization, Grey wolf optimization, Artificial bee colony

***Corresponding author:** *Karabük University, Faculty of Engineering, Department of Mechatronics Engineering, 78050 Karabük, Türkiye*
E mail: fundademir@karabuk.edu.tr (F. DEMİR)
Mustafa GÜNEŞ https://orcid.org/0000-0002-0266-6370
Funda DEMİR https://orcid.org/0000-0001-7707-8496

Received: January 05, 2025
Accepted: February 11, 2025
Published: March 15, 2025

Cite as: Güneş M, Demir F. 2025. Optimization-based PID controller design for DC-DC boost converters in hybrid renewable energy systems. BSJ Eng Sci, 8(2): 455-461.

1. Introduction

In the contemporary world, the diversity and accessibility of energy resources for electricity generation hold significant importance on a global scale. This issue is closely associated with the increasing energy demand driven by population growth, industrialization, and technological advancements (Long and Liu, 2024). In particular, environmental concerns and the increasing awareness of climate change have intensified interest in renewable energy sources. Renewable sources such as wind, solar, hydroelectric, geothermal, and biomass hold significant potential for clean and sustainable electricity generation (Paraschiv, 2023). Moreover, the use of renewable energy sources contributes to energy supply security by diversifying energy resources. In this context, the effective and efficient utilization of various energy sources for electricity generation is crucial in meeting global energy needs (Hassan et al., 2024).

Hybrid energy systems combine different energy sources to enable more efficient and sustainable energy production. These systems typically integrate fossil-based fuels, referred to as primary energy sources, with renewable energy sources such as wind, solar, and hydrogen. Additionally, some hybrid systems are formed by the combination of two or more renewable energy sources (Krishna and Kumar, 2015). The main challenge with renewable energy sources is their dependence on environmental conditions, such as wind speed and solar irradiance, which limits their ability to provide consistent and high-power output (Paliwal et al., 2014). Therefore, using renewable sources like wind, solar, hydro, biogas, and fuel cells within a hybrid system can help mitigate environmental dependency, ensure energy continuity,

This work is licensed (CC BY-NC 4.0) under Creative Commons Attribution 4.0 International License

and increase power output. For example, a hybrid energy system that combines wind turbines and solar panels can continue generating electricity using wind energy even when sunlight is unavailable. The goal of such systems is to enhance energy efficiency, reduce power outages, and promote energy sustainability.

Significant research is currently being conducted on hybrid systems and their applications. Various configurations, systems, and their effects are well-documented in the literature (Olatomiwa et al., 2016). In particular, a general review of the literature on rural electrification shows that renewable energy sources are among the most effective solutions for providing electricity to rural areas that are located far from the electrical grid (Ma et al., 2013; Mekhilef et al., 2012; Harish and Kumar, 2014).

2. Materials and Methods

In this study, a hybrid energy system model has been developed by combining three separate renewable energy systems, namely PV panel, wind turbine, and PEM fuel cell. The objective of this study is to obtain continuous and uninterrupted voltage from each of these three energy systems, each influenced by specific conditions and environmental factors. Additionally, when operating in pairs or trios, the aim is to achieve a high voltage level. The study is prepared in a simulation environment using Matlab/Simulink. The block diagram of the developed model is given in Figure 1.

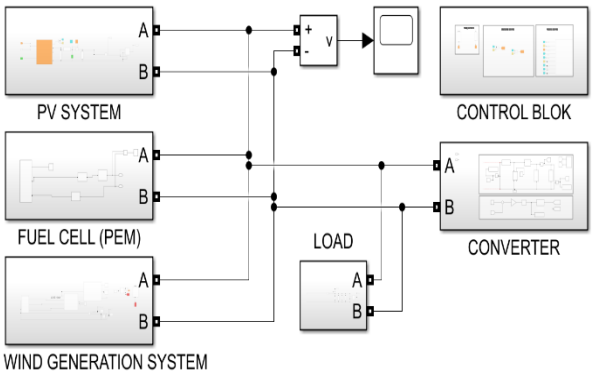


Figure 1. Block diagram of PV panel, fuel cell (PEM) and wind turbine-based hybrid power generation system.

The total voltage obtained from the hybrid system is transferred as an input value to a DC-DC boost converter. In the block diagram, the control unit is responsible for adjusting the converter to raise the incoming voltage to the desired level. Upon closer examination of these blocks and their functions:

2.1. DC-DC Boost Converter

A boost converter is a type of DC-DC power converter that increases the input voltage to a higher output voltage. It operates on the principle of storing energy in an inductor and then releasing that stored energy to the output at a higher voltage level (Liu and Wu, 2023). Boost converters are widely used in various applications where a higher voltage is required from a lower voltage source, such as in battery-powered devices, renewable energy systems, and electric vehicles (Mirzaei et al., 2012).

The primary function of the boost converter is to regulate the charge and discharge cycles between the inductor and capacitor through a control signal that adjusts the voltage level (Paul et al., 2024). In this process, the control signal manages the switching operations of the converter, balancing the storage and release of energy. The circuit of the boost converter used in this study, modelled in the Matlab/Simulink environment, is shown in Figure 2.

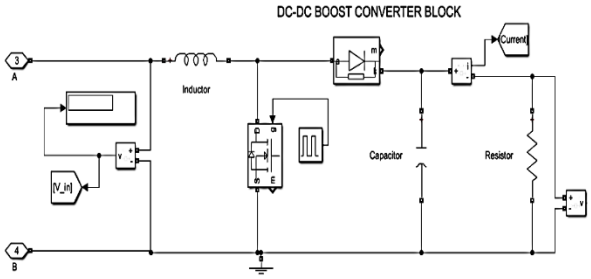


Figure 2. Matlab model of the DC-DC boost converter.

A DC-DC boost converter fundamentally consists of a switching element, a capacitor, an inductor, and a load. The values of these components are calculated based on the system's input voltage and the desired output voltage. Based on this ratio, the duty cycle of the switching element is determined. Since the converter's parameters affect its performance, efficiency, and reliability, they must be selected carefully (Solaiman et al., 2015; Sakly et al., 2017). The key parameters of the boost converter circuit used in this study are provided in Table 1.

Table 1. Parameters of DC-DC boost converter

Parameter	Rated Value
Input Voltage (V_in)	~ 250 V
Output (Reference) Voltage (V_out)	400 V
Inductor (L)	20.50 µH
Capacitor (C)	40 µF
Load (R)	40 Ω
Duty Cycle (D)	0.6

2.2. PID Controller

A PID controller (Proportional-Integral-Derivative controller) is a widely used feedback mechanism in industrial control systems. It continuously calculates the error as the difference between the desired setpoint and the measured process variable, then applies a correction based on proportional, integral, and derivative terms (Ozdemir and Erdem, 2018). Figure 3 presents the PID control algorithm.

The PID control algorithm consists of three fundamental components. The Proportional (P) term generates a

control signal that is proportional to the instantaneous error value. This term adjusts the control signal based on the magnitude of the current error, thereby correcting it (Daraz et al., 2023). The Integral (I) term addresses any persistent errors in the system by accumulating the error signal over time. This enhances the long-term stability of the system and helps to balance slow changes.

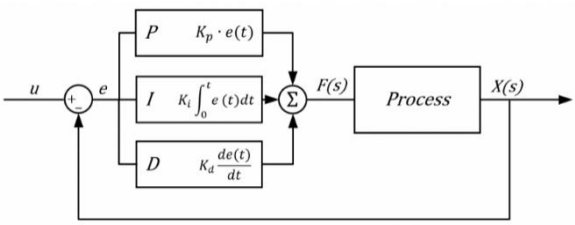


Figure 3. PID control algoritm.

The Derivative (D) term evaluates the rate of change of the error signal over time, thereby controlling the system's response speed. This allows for a quicker response to sudden changes and reduces overshooting, thereby enhancing system stability (Mitra and Swain, 2014). Figure 4 shows the PID control block as prepared in Matlab/Simulink.

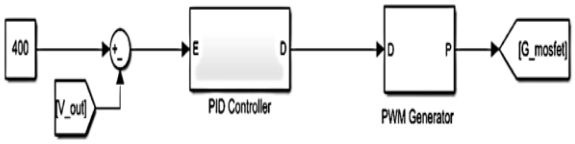


Figure 4. PID control block in Matlab

2.3. Optimization Algorithms for PID Control

Various methods exist for adjusting the parameters of PID controllers, ranging from classical approaches that involve mathematical modeling and system response analysis (Harish and Kumar, 2014) to techniques based on metaheuristic optimization algorithms for determining optimal parameter values (Pareek et al., 2014).

In this study, the PID controller for a DC-DC boost converter connected to a hybrid energy system was tuned using metaheuristic methods. The selected algorithms were Particle Swarm Optimization (PSO), Grey Wolf Optimizer (GWO), and Artificial Bee Colony (ABC).

The performance of the tuned PID controller was evaluated through system response analysis under variable load conditions, as well as by calculating the Root Mean Square Error (RMSE) between the output voltage and the specified reference value. Additionally, the controller's performance was assessed with a focus on overshoot, settling time, and rise time values, as depicted in the obtained graphs.

2.3.1.Particle swarm optimization (PSO) algoritm

The Particle Swarm Optimization (PSO) algorithm is an optimization technique inspired by the behavior of swarms of fish and insects in nature (Kennedy and Eberhart, 1995). In PSO, the problem is divided into segments, each represented by candidate solutions, referred to as 'particles' within the algorithm (Xiao et al., 2024). These particles navigate the search space, proposing solutions to identify the optimal one.

The PSO algorithm consists of the following stages: Initialization, Evaluation, Updating Particle Velocity and Position, Updating Personal and Global Best Positions, and Termination. These stages are illustrated in Fig. 5 (Yousef et al., 2020). The algorithm is widely preferred in fields such as engineering, economics, and data science due to its simplicity, ability to handle complex problems, and efficiency (Le et al., 2019).

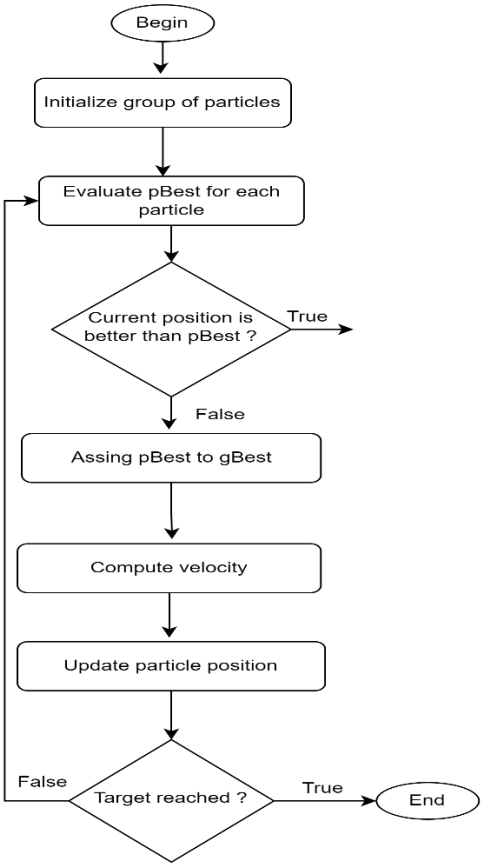


Figure 5. Flow chart of the PSO algorithm (Le et al., 2019).

2.3.2. Grey wolf optimizer (GWO) algoritm

The Grey Wolf Optimizer (GWO) algorithm is inspired by the hunting behaviours of grey wolves (canis lupus), one of nature's most impressive predators (Mirjalili et al., 2014). Wolves, which move in packs, exhibit a strong social hierarchy. This hierarchy includes the alpha (α) wolf, which assumes the leadership role, followed by beta (β) wolves, then delta (δ) wolves, and finally omega (ω) wolves. The algorithm is based on the hunting process of wolf packs, which follows a three-stage strategy: encircling, hunting, and attacking prey to find their target (Prasad et al., 2024). These unique hunting strategies enable the GWO algorithm to achieve successful results in optimization problems. Figure 6 illustrates the GWO algorithm.

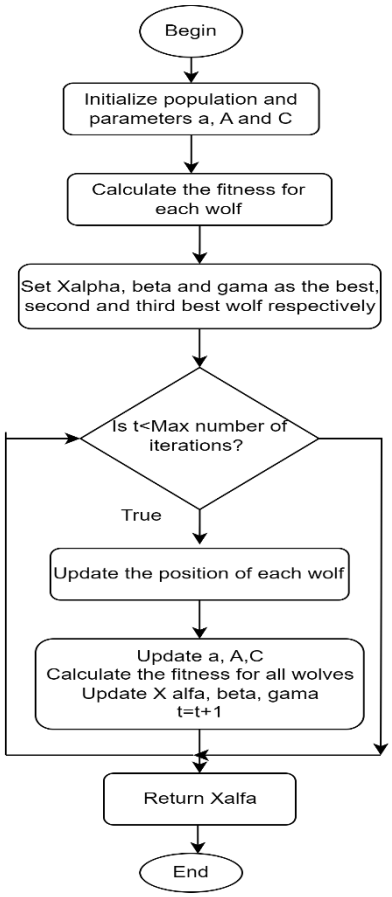


Figure 6. Flow chart of the GWO algorithm (Amirsadri et al., 2018).

Due to its simplicity and ease of implementation, requiring few parameter adjustments, high efficiency, and parallel applicability, Grey Wolf Optimizer (GWO) is recognized as a powerful and innovative tool for solving optimization problems.

2.3.3. Artifical bee colony (ABC) algoritm

The Artificial Bee Colony (ABC) Optimization algorithm is a nature-inspired optimization method based on the foraging strategy of bees (Karaboga, 2005). ABC mimics the foraging behaviour of honeybees as they search for food sources and share information within the colony. In this algorithm, each bee represents a candidate solution and works to optimize a fitness function that evaluates the quality of the solution (Sönmez et al., 2017). The bee colony is composed of employed bees, onlooker bees, and scout bees.

In ABC, the behavior of bees is modeled based on certain assumptions. One key assumption is that only one employed bee is responsible for extracting nectar from each food source. Consequently, the number of food sources in the algorithm is equal to the number of employed bees. Another assumption is that the number of employed bees matches the number of scout bees. However, in practice, if a worker bee returns to a depleted food source, it may transform into a scout bee. The fitness value of a food source is directly proportional to the quality of the food it provides.

The ABC algorithm is highly adaptable to various problem domains and optimization challenges, making it a versatile tool for a wide range of industrial and academic applications. Figure 7 illustrates the ABC algorithm.

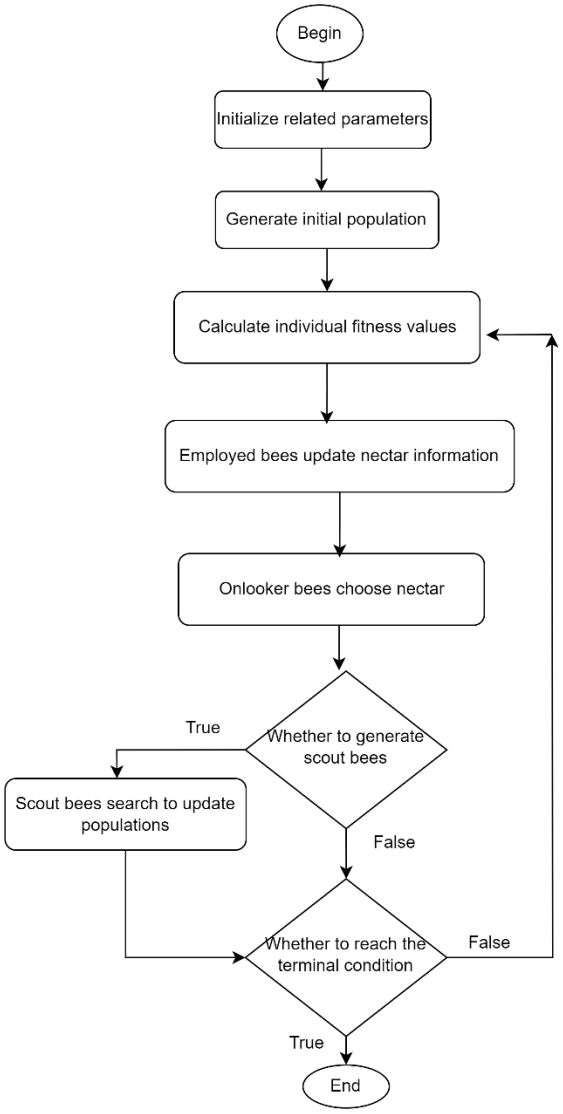


Figure 7. Flow chart of the ABC algorithm (Wang et al., 2019).

3. Simulation and Results

This study focuses on the optimization of PID parameters using PSO, GWO, and ABC algorithms. The selection of appropriate initial values is critically important for effectively tuning the PID parameters and managing the optimization process. These values can significantly influence the success and outcomes of the optimization process. The initial values for the algorithms, each executed over 30 iterations, are provided in Table 2.

After conducting system simulations and optimization using the PSO, GWO, and ABC algorithms, the PID controller gain values were obtained for each scenario. The gain parameters of the PID controller and the RMSE values from the optimization are presented in Table 3.

Table 2. PSO, GWO and ABC Algorithms initial values

Algorithm	Parameters İnitial Values	
	Description	Value
PSO	Number of particles	20
	Number of iterations	30
	Self-adjustment weight	0.9
	Social-adjustment weight	1.2
GWO	Number of Wolves	10
	Number of Iterations	30
ABC	Number of Bees	15
	Number of Iterations	30
	Dimension of problem	3

These results provide a comparative analysis of the performance of the different algorithms and how closely each system achieved the targeted performance. In other words, they demonstrate each algorithm's ability to optimize the PID parameters and its impact on system performance. Table 3 summarizes the optimized parameters and the obtained RMSE values.

Table 3. Optimized parameters and obtained RMSE values

Parameter	Algorithms		
	PSO	GWO	ABC
Kp	5.2307	3.1072	2.2106
Ki	5.5473	6.0041	8.8505
Kd	4.6979	7.8168	1.2033
RMSE	1.8261	2.7458	2.4495

When comparing the results based on RMSE values, it is evident that the PSO algorithm delivers the best performance. PSO achieved the lowest error with an RMSE value of 1.8261, making it the most successful algorithm by a significant margin. The ABC algorithm, with an RMSE value of 2.4495, ranked second, demonstrating approximately 15% lower performance compared to PSO. The GWO algorithm exhibited the lowest performance, with an RMSE value of 2.7458, showing approximately 20% lower performance than PSO. These findings highlight the superior capability of the PSO algorithm in optimizing PID parameters and its significantly greater impact on system performance compared to the other algorithms. The exceptional success of PSO strongly supports its preference in optimization processes.

The output voltages obtained when the PID parameters, determined through the optimization process, were applied to the system are shown in Fig. 8. As illustrated in the figure, the output voltage achieved using the PSO algorithm demonstrates significant success compared to the results from the other algorithms. This success is reflected not only in its low error (RMSE) values but also in its superior dynamic performance metrics, such as overshoot, settling time, and rise time. Specifically, the output signal obtained with the PSO algorithm exhibited minimal overshoot and the fastest settling time to the desired values. These findings clearly demonstrate the effectiveness of the PSO algorithm in optimizing PID parameters and its positive impact on system performance.

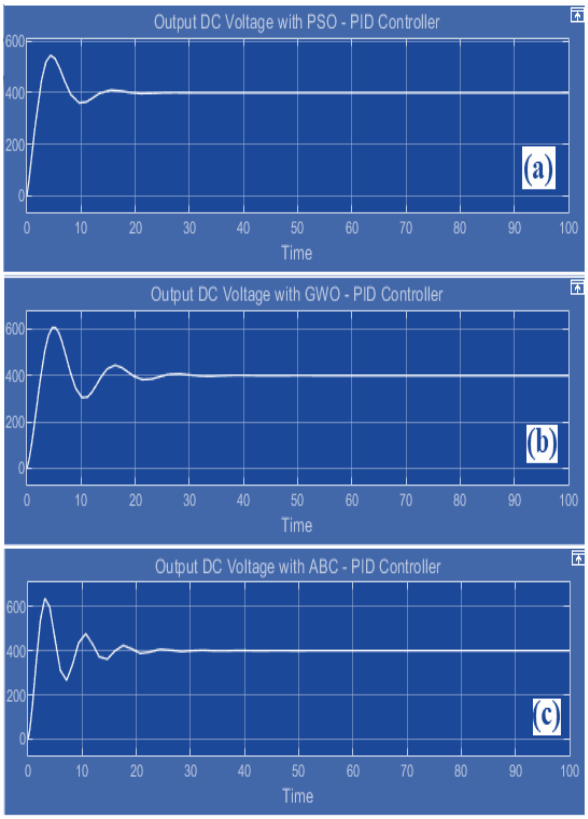


Figure. 8. System response comparison for the PID controller tuned by (a) PSO, (b) GWO and (c) ABC algorithms under output voltage changes.

4. Discussion

With the increasing demand for energy today, the utilization of renewable energy sources is becoming more crucial. In this context, a study was conducted to model a hybrid energy system integrating three different renewable energy sources—PV panels, wind turbines, and PEM fuel cells—using the Matlab/Simulink simulation environment. The system is managed with an optimized control strategy that accounts for the characteristics of each energy source. This control strategy employs a PID controller, which was tuned using various optimization techniques. Specifically, the coordinated operation of these three energy sources depends on solar irradiance for PV panels, wind speed for wind turbines, and the fuel source for fuel cells.

The parameters of the DC-DC boost converter modelled in the Matlab/Simulink environment are critical components that directly influence the system's performance. The PID controller is used to adjust the output voltage of the DC-DC boost converter to approach the desired reference value. In this study, metaheuristic

algorithms such as PSO, GWO, and ABC were employed to optimize the PID controller. The simulations and optimization studies revealed that the PSO algorithm demonstrated the best performance, achieving the lowest RMSE value of 1.8261 and effectively reaching the desired output voltage in the system.

This study demonstrates the effectiveness of metaheuristic optimization methods in optimizing renewable energy systems and enhancing energy efficiency. It makes a significant contribution to the literature by providing a comparative analysis of the impacts of different optimization algorithms on PID controller settings. The results represent a crucial step towards the integration of renewable energy systems, as hybrid systems combining various energy sources offer a potentially effective solution for balancing fluctuations in energy production and ensuring a continuous energy supply.

The study contributes to the development of sustainable and efficient energy production methods to meet future energy demands. It also provides valuable guidance for researchers and industry professionals in the design and optimization of hybrid systems.

In the next stage of the study, the optimization methods will be expanded, and the performances of different hybrid optimization techniques will be evaluated. The study will be further developed by detailing the training and execution times of the algorithms, as well as the validation approaches, to present an original and innovative contribution to the literature.

Author Contributions

The percentages of the authors' contributions are presented below. All authors reviewed and approved the final version of the manuscript.

	M.G.	F.D.
C	50	50
D	50	50
S	50	50
DCP	50	50
DAI	50	50
L	50	50
W	50	50
CR	50	50
SR	50	50
PM	50	50
FA	50	50

C=Concept, D= design, S= supervision, DCP= data collection and/or processing, DAI= data analysis and/or interpretation, L= literature search, W= writing, CR= critical review, SR= submission and revision, PM= project management, FA= funding acquisition.

Conflict of Interest

The authors declared that there is no conflict of interest.

Ethical Consideration

Ethics committee approval was not required for this study because of there was no study on animals or humans.

References

Amirsadri S, Seyed Jalaleddin M, Hossein E-K. 2018. A Levy flight-based grey wolf optimizer combined with back-propagation algorithm for neural network training. Neural Comput Appl, 30(12): 3707–3720. https://doi.org/10.1007/s00521-017-2952-5

Daraz A, Basit A, Zhang G. 2023. Performance analysis of pid controller and fuzzy logic controller for dc-dc boost converter. Plos One, 18(10): e0281122. https://doi.org/10.1371/journal.pone.0281122

Harish VSKV, Kumar A. 2014. Demand side management in ındia: action plan, policies and regulations. Renew Sust Ener Rev, 33: 613-624. https://doi.org/10.1016/j.rser.2014.02.021

Hassan Q, Victor P, Al-Musawi TJ, Ali BM, Algburi S, Alzoubi HM, Khudhair AAJ, Sameen AZ, Salman HM, Jaszczur M. 2024. The renewable energy role in the global energy transformations. Renew Ener Focus, 48: 100545. https://doi.org/10.1016/j.ref.2024.100545

Hossam F, Aljarah I, Al-Betar MA, Mirjalili S. 2018. Grey wolf optimizer: a review of recent variants and applications. Neural Comput Appl, 30(2): 413-435. https://doi.org/10.1007/s00521-017-3272-5

Karaboga D. 2005. An idea based on honey bee swarm for numerical optimization. Erciyes University Engineering Faculty, Computer Engineering Department Technical Report, Kayseri, Türkiye, pp: 1-10.

Kennedy J, Eberhart R. 1995. Particle swarm optimization. In Proceedings of ICNN'95-International Conference on Neural Networks, November 27, Perth, Australia, 4: 1942-1948. https://doi.org/10.1109/ICNN.1995.488968

Krishna KS, Kumar KS. 2015. A review on hybrid renewable energy systems. Renew Sust Ener Rev, 52: 907-916. https://doi.org/10.1016/j.rser.2015.07.187

Le LM, Ly HB, Pham BT, Le VM, Pham TA, Nguyen DH, Tran XT, Le TT. 2019. Hybrid artificial intelligence approaches for predicting buckling damage of steel columns under axial compression. Materials, 12(10): 1670. https://doi.org/10.3390/ma12101670

Liu X, Wu X. 2023. A two-stage bidirectional dc-dc converter system and its control strategy. Energy, 266: 126462. https://doi.org/10.1016/j.energy.2022.126462.

Long Y, Liu X. 2024. Optimal green investment strategy for grid-connected microgrid considering the impact of renewable energy source endowment and incentive policy. Energy, 295: 131073. https://doi.org/10.1016/j.energy.2024.131073

Ma T, Yang H, Lu L. 2013. Performance evaluation of a stand-alone photovoltaic system on an isolated island in Hong Kong. App Ener 112: 663-672. https://doi.org/10.1016/j.apenergy.2012.12.004

Mekhilef S, Saidur R, Kamalisarvestani M. 2012. Effect of dust, humidity and air velocity on efficiency of photovoltaic cells. Renew Sust Ener Rev, 16(5): 2920-2925. https://doi.org/10.1016/j.rser.2012.02.012

Mirjalili S, Mirjalili SM, Lewis A. 2014. Grey wolf optimizer. Adv Eng Software, 69: 46-61. https://doi.org/10.1016/j.advengsoft.2013.12.007

Mirzaei A, Awang J, Zainal S. 2012. Design and implementation of high efficiency non-isolated bidirectional zero voltage

transition pulse width modulated dc-dc converters, Energy, 47(1): 358-369. https://doi.org/10.1016/j.energy.2012.09.035

Mitra L, Swain N. 2014. Closed loop control of solar powered boost converter with pid controller. IEEE International Conference On Power Electronics, Drives And Energy Systems, Decenber 16-19, Mumbai, India, pp: 1-5. https://doi.org/10.1109/pedes.2014.7041973

Olatomiwa l, Mekhilef S, Ismail MS, Moghavvemi M. 2016. Energy management strategies in hybrid renewable energy systems: A review. Renew Sust Ener Rev, 62: 821-835. https://doi.org/ 10.1016/j.rser.2016.05.040

Ozdemir A, Erdem Z. 2018. Double-loop pi controller design of the dc-dc boost converter with a proposed approach for calculation of the controller parameters. J Syst Control Eng, 232(2): 137-148.

Paliwal P, Patidar NP, Nema RK. 2014. Planning of grid integrated distributed generators: a review of technology, objectives and techniques. Renew Sust Ener Rev, 40: 557–570. https://doi.org/10.1016/j.rser.2014.07.200

Paraschiv S. 2023. Analysis of the variability of low-carbon energy sources, nuclear technology and renewable energy sources, in meeting electricity demand. Ener Rep, 9(s11): 276–283. https://doi.org/10.1016/j.egyr.2023.09.008

Pareek S, Kishnani M, Gupta R. 2014. Optimal tuning of pid controller using meta heuristic algorithms. International Conference on Advances in Engineering and Technology Research, August 1-2, Kanpur, India, pp: 1–5. https://doi.org/10.1109/ıcaetr.2014.7012816

Paul AK, Ram BS, Kulkarni SV. 2024. Review of coupled inductors in power electronics: from concept to practice. E-Prime Adv Electr Eng Electron Ener, 8: 100501. https://doi.org/10.1016/j.prime.2024.100501

Prasad T, Raj S, Kundu D. 2024. Artificial neural network framework for the selection of deep eutectic solvents promoted enhanced oil recovery by interfacial tension reduction mechanism. Energy, 307: 132602. https://doi.org/10.1016/j.energy.2024.132602

Sakly J, Abdelghani ABB, Slama-Belkhodja I, Sammoud H. 2017. Reconfigurable dc/dc converter for efficiency and reliability optimization. IEEE J Emerg Selected Topics Power Electron, 5(3): 1216–1224. https://doi.org/10.1109/jestpe.2017.2676027

Solaiman HM, Hasan MM, Mohammad A, Kawsar SR, Hassan MA. 2015. Performance analysis of dc to dc boost converter using different control methods. IEEE International Conference on Electrical, Computer and Communication Technologies (ICECC), March 5-7, Tamilnadu, India, pp: 1–5.

Sonmez M, Akgüngör MA, Bektaş S. 2017. Estimating transportation energy demand in Turkey using the artificial bee colony algorithm. Energy, 122(2017): 301–310. https://doi.org/10.1016/j.energy.2017.01.074

Wang S, Liu H, Gao K, Zhang J. 2019. A multi-species artificial bee colony algorithm and its application for crowd simulation. IEEE Access, 7: 2549–2558.

Xiao X, Zhang X, Song M, Liu X, Huang G. 2024. Npp accident prevention: integrated neural network for coupled multivariate time series prediction based on pso and its application under uncertainty analysis for npp data. Energy, 305: 132374. https://doi.org/10.1016/j.energy.2024.132374

Yousef AM, Ebeed M, Abo-Elyousr FK, Elnozohy A, Mohamed M, Abdelwahab SAM. 2020. Optimization of pid controller for hybrid renewable energy system using adaptive sine cosine algorithm. Int J Renew Ener Res, 10(2): 669–677. https://doi.org/10.20508/ijrer.v10i2.10685.g7938

Black Sea Journal of Engineering and Science
doi: 10.34248/bsengineering.1600119

Open Access Journal
e-ISSN: 2619 – 8991

Research Article
Volume 8 - Issue 2: 462-465 / March 2025

DETERMINATION OF ELEMENTAL CONTENT OF *Allium pervariensis* PLANT USING ICP-OES (INDUCTIVELY COUPLED PLASMA OPTICAL EMISSION SPECTROSCOPY) METHOD

İdris YOLBAŞ[1]*

[1]*Türk Telekom Science High School, 56100, Siirt, Türkiye*

Abstract: In this study, the elemental composition of the endemic *Allium pervariensis* plant was determined using the ICP-OES method. The analysis revealed that calcium (Ca) and potassium (K) had the highest concentrations, with Ca at 6.2278±0.547 ppm and K at 5.5283±0.482 ppm. Additionally, sodium (Na) was measured at 1.0325±0.061 ppm. Furthermore, silver (Ag), arsenic (As), cobalt (Co), chromium (Cr), copper (Cu), iron (Fe), manganese (Mn), nickel (Ni), selenium (Se), silicon (Si), strontium (Sr), and vanadium (V) were also analyzed. These findings suggest that *A. pervariensis* is nutritionally rich and may offer potential health benefits. However, as the study is limited to samples from a specific geographical region, caution is needed when generalizing the results. Further comprehensive biochemical and clinical studies are recommended.

Keywords: *Allium pervariensis*, Calcium, Elemental analysis, ICP-OES, Potassium

***Sorumlu yazar (Corresponding author):** Türk Telekom Science High School, 56100, Siirt, Türkiye
E mail: idrisyolbas@gmail.com (İ. YOLBAŞ)
İdris YOLBAŞ https://orcid.org/0000-0001-7529-3395

Received: December 11, 2024
Accepted: February 14, 2025
Published: March 15, 2025

Cite as: Yolbaş İ. 2025. Determination of elemental content of *Allium pervariensis* plant using ICP-OES (Inductively coupled plasma optical emission spectroscopy) method. BSJ Eng Sci, 8(2): 462-465.

1. Introduction

Ethnobotanical knowledge plays a critical role in preserving traditional cultures, maintaining biodiversity, and contributing to public health and drug development (Khan et al., 2011; Saraçoğlu, 2024; Uslu, 2024; Yolbaş, 2024a, 2024c, 2024d). *Allium pervariensis* is an endemic plant species identified in the Southeastern Anatolia region of Türkiye, particularly in Siirt province (Fırat et al., 2018). It has close relatives such as *A. pustulosum* Boiss. & Hausskn and *A. karyeteini* Post, although it exhibits morphological differences.

Türkiye has a rich diversity of Allium species, attracting global attention. Of approximately 750 Allium species, about 170 are endemic to Türkiye (Rice-Evans et al., 1997). Allium species have been widely used in culinary and medicinal applications (Altunkanat and Tasan, 2023), playing a significant role in health and nutrition (Gürel, 2014).

Minerals are essential inorganic substances that support various biological functions. Their deficiency or excess can negatively impact physiological processes (Soetan et al., 2010). Determining the elemental content in plants is therefore crucial for understanding both plant physiology and human health (Yolbaş, 2024b).

This study aimed to determine the elemental composition of *A. pervariensis* and provide a comprehensive understanding of its biological properties and medicinal potential. For this purpose, ICP-OES was used for detailed elemental analysis.

ICP-OES is widely employed for trace element analysis, allowing simultaneous determination of multiple elements with high accuracy using small sample volumes (Donati et al., 2017; Diğdem and Arslan, 2019).

Trace elements, typically found in low concentrations, play essential roles in biological systems (Narin, 2002). Their determination is critical for plant health and human nutrition (Baytak, 2003). The findings of this study will enhance knowledge of *A. pervariensis*'s elemental composition and potential medicinal uses, inspiring future research.

This study represents the first elemental analysis of *A. pervariensis*. The use of ICP-OES enabled precise identification of its elemental content, providing a valuable reference for future studies.

2. Materials an Methods

2.1. Sample Collection

The *A. pervariensis* plant, naturally growing and commonly used by the local population for cheese-making, was collected in mid-April 2024 from Pervari, Siirt. The above-ground parts were dried in a dark room at 24°C for 30 days, then ground into a fine powder. The powdered plant was stored in a desiccator at the same temperature until analysis.

This work is licensed (CC BY-NC 4.0) under Creative Commons Attribution 4.0 International License

2.2. Elemental Analysis

2.2.1. Sample preparation

For the analyses to be performed using ICP-OES, *A. pervariensis* plant samples (each 1 g) were first ground into a fine powder. Each sample was then placed in separate Teflon vessels (CEM brand MARS 6 One Touch microwave oven, Matthews, NC, USA). A 10 mL portion of 65% concentrated nitric acid solution (Merck, Darmstadt, Germany) was added to the samples, and a blank sample containing only 10 mL of 65% nitric acid was also prepared. The vessels were sealed and placed in a microwave oven for digestion. The temperature was increased from room temperature (22-24°C) to 210°C over 25 minutes and was held at this temperature for 15 minutes. After cooling the samples to 22-24°C, they were transferred to volumetric flasks (50 mL), and ultrapure water was added to obtain the final volume.

2.2.2. ICP-OES analysis

The elements analyzed in the serum samples were as follows: Copper (Cu), Silver (Ag), Arsenic (As), Calcium (Ca), Cobalt (Co), Chromium (Cr), Iron (Fe), Potassium (K), Manganese (Mn), Sodium (Na), Nickel (Ni), Selenium (Se), Silicon (Si), Strontium (Sr), and Vanadium (V). The levels of these elements were determined using the Thermo iCAP 6000 series (ICP-OES) instrument parameters provided in table 1. Each element was measured using the appropriate wavelengths specified in table 2.

Table 1. ICP-OES device parameters

Parameters	Determined values
Plasma gas flow rate	15 L/min
Argon flow rate	0.5 L/min
Sample flow rate	1.51 L/min
Peristaltic pump speed	100 rpm
RF Power	1150 W

Table 2. ICP-OES elemental wavelengths

Element	Wavelength (nm)
Copper (Cu)	324.754
Silver (Ag)	328.068
Arsenic (As)	189.042
Calcium (Ca)	393.366
Cobalt (Co)	228.616
Chromium (Cr)	283.563
Iron (Fe)	259.940
Potassium (K)	766.490
Manganese (Mn)	257.610
Sodium (Na)	588.995
Nickel (Ni)	221.647
Selenium (Se)	196.090
Silicon (Si)	251.611
Strontium (Sr)	407.771
Vanadium (V)	309.311

Each element to be measured was prepared by creating working standard solutions from standard stock solutions (1000 µg/dL) (Chem-Lab NV). Calibration curves for each element were plotted and evaluated using these standard solutions and deionized water as the blank solution before conducting the measurements. The concentrations of the elements in the serum samples, prepared in this way for measurement, were determined using the ICP-OES device by referring to these standard curves.

2.3. Statistical Analysis

The statistical comparison of the results was performed using descriptive analysis. The data are presented as means and standard deviations (X±SD). All analyses were conducted using SPSS (v23.0).

3. Results and Discussion

In this study, the mineral content of *A. pervariensis* was analyzed using ICP-OES, table 3. The results indicate a significant mineral richness, with calcium (Ca) and potassium (K) detected at the highest concentrations. Calcium was the most abundant element at 6.2278±0.547 ppm, followed by potassium at 5.5283±0.482 ppm. Sodium (Na) ranked third at 1.0325±0.061 ppm. In contrast, cobalt (Co), nickel (Ni), vanadium (V), and arsenic (As) were present at the lowest levels, measuring 0.0035±0.011 ppm, 0.0078±0.012 ppm, 0.0079±0.014 ppm, and 0.0106±0.012 ppm, respectively. These findings suggest that calcium and potassium dominate the mineral composition, while trace elements are present in minimal amounts.

The results highlight the potential health contributions of *A. pervariensis*. Calcium plays a critical role in muscle and nerve function, hemostasis, and intracellular signaling (Duyff, 2006). Given its importance for bone health, this plant may help reduce the risk of osteoporosis. Potassium, essential for lowering hypertension and regulating heart rhythm, suggests potential cardiovascular benefits (Ekinci et al., 2004). Sodium is vital for energy production and intercellular transport, but excessive intake increases the risk of hypertension and cardiovascular disease. Therefore, controlled consumption of *A. pervariensis* is advisable.

Iron (Fe) deficiency, a global health issue, leads to anemia (Vandecasteele and Block, 1997). The low iron level in *A. pervariensis* (0.1158±0.087 ppm) suggests it is not a significant iron source. However, the presences of other essential trace elements, such as copper (Cu), enhances its nutritional value. Copper is crucial for human health, and its deficiency can cause various disorders (Yaşar et al., 2016).

Selenium (Se) was detected at low levels, indicating safe consumption without an increased risk of cardiomyopathy (Vandecasteele and Block, 1997). However, given selenium's role in cardiovascular health, further research is needed. Similarly, the low cobalt (Co) levels suggest limited health effects. While cobalt is essential in small amounts, excessive intake can be toxic,

underscoring the importance of evaluating *A. pervariensis*'s trace element content.

Allium species have been historically used to treat various diseases. The Ebers Papyrus from ancient Egypt mentions their benefits for heart conditions, tumors, and infections (Rahman, 2001). Modern studies confirm that *Allium sativum* (garlic) lowers blood pressure, enhances fibrinolysis, and inhibits platelet aggregation. Given these findings, *A. pervariensis* may exhibit similar pharmacological effects. The anti-atherosclerotic properties of *A. sativum* suggest not only disease prevention but also therapeutic potential (Koscielny et al., 1999). Additionally, *Allium* species possess antidiabetic, antibiotic, hypocholesterolemic, and antimicrobial properties (Augusti, 1996), which may extend to *A. pervariensis*.

Despite the significance of these findings, some limitations should be noted. First, mineral analysis was conducted solely using ICP-OES, preventing comparison with other techniques. Second, samples were collected from a single geographic location, limiting the generalizability of the results. Environmental factors such as soil composition and climate variations can influence mineral content, necessitating broader studies across different regions and seasons.

Furthermore, the bioavailability of *A. pervariensis*—the extent to which its minerals can be absorbed and utilized by the human body—remains unexplored. Investigating bioavailability could clarify its nutritional and pharmacological value. Future studies should assess its mineral composition in diverse populations and conditions, along with toxicological and pharmacokinetic evaluations. Such research could uncover the full potential of *A. pervariensis* in both traditional and modern medicine.

Table 3. Elemental analysis results of *A. pervariensis* plant

Element	Value (X±SD) ppm
Silver (Ag)	0.0297±0.016
Arsenic (As)	0.0106±0.012
Calcium (Ca)	6.2278±0.547
Cobalt (Co)	0.0035±0.011
Chromium (Cr)	0.0111±0.011
Copper (Cu)	0.0157±0.012
Iron (Fe)	0.1158±0.087
Potassium (K)	5.5283±0.482
Manganese (Mn)	0.0155±0.016
Sodium (Na)	1.0325±0.061
Nickel (Ni)	0.0078±0.012
Selenium (Se)	0.0121±0.013
Silicon (Si)	0.2126±0.054
Strontium (Sr)	0.0304±0.014
Vanadium (V)	0.0079±0.014

X= mean, SD= standart devition

4. Conclusion

The ICP-OES analysis results indicate that *A. pervariensis* is nutritionally rich, with the highest concentrations of calcium (Ca) and potassium (K), measured at 6.2278±0.547 ppm and 5.5283±0.482 ppm, respectively. Sodium (Na) was also detected at 1.0325±0.061 ppm, along with other elements such as silver (Ag), arsenic (As), cobalt (Co), chromium (Cr), copper (Cu), iron (Fe), manganese (Mn), nickel (Ni), selenium (Se), silicon (Si), strontium (Sr), and vanadium (V). These findings suggest that *A. pervariensis* may have nutritional and potential health benefits. However, as the study is limited to samples from a specific geographical region, caution is needed when generalizing the results. Further comprehensive biochemical, toxicological, and clinical studies involving samples from different regions are necessary to better understand the nutritional and medicinal potential of *A. pervariensis*.

Author Contributions

The percentages of the author' contributions are presented below. The author reviewed and approved the final version of the manuscript.

	İ.Y.
C	100
D	100
S	100
DCP	100
DAI	100
L	100
W	100
CR	100
SR	100
PM	100
FA	100

C=Concept, D= design, S= supervision, DCP= data collection and/or processing, DAI= data analysis and/or interpretation, L= literature search, W= writing, CR= critical review, SR= submission and revision, PM= project management, FA= funding acquisition.

Conflict of Interest

The author declared that there is no conflict of interest.

Ethical Consideration

Ethics committee approval was not required for this study because of there was no study on animals or humans.

Acknowledgments

I would like to thank Mr. Mustafa Yavuz for his contributions and support during the plant identification and collection process.

References

Altunkanat H, Tasan M. 2023. Farklı kurutma ön işlemleri ve yöntemlerinin pirasanin (*Allium porrum* L.) fizikokimyasal ve duyusal özellikleri üzerine etkisi. Bahçe, 52(1): 45–56. https://doi.org/10.53471/bahce.1140541

Augusti KT. 1996. Therapeutic values of onion (*Allium cepa* L.) and garlic (*Allium sativum* L.). Indian J Exp Bio, 34(7): 634–640.

Baytak S. 2003. Mn (II), Co (II), Fe (III), Cr (III) iyonlarının mikroorganizma tutturulmuş amberlite XAD-4 kullanılarak katı faz özütleme tekniği ile zenginleştirme şartlarının araştırılması ve atomik absorpsiyon spektrometrisi ile tayini. PhD thesis, Gazi University, Institute of Science, Ankara, Türkiye, pp: 1-163

Diğdem T, Arslan Y. 2019. İndüktif Eşleşmiş Plazma Optik Emisyon Spektroskopisi (ICPOES) ile siyah çikolata içindeki bazı elementlerin tayini. Mehmet Akif Ersoy Üniv Fen Bil Ens Derg, 7(Özel (Special) 1): 44–50.

Donati GL, Amais RS, Williams CB. 2017. Recent advances in inductively coupled plasma optical emission spectrometry. J Anal At Spectrom, 32(7): 1283–1296.

Duyff RL. 2006. American dietetic association complete food and nutrition guide. John Wiley & Sons Hoboken, New Jersey, USA, pp: 456.

Ekinci N, Ekinci R, Polat R, Budak G. 2004. Analysis of trace elements in medicinal plants with energy dispersive X-ray fluorescence. J Radioanal Nucl Chem, 260(1): 127–131. https://doi.org/10.1023/B:JRNC.0000027071.72742.ee

Fırat M, Koyuncu M, Ekşi G. 2018. Allium pervariensis, sect. Allium (Amaryllidaceae), a new species from Siirt Türkiye. Plant Biosys - An Int J Deal All Aspects Plant Biol, 152(3): 305–310. https://doi.org/10.1080/11263504.2016.1271051

Gürel İ. 2014. İlaçlara ve bitkisel ürünlere bilinçli yaklaşım. TÜBİTAK Pop Bil Kit, pp: 14–17.

Khan KY, Khan MA, Niamat R, Munir M, Fazal H, Mazari P, Ahmed SN. 2011. Element content analysis of plants of genus Ficus using atomic absorption spectrometer. African J Pharm Pharm, 5(3): 317–321.

Koscielny J, Klüssendorf D, Latza R, Schmitt R, Radtke H, Siegel G., Kiesewetter H. 1999. The antiatherosclerotic effect of *Allium sativum*. Atherosclerosis, 144(1): 237–249.

Narin İ. 2002. Bazı eser metal iyonlarının atomik absorpsiyon spektrometrik tayinleri öncesi katı faz ekstraksiyonları. Master's thesis, Niğde University, Institute of Science, Niğde, Türkiye, pp: 1-158

Rahman K. 2001. Historical perspective on garlic and cardiovascular disease. J Nutr, 131(3): 977S-979S. https://doi.org/10.1093/jn/131.3.977S

Rice-Evans C, Miller N, Paganga G. 1997. Antioxidant properties of phenolic compounds. Trends Plant Sci, 2(4): 152–159.

Saraçoğlu HT. 2024. Farklı çözücülerle hazirlanan *Elettaria Cardamomum* (L.) maton ekstraktlarinin antibakteriyel aktivitelerinin incelenmesi. Black Sea J Eng Sci, 7(4): 635–640. https://doi.org/10.34248/bsengineering.1473309

Soetan KO, Olaiya CO, Oyewole OE. 2010. The importance of mineral elements for humans, domestic animals and plants: A review. African J Food Sci, 4(5): 200–222.

Uslu ME. 2024. Investigation of the effects of extraction polarity change on the bioactivity of Eruca vesicaria. Black Sea J Eng Sci, 7(6): 1287–1293. https://doi.org/10.34248/bsengineering.1550408

Vandecasteele C, Block CB. 1997. Modern methods for trace element determination. John Wiley & Sons. New York, USA, pp: 265.

Yaşar S, Üstek MA, Bengü AŞ, Leyla M. 2016. Mardin bölgesi içme sularında ağır metal düzeylerinin araştırılması. Cumhuriyet Üniv Sağlık Bilim Ens Derg, 1(2): 63–71.

Yolbaş İ. 2024a. Bellevalia pseudolongipes Plant: Comprehensive analysis of the elemental composition and total phenolic and flavonoid contents. Black Sea J Eng Sci: 7(6), 13–14. https://doi.org/10.34248/bsengineering.1525176

Yolbaş İ. 2024b. Elemental analysis and determination of total phenolic and flavonoid content of rheum ribes l. Bark. Int J Innovative Eng Appl, 8(1): 17–21. https://doi.org/10.46460/ijiea.1390339

Yolbaş İ. 2024c. Phenolic compound content and antioxidant activity of Rheum ribes Shells. J Chem, 2024(1): 1–8. https://doi.org/10.1155/2024/9151180

Yolbaş İ. 2024d. Phytochemical profiling and antioxidant activity assessment of Bellevalia pseudolongipes via liquid chromatography-high-resolution mass spectrometry. PeerJ, 12: e18046. https://doi.org/10.7717/peerj.18046

Black Sea Journal of Engineering and Science
doi: 10.34248/bsengineering.1608596

Open Access Journal
e-ISSN: 2619 – 8991

Research Article
Volume 8 - Issue 2: 466-472 / March 2025

ANALYSIS OF COMPRESSIVE STRENGTH OF STANDARD POURED MICROSILICA ADDED REACTIVE POWDER CONCRETE

Yakup Murat ÇEBİ[1]* Arif Emre SAĞSÖZ[2]

[1]*Bitlis Eren University, Vocational School of Tatvan, 13200, Tatvan, Bitlis, Türkiye*
[2]*Ataturk University, Vocational School of Pasinler, 25240, Erzurum, Türkiye*

Abstract: Reactive powder concretes (RPC) are new-generation concretes with superior properties that have been continuously developed since 1995. They are the most important concretes that are candidates to be the concrete of the future. In this study, reactive powder concretes were produced by using silica fume and micro silica instead of cement. 5x5x5 cm cube samples were used as samples, and these samples were produced in steel molds. Silica fume was used at 20%, 25%, and 30% rates. Microsilica was used instead of cement at 5%, 10%, and 15% rates. These produced samples were cured under autoclave conditions at 160^{0}C 10 Atm for 4 hours, 175^{0}C 15 Atm for 4 hours, 160^{0}C 10 Atm for 8 hours, and 175^{0}C 15 Atm for 8 hours. The cured samples were broken in an automatically controlled test press loaded at 90 kg/s, and the compressive strengths of these samples were measured. According to the compressive strength results, an increase in compressive strength was detected when the proportions of silica fume samples were increased from 20% to 25%. When the silica fume samples were increased from 25% to 30%, a minimal decrease in compressive strength occurred. When the compressive strengths of microsilica samples were increased from 5% to 10% and 15%, a decrease in compressive strength was observed. As a result, the compressive strengths of microsilica samples were generally found to be higher than those of silica fume samples.

Keywords: Reactive concretes, Silica fume, Micro silica, Compressive strength
***Corresponding author:** Bitlis Eren University, Vocational School of Tatvan, 13200, Tatvan, Bitlis, Türkiye
E mail: ymcebi@beu.edu.tr (Y. M. ÇEBİ)
Yakup Murat ÇEBİ https://orcid.org/0000-0002-7033-751X
Arif Emre SAĞSÖZ https://orcid.org/0000-0002-2388-1280

Received: December 27, 2024
Accepted: February 02, 2025
Published: March 15, 2025

Cite as: Çebi YM, Sağgöz AE. 2025. Analysis of compressive strength of standard poured microsilica added reactive powder concrete. BSJ Eng Sci, 8(2): 466-472.

1. Introduction

RPCs are ultra-high-strength cement-based composites with superior mechanical and physical properties, excellent ductility, and very low permeability (Walraven, 1999; Alaee, 2020; Bajpai et al., 2020). These materials were first developed in the early 1990s by researchers at the Bouygues laboratories in Paris. Reactive powder concretes represent a new generation of concretes with compressive strengths ranging between 200 and 960 MPa, tensile strengths between 25 and 150 MPa, fracture energies of approximately 30000 J/m^2, and unit weights ranging between 2500 and 3000 kg/m^2 (Bayrak, 2024). The internal structure of reactive powder concrete has a tighter grain arrangement, and its microstructure is strengthened by the presence of the strongest cementitious hydrated products compared to high-performance concretes. This remarkable performance is achieved through the following stages:

1. Fine adjustment of the distribution of all grains in the mixture to reach the optimum density matrix,
2. Reduction of the largest size of the aggregate grains for homogeneity of the concrete,
3. Reduction of the water content in the concrete,
4. Effective use of the pozzolanic properties of high-fineness silica fume,
5. Optimum composition of all components,
6. Use of short-cut steel wires for ductility,
7. Hardening under pressure and elevated temperature conditions to reach very high strengths permeability (Walraven, 1999; Richard Cheyrezy, 1994).

RPC owes its superior mechanical and durability properties to its tight microstructure. In order to achieve this tight microstructure, many measures are taken during its production, unlike traditional concrete, and a different design approach is adopted. These can be listed as follows:

1. The maximum aggregate diameter is kept at very small levels (Generally<1 mm) to increase the homogeneity in the matrix.
2. The amount of material to be used for the matrix to reach optimum density should be investigated experimentally, and the aggregate grain distribution should be adjusted appropriately.
3. The water/binder ratio is generally kept between 0.10 and 0.22.

This work is licensed (CC BY-NC 4.0) under Creative Commons Attribution 4.0 International License

4. Hyperplasticizer additives are used in high dosages.
5. Mixers that can mix at high speeds are preferred in its preparation.
6. An effective vibration should be used.
7. Ductility is increased with short-cut wires (mostly steel).
8. Mechanical properties are improved with high-fineness silica fume additive. In addition, mineral additives with high pozzolanic activity are used to reduce cement dosage.
9. In order to increase mechanical performance, in addition to water curing, steam curing and autoclave curing (steam curing under pressure) applications are performed.
10. In addition, if it is kept under pressure in the mold during the production phase, mechanical properties can be increased even more.

Basically, with the production of new generation strong plasticizers, the production of cementitious composites with such low water/cement ratios has become possible. In addition, thanks to the developing microscope and microstructure research technologies, designs are supported by microstructure examinations. In this way, it has become possible to produce strong composites such as RPC with considerably reduced defects (Yazıcı and Yalçınkaya, 2011; Jalal et al., 2012; Ghafari et al., 2014).

When the durability properties of RPCs are examined according to the studies in the literature, it is seen that they are incomparably high with normal concretes. The application of compression pressure increases the unit volume weight of RPC. The increase in unit volume weight means the decrease of the voids in the concrete. For this reason, the already high durability properties will increase even more with the application of compression pressure. For this reason, it can be used in facilities where industrial and nuclear wastes are stored where high durability properties are needed. With the application of compression pressure, thin-walled elements can be produced, as well as the thickness of the existing produced elements or the amount of fiber used in them, which constitutes the biggest cost, can be reduced (İpek and Yılmaz, 2009).

2. Materials and Methods

2.1. Materials

The construction sector is undergoing a major transformation today, where technology is rapidly developing. The transition from traditional methods to innovative and sustainable solutions is reshaping the dynamics of the sector (Cakir and Sofyanli, 2015; Carrasco Vasques and Fernandez Herrera, 2019; Cengiz, 2023a; Cengiz, 2023b). Environmentally friendly and sustainable construction solutions are becoming increasingly important in the sector. Applications such as the use of recyclable materials, high-energy-efficient buildings, and green roof systems aim to minimise environmental impacts (Chithra et al., 2016; Cengiz and Cengiz, 2018; Onur and Efe, 2020; Özer et al., 2021; Cengiz, 2024). In fact, many statistical models are applied to determine the ratio of these materials, aiming to reach the optimum solution (Cengiz and Karakaş, 2015; Cengiz and Aydoğdu, 2015; Cengiz, 2019). In this context, efficiency-based studies continue in today's world.

The materials used in this experimental study, which will serve the purpose of sustainability, are as follows:

a. Crushed Quartz Sand

The crushed quartz sand used in the experimental study is 600–150 μm in size and was supplied by Ankara Sika. Crushed quartz sand is seen in Figure 1.



Figure 1. Crushed quartz sand.

b. Quartz Powder

The quartz powder used in the study is 4 μm in size. Quartz Powder is seen in Figure 2.



Figure 2. Quartz powder.

c. Silica Fume

The silica fume used in the study is 0.1 μm in size. Silica fume at 0.1 μm scale is seen in Figure 3.



Figure 3. Silica fume at 0.1 µm scale.

d. Micro Silica
The microsilica used in the experiments is 0.05 µm in size. Microsilica at a 0.05 µm scale is seen in Figure 4.



Figure 4. Microsilica at a 0.05 µm scale.

e. Hiper Liquefier
The hyperliquefier used is polymer-based. The hyperliquefier used is shown in Figure 5.



Figure 5. The hyperliquefier used.

f. Cement
The cement used is CEM 1 42.5R.

2.2. Tools

The tools used in this experimental study are as follows:
a. Concrete Sample Molds
The concrete sample moulds used in the experiments are made of steel and have dimensions of 5x5x5 cm. The concrete sample moulds are shown in Figure 6.



Figure 6. Concrete sample molds.

b. High-Capacity Concrete Mixer
The high-capacity concrete mixer used to mix the concrete samples is shown in Figure 7.



Figure 7. High-capacity concrete mixer.

c. Autoclave
An autoclave was used to cure the test samples. The samples were cured under the curing conditions of 160 °C at 10 Atm pressure for 4 hours, 175 °C at 15 Atm pressure for 4 hours, 160 °C at 10 Atm pressure for 8 hours, and 175 °C at 15 Atm pressure for 8 hours. The autoclave used in the experiments is shown in Figure 8.



Figure 8. Autoclave.

d. Concrete Press
A concrete press with a crushing capacity of 300 tonnes and a loading of 90 kg/s was used to measure the compressive strength of the test samples. The concrete press is shown in Figure 9.



Figure 9. Concrete press.

2.3. Method

2.3.1. General mixing ratios of RPCs

According to the research conducted within the scope of this study, no local or foreign standards were

encountered for the mixture design of RPCs. Different mixing theories were used to proportion the granular materials forming the mixture to form a tight structure. These theories were derived from Mooney's suspension viscosity model reduced (Larrard and Sedran, 1994; İpek, 2009). Mixing ratios of reactive powder concretes are made according to the absolute weight method.

When the case of only no steel fibre in the mixture (fibreless-powdered) was examined, the mixing ratios given in 1 unit were taken into consideration, and the relationship between the total mixture weight and the amount of cement was converted into a formula as follows in order to facilitate the calculations (equation 1).

1 m³ RPC Mix Weight(kg)=2.909x1 m³ RPC Cement (1)

Amount (kg) If the 1 m³ RPC200 mix weight is 2388 kg, the amount of cement to be used in this mix will be approximately 821 kg as a result of the 2388/2.909 ratio from the formula above. After the amount of cement is found to be 821 kg, the amounts of other materials to be used in the mix are determined according to the following mix ratios. Considering the mix ratios given in 1 unit, in the production of RPC200 without steel fiber, silica fume is prepared as 23% by weight of the cement amount, sand content is 110% by weight of the cement amount, powder content is 39% by weight of the cement amount, hyper plasticizer is 1.9% by weight of the cement amount, mixing water is 17% by weight of the cement amount and the mix is created. Other mix materials and mix ratios according to the amount of 821 kg of cement to be used in 1 m³ mix are shown in Table 1. Table 1 shows the mixing ratios of RPC200 without steel fiber and powdered.

Table 1. Mixing ratios of RPC200 without steel fiber and powd

Materials	Calculation Method	MQFRC (kg/m³)
Cement	2388/2.909	821
Silica Rime	821x023	189
Sand (600-150 pm)	821x1.10	903
Powder (4 urn)	821x0.9	320
Hyper fluidizer/pListkizer	821x0.019	15.5
Steel fibers (L=12 mm)	•	-
Water	821x0.17	1395
Total		2388

MQFRC= material quantity found as a result of calculation

2.3.2. Mixing Ratios of RPCs in the Experimental Study

When the water/binder ratio was taken as 0.17 according to Table 1 in the RPC castings, it was observed that the cement did not show sufficient binding properties. In addition, taking the water/cement ratio instead of the water/binder ratio according to this table caused insufficient water in the castings. In addition, taking the amount of hyperplasticizer according to the water/cement ratio instead of the water/binder ratio and the insufficient percentage of hyperplasticizer caused the cement not to show sufficient binding properties. For this reason, in the experiments, the water/binder ratio was taken, and this value was brought to 0.19, and the samples were poured. In addition, the amount of hyperplasticizer was taken as 0.03 of the water/binder ratio. 5x5x5 cm cube samples were produced in the study. In this experimental study, RPCs were cast in 3 groups as silica fume at 20%, 25%, and 30% ratios, and each group was cured under autoclave conditions of 160 °C 10 Atm for 4 hours, 175 °C 15 Atm for 4 hours, 160 °C 10 Atm for 8 hours, and 175 °C 15 Atm for 8 hours. A total of 3x12=36 silica fume samples were produced, 3 for each cure condition of each group. The microsilica samples produced by using it instead of cement were cast in 3 groups of 5%, 10%, and 15%, and each group was cured in autoclave conditions of 160 °C (10 °A) for 4 hours, 175 °C (15 °A) for 4 hours, 160 °C (10 °A) for 8 hours, and 175 °C (15 °A) for 8 hours. A total of 3x12=36 microsilica samples were produced, 3 for each cure condition of each group. In general, 36+36=72 samples were produced. Table 2 shows the material amounts found as a result of the calculation for 20%, 25%, and 30% RPC. Table 3 shows the mixing ratios of 5%, 10%, and 15% Microsilica RPCs.

Table 2. The material amounts found as a result of the calculation for 20%, 25%, and 30% RPC

Materials	MQFRC (kg/m³)		
	20% silica fume	25% silica fume	30% silica fume
Cement	821	821	821
Silica Fume	164	205	246,5
Sand (600-150 µm)	903	903	903
Powder (4 µm)	345	304	262.5
Hyper fluidizer/plasticizer	30	31	32
Steel Fibers (L=12 mm)	-	-	-
Water	187	195	203
Total	2450	2459	2468

MQFRC= material quantity found as a result of calculation

Table 3. The mixing ratios of 5%, 10%, and 15% Microsilica RPCs

Materials	MQFRC (kg/m3)		
	5% Microsilica	10% Microsilica	15% Microsilica
Cement	780	739	698
Microsilica (0.05 µm)	41	82	123
Silica Fume	189	189	189
Sand (600-150 µm)	903	903	903
Powder (4 µm)	320	320	320
Hyper fluidizer/plasticizer	30	30	30
Steel Fibers (L=12 mm)	-	-	-
Water	192	192	192
Total	2455	2455	2455

MQFRC= material quantity found as a result of calculation

2.3.3. Production Method of RPCs in the Experimental Study

The RPCs in the experimental study were poured as follows:

- First, cement and silica fume were poured into the concrete container and mixed with a high-capacity concrete mixer for 1 minute at 1st speed.
- Then, hyper-fluidiser water was poured onto the mixture while the mixture was being mixed at 1st speed for 1 minute.
- This mixture was mixed at first speed for 1 minute.
- Then, the mixture was mixed at 2nd speed for 1 minute.
- Then, the mixture was mixed at 3rd speed for 1 minute.
- Then, half of the quartz sand and powder were poured onto the mixture and mixed at first speed for 1 minute.
- Then, the other half of the quartz sand and powder were poured onto the mixture and mixed at first speed for 1 minute.
- After this, the resulting mixture was mixed for 5 minutes in the 2nd cycle, and RPC was produced.
- The produced RPCs were placed in 5x5x5 cm steel moulds in 2 passes. Each pass was skewered 35 times with Φ6 iron.
- Then the surfaces of the RPCs were smoothed with light water.
- Finally, a well-wetted cloth was covered on the RPCs.

The production of silica fume RPCs takes 12 minutes. The 8th stage in the production of microsilica RPCs takes 7 minutes. The total production time is 14 minutes. The 2nd stage in the production of nanosilica RPCs is organised as follows: Less than half of the water and hyperfluidizer were collected in one container and mixed. The other part of the water, hyperfluidizer, and nanosilica were collected in another container and mixed to form a suspension. First, hyperliquefied water was added to the mixture for 1 minute, then the suspension was added to the mixture for 1 minute. The total production time is 13 minutes.

In addition, after the autoclave curing process applied to the samples produced in this experimental study, the samples to be broken in the concrete press after leaving the autoclave are shown in Figure 10, and the samples broken in the concrete press are shown in Figures 11 and 12.



Figure 10. Samples to be broken in the concrete press after leaving the autoclave.



Figure 11. Sample broken in the concrete press.

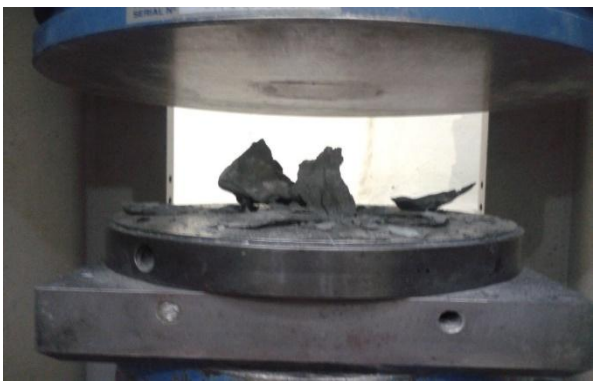


Figure 12. Sample broken in the concrete press.

3. Results

The average strengths of 3 samples in each cure condition of each group of silica fume samples are shown in Table 4, and the average strengths of 3 samples in each cure condition of each group of microsilica samples are shown in Table 5.

Table 4. Average strengths of silica fume samples

25% Silica Fume			
4 Hours		8 Hours	
160 °C	175 °C	160 °C	175 °C
10 Atm	15 Atm	10 Atm	15 Atm
150.5 MPa	152.6 MPa	189.1 MPa	210.5 MPa
25% Silica Fume			
4 Hours		8 Hours	
160 °C	175 °C	160 °C	175 °C
10 Atm	15 Atm	10 Atm	15 Atm
194.4 Mpa	200.5 MPa	203.2 MPa	223.4 MPa
30% Silica Fume			
4 Hours		8 Hours	
160 °C	175 °C	160 °C	175 °C
10 Atm	15 Atm	10 Atm	15 Atm
172.3 MPa	181.1 MPa	200.8 MPa	214.1 MPa

Table 5. Average strengths of micro silica samples

5% Silica Fume			
4 Hours		8 Hours	
160 °C	175 °C	160 °C	175 °C
10 Atm	15 Atm	10 Atm	15 Atm
202.8 MPa	206.8 MPa	205.9 MPa	224 MPa
10% Silica Fume			
4 Hours		8 Hours	
160 °C	175 °C	160 °C	175 °C
10 Atm	15 At tn	10 Atm	IS Atm
195.7 MPa	204.9 MPa	207.2 MPa	211.3 MPa
15% Silica Fume			
4 Hours		8 Hours	
160 °C	175 °C	160 °C	175 °C
10 Atm	15 Atm	10 Atm	15 Atm
186 MPa	186.6 MPa	196.3 MPa	204.2 MPa

The average strengths of the silica fume samples in Table 5 are shown in Figure 10, and the average strengths of the microsilica samples in Table 6 are shown in Figure 11.

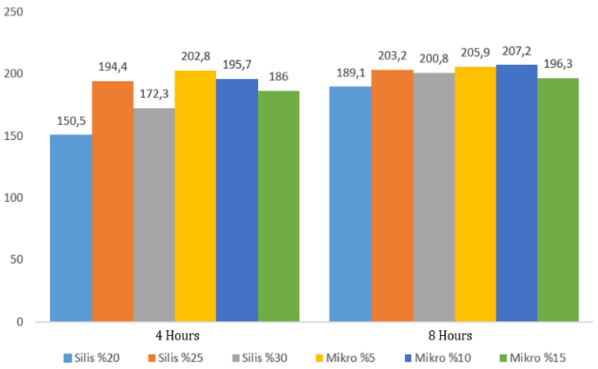


Figure 10. Compressive strength of samples applied with autoclave at 160˚C 10 Atm.

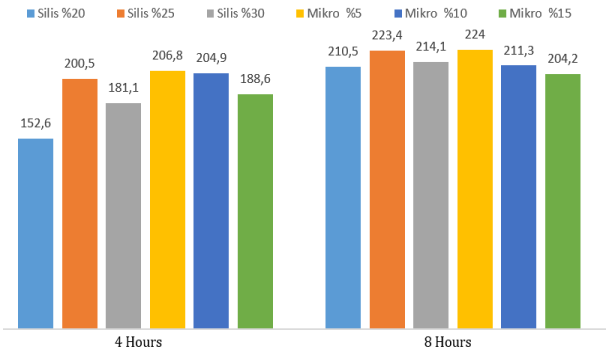


Figure 11. Compressive strength of samples applied with autoclave at 175˚C 15 Atm.

4. Discussion and Conclusions

In each curing condition, when the microsilica samples were increased from 5% to 10%, a slight decrease in the compressive strength of the samples was observed. When the ratio was increased from 10% to 15% in the microsilica samples, a greater decrease in the compressive strength of the microsilica samples was observed. In other words, a decreasing tendency is observed in the strength. It is thought that the reason for this is that since the specific surface of microsilica is higher than that of silica fume, it does not contribute to the strength by agglomeration after 5% and even causes a decrease.

In addition, it is seen that the curing time is more effective in increasing the strength of all samples according to the curing temperature.

Finally, the compressive strengths of the microsilica samples were generally higher than those of the silica fume samples.

Author Contributions

The percentages of the authors' contributions are presented below. All authors reviewed and approved the final version of the manuscript.

	Y.M.Ç.	A.E.S.
C	50	50
D	50	50
S	50	50
DCP	50	50

DAI	50	50
L	50	50
W	50	50
CR	50	50
SR	50	50
PM	50	50
FA	50	50

C=Concept, D= design, S= supervision, DCP= data collection and/or processing, DAI= data analysis and/or interpretation, L= literature search, W= writing, CR= critical review, SR= submission and revision, PM= project management, FA= funding acquisition.

Conflict of Interest

The authors declared that there is no conflict of interest.

Ethical Consideration

Ethics committee approval was not required for this study because of there was no study on animals or humans.

References

Alaee FJ. 2020. Retrofitting of concrete structures using high performance fiber reinforced cementitious composite. PhD Thesis, University of Wales, Cardiff, UK, pp: 220.

Bajpai R, Choudhary K, Srivastava A, Sangwan KS, Singh M, 2020. Environmental impact assessment of fly ash and silica fume based geopolymer concrete. J Clean Prod, 254: 120-147.

Bayrak B. 2024. Trio/hybrid fiber effect on the geopolymer reinforced concrete for flexural and shear behavior. Struct Concrete, 1(1): 1-28.

Cakir Ö, Sofyanli ÖÖ. 2015. Influence of silica fume on mechanical and physical properties of recycled aggregate concrete. HBRC J. 11(2): 157-166.

Carrasco Vasques DJ, Fernandez Herrera LH. 2019. Influencia del Nano-sílice en las propiedades de un concreto de F'c= 350 kg/cm² para obtener un concreto de alta resistencia. Universidad Cesar Valejo. URL: https://hdl.handle.net/20.500.12692/52543 (accessed date: October 12, 2024).

Cengiz C. 2024. The Relationship between electricity consumption from outdoor lighting and economic growth. Light Eng, 32(4): 14-21

Cengiz Ç, Aydoğdu H. 2015. Gamma Renewal functions ın censored data. Bitlis Eren Univ J Sci Technol, 5(2): 97-101.

Cengiz Ç, Metin Karakaş A. 2015. Estimation of weibull renewal function for censored data. Int J Sci Tech Res, 1: 123-132.

Cengiz Ç. 2019. Nonparametric estimation of a renewal function in the case of censored sample. Bitlis Eren Univ J Sci Technol, 9(2): 54-57.

Cengiz MS, Cengiz C. 2018. Numerical analysis of tunnel lighting maintenance factor. Int Isl U Malay. IIUM Engin J, 19(2): 154-163.

Cengiz MS. 2023a. Daylight analysis in terms of building direction and one-way roof. BSJ Eng Sci, 6(4): 535-539.

Cengiz MS. 2023b. The angular use of light in architecture and the concept of space. BSJ Eng Sci, 6(4): 469-476.

Chithra S, Senthil Kumar SRR, Chinnaraju K. 2016. The effect of colloidal nano-silica on workability, mechanical and durability properties of high performance concrete with copper slag as partial fine aggregate. Constr Build Mater, 113: 794-804.

Ghafari E, Costa H, Júlio E, Portugal A, Durães L. 2014. The effect of nanosilica addition on flowability, strength and transport properties ultra high performance concrete. Mater Des, 59: 1-9.

İpek M, Yılmaz K. 2009. Sıkıştırma basıncının reaktif pudra betonunun eğilme dayanımına etkisi. 5. Uluslararası İleri Teknolojiler Sempozyumu, May 13-15, Karabük, Türkiye.

İpek M. 2009. Reaktif pudra betonların mekanik davranışına katılaşma süresince uygulanan sıkıştırma basıncının etkileri. PhD Thesis, Sakarya University, Institute of Science, Sakarya, Türkiye, pp: 182.

Jalal M, Mansouri E, Sharifipour M, Pouladkhan AR. 2012. Mechanical, rheological, durability and microstructural properties of high performance self-compacting concrete containing SiO_2micro and nanoparticles. Mater Des, 34: 389-400.

Larrard F, Sedran T. 1994. Optimization of ultra-high-performance concrete by the use of a packing model. Cement Concrete Res, 24(6): 997-1009.

Onur S, Efe SB. 2020. Elektrikli bisikletle paylaşımlı hareketlilik: Balıkesir Üniversitesi Kampüsü örneği. Akıllı Ulaş Sist Uyg Derg, 3(2): 216-226.

Özer I, Efe SB, Özbay H. 2021. CNN/Bi-LSTM-based deep learning algorithm forclassification of power quality disturbances by using spectrogram images. Int Trans Electr Energ Syst, 31(12): 1-16.

Richard P, Cheyrezy MH. 1994. Reactive powder concretes with high ductility and 200-800 MPa compressive strength. Bouygues Int Rep, Paris, France, pp: 15.

Walraven J. 1999. Structural concrete. J Fib, 1(1): 3-11.

Yazıcı H, Yalçınkaya Ç. 2011. Yeni nesil yüksek performanslı beton: Reaktif pudra betonu. İMO İzmir Şubesi Bülten, 2011: 26-29.

Black Sea Journal of Engineering and Science
doi: 10.34248/bsengineering.1610101

Open Access Journal
e-ISSN: 2619 – 8991

Research Article
Volume 8 - Issue 2: 473-479 / March 2025

OPTIMIZING MICROWAVE DRYING OF BLACK CARROT PRETREATED WITH OSMOTIC DEHYDRATION: TAGUCHI-BASED DESIRABILITY FUNCTION APPROACH

Mehmet GÜLDANE[1]*

[1]*Sakarya University of Applied Sciences, Pamukova Vocational School, Program of Laboratory Technology, 54050, Sakarya, Türkiye*

Abstract: This study aimed to optimize the microwave drying process of black carrot pretreated with ultrasound-assisted osmotic dehydration (UAOD). The effect of salt concentration (2-10%), sonication time (5-15 min), and microwave power (300-600 W) on total phenolic matter (TFM) and drying time was monitored. Single response optimization was performed using the Taguchi method (TM), while the desirability function approach (DFA) was used to optimize multiple responses. The analyses were conducted using Taguchi L_9 orthogonal design. Single response optimization results showed that TFM content was changed between 11.59 and 18.57 mg GAE/g sample dry matter, while the drying time ranged from 8 to 20 min. In multiple response optimization, the DFA with a composite desirability (CD) value of 0.973 demonstrated that the optimal conditions for both maximizing TPC and minimizing drying time were obtained with 10% salt concentration, 15 min sonication, and 600 W microwave power. ANOVA results revealed that microwave power contributed the highest to both responses, followed by salt concentration and sonication time, respectively. However, microwave power and salt concentration had a substantial impact on the CD. Overall results showed that the Taguchi-based DFA was successfully applied to optimize the microwave drying process of black carrots pretreated with UAOD, maximizing the phenolic compound content and minimizing the drying time.

Keywords: Microwave drying, Osmotic dehydration, Sonication, Black carrot, Optimization

***Corresponding author:** Sakarya University of Applied Sciences, Pamukova Vocational School, Program of Laboratory Technology, 54050, Sakarya, Türkiye
E-mail: mehmetguldane@subu.edu.tr (M. GÜLDANE)
Mehmet GÜLDANE https://orcid.org/0000-0001-7321-0496

Received: December 30, 2024
Accepted: February 02, 2025
Published: March 15, 2025

Cite as: Güldane M. 2025. Optimizing microwave drying of black carrot pretreated with osmotic dehydration: Taguchi-based desirability function approach. BSJ Eng Sci, 8(2): 473-479.

1. Introduction

The black carrot (*Daucus carota subsp. sativus var.*) is characterized by its dark purple color, attributable to anthocyanins—water-soluble plant pigments with antioxidant and anti-inflammatory properties. In addition to anthocyanins, black carrots contain a variety of phytonutrients, including carotenoids, flavonoids, and phenolic acids, which have been associated with a range of health benefits (Ayar-Sumer et al., 2024). All these compounds contribute to reducing the risk factors associated with chronic diseases. While carrots are primarily consumed in their fresh form, their extracts are extensively utilized in various food products such as juices, soft drinks, baked goods, confectionery, ice cream, and as natural colorants. In Türkiye, the black carrot has a cultural significance, particularly in producing "shalgam," a traditional fermented beverage (Keskin et al., 2021).

Drying, one of the oldest and most significant preservation methods, plays a crucial role in enhancing storage capacity while preserving the physical and nutritional quality of agricultural products (Kaveh et al., 2021). Hot air drying, a widely employed technique, relies on the concurrent application of heat and mass transfer to facilitate the removal of moisture from fruits and vegetables. However, this conventional technique has several disadvantages, including alterations to physical properties such as texture, color, nutritional value, and shape. Furthermore, it is a time-consuming and energy-intensive process. Consequently, there is an increasing demand for developing novel drying methods that can address these limitations, while offering the advantages of reduced energy consumption and accelerate drying times. Microwave drying has emerged as a promising alternative, offering several advantages over traditional methods. These include enhanced drying efficiency, reduced energy consumption, and decreased drying time. However, it is important to note that microwave drying can result in non-uniform drying, leading to uneven heat distribution within the product. This, in turn, can compromise the quality of the final product. To address these concerns, the employment of non-conventional techniques, including pretreatment methods prior to drying, emerges as a pivotal strategy to enhance the quality of the final product. Pretreatment application can enhance material porosity, thereby facilitating mass transfer, reducing drying time, and minimizing undesired alterations during the drying process. Ultrasound-assisted osmotic dehydration

This work is licensed (CC BY-NC 4.0) under Creative Commons Attribution 4.0 International License

(UAOD) is one such pretreatment technique that can further improve the drying process (Mohammadi et al., 2023).

Osmotic dehydration is a non-thermal, partial drying process that removes water from food by immersing it in a hypertonic solution, thereby creating a concentration gradient that drives water loss and cellular shrinkage. The UAOD enhances this process through acoustic cavitation, where rapid compression and relaxation cycles induce bubble formation and collapse, significantly increasing mass transfer rates. Recent studies have emphasized that ultrasound pretreatment both increases the drying rate and reduces the loss of bioactive components compared to conventional methods. These improvements highlight the potential of UAOD as a technique to improve both process efficiency and product quality (Memis et al., 2024).

The Taguchi method (TM) has been widely utilized in numerous studies to investigate the effects of control parameters on an output response. It provides a structured and systematic approach to optimizing manufacturing processes, ensuring efficient and effective control over process variables to enhance product quality and performance (Dang et al., 2024). The TM employs orthogonal arrays to minimize the experimental trials and reduce the costs. The data obtained from the analysis transform the signal-to-noise ratio (SNR) to optimize response variables. The TM is employed to optimize the process in studies on drying in food processing. In a recent study, Chen et al. (2023) investigated the impact of drying factors on the quality of the final product and energy consumption using the TM. The results revealed that the transition moisture content was the most influential characteristic affecting the MAFD in pineapple drying. Türkan and Etemoğlu (2020) adopted the Taguchi approach to minimize the drying time of cucumber in a convective drier. The optimal levels for air velocity, drying temperature, and sample thickness were determined as 1 m/s, 60 °C, and 5 mm, respectively. A study conducted by Mecha et al. (2024) utilized Taguchi design to optimize the responses such as drying rate, specific moisture extraction rate, color change, and rehydration ratio in the chanterelle mushroom drying process. The drying process was conducted in a heat pump drier, and the experiments were run according to the Taguchi L_9 design to optimize the mushroom shape and the drying air temperature parameters. The results indicated that the mushrooms with cubic shapes dried at 56 °C exhibited optimum characteristics. The aforementioned studies demonstrate the application of the TM in the optimization of single-response problems. On the other hand, hybrid optimization techniques are required for the optimization of multi-response problems. The desirability function approach (DFA) is an optimization method that provides optimal solutions for multi-response problems. The DFA is often integrated into response surface methodology designs to optimize multiple responses in microwave drying studies of pretreated apple slices (Taghinezhad et al., 2023), mango cubes (Shinde and Ramaswamy, 2021), and tomato slices (de Souza et al., 2023).

To the best of our knowledge, no DFA integrated with TM for the optimization of drying processes in food drying. Therefore, the objective of this study was to optimize the drying conditions for UAOD followed by microwave drying of black carrots. The Taguchi L9 experimental design was employed, and the optimization process was conducted using the Taguchi-based DFA method. The process factors were selected as salt concentration, sonication time, and microwave power, while the response variables were identified as total phenolic matter (TFM) content and drying time.

2. Materials and Methods

2.1. Material

Fresh black carrots were procured from a local supplier in Sakarya, Türkiye. After peeling, the samples were cleaned and sliced into spherical by a mechanical slicing machine. The salt and chemicals utilized in the study were of analytical purity.

2.2. Ultrasound-Assisted Osmotic Dehydration (UAOD)

Osmotic dehydration was conducted using aqueous NaCI solutions containing 20, 60, and 100 g of soluble solids per kg of solution. The solutions were prepared at room temperature by dissolving the osmotic agent in distilled water. The sample weight was 35 ± 0.2 g and kept constant throughout the process. Osmotic dehydration experiments were conducted in an ultrasonic water bath (Creworks, PS-30A, China) at a constant temperature (30±2 °C). The ultrasonic bath operated at a fixed power of 150 kW and a frequency of 40 kHz. Samples were exposed to osmotic solutions for various durations (5-15 min) under acoustic treatment.

2.3. Microwave Drying

Osmotic dehydrated samples were gently placed between filter paper for 1 min to remove surface water. Subsequently, the black carrots were placed on the tray of a domestic microwave (Samsung, Model MS23F300EES, Malaysia) and dried at power levels of 300, 450, or 600 W. The weight of the tray was noted at 30 s intervals during the drying process, which continued until the sample achieved a constant moisture content of 10%.

2.4. Analysis

2.4.1. Total phenolic matter (TFM) content

Total phenolic content in black carrot powders was analyzed by a modified assay reported by Sonmez and Sahin (2023). Briefly, 1 g of powder was mixed with 25 mL of 80% (v/v) methanol, agitated at 400 rpm for 15 min. The mixture was then centrifuged (K242R, Centurion Scientific, England) for 15 min at 5000 rpm, and the resulting supernatant was used to determine the TFM. In this method, 0.1 mL of the resulting extract was mixed with 2 mL of distilled water and 0.2 mL of Folin-Ciocalteu reagent. After 5 min, 1 mL of Na_2CO_3 solution

(20% (w/v)) was added into the test tube. The reaction was allowed to proceed for 60 min in the dark and the absorbance was read in a UV-VIS spectrophotometer (Shimadzu, UVmini-1240, Japan) at 765 nm. Various concentration of gallic acid solutions (25-100 mg/L) was used to obtain a calibration curve. The results were calculated as mg gallic acid equivalent (mg GAE) in g sample dry matter (dm).

2.4.2. Drying time

The drying time for each pretreated black carrot was defined as the duration required for the moisture content of the final product to fall below 10%. The moisture content of the samples was measured by drying them in a laboratory oven at 105 °C until a constant weight was achieved.

2.5. Experimental Design

2.5.1. Taguchi optimization technique

The TM was developed to optimize total quality control processes by systematically analyzing the effects of various factors on response characteristics and determining their optimal levels. This method enables the identification of experimental conditions with minimal variability, offering a significant advantage over conventional statistical design approaches (Zolgharnein et al., 2013). Traditional experimental design methods are often complex, with the number of required experiments increasing proportionally to the number of experimental factors, making them less practical for food applications (Li et al., 2024). The TM basically uses orthogonal arrays to quantify the effect of process factors on response variables and then evaluates experimental test results using SNR values. In the present study, the Taguchi L_9 orthogonal array, which was composed of three factors and three levels, was selected (Table 2). The process factors including salt concentration, sonication time and microwave power and their corresponding levels were given in Table 1.

Table 1. Process parameters and levels

Process parameters	Symbol	Unit	-1	0	+1
Salt concentration	A	%	2	6	10
Sonication time	B	min	5	10	15
Microwave power	C	W	300	450	600

Table 2. Taguchi L_9 orthogonal array

Run	Experimental design			Mean values		SNR (dB)	
	A	B	C	TFM	Drying time	TFM	Drying time
1	-1	-1	-1	11.59	20.00	21.28	-26.02
2	-1	0	0	16.27	15.00	24.23	-23.52
3	-1	+1	+1	14.14	11.50	23.01	-21.21
4	0	-1	0	18.57	14.50	25.37	-23.23
5	0	0	1	17.28	9.50	24.75	-19.55
6	0	+1	-1	13.35	17.00	22.51	-24.61
7	+1	-1	1	14.09	8.00	22.98	-18.06
8	+1	0	-1	13.02	16.00	22.29	-24.08
9	+1	+1	0	18.10	9.00	25.15	-19.08

For responses, the "larger is better" function (equation 1) was selected to maximize TFM. However, the "smaller is better" (equation 2) was chosen because drying time was targeted to minimize in this research.

$$S/_N = -10log\left[\frac{1}{n}\sum_{i=1}^{n}\frac{1}{y_i^2}\right] \quad (1)$$

$$S/_N = -10log\left[\frac{1}{n}\sum_{i=1}^{n}y_i^2\right] \quad (2)$$

where i indicates the experimental order, y_i is the result and n is the design parameter.

2.5.2. Desirability function approach (DFA)

The DFA is an effective tool for optimizing multiple responses. The primary advantage of desirability function analysis lies in its ability to address multi-response optimization problems by transforming multiple responses into a normalized scale within the range [0, 1]. A desirability value of "1" represents the most favorable outcome, while "0" indicates the least favorable. Depending on the specific response characteristics, desirability functions are classified into three forms: the nominal-the-best, larger-the-best, and smaller-the-best. In this study, the "larger-the-best" was used for TFM (equation 3). On the other hand, the "smaller-the-best" form given in equation 4 was utilized for drying time.

$$= \begin{cases} 0 & y_i<y_{min} \\ \left(\frac{y_i-y_{min}}{y_{max}-y_{min}}\right)^s & y_{min}\le y_i\le y_{max},\ s\ge 0 \\ 1 & y_i>y_{max} \end{cases} \quad (3)$$

$$= \begin{cases} 0 & y_i<y_{min} \\ \left(\frac{y_i-y_{max}}{y_{min}-y_{max}}\right)^s & y_{min}\le y_i\le y_{max},\ s\ge 0 \\ 1 & y_i>y_{max} \end{cases} \quad (4)$$

where y_{min} and y_{max} denote the lower and upper limits of the response variables. The parameter "s" in equations 1-2 represents the weight value, which is determined using either subjective or objective weighting methods.

Finally, these individual desirability values are then combined using equation 5 to determine the overall desirability (OD), enabling the simultaneous optimization of multiple responses in a straightforward and effective manner (Dang et al., 2024).

$$OD = \sqrt[w]{d_1^{w_1} \times d_2^{w_2} \times \dots\dots\dots\dots d_i^{w_3}} \quad (5)$$

where d_i indicates the desirability value of response "i", while w represents the number of responses.

2.6. Statistical Analysis

Minitab (version 19.0, USA) was used to develop an L_9 orthogonal array based on the Taguchi optimization method for microwave drying black carrot samples pre-treated with UAOD. Additionally, the software was used to conduct ANOVA analysis to evaluate the contribution ratio of independent variables such as salt concentration, sonication time, and microwave power on TFM and drying time, within the context of the Taguchi-based DFA optimization.

3. Results and Discussion

3.1. Taguchi Optimization

The TM was used to obtain optimal process levels for each response variable. Table 2 shows the mean and the corresponding SNR values for the TFM and drying time responses. The TFM content of the nine samples ranged from 11.59 to 18.57 mg GAE/ g sample dm. However, the drying time of the samples exposed to sonication for different durations (5-15 min) in the medium with different salt content (2-10%) varied between 8 and 20 min in the microwave with various powers (300-600 W). One of the most critical stages in the TM is that the results of the responses are transformed into the SNR values (Zhang et al., 2024). In this project, the "larger the better" and "smaller the better" functions were used to convert the response values of TFM and drying time into the SNR values, respectively. To obtain the SNR table, these SNR values were further analyzed through Minitab software. In Table 3, the level with the highest SNR value among each process factor level for a response indicates its optimum setting. Therefore, it can be concluded that the maximum TFM content was determined using %6 salt, 10 min sonication, and 450W microwave power ($A_2B_2C_2$). On the other hand, the optimal drying time could be obtained under experimental conditions using %10 salt, 15 min sonication, and 600W microwave power ($A_3B_3C_3$).

Table 3. The SNR table for the responses

	TFM			Drying time		
Level	A	B	C	A	B	C
1	22.84	23.21	22.03	-23.59	-22.44	-24.90
2	*24.21*	*23.76*	*24.92*	-22.46	-22.39	-21.94
3	23.47	23.56	23.58	*-20.41*	*-21.64*	*-19.61*
Delta	1.37	0.54	2.89	3.18	0.80	5.29
Rank	2	3	1	2	3	1

*Italic values indicate optimal levels.

Analysis of variance (ANOVA) can be used to observe the impact of each control factor (salt, sonication time, microwave power) on the response variable (TFM and drying time). In this study, ANOVA analyses were carried out using Minitab software. Statistical analysis of the results was carried out with a 95% confidence level. The ANOVA results for TFM and drying time are shown in Table 4. It can be deduced from Table 4 that the percent contribution of salt, sonication time, and microwave power on TFM response is 17.75, 1.85, and 76.72, respectively. Similarly, the variation in microwave power is identified as a dominant factor, attributing contribution rates of 72.47% for drying time, followed by 22.86% for salt concentration and 3.14% for sonication time. These findings indicated that microwave power is a critical determinant in optimizing the response variables. Furthermore, salt concentration was observed to have a moderate effect. Sonication time, on the other hand, has a limited effect on the optimization process.

Table 4. ANOVA results for the responses

Factors		df	SS	MS	F-value	Contribution (%)
	A	2	8.653	4.326	4.81	17.75
	B	2	0.901	0.451	0.50	1.85
T*	C	2	37.41	18.703	20.79	76.72
	Error	2	1.799	0.899		
	Total	8	48.76			
	A	2	30.722	15.361	14.95	22.86
	B	2	4.222	2.111	2.05	3.14
D*	C	2	97.389	48.694	47.38	72.47
	Error	2	2.056	1.028		
	Total	8	134.389			

T*= TFM, D*= Drying time.

3.2. Desirability Function Approach (DFA) Optimization

The DFA was applied for multiple response optimization of TFM and drying time responses in the microwave drying process of black carrot slices subjected to UAOD. In this method, firstly, the experimental results obtained using Taguchi L_9 orthogonal design were normalized. In this process, since the TFM response has a maximization objective, the "larger-the-best" (equation 3) was selected. On the other hand, the "smaller-the-best" (equation 4) was used because the aim of the study was to reduce the drying time. Then, the desirability values (d_i) were calculated by considering the weighting factor values of the normalized results obtained for the responses. For a subjective approach, principal component analysis (PCA) was used to calculate the weighting factors for the responses (Güldane, 2023). As a result, these values for TFM and drying time were determined as 0.15 and 0.85, respectively. Composite desirability (CD) values were obtained by using the weighted desirability values in equation 5. Table 5 shows the normalization, d_i and CD values calculated for all experiments. Among the nine runs, Run 9 achieved the highest CD value (CD=0.959), indicating the optimal conditions for both responses, which is referred to as the initial process parameter. This was followed closely by Run 5 (CD=0.930) and Run 7 (CD=0.926). In contrast, Run 1 exhibited the lowest desirability index (CD=0.000), suggesting non-optimal conditions for both TFM and drying time.

Table 6 presents the average impact of each parameter level on CD. In this table, the Max-Min value corresponds to the difference between the highest and lowest level data of each process parameter. This indicates the degree of importance of the respective parameter on CD. Also, in this table, the highest value of the process parameter levels indicates the optimal value for relevant process factor. When the Max-Min results were analyzed, it was determined that the effect of the microwave power parameter was the most significant on CD, followed by salt concentration and sonication time, respectively. In

addition, the optimum parameter combination for maximization of TFM and minimization of drying time was obtained as 10% salt, 15 min sonication, and 600W microwave power ($A_3B_3C_3$).

Table 5. Multi-response optimization with DFA

Run	Normalization		Desirability index (di)		CD	Range
	TFM	Drying time	TFM	Drying time		
1	0.000	0.000	0.000	0.000	0.000	9
2	0.671	0.417	0.942	0.475	0.669	6
3	0.365	0.708	0.860	0.746	0.801	4
4	0.999	0.458	1.000	0.515	0.718	5
5	0.815	0.875	0.970	0.893	0.930	2
6	0.252	0.250	0.813	0.308	0.500	8
7	0.358	1.000	0.857	1.000	0.926	3
8	0.204	0.333	0.788	0.393	0.557	7
9	0.933	0.917	0.990	0.929	0.959	1*

*Initial process parameters, CD= composite desirability.

Table 6. Response table for the mean values of the CD

Factors	Level 1	Level 2	Level 3	Max-Min	Rank
A	0.4899	0.7162	0.8137	0.3238	2
B	0.5479	0.7186	0.7533	0.2054	3
C	0.3523	0.7818	0.8857	0.5334	1

The bold values show the optimal process levels.

Figure 1 plots the effect of control factors on the CD. As shown in the graph, an increase in salt concentration leads to a significant increase in CD. This means that osmotic dehydration at an increasing level from 2% to 10% in osmotic solution had a positive influence on maximizing the TFM and especially minimizing the drying time. The formation of chemical bonds between salt and the plant tissue matrix causes a decrease in the resistance of the cell wall and membrane and an improvement in the diffusion process (Asghari et al., 2024). An increase in water loss and a decrease in solute gain was observed in the osmotic dehydration process of lemon (Deepika and Sutar, 2017), aonla (Alam and Singh, 2010), and cauliflower (Vijayanand et al., 1995) samples in an increasing salt concentration. Figure 1 also revealed that the mean CD value increased with increasing sonication treatment during the osmotic dehydration process. The application of sonication during the osmotic dehydration process leads to the disruption of cell walls due to the cavitation effect and thus accelerates the drying process. Furthermore, this process prevents the degradation of phenolic compounds (Cichowska-Bogusz et al., 2020). Similarly, Guo et al. (2023) studied the effect of ultrasound treatment on hot air drying characteristics of garlic slices. They reported a significant improvement in the drying process in sonicated samples, which had a more porous structure compared to untreated garlic slices. This reduction in drying time was also observed in freeze drying of goji (Wang et al., 2024), air drying of apple cubes (Magalhães et al., 2017), and microwave freeze drying of sea cucumber (Duan et al., 2008). The plot drawn in Figure 1 also indicated that an increase in the level of microwave power leads to an increment in CD value, as expected. Saha et al. (2019) investigated the effect of the microwave drying process at different power levels (300W, 600W, 900W) on antioxidant compounds and the drying time of corncob slices. As a result, microwave power levels higher than 300W had a negative effect on the antioxidant capacity of the dried samples. On the other hand, the drying rate of the samples increased as increasing microwave power levels. Similarly, we observed the SNR values of the black carrot samples dried at higher microwave power levels than 450W (Table 3).

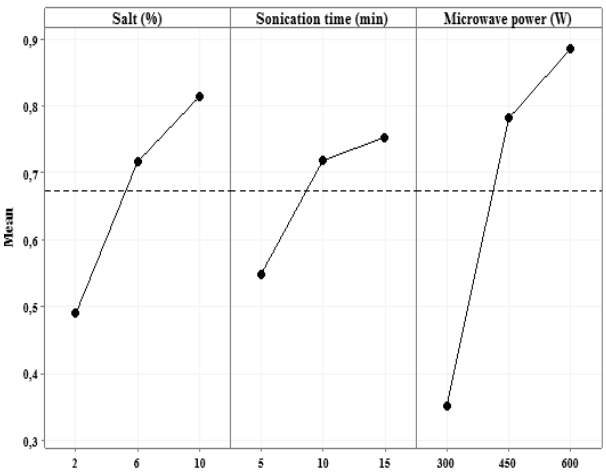


Figure 1. Effect of process variables on CD.

ANOVA results in Table 7 show the effect of process variables on CD. F- and *p*- values were used to evaluate this effect in the black carrot drying process where UAOD pretreatment was applied. Higher F- and lower *p*- values increase effective drying factors' contribution to the process. The results showed that microwave power was the most important parameter affecting CD, followed by salt concentration and sonication time. Microwave power contributed 66.05% on CD, followed by salt

concentration and sonication time with 22.78% and 9.98%, respectively.

Table 7. ANOVA table for composite desirability (CD)

Factors	df	SS	MS	F-value	P-value	Contribution (%)
A	2	0.166	0.083	19.23	0.049	22.78
B	2	0.073	0.036	8.43	0.106	9.98
C	2	0.480	0.240	55.74	0.019	66.05
Error	2	0.009	0.004			
Total	8	0.726				

*Significant at $p<0.05$; S=0.0656. R^2=98.82%. R^2(adj)=95.26. R^2(pred)=76.01.

3.3. Validation Experiments

Confirmation experiments were carried out to determine the enhancement in CD value obtained statistically by the DFA. The hybrid improvement in TFM and drying time responses was evaluated by comparing the values obtained at the initial parameter settings (salt concentration 6%, sonication time 15 min, microwave power 450W) with those obtained at the optimum parameter levels (salt concentration 10%, sonication time 15 min, microwave power 600W). The results were also predicted using Minitab software. To obtain observational data, 3 replicate experiments were performed with the optimum combination of CD values. Table 8 illustrates the average results of the validation studies. As can be seen, the CD for the initial drying parameter setting of black carrot samples pretreated with UAOD was 0.959. While this value increased to 0.973 after the optimization process, an improvement of 1.46%. Consequently, the overall results of this study revealed that the optimal drying conditions, which were determined using a Taguchi-based desirability function approach to reduce drying time and produce a product with a high concentration of phenolic compounds for black carrots subjected to osmotic dehydration via microwave drying, were as follows: a salt concentration of 10%, sonication for 15 minutes, and 600 W microwave power.

Table 8. Results of validation tests

Responses	Initial settings	Optimal process parameters	
		Predicted	Test
	$A_2B_3C_2$	$A_3B_3C_3$	$A_3B_3C_3$
TFM	18.10	15.13	16.42
Drying time	9.00	6.39	7.50
CD	0.959	1.000	0.973

4. Conclusion

This study was carried out to optimize the microwave drying process of black carrot slices with ultrasound-assisted osmotic dehydration pretreatment. Salt concentration, sonication time, and microwave power variables were selected as control factors. The total phenolic matter content and drying time variables of the dried samples were optimized using a hybrid method, Taguchi-based desirability function approach. The study revealed that an increase in the control parameter levels led to an increase in the composite desirability value. Furthermore, the contributions of these parameters to the drying process were determined to be in the following order of importance: microwave power > salt concentration > sonication time. This study demonstrated that the Taguchi-based desirability function approach is effective for optimizing multiple response optimization in similar drying operations.

Author Contributions

The percentages of the author' contributions are presented below. The author reviewed and approved the final version of the manuscript.

	M.G.
C	100
D	100
S	100
DCP	100
DAI	100
L	100
W	100
CR	100
SR	100
PM	100
FA	100

C=Concept, D= design, S= supervision, DCP= data collection and/or processing, DAI= data analysis and/or interpretation, L= literature search, W= writing, CR= critical review, SR= submission and revision, PM= project management, FA= funding acquisition.

Conflict of Interest

The author declared that there is no conflict of interest.

Ethical Consideration

Ethics committee approval was not required for this study because of there was no study on animals or humans.

References

Alam MS, Singh A. 2010. Optimization of osmotic dehydration process of aonla fruit in salt solution. Int J Food Eng, 6. https://doi.org/10.2202/1556-3758.1476

Asghari A, Zongo PA, Osse EF, Aghajanzadeh S, Raghavan V, Khalloufi S. 2024. Review of osmotic dehydration: Promising technologies for enhancing products' attributes, opportunities, and challenges for the food industries. Compr Rev Food Sci Food Saf, 23: 1-28. https://doi.org/10.1111/1541-4337.13346

Ayar-Sumer EN, Nyambe C, Hashim MA. Altin-Yavuzarslan G, El-Messery TM, Ozçelik B. 2024. Optimizing encapsulation of black carrot extract using complex coacervation technique: Maximizing the bioaccessibility and release kinetics in different food matrixes. Lwt, 198: 115995. https://doi.org/10.1016/j.lwt.2024.115995

Chen BL, Lin GS, Amani M, Yan WM. 2023. Microwave-assisted freeze drying of pineapple: Kinetic, product quality, and energy consumption. Case Stud Therm Eng, 41: 102682. https://doi.org/10.1016/j.csite.2022.102682

Cichowska-Bogusz J, Figiel A, Carbonell-Barrachina AA, Pasławska M, Witrowa-Rajchert D. 2020. Physicochemical properties of dried apple slices: Impact of osmo-dehydration, sonication, and drying methods. Molecules, 25: 1078. https://doi.org/10.3390/molecules25051078

Dang X, Al-Rahawi M, Liu T, Mohammed STA. 2024. Single and Multi-response Optimization of Scroll Machining Parameters by the Taguchi Method. Int J Precis Eng Manuf, 25: 1601-1614. https://doi.org/10.1007/s12541-024-01026-3

de Souza AU, Corrêa JLG. Junior RE, Silveira PG, de Mendonça KS, Junqueira JR de J. 2023. Optimization of osmotic pretreatment of tomato slices using response surface methodology and further hot-air drying. Acta Sci Technol, 45: 1-12. https://doi.org/10.4025/actascitechnol.v45i1.62457

Deepika S, Sutar PP. 2017. Osmotic dehydration of lemon (Citrus limon L.) slices: Modeling mass transfer kinetics correlated with dry matter holding capacity and juice sac losses. Dry Technol, 35: 877-892. https://doi.org/10.1080/07373937.2016.1229675

Duan X, Zhang M, Li X, Mujumdar A. 2008. Ultrasonically enhanced osmotic pretreatment of sea cucumber prior to microwave freeze drying. Dry Technol, 26: 420-426. https://doi.org/10.1080/07373930801929201

Güldane M. 2023. Optimizing foam quality characteristics of model food using Taguchi-based fuzzy logic method. J Food Process Eng, 46(8): e14384.

Guo X, Hao, Q, Qiao X, Li M, Qiu Z, Zheng Z, Zhang B, 2023. An evaluation of different pretreatment methods of hot-air drying of garlic: Drying characteristics, energy consumption and quality properties. Lwt, 180: 114685. https://doi.org/10.1016/j.lwt.2023.114685

Kaveh M, Abbaspour-Gilandeh Y, Nowacka M. 2021. Optimisation of microwave-rotary drying process and quality parameters of terebinth. Biosyst Eng, 208: 113-130. https://doi.org/10.1016/j.biosystemseng.2021.05.013

Keskin M, Guclu G, Sekerli Y.E, Soysal Y, Selli S, Kelebek H. 2021. Comparative assessment of volatile and phenolic profiles of fresh black carrot (Daucus carota L.) and powders prepared by three drying methods. Sci Horticult, 287: 110256. https://doi.org/10.1016/j.scienta.2021.110256

Li J, Huang W, Xie Y, Yang J, Zhao M. 2024. The parameters optimization of robotic polishing with force controlled for mold steel based on Taguchi method. J Brazilian Soc Mech Sci Eng, 46: 1-11. https://doi.org/10.1007/s40430-024-04889-9

Magalhães ML, Cartaxo SJM, Gallão MI, García-Pérez JV, Cárcel JA, Rodrigues S, Fernandes FAN. 2017. Drying intensification combining ultrasound pre-treatment and ultrasound-assisted air drying. J Food Eng, 215: 72-77. https://doi.org/10.1016/j.jfoodeng.2017.07.027

Mecha P, Zhu R, Zhang J, Awuah E, Soomro SA, Chen K. 2024. Optimization of chanterelle mushroom drying kinetics under heat pump dryer using taguchi design method. Int J Agric Biol Eng, 16: 273-279. https://doi.org/10.25165/j.ijabe.20231606.6408

Memis H, Bekar F, Guler C, Kamiloğlu A, Kutlu N. 2024. Optimization of ultrasonic-assisted osmotic dehydration as a pretreatment for microwave drying of beetroot (Beta vulgaris). Food Sci Technol Int, 30: 439-449. https://doi.org/10.1177/10820132231153501

Mohammadi S, Karimi S, Layeghinia N, Abbasi H. 2023. Microwave drying kinetics and quality of Allium hirtifolium Boiss: effect of ultrasound-assisted osmotic pretreatment. J Food Meas Charact, 17: 4747-4759. https://doi.org/10.1007/s11694-023-01957-x

Saha SK, Dey S, Chakraborty R. 2019. Effect of microwave power on drying kinetics, structure, color, and antioxidant activities of corncob. J Food Process Eng, 42: 1-13. https://doi.org/10.1111/jfpe.13021

Shinde B, Ramaswamy HS. 2021. Optimization of maltodextrin (10DE)—Sucrose moderated microwave osmotic dehydration of mango cubes under continuous flow spray mode (MWODS) conditions. J Food Process Eng, 44: 1-13. https://doi.org/10.1111/jfpe.13835

Sonmez F, Sahin Z. 2023. Comparative study of total phenolic content, antioxidant activities, and polyphenol oxidase enzyme inhibition of quince leaf, peel, and seed extracts. Erwerbs-Obstbau, 65: 745-750.

Taghinezhad E, Kaveh M, Szumny A, Figiel A, Blasco J. 2023. Qualitative, energy and environmental aspects of microwave drying of pre-treated apple slices. Sci Rep, 13: 1-19. https://doi.org/10.1038/s41598-023-43358-6

Türkan B, Etemoğlu AB. 2020. Optimization of parameters effecting food drying using Taguchi method. Pamukkale Univ. J Eng Sci, 26: 654-665. https://doi.org/10.5505/pajes.2019.93695

Vijayanand P, Chand N, Eipeson WE. 1995. Optimization of osmotic dehydration of cauliflower. J Food Process Preserv, 19: 229-242. https://doi.org/10.1111/j.1745-4549.1995.tb00291.x

Wang J, Liu C, Zheng L. 2024. Effect of ultrasound-assisted osmotic dehydration on the drying characteristics and quality properties of goji. J Food Process Eng, 47(5): e14620. https://doi.org/10.1111/jfpe.14620

Zhang Z, Wang S, Pan M, Lv J, Lu K, Ye Y, Tan D. 2024. Utilization of hydrogen-diesel blends for the improvements of a dual-fuel engine based on the improved Taguchi methodology. Energy, 292: 13047. https://doi.org/10.1016/j.energy.2024.130474

Zolgharnein J, Asanjarani N, Shariatmanesh T. 2013. Taguchi L16 orthogonal array optimization for Cd (II) removal using Carpinus betulus tree leaves: Adsorption characterization. Int Biodeterior Biodegrad, 85: 66-77. https://doi.org/10.1016/j.ibiod.2013.06.010

Black Sea Journal of Engineering and Science
doi: 10.34248/bsengineering.1616966

Open Access Journal
e-ISSN: 2619 – 8991

Research Article
Volume 8 - Issue 2: 480-495 / March 2025

IMPACT ANALYSIS OF BUILDING STRUCTURE ON BUILDING ENVELOPE DESIGN IN THE CONTEXT OF SUSTAINABILITY

Merve ERTOSUN YILDIZ[1]*, Mehmet Akif YILDIZ[1]

[1]Sakarya University, Faculty of Art, Design and Architecture, Department of Arcitecture, 54050, Sakarya, Türkiye

Abstract: This study examines the impact of the building structure on the building envelope in line with sustainable design goals. The building envelope plays a critical role in energy efficiency, conservation of natural resources, and reduction of environmental impacts with its design components such as form, facade, roof, and orientation. In the study, sustainable building examples accepted in the international literature were analyzed, and the building structure's design flexibility and performance advantages were evaluated. The findings show that innovative building systems such as steel, wood, and precast concrete provide significant advantages in sustainable design processes. Structural elements that allow for wide openings and are recyclable increase the building envelope's energy efficiency. The results reveal that the building structure is not only structural durability but also a strategic component in achieving sustainability goals. In this context, it is emphasized that structural elements should be planned at the early design stage.

Keywords: Building envelope, Building structure, Sustainable design, Energy efficiency

***Corresponding author:** Sakarya University, Faculty of Art, Design and Architecture, Department of Architecture, 54050, Sakarya, Türkiye
E mail: merveertosun@sakarya.edu.tr (M. ERTOSUN YILDIZ)
Merve ERTOSUN YILDIZ https://orcid.org/0000-0002-5362-1666
Mehmet Akif YILDIZ https://orcid.org/0000-0001-7248-6191

Received: January 10, 2025
Accepted: February 21, 2025
Published: March 15, 2025

Cite as: Ertosun Yıldız M, Yıldız MA. 2025. Impact analysis of building structure on building envelope design in the context of sustainability. BSJ Eng Sci, 8(2): 480-495.

1. Introduction

In the globalizing world, the depletion of resources due to the climate crisis, the misuse of developing technology, and the consumption and environmental pollution caused by the increasing population have led to the inclusion of sustainable approaches in country policies. In national and international meetings such as the UN Conference on the Human Environment-Stockholm Conference, 1972, the UN Conference on Environment and Development- Rio Conference, 1992, and the World Summit on Sustainable Development- 2002, it was emphasized that environmental pollution has become a widespread problem on a global scale, that ecological, social, cultural and economic development should be addressed together. That importance should be given to sustainable production and consumption (Ministry of Foreign Affairs of the Republic of Turkey, 2023). Increasing environmental awareness has also encompassed the disciplines of architecture, interior architecture, design and planning, and building practices with sustainability principles, which have become widespread. Settlements and buildings that cause global warming with 40% greenhouse gas CO2 emissions, 12% water consumption, 65% waste production, and 71% electricity consumption draw attention to the necessity of sustainable building practices (Environmentally Friendly Green Buildings Association, 2023). Sustainable design in built environments, which constitute a significant amount of the energy used in the world, aims to save energy, resources, and water, to have minimum impact on the environment and economy, and to make a high level of contribution to society.

The most critical design criteria for achieving sustainable targets is to utilize external environmental conditions such as wind, sun, and humidity at a high level in building designs. The building envelope, which brings the external environment and the building together, is the most essential building component for efficiently using energy and resources. In recent years, there have been intensive studies on energy efficiency and user comfort in areas such as thermal insulation, envelope construction systems, materials, thermal utilization, and ventilation in the building envelope. Some of the studies that establish the contemporary technologies of the components that make up the envelope, such as external walls, roofs, windows, foundations, etc., discussed the efficiency conditions for different types of walls, such as trombe walls, solar chimneys, water walls, ventilated walls, and glazed walls (Khedari et al., 2005; Sadineni et al., 2011; Ma et al., 2019; Wang and Lei, 2019; Wang and Lei, 2020; Simões et al., 2021). Studies investigating the potential of window technologies to improve the thermal performance, sunlight, and solar properties of window technologies that allow the most heat flow from the building envelope and allow sunlight to be taken into the indoor environment have examined the physical and thermal transmittance properties of glass and the performance of window joinery (Jelle et al., 2012;

This work is licensed (CC BY-NC 4.0) under Creative Commons Attribution 4.0 International License

Aguilar-Santana et al., 2019; Aburas et al., 2019; Favoino et al., 2022). In addition to these studies, some studies discussed the efficiency of roofs that form the horizontal area of the envelope in areas such as green roofs, photovoltaic roofs, radiant-permeable barriers, and roof cooling systems. These studies discussed solar energy generation, energy efficiency, and ecological designs (Castleton et al., 2010; Shafique et al., 2020; Zheng and Weng, 2020; Catalbas et al., 2021). The area of research most related to the building envelope is energy efficiency and environmental effects of thermal insulation material's types and physical and chemical properties. These studies were in physics, chemistry, health engineering, and architecture, which examine the elements of building insulation materials used for heating and cooling according to climatic conditions, cost, thermal and mechanical properties, life cycle assessment, and health problems (Al-Homoud, 2005; Pargana et al., 2014; Abu-Jdayil et al., 2019; Anh and Pásztory, 2021). The study areas related to the building envelopes discuss the criteria for the design of the envelope together with the external environment. This study contributes to the design features of the building envelope by analyzing the relationship between the building envelope's structure and the building's structure with external environmental conditions for energy-efficient building envelope design with related building examples.

1.1. Research Problem

The increasing demand for energy, the rapid depletion of natural resources, and the growing environmental impacts of the construction industry necessitate the adoption of sustainable building designs. Buildings account for nearly 40% of global energy consumption, exerting significant pressure on natural resources and contributing to extensive environmental degradation. Within this framework, building envelope design plays a critical role in achieving energy efficiency and sustainability objectives. However, the interaction between key building envelope components—such as form, facade, roof, and orientation—and the flexibility and durability provided by structural systems remains insufficiently explored in existing literature.

This research problem raises fundamental questions about how the impact of structural systems on the building envelope can be optimized to align with sustainable design objectives. Furthermore, it is essential to assess the strategic role of structural elements in sustainable design processes. Addressing these issues is crucial to enhancing the effectiveness of sustainable building designs, ensuring both energy efficiency and long-term resilience.

1.2. Research Purpose

The primary objective of this research is to examine the influence of structural systems on the design of building envelope components within the context of sustainable design. This study aims to analyze how building envelope elements, including form, facade, roof, and orientation—are shaped by the flexibility and durability offered by different structural systems.

To achieve this goal, the study evaluates the contributions of various building materials—such as steel, wood, and precast concrete—to energy efficiency, resource conservation, and environmental impact reduction. Additionally, it seeks to optimize the relationship between structural systems and building envelopes, emphasizing the strategic planning of structural components in sustainable building design.

Through a systematic analysis of selected case studies, this research explores the role of innovative structural systems in achieving sustainability goals and aims to provide practical insights that can guide sustainable design processes.

1.3. Research Hypotheses

This study is based on the hypothesis that structural systems play a decisive role in the sustainability performance of building envelope design. Specifically, the research assumes that:

1. Innovative and flexible structural systems (such as steel, wood, and precast concrete) enhance sustainable performance by optimizing the design freedom of the building envelope.
2. The integration of structural and envelope components is essential for achieving energy efficiency, resource conservation, and environmental impact reduction in sustainable building designs.
3. Structural elements serve as strategic components in ensuring durability, adaptability, and resilience while supporting passive design strategies.

By testing these hypotheses, the study aims to clarify the role of structural systems in sustainable building performance and identify key factors that influence the optimization of building envelope components.

1.4. Research Scope

This study systematically examines the relationship between structural systems and building envelope components in sustainable building design. The research is based on an analysis of sustainable building projects recognized in international literature, with a focus on projects that provide accessible and detailed data for in-depth examination.

The study evaluates the contributions of different structural systems—including steel, wood, and precast concrete—to sustainable building performance, particularly in terms of:

- Energy efficiency,
- Resource conservation,
- Material recyclability, and
- Environmental impact reduction.

Additionally, the study explores the interaction between structural flexibility and passive design strategies, such as natural ventilation, daylight utilization, solar energy integration, and water recovery systems. The findings aim to provide a comprehensive understanding of how structural elements contribute to sustainability goals and

offer guidance for optimizing sustainable building design processes.

1.5. Research Methodology

This study adopts a qualitative research framework to analyze the impact of structural systems on the building envelope in sustainable building design. The case study method was employed to identify sustainable building projects acknowledged in international literature, with a focus on projects that provide detailed and accessible data for in-depth analysis.

The selected case studies were examined based on key building envelope components, including form, facade, roof, and orientation, as well as the design flexibility and performance advantages offered by structural systems. The evaluation criteria for this analysis are as follows:

- Energy Efficiency: Assessment of natural ventilation strategies, solar energy utilization, and insulation performance of the building envelope.
- Material Performance: Examination of the sustainability contributions of structural systems, including steel, wood, and precast concrete.
- Design Flexibility: Analysis of the potential of structural systems to facilitate wide openings, recyclability, and adaptable orientation.

By conducting a systematic comparison of data obtained from case studies, this research aims to assess how the interaction between structural systems and the building envelope influences energy efficiency and sustainability outcomes. The integration of theoretical knowledge and empirical data from real-world projects ensures a comprehensive and practical evaluation of sustainable building strategies.

2. Materials and Methods

The structure, a fundamental component of architectural design as the load-bearing system of a building, must support the building envelope, form, and orientation to implement sustainable architectural design correctly. In addition to ensuring safety by protecting the building from loads, ground movements, and other external influences, the structure also plays a vital role in energy-efficient/sustainable architectural design. Various design strategies used to increase energy efficiency affect many elements, from the choice of materials for the structure to the layout of structural systems. The structure, which is the most critical building component that provides the formation of the building form, must have an appropriate design to facilitate the building envelope design according to climatic data. To achieve the desired level of sustainable design components such as building form and orientation according to climatic data, natural ventilation, and lighting strategies, thermal insulation design to maintain indoor conditions, and placement of solar energy generating systems, the structure should allow the free and flexible design to the building envelope. In addition, the building structure contributes to sustainable design with minimum environmental and economic impact during the construction, use, and disposal phases.

The structure is the main building element affecting energy-efficient/sustainable architectural design. The various design strategies used to improve energy efficiency affect many aspects of the structure, from the choice of materials to the layout of structural systems. For example, the structure should have an appropriate thermal mass and support the shell insulation materials for an efficient insulation system. For natural ventilation design, the structure should have openings or ventilation ducts that support natural airflow. Furthermore, there is a need for structural integration to place renewable energy systems, such as solar panels and wind turbines, used for energy generation in appropriate building areas. Therefore, important decisions to improve energy efficiency should be taken at the design stage of the structure and integrated with sustainable design. In line with this information, the issues that should be taken into consideration for energy-efficient/sustainable approaches in the structural design process are summarized below:

Material selection: Material efficiency is linked to savings in using materials by utilizing their strength and stiffness properties. Efficient structural forms are designed with attention to the geometry of the overall structure and its parts and provide the highest structural performance with the least amount of material (Huberman et al., 2015).

Structural system: Structural design and layout influence sustainable design strategies. The structural system should provide more strength with fewer structural elements to have the flexibility to allow for future changes and the energy efficiency of the building (Buschmeyer and Fastabend, 2004).

Insulation: The insulation system can affect the structure's thermal mass while improving energy efficiency. Proper design of the structural thermal mass saves energy by regulating heat transfer. Structural design can help to reduce heat losses and control external heat gains. Optimization of the dimensions of the structural components of a building at the initial design stage, aimed at minimizing operational and total energy consumption, increases the thermal insulation area. Using insulated facade systems or structural details that reduce thermal bridges can limit heat transfer and reduce the building's heating and cooling energy demand (Zilberberg et al., 2021; Kumar et al., 2020; Wang and Adeli, 2014).

Integration: For the construction of systems such as solar panels, wind turbines, or water collection systems used for energy generation, the structural design must be integrated. The layout and strength of the structure are factors to be considered in terms of system safety and enabling the creation of energy-generating systems. In addition, solar panels or collectors can be integrated into structural elements or have structural features (Wang et al., 2021).

Natural ventilation and lighting: The structure is an essential building component for the design effectiveness of natural air intake from the building envelope to the interior spaces. The structural elements of the building should have a design plan that will direct the airflow and provide comfortable air circulation in the interior spaces. Meeting the ventilation and lighting demands expected from the building envelope is possible with appropriate structural design. For example, structural elements with openings that facilitate natural airflow can reduce the need for artificial ventilation in spaces and energy consumption.

Water management: The structure contributes to implementing rainwater harvesting systems or water-saving measures by providing strength and flexibility. Structural design can be integrated into rainwater harvesting areas and drainage systems. It can also be designed to provide structural support for methods used for water saving. For example, structural support elements for green roofs can retain water and grow plants.

Construction Method: Access to the construction site and the duration and environmental impact of on-site construction contribute to the structural system's sustainability. The performance parameters expected from the structure design ensure that the structural element, produced in the factory and has a short transport distance, is assembled quickly and with less labor on-site. The structural design needs to be planned and optimized in line with building efficiency principles to achieve energy efficiency targets.

In order to analyze the research frequency and need for recent studies on building structures for sustainable built environments, the Web of Science website, which provides access to multiple databases and comprehensive citation data for many different academic disciplines, was used. As a result of the Web of Science search with the keywords "structure," "sustainability," "building," and "energy efficiency," 610 studies have been encountered since 2010, and the distribution of the research by years is given in Figure 1. It is seen that there is an increasing graph on the subject of research over the years.

Figure 2 shows the density of research areas of 610 publications on research topics encountered due to keyword searches. While the numerical majority of the studies covered the branch of materials science, it was seen that the numerical ratio of the studies in the fields of civil, chemical, and physical engineering was also high. Although sustainability and energy efficiency are among the keywords, the number of studies in this field could be higher for the research area, and there is no research area where architecture and design are the main branches of science. In the Green Sustainable Science Technology field, which is the closest research area to sustainable architectural approaches, 35 studies have been conducted.

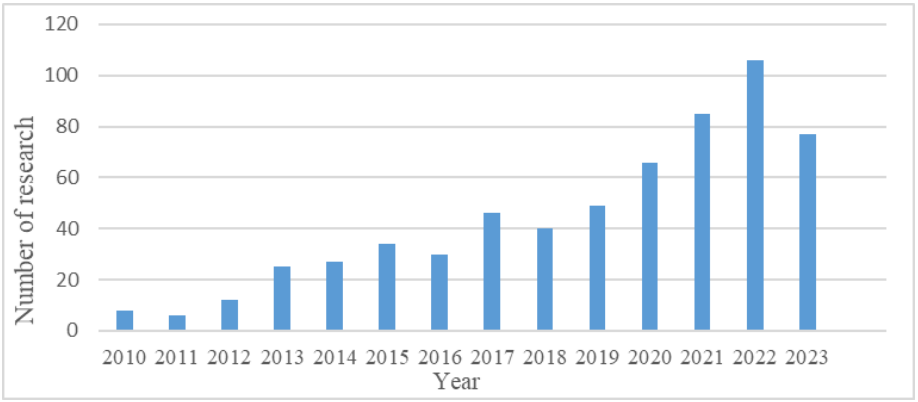


Figure 1. Distribution of research by years.



Figure 2. Scientific fields of published works on research.

To contribute to the limited number of academic studies that examine sustainable design approaches in the context of structure, this study analyses the design criteria for energy conservation and recovery of the structural system through sustainable building designs. In this direction, as a result of the analysis of the literature information, the sustainability features of the structural systems that are most widely used in built environments are explained. Timber, reinforced concrete, masonry, steel, and composite components are used as the primary structural systems in buildings. The structure materials have different environmental impacts and sustainable evaluations, and the envelope design has other effects on energy efficiency.

2.1. Wood

The selection of basic building materials is often made considering the importance of economic, environmental, functional, aesthetic, and health-related criteria, and wood is one of the modern construction materials that offer efficient, economical, and sustainable solutions (Kolb, 2008; Leśniak and Zima, 2018). Efficient, durable, and valuable wood products produced from trees are minimally processed at the construction site or composited and used as highly processed and highly engineered products in a large production facility. The most essential features of wood that contribute to sustainability are low embodied energy and low carbon impact. Wood, a material that requires a minimum amount of energy-based processing in its production, has a low level of embodied energy compared to many other materials used in construction (e.g., steel and concrete) (Falk, 2010). However, while it is used in buildings with fewer stories compared to the usage areas of other materials, it allows large spans to be crossed with small-sized products such as steel.

2.2. Masonry and Concrete

Carbon footprint and the use of natural materials as the material can be supplied near the construction site. In addition, thanks to the thick wall constructions, the insulation feature is provided, allowing the interior to remain warm or cold for a long time. This structure, used in low-rise buildings, has low-free design possibilities for natural lighting and ventilation. However, it can contribute to energy efficiency as a suitable material for passive design systems such as trombe walls (Wang and Adeli, 2014).

Concrete, which consists of aggregate and cement, has a long service life and is a durable system, but the chemical reaction that occurs during its formation can damage the environment by releasing CO_2 gas. In addition, the reinforced concrete system is less used in buildings with sustainable design due to its larger size and less wide span than steel and timber systems.

2.3. Steel

It is the most preferred structural system for sustainable designs thanks to its advantages, such as fast production and assembly of steel, high recycling, high strength and flexibility, and small column dimensions. Despite the high energy requirement to produce steel, its low cost and environmental impact throughout its life cycle due to its production and assembly speed and recycling capacity make it sustainable (Broniewicz and Broniewicz, 2020). While steel can be recycled up to 95% of the time, the amount of energy consumed per ton of steel produced decreases in the subsequent recycling process and reaches a constant value (Brimacombe et al., 2001).

Natural resource consumption, transport, energy consumption throughout the life cycle, waste production, and emission production are frequently discussed in the literature as indicators of the sustainability of steel (Burgan and Sansom, 2006; Landolfo et al., 2011; Aksel and Eren, 2015; Rossi, 2014). Another advantage of steel is that it allows flexible design. Thanks to the flexible design, the sustainable performances expected from the building envelope are realized quickly and efficiently. The ability of steel to pass through wide openings, transform into desired forms, and provide high strength with small dimensions allows passive and active energy efficiency and energy generation designs.

Wood, reinforced concrete, masonry, steel, and composite systems consisting of a combination of these building systems are the most common construction systems used in built environments. Since each system has different sustainable advantages and disadvantages, designers choose suitable construction systems for sustainable building design goals.

3. Results

In sustainable building designs, the contributions of the building envelope to energy efficiency, natural resource use, and environmental impact reduction are generally examined. However, this study differs from other studies in the literature by focusing on the sustainable advantages created by the building structure on the building envelope. In this context, the effects of the building structure on the building envelope design components were analyzed based on ecological values, energy efficiency, and user comfort.

The research examines examples used to achieve sustainable building design goals at different scales and structures. In the selected examples, the effect of the building structure on the building envelope was evaluated through the following four essential design components:

Form: The effect of the shape and geometry of the structure on energy performance and environmental compatibility.

Orientation: Positioning of the building envelope

according to sunlight, wind, and other climate data.

Roof: Designs that increase energy efficiency and provide renewable energy integration.

Facade: Building elements that optimize natural ventilation, lighting, and energy gain targets.

The common feature of the selected sample buildings is that they focus on sustainable design targets. However, the methods of each building to achieve these targets differ. The research focused on buildings with composite structural systems selected from steel, timber, and concrete systems and buildings with steel systems only. These examples were analyzed in tables to evaluate each sustainable design feature in detail.

3.1. Example 1: The Edge Building

The EDGE is a 'smart building' designed for the Deloitte company, whose construction was completed in 2014. The design of the pentagonal office building with a 40,000 m^2 gross floor area and sloping facade belongs to PLP Architecture. Sustainability, comfort, and users' productivity were considered during design and construction. The Edge is one of the world's most significant buildings with BREEAM Outstanding certification. The building core constitutes the starting point of architectural design. The core consists of horizontally and vertically moving bridges and an atrium housing the open elevator. The atrium functions as a giant theater hall. There are offices arranged like an amphitheater around it. At the same time, this atrium turns into a natural gathering area. While the transparent atrium on the north side provides climate control, solar collectors on the south side are integrated into the facade and provide energy gain. The Edge uses energy concepts such as thermal storage, a heat pump system with a district heating connection, a PV in the building (Table 1) (URL-1; URL-2).

3.2. Example 2: Davies Alpine House

Davies Alpine House is an award-winning RIBA building that combines traditional practices with the latest technology, such as a greenhouse developed for the 21st Century. It was designed by Wilkinson Eyre to provide the dry, cool, and windy conditions that alpine plants need. The structural setup of this building, which is 16 meters long and 10 meters high, consists of four prominent steel arches connected to the reinforced concrete floor. Designing the maximum possible glass surface area on the facade allows 90% of the sunlight to be let in. Shading elements integrated into the transparent surface protect from unwanted sunlight during summer months. Three meters below the Alpine House is a maze of concrete slabs. The process mimics the natural system of termite mounds. That is a passive cooling system. Air from the outside is drawn into the 80-meter interlocking labyrinth. The maze cools overnight as the concrete creates thermal mass, which cools the incoming air. Four low-energy fans carry the air into the building through the displacement tubes above, and through these tubes, the cooled air enters the greenhouse at the plant level. Davies Alpine House is an award-winning RIBA building that combines traditional practices with the latest technology, such as a greenhouse developed for the 21st Century. It was designed by Wilkinson Eyre to provide the dry, cool, and windy conditions that alpine plants need. The structural setup of this building, which is 16 meters long and 10 meters high, consists of four prominent steel arches connected to the reinforced concrete floor. Designing the maximum possible glass surface area on the facade allows 90% of the sunlight to be let in. Shading elements integrated into the transparent surface protect from unwanted sunlight during summer months (Table 2) (URL-3; URL-4).

3.3. Example 3: Hawaii Preparatory Academy | Energy Lab

Designed to meet Hawai'i Preparatory Academy's request to create a high school science building that emphasizes energy conservation and recovery, the 6,100 sf Energy Lab offers students the opportunity to experiment with renewable energy technologies. The LEED Platinum building uses photovoltaics and wind turbines to meet its energy needs. It collects rainwater to meet drinking water needs, uses natural ventilation, and has an outdoor view from 100 meters—the percentage of occupied spaces. To promote environmental literacy, students can monitor the building's energy use in real time (URL-5).

The Energy Laboratory responds to the science curriculum it houses, with spaces from project rooms to an extensive research center and laboratory designed to encourage student exploration and experimentation. The building's configuration facilitates indoor and outdoor scientific study by connecting the interior spaces to the surrounding landscape. Students are surrounded by the systems they study and are constantly reminded of their methods (Table 3) (URL-6).

3.4. Example 4: The Crystal Building

Designed by Siemens in response to a green building request, Crystal is the first building to receive the highest sustainable building awards from BREEAM and LEED. Designed by Wilkinson Eyre, the glazed and sharp-lined building creates a new platform for discussion on sustainable urban living and development. With its crystalline shape representing complexities and challenges, the Crystal building is derived from the multifaceted urban life with its design. The facade wings with sporty triangular glass paneled surfaces form a similar external geometry with walls and roofs composed of multiple triangular planes, aiming to represent different aspects of sustainability and the complexity of urban life.

Six different types of highly insulated glass, each with different levels of transparency, have been used in the cladding to reduce solar gain and frame views into and out of the all-glass building facade, focusing more on using advanced technology. The building consists of two steel-framed parallelogram wings covered by a curtain wall. Box-section columns are designed along the roof

ridge to maximize the column-free central area, tapering at the top and bottom on different axes. Cross beams, narrower at the bottom and broader in the perpendicular direction towards the top, are connected at the bases of the load-bearing system, providing strength and stability under wind load at the top and bottom (Table 4) (URL-7; URL-8).

3.5. Example 5: Adnan Menderes Airport

Izmir Adnan Menderes Airport International Terminal, put into service in 2006, serves passengers in an area of 107. 699 m^2. It claims that it can create an attractive, colorful/lively, spatially peaceful effect in terms of the character and design of the materials used, with transparent facades between the air side and passenger waiting for lounges and spacious and wide surfaces in terms of providing sufficient. There are transparent surfaces that will provide sufficient natural lighting in space. Thus, most of the lighting can be provided naturally.

The focal point of the terminal design is the diagrid vaulted roof measuring 200 m x 80 m in plan, covering the check-in hall at the departure floor entrance with a span of 72 m and the "elephant's foot" structure with four diagrid hyperboloid cones. The inside of the four vaulted elephant legs that form the design are commercial spaces; simultaneously, these legs act as vertical chimneys, providing light and ventilation to the check-in area (URL-9).

The glass canopies at the terminal entrance are made of composite material with photovoltaic cells, creating shade and generating green energy from solar energy to the terminal. The connection detail element at the end of the pin-supported steel pipe elements forming the carrying system of the canopy is formed with cast structural steel (Table 5) (URL-9).

4. Discussion

This study analyzes sustainable building examples that aim to reduce resource consumption, increase energy efficiency, and improve user comfort while minimizing environmental impact through an ecological and human-centered approach. The case study analysis highlights that climatic data, which provides critical information about external environmental conditions, plays a key role in sustainable design strategies. Integrating solar energy, wind, and air currents into architectural design reduces the need for mechanical systems and enhances the self-sufficiency of buildings by enabling passive heating, cooling, and ventilation.

The Role of Structural Systems in Climate-Responsive Design

A fundamental prerequisite for achieving high efficiency in form, orientation, and building envelope design is the appropriate structural system selection. The case study analysis demonstrates that for effective natural ventilation, lighting, and passive heating and cooling, the structural system should:

- Enable broad openings for enhanced airflow and daylight penetration,
- Minimize column sections to increase spatial flexibility,
- Allow variable roof slopes and envelope orientations to optimize solar and wind utilization.

Among the structural systems analyzed, steel structures were found to be particularly advantageous due to their small cross-sections, ability to span large distances, and flexibility. Additionally, wood was identified as a sustainable structural material due to its natural properties, small dimensions, and recyclability. However, its limited strength in high-rise buildings restricts its application to low-rise structures. While reinforced concrete remains the most commonly used structural material in traditional buildings, precast concrete has emerged as a preferred alternative in sustainable designs due to its lower environmental impact and reduced construction time.

Integration of Structural Systems and Energy-Efficient Design Strategies

The findings from the case studies, summarized in Table 6, illustrate how structural systems facilitate energy efficiency and environmental performance through various strategies:

- Natural lighting was achieved in all case studies through transparent roof surfaces.
- Natural ventilation via roof openings was incorporated in all cases except The Crystal Building.
- Solar panel integration was enabled by roof structures designed with optimal solar angles in all case studies except Davies Alpine House.
- Rainwater collection and drainage systems were structurally integrated into The Edge Building and The Crystal Building, demonstrating the role of structure in supporting water conservation strategies.
- Solar or wind chimneys, which are critical for enhancing indoor air circulation, were incorporated only in Adnan Menderes Airport.

These examples illustrate that structural systems are not merely load-bearing components but also active design elements that shape the environmental performance of buildings.

Structural Flexibility and Adaptive Building Envelopes

The facade designs of the analyzed buildings highlight the role of structural flexibility in enhancing energy efficiency. A key finding is that all five case studies benefited from the flexibility provided by steel structures, allowing for dynamic facade adaptations that improved solar exposure, ventilation, and lighting performance.

- The Edge Building, The Crystal Building, and Adnan Menderes Airport feature facades optimized for both structural efficiency and solar

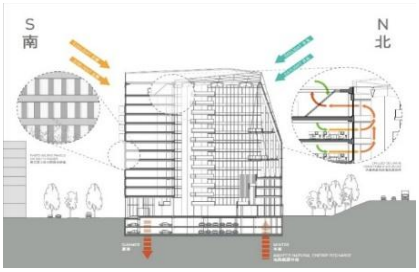
orientation, facilitating solar panel integration.

- The Edge Building and The Crystal Building implemented facade movements and increased facade surface area, improving daylight access and natural ventilation.
- Geothermal and wind energy systems were incorporated in all case studies except Adnan Menderes Airport, demonstrating the potential of site-responsive structural layouts.
- Atrium-based ventilation strategies and the chimney effect were effectively utilized in The Edge Building, Davies Alpine House, and Adnan Menderes Airport.

These findings highlight the importance of structural adaptability in integrating passive design strategies and reducing the reliance on active energy systems.

Table 1. The Edge Building (URL-1; URL-2)

INFORMATION		
Location	Amsterdam	
Year	2014	
Function	Office	
Architect	PLP Architecture	
Material	Precast concrete, Steel and Glass	
STRUCTURE		
Small-sized long span steel carrier system Solar pitched steel roof Steel laced beam Structural design allowing design objectives		 
DESIGN FICTION		
Design Objectives	Zero-energy building design Natural lighting and ventilation Structural design allowing flexible design Energy recovery with solar energy	
Form	Broad facade surfaces in the north-south direction Hollowing out the compact mass to form an atrium Natural ventilation openings in the direction of the prevailing wind	
Orientation	Orientation in accordance with the sun and wind Atrium to the north, solar panels to the south	
Recycling	Recyclable building structure Use of rainwater Recovery of energy consumed by utilising solar energy	
BUILDING ENVELOPE		
Roof	Solar Panels Rainwater collection system Roof windows	
Facade	Transparent surfaces on the north-facing atrium facade Small-sized transparent surfaces on the south-facing facade South facade covered with photovoltaic panels Preventing temperature rise indoors by reducing heat conduction Movements on the facade to control the air flow rate indoors and prevent strong air currents	



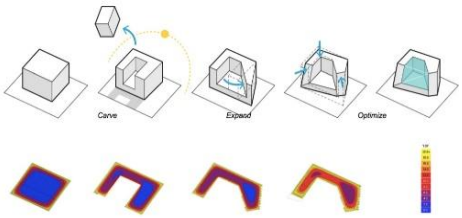
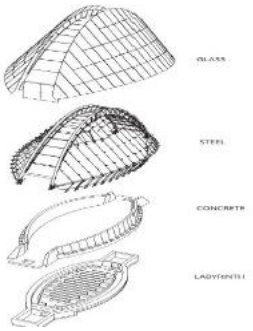




Table 2. Davies Alpine House (URL-3; URL-4)

INFORMATION		
Location	London	
Year	2006	
Function	Greenhouse	
Architect	Wilkinson Eyre	
Material	Steel, glass, Precast concrete	
STRUCTURE		
Small-sized long span steel carrier system Subsoil concrete labyrinth allowing air circulation Steel arch beams Structural design allowing design objectives Construction design allowing maximum daylight gain		
DESIGN FICTION		
Design Objectives	Natural ventilation and lighting Movable structure design / two back-to-back arches Maximum utilisation of daylight Shading system design resembling a peacock	
Form	Organic form in commune with nature Long facade extending on east-west axis Transparent surfaces allowing maximum sunlight transmission A structure that allows warm air to flow into the ventilation shaft on the roof	
Orientation	Orientation in accordance with the direction of sun and wind Orientated from north to south so that it receives direct sunlight but does not overheat.	
Recycling	Recyclable building structure	
BUILDING ENVELOPE		
Roof	Roof windows	

Facade	Bringing a high amount of sunlight into the interior with the structural system supporting the glass facade and glass joint details Shading element in white woven fabric that can cover 70% of the glass panels

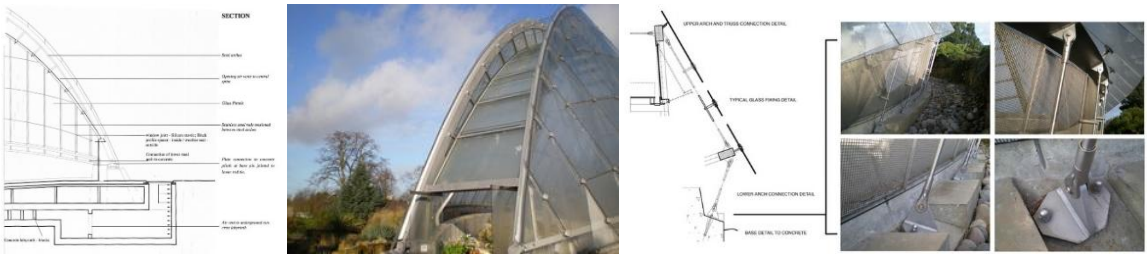


Table 3. Hawaii Preparatory Academy | Energy Lab (URL-5; URL-6)

INFORMATION		
Location	Kamuela, Hawaii	
Year	2010	
Function	Education	
Architect	Flansburgh Architects	
Material	Wood, Steel	
STRUCTURE		
Structural design allowing large area design Pitched roof structure suitable for sunlight Structural design allowing design objectives Use of natural materials		
DESIGN FICTION		
Design Objectives	Net zero energy building design Provide natural ventilation To maximise the benefit of sunlight Avoiding energy consumption for active systems To educate students on the understanding of environmentally sensitive, sustainable living systems	
Form	Form integrating with the ground Positioning on north-south axis Maximum benefit from natural ventilation Roof design that creates negative pressure with the prevailing wind and allows the heated air inside the building to flow out Plan design with courtyards and terraces to maximise the benefit of topography	
Orientation	Orientation that creates a wind corridor interior by using the north wind Orientation that improves the efficiency of solar energy and photovoltaic panels	
Recycling	Recyclable building structure	
BUILDING ENVELOPE		

Roof	Skylights allowing natural ventilation and lighting Pitched roof structure that increases the energy efficiency of photovoltaic panels
Facade	Natural lighting with high light transmission on transparent surfaces Wide eaves providing protection from sun rays

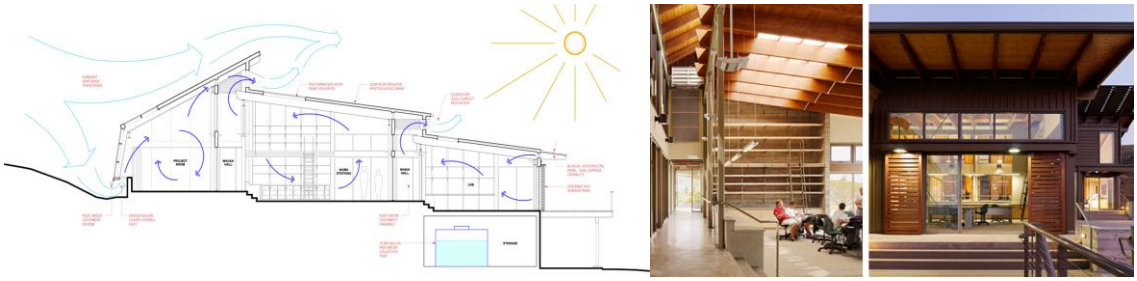


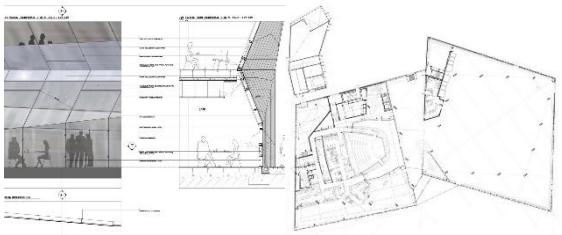
Table 4. Hawaii Preparatory Academy | Energy Lab (URL-7; URL-8)

INFORMATION	
Location	London
Year	2022
Function	Mixed Use
Architect	Wilkinson Eyre Architects
Material	Çelik, cam



STRUCTURE

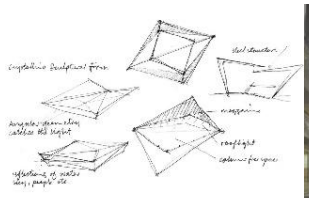
Steel structure combining many triangles
Steel laced beam
Cross steel beams and box section columns allowing wide span crossing
Structural design that allows for design
28 columns and all main beams including edge and ridge beams with box section profile
Frame design minimum steel utilisation and prefabricated system



DESIGN FICTION

Design Objectives	Intelligent building management systems to minimise energy use Ensuring maximum gain from solar energy Zero-energy building design Natural ventilation through automatic windows Use of natural daylight in all spaces Structural design allowing flexible design
Form	Transfer of crystal geometry to architecture Broad facade surfaces in the north-south direction Two steel-framed parallelogram wings covered with glass curtain wall
Orientation	Sun and wind favourable orientation Atrium to the north, solar panels to the south
Recycling	Recyclable building structure Greywater recovery of dirty water (the building is 90% self-sufficient) Recovery of energy consumed by utilising solar energy

BUILDING ENVELOPE	
Roof	Solar Panels Rainwater collection system Transparent roof with varying levels of transparency (six different panes)
Facade	Transparent surfaces with different levels of transparency Facade design that allows natural lighting Controlled sunlight gain Sloping facade structure in accordance with the sun





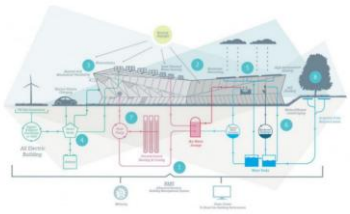
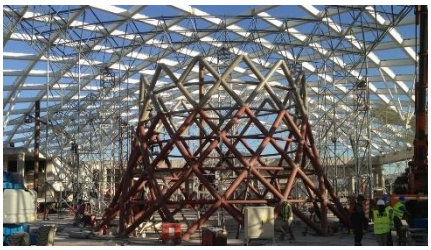


Table 5. Adnan Menderes Airport (URL-9)

INFORMATION		
Location	İzmir	
Year	2014	
Function	Aırport	
Architect	Hazan Architect	
Material	Reinforced concrete, steel, glass	
STRUCTURE		
Steel laced beam Steel frame light chimneys Steel structure allowing skylight formation Ventilation through chimney effect with hollow steel frame system		
DESIGN FICTION		
Design Objectives	Reducing the use of natural resources To ensure that sunlight reaches the depths of the building Maximising the use of natural lighting by increasing the transparent surface area Chimney effect design with vertical voids	
Form	Compact form with linear plan scheme Design elements to ensure visual integrity with the exterior Structure allowing open space organisation	
Orientation	Orientation to natural ventilation and lighting indoors	
Recycling	Recycled Material Recovery of energy consumed by utilising solar energy	
BUILDING ENVELOPE		

Roof	Reflection of sunlight with white standing seam roof structure Solar Panels Roof windows Vertical structure forming light chimneys
Facade	Facade design that allows natural lighting Controlled solar gain - metal solar shading panels Energy production with PV panels on the entrance eaves



Table 6. Energy-efficient and productive approaches to sustainable building examples

	Example 1	Example 2	Example 3	Example 4	Example 5
STRUCTURE					
Wood			✓		
Steel	✓	✓	✓	✓	✓
Precast concrete		✓			
ROOF					
Natural ventilation	✓	✓	✓		✓
Natural lighting	✓	✓	✓	✓	✓
Roof window	✓	✓	✓	✓	✓
Roof solar panel	✓		✓	✓	✓
Rainwater collection	✓			✓	
Solar chimney					✓
FACADE					
Natural ventilation-lighting	✓	✓	✓	✓	✓
Facade solar panel	✓			✓	✓
Broad facade openings	✓	✓	✓	✓	✓
Shading elements		✓	✓		
FORM					
Gaps that increase the facade surface	✓			✓	
Utilising topography	✓	✓	✓	✓	
Broad facade parallel to the sun	✓	✓		✓	✓
Ventilation and lighting with vertical gaps	✓	✓			✓

ORIENTATION					
Roof slope towards the sun	✓		✓	✓	
Sloping facade suitable for sun angle	✓	✓		✓	
Natural ventilation with wind	✓	✓			✓
RECYCLING					
Recycled structure	✓	✓	✓	✓	✓
Recycled material	✓	✓	✓	✓	✓
Energy recovery	✓	✓	✓	✓	✓
Water recovery	✓			✓	

Environmental Adaptability Through Structural Design

The roof and facade slopes in the case studies were designed based on solar incidence angles and wind flow patterns, demonstrating the direct relationship between structural design and environmental adaptability.

- The Edge Building, The Hawai'i Preparatory Academy Building, and The Crystal Building optimized roof slopes for solar energy utilization.
- The Edge Building, Davies Alpine House, and The Crystal Building incorporated facade orientations responsive to wind and sun exposure, reducing energy demand.

Material selection also played a crucial role in sustainability performance. Steel, timber, and precast concrete were selected in the case studies for their recyclability and potential for reuse. The structural system's capacity to integrate renewable energy solutions was evident in:

- Solar panel integration across all case studies, facilitated by structural modulation and load-bearing optimization.

The Edge Building and The Crystal Building incorporated rainwater collection and storage systems, showcasing water efficiency strategies.

4. Conclusion

The high consumption of energy and natural resources, coupled with significant carbon emissions and environmental degradation, underscores the critical importance of sustainability in the built environment. Rapid technological advancements, population growth, and shifting demographic structures have further intensified the threat of resource depletion and environmental pollution, necessitating resource-efficient and ecologically responsible design strategies. Incorporating natural environmental components and climatic data into architectural design is fundamental to achieving sustainability goals related to ecology, human well-being, resource conservation, and economic efficiency. While solar energy is harnessed for heating and electricity generation, wind and air currents contribute to energy production, cooling, and ventilation, reducing reliance on mechanical systems.

Among all building components, the building envelope plays a pivotal role in mediating between outdoor and indoor environments, maximizing the benefits derived from climatic data. The placement of buildings on the land and the design of the envelope—which regulates the entry of solar radiation, wind, rain, and humidity under optimal conditions—are fundamental considerations for sustainable design. However, for the building envelope to function efficiently, the design of the roof, facade, building form, and orientation must be flexible and adaptable to environmental conditions. In this regard, the structural system is a crucial factor, as it not only determines the physical lifespan of a building but also facilitates the flexibility required for optimal envelope performance. The ability of structural systems to support adaptable design solutions directly impacts on the overall sustainability and efficiency of buildings.

The Role of Structural Systems in Sustainable Design

For the building structure to provide flexibility to the envelope, it must allow controlled integration of external environmental conditions into interior spaces. This can be achieved by:

- Optimizing the placement of structural elements in both the envelope and interior spaces.
- Designing the structure to accommodate diverse forms and configurations, ensuring adaptability to environmental conditions.
- Incorporating appropriately sized openings in the building shell to facilitate ventilation, lighting, and energy efficiency.

Wide column spacing and reduced column and beam cross-sections contribute to more adaptable interior layouts, while also enhancing environmental integration. Beyond structural strength and stability, sustainable design requires structural flexibility, enabling the building form and envelopes to respond dynamically to solar angles, wind flows, and climatic conditions. This adaptability allows designers to maximize solar gains, optimize passive ventilation, and integrate renewable energy solutions such as solar panels on facades and roofs.

Material Selection and Lifecycle Considerations

In addition to enhancing passive cooling, heating, lighting, and ventilation, sustainable building structures contribute to long-term environmental sustainability through responsible material selection. The ideal structural materials for sustainability should:

- Be sourced from natural origins.
- Have low energy consumption throughout their life cycle.
- Avoid harmful gas emissions during production and construction.
- Be fully recyclable at the end of their lifecycle.

Among structural materials, wood and steel stand out as highly sustainable options:

- Wood is a renewable material that can be sourced naturally, requiring minimal energy for production and construction. It generates low waste and offers reusability, making it an ideal choice for low-rise sustainable buildings.
- Steel has a long lifecycle, provides durability, safety, and cost efficiency, and is widely regarded as an environmentally friendly construction system. Additionally, steel's recyclability and adaptability make it one of the most versatile materials for sustainable structural design.

This study presents a new perspective in sustainable design research by analyzing the relationship between structural flexibility and the performance of other building components. Unlike conventional studies that primarily focus on material efficiency or energy consumption, this research underscores the fundamental role of structural elements in shaping the building envelope, form, and orientation.

A key conclusion of this study is that sustainable building design should begin with the selection and design of appropriate structural systems. By integrating low-impact, energy-efficient structural elements that respond to environmental conditions, architects and engineers can achieve high-performance, climate-responsive buildings. Moving forward, the consideration of structural sustainability should be given equal priority to structural strength, ensuring that buildings not only meet functional and safety requirements but also contribute to energy conservation and ecological balance.

Author Contributions

The percentages of the authors' contributions are presented below. All authors reviewed and approved the final version of the manuscript.

	M.E.Y.	M.A.Y.
C	50	50
D	50	50
S	50	50
DCP	50	50
DAI	50	50
L	50	50
W	50	50
CR	50	50
SR	50	50
PM	50	50
FA	50	50

C=Concept, D= design, S= supervision, DCP= data collection and/or processing, DAI= data analysis and/or interpretation, L= literature search, W= writing, CR= critical review, SR= submission and revision, PM= project management, FA= funding acquisition.

Ethical Consideration

Since this study did not involve any studies on animals or humans, ethics committee approval was not obtained.

Conflict of Interest

The authors declared that there is no conflict of interest.

References

Abu-Jdayil B, Mourad AH, Hittini W, Hassan M, Hameedi, S. 2019. Traditional, state-of-the-art and renewable thermal building insulation materials: An overview. Constr Build Mater, 214: 709-735. https://doi.org/10.1016/j.conbuildmat.2019.04.102

Aburas M, Soebarto V, Williamson T, Liang R, Ebendorff-Heidepriem H, Wu Y. 2019. Thermochromic smart window technologies for building application: A review. Appl Ener, 255: 113522. https://doi.org/10.1016/j.apenergy.2019.113522

Aguilar-Santana JL, Hasila J, Velasco-Carrasco M, Riffat S. 2019. Review on window-glazing technologies and future prospects. Int. J Low-Carbon Technol, 15: 112-120. https://doi.org/10.1093/ijlct/ctz032

Al-Homoud MS 2005. Performance characteristics and practical applications of common building thermal insulation materials. Build Environ, 40(3): 353-366. https://doi.org/10.1016/j.buildenv.2004.05.013

Aksel H, Eren Ö. 2015. A Discussion on the advantages of steel structures in the context of sustainable construction. Int J Contemp Archit-The New ARCH, 2(3): 46-53.

Anh LDH, Pásztory Z. 2021. An overview of factors influencing thermal conductivity of building insulation materials. J Build Eng, 44: 102604. https://doi.org/10.1016/j.jobe.2021.102604

Brimacombe L, Shonfield P, Buridard M. 2001. Sustainability and steel recycling. SAE Tech Paper 2001-01-3766, URL: https://saemobilus.sae.org/papers/sustainability-steel-recycling-2001-01-3766 (accessed date: January 13, 2025). https://doi.org/10.4271/2001-01-3766

Broniewicz F, Broniewicz M. 2020. Sustainability of steel office buildings. Energies, 13(14): 3723. https://doi.org/10.3390/en13143723

Burgan BA, Sansom MR. 2006. Sustainable steel construction. J Constr Steel Res, 62(11): 1178-1183. https://doi.org/10.1016/j.jcsr.2006.06.029

Buschmeyer W, Fastabend M. 2004. Methods for raising sustainable design of concrete structures. Struct Eng Int, 14(3): 195-197. http://dx.doi.org/10.2749/101686604777963766

Castleton HF, Stovin V, Beck SBM, Davison JB. 2010. Green roofs; building energy savings and the potential for retrofit. Ener Build, 42(10): 1582-1591. https://doi.org/10.1016/j.enbuild.2010.05.004

Catalbas MC, Kocak B, Yenipınar B. 2021. Analysis of photovoltaic-green roofs in OSTIM industrial zone. Int J Hydrog Ener, 46(27): 14844-14856. https://doi.org/10.1016/j.ijhydene.2021.01.205

Environmentally Friendly Green Buildings Association. 2023. Yeşil bina. URL: https://cedbik.org/tr/yesil-bina-7-pg (accessed date: October 27, 2023).

Falk B. 2010. Wood as a sustainable building material. General Technical Report FPL–GTR–190. Madison, U.S. Dept. of Agriculture, Forest Service, Forest Products Laboratory, 2010: pp: 1.1-1.6. URL: https://research.fs.usda.gov/treesearch/37431 (accessed date: January 13, 2025).

Favoino F, Loonen RCGM, Michael M, Michele GD, Avesani S. 2022. 5 - Advanced fenestration—technologies, performance and building integration. In: Gasparri A, Brambilla B, Lobaccaro G, Goia F, Andaloro, A, Sangiorgio A, editors. Rethinking Building Skins. Woodhead Publishing, Sawston, Cambridge, UK, pp: 117-154. https://doi.org/10.1016/B978-0-12-822477-9.00038-3

Huberman N, Pearlmutter D, Gal E, Meir IA. 2015. Optimizing structural roof form for life-cycle energy efficiency. Ener Build, 104: 336-349, https://doi.org/10.1016/j.enbuild.2015.07.008

Jelle JP, Hynd A, Gustavsen A, Arasteh D, Goude H, Hart R. 2012. Fenestration of today and tomorrow: A state-of-the-art review and future research opportunities. Sol Ener Mater Sol Cells, 96: 1-28. https://doi.org/10.1016/j.solmat.2011.08.010

Khedari J, Pongsatirat C, Puangsombut W, Hirunlabh J. 2005. Experimental performance of a partially-glazed modified trombe wall. Int J Ambient Ener, 26(1): 27-36. https://doi.org/10.1080/01430750.2005.9674968

Kolb J. 2008. Systems in timber engineering: Loadbearing structures and component layers. In Lignum - Holzwirtschaft Schweiz and DGfH editors - German Society of Wood Research. Basel, Switzerland, pp: 257.

Kumar D, Alam M, Zou PXW, Sanjayan JG, Memon RA. 2020. Comparative analysis of building insulation material properties and performance. Renew Sustain Ener Rev, 131: 1364-0321. https://doi.org/10.1016/j.rser.2020.110038

Landolfo R, Cascini L, Portioli F. 2011. Sustainability of steel structures: towards an integrated approach to life-time engineering design. Front Archit Civ Eng China, 5: 304-314. https://doi.org/10.1007/s11709-011-0123-9

Leśniak A, Zima K. 2018. Cost calculation of construction projects including sustainability factors using the case based reasoning (CBR) method. Sustainability, 10(5): 1608. https://doi.org/10.3390/su10051608

Ma Q, Fukuda H, Wei X, Hariyadi A. 2019. Optimizing energy performance of a ventilated composite Trombe wall in an office building. Renew Ener, 134: 1285-1294. https://doi.org/10.1016/j.renene.2018.09.059

Simões N, Manaia M, Simões I. 2021. Energy performance of solar and Trombe walls in Mediterranean climates. Energy, 234: 121197. https://doi.org/10.1016/j.energy.2021.121197

Pargana N, Pinheiro MD, Silvestre, JD, Brito, J. 2014. Comparative environmental life cycle assessment of thermal insulation materials of buildings. Ener Build, 82: 466-481. https://doi.org/10.1016/j.enbuild.2014.05.057

Rossi B. 2014. Discussion on the use of stainless steel in constructions in view of sustainability. Thin-Walled Struct, 83: 182-189. https://doi.org/10.1016/j.tws.2014.01.021

Sadineni SB, Madala S, Boehm RF. 2011. Passive building energy savings: A review of building envelope components. Renew Sustain Ener Rev, 15(8): 3617-3631. https://doi.org/10.1016/j.rser.2011.07.014

Shafique M, Luo X, Zuo J. 2020. Photovoltaic-green roofs: A review of benefits, limitations, and trends. Sol Ener, 202: 485-497. https://doi.org/10.1016/j.solener.2020.02.10

Ministry of Foreign Affairs of the Republic of Turkey. 2023. Sürdürülebilir kalkınma. URL: https://www.mfa.gov.tr/surdurulebilir-kalkinma.tr.mfa (accessed date: January 13, 2025).

URL-1. The Edge Building Amsterdam, URL: https://plparchitecture.com/the-edge/ (accessed date: October 30, 2024)

URL-2. PLP unveils world's most sustainable office building, URL: https://archello.com/project/the-edge (accessed date: October 30, 2024).

URL-3. Davies' Alpine House, URL: https://daviesalpinehouse.weebly.com/environment.html (accessed date: October 30, 2024).

URL-4. Royal Botanic Gardens, URL: https://visitworldheritage.com/en/eu/davies-alpine-house/592a6e18-e183-41f6-86ad-98bc12482be0 (accessed date: October 30, 2024).

URL-5. Hawai'i Preparatory Academy | Energy Lab, URL: http://flansburgh.com/portfolio/hawai%CA%BBi-preparatory-academy-energy-lab/ (accessed date: October 30, 2024).

URL 6. Hawaii Prep Academy Energy Lab, URL: https://living-future.org/case-studies/hawaii-prep-academy-energy-lab-2/ (accessed date: October 30, 2024).

URL-7. The Crystal by Wilkinson Eyre Architects: A pavilion in a park, URL: https://www.re-thinkingthefuture.com/case-studies/a4224-the-crystal-by-wilkinson-eyre-architects-a pavilion-in-a-park/ (accessed date: October 30, 2024).

URL-8. The Crystal, URL: https://wilkinsoneyre.com/projects/the-crystal (accessed date: October 30, 2024).

URL-9. Izmir Adnan Menderes Airport New Domestic Terminal. URL: https://www.tucsa.org/en/celik_yapilar_yazi.aspx?yazi=462 (accessed date: October 30, 2024).

Wang H, Lei C. 2020. A numerical investigation of combined solar chimney and water wall for building ventilation and thermal comfort. Build Environ, 171: 106616. https://doi.org/10.1016/j.buildenv.2019.106616

Wang H, Lei C. 2019. Theoretical modeling of combined solar chimney and water wall for buildings. Ener Build, 187: 186-200. https://doi.org/10.1016/j.enbuild.2019.01.025

Wang N, Adeli H. 2014. Sustainable building design. J Civ Eng Manag, 20(1): 1-10. https://doi.org/10.3846/13923730.2013.871330

Wang P, Liu Z, Zhang L. 2021. Sustainability of compact cities: A review of inter-building effect on building energy and solar energy use. Sustain Cities Soc, 72: 103035. https://doi.org/10.1016/j.scs.2021.103035

Zheng Y, Weng Q. 2020. Modeling the effect of green roof systems and photovoltaic panels for building energy savings to mitigate climate change. Remote Sens, 12(15): 2402. https://doi.org/10.3390/rs12152402

Zilberberg E, Trapper P, Meir IA, Isaac S. 2021. The impact of thermal mass and insulation of building structure on energy efficiency. Ener Build, 241: 110954. https://doi.org/10.1016/j.enbuild.2021.110954

Black Sea Journal of Engineering and Science
doi: 10.34248/bsengineering.1606002

Open Access Journal
e-ISSN: 2619 – 8991

Araştırma Makalesi (Research Article)
Cilt 8 - Sayı 2: 496-506 / Mart 2025
(Volume 8 - Issue 2: 496-506 / March 2025)

KAMUSAL ALANLARIN SÜRDÜRÜLEBİLİRLİĞİ: CAMİ AVLUSUNUN AFET SONRASI ESNEK KULLANIMI ÜZERİNE BİR İNCELEME

Melih AK[1]*, Ceyda FESCİ[2], Ebru Melis ÖZDEMİR[3], Bedizhan BAŞKAN[4], Hilal AYCI[1]

[1]*Gazi University, Faculty of Architecture, Department of Architecture, 06000, Ankara, Türkiye*
[2]*Gazi University, Graduate School of Natural and Applied Sciences, Department of Architecture, 06500, Ankara, Türkiye*
[3]*Amasya University, Faculty of Architecture, Department of Restoration, 05100, Amasya, Türkiye*
[4]*Erciyes University, Faculty of Architecture, Department of Building Science, 38000, Kayseri, Türkiye*

Özet: Deprem, sel, yangın gibi doğal afetler ve salgınlar nüfusun yoğun olarak bulunduğu kentleri ve kentte yaşayan insanların hayatlarını önemli derecede etkilemektedir. Bu afetlere hazırlıklı olmak ve sonrasında ortaya çıkan ihtiyaçlara hızlıca cevap vermek, afet sonrası yönetim için son derece gereklidir. Afet sonrasında toplanma, geçici barınma gibi işlevlerde kullanılabilecek kentsel açık alanların kentleşmenin etkisiyle azalması, hatta yok olması başka potansiyel mekânlar bulma arayışını ortaya çıkarmaktadır. Bu bağlamda afet sonrası barınma ve benzeri ihtiyaçlar için kamusal yapıların ve açık alanlarının kullanılması; kısa süreliğine kullanılacak olan bu mekânların erişilebilir olması ve birçok konuda ihtiyaçları karşılama potansiyeli son derece önemlidir. Bu çalışma kapsamında kamusal bir yapı elemanı olan cami avlusunun deprem sonrasında kullanım potansiyelleri araştırılmıştır. Bu bağlamda olası bir deprem sonrası ortaya çıkabilecek fiziksel ve sosyal ihtiyaçlar belirlenerek; cami avlusunun elemanları bu ihtiyaçlar doğrultusunda esnek kullanım potansiyelleri bakımından değerlendirilmiştir. Çalışma sonucunda cami avlularının afet sonrası kullanımına yönelik potansiyelleri değerlendirilmiştir.

Anahtar kelimeler: Cami avlusu, Doğal afet, Esneklik, Deprem, Açık alan

Sustainability of Public Areas: A Study on the Post-Disaster Use of Mosque Courtyards

Abstract: Natural disasters such as earthquakes, floods, fires, and epidemics significantly impact densely populated cities and people's lives. Preparing for these disasters and responding quickly to subsequent needs are extremely necessary for post-disaster management. The decrease or even disappearance of urban open spaces that can be used for functions such as gathering and temporary shelter after disasters due to urbanization leads to the search for other potential spaces. In this context, the use of public buildings and open spaces for post-disaster shelter and similar needs, the accessibility of these spaces that will be used for a short period, and their potential to meet the needs in many areas are critical. Within the scope of this study, the utilization potentials of the mosque courtyard, a public building element, were investigated after the earthquake. In this context, the physical and social needs that may arise after a possible earthquake were determined within the scope of the study, and the potential use of mosque courtyard elements for these needs was evaluated. As a result of the study, mosque courtyards potential to be assessed for post-disaster use.

Keywords: Mosque courtyard, Natural disaster, Flexibility, Earthquake, Open space

***Sorumlu yazar (Corresponding author):** Gazi University, Faculty of Architecture, Department of Architecture, 06500, Ankara, Turkey
E mail: melihak@gazi.edu.tr (M. AK)
Melih AK https://orcid.org/0000-0002-6296-8063
Ceyda FESCİ https://orcid.org/0000-0002-0202-7886
Ebru Melis ÖZDEMİR https://orcid.org/0000-0002-4882-7520
Bedizhan BAŞKAN https://orcid.org/0000-0002-2609-7790
Hilal AYCI https://orcid.org/0000-0001-5101-4873

Gönderi: 23 Aralık 2024 **Kabul:** 05 Şubat 2025 **Yayınlanma:** 15 Mart 2025
Received: December 23, 2024 **Accepted:** February 05, 2025 **Published:** March 15, 2025

Cite as: Ak M, Fesci C, Özdemir EM, Başkan B, Aycı H. 2025. Sustainability of public areas: A study on the post-disaster use of mosque courtyards. BSJ Eng Sci, 8(2): 496-506.

1. Giriş

Doğal afetler sonrasında afetzedelerin kısa sürede ulaşabileceği, fiziksel ve sosyal ihtiyaçlarını karşılayabileceği toplanma alanları günümüz kentlerinin olmazsa olmazı haline gelmiştir. Afet sonrası ortaya çıkabilecek en önemli problemlerden biri bu toplanma alanlarının nasıl tasarlanacağıdır. Afetzedeler bulundukları yapılardan uzaklaşarak, kentlerdeki yoğun yapılaşmanın içerisinde yer alan kentsel boşlukları, kamusal alanları, açık ve yeşil alanları tercih ederek bu alanları geçici olarak farklı işlevlerle kullanmaktadır. Bu alanlar afet sırasında ya da sonrasında toplanma alanı olarak kullanıldığı için kolay erişilebilir, yeterli büyüklüğe sahip ve geçici barınmaya olanaklı olması gerekmektedir. Afet sırasında kamusal alanın sadece acil durumda değil aynı zamanda yeniden inşa aşamasında da son derece önemli bir rolü vardır. Sokaklar ve meydanlar sadece barınak olarak değil, aynı zamanda yiyecek toplama ve yeniden inşa çalışmaları için stratejik noktalar olarak da kullanılabilir (Montejano ve Moreno, 2016). Toplanma alanlarının önemi yaşanılan afetler ve sonrasında elde edilen verilerle tartışılmaz bir konu

This work is licensed (CC BY-NC 4.0) under Creative Commons Attribution 4.0 International License

haline gelmiştir. 1906 yılında gerçekleşen San Francisco depremi ve ardından ortaya çıkan yangının, Şili'nin Concepción şehrinde 1835 yılında yaşanan büyük deprem ve depremin etkisiyle oluşan tsunaminin olumsuz etkilerinden korunmada kentteki toplanma alanlarının etkili olduğu tespit edilmiştir (Allan ve Bryant, 2011). Bu bağlamda toplanma alanları, afet sonrası durumlarda afetzedelerin güvenli bir şekilde ulaşabildiği temel ihtiyaçlarına cevap veren alanlar olarak tanımlanabilir. Bu alanlar, afet sonrasında hızlı bir şekilde toplanma ve barınma amacıyla kullanılan, ilk yardım gibi hizmetlerin verildiği, temel ihtiyaçların karşılandığı güvenli alanlardır. Deprem sonrası sürecin minimum hasar ve kayıpla atlatılabilmesi için bu alanların etkin ve doğru şekilde planlanması ve tasarlanması gerekmektedir (Uyar ve Özkan, 2023). Afetler ve kentsel/yapısal etkileri birçok çalışmada ele alınmıştır (Halı Kabataş vd., 2023; Saçlı vd., 2023; Gökşen vd., 2024). Bu çalışmada ise 6 Şubat 2023 tarihinde Türkiye'de gerçekleşen deprem sonrasında yaşanan kamusal alanda koordinasyon mekânlarının sorunları üzerine (Yılmaz vd., 2023) cami avlularının esnek kullanım potansiyelleri soruşturulmaktadır.

6 Şubat 2023'te Türkiye'de yaşanan, çevre illerde de büyük çaplı yıkıma neden olan Kahramanmaraş merkezli deprem sonrasında birçok ilde koordinasyon merkezi eksikliği yaşanmıştır. Karakuş'un aktardığına göre koordinasyon merkezi eksikliği yaşanan Adıyaman'da, Adıyaman Üniversitesi İktisadi ve İdari Bilimler Fakültesi binası koordinasyon merkezi olarak kullanılmıştır. Bu durum deprem sonrası koordinasyonun sağlanacağı merkezin konumu, güvenliği ve temel ihtiyaçlara cevap verebiliyor olmasının deprem sonrası acil ihtiyaçların yönetimi açısından ne kadar önemli olduğunu göstermektedir. Buradan hareketle bu çalışma kapsamında merkezi konumdaki cami avlularının koordinasyon merkezi olarak kullanımı, afetzedelerin fiziksel ve sosyal ihtiyaçlarını karşılama potansiyelleri esnek kullanım bağlamında araştırılmaktadır.

2. Materyal ve Yöntem

Bu çalışma kapsamında cami avlularının güncel esnek kullanım durumları ve afet sonrasındaki kullanım potansiyelleri incelenmiştir. Olası bir afet durumunda cami avlularının hangi fiziksel ve sosyal ihtiyaçları karşılayabileceği soruşturulmuştur. Afet anındaki fiziksel ihtiyaçlar toplanma alanı, barınma, ilk yardım (acil müdahale), depolama alanı, yemek, temiz su (içme suyu), tıbbi bakım, erişilebilirlik ve dağıtım olarak; sosyal ihtiyaçlar ise sosyal hizmetler, eğitim/bilgilendirme, güvenlik, danışma ve kişisel bakım olarak sıralanabilir (Kılıç Özkaynar, 2023). Aynı zamanda sosyal birer odak noktası olan cami avluları gündelik hayatta ibadet mekânı, sosyal mekân, buluşma mekânı, ibadete hazırlık, temizlik-hijyen, çocuk oyun alanları gibi amaçlar için kullanılmaktadır. Bu bağlamda çalışmanın konusunu da oluşturan camilerin avluları afet sonrasında kullanım için önem kazanmaktadır. Bununla birlikte doğrudan avluların kullanımı işaret edilmese de camilerin afet sonrası kullanımına yönelik öneriler Diyanet İşleri Başkanlığı'nın tasarım kılavuzu kapsamında da vurgulanmaktadır. Kamusal yapı olarak nitelendirilebilecek camilerin afet sonrasında kullanımına dair veriler Cumhurbaşkanlığı Diyanet İşleri Başkanlığının Cami Planlama ve Tasarımı Kılavuzu'nda şu maddelerle yer almaktadır:

- Madde 1.2. Yer seçim ilkeleri başlığının h alt maddesi "Camiler, olası doğal afet veya seferberlik durumlarında toplanmaya yönelik ihtiyacı karşılayabilecek konumlarda yer almalıdır" (T.C. Cumhurbaşkanlığı Diyanet İşleri Başkanlığının Cami Planlama ve Tasarımı Kılavuzu, 2021).
- Madde 2.6. Statik sistem başlığının d maddesi "Camiler, kullanım amaçları göz önüne alındığında herhangi bir afet sonrasında toplanma alanı ve sığınma yeri olarak kullanılacağı öngörülerek tasarlanmalı ve üst düzeyde yapı güvenliği tesisi açısından statik hesaplamalarda hassasiyet gösterilmelidir" (T. C. Cumhurbaşkanlığı Diyanet İşleri Başkanlığının Cami Planlama ve Tasarımı Kılavuzu, 2021).

Bu maddeler de göz önünde bulundurulduğunda, afet sonrası acil durumlarda cami avlularının kullanılmasına önem verilmesi ve yeni inşa edilecek camilerde avlu tartışmasının bu bağlam çerçevesinde yapılması çalışma için önem arz etmektedir. Bu amaçla çalışmada ilk önce konuyla ilgili yapılmış çalışmalar üzerinden literatür taraması yapılmıştır. Ayrıca deprem sonrası ortaya çıkan ve tespit edilen fiziksel ve sosyal ihtiyaçlar belirlenerek (Ünkaracalar ve Aycı, 2023; Melikeoğlu ve Kayıhan, 2023) giriş kapısı (taçkapı), açık alan, yarı açık alan (revak ve son cemaat yeri), su öğesi (havuz-şadırvan), ıslak hacim gibi avlu elemanlarının bu ihtiyaçlar için kullanım potansiyelleri değerlendirilmiştir. Çalışmanın son bölümünde; bu değerlendirmeler sonucunda elde edilen veriler tablolaştırılmış ve cami avlularının afet sonrası fiziksel ve sosyal ihtiyaçların karşılanmasına yönelik potansiyelleri analiz edilmiştir.

2.1. Literatür Araştırması

Literatürde avlunun yeri incelendiğinde farklı yapı türlerinde farklı işlevlerle tasarlandığı görülmektedir. Hititlere başkentlik yapmış olan Boğazköy'de avlunun çarşı meydanı olarak karşımıza çıkması, İslamiyet'in farklı dönemlerinde hazire bölümünün avluda bulunması, revakların dini eğitimlerin verildiği mekânlara dönüşmesi, mahkemelerin bu kamusal alanlarda görülmesi, önemli duyuruların halka bu alanlarda bildirilmesi bu veriyi doğrulamaktadır (Okuyucu, 2011). Tarihsel süreç içerisinde incelendiğinde avlu, iç ve dış mekânların birbiriyle olan ilişkilerini sağlayarak iç mekânların dış mekânlarla, dış mekânların da iç mekânlarla bağlantısını kurmuştur (Erdoğan, 1996). Avluların işlevsel, biçimsel ve simgesel değerleri bir mimari yapıyı tasarlarken önemli birer kriter olarak karşımıza çıkmaktadır. Bu kriterler

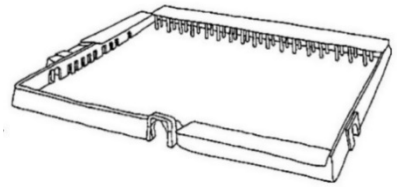
mekânsal kurgu çözümlenirken önemli derecede etkili olmuştur ve mekânsal çözümlemede kolaylık sağlamıştır. Tarihi yapı olarak nitelendirilebilecek mimari eserlerde avlu tasarım programına dahil edildiğinde yapı formunu etkileyen temel elemanlardan biri olarak karşımıza çıkmaktadır (Özbudak Akça ve Halifeoğlu, 2018).

2.1.1. Avlu ve caminin tarihi

Avlu, bir yapı veya yapı organizasyonunun genellikle çekirdeğini oluşturan mimari özelliklerine bağlı olarak revaklı avlu, şadırvan avlusu, dış avlu gibi çeşitli isimlendirmelerle anılan önemli bir mimari öğedir. Üstü açık ya da kapalı olabilen avlular, gölgeli revakları, merkezinde yer alan havuz ve şadırvanlarıyla Türk ve İslam mimarisinin temel unsurları arasında yer almaktadır (Cantay, 1991; Ak ve Karamağaralı, 2023). Toplayıcı ve dağıtıcı bir eleman olan avlular yapıdaki konumuna göre ön avlu, arka avlu, iç avlu, yan avlu şeklinde tanımlanabilir. Cami avlusu, herkese açık bir dış mekân niteliğine sahip olmasına rağmen, cami kompleksi içinde içselleşen bir mekân öğesidir (Aydın, 2000). Bununla birlikte hem ortak hem özel kullanıma açık olduğu için cami avluları yarı kamusal avlu olarak nitelendirilebilir.

Mimari eleman olarak avlunun kökeni Neolitik Çağ'a kadar uzanmaktadır. Bununla birlikte Mezopotamya konutlarında coğrafi koşullara bağlı olarak iç avlunun varlığı bilinmektedir. Hitit, Helen, Mısır, Roma gibi uygarlıklarda birçok farklı yapı tipinde yine avlu kullanımı karşımıza çıkmaktadır (Özköse, 1995). Türk mimarisinde ise avlu kavramı İslamiyet öncesinde Göktürk Dönemi'ne tarihlenen mezar külliyelerinde, Uygur Dönemi'ne tarihlenen Budist tapınaklarında ve hanlarda karşımıza çıkmaktadır. Türklerin İslamiyet'i kabulünden sonra da cami, medrese, han, kervansaray, saray, konut gibi birçok yapı türünde avlu kullanılmaya devam etmiştir (Ak ve Karamağaralı, 2023).

Camiler "toplanılan yer" anlamına gelmektedir. Camilerde bulunan avlular ibadetin yanı sıra sosyal ve kültürel işlevleri de barındırarak camilerin birer toplanma mekânı olmasında kritik bir role sahiptir (Güleç Demirel ve Kara Pilehvarian, 2018). Camide avlu kavramı Hz. Muhammed'in evi olarak nitelendirilen, aslında çok fonksiyonlu bir yapı ile karşımıza çıkmaktadır. Bilinen ilk cami olan bu yapı yerleşim alanı büyük olduğu için hem bir toplanma alanı hem de Hz. Muhammed'in ailesinin kaldığı özelleşmiş bir mekân olarak kullanılmaktaydı. Bunun yanında bu komplekste kimsesiz yoksulların da barındığı bilinmektedir. Yapıda bulunan çeşitli derinlikteki revak olarak nitelendirilebilecek mekânlar kötü hava koşullarına karşı cemaati korumaktadır. Yapının avlusunun da toplu ibadetler ve eğitimler için kullanılmakta olduğu düşünülmektedir. Bu bağlamda cami avlusunun işlevleri gölge ve ışık sağlama, cemaati karşılama ve toplanma şeklinde sıralanabilir. Aynı zamanda avlu camiye gelen insanların buluşma ve sosyalleşme yeridir. İktidarın simgesi haline gelen, resmî açıklamaların da yapıldığı cami avlusu, eğitim, hastane ve sığınak gibi işlevlerle de zaman zaman kullanılmıştır (Özköse, 1995; Grabar, 2007: 41).

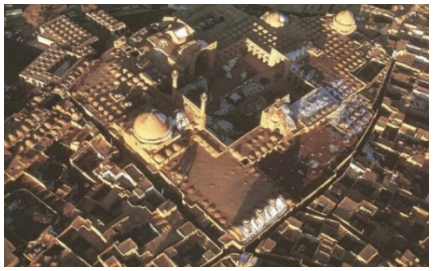


Şekil 1. Hz. Muhammed'in Medine'deki Evinin (Mescid-i Nebevi) Sonradan Yapılmış Bir Çizimi (Grabar, 2007).

Türk cami mimarisinde avlu kavramı merkezindeki havuz-şadırvanı ile birlikte ilk olarak Tolunoğlu Ahmed Camii'nde karşımıza çıkmaktadır. Karahanlı eseri olan ve Türk cami mimarisinde önemli bir yeri olan Talhatan Baba Camii de avlulu plana sahiptir. Avlu Büyük Selçuklu Dönemi'ne gelindiğinde ise artık simgesel bir değer kazanmıştır. Dört eyvanlı avluda eyvanlardan geçen eksenlerin kesiştiği yere bir de havuz-şadırvan eklenmiştir (Ak, 2022; Akgül (Karamağaralı), 1997).



Şekil 2. Tolunoğlu Ahmed Camii revaklı avlusu (Yetkin, 1984).



Şekil 3. İsfahan Cuma Camii (Blair ve Bloom, 2007).

Bir mikrokozmos temsili olan dört eyvanlı ve merkez vurgulu avlu planının kökeni çok eskiye dayanmaktadır. Gazneli saraylarında, Büyük Selçuklu medreselerinde; İsfahan, Ardistan, Zevvare ve Gülpayegan Camilerinde anıtsal düzeye ulaşmış merkezi avlulu mekân düzeni Anadolu'da medrese, şifahane ve kervansaraylarda benzer şekilde karşımıza çıkmaktadır (Ögel, 1994). Büyük Selçuklularda 12. yüzyılda başlayan, camide dört eyvanlı avlu kullanımı simgesel boyutuyla birlikte cami mimarisinde çok önemli bir yere sahiptir (Akın, 1990).

Anadolu Selçuklu camilerinde ise eyvanlı avlulu şema bir temsil niteliğine indirgenmiştir. Bu temsiliyet aydınlık fenerli kubbe ve altında bulunan havuzla gerçekleşmektedir (Ögel, 1994; Akgül (Karamağaralı), 1997; Ak, 2022). Bu aydınlık açıklıklı birimin en önemli

işlevlerinden biri yeterince aydınlatılamayan Anadolu Selçuklu ulu camilerinin aydınlatma problemini çözmektir. Bir aydınlatma elemanı olarak nitelendirilebilecek bu aydınlık fenerlerinin altında bulunan havuz, aydınlık açıklığından gelen ışığı yansıtarak ikinci bir aydınlatma elemanına dönüşmektedir. Bu havuzun durağan suyu, ışığı yansıtarak mekânın aydınlatılmasına katkıda bulunmaktadır. Aydınlık fenerli ve havuzlu bu birimin yapının merkezinde konumlandırılmasında mekânın eşit bir şekilde aydınlatılma amacı da yatmaktadır. Aynı zamanda bu su elemanı çıkardığı ses ile mekânı huzurlu ve sakin kıldığı gibi, mekânın iklimlendirilmesinde de önemli katkıları vardır. Bu plan tipi olgunlaşarak Erken Osmanlı Dönemi eseri olan Bursa Ulu Camii'nde en olgun halini almıştır (Ak, 2022).



(a) (b) (c)

Şekil 4. (a) Bursa Ulu Camii aydınlık açıklıklı birim (Melih Ak Arşivi), (b) Üç Şerefeli Camii revaklı avlusu (Melih Ak Arşivi), (c) Selimiye Camii kesitli aksonometri (Kuban, 2007).

2.1.2. Cami avlusunun kent merkezindeki yeri ve esnek kullanımı

Ulu camiler Türk kentlerinin merkezinde bulunmaktadır ve kent, ulu camilerin etrafında gelişmektedir (Çelik, 1993). İbadet gereği günün beş vaktinde toplanılan bir merkez olan camiler, bu toplanma eyleminin bir sonucu olarak toplum hayatında önemli bir yer edinmiştir. Camilerin avlularında ibadetin yanında, cenaze ve bayramlaşma merasimleri de düzenlenmektedir. Tarihsel süreçte baktığımızda bu avlularda pazarların kurulduğu, insanların alışveriş yaptığı, sosyalleştiği ve hatta mahkemelerin kurulduğu bilinmektedir. Dönemin sanatçıları tarafından yapılan resim ve gravürlerde de bu anlatıları görebilmekteyiz. 1843 yılında Ressam Preziosi'nin yaptığı bir resimde Beyazıt Camii'nin avlusunda satış için tezgâhların kurulduğu ve halkın alışveriş yaptığı görülmektedir (Güleç Demirel ve Kara Pilehvarian, 2018).



Şekil 5. Ressam Preziosi'nin 1843 yılında yaptığı Beyazıt Camii avlusunu gösteren resim (Güleç Demirel ve Kara Pilehvarian, 2018).

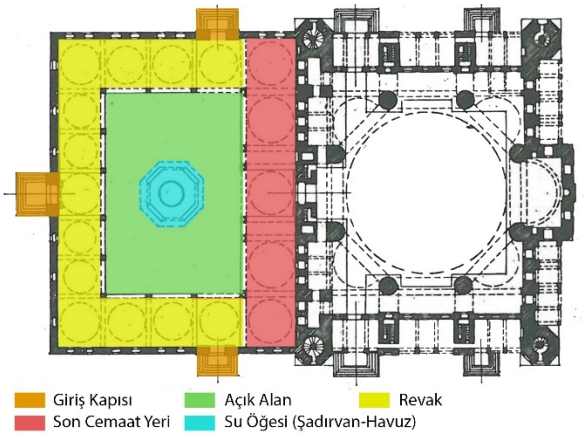


Şekil 6. Şehzade Camii revaklı avlusu (Melih Ak Arşivi).

Cami avluları incelendiğinde avlu elemanları giriş kapısı (taçkapı) açık alan, yarı açık alan (revak ve son cemaat yeri), su öğeleri (havuz-şadırvan) ve ıslak hacim şeklinde sıralanabilir. Cami mimarisinde giriş kapısı (taçkapı), genellikle caminin ana giriş kapısını vurgulayan bir mimari unsur olarak karşımıza çıkmaktadır. Taçkapılar, Selçuklu ve Osmanlı dönemlerinde İslam mimarisinin karakteristik özelliklerinden biri olarak öne çıkmaktadır. Çoğunlukla geometrik motifler, bitkisel süslemeler, mukarnaslar ve kitabelerle bezeli olan bu girişler, yapının ihtişamını ve sanatsal detaylarını sergilemektedir. Giriş kapıları (taçkapılar), hem estetik bir odak noktası oluşturur hem de ziyaretçiyi kutsal mekâna yönlendiren sembolik bir geçit görevi görür. Revak ise genellikle ön yüzü kemerli ve açık, arkası duvarla kapalı, üstü tonoz, kubbe veya düz tavanla örtülü galeriler şeklinde tanımlanabilir. Revaklar etrafı duvarlarla çevrili korunaklı bir alan haline gelen avlunun çeperinde daha

özelleşmiş alanlar oluşturmaktadır. Bu alanlar günümüzde güneşten ve yağmurdan korunmak için veya cemaat camiye sığmadığında ibadet için kullanılmaktadır. Hatta harimin cephesine bitişik olan revaklar son cemaat yeri olarak tanımlanmaktadır ve namaza geç kalanlar bu alanda namaza durmaktadır. Avlunun bir diğer önemli elemanı olan havuz-şadırvanlar ortasında yüksekçe bir yerden su akan, havuzu veya çevresinde abdest almak için musluk bulunan çevresi duvarla çevrilmiş su haznesi olarak tanımlanabilir. Şadırvanların abdest almak için camilerin iç avlularına yapılan, üstü açık veya kapalı şekilleri de bulunmaktadır (Hasol, 1990).

Avluların diğer bileşenleri olan açık alan ve peyzaj öğeleri, diğer elemanlardan birbirine geçiş ve mekânsal akış için önem arz etmektedir. Mekânı kullanan insanları yönlendirmesi, onlara birer toplanma veya sosyalleşme yeri oluşturması açısından avludaki açık alan ve diğer peyzaj öğeleri önemli birer eleman olarak karşımıza çıkmaktadır. Islak hacimler benzer şekilde ibadetin ön şartlarını yerine getirebilmek için cami kompleksinde olmazsa olmaz yapılardan biridir. Yapıdaki konumu oldukça önemli olan bu birim kolay ulaşılır olmalıdır.



Şekil 7. Selimiye camii planı (Aslanapa, 1989) üzerinden avlu elemanlarının gösterimi.

Kentin merkezinde kendine yer bulan ve toplumun hafızasında bir toplanma mekânı olarak yer edinmiş camiler tüm bu elemanlarıyla bizlere toplumsal yaşam için önemli potansiyeller sunmaktadır. Bu bağlamda cami avlusu toplumsal hayatta sosyal bir mekân olarak kullanılmasının yanında afet durumlarında da kullanılabilir bir mekân öğesidir. Olası bir afet sonrasında cami avlularının kullanımı birçok avantaj sağladığı gibi dezavantajları da mevcuttur. Avlulu camilerin tüm kentlerde olması, günlük yaşamda aktif olarak kullanılması, çevreden kolay algılanabilir olması afet sonrası kullanım için bu yapıları avantajlı kılmaktadır. Açık ve yarı açık alanlara sahip olan bu cami avluları afet sonrasında ortaya çıkabilecek toplanma, geçici barınma, su ihtiyacı, tuvalet ihtiyacı gibi temel ihtiyaçları karşılayabilecek potansiyele sahiptir. Bununla birlikte yüksek kütle ve minaresi, mülkiyetinin kimde olduğu (diyanet, vakıflar, dernekler, belediyeler, özel şahıslar vb.), konumu ve çevre yapılanması (tarihi bir kent merkezinde bulunması) ile afet sonrası kullanım için dezavantajları da mevcuttur (Tablo 1).

Tablo 1. Cami avlusunun afet sonrası kullanımı için ortaya çıkan avantajlar ve dezavantajlar

Avantajlar	Dezavantajlar
Çevreden Kolay Algılanabilir Olma	Yüksek Kütle ve Yüksek Minare
Açık ve Yarı Açık Alana Sahip Olma	Mülkiyet Problemi
Su Elemanının (Havuz-Şadırvan) Bulunması	Konumu ve Çevre Yapılanması
Toplanma ve Geçici Barınmaya Olanak Sağlaması	
Kentte Odak Noktasında Yer Alma	
Günlük Yaşamda Aktif Olarak Kullanılma	

Camilerden bağımsız olarak avluların kentsel avlu bağlamında son dönem kullanımlarına bakıldığında birçok farklı amaçla kullanıldığı görülmektedir. Özellikle esneklik kavramının kentsel alanda avlu ile birlikte kullanıldığı ilk yerleşim yerlerinden bu yana avluların tarihte kent merkezi, pazar yeri, kutsal mekân, toplanma alanı gibi birçok işlevi aynı anda barındırabilen esnek mekânlar olduğu görülmektedir. Tarihsel süreçte birbirinden farklı amaçlarla kullanılan kentsel avlular bu özelliklerini günümüzde de sürdürmektedir. Literatürde kentsel açık mekânların sürdürülebilirlik kapsamında değişen yaşam koşullarına uygun olarak esnek tasarlanmasının gerekliliğini vurgulayan (Sınmaz, 2015) ve tasarım önerileri sunan çalışmalar (Alpak ve Düzenli 2018; Bayramoğlu ve Cındık Akıncı 2018; Sanei vd., 2018) bulunmaktadır. Bu çalışmalara ek olarak kentsel açık alanların salgın, doğal afet gibi acil durumlarda kullanım senaryolarına yönelik yapılan çalışmalarda (Sepe, 2021; Özdede vd., 2021; Doostvandi vd., 2022) esnek tasarımın ön plana çıkarıldığı görülmektedir.

Birçok araştırmaya konu olan avlular özellikle son dönemlerde sürdürülebilirlik ve esneklik kavramıyla ilişkilendirilmektedir. Son beş yılda avlu üzerine yapılan tez çalışmaları incelendiğinde avluların sürdürülebilirlik bağlamında çoğunlukla enerji verimliliği, termal konfor gibi kavramlar çerçevesinde incelendiği çalışmalar karşımıza çıkmaktadır (Çelik, 2022; Elfallah, 2023, Mousighichi, 2023). Son dönemlerde yapılmış olan uluslararası çalışmalarda da benzer şekilde avlularda esneklik, değişen iklimsel şartlara uyum sağlayabilme anlamında kullanıldığı örnekler çoğunluktadır. Örneğin Wang vd. (2024) Çin'in kıyı bölgelerindeki avlulu yerleşimlerin rüzgâr etkisini nasıl etkilediğini, Zhang vd. (2024) Çin'de geleneksel avlulu konutların iklim

şartlarına uyumunu ve stratejik uygulamayı etkileyen faktörleri simülasyon yöntemiyle araştırmıştır. Fesci ve Aycı (2024) çalışmalarında bibliyometrik analiz yöntemiyle avluların esnek kullanımına yönelik yapılan çalışmalarda esneklik kavramının daha çok değişen iklimsel şartlara uyarlanabilirlik anlamında ele aldığını belirtmişlerdir. Bulgulara göre çalışmalarda ele alınan avluların çoğunlukla geleneksel konut dokusundaki avlular olduğu dikkat çekmektedir. Avluların kentsel kimlikleri ve gündelik yaşamdaki rolleri geri planda bırakılmıştır.

Literatürdeki bu incelemeler sonucunda avluların sürdürülebilirliğinin kentsel kamusal mekân özellikleri ile kentsel yaşama katkısı çerçevesinde tartışılması gerekliliği ortaya çıkmaktadır. Buradan hareketle bu çalışmada kentin etrafında şekillendiği açık kamusal alan olarak cami avlularının esnek kullanım potansiyelleri incelenmektedir.

3. Bulgular

Cami avlularının afet sonrası kullanımına yönelik potansiyel analizleri incelendiğinde;

Yeri ve zamanı öngörülemeyen afet durumlarında en önemli önlem afetlere hazırlıklı olmaktır. Kent ölçeğinde yapılan planlamalarda afet öncesi ve sonrası süreçler göz önüne alınması gerektiği gibi afet esnasındaki süreci yönetmek de büyük önem teşkil etmektedir. Afet öncesi acil kurtarma ve yardım için hazırlıkların etkin bir biçimde yapılması, afet esnasında kentlilerin toplanması ve afet sonrasında da geçici barınma ihtiyaçlarını karşılamaya yönelik stratejilerin üretilmesine yönelik ihtiyaç bulunmaktadır. Acil durumlarda tahliye, geçici barınma gibi işlevlerde kullanılabilecek kentsel boşlukların günümüz kentlerinde hızlı kentleşmenin etkisiyle azalması, hatta yok olması başka potansiyel mekânlar bulma arayışını ortaya çıkarmaktadır (Zengin Çelik vd., 2017). Bu alanlar afet durumuna bağlı olarak sadece toplanma alanı olarak değil, ayrıca afete maruz kalan bireylerin bilgi alması, ilk yardım uygulamalarından ve yardımlardan yararlanması, gerektiği durumda geçici barınma alanlarına yönlendirilmesi gibi faaliyetlerin de yürütüldüğü alanlar olmaktadır (Japon Uluslararası İşbirliği Ajansı ve İstanbul Büyükşehir Belediyesi, 2002; Aksoy vd., 2009; Çınar vd., 2018; Gerdan ve Şen, 2019). Çalışmanın bu bölümünde acil durumlarda ortaya çıkan erişilebilirlik-ulaşılabilirlik, ilk toplanma, acil barınma, ilk yardım, depolama-tedarik, dağıtım, temiz su, ıslak hacim ve alt yapı gibi fiziksel; psikososyal hizmetler, eğitim-bilgilendirme ve güvenlik gibi sosyal ihtiyaçlar analiz edilerek, cami avlularının bu ihtiyaçlara cevap verebilme potansiyelleri tablolaştırılarak incelenmiştir.

3.1. Fiziksel İhtiyaçlar

3.1.1. Erişilebilirlik - ulaşılabilirlik

Afet durumunda toplanma alanı olarak kullanılacak alanların kentliler tarafından kolay ve güvenli bir şekilde erişilebilir olması gerekmektedir. Bu durumda toplanma alanlarının çevresindeki yapılara çok yakın olmaması aynı zamanda da yürüyüş mesafesinde olması oldukça önemlidir (Çınar vd., 2018). Buradan hareketle kentlerde tek bir toplanma noktası seçilmesi yerine mahalle gibi küçük ölçekli kent birimlerinde toplanma alanlarının belirlenmesi gerekmektedir (Maral vd., 2015). Hemen her mahallede birden fazla sayıda bulunan camiler, kentte kolay ulaşılabilen ve simge yapılar olmaları nedeniyle acil durumlarda toplanmak için başvurulan mekân olma potansiyeli taşımaktadır. Ayrıca alanların yiyecek, içecek ve diğer tedarik edilmesi gerekli malzemelerin temini için, market, depo gibi noktalara yakınlığı da oldukça önemlidir (Özdemir, 2002). Camilerin genellikle merkezi noktalarda konumlanmaları; afet anında ulaşım ağı üzerinden gelecek yardımlara, gerekli malzemelere, sağlık kuruluşlarına, erişimin kolay olmasını sağlamaktadır. Avluların giriş kapılarının genellikle geniş ve yüksek tasarlanmış olması da erzak, kıyafet gibi ihtiyaçların, çadırların, gerekli tıbbi malzemelerin taşınmasına olanak tanımaktadır.

3.1.2. İlk Toplanma

Özellikle deprem gibi afetlerde insanların ilk tepkisi yapılı alanlardan uzaklaşmak ve açık alanlara yönelmektir. Bu durumda kamusal açık alanlar acil sığınma ve tahliye alanı olarak görülmektedir (Atalay, 2008). Ancak zamanı, yeri öngörülemeyen afetlerin hangi hava koşullarında gerçekleşeceği ve sonrasında gündelik yaşama ne kadar süre içinde dönülebileceği de belirsizdir. Bu nedenle toplanma alanının salt açık mekâna değil aynı zamanda kapalı ve yarı açık mekân kurgusuna da sahip olması avantajlı bir durumdur (Erdin vd., 2023). Bu bağlamda merkezindeki açık alanı ve onu çevreleyen revaklı yarı açık mekân kurgusuna sahip cami avlusu, afet sonrası ilk toplanma alanı olarak kullanım potansiyeline sahiptir. Mekân kurgusundaki bu çeşitlilik avlunun birden çok amaçla kullanımına da olanak tanımaktadır. Ayrıca kent ile cami kütlesi arasında geçiş mekânı niteliğinde olan avlular, güvenli sınırlar içinde korunmaya olanak sağlamaktadır.

3.1.3. Barınma

Afet durumunda konutları zarar gören insanların özellikle ilk birkaç gün acil barınma ihtiyacı ortaya çıkmaktadır. Toplanma alanlarının gerektiğinde bu ihtiyaca da cevap verebilmesi önemlidir (Atalay, 2008). Kentteki mevcut yapılaşmanın afet sonrası kullanışsız hale gelmesi durumunda, barınma için ilk çözümler genellikle kentsel açık alanlarda kurulan çadır ve konteyner gibi geçici strüktürel yapılar olmaktadır (Özdemir, 2002). Cami avlusunda yer alan yarı açık mekân kurgusundaki revaklar, geçici strüktürel elemanlar ile kapalı birimler oluşturularak kullanılabilir. Böylece yardımlar bölgeye ulaşana kadar geçen süreçte geçici barınma ve çeşitli mekân ihtiyaçları karşılanabilir. Revaklarda gerektiğinde kaldırılabilen mobilyalar tasarlanarak bu mobilyalar afet anında oturma/yatma birimleri, sedye ya da gündelik yaşamda oturma, stant gibi birimler olarak kullanılabilir. Gerekli kapasiteyi sağlayabilecek büyüklükte olan cami avlularında sert

zemin üzerine barınma ve diğer ihtiyaçlar için kullanılabilecek çadırların kurulması mümkündür.

3.1.4. İlk Yardım ve Tıbbi Bakım

Yardımlar bölgeye ulaşana kadar tıbbi müdahalelerin gerçekleşmesi için toplanma alanları kullanılmaktadır. İlk yardım müdahalelerinin ve sonraki süreçte gerekecek tıbbi bakımın tamamen açık alanlarda yapılması iklim ve hava koşulları, mahremiyet gibi sebeplerden ötürü her zaman mümkün olmamaktadır. Bu durumda özel ya da yarı özel mekânlara ihtiyaç duyulmaktadır. Ayrıca yaraların ve sağlık ekipmanlarının temizlenmesi gerekliliği düşünüldüğünde temiz su hem hijyen hem de sağlık amaçlı önem kazanmaktadır. Toplanma alanında temiz su ihtiyacını karşılayacak birimlerin bulunması gerekmektedir (Erdin vd., 2023). Cami avlularında yarı açık ve tek katlı kapalı birimlerin olması ilk yardım müdahalelerinin yapılması için olanak sunmaktadır. Özellikle afet sonrası kritik zaman diliminde cami avlularında inşa edilen tek katlı ıslak hacim birimleri önem kazanmaktadır. Ayrıca abdest almak ve temizlik için kullanılan şadırvanlar hijyen ihtiyacını karşılamak için kullanılabilir.

3.1.5. Depolama ve Tedarik

Yeri, zamanı, şiddeti ön görülemeyen ve insan eliyle engellenemeyen afet durumunda hazırlıklı olmak büyük önem taşımaktadır. Afet durumunda oluşan hasar, bölgeye ulaşacak yardımları aksatabilmektedir. İlk yardım malzemeleri, erzak, kıyafet yardımlarının halihazırda bir depoda bulunması en azından bir ya da birkaç günün rahat geçirilmesine olanak sağlayacaktır. Bu nedenle uzun süre muhafaza edilebilecek malzemelerin (kıyafet, battaniye, ilk yardım malzemeleri, hazır yiyecekler gibi) belirli noktalarda depolanması afet anında önem kazanmaktadır (Önsüz ve Işıktekin Atalay, 2015). Bu bağlamda cami avlularındaki tek katlı kapalı birimlerde olası afet durumunda kullanılmak üzere gerekli malzemelerin depolanabileceği mekânlar oluşturulabilir.

3.1.6. Dağıtım

Gerekli yardım malzemeleri afet durumu bölgesine ulaştığında dağıtım; kentlilerin barındıkları alana yakın, kolay ulaşabilir merkezi noktalarda gerçekleştirilmelidir. Bu bağlamda toplanma alanı olma potansiyeli yüksek olan cami avlularında yer alan açık ve yarı açık mekânlar dağıtım noktası olarak kullanılabilir. Nitekim 6 Şubat Kahramanmaraş depremi sonrasında Diyarbakır Ulu Camii'nde insanların barındıkları (Şekil 8) ve cami avlusunda yardım dağıtımı gerçekleştiği (Şekil 9) görülmektedir. Özellikle yarı açık alanların bu durumda kullanımı dağıtılan malzemelerin iklim ve hava koşullarından korunmasını sağlar ve dağıtımın daha düzenli bir şekilde yapılmasına olanak tanır.

3.1.7. Temiz su

Afet durumlarında ulaşılması en zor ve en önemli olan unsur temiz su olmaktadır. Hem hijyen hem de sağlık için hayati önem taşıyan temiz suyun tedarik edilememesi oldukça büyük sorunlara yol açmaktadır. Deprem sonrasında zarar görebilecek olan temiz su altyapısı afetzedelerin sağlığını tehlikeye atabilmektedir. Bununla birlikte bu durum tıbbi müdahalelerin hijyenik koşullarda yapılamamasına neden olmaktadır (Ekşi, 2016). Cami avlularında yer alan şadırvan ve umumi tuvaletler afet durumunda hijyen açısından oldukça önemli bir potansiyele sahiptir. Ayrıca temiz su çeşmeleri de içme suyu sorununa bir çözüm getirebilmektedir. Şebeke sularının içmek için uygun olmaması, temiz su çeşmelerinin yeterli olmaması veya afetten kaynaklı olarak şebeke hatlarında sorun oluşması durumları da göz önüne alınarak camilerde yağmur suyu toplama ve arıtma sistemleri kurularak temiz su ihtiyacı karşılanabilir.



Şekil 8. 6 Şubat 2024 Kahramanmaraş depremi sonrası Diyarbakır Ulu Camii'nde geçici olarak barınan depremzedeler avlusunda yardım dağıtımı (Bestami Bodruk vd., 2023).



Şekil 9. 6 Şubat 2024 Kahramanmaraş depremi sonrası Diyarbakır Ulu Camii avlusunda yardım dağıtımı (Bestami Bodruk vd., 2023).

3.1.8. Islak hacim

Yaşam alanları kullanılamaz hale gelen afetzedelerin acil/geçici barınma alanlarında yaşam koşullarının mümkün olduğu kadar rahat ve insani olması göz önünde bulundurulmalıdır (Maral vd., 2015). Bu durumda tuvalet, duş alma, temizlik gibi temel ihtiyaçların da bu alanlarda giderilebilmesi gerekmektedir. Cami avlularında abdest alma ve temizlik amacıyla inşa edilen tek katlı umumi tuvaletler afet durumunda yaşam şartlarını kolaylaştırmayı sağlar (Atalay, 2008). Karakuş'un aktardığına göre 6 Şubat Kahramanmaraş depremi sonrasında bazı camilerde tek katlı ıslak hacimler halk tarafından bahsedilen ihtiyaçları karşılama amacıyla kullanılmıştır.

3.1.9. Altyapı

Toplanma alanlarının seçiminde önemli olan kriterlerden biri de alanın afet durumuna karşı risk taşımıyor olmasıdır. Bu durumda toplanma alanları fiziksel, jeolojik ve coğrafi olarak da ele alınarak afete dayanıklı alanlar olarak belirlenmelidir (Maral vd., 2015; Gerdan ve Şen, 2019). Afet anından itibaren kullanılacak toplanma ve acil barınma alanları temel ihtiyaçlara cevap verebilecek elektrik, su, kanalizasyon, haberleşme gibi alt yapı şartlarını sağlamalıdır (Özdemir, 2002). Depreme dayanıklı inşa edilen camiler ve avluları elektrik, haberleşme, ıslak hacimler için su kanalları ve kanalizasyon altyapısı gibi şartları sağladığı varsayıldığından, toplanma ve acil barınma ihtiyaçlarında tercih edilebilecek mekânlardır.

3.2. Sosyal İhtiyaçlar

3.2.1. Yeşil alan

Afet sonrasında yeşil alanlar sahip oldukları doğal ve yapay peyzaj elemanları ile afetzedeler için hem psikolojik hem de sosyolojik ihtiyaçlarını gidermek için önemli potansiyeller taşımaktadır. Yeşil alanlar, gündelik yaşamda rekreasyon alanı olmanın yanında iklim koşullarını iyileştirmesi, gürültüyü önlemesi ve estetik değer katması nedeniyle de önemlidir. Ayrıca yeşil alanlar yukarıda bahsedildiği gibi kent sakinlerinin fiziksel ve ruhsal sağlıkları açısından da önemlidir (Atalay, 2008). Son yıllarda yaşanan Covid-19 pandemisi, kentlerde kamusal yeşil alanların hayati önemine vurgu yapmıştır. Sosyal mesafenin önem kazandığı bu dönemde özellikle mahalle ölçeğinde, kolay ulaşılabilir yeşil alanların olması gerekliliği ortaya çıkmıştır (Özdede vd., 2021). Gerekli alan büyüklüğünü sağlayan cami avlularında yeşil alana yer verilmesinin hem psikolojik anlamdaki olumlu etkileriyle hem de afet sonrası gündelik yaşama dönmeyi kolaylaştırmasıyla önemli olacağı düşünülmektedir.

3.2.2. Psikososyal hizmetler

Afet sonrasında afetzedelerin hakları koruma altına alınmalı ve suistimal edilmelerinin önüne geçilmelidir. Yaşadıkları yerlerden olan, bir anda maddi ve manevi olarak zor şartlarda kalan bireylerin bu duruma uyum sağlayabilmesi ve bu süreçte yaşanması muhtemel psikolojik sorunları atlatabilmesi adına sosyal hizmetler afet bölgesinde görev almalıdır. Afetzedelerin sosyal hizmet görevlileri tarafından psikolojik, sosyal anlamda destek alması, bireylerin gündelik yaşamlarına dönebilmeleri ve yeniden sosyal ilişkiler kurabilmeleri için en az fiziki şartların düzenlenmesi kadar önemlidir (Ekşi, 2015; Gebel vd., 2023). 6 Şubat Kahramanmaraş depremi sonrasında kurulan çadırkentlerde psikososyal destek çadırlarının, psikolojik danışma ve rehberlik birimlerinin ve çocuk oyunları için ayrılan çadırların olduğu belirtilmiştir. Bu durum depremzedelerin psikolojik açıdan daha kolay bir şekilde süreci atlatabilmesini sağlamıştır (Gebel vd., 2023). Cami avlularında revaklar veya açık alanda kurulacak çadırlar sosyal hizmet amacıyla kullanılabilir. Afet sonrası dönemde de acil barınma ihtiyacının ortadan kalkıp bireylerin geçici yerleşim yerlerine ya da çadırkentlere yerleştirildiği dönemde, cami avluları psikolojik ve sosyal destek amacıyla kullanılmaya devam edilebilir. Ayrıca kentlilerin fiziksel ve ruhsal sağlıkları açısından da yararlı olduğu görülmektedir (Atalay, 2008).

3.2.3. Eğitim ve bilgilendirme (danışma)

Afet anı yaşanmadan önce gerekli önlemlerin alınması afet yönetiminin en önemli aşamasıdır (Şengün ve Küçükşen, 2019). Afet yaşandıktan sonraki, özellikle ilk 12 ve 24 saatlik, süreçte ise doğru bilgi aktarımının önemi ön plana çıkmaktadır. Bu süreçte toplanma alanlarında afete maruz kalan bireylerin afet hakkında, geçici barınma ile ilgili sahip oldukları haklar, dağıtım organizasyonunun en az sorunla işlemesi için yapılması gerekenler, ortaya çıkan sorunlarda nerelere başvurulabileceği gibi bilgilerin yetkililer tarafından duyurulması gerekmektedir. Toplanma alanları ise afet durumundan önce halka duyurulmuş olmalıdır. Böylece olası kargaşaların önüne geçilebilir (Maral vd., 2015). Camiler afet öncesi dönemde yani gündelik yaşamda da insanların toplandığı, buluştuğu yerler olduğundan afet öncesi eğitimlerin verilmesi ve gerekli duyuruların yapılması için uygun mekânlar olabilir. Cami avlularındaki revaklar kapalı birimlere çevrilerek ya da mevcutta inşa edilmiş tek katlı birimler, sosyal hizmet verilen mekânlar olarak kullanılabilir. Açık alanda kurulacak çadırlar da eğitim, bilgilendirme ve danışma merkezi olarak kullanılabilir.

3.2.4. Güvenlik

Özellikle deprem gibi, yapı stoğuna zarar veren afet durumlarında bireyler içgüdüsel olarak korunma ve güvenlik kaygısıyla kentsel açık alanlara yönelmektedir (Gebel vd., 2023). Ancak kentsel açık alanların toplanma alanı ve barınma alanı olabilmesi için gerekli şartları sağlaması gerekmektedir. Bu şartlardan biri güvenliktir. Güvenliğin sağlanması için acil ve geçici süre ile kentsel açık alanlara kurulan çadırkentlerin tel örgü ile çevrelenmesi gerekmektedir çünkü insanlar giriş çıkışların kontrollü sağlandığı mekânlarda daha güvende hissetmektedir. Cami avluları toplanmak için uygun noktalar olmalarının yanı sıra aynı zamanda kentten geçirgen sınırlar ile ayrılarak güvenli alanlar oluşturmaktadır. Bu durum giriş çıkışların kontrollü sağlanmasına olanak tanımaktadır.

4. Tartışma

Tablo 2'de de özetlendiği üzere cami avlularının elemanları afet durumunda birden fazla fiziksel ve psikososyal işlevle kullanım potansiyeline sahiptir. Bu potansiyellerden yola çıkarak, cami avlularının sahip olduğu giriş kapısı, açık alan, revak, son cemaat yeri, su öğesi ve ıslak hacimler değerlendirilmiş ve cami tasarımları için esnek kullanım potansiyelleri ele alınmıştır. Açık alanı çevreleyen avlu duvarı güvenli bir alan oluşturmaktadır. Bu güvenlikli alan çadır ve mobil mekânların kurulmasına uygun koşulları sağlamaktadır. Ayrıca hava koşulları uygun olduğunda yardım dağıtımlarının yapılabileceği bir alan olarak da

kullanılabilme potansiyeli mevcuttur. Açık alanda yer alan şadırvan ise afet anında temiz su ihtiyacına cevap verebilecek bir su elemanıdır. Cami avlularındaki temiz su çeşmeleri de afetzedelerin sağlığı için oldukça önemlidir. Bu elemanlara yağmur suyunu depolama ve arıtma gibi sistemleri entegre ederek olası afet durumunda şebekelerde meydana gelebilecek hasarlara rağmen su ihtiyacının karşılanması sağlanabilir.

Tablo 2. Cami avlu elemanlarının afet sonrası kullanım potansiyelleri ve öneriler

Avlu Elemanları	Avlu Elemanlarının Afet Sonrası Kullanım Potansiyelleri ve Öneriler
Giriş Kapısı (Taçkapı)	Afet sonrası bireyler ilk olarak kentsel açık alanlara yönelmektedir. Camilerin ve cami avlularının, kent ve mahalle merkezlerinde belirli aralıklarla ve yürüyüş mesafesinde yer alması nedeniyle bu mekânlara afet sonrasında kolayca erişilebilmektedir. Kolay algılanabilir, geniş ve yüksek oluşu bakımından giriş kapıları korunaklı bir alan olan avluya erişim açısından önemlidir. Bu bağlamda yeni tasarlanacak camilerin giriş kapıları (taçkapı) kolay algılanabilir ve ulaşılabilir bir şekilde tasarlanması öngörülmektedir.
Açık Alan	Avlu, açık alanında çadır ve mobil mekânlar kurularak afet sonrası ortaya çıkan barınma, eğitim, bilgilendirme, koordinasyon merkezi, yardım dağıtımı (yemek, kıyafet), ilk yardım ve tıbbi bakım gibi ihtiyaçlara karşılık çözüm getirme potansiyeline sahiptir. Bunun dışında avlu peyzajında yeşil alana yer verilmesiyle çocuklar için oyun alanı, buluşma mekânı elde edilmiş olur. Bu durum hem psikolojik anlamdaki olumlu etkileriyle hem de afet sonrası gündelik yaşama katkısıyla önemli olmaktadır.
Revak	Avlunun revaklarla çevrilerek bir sınır oluşturması güvenlik açısından önemlidir. Yarı açık alanlar olarak nitelendirilebilecek revaklar kapalı alanlara çevrilerek barınma, depolama, dağıtım, psikososyal hizmetler, danışma, ilk yardım ve tıbbi müdahalelere uygun korunaklı birer hacme dönüştürülebilir.
Son Cemaat Yeri	Avlunun bir elemanı olarak son cemaat yerinin revaklardan farkı caminin kapalı mekânı olan ana ibadet mekânı (harim) ile ilişkili olmasıdır. Bu bağlamda esnek kullanıma uygun daha çok sosyal ihtiyaçlara (psikososyal hizmetler, eğitim, bilgilendirme) yönelik mekânlara sahip olma potansiyeli taşımaktadır.
Su Öğeleri (Havuz-Şadırvan)	Temiz su çeşmeleri içme suyuna erişim için kaynak potansiyeline sahiptir. Şebeke sularının içmek için uygun olmaması, temiz su çeşmelerinin yeterli olmaması veya afetten kaynaklı olarak şebeke hatlarında sorun oluşması durumları da göz önüne alınarak yeni inşa edilecek camilerde yağmur suyu toplama ve arıtma sistemleri kurularak temiz su ihtiyacı karşılanabilir.
Islak Hacimler	Islak hacimler afet sonrasında ortaya çıkan temel ihtiyaçların giderilebilmesi için önemlidir. Cami avlularında yapılacak bağımsız girişli ıslak hacimler, deprem sonrası ihtiyaç durumuna göre aynı işlevini sürdürebileceği gibi çamaşırhanelere de dönüştürülebilme potansiyeline sahip mekânlardır.

Revaklar ise yarı açık mekân organizasyonuyla esnek kullanım potansiyeline sahiptir. Afet anında afetzedelerin yapılardan uzak durma içgüdüsü düşünüldüğünde ilk toplanma için yarı açık mekânların varlığı hava ve iklim koşullarından korunma (yağmur, güneş etkisi gibi) açısından büyük önem taşımaktadır. Afet sonrası dönemde ise gerektiğinde geçici strüktürel elemanlar ile kapalı mekân elde edebilme gibi esnek kullanım potansiyelleri ile çok amaçlı kullanımı mümkündür. İhtiyaç durumuna göre dönüşebilecek mobilyalarla revakların afet durumunda ve gündelik yaşamda farklı işlevlerle kullanılabilme olanağı vardır. Cami avlularında yer alan tek katlı birimlerin afet durumunda kapalı mekân ihtiyacını kısmen de olsa karşılayacağı düşünülmektedir. Özellikle umumi tuvaletler ve ticari birimler afet durumunda ıslak hacim, depo gibi ihtiyaçları karşılamaya uygun mekânlardır.

5. Sonuç

Son yıllarda yaşanan afetler toplanma alanlarının sayı ve imkân bakımından yetersiz olduğunu göstermektedir. Bu nedenle afet durumunda kullanım potansiyeli sunan mekânların araştırılması önemlidir. Camilerin hemen her mahallede bulunması, depreme dayanıklı inşa edilmesi ve kolay algılanabilir birer simge yapı olması afet sonrasında kullanım potansiyelleri olduğunu göstermektedir. Toplanma alanları afet sonrasında barınma, ilk yardım ve bilgilendirme merkezi gibi işlevlere hizmet edebilecek alanlar olarak tasarlanmalıdır. Deprem ve salgın gibi afetlerde açık alanların kullanımı oldukça önem kazanmıştır. Ancak yeri ve zamanı öngörülemeyen afetlerin hangi hava ve iklim koşullarında gerçekleşeceği bilinmediğinden toplanma alanlarında yarı açık ve kapalı mekânlara da ihtiyaç duyulmaktadır. Cami avluları yarı açık, açık ve kapalı mekânlardan oluşan zengin mekân organizasyonu ile esnek kullanıma olanak tanımaktadır.

Çalışmada cami avlularının afet sonrasında kullanım potansiyelleri analiz edilmiş ve tablo halinde özetlenmiştir (Tablo 2). Cami avlularının toplanma alanı olarak kullanılmasındaki dezavantajlar da gözetilerek birtakım önerilere yer verilmiştir. Sonuç olarak bu çalışmada, kentte birer arayüz mekânı olan cami

avlularının toplanma alanı olarak kullanımına yönelik potansiyeller analiz edilerek tartışmaya açılmıştır. Bu çalışma kapsamında ele alınan dezavantajların iyileştirilmesi ya da yeni inşa edilecek camilerin tasarımında düşünülmesi gerektiği konusunda literatüre katkı yapmaktadır. Buradan hareketle gelecek araştırmalarda, farklı kamusal mekânların afet anında esnek kullanım potansiyelleri araştırma konusu olarak önemli tartışma zeminleri oluşturmaktadır. Aynı zamanda çalışmada ele alınan alan çalışması olan cami örneğinden hareketle, tasarım aşamasında kamusal alan kullanımları esnek ve ortak kullanım potansiyelleri taşıyan kamusal mekânların tasarım kararlarına ilişkin araştırmalar da literatüre önemli katkılar sağlayacaktır.

Katkı Oranı Beyanı

Yazarların katkı yüzdeleri aşağıda verilmiştir. Yazarlar makaleyi incelemiş ve onaylamıştır.

	M.A.	C.F.	E.M.Ö	B.B.	H.A.
K	20	20	20	20	20
T	20	20	20	20	20
Y	20	20	20	20	20
VTI	20	20	20	20	20
VAY	20	20	20	20	20
KT	20	20	20	20	20
YZ	20	20	20	20	20
KI	20	20	20	20	20
GR	20	20	20	20	20
PY	20	20	20	20	20
FA	20	20	20	20	20

K= kavram, T= tasarım, Y= yönetim, VTI= veri toplama ve/veya işleme, VAY= veri analizi ve/veya yorumlama, KT= kaynak tarama, YZ= Yazım, KI= kritik inceleme, GR= gönderim ve revizyon, PY= proje yönetimi, FA= fon alımı.

Çatışma Beyanı

Yazarlar bu çalışmada hiçbir çıkar ilişkisi olmadığını beyan etmektedirler.

Etik Onay Beyanı

Bu araştırmada hayvanlar ve insanlar üzerinde herhangi bir çalışma yapılmadığı için etik kurul onayı alınmamıştır.

Destek ve Teşekkür Beyanı

Makalenin İngilizce bölümlerini dil bilgisi ve yazım kuralları bakımından kontrol eden Gazi Üniversitesi Akademik Yazma Uygulama ve Araştırma Merkezi'ne teşekkür ederiz. Çalışma boyunca ufuk açıcı yönlendirmeleri ile makaleye katkıda bulunan değerli hocamız Doç. Dr. Hilal Aycı'ya teşekkür ederiz.

Kaynaklar

Ak M, Karamağaralı CN. 2023. Anadolu Türk Camilerinde avlunun gelişimi. Türkiye Cumhuriyeti'nin 100. Yılında Uluslararası Genç Araştırmacılar Sempozyumu: Dünden Bugüne Türk Mimarlığı Sempozyumu Bildirileri, 22-24 Mart, Ankara, Türkiye, ss: 299-317.

Ak M. 2022. Anadolu Türk Camilerinde mimari öğe olarak su kullanımı (11-15. yüzyıl). Yüksek Lisans Tezi, Gazi Üniversitesi Fen Bilimleri Enstitüsü, Ankara, Türkiye, ss: 182.

Akgül (Karamağaralı) N. 1997. Some cosmic motifs and elements in Seljuk and Ottoman Architecture. Erdem, 9(27): 903-910.

Akın G. 1990. Asya merkezi mekân geleneği. Kültür Bakanlığı, Ankara, Türkiye, ss: 264.

Aksoy Y, Turan AÇ, Atalay H. 2009. İstanbul Fatih ilçesi yeşil alan yeterliliğinin Marmara Depremi öncesi ve sonrası değerleri kullanılarak incelenmesi. Uludağ Üniv Müh-Mim Fak Derg, 14(2): 137-150.

Allan P, Bryant M. 2011. Resilience as a framework for urbanism and recovery. J Landsc Archit, 6(2): 34-45.

Alpak EM, Düzenli T. 2018. Kentsel tasarımda esneklik ve adaptasyon: Kentsel meydan senaryoları üretimi. Int Soc Hum Sci Res, 5(16): 16-22.

Aslanapa O. 1989. Türk Sanatı. Remzi Kitabevi, İstanbul, Türkiye, ss: 454.

Atalay H. 2008. Deprem durumunda kentsel açık ve yeşil alanların kullanımı - Küçükçekmece Cennet Mahallesi örneği. Yüksek Lisans Tezi, İstanbul Teknik Üniversitesi, Fen Bilimleri Enstitüsü, İstanbul, Türkiye, ss: 154.

Aydın Ö. 2000. Anadolu mimarlığında avlu (neolitik dönemden tunç çağı sonuna). Yüksek Lisans Tezi, Gazi Üniversitesi, Fen Bilimleri Enstitüsü, Ankara, Türkiye, ss: 119.

Bayramoğlu E, Cındık Akıncı Y. 2018. Kentsel açık alanlarda dönüşümlü etkinlik yaratıcılığı. J Int Soc Res, 11(59): 448-454.

Blair S, Bloom J. 2007. Isfahan Cuma Camisi. Hattstein M, Delius P. (editörler), İslam Sanatı ve Mimarisi. Literatür Yayınları, İstanbul, Türkiye, ss: 368-369.

Bodruk B, Sincar Hİ, Kaplan A. 2023. Diyarbakır'da tarihi camiler depremzedeleri misafir ediyor. URL: https://www.aa.com.tr/tr/gundem/diyarbakirda-tarihi-camiler-depremzedeleri-misafir-ediyor/2812961# (erişim tarihi: 23 Aralık 2024).

Cantay T. 1991. Avlu. İslâm Ansiklopedisi IV, Türkiye Diyanet Vakfı, İstanbul, Türkiye, ss: 120-123.

Çelik M. 2022. Avlu bahçelerinin termal konforunun envi-met ile belirlenmesi; Diyarbakır örneği. Yüksek Lisans Tezi, Atatürk Üniversitesi, Fen Bilimleri Enstitüsü, Erzurum, Türkiye, ss: 108.

Çelik N. 1993. Bursa Ulu Camii'nin mimarlık tarihi bakımından analizi ve değerlendirilmesi. Yüksek Lisans Tezi, Gazi Üniversitesi, Fen Bilimleri Enstitüsü, Ankara, Türkiye, ss: 152.

Çınar AK, Akgün Y, Maral H. 2018. Afet sonrası acil toplanma ve geçici barınma alanlarının planlanmasındaki faktörlerin incelenmesi: İzmir-Karşıyaka örneği. Planlama, 28(2): 179-200.

Doostvandi M, Akbari M, Ketabollahi K. 2022. The flexibility of urban spaces during the Covid-19 pandemic. J Place Space Res, 4(23): 25-44.

Ekşi A. 2015. Afet yönetiminde içsel denetim aracı olarak etik. Int J Econ Admin Stud, 8(15): 89-102.

Ekşi A. 2016. Afetlerden sonra ortaya çıkabilecek çevresel risklerin yönetimi. Hastane Öncesi Derg, 1(2): 15-25.

Elfallah S. 2023. Energy efficient housing: Through the courtyard concept in Benghazi Libya. Yüksek Lisans Tezi Bahçeşehir Üniversitesi, Lisansüstü Eğitim Enstitüsü, İstanbul, Türkiye, ss: 137.

Erdin HE, Zengin Çelik H, Sılaydın MB, Partigöç NS. 2023. Afet ve acil durumlarda sosyal altyapı alanlarının toplanma alanı olarak belirlenme kriterleri ve yöntemi. Türk Deprem Araş Derg, 5(1): 1-21.

Erdoğan E. 1996. Anadolu avlularının özellik ve düzenleme ilkeleri üzerinde karşılaştırmalı bir araştırma. Doktora Tezi, Ankara Üniversitesi, Fen Bilimleri Enstitüsü, Ankara, Türkiye, ss: 259.

Fesci C, Aycı H. 2024. A bibliometric study on the flexible use

potentials of courtyards. BSJ Eng Sci, 7(6): 1118-1130

Gebel Ş, Koç D, Aycı H. 2023. Spor komplekslerinin deprem sonrası kullanımı ve potansiyelleri: Kahramanmaraş ve Gaziantep örnekleri. J Archit Sci Appl, 8(Special Issue): 198-22.

Gerdan S, Şen A. 2019. Afet ve acil durumlar için belirlenmiş toplanma alanlarının yeterliklerinin değerlendirilmesi: İzmit örneği. İdealkent, 10(28): 962-983.

Gökşen F, Takva Ç, Takva Y, İlerisoy ZY. 2024. Post-earthquake fires: risk assessment and precautions. Mehran University Res J Eng Technol, 43(1): 1-16.

Grabar O. 2007. İslam Dünyasında sanat ve kültür. Hattstein M, Delius P (Editör) İslam Sanatı ve Mimarisi. Literatür Yayınları, İstanbul, Türkiye, ss: 34-43.

Güleç Demirel BN, Kara Pilehvarian N. 2018. Osmanlı Sultan Camilerinde 'Avlu'. Yakın Mim Derg, 1(2): 11-33.

Halı Kabataş F, Ak CN, Işıldak NA, Aycı H. 2023. Tabhaneli Camilerin afet sonrası süreçte çok fonksiyonlu kullanım potansiyelleri üzerine bir değerlendirme. J Architect Sci Appl, 8(Special Issue): 298-317.

Hasol D. 1990. Ansiklopedik Mimarlık Sözlüğü. Yem Yayın, İstanbul, Türkiye.

Japon Uluslararası İşbirliği Ajansı ve İstanbul Büyükşehir Belediyesi. 2002. Türkiye Cumhuriyeti İstanbul İli Sismik Mikro-Bölgeleme Dahil Afet Önleme/Azaltma Temel Planı Çalışması Sonuç Raporu (Doküman V). Japon Uluslararası İşbirliği Ajansı (JICA) ve İstanbul Büyükşehir Belediyesi (İBB), İstanbul, Türkiye.

Kılıç Özkaynar G. 2023. Afet döneminde yönetim fonksiyonlarının uygulanma sürecine yönelik bir araştırma: Kahramanmaraş Depremi özelinde Sivas Cumhuriyet Üniversitesi örneği. Türk Deprem Araş Derg, 5(2): 105-127.

Kuban D. 2007. Osmanlı mimarisi. YEM Yayın, İstanbul, Türkiye, ss: 720.

Maral H, Akgün Y, Çınar AK, Karaveli AS. 2015. İzmir'deki afet sonrası toplanma ve acil barınma alanları üzerine bir değerlendirme. 3. Türkiye Deprem Mühendisliği ve Sismoloji Konferansı, 14-16 Ekim, İzmir, Türkiye.

Melikoğlu Y, Sevinç Kayıhan K. 2023. Günümüz kentlerinde camilerin deprem yönetiminde kullanım potansiyelleri: Diyarbakır örneği. J Architect Sci Appl, 8(Special Issue): 1-25.

Montejano-Castillo M, Moreno-Villanueva M. 2016. The adaptability of public space in Mexico City after an earthquake: a preliminary classification. Int J Saf Secur Eng, 6(2): 104-113.

Mousighichi P. 2023. Comparison of courtyards in traditional Iranian houses in different climates of Iran. Yüksek Lisans Tezi, İzmir Ekonomi Üniversitesi, Lisansüstü Eğitim Enstitüsü, İzmir, Türkiye, ss: 108.

Okuyucu ŞE. 2011. Çağdaş eğitim yapılarında avlunun göstergebilimsel açıdan değerlendirilmesi. Doktora Tezi, Selçuk Üniversitesi Fen Bilimleri Enstitüsü, Konya, Türkiye, ss: 286.

Ögel S. 1994. Anadolu'nun Selçuklu çehresi. Akbank Yayınları, İstanbul, Türkiye.

Önsüz MF, Işıktekin Atalay B. 2015. Afet lojistiği. Osmangazi Tıp Derg, 37(3): 1-6.

Özbudak Akça B, Halifeoğlu FM. 2018. Avlunun kentsel yerleşim düzenindeki rolünün tarihi Diyarbakır camileri üzerinde değerlendirilmesi. Tasarım Koruma (Prof. Dr. Zülküf Güneli'ye Armağan). Birsen Yayınevi, İstanbul, Türkiye, ss: 107-119.

Özdede S, Hazar Kalonya D, Aygün A. 2021. Pandemi sonrası dönemde kişi başına düşen kentsel yeşil alan ihtiyacını yeniden düşünmek. İdealkent, 12(Covid-19 Özel Sayısı): 362-388.

Özdemir H. 2002. İstanbul Avrupa Yakası olası afet sonrası geçici iskan alanlarının coğrafi etüdü, Yüksek Lisans Tezi, İstanbul Üniversitesi, Sosyal Bilimler Enstitüsü, İstanbul.

Özköse A. 1995. Avluların tarihsel süreç içindeki evrimi. Doktora Tezi, Gazi Üniversitesi, Fen Bilimleri Enstitüsü, Ankara, Türkiye, ss: 358.

Saçlı ZA, Arı BN, Aycı H. 2023. Deprem sonrası kültürel miras varlıklarının kullanımı: Hatay örneği, Cumhuriyetimizin 100. yılı anısına peyzaj mimarlığı, mimarlık ve çevre, Platanus Publishing, Ankara, Türkiye, ss: 231-252.

Sanei M, Khodadad S, Khodadad M. 2018. Flexible urban public spaces and their designing principles. J Eng Urban, 8(4): 39-43.

Sepe M. 2021. Covid-19 pandemic and public spaces: improving quality and flexibility for healthier places. Urban Des Int, 26(2): 159-173.

Sınmaz S. 2015. Gelişen iletişim teknolojilerinin kentsel yaşam ve kamusal mekânlar üzerindeki yansımaları. Tasarım+Kuram, 11(20): 63-75.

Şengün H, Küçükşen M. 2019. Afet yönetimi eğitimi niçin gerekli? Erciyes Üniv Sos Bil Enst Derg, 33(46): 193-211.

T.C. Cumhurbaşkanlığı Diyanet İşleri Başkanlığı. 2021. Cami Planlama ve Tasarımı Kılavuzu, Yönetim Hizmetleri Genel Müdürlüğü Yatırım Emlak ve Teknik Hizmetler Daire Başkanlığı.

Uyar HE, Özkan E. 2023. Deprem sonrası ilk durak: İstanbul'da toplanma alanlarına dair bir inceleme. Afet Risk Derg, 6(1): 226-242.

Ünkaracalar SS, Aycı H. 2023. Open urban spaces for flexible urbanism: An analysis of parks in Gaziantep, Hatay, and Kahramanmaras as earthquake parks. Gazi Univ J Sci Part B: Art Human Design Plan, 11(2): 337-352.

Wang Z, Huang T, Wang Y, Dai S, Zeng Y, Chen J, Tang F. 2024. Evaluation of the ımpact of courtyard layout on wind effects on coastal traditional settlements. Land, 13(11): 1813.

Yetkin SK. 1984. İslâm ülkelerinde sanat. Cem Yayınevi, İstanbul, Türkiye, ss: 245.

Yılmaz E, Göbel İE, Aycı H. 2023. Deprem parkları: Hatay örneği, Cumhuriyetimizin 100. yılı anısına peyzaj mimarlığı, mimarlık ve çevre. Platanus Publishing, Ankara, Türkiye, ss: 117-137.

Zengin Çelik H, Özcan NS, Erdin HE. 2017. Afet ve acil durumlarda halkın toplanma alanlarının kullanılabilirliğini belirleyen kriterler. 4. Uluslararası Deprem Mühendisliği ve Sismoloji Konferansı, 11-13 Ekim, Eskişehir, Türkiye.

Zhang M, Fang Z, Liu Q, Zhang F. 2024. Simulation and analysis of factors influencing climate adaptability and strategic application in traditional courtyard residences in hot-summer and cold-winter regions: a case study of Xuzhou, China. Sustain, 16(19): 8676.

Black Sea Journal of Engineering and Science
doi: 10.34248/bsengineering.1605086

Open Access Journal
e-ISSN: 2619 – 8991

Research Article
Volume 8 - Issue 2: 507-516 / March 2025

RECONSTRUCTION OF METAL OBJECTS - 3D PHOTOGRAMMETRY AND CLAY COATING

Hasan Kemal SÜRMEN[1]*

[1]*Istanbul University - Cerrahpasa, Department of Motor Vehicles and Transportation Technologies, 34500, Istanbul, Türkiye*

Abstract: This work focuses on the development of a reconstruction process using 3D photogrammetry for metal objects, which are often difficult to scan in three-dimensional (3D) due to their shiny, smooth and featureless surfaces. Usually, expensive 3D scanning technologies are used for high accuracy reconstructions. This research presents a novel approach using clay powder to improve the geometric accuracy of 3D reconstructions through a coating process, a first in the literature. Twelve metal objects with cubic, cylindrical and spherical geometries were selected for the study. They were photographed in a controlled environment using a turntable, camera and 18-135 mm lens. 3D reconstructions of these objects were obtained initially without coating and then by applying clay powder. The reconstructions were then compared for geometric accuracy and mesh quality. The main findings from the study show that clay coating significantly improves the geometric accuracy of the reconstruction process. In addition, it also improves the homogeneity of the mesh structures. These improvements were confirmed by deviation analysis, which compared the models generated by the reconstruction process with computer-aided design (CAD) models drawn according to the actual dimensions of the objects. The study highlights the potential of clay coating as a viable alternative method to improve geometric accuracy in the 3D reconstruction process.

Keywords: 3D Photogrammetry, Coating, Computer aided design (CAD), Image based modeling, Reconstruction, Reverse engineering

***Sorumlu yazar (Corresponding author):** Istanbul University - Cerrahpasa, Department of Motor Vehicles and Transportation Technologies, 34500, Istanbul, Türkiye
E mail: hksurmen@iuc.edu.tr (H.K. SÜRMEN)
Hasan Kemal SÜRMEN https://orcid.org/0000-0001-8045-9193

Received: December 21, 2024
Accepted: February 05, 2025
Published: March 15, 2025

Cite as: Surmen HK. 2025. Reconstruction of metal objects - 3D photogrammetry and clay coating. BSJ Eng Sci, 8(2): 507-516.

1. Introduction

Three-dimensional (3D) reconstruction is a rapidly evolving field encompassing various technologies to create precise models of physical objects. It finds extensive applications in engineering, biomedical sciences, industrial design, and manufacturing, providing efficient capture of geometric data (Reis, 2018; Javaid et al., 2021). One challenge it addresses is the scanning of free-form objects that are difficult to model using traditional 3D drafting software. Technologies such as 3D laser scanning (Yaman et al., 2017; Yang et al., 2018), computed tomography (Cansiz et al., 2014), structured light (Gessner et al., 2022), and 3D photogrammetry (Mathys et al., 2019; Surmen, 2023) each offer distinct advantages and drawbacks. However, high initial costs and specialized equipment remain significant barriers to widespread adoption (Cansiz et al., 2014; Yang et al., 2018).

3D photogrammetry is increasingly popular due to its affordability, portability, ability to capture color, and wide scanning range. Also known as image-based 3D modeling (Remondino and El-Hakim, 2006) or photo scanning (Seeberger et al., 2016), photogrammetry finds applications in diverse fields including architecture (Pepe and Costantino, 2020), engineering (Kanun, 2021), archaeology (Molnár, 2019), cultural heritage (Kingsland, 2020), medical sciences (Orun et al., 2018; Kurilová et al., 2023), forensics (Tóth et al., 2021), biomedical research (Struck et al., 2019), biology (Eulitz and Reiss, 2015), and geology (Gomez and Kennedy, 2018). This technique involves capturing multiple photographs of an object from different angles, which are then processed using specialized software to create point cloud models, triangular mesh polygon models, or photorealistic textured 3D models. However, challenges arise when dealing with objects that have shiny or reflective surfaces (Valinasab et al., 2015; Kohtala et al., 2021).

The reconstruction of metal objects, including parts and devices, using 3D scanning is crucial for applications such as reverse engineering and archival purposes in fields like engineering, biomedical sciences, and archaeology (Wang et al., 2016; Helle and Lemu, 2021). The glossy and reflective surfaces of metallic materials pose significant challenges even for advanced technologies such as structured light scanning (Surmen et al., 2018). Most 3D scanning methods rely on capturing the way light reflects off an object to create a detailed 3D model. On reflective surfaces, this process becomes problematic for a few key reasons such as specular reflection and glare. Metallic surfaces tend to reflect light in a mirror-like, specular manner, meaning the light doesn't scatter in all directions but instead reflects at specific angles. This causes the scanning system to miss important data

This work is licensed (CC BY-NC 4.0) under Creative Commons Attribution 4.0 International License

about the object's geometry since the reflected light might not reach the sensor or might be misinterpreted. In addition, highly reflective materials can cause glare, which overwhelms the sensor's ability to capture the correct pattern or laser light. This can lead to the sensor being "blinded" by the reflection, resulting in data loss or errors in measuring the shape of the object. Surface preparation, including the application of coatings, may be necessary to facilitate accurate scanning. Furthermore, post-processing and editing of models derived from the reverse engineering process are often required (Wang et al., 2016; Helle and Lemu, 2021). Therefore, improving the accuracy of initial 3D reconstructions can minimize subsequent editing efforts, thereby saving time, labor, and costs.

This study aims to evaluate and enhance the effectiveness of 3D photogrammetry in reconstructing metal objects. Additionally, it explores the use of clay powder as a coating material in photogrammetric modeling—an approach valued for its affordability, natural composition, ease of application, and environmental friendliness compared to commercial alternatives. Comparative analyses of clay-coated and uncoated object reconstructions focus on geometric accuracy and mesh structures. Twelve reconstructions were performed using 3D photogrammetry, and results include solid and mesh models alongside deviation analyses referencing CAD models based on actual object dimensions. Maximum and minimum geometric deviations are quantified, and 3D color maps illustrating deviation regions are presented. Ultimately, the study assesses how clay coating influences geometric accuracy and mesh structures in generated reconstructions.

2. Materials and Method

Photogrammetry enables the acquisition of dimensions, position, shape, and texture of objects through the analysis of photographs, providing both measurement data and visual information. The process of photogrammetric modeling involves several stages: planning the photography session based on the objects' shapes and geometric details, camera calibration, generation of a point cloud using specialized software, and conversion of this point cloud into solid, mesh, and textured 3D models. The fundamental principle underlying both digital close-range photogrammetry (Awange and Kiema, 2019) and aerial photogrammetry (Axelsson, 1991) is central perspective projection, illustrated in Figure 1.

Collinearity equations, which are the basic mathematical equations underlying photogrammetry, are used to unify the coordinate system of the obtained image with the object being photographed (equations 1 and 2):

$$x_p = -c\frac{r_{11}(X_p-X_0)+r_{12}(Y_p-Y_0)+r_{13}(Z_p-Z_0)}{r_{31}(X_p-X_0)+r_{32}(Y_p-Y_0)+r_{33}(Z_p-Z_0)} \quad (1)$$

$$y_p = -c\frac{r_{21}(X_p-X_0)+r_{22}(Y_p-Y_0)+r_{23}(Z_p-Z_0)}{r_{31}(X_p-X_0)+r_{32}(Y_p-Y_0)+r_{33}(Z_p-Z_0)} \quad (2)$$

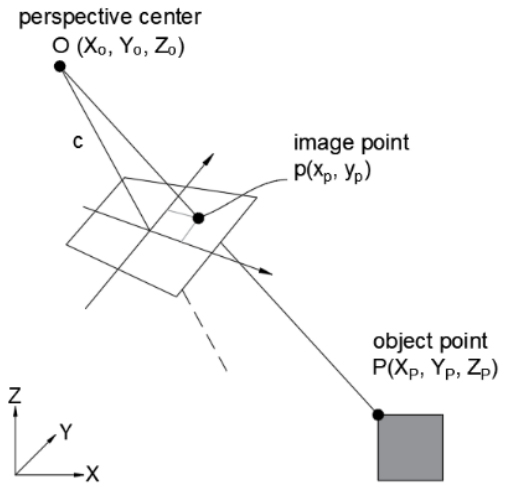


Figure 1. Principle of central perspective.

Where Xp, Yp represent the coordinates of the image point (p); c is the calibrated focal length or also called the principal distance. Xo, Yo, and Zo indicate the position of the perspective center in the object's space; rij for i, j = 1, 2, 3 are the elements of the orthogonal rotation matrix comprising the three angles ω, φ and κ. Xp, Yp, Zp are the coordinates of the object point (P). The six parameters (ω, φ, κ, Xo, Yo, Zo) represent the elements of exterior orientation, which define the position of the camera in space. This study employs 3D photogrammetry to investigate the reconstruction of metal objects and assess the influence of clay powder coating. The chosen objects include basic geometric shapes commonly found in mechanical parts: prisms, cylinders, spheres, and surfaces with concave and convex edges. These objects, such as cubes, cylinders, spheres, and their variants created through constructive solid geometry techniques (Ghali, 2008), serve as subjects for exploring various applications of 3D reconstruction, as illustrated in Figure 2.

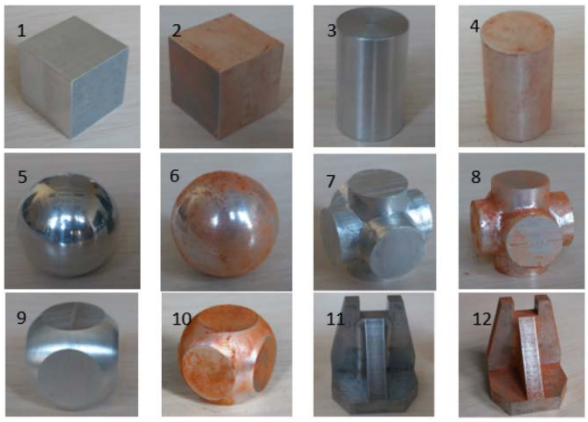


Figure 2. Uncoated and clay coated objects used in 3D photogrammetry.

In this study, aluminum metal objects were manufactured using the CNC method and subsequently prepared for accurate 3D reconstruction via

photogrammetry. The surfaces of these objects, known for their inherent shine and smoothness, posed a challenge to achieving precise reconstructions, a critical factor highlighted in prior research (Puerta et al., 2020). To address this, a novel approach was introduced wherein clay, selected for its matte texture and perceptibility, was employed as a coating material. Notably, this study marks the first use of clay for such purposes, leveraging its affordability, accessibility, safety, and ease of handling and storage over extended periods. Clay powder was used in the coating process. It was obtained from the dry form of the clay material, which was carefully pulverized. The powder was then gently applied to the surfaces manually using a soft brush. Clay coating was applied in a thin layer to surfaces for specific objects (2, 4, 6, 8, 10, and 12), thereby enhancing their perceptibility during the subsequent photographing phase. This coating process aimed to mitigate the challenges posed by shiny or transparent surfaces, thereby facilitating more accurate 3D reconstructions. The workflow of the 3D photogrammetry technique employed in this study encompassed three primary phases: photographing, uploading images to cloud-based software, and generating 3D models, as depicted in Figure 3. Each phase was meticulously executed to ensure comprehensive data acquisition and processing integrity.

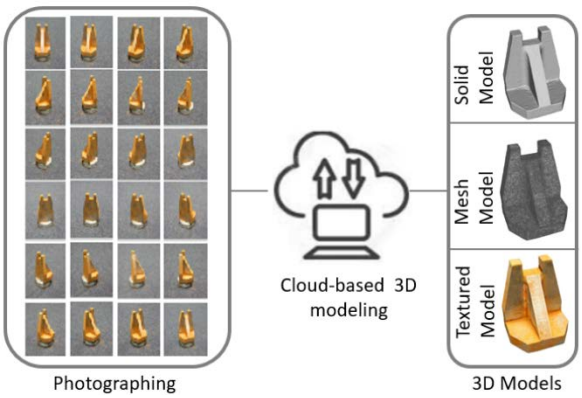


Figure 3. Stages of 3D photogrammetric modeling.

In the context of 3D photogrammetric modeling, ensuring high-quality outcomes necessitates adhering to established best practices. It is widely recommended in the literature that photographs for such applications should exhibit a minimum overlap of 60% (Matthews, 2008; Slaker and Mohamed, 2017). This overlap is crucial as it enables the software to effectively stitch together the images and maintain geometric continuity throughout the 3D model generation process. To achieve this, photographs should be captured in a manner that ensures comprehensive coverage of all surfaces of the object from various angles. Each image should overlap sufficiently with adjacent ones, facilitating robust reconstruction of the object's geometry and texture.

To mitigate potential errors arising from environmental conditions or operator variability during the photographing phase, a straightforward mechanism has been developed. This mechanism, depicted in Figure 4, serves to standardize the photographic process, thereby enhancing consistency and reliability across multiple trials or comparisons. Such procedural consistency is essential for ensuring the accuracy and reproducibility of 3D photogrammetric modeling results.

This mechanism is mounted on a fixed stand equipped with an indicator to precisely measure its rotational angle. It consists of a turntable with a pointer indicating the angle position, along with a Canon EOS 50D camera paired with an 18-135 mm lens. The photographs were taken indoors in a controlled environment devoid of natural daylight. Illumination was provided by a fluorescent light positioned above the turntable. To minimize potential reflections, both the turntable and the background were covered with dark, non-reflective fabric.

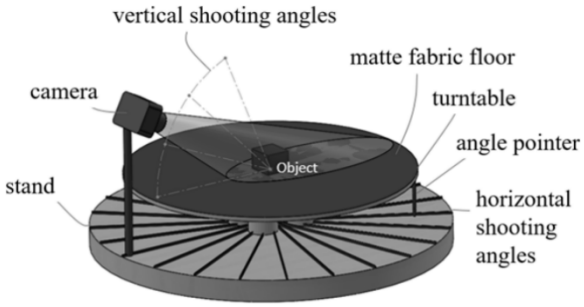


Figure 4. Stages of 3D photogrammetric modeling.

The photography methodology involved rotating the turntable approximately 15 degrees around its axis to ensure sufficient overlap (60-90%) between successive photographs. This approach draws inspiration from the photo-sculpture technique (Beaman et al., 1997), historically used to replicate objects in the 19th century. It was selected due to the limitations of capturing all geometric details of objects from a single vertical angle. Hence, photographs were taken at multiple vertical angles: one shot at a 35-degree angle, and two shots at 0 degrees and 45 degrees, respectively.

The camera was positioned approximately 40 cm away from the object, and no flash was utilized to avoid unwanted reflections. Photographs were captured at a resolution of 15.1 megapixels (4752 x 3168 pixels). Following capture, the photos were uploaded to a computer equipped with Autodesk ReCap Photo, a 3D photogrammetry software that supports cloud-based processing. The software facilitated the upload of photos to the cloud system for 3D modeling. Once processed, the resulting 3D models were downloadable in RCM (Reality Computing Mesh) format, which supports surface models. Additionally, models could be exported in various formats including OBJ, OBJ (Quads), FBX, STL, PLY, PTS, and RCS.

Mesh data reports were generated to meticulously examine the structure of the 3D mesh models. After

assessing visual accuracy, a comprehensive deviation analysis was conducted for each reconstructed object to ascertain geometric accuracy and any discrepancies. The workflow illustrated in Figure 5 guided this deviation analysis.

Initially, physical object dimensions were meticulously measured, and 3D CAD models were meticulously crafted based on these precise measurements. These CAD models served as the gold standard reference models against which the accuracy of the reconstructed 3D models was evaluated. Post-scaling the 3D reconstructed models to match the real-world objects, they underwent rigorous comparison with the CAD models using the advanced 'Difference Analysis' tool available within the ReCap software.

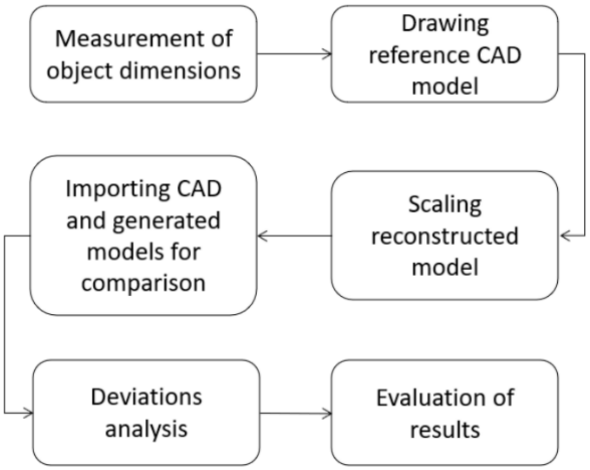


Figure 5. Workflow chart for deviation analysis.

3. Results and Discussion

3.1 Evaluation of Visual and Geometric Accuracy of the Reconstructed 3D Models

Figure 6 showcases 3D solid models reconstructed from both uncoated and clay-coated metal objects using 3D photogrammetry within the scope of this study. When examining the cube-shaped Model 1 and its clay-coated counterpart, Model 2, it is evident that Model 2 exhibits reduced surface roughness compared to Model 1. Additionally, the edges of Model 2 appear smoother and sharper.

There is a noticeable difference in shape between Model 3 and Model 4, which were generated from cylindrical metal objects. Due to the glossiness caused by their cylindrical shape, Model 3 was not accurately reconstructed. However, Model 4 shows significant improvement in geometric accuracy with the application of clay coating. The clay coating not only minimized reflections on the object's surface but also imparted a discernible texture.

Similar improvements were observed in the sphere-shaped Object 5 and its clay-coated version, Object 6. Object 7 consists of three cylindrical parts with identical geometry along the x, y, and z axes. Despite some superficial surface issues, the 3D model of Object 7 was successfully generated. The reconstruction process was repeated with the application of clay powder to the objects, resulting in improved geometric accuracy. Objects 9 and 10 feature geometries derived from the intersection of cube and sphere shapes. It was observed that model 10 achieved higher geometric precision compared to model 9, attributed to the clay coating. Examining model 11, reconstructed from a metal machine part, revealed inaccuracies particularly in concave edges.

Following the application of clay coating and subsequent reconstruction, it was noted that concave edges could be accurately reproduced. Moreover, improvements were observed in the accuracy of edges, corners, and overall surface details of the model.

3.2 Deviation Analysis Results

Deviation analysis plays a critical role in both the numerical and visual assessment of geometric accuracy when comparing different models. In our study, we conducted deviation analysis to meticulously observe the geometric differences between models reconstructed from uncoated and clay-coated metal objects. This analysis followed the structured approach outlined in Figure 5, utilizing Autodesk ReCap Photo's 'Difference Analysis' tool.

The CAD models used for comparison were meticulously created to match the exact dimensions of the objects using CAD software, and then converted into STL format to facilitate the deviation analysis. Prior to analysis, all models were scaled to ensure alignment with the original object dimensions. A tolerance threshold of 0.2 mm was set based on the bounding box of the models, which on average enclosed objects within 125,000 mm^3. The results of the deviation analysis are visualized in Figure 7, where colored zones on the models indicate deviations from the CAD models. Green zones represent areas where deviations fall within the ±0.2 mm tolerance range, highlighting high geometric accuracy. Zones colored in shades from purple to blue signify areas where deviations exceed this tolerance. Notably, models treated with clay coating showed an increase in the proportion of green zones, indicating enhanced geometric precision. This improvement underscores the positive impact of clay coating on the accuracy of reconstructed objects across various surface types, including flat, cylindrical, and spherical geometries.

Table 1 provides a detailed summary of the maximum and minimum deviations observed in both uncoated (odd-numbered models) and clay-coated (even-numbered models) processes. Maximum deviations indicate positive geometric differences, while minimum deviations indicate negative differences.

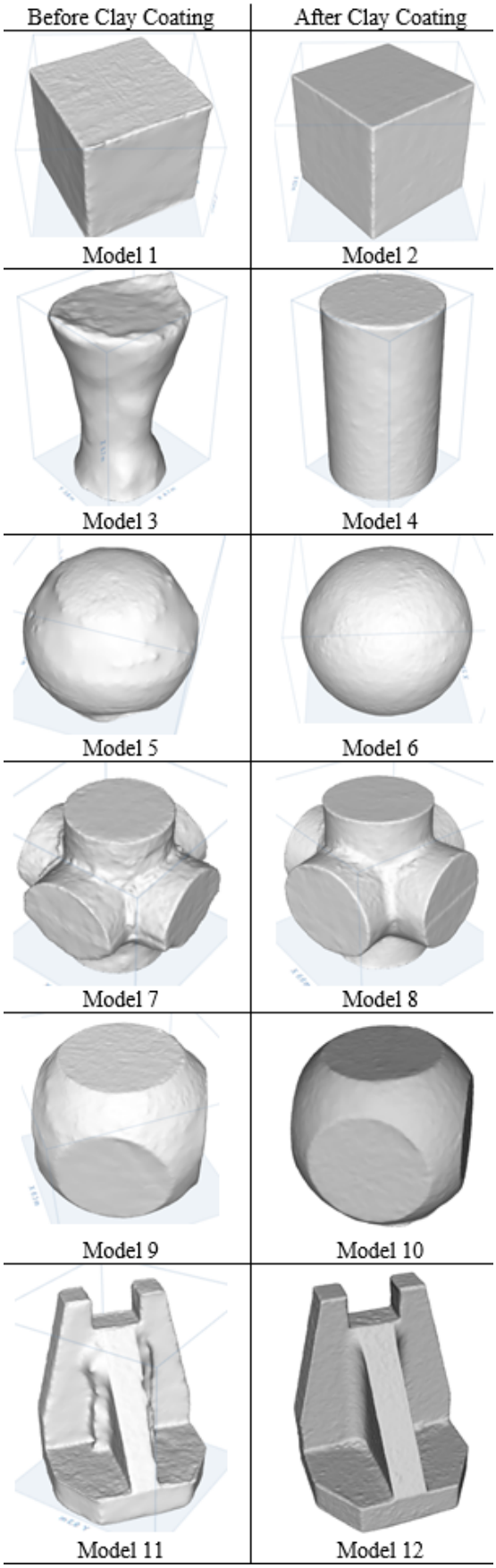


Figure 6. 3D models generated by 3D photogrammetry: The left column shows the 3D models reconstructed without the clay-coating process. The right column shows the 3D models reconstructed with the clay coating process.

Both the graphical representation in Figure 7 and the tabulated data in Table 1 demonstrate a significant reduction in both maximum and minimum deviations with the application of clay coating. Furthermore, the spread and magnitude of deviations across the surfaces of the models were notably reduced, indicating overall improvement in geometric fidelity.

The clay coating process also contributed to smoother and more accurately defined edges in all models, with particularly noticeable benefits in cylindrical and spherical surfaces. Moreover, it effectively addressed significant negative deviations observed on concave edges, further highlighting its role in enhancing geometric accuracy.

In conclusion, our study illustrates that clay coating not only minimizes surface reflections but also enhances the geometric accuracy of reconstructed 3D models. This improvement is evident across a variety of object geometries and underscores the efficacy of clay coating in advanced 3D photogrammetry applications.

Table 1. Maximum and minimum deviations of the reconstructed objects

Model No	Max. Deviation (mm)	Min. Deviation (mm)
1	1.8382	-0.6253
2	0.1491	-0.2530
3	2.9515	-2.1976
4	0.3177	-0.4748
5	1.8390	-0.6571
6	0.7467	-0.3313
7	1.3446	-0.5016
8	0,6259	-0.3205
9	1.2879	-0.7724
10	0.4671	-0.3819
11	1.0938	-2.1024
12	0.7072	-0.6389

3.3 Mesh Structure

In the study, 3D mesh models were generated for each metal object. These models are triangular polygon models that contain vertex, edge, and face data.

The 3D mesh models also provide information about the mesh structures of the models, their density, and their homogeneity. As the mesh homogeneity increase, the quality of the reconstruction also increases and the 3D model more accurately represents the object geometry (Rues et al., 2021).

The quality of the mesh structure becomes more important in ensuring dimensional accuracy, especially for objects with curved surfaces. Images of mesh models are shown in Figure 8. The difference in mesh structure between models generated from coated and uncoated objects can be clearly seen. In addition, the mesh reports for each model, containing the number of vertices and faces, are shown in Table 2.

When the mesh models of each object are examined, it is generally observed that the clay coating process homogenizes the mesh structures. The heterogeneous mesh structures are generally observed on the models generated from uncoated objects. It is seen that the mesh structures become denser at the edges and corners.

Table 2. Mesh reports of the reconstructed objects

Model No	Vertice Number	Face Number
1	35.646	64.740
2	20.204	35.478
3	13.609	24.106
4	18.758	34.144
5	25.074	43.018
6	32.448	57.282
7	36.591	63.536
8	48.233	83,072
9	32.867	58.148
10	20.273	35.198
11	69.680	125.482
12	61.217	111.500

The clay coating process reducing the glossiness of the surfaces also provided a featured texture to the surfaces. Thus, homogeneity has improved along with the geometric accuracy of the edges and surfaces.

The mesh reports of the models presented in Table 2 showed that while the clay coating increased the homogeneity, it decreased the mesh element numbers for some models.

Considering the mesh model obtained after the clay coating process of object 1, it was determined that the number of vertices decreased from 35.646 to 20.204, and the number of faces decreased from 64.740 to 35.478. Thereby, it can be said that the clay coating reduces the number of vertices by 43% and the number of faces by 45% for object 1.

Considering models 9 and 10, it is seen that the number of vertices has decreased from 32.867 to 20.273 and the number of faces has decreased from 58.148 to 35.198 after the clay coating process. Thereby, the number of vertices decreased by 38%, and the number of faces decreased by 39% for object 5.

Considering models 11 and 12, it is seen that the number of vertices has decreased from 69.680 to 61.217 and the number of faces has decreased from 125.482 to 111.500 after the clay coating process. Thereby, the number of vertices decreased by 12%, and the number of faces decreased by 11% for object 6.

However, for objects 2, 3, and 4 the coating process increased the number of mesh elements. Within the scope of these results, it may be said that the clay coating causes an increase in the number of mesh elements in models with curved, cylindrical, and spherical surfaces, and a decrease in models with flat surfaces. It is understood that both effects in the number of mesh elements are a result of the clay coating increasing the geometric accuracy.

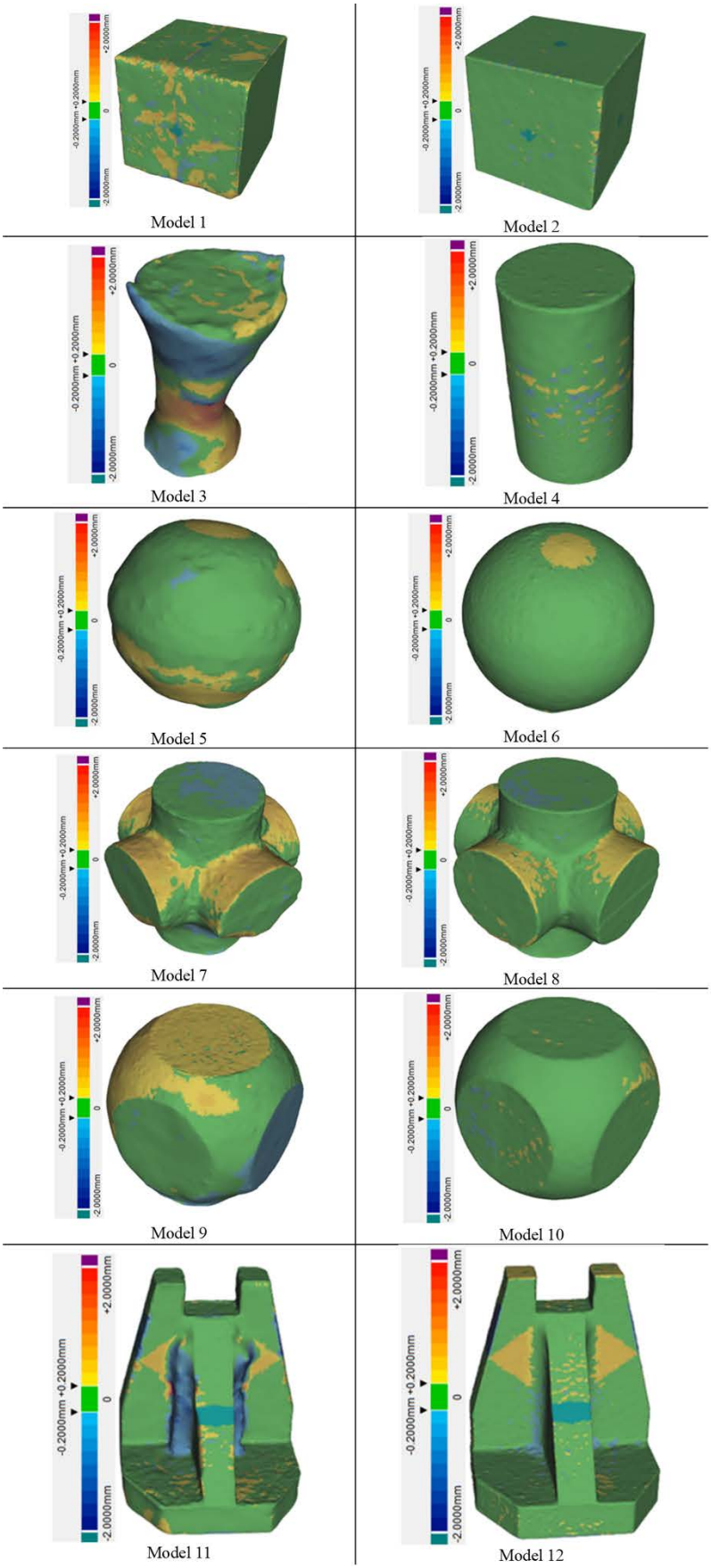


Figure 7. Results of difference analysis of the models: The left column shows the 3D models reconstructed without the coating process. The right column shows the 3D models reconstructed with the clay-coating process. Notice how the clay coating process increases the green areas within 0.2mm tolerances.

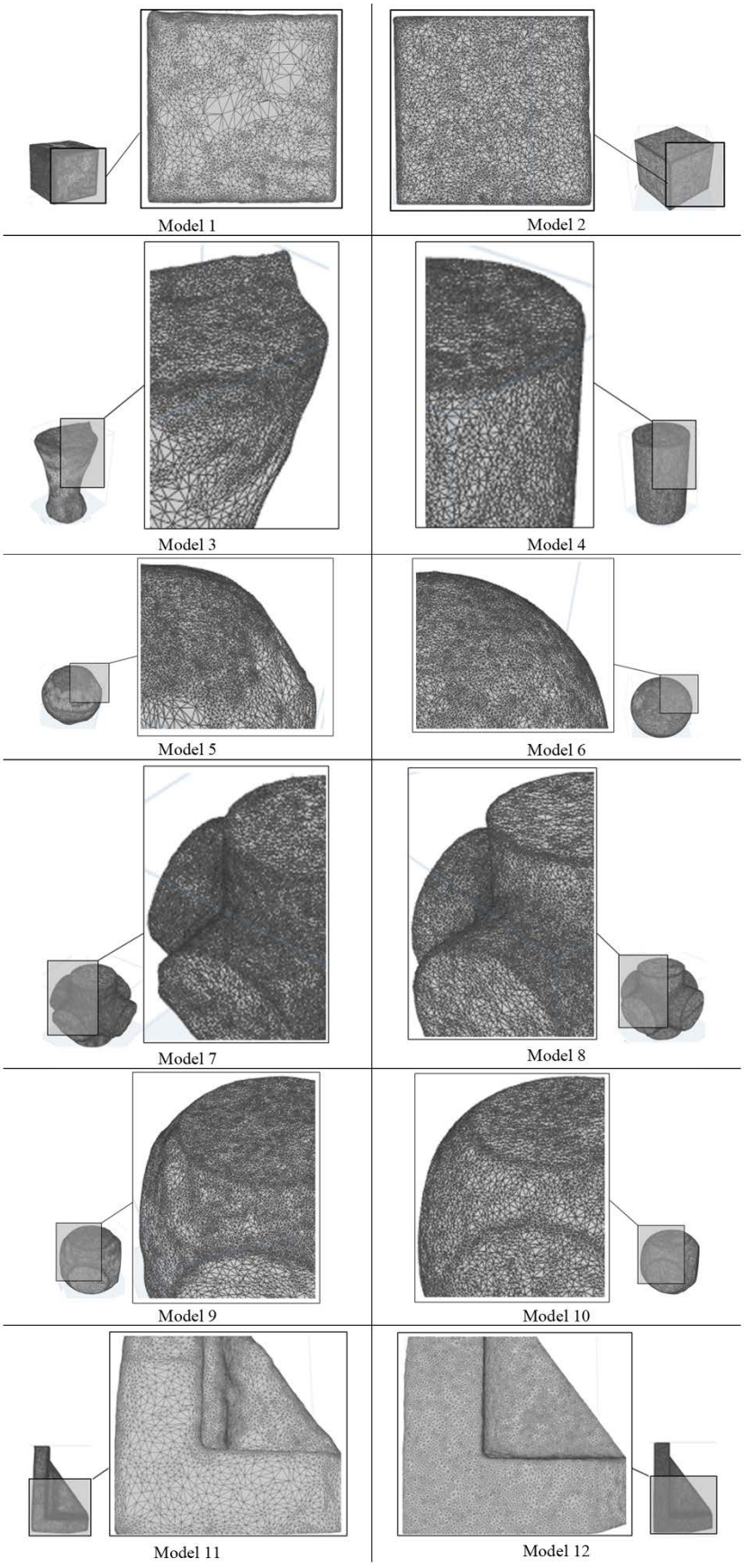


Figure 8. Mesh structures of reconstructed metal objects: The left column shows the mesh structures of the models reconstructed without the coating process. The right column shows mesh structures of the models reconstructed with the clay-coating process. Notice how the clay coating process improves mesh homogeneity in addition to improving model geometry.

This study has some limitations. The coating process was performed manually. The coating was made using clay powder obtained from the dry form of the clay material. The clay powder was crushed as much as possible. The powder was then applied in a thin layer to the surfaces using a soft brush. The objects used in the study, in addition to being metallic, have polished and very smooth surfaces. The adhesion of the clay powder was more difficult on cylindrical and spherical surfaces. The fineness of the powder enhanced the coating ability. No chemicals were used in this study to either aid in the adhesion of the powder to the surface or as part of the coating material. The clay powder can be coated using a spraying device, and coating performance can be observed. The metal objects included in the study were selected from various objects with prismatic, cylindrical, and spherical shapes to observe the effects of geometric differences accordingly. Although the reconstructed objects have various shapes, they are not very geometrically detailed objects. The photographs were taken in a closed environment to isolate external factors for the comparisons. The contribution of the clay coating to the outdoor 3D photogrammetry applications can be evaluated by the daylight applications.

4. Conclusions

This study introduced and evaluated the novel application of the clay coating process in conjunction with 3D photogrammetry for reconstructing metal objects with diverse geometric surfaces. The findings clearly demonstrate that the clay coating process significantly enhances the geometric accuracy and mesh structure of 3D models compared to uncoated objects. Both solid models and deviation analyses confirm marked improvements in edge definition, corner sharpness, and overall surface fidelity due to clay coating. Notably, the process reduces geometric deviations, evidenced by minimized maximum and minimum deviations and fewer instances of deviations beyond tolerance thresholds. Moreover, the impact on mesh structure was notable, with a reduction in irregularities and a more uniform mesh pattern observed post-coating. Clay, being a natural, cost-effective material with light-absorbing properties and a tactile texture, effectively enhances reconstruction outcomes and dimensional precision. The integration of clay coating with 3D photogrammetry presents a viable alternative to expensive 3D scanning techniques characterized by high initial costs and limited flexibility. This approach not only offers enhanced accuracy but also expands the accessibility of high-quality 3D reconstruction to diverse applications. Future research may further explore optimization strategies and broader applicability of this combined method in various fields requiring precise geometric modeling.

Author Contributions

The percentages of the author' contributions are presented below. The author reviewed and approved the final version of the manuscript.

	H.K.S.
C	100
D	100
S	100
DCP	100
DAI	100
L	100
W	100
CR	100
SR	100

C=Concept, D= design, S= supervision, DCP= data collection and/or processing, DAI= data analysis and/or interpretation, L= literature search, W= writing, CR= critical review, SR= submission and revision.

Conflict of Interest

The author declared that there is no conflict of interest.

Ethical Consideration

Ethics committee approval was not required for this study because of there was no study on animals or humans.

References

Awange J, Kiema J. 2019. Fundamentals of photogrammetry, environmental geoinformatics. Springer, Cham, Germany, pp: 161-178.

Axelsson P. 1991. Fundamentals of real-time photogrammetry, ISPRS J Photogrammet Remote Sens, 46(2): 114-115.

Beaman JJ, Barlow JW, Bourell DL, Crawford RH, Marcus HL, McAlea KP. 1997. Polymers in solid freeform fabrication, solid freeform fabrication: A new direction in manufacturing. Springer, Boston US.

Cansiz E, Arslan YZ, Turan F, Atalay B. 2014. Computer-assisted design of patient-specific sagittal split osteotomy guide and soft tissue retractor. J Medic Biol Eng, 34(4): 363.

Eulitz M, Reiss G. 2015. 3D reconstruction of SEM images by use of optical photogrammetry software. J Struct Biol, 191(2): 190-196.

Gessner A, Ptaszyński W, Adam W. 2022. Accuracy of the new method of alignment of workpiece using structural-light 3D scanner. Advan Sci Technol Res J, 16(1): 1-14.

Ghali S. 2008. Constructive solid geometry, Introduction to geometric computing. Springer, London, UK, pp: 277-283.

Gomez C, Kennedy B. 2018. Capturing volcanic plumes in 3D with UAV-based photogrammetry at Yasur Volcano – Vanuatu. J Volcanol Geothermal Res, 350: 84-88.

Helle RH, Lemu HG. 2021. A case study on use of 3D scanning for reverse engineering and quality control. Mater Today, 45: 5255-5262.

Javaid M, Haleem A, Pratap SR, Suman R. 2021. Industrial perspectives of 3D scanning: Features, roles and it's analytical applications. Sensors Int, 2: 100-114.

Kanun E. 2021. Using photogrammetric modeling in reverse engineering applications: Damaged turbocharger example. Mersin Photogrammet J, 3(1): 21-28.

Kingsland K. 2020. Comparative analysis of digital photogrammetry software for cultural heritage. Digital Appl

Archaeol Cultural Herit, 18: 157.

Kohtala S, Erichsen JF, Wullum OP, Steinert M. 2021. Photogrammetry-based 3D scanning for supporting design activities and testing in earlystage product development. Procedia CIRP, 100: 762-767.

Kurilová V, Bemberáková D, Kocián M, Šterbák D, Knapčok T, Palkovič M, Hančák S. 2023. Unexpected corneal reflection phenomenon alters smartphone 3D image-based models of the eye. J Elect Eng, 74(6): 513-520.

Mathys A, Semal P, Brecko J, Van den Spiegel D. 2019. Improving 3D photogrammetry models through spectral imaging: Tooth enamel as a case study. Plos ONE, 14(8): 1-33.

Matthews NA. 2008. Aerial and close-range photogrammetric technology: providing resource documentation, interpretation, and preservation. US Department of the Interior, Bureau of Land Management, National Operations Center, Denver, Colorado, US.

Molnár A. 2019. Surveying archaeological sites and architectural monuments with aerial drone photos. Acta Polytech Hungarica, 16(7): 217-232.

Orun AB, Goodyer E, Smith G. 2018. 3D non-invasive inspection of the skin lesions by close-range and low-cost photogrammetric techniques. Image Analy Stereol, 37(1): 63-70.

Pepe M, Costantino D. 2020. UAV photogrammetry and 3D modelling of complex architecture for maintenance purposes: The case study of the Masonry Bridge on the Sele River, Italy. Period Polytech Civil Eng, 65: 1-13.

Puerta APV, Jimenez-Rodriguez RA, Fernandez-Vidal S, Fernandez-Vidal SR. 2020. Photogrammetry as an engineering design tool. In Alexandru C, Jaliu C, Comşit M eds., Product design, IntechOpen, London, UK, pp: 41.

Reis HC. 2018. Detection of foot bone anomaly using medical photogrammetry. Int J Eng Geosci, 3(1): 1-5.

Remondino F, El-Hakim S. 2006. Image-based 3D modelling: A review. Photogrammet Record, 21(115): 269-291.

Rues S, Waldecker M, Rammelsberg P, Zenthöfer A. 2021. Effect of mesh homogeneity and choice of target surface on statistical evaluation of mesh differences. Biotribology, l(26): 100-176.

Seeberger R, Hoffmann J, Freudlsperger C, Berger M, Bodem J, Horn D, Engel M. 2016. Intracranial volume (ICV) in isolated sagittal craniosynostosis measured by 3D photocephalometry: A new perspective on a controversial issue. J Cranio-Maxillofacial Surg, 44(5): 626-631.

Slaker B, Mohamed K. 2017. A practical application of photogrammetry to performing rib characterization measurements in an underground coal mine using a DSLR camera. Int J Mining Sci Technol, 27(1): 83-90.

Struck R, Cordoni S, Aliotta S, Pérez-Pachón L, Gröning F. 2019. Application of photogrammetry in biomedical science. In: Rea P (eds) Biomedical Visualisation. Advances in Experimental Medicine and Biology, vol 1120. Springer, Cham, pp: 121-130. https://doi.org/10.1007/978-3-030-06070-1_10

Surmen HK, Akalan NE, Fetvaci MC, Arslan YZ. 2018. A Novel dorsal trimline approach for passive-dynamic ankle-foot orthoses. Strojniški Vestnik J Mechan Eng, 64(3): 185-194.

Surmen HK. 2023. Photogrammetry for 3D reconstruction of objects: Effects of geometry, texture and photographing. Image Analy Stereol, 42(2): 51-63.

Tóth D, Petrus K, Heckmann V, Simon G, Poór VS. 2021. Application of photogrammetry in forensic pathology education of medical students in response to COVID-19. J Forensic Sci, 66(4): 1533-1537.

Valinasab B, Rukosuyev M, Lee J, Ko J, Jun MBG. 2015. Improvement of optical 3D scanner performance using atomization-based spray coating. J Korean Soc Manufact Technol Eng, 24(1): 23-30.

Wang H, Zhou J, Zhao T, Tao Y. 2016. Springback compensation of automotive panel based on three-dimensional scanning and reverse engineering. Int J Advan Manufact Technol, 85(5): 1187-1193.

Yaman A, Yılmaz HM. 2017. The effect of object surface colors on terrestrial laser scanners. Int J Eng Geosci, 2(2): 68-74.

Yang S, Shi X, Zhang G, Lv C. 2018. A dual-platform laser scanner for 3D reconstruction of dental pieces. Engineering, 4(6): 796-805.

Black Sea Journal of Engineering and Science
doi: 10.34248/bsengineering.1634974

Open Access Journal
e-ISSN: 2619 – 8991

Research Article
Volume 8 - Issue 2: 517-523 / March 2025

PRODUCTION OF PURE PVC, GRAPHENE AND CARBON NANOTUBE-DOPED PVC ELECTROSPUN NANOFIBER MEMBRANES: A HIGHLY EFFECTIVE METHOD FOR REMOVING ACID BLUE 74 DYE FROM WASTEWATER

Vildan ÖZKAN[1]*, Pınar BOZBEYOĞLU[2]

[1]Iskenderun Technical University, Faculty of Engineering and Natural Sciences, 31200, Hatay, Türkiye
[2]Gümüşhane University, Gümüşhane Vocational School, Biomedical Device Technology Program, 29000, Gümüşhane, Türkiye

Abstract: Dyeing wastewater is produced by various industries, including textiles, cosmetics, tanning, and plastics. Annually, about 1.6 million tons of dyes are manufactured, with 10-15% released into the environment as wastewater. Organic dyes are particularly harmful pollutants, even at low concentrations. The adsorption technique has proven effective for removing these pollutants from water, significantly relying on the properties and efficiency of the adsorbent. Nanofibers are emerging as promising adsorbents for dye removal due to their unique properties and high efficiency. This research focuses on polymeric nanofibers to address global dye pollution, as they effectively eliminate various dyes and contaminants. However, their mechanical properties can be a limitation under harsh conditions. To enhance their strength and hydrophilicity, incorporating nanofillers like carbon nanotubes and graphene oxide has shown significant benefits. This study examines the impact of different nanofibers on the adsorption of Acid Blue 74 (AB74) dye. Pure, carbon nanotube-doped, and graphene-doped PVC nanofibers were produced via electrospinning. Their properties were analyzed using FTIR and SEM, while key parameters such as contact time, adsorbent dosage, dye concentration, and pH were assessed to understand the adsorption behavior. Additionally, dye adsorption isotherms and kinetics were investigated.

Keywords: Nanofibers, Wastewater treatment, Electrospinning, Dyes, Adsorption

***Sorumlu yazar (Corresponding author):** Iskenderun Technical University, Faculty of Engineering and Natural Sciences, 31200, Hatay, Türkiye
E mail: vildan.ozkan@iste.edu.tr (V.OZKAN)
Vildan ÖZKAN https://orcid.org/0000-0001-8719-9099
Pınar BOZBEYOĞLU https://orcid.org/0000-0002-3704-2701

Received: February 07, 2025
Accepted: March 04, 2025
Published: March 15, 2025

Cite as: Ozkan V, Bozbeyoglu P. 2025. Production of pure PVC, graphene and carbon nanotube-doped PVC electrospun nanofiber membranes: A highly effective method for removing acid blue 74 dye from wastewater. BSJ Eng Sci, 8(2): 517-523.

1. Introduction

Textile industries utilize large amounts of dyes to provide distinctive textures to fabric materials. Approximately 10% of the colors used in textile processes are discharged into wastewater. Wastewater from textile manufacturing facilities is recognized as one of the most polluting among various industries due to its significant content of hazardous waste. Treating contaminated water, such as non-industrial waste, is an effective method for recycling lost water (water treatment) (Mo et al., 2008). Various conventional technologies are employed to remove different pollutants (inorganic, organic, biological, and radiological) from aqueous solutions (Kaczyk et al., 2020). These technologies include ion exchange, chemical oxidation, reduction, precipitation, biological, electrodialysis, (Altıntaş et al., 2023) coagulation, electrocoagulation, flocculation, liquid-liquid extraction, evaporation (Fadlalla et al., 2020), phytoremediation, filtration/adsorption, reverse osmosis, and ultra-, nano-, or micro-filtration (Kurniawan et al., 2006; Ayodhya and Veerabhadram, 2018).

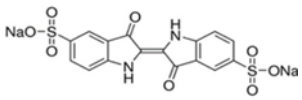
In the textile industry, Acid Blue 74 (AB74) is one of the most commonly used dyes for dyeing wool and silk (Ghanavati et al., 2021). This dye is highly toxic and carcinogenic. Exposure to AB74 can cause skin and eye irritation in humans (Li et al., 2012). Acid Blue 74, also known as Indigo Carmine or Indigotine, is a synthetic dye widely used in textiles, food, and the pharmaceutical industry. It is derived from indigo and is recognized for its vibrant color and stability. In environmental science, indigo carmine is often studied as a model pollutant due to its widespread use and potential impact on water quality. Its removal from wastewater is a significant focus in developing effective nano adsorbents and filtration techniques (Wang Q et al., 2019; Wang W et al., 2019; Wang et al., 2015). Below is an exploration of its properties, including its chemical structure, uses, and environmental impact in wastewater.

Acid Blue 74 (AB74) is a sulfonated derivative of indigo. It consists of a central indole structure with two aromatic rings linked by a double bond between two carbon atoms. The sulfonic acid group ($-SO_3H$) makes it water-soluble and allows it to dissociate in aqueous solutions (Attia et al.,, 2006). The presence of the sulfonate group enhances its solubility compared to the original indigo

This work is licensed (CC BY-NC 4.0) under Creative Commons Attribution 4.0 International License

dye, making it suitable for various applications. Textiles are traditionally used in dyeing fabrics, especially in textile industries, for their vibrant blue color and in food and beverages (Rehorek et al., 2004). It is employed as a food colorant (E132) for various products, giving them an appealing blue hue. In medicinal, it is sometimes used in pharmaceutical formulations and as a color indicator in biological studies (Yagub et al., 2014). In cosmetics, found in personal care products for coloring purposes. By electrospinning technique, it is possible to produce PVC nanofiber membrane material with high specific surface area and high porosity, which is useful for adsorption and filtration applications (Wang et al., 2022).

Table 1. Characteristic properties of Acid Blue 74 (AB74) dyes

Properties of Dye	Acid Blue 74 (AB74)
Common name	Indigo Carmine
Color index number	73015
Chemical name(IUPAC)	Disodyum [2(2′)E]-3,3′-diokso-1,1′ ,3,3′ -tetrahidro [2,2′-biindoliliden]-5,5′-disülfonat
Molecular weight	466.35 g mol^{-1}
	
Chemical formula	$C_{16}H_8N_2Na_2O_8S_2$
Suitablefor detection wavelength	650 nm

The interaction of AB74 dye with nano adsorbents is governed by multiple adsorption mechanisms, primarily involving physisorption and chemisorption (Ahmed and Lalia, 2015). Key factors like pH, temperature, initial dye concentration, contact time, and the specific properties of the nano adsorbents play crucial roles in determining the extent and efficiency of adsorption. For effective wastewater treatment solutions, it's essential to optimize these parameters and tailor nano adsorbent materials to effectively capture and remove contaminants like AB74 dye. Adding graphene or carbon nanotubes can significantly enhance the adsorption properties of PVC. These materials possess high surface areas and can provide additional adsorption sites. They may also improve mechanical properties and electrical conductivity. In this study the AB74 dye adsorption of the synthesized nanofibers was described exploring the influence of several parameters, including contact time, adsorbent dosage, dye concentration, and pH of solution.

2. Materials and Methods

2.1. Materials

The PVC used in the study was supplied by Sigma-Aldrich; its viscosity is 0.80 dL / g, density is 1.4 g / mL (at 25 °C), and molecular weight is Mw = ~80,000. The supplied PVC was dissolved in a mixture of THF and DMF prepared in a weight ratio of (1:1) to 15% by weight. Indigoid dye AB74 (Mw = 466 g mol^{-1}) was obtained from Sigma–Aldrich as a commercially available dye (85%) and used without further purification (Briesemeister et al., 2024).

2.2.Methods

2.2.1. Nanofiber production

The polymer solution was placed into 10 mL syringes in the pump unit. Nanofibers were produced at 27 kV voltage and 0.6 mL/h feed rate. During production, the ambient temperature was 25 °C on average, and the relative humidity was between 50%-60%. The distance between the syringe tip and the drum was 24 cm (Xue et al., 2019). Under the given conditions, the nanofiber sheets obtained were kept at ambient temperature for 3 days so that the solvent that might remain on them could evaporate. The thickness of the nanofiber sheets obtained varied between 0.004-0.005 mm. Three different types of PVC nanofiber sheets were produced. Three different products were obtained pure PVC nanofiber sheets, 2% carbon nanotube-doped PVC nanofiber sheets, and 2% graphene-doped PVC nanofiber sheets. For the PVC solution to be as homogeneous as possible, the solution was first placed in the magnetic stirrer for about half an hour until the solid particles dissolved and then kept in an ultrasonic bath for 1 hour (Ozkan et al., 2019). For our study, the electrospinning production method was preferred among nanofiber production methods. The electrospinning device used in production is given in Figure 1.

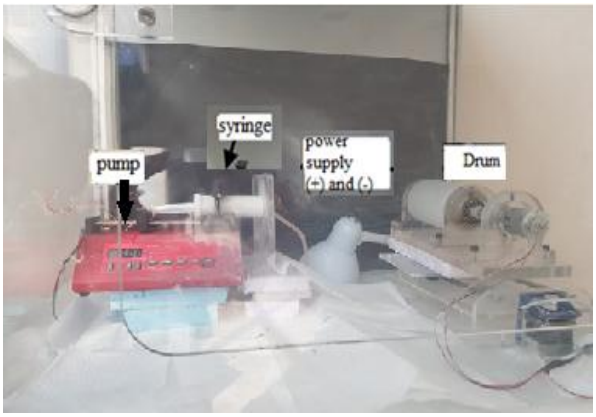


Figure 1. Electrospinning device used in nanofiber production.

2.2.2. Characterization of adsorbents

The FTIR spectra of untreated pure PVC nanofibers membranes, PVC/CNT nanofiber membranes, and PVC/G nanofiber membranes were analyzed using a PerkinElmer 1600 Fourier Transform Infrared (FTIR) spectrometer, covering a range from 4000 to 400 cm^{-1}. The surface morphology and topography of the electrospun nanofibers were examined with a Jeol JSM-6335F scanning electron microscope (Wang et al., 2015;Wang et al., 2016). Infrared (IR) spectra were also

collected during the study. To determine the thermal properties of the produced nanofibers, DSC analyses were carried out in the presence of nitrogen gas (N_2) in the Perkin Elmer DSC-4000 model Differential Scanning Caliper (DSC) device at a heating rate of 20 °C min^{-1} and the range of 30-400 °C (Ozkan, 2019)

2.2.3. Adsorption tests

This study obtained three different adsorbents by electrospinning with PVC on different nanofiber membranes. The adsorption performance of all three adsorbents in the aqueous solution and the samples was tested. As the adsorbate, AB74, a basic anionic dye, was used to represent the total dyes in the adsorption studies. To evaluate the adsorptive removal capacity of PVC nanofiber membranes for the AB74 dye, 0.030 g of the adsorbents were weighed, mixed with 25 mL of AB74 solutions between 50 and 500 mg/L, and treated separately until equilibrium was reached for ten hours. Each flask was shaken in a Nuve ST 402 shaking water bath at a constant speed of 150 rpm. Then, adsorbent particles and adsorbate molecules were separated with the help of a vacuum filtration device. The concentrations of AB74 remaining in the filtrate were determined at 650 nm in a UV-VIS spectrophotometer in the mg/L concentration unit. The results were then converted to mg/g by Formula (1) and % by Formula (2).

$$Q_e\ (mg/g) = \frac{C_o - C_e}{m} \quad (1)$$

$$Q_e\ (\%) = \frac{C_o - C_e}{C_o} \times 100 \quad (2)$$

Where Qe (mg/g) and Qe (%) mean the amount of AB74 molecules adsorbed on the adsorbent at equilibrium, Co and Ce represent the initial and equilibrium AB74 concentrations (mg/L), respectively. m is the adsorbent mass (g).

The experiments were conducted at three different temperatures: 5 °C, 15 °C, 25 °C, 35 °C, and 50 °C, to assess the effect of temperature. Additionally, the pH of the dye solutions was varied between 2 and 12 to investigate the impact of pH, with the shaking duration set at 10 hours. After filtering the dye solutions, absorbance values were measured at 650 nm. The measured absorbance data were then converted to concentration data using a calibration graph specific to the dye.

3. Results and Discussion

3.1. Results of Characterization Analysis of Adsorbents

3.1.1. SEM analysis

SEM analysis is a crucial tool for characterizing the surface morphology and physical properties of adsorbent materials. It helps determine the particle shape, porosity, and size distribution of the adsorbent. Additionally, nanofibers with high porosity exhibit superior dye removal capabilities due to their increased surface area and greater availability of adsorption sites.

In the study, SEM images of PVC, carbon nanotube-doped PVC, and graphene-doped PVC nanofibers obtained by electrospinning were obtained with the ZEISS GeminiSEM brand SEM device, which is shown in Figure 3. (Zakaria, 2021).



Figure 2. Nanofiber membranes obtained from PVC polymer, a) Pure PVC Nanofiber membranes, b) 2% carbon nanotube-doped PVC nanofiber sheets, c) 2% graphene-doped PVC nanofiber sheets.

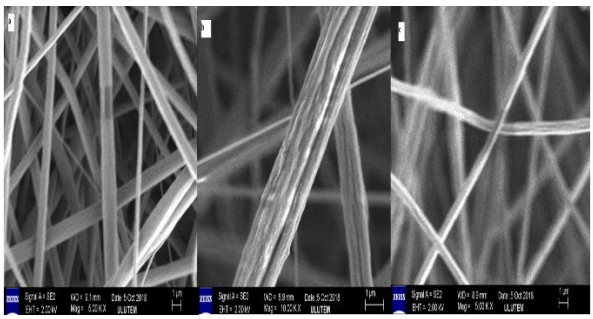


Figure 3. SEM Analysis a) PVC b) PVC-CNT c) PVC-G nanofibers.

The random distribution of nanofibers of all examined membranes is seen in the SEM image in Figure 3. The SEM images also show that all of the nanofibers produced are obtained in a droplet-free and homogeneous distribution (Ray et al., 2016).

3.1.2. FTIR analysis

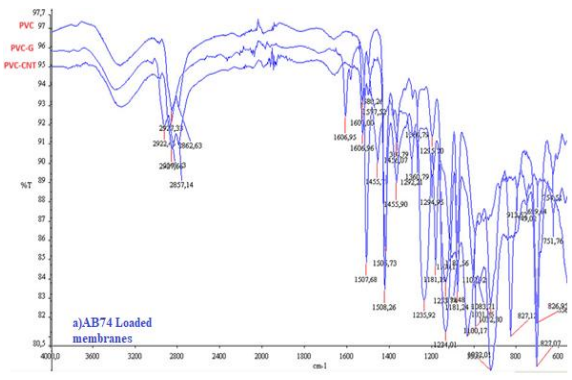


Figure 4. a) IR spectra for AB74 loaded nanofiber membranes.

The spectra of AB74 and AB74 loaded PVC, PVC/CNT, and PVC/G in Figure 4 are similar. Since AB74 covers the surface, the spectrum of AB74-loaded adsorbents is similar to the original AB74 spectrum. The adsorption capacity of adsorbents for AB74 is high. The shift in

permeability can explain the formation of similar spectra. After AB74 dye adsorption, first of all, it is seen that the relative permeability (T) percentages increase compared to the original adsorbents.

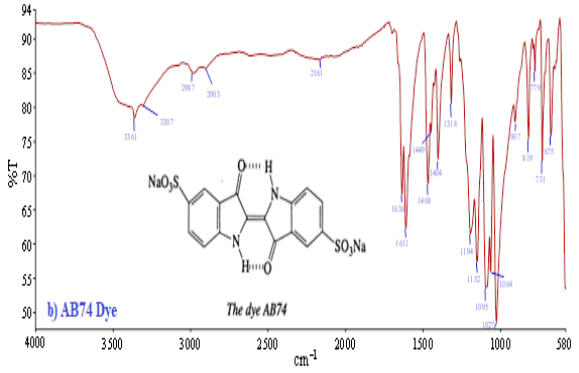


Figure 4. b) Spectrum of original AB74 dye.

The increase in permeability is a natural result resulting from the occupation of functional groups by dye molecules. The spectra taken after adsorption show that PVC nanofiber membrane has extra peaks compared to other adsorbents, and some peaks have shifts in wavelength values. The most significant change occurs after adsorption with PVC/G nanofiber membrane. When the IR spectra of the AB 74 dye given in Figure 4 are examined, typical AB74 peaks appear between 1517–1623 cm^{-1} due to the surface coating feature. This situation is also seen in the spectra of many other adsorbents taken after AB74 adsorption. In the IR spectra taken after dye adsorption for membranes, extra peaks consisting of hydroxyl groups are seen around 2850 cm^{-1} compared to the pure PVC. However, since the groups characterizing the adsorbents are generally the peaks that appear toward the right side of the spectrum, this situation does not constitute a problem (Zakaria, 2021).

3.1.3. TGA/DSC analysis

Thermal analysis measurements were performed with TGA Shimadzu, a TGA-50 device (thermogravimetric analysis) from room temperature to 400 °C (at a heating rate of 10 °C/min), and with DSC Shimadzu, a DSC-50 device (differential scanning calorimeter) from room temperature to 200 °C (at a heating temperature of 20 °C/min) under a dynamic nitrogen atmosphere (10 mL/min low flow rate).

Figure 5 shows DSC graphs of pure, carbon nanotube-doped, and graphene-doped PVC nanofiber membranes. The DSC curves of the samples are given in graphs and interpreted comparatively. Accordingly, they showed exothermic behavior. The glass transition temperature is high for PVC nanofibers.

As seen in Table 2, the highest glass transition temperature belongs to the CNT-doped PVC-nanofiber membrane, while the lowest belongs to the pure PVC-nanofiber membrane. The peak length is the longest for the pure PVC-nanofiber membrane, which shows that it has the lowest exothermic reaction rate among all materials.

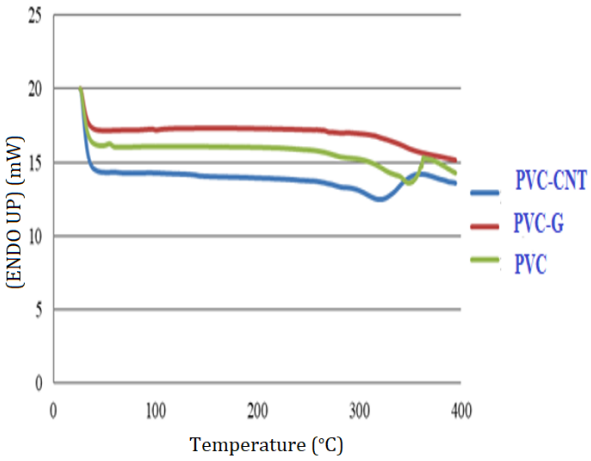


Figure 5. DSC graphs of pure, carbon nanotube-doped, and graphene-doped PVC nanofiber membranes.

Table 2. DSC test results of the produced nanofiber membranes

	PVC-CNT	PVC-G	Pure PVC
T_g	95 °C	94 °C	51 °C
T_{on}	288 °C	267 °C	321 °C
T_{max}	322 °C	270 °C	348 °C
ΔH	-165.8641 J/g	-2.0228 J/g	-174.9227 J/g
P_H	1.4048 mW	0.0677 mW	1.7277 mW
T_{off}	348 °C	258 °C	362 °C

3.2.Results of Adsorption Of AB 74 Dyes on Nanofiber Membranes

3.2.1. Effect of pH on adsorption of AB 74 dye on PVC nanofibers

250 mg/L batch dye solution with pH adjusted between 2-12 was prepared and treated with 3.0 g/L adsorbent for 10 hours. After filtration, the remaining dye concentrations in the solution without being adsorbed were determined by UV-VİS spectrophotometer. According to Figure 6, it has been determined that there is a possibility of working in a wide pH range, especially for AB74 adsorption. Although it was determined that acidic conditions were suitable for AB 74, pH five would be more suitable. As seen in Figure 6, the highest adsorption capacity (qt) was obtained at pH =5 and 43.57 with a CNT-doped PVC nanofiber membrane. However, the decrease in adsorption capacity with increasing pH value to 8 is related to the decrease in dye adsorption due to the competitive effect of OH- and anionic dye to be adsorbed on the solid surface. The wide adaptation of the surface and pore structure of the copolymer particles to HR molecules can be considered the main factor in removing dyes (Ahmed et al., 2017).

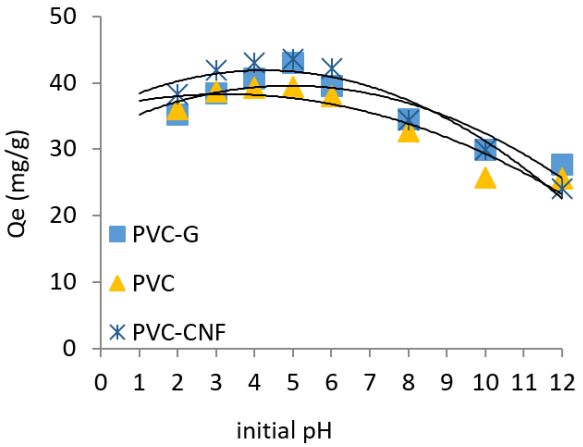


Figure 6. Effect of initial solution pH on adsorption of AB74 (Initial dye concentration: 250 mg/L, ads. dose: 3.0 g/L, agitation time: 10 h).

3.2.2. Effect of temperature on adsorption of AB 74 dyes and adsorption ısotherms

B250 mg/L dyestuff solutions were treated with 3.0 g/L adsorbents at room temperature for 10 hours. The concentrations of dyestuff remaining without adsorbing in the solution were determined by UV-VİS spectrophotometer. That is, the adsorption of dyestuffs on the adsorbents occurs spontaneously and voluntarily (Figure 7).

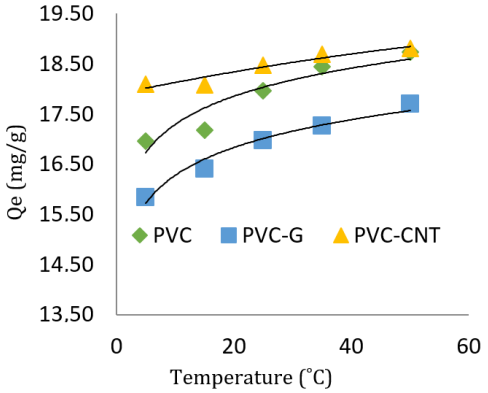


Figure 7. Effect of temperature (Initial dye conc.: 250 mg/L, pH: 5.0, ads. dose: 3,00 g/L).

The adsorption equilibrium isotherm is important because it gives a clear clue about the distribution pattern of dye molecules between the liquid and solid phases when the adsorption process reaches an equilibrium state. The isotherm is vital for the design of adsorption systems, and its shape can explain the homogeneity and heterogeneity of the adsorbent surface. The equilibrium data of dyes were analyzed by fitting them to the Langmuir equations to find the appropriate model to describe the adsorption mechanism. Langmuir isotherm equation 3 is;

$$\frac{C_e}{q_e} = \frac{C_e}{q_{max}} + \frac{1}{bq_{max}} \qquad (3)$$

Table 3. Adsorption constants obtained according to the Langmuir model in the adsorption of AB 74 onto PVC nanofibers

	Qmaks(mg/g)	*b*(L/mg)	slope	R^2
PVC	39.42	0.0107	0.0136	0.999
PVC-G	40.26	0.0095	0.0112	0.996
PVC-CNT	43.57	0.0109	0.0121	0.997

3.2.3. Effect of contact time on adsorption of dyes

The time dependence of the adsorption process is called adsorption kinetics. The equilibrium time for AB 74 dye adsorption on PVC nanofibers was determined in the 0–12 h range. For this purpose, a series of dye solutions containing 500 mg/L and pHs between 4–6 were treated with 3.0 g/L adsorbents at different intervals. After the mixtures taken at different time intervals were filtered, the AB 74 dye remaining in the filtrate was determined by UV-GB at 630 nm wavelength (Bozbeyoğlu and Gündoğdu, 2023). Dye adsorption (%) graphs were drawn against shaking time (min) from the results.

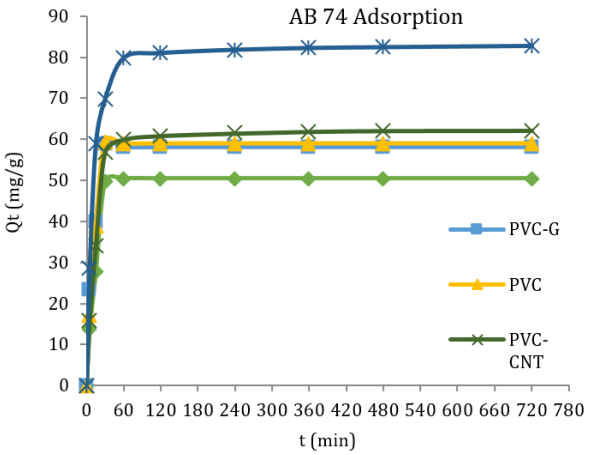


Figure 8. Changes in dye adsorption over time.

Figure 8 shows a sharp rise in the dye concentration during the 60-minute contact time due to the adsorption of anionic dye onto the negatively charged PVC nanofiber membrane material via electrostatic attraction forces. After 120 min, no significant change in the dye concentration was observed for the membrane material AB 74 system.

3.2.4. Desorption and reuse experiments

Acetone, ethanol, NaCl, and HCl were used as eluents to investigate the reusability of PVC nanofiber membrane material. Before the desorption experiment, AB 74 dye (25 mL, 3.5×10-5 mol.L^{-1}) was loaded onto 0.0030 g of membrane material for 10 h. Then, AB74-loaded PVC nanofiber membrane materials were separately transferred to Erlenmeyer flasks containing 25 mL of ethyl alcohol, 0,1 M HCl, 0,1 M NaCl, and acetone and shaken at 25 °C for 10 h. Desorbed AB 74 concentrations were measured using the spectrophotometric method, and the dye desorption efficiency of the spent membrane

material was calculated. The desorption studies, shown in Figure 9, showed that the desorption performance of acetone and ethanol used in a 1:1 ratio was better than that of NaCl and HCl (Gundogdu, 2022).

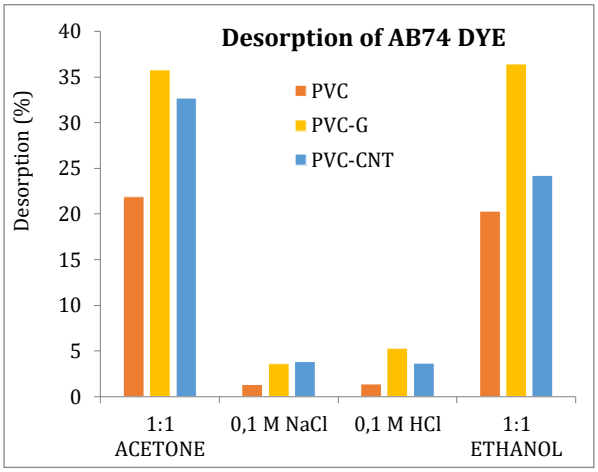


Figure 9. Desorption studies.

4. Conclusion

AB 74 dye is a widely used synthetic dye with important applications across industries, but its environmental implications require careful management. Effective waste treatment solutions to minimize the discharge of indigo carmine into water systems are critical to protecting aquatic ecosystems and ensuring water quality.

- In the studies, suitable conditions for factors such as pH, temperature, and time's effect on AB 74 dye solutions were determined using a model solution, and dye removal from wastewater was carried out.
- It was determined that the optimum pH range for AB 74 dyes was around five and that the shaking time increased the adsorption capacity to 60 minutes, reaching equilibrium after 60 minutes.
- It was determined that the adsorption capacity of pure PVC nanofiber membrane was lower than that of graphene-doped PVC nanofiber membrane, and the adsorbent with the best adsorption capacity belonged to the carbon nanotube-doped PVC nanofiber membrane.
- When the equilibrium data of AB 74 dye were examined, the Langmuir isotherm model was determined to be the most suitable model with a high R^2 value for describing the adsorption mechanism.

Author Contributions

The percentages of the authors' contributions are presented below. All authors reviewed and approved the final version of the manuscript.

	V.Ö.	P.B
C	50	50
D	50	50
S	50	50
DCP	50	50
DAI	50	50
L	50	50
W	50	50
CR	50	50
SR	50	50
PM	50	50
FA	50	50

C=Concept, D= design, S= supervision, DCP= data collection and/or processing, DAI= data analysis and/or interpretation, L= literature search, W= writing, CR= critical review, SR= submission and revision, PM= project management, FA= funding acquisition.

Conflict of Interest

The authors declared that there is no conflict of interest.

Ethical Consideration

Ethics committee approval was not required for this study because of there was no study on animals or humans.

References

Ahmed FE, Lalia BS. 2015. A review on electrospinning for membrane fabrication: Challenges and applications. Desalination, 356: 15-30.

Ahmed MA, Brick AA, Mohamed AA. 2017. An efficient adsorption of indigo carmine dye from aqueous solution on mesoporous Mg/Fe layered double hydroxide nanoparticles prepared by controlled sol-gel route. Chemosphere, 174: 280-288.

Altıntaş F, Delimanlar M, Kolcu E, Olgaç BM. 2023. Filtration with Nanofibers. Res J Biomedic Biotechnol, 4(1): 1-11.

Attia AA, Rashwan WE, Khedr SA. 2006. Capacity of activated carbon in the removal of acid dyes subsequent to its thermal treatment. Dyes Pigment, 69: 128-136.

Ayodhya D, Veerabhadram G. 2018. A review on recent advances in photodegradation of dyes using doped and heterojunction-based semiconductor metal sulfide nanostructures for environmental protection. Mater Today Ener, 9: 83-113.

Bozbeyoglu P, Gündoğdu A. 2023. Adsorption of hexavalent chromium from aqueous solution onto corn cobs – activated carbon. Turkish J Analyt Chem, 5(2): 107-117.

Briesemeister M, Gómez-Sánchez JA, Bertemes-Filho P, Pezzin SH. 2024. PVC/CNT electrospun composites: morphology, thermal and impedance spectra. Polymers, 16(20): 2867.

Fadlalla MI, Kumar PS, Selvam V, Babu SG. 2020. Emerging energy and environmental application of graphene and their composites: a review. J Mater Sci, 55: 7156-7183.

Ghanavati L, Hekmati AH, Rashidi A, Shafiekhani A. 2021.

Application of electrospun polyamide-6/modified zeolite nanofibrous composite to remove Acid Blue 74 from textile dyeing wastewater. J Textil Inst, 112: 1730-1742.

Gundogdu A, Bozbeyoglu, P, Imamoglu M, Baltaci C, Duran C, Bulut VN. 2022. Characterization of the adsorption mechanism of cadmium(II) and methylene blue upon corncobs activated carbon. Analyt Lett, 56(3): 433-448.

Kaczyk A, Mitrowska K, Posyniak A. 2020. Synthetic organic dyes as pollutants of the aquatic environment and their effects for ecosystems: A review. Sci Total Environ, 717: 137222.

Kurniawan TA, Chan GYS, Lo WH, Babel S. 2006. Physico-chemical treatment techniques for wastewater laden with heavy metals. Chem Eng J, 118: 83-98.

Li M, Wang H, Wu S, li F, Zhi P. 2012. Adsorption of hazardous dyes indigo carmine and acid red on nanofiber membranes. RSC Adv, 2: 900-907.

Mo JH, Lee YH, Kim J, Jeong JY, Jegal J. 2008. Treatment of dye aqueous solutions using nanofiltration polyamide composite membranes for reuse of dye wastewater. Paint Pigment, 76: 429-434.

Ozkan V, Yapici A, Karaaslan M, Akgol O. 2019. Investigation of electromagnetic properties of glass-fiber reinforced epoxy composites containing PAN nanofibers with MWCNT/Graphene additive. Fresenius Environ Bull, 28(3): 2238-2246.

Ozkan V. 2019. Production and characterization of nanocomposite materials by adding nanoparticles to petroleum-derived polymers. PhD Thesis, Iskenderun Technical University, Institute of Engineering and Science, Hatay, Turkiye, pp: 200.

Ray SS, Chen SS, Li CW, Nguyen NC, Nguyen, HT. 2016. A comprehensive review: Electrospinning technique for fabrication and surface modification of membranes for water purification applications. RSC Adv, 6: 85495-85514.

Rehorek A, Tauber M, Gübitz G. 2004. Application of power ultrasound for azo dye degradation. Ultrason Sonochem, 11: 177-182.

Wang W, Fan Z, Zhu Q, Li M, Liu K, Yan K, Wang D. 2019. Efficient adsorption properties of dyes from aqueous solution by poly(vinyl alcohol-co-ethylene) nanofiber membranes modified with β-cyclodextrin. Color Technol, 135: 244-249.

Wang Q, Ju J, Tan Y, Hao L, Ma Y, Wu Y, Zhang H, Xia Y, Sui K. 2019. Controlled synthesis of sodium alginate electrospun nanofiber membranes for multioccasion adsorption and separation of methylene blue. Carbohydr Polym, 205: 125-134.

Wang SX, Yap CC, He J, Chen C, Wong SY, Li X. 2016. Electrospinning: A facile technique to produce functional nanofibers for environmental applications. Nanotechnol Rev, 5: 51-73.

Wang X, Dong J, Gong C, Zhang S, Yang J, Zhang A, Feng Z. 2022. Bendable poly(vinylidene fluoride)/ polydopamine/β-cyclodextrin composite electrospun membranes for highly efficient and bidirectional adsorption of cation and anion dyes from aqueous media. Compos Sci Technol, 219: 109256.

Wang X, Fu Q, Wang X, Si Y, Yu J, Wang X, Ding B. 2015. In situ cross-linked and highly carboxylated poly(vinyl alcohol) nanofibrous membranes for efficient adsorption of proteins. J Mater Chem B, 3: 7281-7290.

Wang Y, Zhu J, Dong G, Zhang Y, Guo N, Liu J. 2015. Ulfonated halloysite nanotubes/polyethersulfone nanocomposite membrane for efficient dye purification. Sep Purif Technol, 150: 243-251.

Xue J, Wu T, Dai Y, Xia Y. 2019. Electrospinning and electrospinning nanofibers: Methods, materials and applications. Chem Rev, 119: 5298-5415.

Yagub MT, Sen TK, Afroze S. 2014. Ang, HM Dye and its removal from aqueous solution by adsorption: A review. Adv Colloid Interf Sci, 209: 172-184.

Zakaria AF, Kamaruzaman S, Abdul Rahman N. 2021. Electrospun polyacrylonitrile/lignin/poly(ethylene glycol)-based porous activated carbon nanofiber for removal of nickel(II) ion from aqueous solution. Polymers, 13: 3590.

Black Sea Journal of Engineering and Science
doi: 10.34248/bsengineering.1629319

Open Access Journal
e-ISSN: 2619 – 8991

Research Article
Volume 8 - Issue 2: 524-536/ March 2025

FROM SIMULATORS TO SKIES: ENGINEERING AND EDUCATIONAL ADVANCEMENTS IN PILOT TRAINING: A BIBLIOMETRIC PERSPECTIVE

Ayşe Aslı YILMAZ[1]*

[1]*Atılım University, School of Civil Aviation, Department of Pilot Training, 06830, Ankara, Türkiye*

Abstract: The integration of advanced engineering innovations into pilot training has brought transformative changes to aviation education, emphasizing the role of technologies such as flight simulators, virtual reality (VR), augmented reality (AR), and artificial intelligence (AI). This study employs a bibliometric analysis to explore research trends, influential contributors, and thematic focuses in pilot training from 2000 to 2025, using data from 350 peer-reviewed articles indexed in the Web of Science. Findings reveal a significant rise in publications during the last decade, driven by advancements in simulation technologies, competency-based training, and human factors research. While the field has experienced rapid technological evolution, challenges such as cost barriers, integration complexities, and gaps in long-term performance evaluation remain. This paper highlights emerging trends, including competency-based training and assessment (CBTA) and scenario-based training (SBT) as well as physiological monitoring, offering a comprehensive roadmap for future research and innovation in aviation training.

Keywords: Flight simulation, Virtual reality (VR), Artificial Intelligence (AI), Competency-based training, Human factors in aviation training

***Corresponding author:** Atılım University, School of Civil Aviation, Department of Pilot Training, 06830, Ankara, Türkiye
E mail: asli.yilmaz@atilim.edu.tr (A. A. YILMAZ)
Ayşe Aslı YILMAZ https://orcid.org/0000-0003-1784-7307

Received: January 29, 2025
Accepted: March 01, 2025
Published: March 15, 2025

Cite as: Yilmaz AA. 2025. From simulators to skies: Engineering and educational advancements in pilot training: A bibliometric perspective. BSJ Eng Sci, 8(2): 524-536.

1. Introduction

The aviation industry has consistently emphasized the critical role of pilot training in ensuring safety, operational efficiency, and adaptability in increasingly complex flight environments. Over the decades, advancements in training methodologies have been instrumental in reducing human error, which remains a leading factor in aviation incidents and accidents (Helmreich et al., 1999). Engineering innovations, particularly the development and refinement of simulation technologies, have revolutionized traditional pilot training practices. These technologies provide realistic and risk-free environments for trainees to master critical skills and experience a wide range of scenarios, including emergency situations, adverse weather conditions, and equipment failures (Salas et al., 2010). As the aviation industry continues to expand, especially in emerging markets, the demand for efficient, scalable, and innovative training solutions has grown significantly (ICAO, 2018).

The integration of virtual reality (VR) and augmented reality (AR) into training programs has further enhanced the immersive quality of these technologies, enabling pilots to engage in highly interactive and lifelike training exercises. VR-based training modules, for example, have been shown to improve situational awareness, decision-making, and overall pilot performance (Zhu et al., 2021). Similarly, AR applications, such as cockpit overlays and real-time system monitoring, have bridged the gap between theoretical learning and practical application, offering dynamic and context-rich educational experiences (Gavrilov et al., 2020). These advancements align with broader trends in CBTA, which focus on measurable learning outcomes and align with international aviation standards (ICAO, 2018).

Artificial intelligence (AI) represents another transformative force in pilot training, enabling the development of adaptive learning systems that personalize training based on individual performance metrics. AI-driven simulators analyse trainee behaviour in real-time, identifying weaknesses and tailoring training modules to address specific needs. Such systems not only enhance learning efficiency but also contribute to early identification of potential deficiencies that could impact long-term performance (Rathinam et al., 2019). Additionally, AI-powered predictive analytics have been employed to optimize training schedules, improve resource allocation, and anticipate trainee performance

This work is licensed (CC BY-NC 4.0) under Creative Commons Attribution 4.0 International License

trends, making pilot training programs more efficient and data-driven (Endsley, 1995).

Despite these advancements, several challenges persist. The high cost of high-fidelity simulators, VR systems, and AI-driven tools presents financial barriers, particularly for smaller training institutions in developing regions. Furthermore, the integration of these technologies into traditional curricula requires significant organizational readiness and expertise, which can hinder widespread adoption (Zhu et al., 2021). In addition, human factors such as stress, cognitive overload, and fatigue remain critical considerations in the design and implementation of training programs (Helmreich et al., 1999). Addressing these challenges will require not only technological innovation but also a comprehensive understanding of the psychological, organizational, and regulatory dimensions of pilot training.

Given these trends, this study aims to examine the convergence of engineering innovations and educational methodologies in pilot training using a bibliometric approach. By analysing 350 peer-reviewed articles published between 2000 and 2025, this paper identifies dominant research themes, leading contributors, and future research directions. Through this lens, it seeks to provide a roadmap for addressing existing challenges while capitalizing on emerging opportunities to enhance the safety, efficiency, and scalability of pilot training programs. This bibliometric analysis contributes to the broader discourse on the role of engineering in advancing aviation education, highlighting the synergies between technological innovation and pedagogical practice in shaping the future of flight training.

2. Literature Review

2.1. The Evolution of Pilot Training

Pilot training is a critical component of aviation safety and efficiency, and its evolution reflects technological and educational advancements over the decades. Traditional pilot training methods primarily relied on classroom instruction and basic in-flight exercises, often with limited opportunities for trainees to practice complex scenarios. However, the integration of engineering advancements, particularly simulation technologies, has revolutionized this field. Initial pilot training programs were designed around a teacher-centred approach, emphasizing rote learning of procedures and theoretical knowledge. Practical exposure was restricted to actual flights, which carried significant risks for both trainees and equipment (Lintern et al., 2000). The introduction of flight simulators marked a paradigm shift, allowing trainees to practice in a controlled environment that mimicked real-world conditions. Today, pilot training incorporates state-of-the-art technologies such as high-fidelity flight simulators, virtual reality (VR), and augmented reality (AR). These tools enable immersive training experiences, significantly reducing risks while improving knowledge retention and skill transferability (Salas et al., 2010). The evolution of pilot training reflects a broader shift toward competency-based education, where the focus is on measurable outcomes rather than time spent in training (Airbus, 2023; Boeing, 2023; Boeing and Airbus. 2023). ICAO has also been updating its documents to include competency based training and assessment programs (Tuncal and Çınar, 2024).

ICAO has also been updating its documents to include competency-based training and assessment programs (Tuncal and Çınar, 2024).

2.2. Engineering Innovations in Pilot Training

2.2.1. Flight simulators

Flight simulators are one of the most impactful engineering contributions to pilot training (IATA, 2023). These devices replicate aircraft systems and flight conditions, enabling trainees to practice a range of scenarios, from routine procedures to emergency situations. High-fidelity simulators, equipped with motion platforms and realistic visuals, provide an unparalleled level of immersion (Zhu et al., 2021). Research by Salas et al. (2010) highlights the effectiveness of simulators in reducing training costs while maintaining high safety standards. Advanced simulators allow for SBT, where trainees practice handling rare but critical events such as engine failures or extreme weather conditions (Kanki et al., 2019). These capabilities make simulators an indispensable tool in modern pilot training.

2.2.2. Virtual reality (VR) and augmented reality (AR)

The application of VR and AR technologies in pilot training has gained traction in recent years. VR offers fully immersive environments where trainees can practice cockpit procedures and emergency responses without the need for physical equipment. For example, Zhu et al. (2021) found that VR-based training improved pilot decision-making and situational awareness. AR complements VR by overlaying digital information onto the real world, enhancing the learning experience. Gavrilov et al. (2020) explored the use of AR in navigation training and found it particularly effective for understanding complex systems and spatial relationships. These technologies bridge the gap between theoretical knowledge and practical application, making them valuable tools for both novice and experienced pilots.

2.2.3. Artificial intelligence (AI)

AI-powered systems are increasingly being used to enhance pilot training by personalizing learning experiences. AI algorithms analyse trainee performance, identify weaknesses, and adjust training modules accordingly. Rathinam et al. (2019) demonstrated the potential of AI-driven simulators to improve training outcomes by providing real-time feedback and adaptive scenarios. These systems also enable predictive analytics, helping identify trainees who may need additional support.

2.3. Educational Trends in Aviation

2.3.1. Competency-based training and assessment (CBTA)

CBTA has emerged as a cornerstone of aviation education, shifting the focus from time-based to outcome-based training. According to the International Civil Aviation Organization (ICAO, 2018), CBTA ensures that trainees acquire the skills and competencies required for safe and efficient flight operations. This approach is particularly effective when combined with engineering innovations such as simulators and VR, which provide measurable outcomes for skill assessment (Flight Safety Foundation, 2022).

2.3.2. Scenario-based training (SBT)

Scenario-based training involves realistic exercises that mimic real-world challenges, enhancing decision-making and problem-solving skills. Wiggins (2015) emphasized the importance of SBT in preparing pilots for high-stress situations, such as engine failures or runway incursions. SBT is widely used in conjunction with simulation technologies, providing a safe environment for trainees to practice critical skills.

2.3.3. Crew resource management (CRM)

CRM training addresses the human factors that contribute to aviation safety, including communication, teamwork, and decision-making. Helmreich et al. (1999) noted that CRM has evolved from a focus on interpersonal skills to a comprehensive approach that includes error management and leadership. Advances in simulation technology have enabled more realistic CRM training scenarios, improving the transfer of these skills to real-world operations.

2.4. Challenges and Opportunities

2.4.1. Challenges

One of the primary challenges in modern pilot training is the cost of technology. High-fidelity simulators, virtual reality (VR) systems, and artificial intelligence (AI)-driven tools are expensive to develop, procure, and maintain. This creates significant financial barriers, especially for smaller institutions or training centres in developing countries (Salas et al., 2010). The initial investment and ongoing operational expenses often limit access to these advanced technologies, which can result in disparities in training quality worldwide.

Another challenge is the complexity of integration. Advanced technologies, while beneficial, require significant changes to existing training programs and infrastructures. Incorporating tools such as AI-powered systems or VR simulations into traditional curricula demands specialized expertise and resources. Zhu et al. (2021) emphasize that integrating such technologies can disrupt established methods and require substantial organizational adjustments to align with technological innovations.

Despite the advantages of engineering advancements, human factors continue to be a critical concern. Stress, fatigue, and cognitive overload remain significant obstacles, even in highly controlled training environments. These factors can impact trainees' performance and their ability to absorb and apply new skills effectively (Endsley, 1995). Additionally, cybersickness, often associated with VR-based training, poses a challenge to trainee comfort and acceptance of the technology (Marron and Dungan, 2023a).

2.4.2. Opportunities

The integration of engineering innovations also presents opportunities to enhance training effectiveness. Advanced tools such as simulators and AI-driven adaptive systems allow for personalized and immersive learning experiences. These technologies enable trainees to practice high-risk scenarios in a safe, controlled environment, improving both skill acquisition and retention (Zhu et al., 2021). Additionally, VR and AR technologies offer a sustainable approach to training by reducing the need for physical aircraft, thereby lowering costs and environmental impact (Marron and Dungan, 2023b).

Another significant opportunity lies in global standardization. CBTA and other outcome-based methodologies provide frameworks to unify pilot training standards worldwide. These approaches align training programs with international safety and proficiency benchmarks, as recommended by the International Civil Aviation Organization (ICAO, 2018). By leveraging these frameworks, training organizations can enhance global aviation safety and ensure consistent pilot competency across regions. While challenges persist, the opportunities for technological advancements to transform pilot training are immense. With strategic investment and innovation, the aviation industry can overcome these obstacles and continue to advance the quality and accessibility of training worldwide.

Despite significant advancements in pilot training through engineering innovations and educational methodologies, several research gaps persist in the literature. First, the long-term impact of VR and AR technologies on pilot skill retention and real-world performance remains underexplored. While studies have demonstrated the short-term benefits of these technologies, their effectiveness in ensuring long-term competency and adaptability in real-world flight conditions requires further investigation (Zhu et al., 2021). Second, the effectiveness of AI-driven adaptive learning systems in addressing individual differences among trainees is another area that warrants deeper exploration. While AI shows promise in tailoring training modules to individual needs, there is limited empirical evidence on how well these systems accommodate varying cognitive and emotional profiles among pilot trainees (Rathinam et al., 2019). Third, the role of organizational culture and regulatory frameworks in the adoption of engineering innovations in pilot training is poorly understood. The successful implementation of advanced technologies often depends on institutional support, regulatory compliance, and cultural acceptance

within training organizations (ICAO, 2018). These factors are critical in determining the scalability and sustainability of technological adoption across diverse regions.

Given these gaps, the following research question emerges:

"How do engineering innovations such as VR, AR, and AI impact long-term skill retention, trainee adaptability, and organizational readiness in pilot training programs?" Addressing this question requires a comprehensive approach that combines bibliometric analysis with thematic exploration to uncover existing trends, research gaps, and influential contributors in the field. The next section outlines the methodology employed to systematically examine the academic literature and answer this research question.

3. Materials and Methods

This study employs a bibliometric analysis to systematically explore the academic literature on engineering innovations and educational advancements in pilot training. The methodology is designed to address the research question: "How do engineering innovations such as VR, AR, and AI impact long-term skill retention, trainee adaptability, and organizational readiness in pilot training programs? "The bibliometric approach provides a comprehensive overview of publication trends, key contributors, thematic focuses, and research gaps in the many areas of the science (Bozkurt Uzan et al., 2025; Önder, 2025).

3.1. Data Collection

The bibliometric analysis for this study was conducted using the Web of Science (WoS) database, renowned for its comprehensive coverage of peer-reviewed academic literature. WoS was chosen for its ability to provide high-quality metadata and access to a wide range of scholarly publications relevant to engineering and aviation education. To ensure the relevance and accuracy of the dataset, a systematic approach was adopted, comprising several key steps.

The first step involved the development of a targeted search query to capture the intersection of engineering innovations and pilot training. The query was designed to include specific terms reflecting the technological and educational aspects of the field. The following Boolean search string was used:

TS=("pilot training" OR "aviation education") AND TS=("virtual reality" OR "augmented reality" OR "artificial intelligence" OR "simulation technology"). This search strategy ensured that the dataset focused on studies integrating advanced technologies, such as virtual reality (VR), augmented reality (AR), artificial intelligence (AI), and simulation systems, within the context of aviation training. The search was restricted to publications between 2000 and 2025, reflecting the most recent and relevant research developments. Additionally, only peer-reviewed articles, reviews, and conference proceedings written in English were included to maintain the quality and consistency of the dataset. To further refine the dataset, inclusion and exclusion criteria were applied. Studies selected for inclusion had to focus explicitly on pilot training and the application of engineering technologies, addressing topics such as skill retention, learning adaptability, or organizational frameworks in aviation education. Moreover, the selected articles were required to be published in high-impact journals or presented at reputable conferences in the fields of aviation and engineering. Conversely, studies unrelated to aviation or pilot training were excluded, along with duplicate entries and articles with incomplete metadata, to ensure the integrity and reliability of the dataset.

After applying these criteria, a final dataset comprising 350 records was extracted. Each record included metadata such as publication titles, abstracts, keywords, authors, institutions, journals, and citation count. This comprehensive dataset provided a solid foundation for conducting a detailed bibliometric analysis.

3.2. Data Analysis

The data collected from the WoS database were subjected to rigorous quantitative bibliometric techniques to identify key trends and relationships within the literature. Various analytical dimensions were explored to gain a holistic understanding of the academic landscape surrounding engineering-driven pilot training.

The first dimension of analysis focused on publication trends over time. The distribution of articles by year was examined to identify growth patterns, milestone years, and potential shifts in research priorities. This temporal analysis provided insights into how research interest in the field has evolved, highlighting periods of rapid growth, peak activity, and potential decline.

Next, authorship and institutional contributions were analysed to identify the most prolific researchers, influential institutions, and patterns of international collaboration. This analysis provided a clear picture of the key contributors driving advancements in the field, as well as the collaborative networks that underpin much of the research.

Keyword co-occurrence analysis was another critical component of the bibliometric analysis. Frequently used keywords were examined to identify thematic clusters and emerging research topics. By visualizing the co-occurrence of keywords using tools like VOS viewer, this analysis revealed the interconnectedness of various themes, such as VR, AR, AI, human factors, and competency-based training. The resulting network maps highlighted central topics and potential research gaps.

Citation and co-citation analysis were conducted to assess the impact of individual articles and references within the field. Highly cited articles and frequently co-cited references were identified, shedding light on foundational studies and influential works that have shaped the discourse around engineering innovations in pilot training.

Finally, thematic evolution over time was explored to capture shifts in research focus. This dimension of analysis highlighted the transition from traditional training methods to the integration of advanced technologies, such as AI-driven adaptive systems, digital twins, and immersive simulations. By mapping these thematic changes, the analysis provided a dynamic view of the field's development.

3.3. Statistical Analyses

To ensure the accuracy and depth of the analysis, several specialized tools and software were employed. The Web of Science Analytics platform was used for data retrieval and initial citation analysis, offering robust tools for identifying publication trends and key contributors.

VOSviewer, a widely used tool for bibliometric visualization, was utilized to generate keyword co-occurrence maps, co-citation networks, and thematic clusters. This software allowed for a clear graphical representation of the relationships between various research themes, enabling a deeper understanding of the field's structure.

Additionally, the Bibliometrix R package was employed to perform advanced statistical analyses on the bibliometric data. This open-source package provided extensive functionality for descriptive and inferential analysis, enhancing the rigor and comprehensiveness of the study.

By combining these tools and techniques, the bibliometric analysis offered a detailed and multifaceted perspective on the academic literature, uncovering trends, contributors, and research gaps in the integration of engineering innovations into pilot training.

4. Results

The findings of this bibliometric analysis shed light on the evolving landscape of engineering innovations and educational methodologies in pilot training. By examining 350 publications spanning from 2000 to 2025, the analysis identifies key research trends, influential contributors, and thematic clusters in the field. Significant growth in publications over the years reflects an increasing interest in integrating technologies such as virtual reality (VR), augmented reality (AR), and artificial intelligence (AI) into aviation education. This section presents insights into publication trends, author contributions, institutional influence, and keyword co-occurrence, revealing the interconnectedness of emerging technologies and educational practices in shaping modern pilot training programs.

4.1. Publication Trends over Time

As shown in Figure 1, the analysis reveals four distinct phases in publication activity: the early years (1989–2016), a growth period (2017–2021), peak activity (2022–2023), and a recent decline (2024–2025). Each phase is marked by unique characteristics that reflect shifts in research focus, technological advancements, and industry needs.

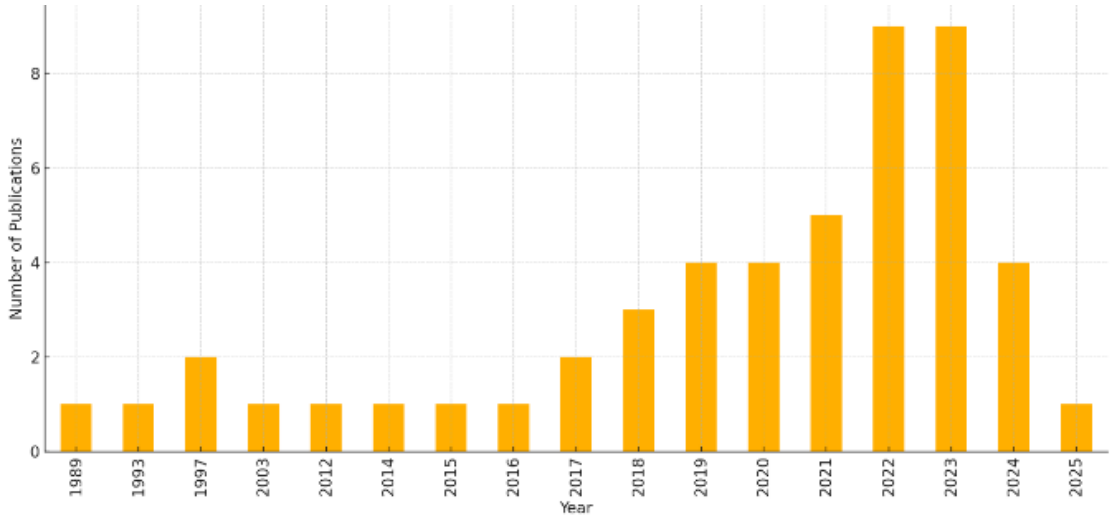


Figure 1. Publication trends over time.

During the early years (1989–2016), the number of publications remained consistently low, with fewer than two articles published annually. Research in this phase primarily focused on traditional simulation techniques and the initial adoption of computer-based training methods. The limited technological advancements in virtual reality (VR) and artificial intelligence (AI) during this period contributed to the modest research activity. Despite the slow growth, foundational studies on human factors and basic flight simulation methodologies laid the groundwork for future advancements in the field.

The growth period from 2017 to 2021 marked a significant increase in research activity, reflecting rapid advancements in high-fidelity simulations, VR, and AI technologies. These developments were accompanied by heightened industry demand for innovative and cost-effective pilot training solutions. Key research topics during this period included SBT, CBTA, and immersive learning environments. The substantial growth in

publications highlights the growing recognition of engineering innovations as critical to modernizing pilot education.

Peak activity was observed during 2022 and 2023, with a dramatic increase in publication numbers. This heightened research interest can be attributed to several factors, including the integration of AI for personalized training, the widespread adoption of VR/AR technologies, and increased collaboration between academic and industry stakeholders. The COVID-19 pandemic further accelerated innovation in training methodologies, emphasizing the importance of remote and virtual learning tools. Research themes during this period expanded to include digital twins, adaptive learning systems, and advanced training technologies, underscoring the field's dynamic nature.

In contrast, the years 2024 and 2025 saw a decline in research activity, with a sharper drop in 2025. This decline may reflect saturation in certain areas of study, shifts in funding priorities, or a transition toward emerging fields such as UAV training and autonomous systems. Despite this downturn, opportunities remain to explore under-researched topics, including the long-term impact of VR/AR tools and AI systems on pilot skill retention. These areas hold significant potential for driving the next wave of innovation in pilot training methodologies.

4.2. Most Prolific Contributors

The chart highlights the top 10 most prolific authors contributing to the field of pilot training and associated technologies. These authors have significantly shaped the research landscape by exploring diverse themes such as engineering innovations, training methodologies, and simulation technologies.

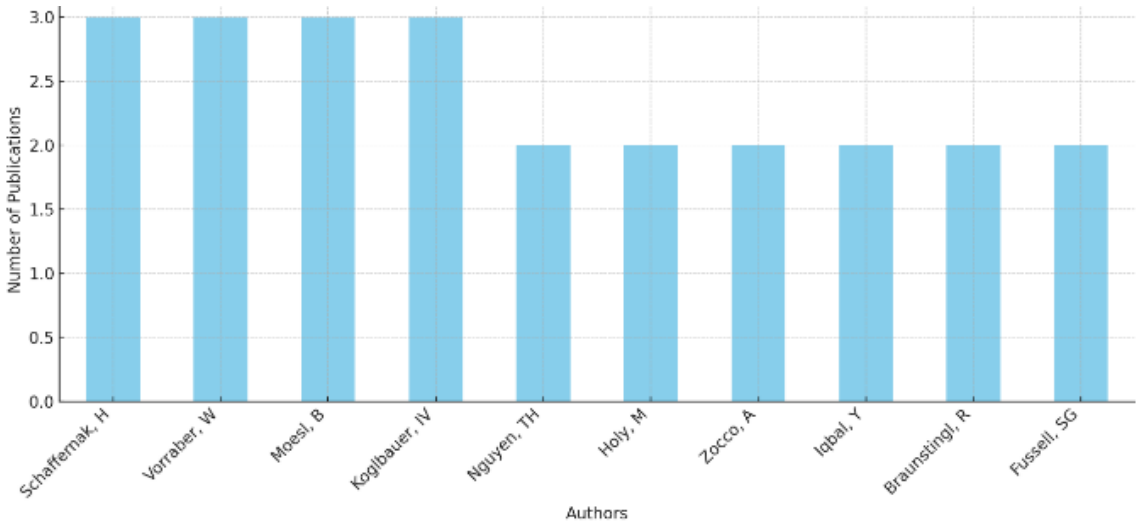


Figure 2. Top 10 most prolific author.

As seen Figure 2, the bibliometric analysis identifies several prolific authors who have significantly contributed to the field of pilot training and its associated technologies. Leading the list is Schaffenrok and Vorraber (2022), who has authored three publications, focusing primarily on the intersection of simulation technologies and human-machine interaction in pilot training. His research provides critical insights into how engineering advancements can enhance training methodologies, particularly in reducing errors and improving situational awareness.

Wolfgang Vorraber shares the top spot with Schaffenrok and Vorraber (2022), demonstrating expertise in virtual reality (VR) and augmented reality (AR) applications within competency-based training programs. His work highlights the growing importance of immersive technologies in modernizing pilot education and creating measurable learning outcomes. These contributions underscore his significant influence in integrating advanced engineering solutions into aviation training practices.

Another notable contributor is Birgit Moesl, who brings extensive expertise in aviation psychology. Her research focuses on crew resource management (CRM) and decision-making in high-stress scenarios, reflecting a strong emphasis on human factors in aviation safety. By addressing psychological and interpersonal dimensions of pilot training, her work complements technological advancements and emphasizes the importance of human-centric approaches.

Robert Koglbauer is recognized for his work on human factors, particularly in exploring how simulation technologies enhance situational awareness and minimize errors during training. His contributions bridge the gap between engineering advancements and cognitive performance, ensuring that training tools align with the psychological needs of trainees.

T. H. Nguyen is another key contributor whose research focuses on advanced engineering applications such as artificial intelligence (AI) in adaptive learning systems. His work highlights the potential of AI to personalize training modules based on individual performance,

improving skill retention and adaptability. Nguyen's studies represent a forward-looking approach to leveraging AI in aviation education.

M. Holy has made significant contributions to understanding the effectiveness of immersive technologies in improving pilot skill retention. His work aligns closely with educational trends, emphasizing the use of VR and AR to create engaging and effective learning experiences. This focus on immersive tools highlights their growing relevance in pilot training.

Zocco et al. (2023) is known for his exploration of training standardization and the integration of international frameworks such as the International Civil Aviation Organization's (ICAO) competency-based training guidelines. His work emphasizes the importance of aligning training methodologies with global standards, ensuring consistency and quality across diverse regions.

Y. Iqbal has contributed to studies on the global implications of innovative training technologies, particularly their adoption in developing regions. His research underscores the importance of making advanced training tools accessible to underserved areas, addressing disparities in aviation education worldwide.

Braunstingl et al. (2023) focuses on SBT, with a particular emphasis on emergency response and teamwork skills. His work highlights the role of realistic scenarios in preparing pilots for high-stress situations, contributing to the development of robust and practical training programs.

Finally, Fussell and Vorraber (2021) has contributed significantly to the development of high-fidelity simulation systems for pilot decision-making in dynamic environments. His work emphasizes the importance of accurate and immersive simulations in improving trainee performance and confidence.

Several observations emerge from analyzing the contributions of these authors. First, many of these researchers collaborate with institutions and industry stakeholders, reflecting the applied nature of their work. This collaboration ensures that their research addresses real-world challenges and contributes directly to advancements in pilot training technologies.

The thematic focus of these authors spans diverse areas, including VR/AR integration, AI-driven learning systems, and human factors in training. Scenario-based training and competency-based frameworks are recurring themes, highlighting their centrality to modern pilot education. This thematic diversity demonstrates how engineering innovations intersect with educational practices to create comprehensive training methodologies.

These authors also have a notable global influence. Their work is recognized across academic and industrial contexts, emphasizing the relevance of their contributions to both research and practice. The international scope of their research underscores the universal challenges and opportunities in aviation education.

4.3. Top Ten Contributing Instutitions

4.3.1. Leading institutions

The analysis highlights key institutions that have emerged as leaders in the domain of aviation and engineering research, particularly in pilot training. Among the top contributors, institutions based in Toulouse, France, such as ISAE SUPAERO and affiliated research centres, play a prominent role. Their focus on aeronautical sciences and pilot education positions them at the forefront of engineering-driven advancements in aviation. These institutions are recognized for their expertise in simulation technologies, virtual reality (VR), and competency-based training, reflecting their commitment to enhancing pilot education methodologies.

Prominent individual researchers, including Schaffenrok and Vorraber (2022), are affiliated with institutions that emphasize robust aviation engineering programs. Their recurring contributions to the field further underscore the importance of institutional support in driving impactful research. Similarly, Zhang Chen from Shenyang Aerospace University in China represents the growing influence of Asian institutions in aviation innovation. Shenyang Aerospace University has made significant strides in integrating human factors into aviation education, highlighting its contribution to the interdisciplinary nature of pilot training research.

The global distribution of contributing institutions demonstrates the international scope of aviation research. Institutions from Europe, such as those in France and Germany, and Asia, particularly China, dominate the landscape. This geographic diversity underscores the universal relevance of pilot training innovations and the need for collaborative approaches to address global challenges in the field.

4.3.2. Institutional impact

Institutions contributing to pilot training research often operate within extensive collaborative networks. These networks involve universities, private companies, and aviation authorities, creating a synergy that accelerates the development and implementation of cutting-edge technologies. Collaborative research efforts have been instrumental in advancing simulation technologies, VR applications, and artificial intelligence (AI)-driven systems, addressing critical needs in modern pilot education.

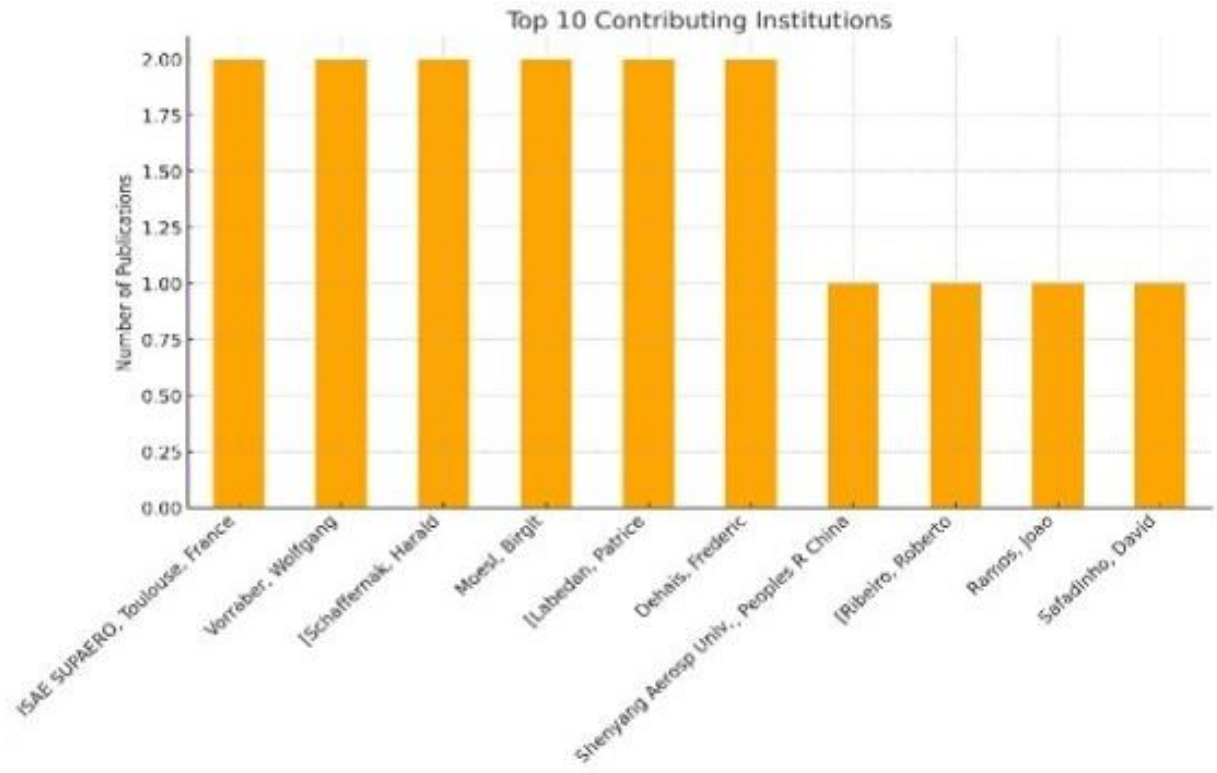


Figure 3. Top ten contributing institutions.

Specialization als efines the impact of leading institutions. For instance, ISAE SUPAERO is renowned for its focus on competency-based pilot training, scenario-based learning, and the integration of advanced engineering solutions into educational frameworks. Such institutions play a pivotal role in setting standards and benchmarks for effective training methodologies.

Emerging regions, particularly in Asia, are becoming increasingly prominent contributors. Chinese institutions, such as Shenyang Aerospace University, have shown a rapid increase in their research output. This growth is driven by the country's expanding aviation sector and its investment in research-led innovation. These institutions are shaping the future of aviation training by introducing innovative approaches that address both regional and global challenges.

4.3.3. Research themes and focus areas

The research themes explored by leading institutions reflect the multidisciplinary nature of pilot training innovations. A significant emphasis is placed on human factors and training, with studies prioritizing human-machine interaction, situational awareness, and overall training efficiency. These areas are critical in ensuring that technological advancements align with the cognitive and psychological needs of trainees.

The integration of VR and AR technologies is another focal area for many institutions. Immersive technologies are being utilized to create dynamic and interactive learning environments, enhancing the effectiveness of pilot training programs. These contributions underscore the potential of VR and AR to bridge the gap between theoretical knowledge and practical application.

Additionally, competency-based training has emerged as a key research focus. Institutions aim to develop frameworks that ensure measurable outcomes for pilot proficiency. This approach aligns with international standards, such as those set by the International Civil Aviation Organization (ICAO) and highlights the importance of creating globally consistent training methodologies.

4.4. Keyword Co-occurrence Analysis

As seen in Figure 4 the keyword co-occurrence network provides valuable insights into the thematic structure and research priorities in pilot training and its associated technologies. The network, composed of nodes and edges, reflects the frequency and strength of connections between keywords in academic literature. Larger nodes and stronger edges signify highly researched areas and their interdependencies, offering a clear representation of dominant themes and emerging trends in the field.

4.4.1. Core themes

A detailed analysis of the network reveals several core themes that dominate the research landscape. One of the most prominent themes is Simulation and Virtual Reality (VR).

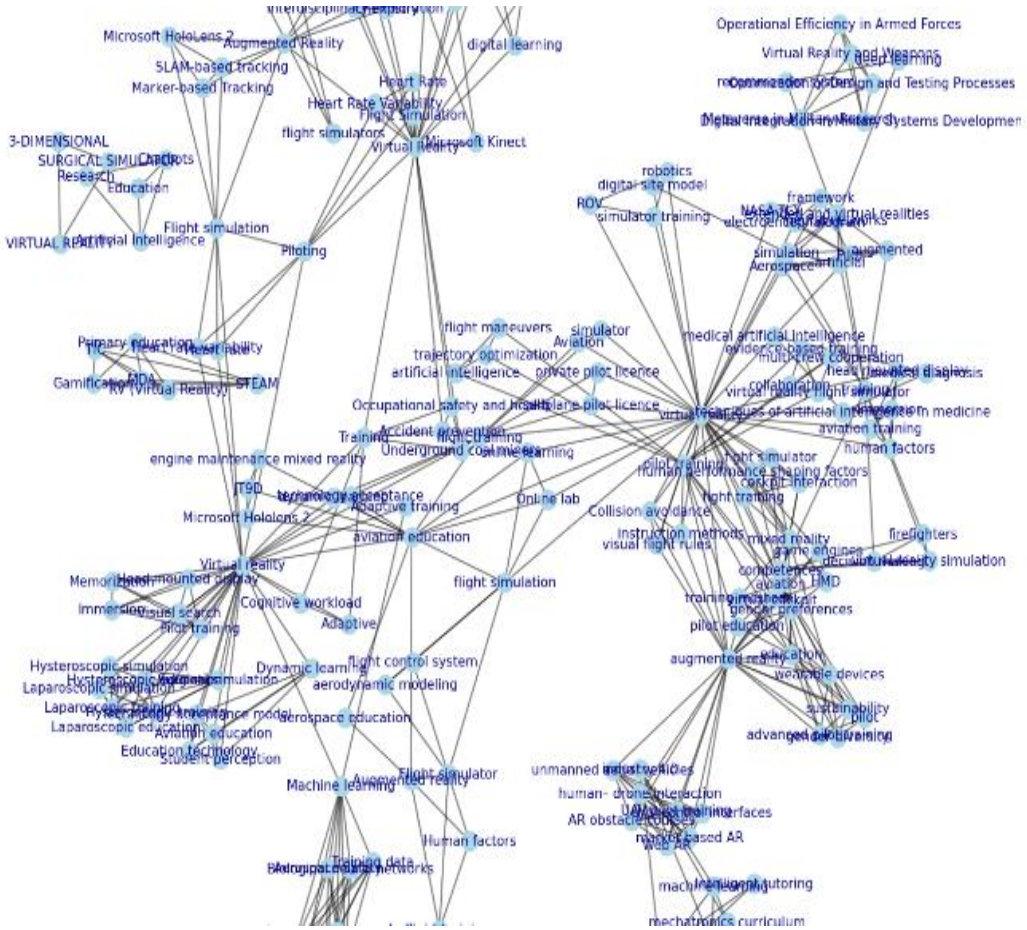


Figure 4. Keyword co-occurrence analysis.

Keywords such as "flight simulation," "virtual reality," and "augmented reality" form a dense cluster, underscoring the central role of immersive technologies in improving pilot training outcomes. These tools are widely recognized for their ability to replicate real-world scenarios in controlled environments, thereby reducing risks and enhancing skill development. The cluster's strong connections to "cognitive workload" and "human factors" further highlight the importance of VR in addressing psychological aspects of pilot training, such as stress management and decision-making under pressure.

Another significant theme is Artificial Intelligence (AI) and Machine Learning, which reflects the growing interest in personalized and adaptive training solutions. Keywords like "artificial intelligence," "machine learning," and "adaptive systems" appear prominently, pointing to the use of AI for tailoring training programs to individual needs. The close links between AI-related keywords and "trajectory optimization" and "human-machine interaction" emphasize the role of AI in improving decision-making, flight manoeuvre training, and overall operational efficiency.

The theme of Human Factors and Safety is also prominent, with keywords such as "human factors," "occupational safety," and "situational awareness" forming a cohesive cluster. These studies are essential for understanding and mitigating human error, which remains a critical challenge in aviation safety. Research in this area often overlaps with Crew Resource Management (CRM), highlighting the importance of teamwork, communication, and leadership in training programs.

Competency-Based Training represents another core theme, focusing on measurable training outcomes. Keywords like "competency-based training," "scenario-based training," and "evaluation processes" are closely linked, indicating an emphasis on aligning training methodologies with international standards. Connections to "digital learning" and "online labs" further demonstrate the shift toward remote and technology-driven education, which has gained prominence in response to global challenges such as the COVID-19 pandemic.

4.4.2. Emerging trends

Beyond the core themes, the network reveals several emerging research areas that indicate the future direction of pilot training innovations. One notable trend is the growing interest in Digital Twins and Advanced Engineering. Keywords such as "digital twins," "advanced engineering," and "mechatronics education" highlight efforts to integrate physical and virtual systems for error-free training. These technologies are strongly connected to "maintenance simulation" and "engine

performance modelling," reflecting their applications in technical and operational training.

Augmented Reality (AR) also stands out as an emerging trend, with keywords like "augmented reality," "Microsoft HoloLens," and "mixed reality" indicating an increased focus on enhancing situational awareness and interactive learning experiences. AR technologies offer unique advantages by overlaying digital information onto the real world, making them particularly effective for navigation training and understanding complex systems.

Another emerging theme is Health and Performance Monitoring, which involves integrating physiological monitoring into training systems. Keywords such as "heart rate variability," "sensor fusion," and "cognitive workload" suggest a growing interest in assessing and optimizing trainee performance. These tools enable trainers to measure stress levels, fatigue, and other factors that impact learning and operational efficiency.

4.4.3. Interconnections and clusters

The keyword co-occurrence network also reveals interconnected clusters that reflect the multidisciplinary nature of pilot training research. The first major cluster revolves around Simulation and VR, which forms the foundation of modern training methodologies. This cluster is connected to both AI and safety-related themes, demonstrating its multifaceted applications in addressing technical, cognitive, and operational challenges.

The second cluster focuses on Adaptive and Personalized Training, encompassing keywords such as "adaptive systems" and "personalized training." This cluster highlights the growing emphasis on trainee-centric approaches, where training programs are tailored to individual strengths, weaknesses, and learning styles.

The third cluster, centered on Human-Drone Interaction, points to an emerging focus on training for unmanned aerial vehicle (UAV) operators. Keywords like "human-drone interaction" and "unmanned systems" suggest that researchers are increasingly exploring the unique challenges and requirements of UAV training, which is expected to become a critical component of aviation education in the coming years.

5. Discussion

The findings of this bibliometric analysis reveal the dynamic and evolving nature of research on engineering-driven pilot training. The trends in publication activity provide a clear picture of how interest in this field has grown over time, shaped by technological advancements, industry needs, and global challenges. In the early years, spanning from 1989 to 2016, research output remained relatively low, reflecting the nascent stage of pilot training innovations. During this period, traditional simulation techniques and basic computer-based training dominated the landscape. Limited technological progress in virtual reality (VR), augmented reality (AR), and artificial intelligence (AI) constrained the scope of academic exploration, resulting in fewer than two publications annually. However, foundational studies focusing on human factors and basic simulation methodologies laid the groundwork for future advancements.

A turning point occurred between 2017 and 2021, marking a period of significant growth in research activity. This coincided with rapid advancements in high-fidelity flight simulators, VR, and AI technologies, as well as increasing demand from the aviation industry for innovative and cost-effective training solutions. Research during this time emphasized immersive learning environments, SBT, and CBTA. The integration of these advanced tools into training methodologies addressed critical gaps in pilot preparation, paving the way for safer and more effective training protocols. By 2021, research output had reached a level indicative of sustained academic and industry interest, with new studies focusing on tailoring training programs to meet evolving needs.

The period of peak activity, from 2022 to 2023, saw a dramatic increase in publication numbers, reflecting a heightened focus on integrating cutting-edge technologies into pilot training. This surge can be attributed to several factors, including the growing adoption of digital twins, adaptive learning systems, and AI-driven training tools. These years also witnessed increased collaboration between academia and industry, enabling researchers to address real-world challenges with innovative solutions. The COVID-19 pandemic played a pivotal role in accelerating research on remote and virtual training methods, as traditional in-person training faced significant disruptions. Key themes during this time expanded to include the role of AI in personalized training, the effectiveness of VR/AR in skill development, and the use of digital twins for error-free simulation.

Despite this peak, a decline in research activity is observed in the years 2024 and 2025. This may be indicative of saturation in certain areas of study, a shift in focus toward emerging fields such as unmanned aerial vehicle (UAV) training, or changes in funding priorities. However, this decline also underscores opportunities to explore under-researched areas, such as the long-term impact of VR/AR technologies on skill retention and the organizational readiness required for systemic adoption of AI-driven tools in training programs. These areas remain critical for advancing pilot training methodologies and ensuring their relevance in a rapidly evolving aviation landscape.

In terms of author contributions, the analysis highlights the significant impact of a select group of researchers who have shaped the field through their innovative studies. Leading contributors, such as Schaffenrok and Vorraber (2022), have focused on simulation technologies and the application of VR/AR in competency-based training programs. Their work, along with that of other prolific authors, such as Birgit Moesl and Robert Koglbauer, underscores the importance of human factors in training. Research by these authors

spans diverse themes, including scenario-based training, AI-driven learning, and the psychological dimensions of pilot education. Collaborative networks among these researchers and their institutions reflect the applied nature of their work, which bridges the gap between academic theory and industry practice.

Institutional contributions further illustrate the global nature of this research field. Leading institutions, such as ISAE SUPAERO in Toulouse, France, and Shenyang Aerospace University in China, have played pivotal roles in advancing pilot training research. Their focus on engineering innovations, immersive learning, and human factors demonstrates their commitment to addressing critical challenges in aviation education. Collaborative efforts between universities, private companies, and aviation authorities have led to significant advancements in simulation technologies, VR/AR integration, and AI applications. The rise of Chinese institutions, in particular, highlights a shift in the global research landscape, emphasizing the importance of fostering international collaboration to address shared challenges, such as pilot shortages and training standardization.

The keyword co-occurrence analysis provides deeper insights into the thematic structure of this research field. Central themes, such as flight simulation, virtual reality, and augmented reality, dominate the landscape, reflecting their foundational role in pilot training innovations. These themes are closely connected to human factors and cognitive workload, highlighting the multidisciplinary nature of this research. Emerging trends, such as digital twins, advanced engineering, and physiological monitoring, point to the field's evolution toward integrating physical and virtual systems for seamless training. However, the analysis also reveals gaps, such as limited studies on the long-term effectiveness of VR/AR and AI in real-world applications, and the lack of focus on regulatory frameworks and institutional readiness for adopting these technologies.

Overall, the findings of this analysis underscore the transformative impact of engineering innovations on pilot training. While significant progress has been made, the field continues to evolve, presenting new challenges and opportunities. Future research must focus on interdisciplinary collaboration, the exploration of emerging technologies, and the development of global standards to ensure that pilot training remains effective, accessible, and aligned with the demands of modern aviation. These efforts will not only enhance the safety and efficiency of pilot training programs but also ensure their continued relevance in an era of rapid technological change.

6. Conclusion

The integration of engineering innovations into pilot training represents a significant evolution in aviation education, blending technological advancements with educational methodologies to enhance pilot competency, safety, and efficiency. This bibliometric study provides a comprehensive analysis of the key trends, research contributions, and emerging technologies that have shaped modern pilot training programs. By analysing 350 peer-reviewed articles from 2000 to 2025, this study highlights the transformative role of flight simulation technologies, virtual reality (VR), augmented reality (AR), artificial intelligence (AI), and competency-based training (CBT) in aviation education.

6.1. Engineering Innovations and Pilot Training Advancements

The findings reveal a progressive shift from traditional training methods—which relied heavily on in-flight training and theoretical instruction—to high-fidelity simulation environments, AI-driven learning models, and immersive VR/AR systems (Salas et al., 2010). Flight simulators, a longstanding component of pilot training, have evolved into highly sophisticated, full-motion systems that allow pilots to experience realistic, high-risk scenarios without exposure to physical danger (Lintern et al., 2000). SBT within these simulators has been particularly effective in developing decision-making skills, situational awareness, and crisis management abilities (Kanki et al., 2019).

The emergence of virtual reality (VR) and augmented reality (AR) in aviation training has introduced new levels of immersion and interaction. VR-based training platforms provide 360-degree simulation environments, allowing pilots to practice cockpit procedures, emergency responses, and navigation techniques in a highly controlled, interactive setting (Zhu et al., 2021). AR, on the other hand, overlays real-time information on cockpit displays, enhancing spatial orientation and navigation accuracy (Gavrilov et al., 2020). These technologies bridge the gap between theoretical learning and practical experience, offering a cost-effective and scalable alternative to traditional aircraft-based training.

Artificial intelligence (AI) has further revolutionized pilot education by introducing adaptive learning systems that personalize training based on individual performance metrics (Rathinam et al., 2019). AI-powered simulators analyse trainee behaviour in real-time, adjusting training modules to address knowledge gaps, weaknesses, and cognitive workload limitations (Endsley, 1995). Moreover, AI-based predictive analytics can assess pilot readiness, skill retention, and learning trajectories, helping instructors tailor training programs more effectively (Marron and Dungan, 2023a).

6.2. Challenges in Engineering-Based Pilot Training

Despite these advancements, several challenges hinder the widespread adoption of these technologies in pilot training. The high cost of high-fidelity simulators, VR systems, and AI-driven adaptive learning platforms presents a significant financial barrier for smaller flight training schools and developing aviation markets (Helmreich et al., 1999). The initial investment required for hardware, software integration, and instructor training is often prohibitively expensive, limiting access to cutting-edge aviation education tools (Wiggins, 2015).

Additionally, the complexity of integrating emerging technologies into existing training frameworks presents an organizational and regulatory challenge (ICAO, 2018). Many aviation authorities and training institutions lack the technical expertise and infrastructure necessary to support AI-driven learning models and immersive VR/AR environments. Furthermore, cybersickness and cognitive overload in VR-based training modules remain significant human factors concerns, requiring further research into ergonomic optimization and trainee adaptability (Marron and Dungan, 2023).

This study is limited to 350 articles indexed in the Web of Science (WoS) database, excluding relevant research from other sources such as Scopus, IEEE Xplore, and Google Scholar. Additionally, the analysis covers the period 2000–2025, which may not account for emerging technological developments beyond this timeframe.

6.3. Opportunities for Future Research and Development

Despite these challenges, the opportunities presented by engineering-driven training technologies are substantial. The use of digital twins, CBTA, and AI-powered adaptive learning models is expected to further enhance training effectiveness while reducing operational costs (ICAO, 2018). VR and AR systems offer a sustainable approach to pilot training, minimizing reliance on physical aircraft for training, thus reducing fuel consumption and carbon emissions (Rathinam et al., 2019).

The global push for standardized pilot training frameworks under ICAO's CBTA initiative provides a unique opportunity for research institutions, regulatory bodies, and aviation training centers to develop uniform training methodologies that ensure competency and safety across international aviation markets (ICAO, 2018).

This study highlights several research gaps that require further investigation:

Longitudinal Studies on Skill Retention – While VR, AR, and AI-based training modules have shown short-term improvements in pilot competency, their long-term effectiveness in real-world flight operations remains underexplored (Zhu et al., 2021).

Scalability of AI-Driven Training – The effectiveness of AI-based adaptive learning systems in customizing training for diverse cognitive profiles needs further empirical validation (Rathinam et al., 2019).

Regulatory Challenges in Implementing Advanced Technologies – There is a lack of policy-driven research addressing the regulatory, ethical, and operational challenges of incorporating AI, VR, and digital twins into pilot training curricula (ICAO, 2018).

Human Factors Research in VR-Based Training – More studies are needed to optimize user experience, minimize cybersickness, and assess cognitive workload in VR-based training environments (Endsley, 1995).

AI and Big Data Integration in Flight Training – AI-powered analytics and machine learning algorithms can improve error prediction, skill evaluation, and dynamic training module adjustments, but their real-world application remains limited (Marron and Dungan, 2023b).

The transformative impact of engineering innovations on pilot training is undeniable. Flight simulators, virtual reality, augmented reality, artificial intelligence, and competency-based training methodologies have significantly enhanced pilot education by providing realistic, immersive, and data-driven learning experiences. However, the successful implementation of these technologies requires strategic investment, interdisciplinary research collaboration, and regulatory standardization to maximize their impact.

The aviation industry stands at a critical juncture, where the adoption of advanced training technologies can improve safety, accessibility, and efficiency in pilot education. Future research should focus on long-term effectiveness assessments, scalability across diverse aviation training environments, and the development of standardized frameworks for technology-driven pilot training.

By addressing these challenges and research gaps, the aviation industry can ensure that pilot training remains at the forefront of technological innovation, equipping future pilots with the skills, competences, and adaptability required to navigate an increasingly complex aviation landscape.

Author Contributions

The percentages of the author' contributions are presented below. The author reviewed and approved the final version of the manuscript.

	A.A.Y.
C	100
D	100
S	100
DCP	100
DAI	100
L	100
W	100
CR	100
SR	100

C=Concept, D= design, S= supervision, DCP= data collection and/or processing, DAI= data analysis and/or interpretation, L= literature search, W= writing, CR= critical review, SR= submission and revision.

Conflict of Interest

The author declared that there is no conflict of interest.

Ethical Consideration

Ethics committee approval was not required for this study due to there is no experimental study on research material.

References

Airbus. 2023. Global services forecast 2023–2042. Airbus SE. URL: https://www.airbus.com/en/services/global-services-forecast (accessed date: December 27, 2024).

Boeing and Airbus. 2023. The Future of aviation training: A market forecast report. Boeing Technical Publications, New York, USA, pp: 26.

Boeing. 2023. Pilot and technician outlook 2023–2042. The Boeing Company. URL: https://www.boeing.com/commercial/market/pilot-technician-outlook (accessed date: December 12, 2024).

Bozkurt Uzan Ş, Manav Mutlu N, Arberk İD. 2025. Bibliometric analysis of math and artificial intelligence. BSJ Eng Sci, 8(1): 149-160.

Braunstingl R, Nguyen TH, Holy M. 2023. Scenario-based training in aviation: Current trends and future directions. J Aviation Psychol, 15(3): 45-60.

Endsley MR. 1995. Toward a theory of situation awareness in dynamic systems. Human Factors, 37(1): 32-64.

Flight Safety Foundation. 2022. Advancing pilot training with emerging technologies. Flight Safety Foundation. URL: https://www.flightsafety.org/ (accessed date: December 25, 2024).

Fussell SG, Vorraber W. 2021. Enhancing pilot training with AI and digital twins: Challenges and opportunities. Aerospace Res J, 9(2): 101-119.

Helmreich RL, Merritt AC, Wilhelm JA. 1999. The evolution of crew resource management training in commercial aviation. Int J Aviation Psychol, 9(1): 19-32.

ICAO. 2018. Manual on competency-based training and assessment for pilots. International Civil Aviation Organization.

International Air Transport Association (IATA). 2023. Future of the aviation workforce: Training and development strategies. URL: https://www.iata.org/ (accessed date: December 10, 2024).

International Air Transport Association. 2023. Pilot Training in a Post-COVID Era: Adaptations and New Standards. IATA Publications.

International Civil Aviation Organization (ICAO). 2019. Manual on competency-based training and assessment (CBTA) for pilots. ICAO. URL: https://www.icao.int/ (accessed date: December 09, 2024).

Kanki BG, Helmreich RL, Anca J. 2019. Crew resource management. Academic Press, Cambridge, US, pp: 664.

Lintern G, Roscoe SN, Koonce JM, Segal LD. 2000. Transfer of landing skills in beginning flight training. Human Factors, 32(3): 319-327.

Marron J, Dungan B. 2023a. Virtual reality and pilot training effectiveness: A review of human factors. Aerospace Res, 11(1): 58-74.

Marron M, Dungan B. 2023b. Cybersickness and adaptation in virtual reality pilot training. Aerospace TrainRev, 14(1): 71-89.

Önder OK. 2025. Analysis of published manuscripts on Napoleon Bonaparte. BSJ Pub Soc Sci, 8(1): 1-6.

Rathinam S, Subramanian R, Gupta N. 2019. AI-driven adaptive learning in flight simulators: Challenges and opportunities. Aerospace Res Cent, 8(1): 35-50.

Salas E, Wilson KA, Burke CS, Wightman DC. 2010. Does crew resource management training work? An update, extension, and some critical needs. Human Factors, 42(4): 641-674.

Schaffenrok H, Vorraber W. 2022. Competency-Based Training with AR/VR Simulators. Int J Aviation Educ, 20(4): 300-320.

Tuncal A, Çınar E. 2024. A scale development study for evaluating the competency perception of air traffic controllers. Int J Aviation Aeronaut Aerospace, 11(3). https://doi.org/10.58940/2374-6793.1942

Wiggins M. 2015. The impact of scenario-based training on critical decision-making. Int J Aviation Psychol, 25(3): 211-227.

Zhu M, Lu Q, Wang H. 2021. Application of Virtual reality technology in aviation training. J Aviation Technol Eng, 10(3): 45-55.

Zocco A, Moesl B, Iqbal Y. 2023. Globalperspectives on AI integration in flight training. J Aerospace Res, 12(2): 150-170.

Black Sea Journal of Engineering and Science
doi: 10.34248/bsengineering.1626358

Open Access Journal
e-ISSN: 2619 – 8991

Research Article
Volume 8 - Issue 2: 537-545/ March 2025

TRADITIONAL USAGE OF NATURAL VASCULAR PLANTS IN TAŞKÖPRÜ AND KAYAÜSTÜ PLATEAUS (GÜMÜŞHANE) AND EVALUATION OF CURRENT PRODUCTION METHODS

Arzu ERGÜL BOZKURT[1]*,Nebahat ÇİMEN[2], Diren Uycan SARAÇ[2]

[1]*Artvin Çoruh University, Faculty of Forestry, Department of Forest Engineering, 08000, Artvin, Türkiye*
[2]*Karadeniz Technical University, Faculty of Forestry, Department of Forest Engineering, 61000, Trabzon, Türkiye*

Abstract: Ethnobotanical studies have recorded the interaction between plants and people over the centuries, enabling this interaction to be used for the development of rural areas. The aim of this study, which was conducted in Taşköprü and Kayaüstü plateaus in Gümüşhane province, was to reveal the ethnobotanical uses of natural vascular plants by the local people and to evaluate and recommend the current production methods of these plant species. As a result of interviews with local people in Taşköprü and Kayaüstü plateaus, natural vascular plant taxa used by local people were identified. Information such as local names of these plants, areas of use, parts used, preparation methods were recorded. Twenty-seven natural vascular plant taxa were identified in the study; these plant taxa are *Alchemilla erythropoda* Juz., *A. sericea* Willd., *A. mollis* (Buser) Rothm, *Astragalus acmophyllus* Bunge, *Berberis vulgaris* L., *B. integerrima* Bunge, *Caltha palustris* L., *Crataegus orientalis* Pall. ex M.Bieb. subsp. *orientalis*, *Foeniculum vulgare* Mill., *Pyrus elaeagrifolia* Pall., *Rosa canina* L., *R. boissieri* Crep., *R. spinosissima* L., *Rubus canescens* DC. var. *canescens*, *R. idaeus* L. subsp. *idaeus*, *R. saxatilis* L., *Rumex alpinus* L., *R. angustifolius* Campd. subsp. *angustifolius, R. ponticus* E.H.L. Krause, *R. scutatus* L., *Sempervivum davisii* Muirhead subsp. *furseorum* (Muirhead) Karaer, *Smilax excelsa* L., *Thymus nummularius* M.Bieb., *T. sipyleus* Boiss., *Urtica dioica* L., *Vaccinium myrtillus* L. and *V. uliginosum* L. Taking into account previous studies in the literature, It was concluded that the most common techniques used to production the 27 plant taxa identified in the research area were seed (52%), tissue culture (27%) and cuttings (21%). This study is significant because it demonstrates the diversity of plant capacity in the plateaus, the breadth of traditional plant knowledge, and the recommendations it makes for production methods. Pharmacologists, botanists, economists, and planners working on local development projects are expected to find significant value in the study's findings.

Keywords: Gümüşhane, Traditional usage, Taşköprü and Kayaüstü Plataeus, Production techniques

***Corresponding author:** Artvin Çoruh University, Faculty of Forestry, Department of Forest Engineering, 08000, Artvin, Türkiye
E mail: arzu.ergulbozkurt@artvin.edu.tr (A. ERGÜL BOZKURT)
Arzu ERGÜL BOZKURT https://orcid.org/0000-0003-0612-8120
Nebahat ÇİMEN http://orcid.org/0000-0002-1795-050X
Diren Uycan SARAÇ https://orcid.org/0000-0002-7859-3972

Received: January 24, 2025
Accepted: March 07, 2025
Published: March 15, 2025
Cite as: Ergül Bozkurt A, Çimen N, Saraç DU. 2025. Traditional usage of natural vascular plants in Taşköprü and Kayaüstü plateaus (Gümüşhane) and evaluation of current production methods. BSJ Eng Sci, 8(2): 537-545.

1. Introduction

Türkiye's geographic location, geomorphological structure, and variety of ecological circumstances all contribute to its abundant flora (11,473 plant taxa. Due to this diversity and richness of plant species, the interest in traditional usage of natural vascular plants have a long research history in Türkiye (Güner et al., 2000; Özhatay et al., 2011; Polat et al., 2015)

Ethnobotanical studies not only record the interaction between plants and humans for centuries, but also pave the way for the utilization of the benefits of this interaction for the development of rural areas, the protection of biodiversity, the identification of used, exported and endangered species, and legal regulations in this regard. The number of plants that is collected from various places of Anatolia and used in kitchen is pretty much. This feature is an important example that reflects the relationship between man and geographical environment as well. Human beings have been using plants for food, medicinal, feed, dye, cosmetic and psychological purposes for hundreds of years (Özkan and Akbulut, 2012; Saraç et al., 2013). However, due to unconscious harvests of some plants, these plants are faced with seperation and extinction from the ecosystem. Medical and aromatic plants need to be met from natural sources, determination of the inventory of these species in order to ensure participation to its national economy, being made in accordance with the techniques of harvesting and using methods and also knowing production methods and making production to ensure its sustainability (Atar et al., 2017).

In the Black Sea Region, ethnobotanical research has been done before (Fidan et al., 2004; Ezer and Arısan, 2006; Türkan et al., 2006; Cansaran and Kaya, 2010; Koca and Yıldırımlı, 2010; Sağıroğlu et al., 2012; Akbulut and Bayramoğlu, 2014; Polat et al., 2015). Although ethnobotanical studies (Özkan et al., 2002; Kandemir and

This work is licensed (CC BY-NC 4.0) under Creative Commons Attribution 4.0 International License

Beyazoğlu, 2002; Korkmaz, 2014; Korkmaz and Karakurt, 2015) have been carried out in Gümüşhane region before, it has been determined that no study has been carried out on the highlands that locally represent the high mountain sections of the region. This study is unique in terms of representing the plant species diversity and utilization in the high altitude plateaus of Gümüşhane region. In this study aim to transfer of knowledge about the traditional usage of natural vascular plant taxa in Taşköprü and Kayaüstü Plateaus (Gümüşhane). In addition, since the production of plant taxa is very important in terms of regional development and continuity, the current production methods of these plant taxa identified in the region were investigated according with literature and suggestions were made about the production methods.

2. Materials and Methods

This study was carried out during the spring and summer of 2017-2018, as this is when people typically visit the plateau. In the province of Gümüşhane, twenty-seven species are gathered as study materials from the Taşköprü and Kayaüstü plateaus, and their intended application is identified. Taşköprü Plateau is 2140 meters and Kayaüstü Plateau is 1950 meters above sea level (Figure 1). At least one plant sample was prepared and deposited at Herbarium of Karadeniz Technical University Faculty of Forestry (KATO). Plant taxa were given Turkish names in accordance with Güner et al. (2012). Before each interview began, an oral Prior Informed Consent (PIC) was obtained. Information about the usage of these plants are obtained from the face to face interviews of the people living at those places. In this study, 30 people (25 women and 5 men) from Taşköprü plateau and 22 people (18 women and 4 men) from Kayaüstü plateau were interviewed. Furthermore, these species production techniques was based on the findings in previous studies.



Figure 1. Location of the Taşköprü and Kayaüstü Plataeus on Turkiye Map (Adapted from Google Earth, 2024, Wikipedia, 2024).

3. Results and Discussion

Twenty-seven natural vascular plant taxa were identified as a result of interviews with 52 people. The majority of the interviewees are primary school graduates. They mostly consist of local people who make their livelihood with animal husbandry. Of the total 52 people; 45 are primary school graduates, 5 are secondary school graduates and 2 are university graduates. The majority of the people surveyed in the region were in the 45-55 age group. As a result of the study, it was determined that *Alchemilla erythropoda* Juz., *A. sericea* Willd., *A. mollis* (Buser) Rothm, *Astragalus acmophyllus* Bunge, *Berberis vulgaris* L., *B. integerrima* Bunge, *Caltha palustris* L., *Crataegus orientalis* Pall. ex M.Bieb. subsp. *orientalis*, *Foeniculum vulgare* Mill., *Pyrus elaeagrifolia* Pall., *Rosa canina* L., *R. boissieri* Crep., *R. spinosissima* L., *Rubus canescens* DC. var. *canescens, R. idaeus* L. subsp. *idaeus*, *R. saxatilis* L., *Rumex alpinus* L., *R. angustifolius* Campd. subsp. *angustifolius*, *R. ponticus* E.H.L. Krause, *R. scutatus* L., *Sempervivum davisii* Muirhead subsp. *furseorum* (Muirhead) Karaer, Smilax excelsa L., Thymus *nummularius* M.Bieb., T. *sipyleus* Boiss., *Urtica dioica* L., *Vaccinium myrtillus* L. and *V. uliginosum* L. plant taxa were intensively used for food purposes in Taşköprü and Kayaüstü plateaus. At the same time, it was determined that these plant taxa were consumed intensively for the treatment of various diseases.

At the end of the study, according with the literature the most commonly used production techniques of the identified 27 plant taxa were seed (52%), tissue cultere (27%) and cuttings (21%) (Figure 2). Rosaceae (11 taxa) and Polygalaceae (4) were the most often used families (Figure 3). Fruits (13 taxa) were the most commonly employed plant components in the preparations and applications, followed by leaves (11 taxa) and aerial parts (8 taxa) (Figure 4). General views of Taşköprü and Kayaüstü plateaus and some pictures of the plant taxa growing naturally there are shown in Figure 5 and Figure 6.

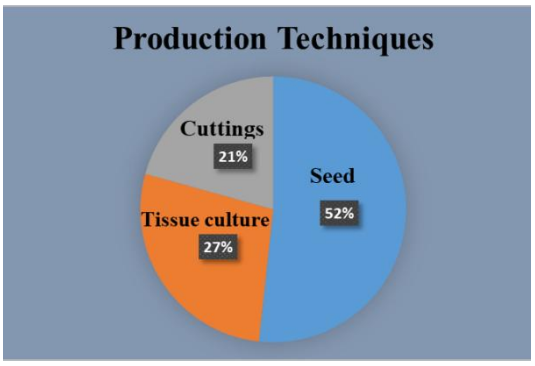


Figure 2. Percentage of plant taxa about production techniques.

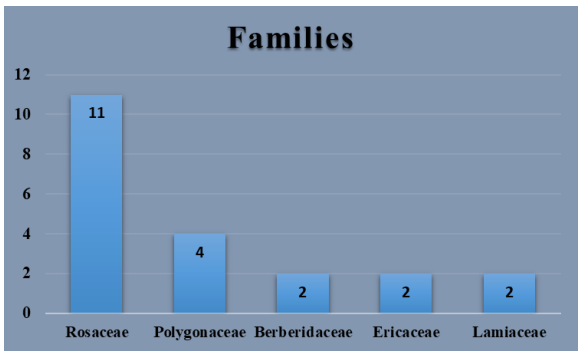


Figure 3. Families include the most number of taxa.

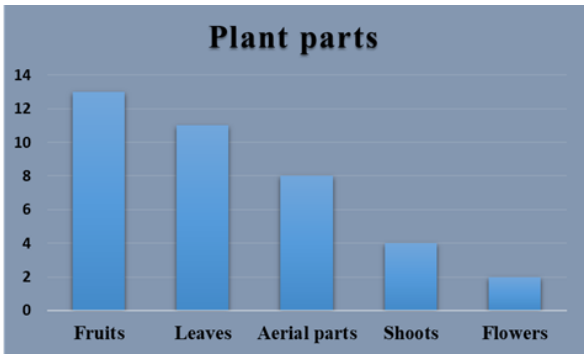


Figure 4. The most frequently used plant parts.

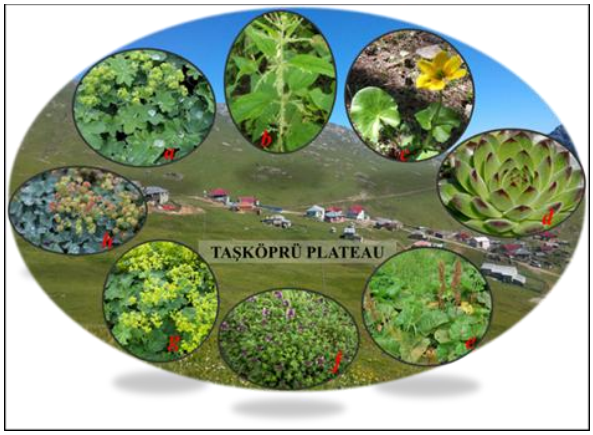


Figure 5. Images of Taşköprü Plateau and some natural vascular plant taxa (a: *Alchemilla sericea*, b: *Urtica dioica*, c: *Caltha palustris*, d: *Sempervivum davisii* subsp. *furseorum*, e: *Rumex alpinus*, f: *Thymus nummularius*, g: *Alchemilla mollis*, h: *Alchemilla erythropoda*).



Figure 6. Images of Kayaüstü Plateau and some natural vascular plant taxa (a: *Vaccinium uliginosum*, b: *Rosa canina*, c: *Smilax excelsa*, d: *Berberis vulgaris*, e: *Crataegus orientalis* subsp. *orientalis*, f: *Astragalus acmophyllus*, g: *Foeniculum vulgare*, h: *Vaccinium myrtillus*).

3.1. *Alchemilla erythropoda* Juz., *A. sericea* Willd. and *A. mollis* (Buser) Rothm

Alchemilla spp. naturally dominates the Eastern Black Sea Region and Türkiye. The perennial herbaceous plant Alchemilla L. is a member of the Rosaceae family, which includes species with significant therapeutic uses. With around 1000 species worldwide and 74 in Türkiye, it holds the distinction of being one of the most abundant genera within the Rosaceae family. The leaves of the plant taxon *A. erythropoda* Juz. are evaluated ethnobotanically. This plant taxon, whose leaves are usually consumed as tea, is used as a painkiller, diuretic and for the treatment of gynecological diseases. *A. sericea* Willd. A. sericea Willd. taxon is used in the treatment of Painkiller- AntiInflammation, Diuretic diseases. In traditional medicine, *A. mollis* (Buser) Rothm. is used to cure wounds and heavy menstruation (Küplemez et al., 2022; Ergene et al., 2025) . The production technique of these plant taxa are seed + tissue culture (Evenor et al., 2001; Anowska et al., 2016).

In the research areas, the above-ground parts of Alchemilla sp., which was called Keltat, plant taxa are utilized in the regions. It is intensively used as animal feed since it is known to increase the milk of animals. Local people use these plant taxa to treat diuretic diseases.

3.2. *Astragalus acmophyllus* Bunge

With 425 taxa, Astragalus L. (Fabaceae) is the most abundant genus in Turkish flora. *Astragalus acmophyllus* Bunge has the high antioxidant and antimicrobial activity Traditionally, astragalus has been used to treat leukemia and promote wound healing (Bedir et al., 2000; Albayrak and Kaya, 2018). This plant taxon is produced using seed + tissue culture (Kunz et al., 2016; Atalay et al., 2017).

The aboveground portions of *Astragalus acmophyllus* Bunge, known as Geven, are used in the study areas. It is widely utilized in the area for firewood and beekeeping. This taxon of plants is used by the locals to treat tuberculosis.

3.3. *Berberis vulgaris* L. and *B. integerrima* Bunge

In Türkiye, there are four species of Berberis that grow naturally: *B. vulgaris* L., *B. integerrima* Bunge, *B. cretica* L., and *B. crataegina* (Davis, 1965-1985). Fruits' anti-inflammatory, antibacterial, and antioxidant qualities, as well as their abundance of healthy ingredients, make them popular food supplements that boost immunity and nutrition. While the roots are used to cure jaundice, bronchitis, and colds, the leaves are used to treat wounds and cuts in cases of intestinal problems, and the fruits are used to treat hypertension, stomach and intestinal disorders, and colds (Ercan, 2024; Yaman et al., 2024). The easiest production technique of this species is by seeds and cuttings (Mammadov and Salakhova, 2018).

The entire aerial parts part of *Berberis vulgaris* L. and *B. integerrima* Bunge are used as a broom in Kayaüstü plateau. Local people call it Karamuk. Local people cut and tie the branches of this species and use it as a broom for cleaning the garden. Its fruits are consumed. These plant taxa are used by locals to treat wounds, common colds, and diuretics.

3.4. *Caltha palustris* L.

With 204 species spread across 20 genera, the Ranunculaceae family is one of the largest families of Turkish flora. It includes both herbaceous and climbing woody taxa. There are six species of Caltha L. (Lilpar) throughout the globe. *Caltha palustris* L. species is the sole species of the genus found in Türkiye (Davis, 1965-1985; Güner et al., 2012; Yücel et al., 2019). For renal and digestive diseases, infusion is used as a diuretic, laxative, and sedative. Preliminary blanching eliminates the toxicity of leaves used to make sarma (Tiţă et al., 2009; Dogan et al., 2015; Paniagua-Zambrana et al., 2024). Foot pain was treated using the aerial portions of *Caltha palustris* L. It is well known that this plant's extracts contain immunomodulatory qualities. According to reports, the plant was used to cure skin conditions in China and to treat broken horns and wounds in India (Pande et al., 2007; Shen et al., 2010; Suszko et al., 2012; Akbulut and Özkan, 2022). The production technique of this plant taxon is seed (Blomqvist et al., 2006).

Caltha palustris L., formerly known as Gongoroş, is a plant species used in the plateaus of Taşköprü and Kayaüstü. Its leaves used for food. People in the area treat diuretic diseases with this plant taxon.

3.5. *Crataegus orientalis* Pall. ex M.Bieb. subsp. *orientalis*

The Rosaceae family is the taxonomic home of the genus Crataegus L. across the Northern Hemisphere, there are 1060 species of Crataegus L. across Asia and Europe. Only two of the twenty-one species found in Türkiye are farmed (Dönmez, 2004; Ünsal, 2012). Since ancient times, people have traditionally employed tinctures or extracts made from Crataegus leaves, flowers, and fruits. The primary purpose of the facility is to cure heart conditions. Furthermore, pharmacological research suggests that Crataegus extracts could be employed as antioxidants and anti-inflammatory agents (Mills and Bone, 2000; Barnes et al., 2002; Bahorun et al., 2003; Bor et al., 2012). The production technique of these plant taxon is seed + cuttings propagation (Yahyaoğlu et al., 2006; Ahmadloo et al., 2016).

Crataegus orientalis Pall. ex M.Bieb. subsp. *orientalis*, famously known as Alıç, are used in the Kayaüstü areas. Its fruits are widely consumed as food. Locals believe that this plant taxon has healing properties against cardiovascular diseases.

3.6. *Foeniculum vulgare* Mill.

Grown in nations with a Mediterranean climate, fennel is a useful fragrant and medicinal plant belonging to the Apiaceae family. The food, fragrance, and medicinal industries all make extensive use of fennel fruits. Carminative, diuretic, laxative, antibacterial, sedative, and stimulating properties are all present in fennel fruits. Teas prepared by mothers using fennel fruits help babies with their flatulence and extend the nursing period (Şanlı et al., 2008). This plant taxon is produced via the seed method (Matthäus et al., 2015).

Within the study locations, plant taxa known as Çaşır—the aboveground portions of Foeniculum vulgare Mill.—are used in the Kayaüstü areas. It is extensively utilized as animal and human food. People in the area treat kidney diseases with this plant taxon.

3.7. *Pyrus elaeagrifolia* Pall.

One of the most well-known wild-grown pear species, belonging to the Rosaceae family, is the oleaster-leafed pear (*Pyrus elaeagrifolia* Pall. subsp. *elaeagrifolia*). It is indigenous to Türkiye's central, eastern, and southern Anatolia regions. The fragrant fruit turns soft and tasty once it has been harvested and allowed to ripen. In Turkish traditional medicine, the fruits are mostly used to alleviate diarrhea and cleanse the body of toxins from snake bites (Yerliturk et al., 2008; Baltas, 2017; Sagbas et al., 2021). Seeds and cuttings are used in production (Kucher et al., 2024).

Marmalade is made from the ripe fruits of *Pyrus elaeagrifolia* Pall., which are gathered from the Kayaüstü plateau. It is eaten as fruit as well. This plant taxon is used by locals to treat kidney disorders. Seeds and cuttings are used in production.

3.8. *Rosa canina* L., *R. boissieri* Crep. and *R. spinosissima* L.

Roses are members of the Rosaceae family, specifically the species Rosa. There are more than 100 species of the genus Rosa, and they are found in North America, Europe, Asia, and the Middle East. There are about 25 species of roses known to exist in Türkiye. (Kutbay and Kilinc, 1996; Nilsson, 1997). In Türkiye, rose fruits have long been used for food, medicine, and a variety of other reasons. Rose fruits have been used medicinally in Türkiye to cure a variety of ailments, including the common cold, rheumatism, and osteoarthritis (Selahvarzian et al., 2018). They are also used to make a number of unique traditional goods, including rose hip fruit juice, jam, marmalade, pestil and syrup, and tea (Kurt and Yamankaradeniz 1983; Ercisli and Guleryuz

2005; Kazaz et al., 2009). Seed and cuttings propagation is the method used to produce this plant taxon (Sarıbaş, 2000; Ercişli and Güleryüz, 1999).

Rosa canina L., *R. boissieri* Crep. and *R. spinosissima* L. known as Kuşburnu, are used in the research regions for its fruits. Jam, marmalade, fruit juice, pestil, tea, and syrup are among its many culinary uses. These plant taxa are used by locals to treat common colds.

3.9. *Rubus canescens* DC. var. *canescens, R. idaeus* L. subsp. *idaeus* and *R. saxatilis* L.

With 12 subgenera, including four highly valuable fruiting species, Rubus is one of the most varied plant genera (Jennings, 1988; Deighton, 2000). For millennia, people have grown rubus species (family Rosaceae) for their fruits. Traditionally, these and other plant parts have been utilized for medicinal purposes (Patel et al., 2004). The fruits are nutritious, therapeutic, and aesthetically pleasing. These plants' strong anti-oxidant, anti-inflammatory, anti-neurodegenerative, and anti-cancer properties are attributed to the high concentration of polyphenols, vitamins, and minerals found in their fruits, roots, shoots, and leaves. The use of Rubus species in the prevention and treatment of chronic illnesses like diabetes, heart disease, and some types of cancer is supported by their varied phytochemical profiles (Zia-Ul-Haq et al., 2014; Buczyński et al., 2024). Production is by seed, cuttings and tissue culture (Wei et al., 1992; Busby and Himelrick, 1998).

The fruits of *Rubus canescens* DC. var. *canescens, R. idaeus* L. subsp. *idaeus* and *R. saxatilis* L. taxa are collected intensively in both plateaus. The fruits are used for making compote and jam. In addition, leafy shoots are collected in Taşköprü plateau and given to animals as feed.

3.10. *Rumex alpinus* L., *R. angustifolius* Campd. subsp. *angustifolius*, *R. ponticus* E.H.L. Krause and R. scutatus L.

With 22 species, the genus Rumex is widely distributed in Turkish flora. The Polygonaceae Juss. family includes the genus Rumex. High mountains in western, central, and eastern Europe, such as the Apennines, the mountains of the Caucasus and Balkan Peninsula, Armenia, and North Anatolia, are home to *Rumex alpinus* L. (Cullen, 1972; Šťastná et al., 2010). In Türkiye, the genus has been widely utilized in traditional medicine to treat a range of conditions, including eczema, diarrhea, and constipation. According to Baytop (1996) and Suleyman et al. (1999), the genus also has antipyretic, laxative, diuretic, wound-healing, and anti-inflammatory qualities (Ozturk and Ozturk, 2007). This plant taxon is produced by seed and tissue culture (Yazdi et al., 2013; Ćulafić et al., 1987).

The leaves of *Rumex alpinus* L., *R. angustifolius* Campd. subsp. *angustifolius*, *R. ponticus* E.H.L. Krause and *R. scutatus* L. sometimes referred to as Lapaza and Kuzukulağı, are consumed as food in the study areas. People in the area utilize these plant taxa to cure skin disorders.

3.11. *Sempervivum davisii* Muirhead subsp. *furseorum* (Muirhead) Karaer

There are roughly fifty species of Sempervivum (Crassulaceae), most of which are found in the highlands of southern Europe, Anatolia, and the Caucasus (Stevens et al., 1996). Fresh juice made from the crushed leaves of different Sempervivum plants is widely used in Türkiye to cure dermatological infections and earaches (Yeşilada et al., 1999; Uzun et al., 2017). Seed and tissue culture is the method used to produce this plant taxon (Giménez-Benavides et al., 2005; Dobos et al., 1994).

In the research locations, the rosette leaves of *Sempervivum davisii* Muirhead subsp. *furseorum* (Muirhead) Karaer, known locally as Etlikulak, are eaten as food in the Taşköprü area. The local population uses this taxon of plants to heal wounds.

3.12. *Smilax excelsa* L.

One of the most prevalent and varied climbing plants in many Old and New World habitats is the Smilacaceae family, which includes the genera Smilax L. and Heterosmilax Kunth. The family's core genus, Smilax, has over 200 species (Gentry, 1991; Cameron and Fu, 2006). Syphilis, acute bacillary dysentery, acute and chronic nephritis, eczema, and silver poisoning are among the illnesses that can be treated using Smilax species (Ivanova et al., 2010; Atar et al., 2020). For this plant taxon, seed and cuttings propagation is the method of production (Martins et al., 2011; Rugna et al., 2010).

The fruits and shoots of Smilax excelsa L., referred to locally as Zimlanga, are consumed as food at the study sites. Residents of the area utilize this plant taxon to cure wounds and eczema.

3.13. *Thymus nummularius* M.Bieb. and *T. sipyleus* Boiss.

Thymus L. (Lamiaceae) is a large genus with over 350 species, of which 66 are found growing wild in Europe. This group consists of 38 species and 64 taxa, 24 of which are indigenous to Türkiye. According to Ozen et al. (2011), one species of this genus is known as "kekik" in Turkish and is used as herbal tea, condiments, and traditional medicine (Ozen and Demirtas, 2015). Folk medicine has utilized thymus species as medicinal herbs and condiments for ages to treat rheumatism, coughs, diarrhea, bronchitis, asthma, arteriosclerosis, and colic (Tammar et al., 2018; Gül et al., 2022). Seed, tissue culture, and cuttings propagation are the methods used to produce these plant taxa (Nasiri et al., 2016; Bakhtiar et al., 2016; Bahadori and Sharifi Ashorabadi, 2017).

Known locally as Yaylaçayı, the leaves and flowers of *Thymus nummularius* M.Bieb. and T. *sipyleus* Boiss. are eaten as food (for tea and soup) at the study locations. Locals treat common colds using this plant taxon.

3.14. *Urtica dioica* L.

Urtica dioica L. of family Urticaceae, is a perennial plant which is commonly known as stinging nettle. It is widely distributed throughout the temperate and tropical areas around the world (Krystofova et al., 2010). The plant's leaves and roots have long been used internally to treat

rheumatism, eczema, anemia, nephritis, haematuria, jaundice, menorrhagia, diarrhea, nasal and menstrual hemorrhage, emmenagogue, diuretic, and blood purification (Khare, 2007; Tucakov, 1997; Wetherilt H. 1992). Turkish traditional medicine uses *Urtica dioica* L. plants to alleviate stomachaches. Furthermore, this plant is utilized to treat liver insufficiency, colds, coughs, and rheumatic discomfort (Yeşilada et al., 1993, 2001; Sezik et al., 1997; Joshi et al., 2014). According to Radman et al. (2015), this plant taxon is produced using the seed method.

The aerial parts of Urtica dioica L., commonly referred to as Isırgan, are consumed as food in the research areas. Rheumatism and gastrointestinal issues are treated by locals using this plant taxon.

3.15. *Vaccinium myrtillus* L. and *V. uliginosum* L.

There are around 450 species in the 36 sections that make up the genus Vaccinium (Ericaceae), subfamily Vaccinioideae, and tribe Vaccinieae. It is cosmopolitan, mainly of the Northern Hemisphere, but particularly in Southeast Asia and Malaysia, and primarily montane in the tropics (Lutein, 2007). *Vaccinium myrtillus* L., *V. vitis-idea* L., *V. uliginosum* L. and *V. arctostaphylos* L. are native to North Eastern Anatolia (Eastern Black Sea) in Türkiye. These species are significant for the local wildlife as well as residents and foresters (Celik, 2012; Celik, 2016). 36 species of Vaccinium have over 70 recorded ethnomedical and dietary uses, primarily in the genitourinary, digestive, and endocrine/metabolic systems. Astringent, diuretic, urinary antiseptic, antidiarrheal, antipyretic, and antidiabetic were the most commonly reported uses, aside from food use (Abreu et al., 2014). Production is by seed and cuttings propagation (Debnath, 2007)

Vaccinium myrtillus L. and *V. uliginosum* L. are collected and used intensively by the highlanders of Taşköprü. It is locally known as ligarba and used in jam and marmalade production. These plant taxa are used by the locals to cure urinary problems.

In the research areas, the local uses of the plant taxa and which plant taxon is used in the treatment of which disease were investigated. In addition, the production techniques of the plant taxa identified in the research area were also tried to be determined (Suplementary Table).

4. Conclusion

The current study details how the indigenous Taşköprü and Kayaüstü plateau people employ natural plant species. Based on the study's findings, it can be said that the people who live in the rural settlements of Kayaüstü and Taşköprü Plataeus are quite informed about the edible and therapeutic applications of natural plant species. The findings demonstrate the significance of twenty-seven types of medicinal plants to rural populations. This study also attempted to provide an explanation of the production methods of plant taxa that are important to ethnobotany. To improve the local population's economy and standard of living, it is crucial to apply the traditional knowledge of using plants.The results highlight how crucial it is to protect traditional knowledge and encourage the long-term usage of medicinal plants in rural healthcare.

Author Contributions

The percentage of the authors' contributions are below. All authors reviewed and approved the final version of the manuscript.

	A.E.B.	N.Ç.	D.U.S.
C	50	30	20
D	50	30	20
S	50	30	20
DCP	50	30	20
DAI	50	30	20
L	50	30	20
W	50	30	20
CR	50	30	20
SR	50	30	20

C=Concept, D= design, S= supervision, DCP= data collection, and/or processing, DAI= data analysis and/or interpretation, L= literature search, W= writing, CR= critical review, SR= submission and revision.

Conflict of Interest

The authors declared that there is no conflict of interest.

Ethical Consideration

Before each interview began, an oral Prior Informed Consent (PIC) was obtained.

Acknowledgment

We appreciate the participation of all Gümüşhane residents who provided insightful information in this survey. This study was presented as oral presentation at the "International Forestry & Environment Symposium (07-10 November 2017, Trabzon / Türkiye)" and printed as abstract.

References

Abreu OA, Barreto G, Prieto S. 2014. Vaccinium (Ericaceae): Ethnobotany and pharmacological potentials. Emir J Food Agric, 26 (7): 577-591.

Ahmadloo F, Kouchaksaraei MT, Goodarzi GR. 2016. Effects of IBA, bacterial and mycorrhizal treatments on the rooting of *Crataegus pseudohetrophylla* Pojark. Iran J For Poplar Res, 24 (2): 345-355.

Akbulut S, Bayramoğlu MM. 2014. Reflections of socio-economic and demographic structure of urban and rural on the use of medicinal and aromatic plants: the sample of Trabzon province. Stud Ethno-Med, 8: 89–100.

Akbulut S, Özkan ZC. 2022. An ethnoveterinary study on medicinal plants used for animal diseases in Rize (Turkey). Appl Ecol Environ Res, 20 (5): 4109-4119.

Albayrak S, Kaya O. 2018. Antioxidant and antimicrobial activities of four Astragalus species growing wild in Turkey.

Turk J Biochem, 4(4): 425-434.

Anowska B, Jakubowska P, Antkowiak A, Nawrot D, Krzaczkowska A, Andrzejak R. 2016. The effect of growth regulators on post-harvest *Alchemilla mollis* (Bauser) Rothm. leaf longevity. Folia Hortic, 28 (2): 137-142.

Atalay E, Erkoyuncu MT, Erişen S, Yorgancılar M. 2017. Micropropagation of Endemic *Astragalus trojanus* Stev. with Nodal Culture. Yuz Yil Univ J Agric Sci, 27 (2): 268-275.

Atar F, Bayraktar A, Yıldırım N, Turna İ, Güney D. 2020. Fruit and seed diversity of Smilax excelsa in the Black Sea Region, Turkey. Turk J For Res, 7 (1): 1-8.

Atar F, Turna H, Turna İ. 2017. Production techniques of some woody medicinal and aromatic plants naturally found in Eastern Black Sea Region, 1st International Congress on Medicinal And Aromatic Plants, May 9-12, Konya, Türkiye, pp: 827-827.

Bahadori F, Sharifi Ashorabadi E. 2017. Effects of different concentrations of IBA and IAA on rooting of *Thymus kotschyanus* Boiss. Cuttings. Iran J Med Aromat Plants Res, 33 (1): 148-156.

Bahorun T, Aumjaud E, Ramphul H, Rycha M, Luximon Ramma A, Trotin F, Aruoma OI. 2003. Phenolic constituents and antioxidant capacities of Crataegus monogyna (Hawthorn) callus extracts. Nahrung, 47: 191-198.

Bakhtiar Z, Mirjalili MH, Sonboli A. 2016. In vitro callus induction and micropropagation of *Thymus persicus* (Lamiaceae), an endangered medicinal plant. Crop Breed Appl Biotechnol, 16 (1): 48-54.

Baltas N. 2017. Investigation of a wild pear species (Pyrus eaeagnifolia subsp elaeagnifolia Pallas) from Antalya, Turkey: Polyphenol oxidase properties and anti-xanthine oxidase, and antioxidant activity. Int J Food Prop, 20: 585–595.

Barnes J, Anderson LA, Phillipson JD. 2002. Herbal medicines: a guide for health care professionals. London: Pharmaceutical Press, Royal Pharmaceutical Society, London, UK, pp: ix + 296.

Baytop T. 1996. Türkiye'de Bitkiler ile Tedavi. Istanbul Universitesi Basimevi, Istanbul, Turkey, I.U. Yayinlari No: 3255, Eczacilik Fak, No: 40, pp: 444 (in Turkish).

Bedir E, Pugh N, Calıs I, Pasco DS, Khan IA. 2000. Immunostimulatory effects of cycloartane-type triterpene glycosides from Astragalus species. Biol Pharm Bull, 23: 834-837.

Blomqvist MM, Tamis WLM, Bakker JP, Van der Meijden E. 2006. Seed and (micro) site limitation in ditch banks: Germination, establishment and survival under different management regimes. J Nat Conserv, 14 (1): 16-33.

Bor Z, Arslan R, Bektaş N, Pirildar S, Dönmez AA. 2012. Antinociceptive, antiinflammatory, and antioxidant activities of the ethanol extract of *Crataegus orientalis* leaves. Turk J Med Sci, 42 (2): 315-324.

Buczyński K, Kapłan M, Jarosz Z. 2024. Review of the report on the nutritional and health-promoting values of species of the Rubus L. genus. Agri, 14 (8): 1324.

Busby AL, Himelrick DG. 1998. Propagation of blackberries (Rubus spp.) by stem cuttings using various IBA formulations. ISHS Acta Horticulturae 505: VII International Symposium on Rubus and Ribes, June 23 – 27, Palencia, Spain, pp: 327-332.

Cameron KM, Fu CX. 2006. A nuclear rDNA phylogeny of Smilax (Smilacaceae). Aliso: J Syst Floris Bot, 22 (1): 598-605.

Cansaran A, Kaya ÖF, 2010. Contributions of the ethnobotanical investigation carried out in Amasya district of Turkey (Amasya-Center, Bağlarüstü, Boğaköy and Vermiş villages; Yassıçal and Ziyaret towns). BioDiCon, 3: 97–116.

Celik H. 2012. Highbush blueberry growing. Edition: 1, Publisher: GIFİMEY, London, UK, pp: 152.

Celik H. 2016. Blueberry culture in Turkey, today and in the future. In XI International Vaccinium Symposium, April 10-14, Orlando, FL, USA, pp: 85-92.

Ćulafić L, Samofalova A, Nešković M. 1987. In vitro organogenesis in two dioecious species, *Rumex acetosella* L. and *R. acetosa* L. (Polygonaceae). Plant Cell Tissue Organ Cult, 11: 125-131.

Cullen J. 1972. Rumex. In: Davis PH, ed., Flora of Turkey and East Aegean Islands, Vol 2. Edinburgh, Edinburgh University press, Edinburgh, Scotland, pp: 281–293.

Davis PH. 1965-1985. Flora of Turkey and the East Aegean Island Vol.:I and Supplament, Edinburg: Edinburg Univesity Press, Edinburgh, Scotland, pp: 567.

Debnath SC. 2007. Propagation of Vaccinium in vitro: A review. Int J Fruit Sci, 6 (2): 47-71. https://doi.org/10.1300/J492v06n02_04.

Deighton N, Brennan R, Finn C, Davies HV. 2000. Antioxidant properties of domesticated and wild Rubus species. J Sci Food Agric, 80 (9): 1307-1313.

Dobos É, Dános B, László-Bencsik Á. 1994. Callus induction and shoot regeneration in *Sempervivum tectorum*. Plant Cell Tissue Organ Cult, 36: 141-143.

Dogan Y, Nedelcheva A, Łuczaj Ł,Drăgulescu C, Stefkov G, Maglajlić A, Ferrier J, Papp N, Hajdari A, Mustafa B, Dajić-Stevanović Z, Pieroni A. 2015. Of the importance of a leaf: the ethnobotany of sarma in Turkey and the Balkans. J Ethnobiol Ethnomed, 11: 26. https:// doi.org/10.1186/s13002-015-0002-x.

Dönmez AA. 2004. The Genus Crataegus L. (Rosaceae) with special reference to hybridization and biodiversity in Turkey. Turk J Bot, 28 (1): 29-37.

Ercan L. 2024. Bioactive components, antioxidant capacity, and antimicrobial activity of Berberis crataegina fruit. Pharmacolog Res Nat Produc, 2: 100020. https://doi.org/10.1016/j.prenap.2024.100020.

Ercişli S, Güleryüz M. 1999. A study of the propagation of the hardwood cuttings of some rose hips. Turk J Agric For, 23 (8): 305-310.

Ercisli S, Guleryuz M. 2005. Rose hip utilization in Turkey. Acta Hortic, 490: 77–83.

Ergene Öz B, İlhan M, Ozbilgin S, Küpeli Akkol E, Bahadır Acıkara Ö, Saltan G, Keleş H, Süntar İ. 2025. Effects of *Alchemilla mollis* and *Alchemilla persica* on the wound healing process. Bangladesh J Pharmacol, 11 (3): 577-584.

Evenor D, Shlomo E, Reuveni M. 2001. In: Plant cell, Tiss Org Cult, 65 (2): 169-172.

Ezer N, Arısan ÖM, 2006. Folk medicines in Merzifon (Amasya, Turkey). Turk J Bot, 30: 223–230.

Fidan MS, Alma MH, Çınar İ, Ertaş M, Köse E. 2004. Ethnobotanical characteristics of traditional plants used in Tokat regions (Turkey). Yüzüncü Yıl Üniversitesi 1. Geleneksel Gıdalar Sempozyumu, September 23-24, Van, Türkiye, pp: 63.

Gentry AH. 1991. The distribution and evolution of climbing plants. Putz, R.E., Mooney, H.A. (eds.), The biology of vines, New York: Cambridge University Press, New York, USA, pp: 3-49.

Giménez-Benavides L, Escudero A, Pérez-García F. 2005. Seed germination of high mountain Mediterranean species: altitudinal, interpopulation and interannual variability. Ecol Res, 20 (4): 433-444.

Google Earth. 2024. URL: https://earth.google.com/web/search (accessed date: December 23, 2024).

Gül LB, Özdemir N, Gül O, Çon A. 2022. Evaluation of *Thymus pseudopulegioides* plant extracts for total phenolic contents, antioxidant and antimicrobial properties. Eur Food Sci Eng, 3

(1): 1-4.

Güner A, Özhatay N, Ekim T, Başer KHC. (Eds.) 2000. Flora of Turkey and the East Aegean Islands, vol. 11. Edinburgh University Press, Edinburgh, Scotland, pp: 656.

Güner A, Aslan S, Ekim T, Vural M, Babaç MT. (edlr.) 2012. Türkiye bitkileri listesi (damarlı bitkiler). Nezahat Gökyiğit botanik bahçesi ve flora araştırmaları derneği yayını, İstanbul, Türkiye, pp: 1290.

Ivanova A, Mikhova B, Kostova I, Evstatieva L. 2010. Bioactive chemical constituents from *Smilax excelsa*. Chem Nat Compd, 46: 295-297.

Jennings DL. 1988. Raspberries and Blackberries: Their Breeding, Diseases and Growth, Academic Press, London, UK, pp: 230.

Joshi BC, Mukhija M, Kalia AN. 2014. Pharmacognostical review of *Urtica dioica* L. Int J Green Phar, 8 (4): 201-209.

Kandemir A, Beyazoğl O. 2002. Köse Dağları'nın (Gümüşhane) tıbbi ve ekonomik bitkileri, Süleyman Demirel Üniv Fen Bilim Enst Derg, 6 (3): 148-157.

Kazaz S, Baydar H, Erbaş S. 2009. Variations in chemical compositions of *Rosa damascena* Mill. and *Rosa canina* L. fruits. Czech J Food Sci, 27(3): 178-184.

Khare CP. 2007. Indian Medicinal Plants an Illustrated Dictionary. First Indian Reprint, Springer (India) Pvt. Ltd., New Delhi, India, pp: 910.

Koca AD, Yıldırımlı S. 2010. Ethnobotanical properties of Akçakoca district in Düzce (Turkey). Hacettepe J Biol Chem, 38: 63–69.

Korkmaz M. 2014. Kelkit (Gümüşhane) aktarlarında satılan tıbbi bitkilerin etnobotanik özellikleri. Süleyman Demirel Üniv Fen Bilim Enst Derg, 18 (3): 60-80.

Korkmaz M, Karakurt E. 2015. An ethnobotanical investigation to determine plants used as folk medicine in Kelkit Gümüşhane/Turkey district. BioDiCon, 8 (3): 290-303.

Krystofova O, Adam V, Babula P, Zehnalek J, Beklova M, Havel L, et al. 2010. Effects of various doses of selenite on stinging nettle (*Urtica dioica* L.). Int J Environ Health Res Public Health, 7: 3804-15.

Kucher N, Hrabovyi V, Opalko O, Zamorskyi V, Opalko A. 2024. In vitro propagation of Pear (Pyrus L.). Біологічні студії/ Stud Biologica, 18 (4): 157-174. doi: https://doi.org/10.30970/sbi.1804.797.

Kunz M, Randall JL, Gray JB, Wall WA, Hohmann MG. 2016. Germination and propagation of *Astragalus michauxii*, a rare southeastern US endemic legume. Native Plants J, 17 (1): 47-52.

Küplemez H, Aykutlu AÖ, Yurteri E, Seyis F. 2022. Distribution of Alchemilla species in Rize and their usage in folk medicine. Diff Pers Med Aromat Plants, 6: 133-148.

Kurt A, Yamankaradeniz R. 1983. The composition of rose hip is grown naturally in Erzurum province and their processing possibilities to different products. Turk J Agric For, 7: 243–248.

Kutbay HG, Kilinc M. 1996. Taxonomic properties of rose hip species are grown in Turkey. In: Proceedings of Rose Hip Symposium, September 5–6, Gümüşhane, Türkiye, pp: 75–83. (in Turkish)

Lutein J. 2007. New York Botanical Garden. Ericaceae-Ethnobotanical Studies. URL: http://www.nybg.org/bsci/res/lut2/ name-use.htm (accessed date: December 24, 2012).

Mammadov T, Salakhova E. 2018. The propagation and morphogenesis of sprouting of some Berberis L. species. Int J Agric Innov Res, 7 (3): 308-311.

Martins AR, Pütz N, Novembre ADDLC, Piedade SMDS, Glória BAD. 2011. Seed germination and seedling morphology of Smilax polyantha (Smilacaceae). Biota Neotrop, 11: 31-37.

Matthäus B, Özcan MM, Al Juhaimi F. 2015. Variations in oil, fatty acid and tocopherol contents of some Labiateae and Umbelliferae seed oils. Qual Assur Saf Crop, 7 (2): 103-107.

Mills S, Bone K. 2000. Principles and practice of phytotherapy. Churchill Livingstone; 1st edition, Edinburgh, pp 664.

Nasiri M, Seedian SE, Sharifi Ashorabadi E. 2016. Investigation of seed germination, establishment and identification of different Thymus species available in natural resources gene bank of Iran. Iran J Med Aromat Plants Res, 32 (1): 115-126.

Nilsson O. 1997. Rosa. In: Davis P.H. (ed.): Flora of Turkey and the East Aegean Islands. Edinburgh University Press, Edinburgh, 4: 106–128.

Ozen T, Demirtas I, Aksit H. 2011. Determination of antioxidant activities of various extracts and essential oil compositions of *Thymus praecox* subsp. *skorpilii* var. *skorpilii*. Food Chem, 124: 58-64.

Ozen T, Demirtas I. 2015. Antioxidative properties of *Thymus pseudopulegioides*: comparison of different extracts and essential oils. J Essent Oil-Bear Plants, 18 (2): 496-506.

Özhatay N, Kültür Ş, Güldal MB. 2011. Check-List of additional taxa to the Supplement Flora of Turkey V. Turkish Journal of Botany, 35; 589–624.

Özkan ZC, Merev N, Terzioğlu S, Üçler AÖ, Gümüş C, Toksoy D. 2002. Gümüşhane yöresi doğal tıbbi bitkilerinin tanınması. yetiştirilmesi ve değerlendirilmesi, Proje sonuç raporu, Gümüşhane Valiliği, Gümüşhane.

Özkan ZC, Akbulut S. 2012. Trabzon İli'nin etnobotanik özellikleri., KTÜ BAP Proje Kod No: 1098.

Ozturk S, Ozturk A. 2007. Antibacterial activity of aqueous and methanol extracts of *Rumex alpinus* and *Rumex caucasicus*. Pharm Biol, 45 (2): 83-87.

Pande PC, Tiwari L, Pande HC. 2007. Ethnoveterinary plants of Uttaranchal - A review. – Indian J Tradit Know, 6 (3): 444-458.

Paniagua-Zambrana NY, Bussmann RW, Jan HA. 2024. *Caltha palustris* L. Ranunculaceae. In Ethnobotany of the Mountain Regions of Eastern Europe: Carpathians. Cham: Springer International Publishing, London, UK, pp: 1-5.

Patel AV, Rojas-Vera J, Dacke CG. 2004. Therapeutic constituents and actions of Rubus species. Curr Med Chem, 11 (11): 1501-1512.

Polat R, Cakilcioglu U, Kaltalioğlu K, Ulusan MD, Türkmen, Z. 2015. An ethnobotanical study on medicinal plants in Espiye and its surrounding (Giresun-Turkey). J Ethnopharmacol, 163: 1-11.

Radman S, Žutić I, Fabek S, Frkin A, Benko B, Toth N. 2015. Influence of temperature and light on seed germination of stinging nettle (*Urtica dioica*). 50th Croatian & 10th International Symposium on Agriculture, February 16-20, Opatija, Crotia, pp: 271-275.

Rugna AZ, Romero O, Mazzeo M, Santamaría JM, Gurni AA, Wagner ML. 2010. Polyphenols production from specimens of *Smilax campestris* Griseb. (Smilacaceae) growing under controlled conditions culture. Museo Farmacobot, Univ Buenos Aires, 26 (2): 21-36.

Sagbas HI, Ilhan G, Ercisli S, Anjum MA, Holubec V. 2021. Characterization of Oleaster-Leafed Pear (*Pyrus elaeagrifolia* Pall. subsp. *elaeagrifolia*) Fruits in Turkey. Agron, 11(3): 430.

Sağıroğlu M, Arslantürk A, Akdemir ZK, Turna M. 2012. An ethnobotanical survey from Hayrat (Trabzon) and Kalkandere (Rize/Turkey). BioDiCon, 5: 31–43.

Şanlı A, Karadoğan T, Baydar, H. 2008. Doğal olarak yetişen tatlı rezene (*Foeniculum vulgare* Mill. var. *dulce*)'nin farklı büyüme ve gelişme dönemlerinde uçucu yağ miktarı ile bileşenlerinin

belirlenmesi. Ziraat Fak. Derg, 3 (2): 17-22.

Saraç DU, Özkan ZC, Akbulut S. 2013. Ethnobotanic features of Rize/Turkey province. BioDiCon, 6 (3): 57-66.

Sarıbaş M. 2000. Activation of the Germination on the Seeds of Some Plants. Turk J Agric For, 24 (5): 579-584.

Selahvarzian A, Alizadeh A, Baharvand PA, Eldahshan OA, Rasoulian B. 2018. Medicinal properties of *Rosa canina* L. Herb Med J, 3 (2): 77-84.

Sezik E, Yeşilada F, Tabata M, Honda G, Takaishi Y, Fujita T, Tanaka T, Takeda Y. 1997. Traditional medicine in Turkey VIII. Folk medicine in East Anatolia Erzurum Erzincan Ağrı, Kars, Iğdır provinces. Econ Bot, 51: 195–211.

Shen S, Qian J, Ren J. 2010. Ethnoveterinary plant remedies used by Nu people in NW Yunnan of China. J ethnobiol ethnomed, 6: 1-10.

Šťastná, P, Klimeš L, Klimešová J. 2010. Biological flora of Central Europe: *Rumex alpinus* L. Perspect. Plant Ecol. Evol. Syst, 12 (1): 67-79.

Stevens JF, Hart HT, Elema ET, Bolck A. 1996. Flavonoid variation in eurasian Sedum and Sempervivum. Phytochem, 41 (2): 503-512.

Suleyman H, Demirezer LO, Kuruuzum A, Banoglu ZN, Gocer F, Ozbakir G, Gepdiremen A. 1999. Antiinflammatory effect of the aqueous extract from *Rumex patientia* L. roots. J Ethnopharmacol, 65: 141–148.

Suszko A, Szczypka M, Lis M, Kuduk-Jaworska J, Obminska-Mrukowicz B. 2012. Influence of polysaccharide fraction C isolated from *Caltha palustris* L. on T and B lymphocyte subsets in mice. Cent. Eur. J. Immunol, 37(3): 193- 199.

Tammar S, Salem N, Bettaieb Rebey I, Sriti J, Hammami M, Khammassi S, Marzouk B, Ksouri R, Msaada K. 2018. Regional effect on essential oil composition and antimicrobial activity of *Thymus capitatus* L. J Essent Oil Res, 31 (2): 129-137. doi:10.1080/10412905.2018.1539415

Tiţă I, Mogoşanu GD, Tiţă MG. 2009. Ethnobotanical inventory of medicinal plants from the South-West of Romania, Farm, 57 (2): 141.

Tucakov J. 1997. Lecenje biljem-fitoterpija. Beograd: Rad; p. 405.

Türkan Ş, Malyer H, Aydın SÖ, Tümen G. 2006. Ordu ili ve çevresinde yetişen bazı bitkilerin etnobotanik özellikleri. Süleyman Demirel univ fen bilim enst derg, 10: 162–166.

Ünsal G. 2012. Alıcın (*Crataegus orientalis* Pallas ex. Bieb. var. *orientalis*) odun ve yarı odun çelikleriyle çoğaltılma performansının belirlenmesi, Master's thesis, Fen Bilimleri Enstitüsü, Gaziosmanpaşa Üniversitesi, Tokat, Türkiye, pp: 25.

Uzun Y, Dalar A, Konczak I. 2017. Sempervivum davisii: phytochemical composition, antioxidant and lipase-inhibitory activities. Pharm Biol, 55 (1): 532-540.

Wei J, Ying G. Shen-Zhi Z. 1992. In vitro propagation of Rubus species. Sci Hortic, 49 (3-4): 335-340.

Wetherilt H. 1992. Evaluation of urtica species as potential sources of important nutrients. Dev Food Sci, 29: 15-25.

Wikipedia. 2024. URL: https://tr.wikipedia.org/wiki (accessed date: December 26, 2024).

Yahyaoğlu Z, Ölmez Z, Göktürk A, Temel F. 2006. Effects of cold stratification and sulphuric acid pretreatments on germination of Hawthorn (Crataegus spp.) seeds. J Bartın Fac For, 8 (10): 74-79.

Yaman M, Sun M, Sümbül A, Demirel F, Tunç Y, Khadivi A, Yılmaz KU. 2024. Multivariate analysis of morphological variation, biochemical content, antioxidant activity, and molecular characteristics of autochthonous *Berberis crataegina* DC. genotypes in Central Türkiye. BMC Plant Biol, 24 (1): 1155.

Yazdi SAF, Rezvani M, Mohassel MHR, Ghanizadeh H. 2013. Factors affecting seed germination and seedling emergence of sheep sorrel (*Rumex acetosella*). Rom Agric Res, 30 (1): 373-380.

Yerliturk FU, Arslan O, Sinan S, Gencer N, Ozensoy GO. 2008. Characterization of polyphenoloxidase from wild pear (*Pyrus elaegnifolia*). J Food Biochem, 32: 368–383.

Yeşilada E, Honda G, Sezik E, Tabata M, Goto K, Ikeshir, Y. 1993. Traditional medicine in Turkey IV. Folk medicine in the Mediterranean subdivision. J Ethnopharmacol, 39: 31–38.

Yeşilada E, Sezik E, Honda G, Takaishi Y, Takeda Y, Tanaka T. 1999. Traditional medicine in Turkey IX: folk medicine in north-west Anatolia. J Ethnopharmacol, 64: 195–210.

Yeşilada E, Sezik E, Honda G, Takaishi Y, Takeda Y, Tanaka T. 2001. Traditional medicine in Turkey X. Folk medicine in Central Anatolia. J Ethnopharmacol, 75: 95–115.

Yücel TB, Fandaklı S, Terzioğlu S, Yaylı N. 2019. *Caltha palustris* L. bitkisinin çiçek ve yaprak kısmının uçucu yağlarının kimyasal bileşimi ve antimikrobiyal aktiviteleri. Gümüşhane Üniv Fen Bilim Enst derg, 9 (2): 189-195.

Zia-Ul-Haq M, Riaz M, De Feo V, Jaafar HZ, Moga M. 2014. *Rubus fruticosus* L.: constituents, biological activities and health related uses. Mol, 19 (8): 10998-11029.

Black Sea Journal of Engineering and Science
doi: 10.34248/bsengineering.1557501

Open Access Journal
e-ISSN: 2619 – 8991

Review
Volume 8 - Issue 2: 546-557 / March 2025

A SOLUTION TO WASTE ECONOMY AND WATER SCARCITY; AIR CONDITIONING WASTEWATER

Hülya SAYĞI[1]*

[1]*Çukurova University, Yumurtalık Vocational School, Department of Plant and Animal Production, 01680, Adana, Türkiye*

Abstract: The waste economy, which is based on the use of wastes that are previously produced and/or produced during the production/consumption process and contain valuable substances for production and pose a significant threat to nature, humans and other living beings, as an alternative to depleting production resources, is a mandatory activity that must be implemented. The waste economy is the process of obtaining production inputs necessary to meet human needs from wastes. The aim of this study is to examine whether wastewater produced by air conditioners at zero cost can be used as an alternative water source to meet the increasing water demand. The study method is the literature review method and scientific studies on the subject, academic publications, digital resources, documents, reports, opinions and evaluations published by authorized and expert national/international persons, institutions and organizations on the subject were used as the study material. The study findings support the fact that waste is an important source of raw materials when evaluated correctly, and that the costs incurred to manage these wastes are instantly transformed into production investments (waste recycling revenue in the world in 2020 was 135 billion dollars). Similarly, the study findings support the fact that evaluating air conditioning wastewater will create significant economic value. Tons of water produced by approximately 2 billion air conditioners in the world (a 1-ton air conditioner produces 1.10 litres of wastewater per hour) and used for various purposes such as drinking and irrigation, which should be used for the economy, are wasted. According to the study findings, wastes (water, plastic, electronics, organic, etc.), which could provide significant economic gains but are not evaluated and cause great economic losses and costs, provide strong evidence that they will be a source of raw materials that meet our needs.

Keywords: Waste, Waste management, Waste economy, Air conditioners, Air conditioner wastewater

***Corresponding author:** Çukurova University, Yumurtalık Vocational School, Department of Plant and Animal Production, 01680, Adana, Türkiye
E mail: hulutas@cu.edu.tr (H. SAYĞI)
Hülya SAYĞI https://orcid.org/0000-0002-2327-566X

Received: September 28, 2024
Accepted: January 14, 2025
Published: March 15, 2025

Cite as: Sayğı H. 2025. A solution to waste economy and water scarcity; air conditioning wastewater, BSJ Eng Sci, 8(2): 546-557.

1. Introduction

In order to sustain their existence, people have to meet their material and spiritual needs that arise at various levels, either directly or indirectly, through production activities consisting of a series of exchange and transformation processes consisting of various economic processes, using scarce resources in nature (air, water, soil, minerals, all living and non-living entities) (Sırım, 2018). Due to the rapid depletion of scarce natural resources used to meet human needs, the search for alternative solutions to reduce the pressure on these resources (Wang et al., 2023; EC, 2023), and to protect, improve and develop the current status of these resources, thus creating a sustainable production/consumption structure, is becoming increasingly important (Sayğı, 2023). On the one hand, the inputs (raw materials) required for production processes must be produced continuously in order to meet human needs (Lahmo, 2024), while on the other hand, these raw material resources (nature) are rapidly consumed due to excessive use and cause great damage to the natural balance (Sayğı, 2023).

In this sense, the evaluation of the wastes of manufactured products or the wastes generated in various production/consumption processes in the supply of inputs needed in the production process has become an important field of economic activity (Mısır and Arıkan, 2023). These activities, expressed with the concept of circular economy, are the most important starting point and component of sustainable economic activities (Mandpe et al., 2022). Sustainable economic activities should foresee the costs incurred in the production/consumption processes and environmental costs (Sayğı, 2023). In this sense, one of the most important environmental costs is waste that poses a threat to nature, humans and other living beings (Sayğı, 2022; Mishra et al., 2023). While the re-use of these wastes as inputs in the production process required high costs until a certain period, rapidly developing technology has made these costs bearable and even more profitable in some cases (Mashudi et al, 2023). One of the main objectives of sustainable economic activities is to destroy and/or preserve these wastes correctly if they cannot be used; and to evaluate them correctly if they can be used and to direct them back to production processes as a production input (Güllü, 2023).

This work is licensed (CC BY-NC 4.0) under Creative Commons Attribution 4.0 International License

The scarcity and rapid consumption of natural resources that meet human needs, and the constraints related to the necessity of continuously providing these resources to the production process are important problems waiting for solutions. On the other hand, the production of these resources causes great damage to nature, and these damages pose a threat to the existence of nature, humans and other living beings (Mashudi et al., 2023; Mishra et al., 2023). These problems have made wastes, which can be converted into raw materials that can be used in the production process at lower costs with the developing technology, very valuable as a new raw material source (Mishra et al., 2023). In the new economic process, waste management (return, rethink, reduce, recycle and reuse) has created the circular economy model, which is an important area of economic activity, by transforming the waste taken from consumption points into very valuable raw materials through the reverse logistics chain (Güllü, 2023; Mısır and Arıkan, 2023). The circular economy model not only provides added value by producing the raw materials needed by production processes at a more affordable cost, but also, more importantly, eliminates the environmental costs of these wastes (Güllü, 2023; Mısır and Arıkan, 2023).

Sustainable economic activities are the design of production/consumption processes that protect, improve and develop nature, humans and other living beings. In this sense, waste management processes have gained importance in order to preserve, destroy and recycle the wastes generated in the production/consumption processes in accordance with sustainable purposes. Wastewater management is the management processes that find application areas in order to evaluate every drop of water, which is a scarce and vital resource, to protect natural water resources and to purify polluted water. In this sense, it covers the processes of recycling and purifying water used in domestic, industrial and agricultural production/consumption activities for various purposes without harming nature, humans and other living beings. Thanks to wastewater management, water resources are protected and the clean water needs of future generations are also met. In order to protect a sustainable environment and natural ecosystem, wastewater management is supported by governments and the private sector. It can be said that conscious initiatives in the world and in Türkiye regarding wastewater management can be considered very new and insufficient (Saraoğlu, 2014). The first legal document in the world on wastewater management is the 'Reuse of effluents: methods of wastewater treatment and health safeguards' document published by the World Health Organization (WHO) in 1973 as a guideline for the protection of water resources and public health (WHO, 1973). The guideline document 'Health guidelines for the use of wastewater in agriculture and aquaculture' was published in 1989, based on this document (WHO, 1989). In the United States of America (USA), the California Title 22 criteria published in 1978 by the State of California (CCR, 1978), and the wastewater use guide documents 'Waste Water Treatment Manuals' published by the Environmental Protection Agency (EPA) in 1992 (EPA, 1992), the EU Water Framework document numbered 2000/60/EC published by the European Union (EU) in 2000, and the 'Water Pollution Control Regulation' in 2004 and the 'Urban Wastewater Treatment Regulation' in 2006 based on the Environmental Law numbered 2872 in Türkiye are legal regulations regarding wastewater management (Saraoğlu, 2014). Pressure of the conscious society and the regulations in the legal field have made wastewater management mandatory. With wastewater management, wastewater does not harm nature, humans and other living beings, and the sustainable use of water resources is ensured by protecting, improving and developing water resources. There are traditional methods consisting of physical, chemical and biological treatment processes in the evaluation of wastewater in wastewater management (Xu et al. 2020; Kulkarni, 2023). Nanotechnology, biotechnology and membrane technologies are used to make wastewater treatment processes more effective and efficient (Kulkarni, 2023). In this way, wastewater is evaluated quickly and at a low cost and in accordance with the purpose. In order for these processes to be successful, it is necessary to create social awareness in water use (Saraoğlu, 2014).

As water resources are insufficient to meet the water needs of the increasing human population, the evaluation of wastewater produced by air conditioners within the scope of wastewater management has become the subject of scientific studies. The findings obtained in these studies indicate that wastewater produced by air conditioners should be evaluated (Matarneh et al., 2024). This study was conducted to examine whether the wastewater produced by air conditioners used in ambient climate control will provide a solution to the increasing water demand.

2. Review

In this study conducted on whether air conditioners used to control the ambient climate conditions in buildings used for various purposes will meet the increasing water demand, literature review was used as a research method. The research data set was formed from scientific studies, academic studies, journals, digital publication sources on the subject; publications of national/international experts, private and public institutions and organizations on the subject, and documents in which their opinions were published. Accordingly, firstly waste economy, amount of waste water produced by air conditioners, water quality, water usage possibilities were examined.

3. Waste Economy

One of the most important stages of sustainable economic activities is the proper disposal, preservation and evaluation of wastes arising from various production/consumption processes in terms of managing their environmental costs (Sayğı, 2023). In this process, it is expressed as waste economy as a result of the activities carried out especially for the purpose of re-evaluating the wastes and bringing them into the production process (Seyhan, 2023). As it is understood that natural raw material resources are being depleted and that using these resources is no longer sustainable, the components in previously produced products that have become waste have begun to gain value as new raw material resources (Usón, 2013). Table 1 shows the economic data of the waste economy in the world, the United States of America (USA), the European Union (EU) and Türkiye.

Table 1. Estimated economic value of waste economy in the world, USA, EU and Türkiye

Estimated	*UN Unit Income/Cost (USD)	World 2020 (USD)	USA 2018 (USD)	EU 2018 (USD)	Türkiye 2020 (USD)
Direct economic cost	118.67	252,300,000,000.00	34,700,150,517.40	27,734,012,229.54	12,436,989,651.93
Indirect economic cost	114.44	243,300,000,000.00	33,462,333,019.76	26,744,689,557.86	11,993,339,604.89
Recycling earned	202.39	135,600,000,000.00	29,589,134,328.36	25,824,756,895.52	11,941,381,253.73
Annual cost net	169.80	361,000,000,000.00	49,650,235,183.44	39,682,831,608.65	17,795,296,331.14
Total amount of waste (tons)		2,126,000,000.00	292,400,000.00	233,700,000.00	104,800,000
Amount recovered (tons)		670,000,000.00	146,200,000.00	127,600,200.00	59,002,400
Number of jobs created (units)		6,300,000.00	681,000.00	700,000.00	350,000

*Unit cost/income values were obtained by proportioning the waste amounts to the UN waste values. UN= United Nations; USA= United States of America; EU= European Union.

According to Table 1, the total volume of the waste economy in the world and Türkiye according to the United Nations (UN) unit values in 2020 was approximately 495 billion dollars (UNEP, 2024) and 24 billion dollars (TÜİK, 2024), respectively. According to the UN environmental program report, the amount of solid waste collected by municipalities, which was 2.126 billion tons in 2020, is estimated to increase by 56% and reach 3.8 million tons in 2050 (UNEP, 2024). Based on 2020, 810 million tons of this amount was thrown into the environment or burned (uncontrolled), 400 million tons was recycled and re-evaluated, 640 million tons was stored in landfills and 270 million tons was burned and used in energy production (UNEP, 2024). According to 2018 data in the USA, 292 million tons of municipal solid waste were collected, approximately 69 million tons of this amount was recycled, 25 tons were used in compost production, 17.7 million tons were used with different methods and 35 million tons were used in energy production, a total of 146.7 million tons were recycled into the economy and the remaining 146 million tons were placed in landfills (EPA, 2020). According to 2018 data in the USA, the income from the waste economy was 106.83 billion dollars and 145.7 billion dollars in 2023 (statista, 2024). According to 2018 data in EU countries, 233.7 million tons of municipal solid wastes were collected, 37.9% of this amount was recycled, 10.7% was refilled and 6% was used for energy production, a total of 54.6% was recycled and reintroduced to the economy (Magazzino and Falcone, 2022). In 2020, 56.3% of the total waste in Türkiye was evaluated in the recycling process, 24.2% in regular storage areas, 14.1% in the workplace area/within the facility producing the waste, 3.2% within the management of municipalities or organized industrial zones, 1.7% in incineration facilities, 0.4% in nature as filling material, and 0.1% in different areas with other methods (TÜİK, 2024).

The waste economy is divided into important sub-branches in terms of waste type and has created unique features. One of these sub-branches and an important area is plastic waste, which is one of the most damaging waste types to the environment, and is a very valuable waste type suitable for processing. According to a report by WWF in 2019, annual plastic production is approximately 200 million tons and about half of this amount is evaluated incorrectly, 11 million tons of waste is thrown into the environment every year and the damage this waste causes to nature, humans and other living beings has a cleaning cost of 3.7 trillion dollars as a measure (WWF, 2021). Nayanathara et al. (2024) reported that an estimated 6.30 billion tons of plastic materials were produced between 1950 and 2015, approximately 80% of these materials were dumped into the natural environment, and it takes 100 to 1000 years for these plastics to break down and transform in the natural environment. According to 2018 data, the annual cleaning cost of plastic waste dumped into the environment could be up to 15 billion dollars, the cleaning cost of plastic waste accumulated in the seas alone is 7 billion dollars, and according to 2019 data, the management cost of all plastic waste is estimated to be 32 billion dollars annually (WWF, 2021). The export value of waste plastics, one of the important components of the circular economy, was 254 million tons of plastic waste between 1988 and 2022, with an import value of 8.8 billion dollars and a total trade volume of 20.4 billion

dollars (Xu et al. 2020).

Electronic waste is another important type of waste. According to a report published by the UN, as of 2019, 53.6 million tons of electronic waste were generated in the world, and only 17% of this waste (total economic value of 10 billion dollars recovered) can be collected and utilized, while a large portion of 83% cannot be utilized (Forti, 2020; WEF, 2023). Scientific studies have shown that the annual value of electronic waste on a global scale is approximately 62.5 billion dollars (Ali and Shirazi, 2023). 90% of electronic waste consists of the most widely used metals, such as iron, copper, tin and aluminium, which provide high added value from recycling these wastes, while metals such as palladium and platinum, which are relatively less in quantity but have the highest value, increase this added value even more (WEF, 2023). The American Coalition for Electronics Recycling (CAER) estimates that the need to recycle waste computers will require approximately 42,000 jobs annually and will add more than $1 billion in economic value to this workforce (Rabbi, 2021).

Another important type of waste is organic waste. Organic waste consists of plant and animal wastes generated during agricultural production, household wastes generated from household consumption, and industrial wastes generated during the production of goods (Sayğı, 2023). The vast majority of organic waste is household waste (49%), and the vast majority of this waste is food (39%). Food worth 940 billion dollars (1/3 of total food production; 1.3 billion tons) is thrown away every year in the world (Ricci-Jürgensen et al., 2020). According to 2016 data, the total annual amount of domestic waste in the world is 2,017 million tons; 935 million tons of this amounts consists of organic waste (Ricci-Jürgensen et al., 2020), however, 19% of municipal solid waste in the world is recycled (UNEP, 2024). If 33% of this amount (309 million tons $year^{-1}$) is made into organic plant nutrition fertilizer compost and applied to the soil at an amount of 10 tons ha^{-1}, approximately 31 million ha of land can be cultivated, representing 2.4% of the total agricultural land in the world (Ricci-Jürgensen et al., 2020). In Türkiye, approximately 30 million tons of household waste is recycled annually, contributing 10 billion TL to the country's economy (Kök, 2021). Scientific studies have proven that fertilizers produced from organic waste not only eliminate organic matter deficiency caused by faulty agricultural production methods, but also improve soil quality by regulating the chemical and physical structure of the soil (Sayğı, 2022)

There are costs that must be incurred for the proper disposal, preservation and recycling of wastes, the protection, improvement and development of nature, humans and other living beings, and the creation of a sustainable economic structure (Sayğı, 2022). These costs, which are inevitably incurred, can be transformed into investments that serve the purpose of production with the circular economy (sustainable economic structure). It is estimated that coal, from non-renewable natural resources, will meet the demand under current conditions for 188 years, oil for 46.2 years, and natural gas for 58.6 years (The World Counts, 2024). As the scarce resources in nature used to meet human needs are rapidly depleted, the wastes resulting from various production/consumption processes have great potential as a new production raw material source. As a result, when non-resource and external benefits are taken into account, it is estimated that the circular economy will produce a total economic value of 1.8 trillion EURO (Biniş, 2023).

Although water, a vital resource, covers 70% of the world's surface, the majority of this amount is in the form of ice at the poles, and 2.5% is freshwater (Mishra, 2023; The World Counts, 2024). According to 2020 data, approximately 26% of the world's population (2 billion people) did not have access to safe drinking water, and 46% (3.6 billion people) did not have access to clean water resources (Unesco, 2023). According to Food and Agriculture Organization (FAO) data, it is estimated that 34% of the world's countries will experience water stress, 15% will experience water scarcity, and 40% of the world's population, which is estimated to be 9.4 billion in 2050, will experience water shortages (Koşar, 2024). In Türkiye, which is among the countries that will experience water stress, it is estimated that with the increasing population, the annual amount of usable water per capita will decrease to 1,200, 1,116 and 1,069 cubic meters in 2030, 2040 and 2050, respectively, and Türkiye will become a country suffering from water scarcity (WWF, 2023). Water and water resource scarcity is one of the most important problems awaiting solutions in the coming years. In this sense, whether wastewater produced by air conditioners within the scope of the waste economy will provide a solution to this problem has been and is being the subject of various scientific studies.

4. Amount of Wastewater Produced by Air Conditioners

Air conditioners, which were offered to people with the patent of "Air Processing Apparatus" by Engineer Willis Carrier, who played an important role in the first emergence of the idea of artificial cooling, are one of the indispensable comfort-providing tools of modern life (ENERGY.GOV, 2015). As with every technological innovation that makes human life easier and increases comfort, air conditioners also have negative effects on human health and nature (Elveren et al., 2018), although the use of air conditioners continues to increase (Khan et al., 2018). Approximately 4% of global greenhouse gas emissions that cause climate change are caused by air conditioners, which consume 10% of global electricity (Elveren et al., 2018; Woods et al., 2022). When air conditioners are not used correctly, they affect human health and cause skin dryness, respiratory dysfunction, cardiovascular diseases, and constant physical fatigue

(Khan et al., 2018). Despite this, since the benefit produced by the use of air conditioners is greater, their production and use are increasing (Dünya Gazetesi, 2024). As the pressure on natural resources that meet human needs increases and these resources are depleted, the use of previously produced and inactive wastes in meeting human needs is seen as an economical solution (Wang and Azam, 2024). Similarly, water resources, one of the scarce resources in the world, are rapidly depleting, becoming polluted, or the cost of accessing water is increasing (Yıldız, 2016). This situation has brought air conditioner wastewater to the agenda as a new water source to meet the increasing water demand.

Snidvongs and Vongsumran (2020) investigated the possibility of using wastewater produced by air conditioners as safe drinking water for humans, and observed that a 1 horsepower (0.58-0.67 ton; 12000 BTU = 1 ton) air conditioner can produce approximately 9 litres of water in 6 hours in a high humidity environment (Guarnieri et al. 2023, 40-60% normal humidity). AlGhamdi et al. (2024) investigated the quality of wastewater produced by different types of air conditioners, and observed that a window air conditioner operated for 8 hours per day in the low temperature and high humidity southern region of Jeddah City, Saudi Arabia, produced 8,725 litres of water per year, and a split air conditioner produced 20,614 litres of water per year. Sabnis et al. (2020) reported in their study examining the quality and usage possibilities of air conditioning wastewater that modern air conditioners generally produce 15-70 litres per day, depending on the air conditioning capacity and the amount of relative humidity in the air, and that a 1 ton air conditioner operating for 7-8 hours can produce up to 10 litres of pure water when collected under aseptic conditions. Sabnis et al. (2020) reported that approximately 6 million active air conditioners in residential and commercial premises in India produce approximately 50-100 million litres of wastewater per day for most of the year and that this resource should be utilized.

Scalize et al. (2018) studied the usability of air conditioner wastewater in a laboratory environment in Goiânia City, Goiás State, Brazil, and observed that operating air conditioners between 8-6 a.m. provided a water flow of 2.7-4.1 litres in 1 hour, and as a result, an average of 3.08 litres of water was produced in 1 hour. Khan (2023) evaluated the quality and quantity of air conditioning wastewater in a study conducted at the European University of Bangladesh and found that air conditioners with 1 ton, 2 ton and 4 ton power produced 97, 177 and 354 litres of water in a month, respectively. In a study conducted by Alom et al. (2021) evaluating the usability options of air conditioning wastewater, it was found that air conditioners with 3, 4 and 4.5 ton/h power operated for 9 hours a day produced 2.159, 2.997 and 3.101 litres of water during the day, respectively, and air conditioners operated for 5 hours at night produced 1.849, 2.695 and 2.702 litres of water, respectively. In a study conducted by Noutcha et al. (2016) on the ground destruction of air conditioner wastewater, it was recorded that a total of 1,459.5 litres were produced in the first month by operating air conditioners of different brands for 48 hours, and 965.5 litres were produced in the second month by operating them for 36 hours. In a study conducted by Akram et al. (2018) evaluating the physical and chemical properties of air conditioner wastewater, it was recorded that in the climatic conditions of Dhaka City, Bangladesh, a 2 ton air conditioner produced 3.5-4.5 litres of water in 1 hour and 25 litres of water in a day.

In a study conducted by Uddin et al. (2019) evaluating the possible usage areas of air conditioner wastewater, it was observed that 19 air conditioners of different powers and brands produced an average of 1.10 litres of water per ton according to the wastewater production values in the climatic conditions of Gazipur and Dhaka Cities, Bangladesh. Galindo (2019) investigated the possibility of air conditioning wastewater as an alternative water source and observed that a window-type 0.75 hp air conditioner produced 25.92-36.72 litres of wastewater per day. In a study conducted by Okeyinka et al. (2021) on the possibility and quality of air conditioning wastewater use in institutional buildings, it was reported that an average of 15.33 millilitres of water was produced when operated for 8 hours in an environment where the air temperature was 24.9 degrees and the humidity rate was 60.1%, and a total of 7.40 litres of wastewater was produced per day. In a study examining the physical and chemical properties of air conditioning wastewater conducted by Matarneh et al. (2024), it was determined that 1 ton (38 units), 2 ton (40 units) and 3 ton (36 units) air conditioners operated at an average temperature of 18 degrees in June and July 2023 produced 480, 650 and 870 litres of wastewater in a month, respectively. Siam et al. (2019) evaluated the possibility of air conditioning wastewater as a water source in terms of quality and quantity in Palestine, where water shortage is severe. They observed that in Ramallah, air conditioners with 1, 2 and 3 tons of power operated for an average of 6.64 hours per day produced approximately 9.63, 18.46 and 25.1 litres per day, respectively, and an average of 259 litres per month. In Jericho, air conditioners with 1, 2 and 3 tons of power operated for an average of 6.64 hours per day produced approximately 15.40, 36.09 and 43.34 litres per day, respectively, and an average of 453 litres per month.

According to the International Energy Agency (IEA) data, the number of air conditioners in the world, which was approximately 2 billion by 2024, is expected to almost triple by 2050, reaching 5.5 billion (Ritchie, 2024). According to a study conducted by Marketing Türkiye in 2021, the air conditioner usage rate in Türkiye is 21.7%, with the highest air conditioner usage in the Mediterranean (28.8%) and the Aegean (27.1%) regions, while the lowest usage rate was in the Northeastern Anatolia Region (15.7%). According to the report

published by the Air Conditioning and Cooling Air Conditioning Manufacturers Association in Türkiye, approximately 1.9 million split air conditioners were sold in 2023 (Dünya Gazetesi. 2024). On a Türkiye scale, based on air conditioner sales in 2023, according to these data, assuming that all 1.9 million split air conditioners have a power of 1 ton, operate for approximately 7 hours per day, and produce approximately 9 litres of water per day (Siam et al., 2019), they can produce a total of 17,100 tons of water per day. When evaluated alone, this value is small, but when combined, its impact is large. Another important issue is whether the water produced by air conditioners meets certain standards for collection and use.

5. Analysis Values of Wastewater Produced by Air Conditioners

According to the working principles of air conditioners, wastewater is produced as a result of the air conditioners collecting water vapour particles in the air due to their instant heating and cooling functions, condensing them and converting them from gaseous to liquid (Snidvongs and Vongsumran, 2020). Like all other wastes generated in production/consumption processes, air conditioner wastewater is a waste produced by air conditioners while they are providing their service in controlling the ambient climate. The effect created by the waste economy, the idea of how to make more use of waste, and more importantly, the need for a vital resource such as water, has brought the wastewater produced by air conditioners to the agenda (Knight, 2023). Water is a vital resource for the continuation of life, but not every water source can be used to meet every water need. In this sense, water resources must meet certain standards in order to meet a specific need such as drinking water and irrigation water (Dinka, 2018).

The possibility of using air conditioning wastewater and its areas of use also depend on the capacity to meet the standards determined in this area. The waste produced by air conditioners can be used as drinking water if it has the characteristics determined by WHO (water does not contain chlorine, sodium, potassium, volatile organic chemicals and inorganic trihalomethanes, microbial pathogens and pesticides).

Table 2. Comparison of heavy metal values in air conditioning wastewater with WHO water standards

Heavy Metals	[1]WHO max (mg L^{-1})	[2]AC (mg L^{-1})	[3]AC (mg L^{-1})	[4]AC (mg L^{-1})	[5]AC (mg L^{-1})	[6]AC (mg L^{-1})	[7]AC (meq L^{-1})
Arsenic As	0.010	<0.010	0.00079	-	-	-	0.0019-0.0048
Antimony Sb	0.005	<0.001	-	-		-	
Lead Pb	0.010	<0.010	0.00051	0.015-0.049	-	-	0.0081-0.0261
Mercury Hg	0.001	<0.001	-	-		-	0.0035-0.0318
Chromium Cr	0.050	<0.010	0.00102	0.001-0.002	0.021-0.19	-	
Cadmium Cd	0.003	<0.001	0.00022	0.001	-	-	0.0008-0.0061
Calcium Ca	-	0.050	-	-		-	
Copper Cu	2.000	0.900	0.00119	0.008-0.061	0.068-1.81	0.23	0.4587-1.4270
Iron Fe	0.300	<0.010	0.062	0.001-0.012	0.032-9.29	0.543	0.1870-1.1427
Zinc Zn	3.000	<0.020	0.00053	0.013-0.325	0.020-0.56	0.18	0.0935-0.4654
Selenium Se	0.010	<0.010	-	-	-	-	
Beryllium Be	-	<0.010	-	-		-	
Magnesium Mg	-	0.030	-			0.59	
Manganese Mn	0.500	<0.010	-	0.005-0.014	0.013-0.19	-	
Barium Ba	0.700	<0.100	-	-	0.033-0.75	-	0.0135-0.1421
Boron Br	0.300	<0.010	-	-		-	
Molybdenum Mo	0.070	<0.010	-	-	-	-	
Nickel Ni	0.020	<0.010	0.00066	0.013-0.096	-	0.171	
Aluminium Al	0.200	<0.010	0.0305	-	0.056-11.50	0.226	

mg L^{-1}= milligrams per litre, µg L^{-1}= micrograms per litre, meq L^{-1}= milliequivalents per litre (to express the concentration of ions in solution), AC= air conditioning. WHO= World Health Organization. [1]WHO, 2019; [2]Snidvongs and Vongsumran, 2020; [3]Matarneh et al., 2024; [4]AlGhamdi et al., 2024 (Values µg L^{-1} were converted to 'mg L^{-1}'); [5]Siam et al., 2019; [6]Glawe et al., 2016; [7]Bautista-Olivas et al., 2017.

Table 2 presents data from different scientific studies that determine the heavy metals in air conditioning wastewater and compare them with the standards determined by WHO.

According to the analysis of air conditioning wastewater by Snidvongs and Vongsumran (2020), it was concluded that the heavy metals that can harm humans in air conditioning wastewater are within the WHO standards and can be used as drinking water (Table 2). Matarneh et al. (2024) reported that the values in water content according to the heavy metal detection test results of air conditioning wastewater are much lower than the

maximum limits determined by Jordan and FAO for drinking water and agricultural irrigation water (Table 2). In their study, AlGhamdi et al. (2024) concluded that the content of heavy metals and all other elements in water samples of air conditioning wastewater produced by window and split air conditioners met the standards determined for drinking water and irrigation and were within acceptable thresholds (Table 2). Siam et al. (2019) reported that according to the heavy metal detection test results of a total of 59 samples of water, the heavy metals lead, cadmium, arsenic, selenium, tin, molybdenum, nickel, cobalt and lithium were not found in the air conditioning wastewater content; some samples contained copper, iron, aluminium, chromium, barium, zinc and manganese; in some samples, the values of iron, aluminium, chromium, barium and zinc were below the acceptable limits within the drinking water standards (Tablo 2).

Glawe et al. (2016) compared the analysis results of wastewater samples taken from 19 central air conditioning systems with more than 5.42 ton in San Antonio, USA, with the standards in the National Primary Drinking Water Regulations and concluded that the quality of air conditioning wastewater is relatively high; heavy metal content is low, microbial content has the potential to increase depending on temperature; and it needs to undergo a series of processes for use for certain purposes (Table 2). Bautista-Olivas et al. (2017) observed that the content of heavy metals in water obtained by condensing atmospheric water vapour in day/night, humid/dry weather conditions in three cities of Mexico (Tlaxcala, Hidalgo and Mexico City) was above WHO standards with Pb (91.66%), Fe (58.33%) and Cd (33%) values, respectively, and the remaining heavy metals were within WHO standards (Table 2).

Table 3 presents data from different scientific studies comparing the water quality of air conditioning wastewater with the standards set by WHO.

Table 3. Comparison of air conditioning wastewater quality values with WHO water standards

Water Quality Characteristics	[1]WHO max	[2]AC	[3]AC	[4]AC	[5]AC	[6]AC	[7]AC	[8]AC
Colour (Pt-Co)	15	<5	-	0.42-0.83	-	Colorless	32	-
Turbidity (NTU)	5	<1	1.12	078-0.42	-	0.69-1.66	1.57	5
pH (Acidity/Alkanity)	-	6.6	7.20	0.86-0.10	6.94-7.03	6.50-8.50	7.26	7.07-7.35
Conductivity (µ.m cm^{-1})	-	21	82	0.96-0.09	15-108.5	-	75.5	20.30-29.16
Taste (Tongue)	OK	OK	-	-	-	-	-	-
Odour (Smelling)	OK	OK	-	-	-	Odorless	-	-
TDS (mg L^{-1})	1000	1	41.15		12-91	190-240	-	11.90-22.09
Total Alkalinity (mg L^{-1})	-	<1		093-0.08	-	40-45	-	12-17
Total hardness (mg L^{-1})	-	<1	34.51	0.71-0.41	1-18	-	-	10.12-15.44
Nitrate nitrogen	11.3	<0.01	12.80	-	-	-	-	13.20-18.32
Fluoride (mg L^{-1})	1.5	0.3	-	-	-	-	-	-
Chloride (mg L^{-1})	250	1	-	-	-	26.63-35.50	-	10.85-16.44
Sulphate (mg L^{-1})	250	1.7	-	-	-	-	-	-
Sodium (mg L^{-1})	-	0.2	-	-	-	-	-	-
Phosphate (mg L^{-1})	-	<0.01	-	-	-	-	-	3.39-5.62
Silica (mg L^{-1})	-	0.04	-	-	-	-	-	-
Total PCA (cfu mL^{-1})	-	110	-	-	-	-	-	-
Coliforms (cfu 100 mL^{-1})	-	0	-	-	0	-	160	$1.5\text{-}4.4x10^3$
TTHM (100 µg L^{-1})	-	<0.005	-	-	-	-	-	-

Pt-Co= platinum-cobalt, NTU= nephelometric turbidity unit, AC= air conditioning, TDS= total dissolved solids PCA= plate count agar, CFU= colony forming units, TTHM= total trihalomethanes, WHO= world health organization. [1]WHO, 2019; [2]Snidvongs and Vongsumran, 2020; [3]Matarneh et al., 2024; [4] Scalize et al., 2018; [5]Sabnis et al., 2020; [6]Khan, 2023; [7]Alom et al., 2021; [8]Noutcha et al., 2016.

Snidvongs and Vongsumran (2020) concluded that the quality characteristics of air conditioning wastewater are better than WHO standards and can be used as drinking water as a result of their analysis of air conditioning wastewater (Table 3). AlGhamdi et al. (2024) observed that the water quality characteristics of air conditioning wastewater (pH, total dissolved solids, electrical conductivity, dissolved and chemical oxygen values, phosphate, chlorine, sulphate) meet the standards set for drinking water and irrigation, and that split air conditioners produce more air conditioning wastewater than window-type air conditioners and are better in terms of water quality (Table 3). Siam et al. (2019) reported that according to the physical, chemical and microbial analysis results of air conditioning wastewater, the pH value is at a neutral level, the total dissolved solids, electrical conductivity and dissolved oxygen values are within the standards of the State of Palestine; in terms of other characteristics, the water quality of air conditioning wastewater is of good quality in accordance with irrigation water standards, but it is controversial because the biological and chemical oxygen demand measurement values do not meet the drinking water standards.

According to the results of the physicochemical and bacteriological analysis of air conditioning wastewater, Scalize et al. (2018) determined that the water quality of air conditioning wastewater is in the range of distilled

water, more like pure water, and that it has the potential to be used in Water Analysis Laboratory activities (Table 3). Matarneh et al. (2024) compared the quality characteristics of air conditioning wastewater and found that pH was at neutral level, total dissolved solids, electrical conductivity, biochemical oxygen demand, and hardness levels met Jordanian and FAO drinking water standards (Table 3). According to these results, Matarneh et al. (2024) test results of air conditioning wastewater samples show that it meets the standards and safety requirements determined by the State of Jordan and the FAO in terms of drinking water and irrigation water. Sabnis et al. (2020) concluded that according to the results of the physicochemical and bacteriological analysis of air conditioning wastewater, no Echolium was found in all water samples, the water quality of the air conditioning wastewater was at a neutral pH level and in terms of other properties, the air conditioning wastewater was suitable for domestic and industrial use. According to the results of the physical, chemical and bacteriological analysis of air conditioning wastewater, Khan (2023) found that air conditioning wastewater generally met the quality standards determined by the Bangladesh Government for drinking water and domestic use. According to the physical, chemical and bacteriological analysis results of air conditioning wastewater conducted by Alom et al. (2021), the waste air conditioning water does not meet the drinking water standards of Bangladesh because it contains a large number of E coli and a high level of BOD, but according to the test results in the laboratory, they reported that this water is suitable for drinking water after filtering and boiling on air conditioning wastewater. Noutcha et al. (2016) found that the physicochemical properties of the air conditioning wastewater were generally within the limits determined by the WHO, while the microbial values did not meet the quality standards determined for drinking water use, and therefore these waters could be used for cleaning purposes in a laboratory environment.

Akram et al. (2018) reported that according to the results of the physical-chemical and bacteriological analysis of air conditioning wastewater, the water quality of air conditioning wastewater is very close to the quality of distilled water and can be used like pure water. Uddin et al. (2019) concluded that the analysis results of air conditioning wastewater meet the Bangladesh Government water standards and the standards set by WHO in terms of water quality drinking water and that this water can be used for drinking, washing and other domestic purposes, irrigation and fishing purposes. Okeyinka et al. (2021) concluded that the analysis results of air conditioning wastewater did not meet the water quality drinking water standards, but it was of sufficient quality for domestic use and in the amount determined by WHO for individual use.

In general, the quantity and quality characteristics of air conditioning wastewater vary depending on factors such as the climate characteristics of the environment, the power of the air conditioner, and the water collection and storage system (Scalize et al. 2018).

6. Possible Usage Areas of Air Conditioning Wastewater

Sustainability and sustainable economic activities have emerged from the necessity to make new production/consumption processes dominant in economic, social and environmental areas in order to minimize or eliminate the effects of risks (such as climate change, acid rain, loss of biodiversity, pollution of air, water and soil resources) that threaten the existence of nature, humans and other living beings, resulting from the excessive consumption of nature (production factors, living space) used to meet human needs. In this respect, the correct management, destruction, preservation and evaluation of wastes resulting from various production/consumption processes that cause great harm to nature and their recycling into the economy and the relieving of the burden of these wastes on nature are essential for the continuation of human existence. The waste economy, expressed with the concept of circular economy, processes these wastes with developing technology, adds economic value and produces solutions to many problems, especially environmental pollution costs, by transforming them into inputs that replace the scarce resources required for production. At this point, the advantage of processing waste is that it has lower production costs than other resources, and also saves the need to incur a considerable cost to manage these wastes, making the waste economy very valuable.

Water, which constitutes 75% of the world (ATO, 2023) and the human body (SUDER, 2024) and is the source of life in both, is a very valuable resource and according to projections, the amount of water needed for human life is decreasing (WWF, 2023). In this sense, the possibilities of evaluating every drop of water should be calculated. Air conditioning wastewater is produced by air conditioners without any production cost, under suitable conditions; a 1 ton air conditioner produces 1.10 litres of water per hour; (Uddin et al., 2019). A significant amount (there are 2 billion air conditioners in the world; Ritchie, 2024) is produced without any cost and is thrown away without being evaluated. In addition to the negative environmental and social effects, the economic loss experienced is incredible. Scientific research conducted on the evaluation of air conditioning wastewater within the scope of waste economy provides scientific evidence that air conditioning wastewater can be an alternative solution to water scarcity. Accordingly, in these studies: Studies by Snidvongs and Vongsumran (2020), Khan (2023), AlGhamdi et al. (2024), and Matarneh et al. (2024) reported that air conditioning wastewater is a suitable source for irrigation and domestic use, including drinking water. Uddin et al. (2019) expressed a wider scope for the use of air conditioning wastewater and reported that air conditioning wastewater can be used

for drinking, washing and other domestic purposes, irrigation and fishing purposes. Sabnis et al. (2020) reported that air conditioning wastewater can be collected with a simple arrangement and used for both domestic and industrial purposes, while Noutcha et al. (2016) and Scalize et al. (2018) reported that air conditioning wastewater can be used for cleaning purposes in Laboratory activities. A similar finding was reached in the study conducted by Galindo (2019), who concluded that air conditioning wastewater could be considered as a potential alternative water source other than drinking water use. In the study conducted by Okeyinka et al. (2021), according to the results of the physico-chemical analysis of air conditioning wastewater, they concluded that air conditioning wastewater has an acidic structure and this acidic structure can be neutralized with pH correction processes and become suitable for domestic use. Okeyinka et al. (2021) concluded that air conditioning wastewater can be used for domestic purposes, Akram et al. (2018) in pure water usage areas, and Siam et al. (2019) as irrigation water.

Abdullah and Mursalin (2021) reported in their study that a 2-ton air conditioner produces an average of 25 litres of wastewater per day, and that this air conditioner wastewater can be used in various applications including vehicle batteries, radiator water, toilet flushing, industrial purposes, laundry, aquarium fish culture and irrigation. In a study conducted by Elveren et al. (2018), while the crop productivity decreased in wheat and barley production grown with irrigation water mixed with air conditioning wastewater at different rates, the negative result was that the products decreased and toxic substances accumulated in the product, Siam et al. (2019) concluded that it can be used as irrigation water. In a case study conducted by Bastos and Calmon (2013) to reduce water costs in a workplace, It was found that the air conditioners in a workplace produced 4.8 litres of water per hour, which corresponds to a significant amount of water used in the toilets in the workplace, and that 5,530 litres of this water was used by 820 employees to clean the toilets, of which 4,298.10 litres was produced by air conditioners, and it was expected that an economic gain of 77.72% would be achieved.

7. Conclusion

The continuation of human existence depends on sustainable economic activities, sustainable economic activities depend on effective and efficient resource use, effective and efficient resource use depends on using each resource while preserving its ability to renew itself, and the ability of each resource to renew itself depends on the correct disposal, preservation and evaluation of wastes resulting from various production/consumption processes and their reintroduction into the economy. In the world, 2.1 billion tons of waste is produced with a management cost of 495 billion dollars and a very small portion of this waste, 400 million tons, is recycled to the economy, providing 130 billion dollars of income. Especially 80% of the 6.8 billion tons of plastic waste that is suitable for recycling, 83% of the 56.3 million tons of electronic waste and 81% of the 935 billion tons of organic waste are thrown into nature. When the situation is evaluated in terms of water source, which is a very valuable resource, tons of waste water produced by approximately 2 billion air conditioners in the world at zero cost (a 1 ton air conditioner can produce 1.10 litres of water per hour) is wasted while it could meet many water needs. Scientific studies on the subject provide evidence supporting that air conditioning wastewater can be an alternative water source. The amount of air conditioning wastewater production depends on the power of the air conditioner, the climate characteristics of the environment and the operating time of the air conditioner. There are scientific studies that conclude that the wastewater values produced by air conditioners are in compliance with the WHO drinking water standards. There are also scientific studies that conclude that the particles in the working environment of air conditioners do not meet the WHO standards due to the high content of heavy metals (such as copper, iron, aluminium, chromium, barium, zinc and manganese) and the high content and density of microbial pathogens and pesticides harmful to humans. However, in general, most studies provide evidence supporting that these wastewaters can be used for different purposes and needs such as drinking, irrigation, domestic and industrial use and that significant economic gains will be achieved. The study results provide strong evidence that significant economic values will be gained from both the environmental costs incurred due to these wastes and the production costs by obtaining the raw materials required for production by managing wastes correctly. More scientific studies should be conducted on wastes, which are a very sensitive issue, and effective waste management should be provided all over the world by sharing knowledge and experience.

Author Contributions

The percentages of the author contributions are presented below. The author reviewed and approved the final version of the manuscript.

	H.S.
C	100
D	100
S	100
L	100
W	100
CR	100
SR	100

C=Concept, D= design, S= supervision, L= literature search, W= writing, CR= critical review, SR= submission and revision.

Conflict of Interest

The author declared that there is no conflict of interest.

References

Abdullah MA, Mursalin R. 2021. Condensed water recycling in an air conditioning unit. IJRDO, 18(3): 13-19. https://doi.org/10.9790/1684-1803021319

Akram MW, Mursalin R, Hassan MM, Islam MR, Choudhury SK. 2018. Recycling of condensed water from an air conditioning unit. In: Proceedings of the 2018 International Conference on Computer, Communication, Chemical, Material and Electronic Engineering (IC4ME2), 8-9 February, Rajshahi, Bangladesh, pp: 1-5. https://doi.org/10.1109/IC4ME2.2018.8465612

AlGhamdi SA, Alromi D, Jambi E, Alzughaibi T, Al-Ansari A. 2024. Heavy metals and microbial assessment of air conditioning condensate water in Jeddah city-Saudi Arabia: concept of sustainable water resources. Sustain. Water Resour Manag, 2024: 1-10. https://doi.org/10.1007/s40899-024-01122-2

Ali S, Shirazi F. 2023. The Paradigm of circular economy and an effective electronic waste management. Sustainabil, 15(3): 1998. https://doi.org/10.3390/su15031998

Alom MdM, Ahsanb A, Imteaz M. 2021. Quantity and quality of condensate air conditioner water for potential use in drinking purpose. Desalination Water Treat, 210: 164–169. https://doi.org/10.5004/dwt.2021.26571

ATO, 2023. Su raporu. Ankara Ticaret Borsası (ATO). URL: https://www.ankaratb.org.tr/lib_upload/Su%20raporu.pdf (accessed date: August 28, 2024)

Bastos CS, Calmon JL. 2013. Using condensed water of air conditioners for toilet flushing: A Case Study in Brazil J Archit Civ Eng, 7(1): 98-104. URL: https://www.davidpublisher.com/Public/uploads/Contribute/5553107865bb7.pdf (accessed date: August 28, 2024)

Bautista-Olivas AL, Cruz-Bautista F, Álvarez-Chávez CR, Zavala-Reyna AG, Sánchez-Landero LA, Alvarado-Ibarra J. 2017. Concentration of heavy metals in condensed atmospheric water vapor at three Mexican localities. Atmósfera, 30(3): 209-220. https://doi.org/10.20937/atm.2017.30.03.02

Biniş M. 2023. Türkiye'de çevresel sürdürülebilirliğe yönelik mali teşvikler: Geri Dönüşüm Örneği. Dumlupınar Üniv Sosy Bil Derg, 77: 31-52. https://doi.org/10.51290/dpusbe.1246296

CCR, 1978. California code of regulations, Title 22 Social Security. URL: https://www.law.cornell.edu/regulations/california/title -22 (accessed date: December 27, .2024)

Dinka MO. 2018. Safe drinking water: concepts, benefits, principles and standards. In: Glavan M. editor. Water Chal Urb World. Intechopen, London, UK, pp: 163-182. https://doi.org/10.5772/intechopen.71352

Dünya Gazetesi. 2024. Split klima pazarı yüzde 35 büyüdü ihracat 2 kat arttı. URL: https://www.dunya.com/sektorler/split-klima-pazari-yuzde-35-buyudu-ihracat-2-kat-artti-haberi-726836 (accessed date: August 28, 2024).

EC. 2023. Aggravating resource scarcity. European Commission (EU), Knowledge for policy, Megatrends Hub. https://knowledge4policy.ec.europa.eu/navigation-page/megatrends-hub_en

Elveren M, Varol T, Osma E. 2018. klima atik sularinin, buğday ve arpa üzerindeki etkilerinin araştirilmasi. Erzincan Üniv Fen Bilim Enst derg, 11(3): 467-477. https://doi.org/10.18185/erzifbed.408094

ENERGY.GOV. 2015. History of air conditioning. Author: Paul Lester. URL: https://www.energy.gov/articles/history-air-conditioning (accessed date: August 28, 2024)

EPA. 1992. Waste water treatment manuals. Envir Protec Agen. URL: https://www.epa.ie/publications/compliance--enforcement/waste-water/EPA_water_treatment_manual_-small-comm_business.pdf (accessed date: December 27, 2024)

EPA. 2020. National Overview: Facts and figures about materials, waste and recycling. URL: https://www.epa.gov/facts-and-figures-about-materials-waste-and-recycling/national-overview-facts-and-figures-materials (accessed date: August 28, 2024)

Forti V. 2020. Global electronic waste up 21% in five years, and recycling isn't keeping up. URL: https://ourworld.unu.edu/en/global-electronic-waste-up-21-in-five-years-and-recycling-isnt-keeping-up (accessed date: August 28, 2024)

Galindo RM. 2019. Air conditioning condensate: a potential water source and a creeping destroyer. URL: http://conf.e-jikei.org/ICTCBW/2019/proceedings/materials/proc_files/GS_papers/camerareadymanuscript_GS_ICTCBW2019_A017.pdf (accessed date: August 28, 2024)

Glawe D, Wooten M, Lye B. 2016. Quality of condensate from air-handling units. ASHRAE J, 58(12): 14-23. URL: https://core.ac.uk/download/pdf/216391004.pdf (accessed date: August 28, 2024)

Guarnieri G, Olivieri B, Senna G, Vianello A. 2023. Relative humidity and its impact on the immune system and infections. Int J Mol Sci, 24(11): 9456. https://doi.org/10.3390/ijms24119456

Güllü G. 2023. Good practice examples of recyling in local governments. in: aydin me, engin g. editors. cleaner production, green consensus and sustainable waste management. Turkish Acad Sci Publ, Ankara, Türkiye, pp: 225-243. https://doi.org/10.53478/TUBA.978-625-8352-57-3.ch12

Khan MN, Khan MA, Khan S, Khan MM. 2018. Chapter 5 effect of air conditioning on global warming and human health. In: M. Oves et al., editors. Modern Age Environmental Problems and their Remediation. Springer Intern Publ AG, New York, USA, pp: 83-94. https://doi.org/10.1007/978-3-319-64501-8_5

Khan MO. 2023. Quality assessment of condensate water generating from air conditioning units. Preprints. https://doi.org/10.20944/preprints202310.1639.v1

Knight C. 2023. What is the linear economy? European Investment Bank (EIB). URL: https://www.eib.org/en/stories/linear-economy-recycling (accessed date: August 28, 2024)

Kök F. 2021. Organik atiklarin yönetimi, geri dönüşümü ve uygulamaları. Ulusal Çevre Bilim Araşt Derg, 4(2): 99-108.

Koşar A. 2024. Suyun değeri kuyu kuruyunca anlaşılır. Güney Gazatesi. URL: https://www.guneygazetesi.com/yazi/4216/suyun-degeri-kuyu-kuruyunca-anlasilir.html (accessed date: August 28, 2024)

Kulkarni SJ. 2023. Combinations of biotechnology and nanotechnology in industrial wastewater treatment. In: Mishra BK, editor. Sustainable Science and Intelligent Technologies for Societal Development, IGI Global Scientific Publishing. Chennai, India, pp: 96-106. https://doi.org/10.4018/979-8-3693-1186-8.ch006

Lahmo P. 2024. Beyond batch: The transformative force of continuous manufacturing. URL: https://www.rootsanalysis.com/blog/transformative-force-of-continuous-manufacturing/ (accessed date: August 30, 2024).

Magazzino C, Falcone PM. 2022. Assessing the relationship among waste generation, wealth, and GHG emissions in Switzerland: Some policy proposals for the optimization of the municipal solid waste in a circular economy perspective. J

Clean Prod, 351: 131555. https://doi.org/10.1016/j.jclepro.2022.131555

Mandpe A, Paliya S, Gedam VV, Patel S, Tyagi L, Kumar S. 2022. Circular economy approach for sustainable solid waste management: A developing economy perspective. Waste Manag Res, 41(3): 499-511. https://doi.org/10.1177/0734242X221126718

Marketing Türkiye. 2021. Yazın süper kahramanı: klimalar. Yazan; Nafizcan Önder. URL: https://www.marketingturkiye.com.tr/haberler/yazin-super-kahramani-klimalar/ (accessed date: August 28, 2024)

Mashudi, Sulistiowati R., Handoyo S, Mulyandari E, Hamzah N. 2023. Innovative strategies and technologies in waste management in the modern era integration of sustainable principles, resource efficiency, and environmental impact. Int J Sci Soc, 5(4): 87-100. https://doi.org/10.54783/ijsoc.v5i4.767

Matarneh S, AlQaraleh L, Alkhrissat T, Abdel-Jaber M, 2024. Assessing water production from air conditioning systems as an unconventional supply source: A focus on water quality and social acceptance perspectives. Case Stud Chem Environ Eng, 9: 100585. https://doi.org/10.1016/j.cscee.2023.100585

Mishra K, Siwal SS, Nayaka SC, Guan Z, Thakur VK. 2023. Waste-to-chemicals: Green solutions for bioeconomy markets. Sci Total Environ. 887: 164006. https://doi.org/10.1016/j.scitotenv.2023.164006

Mishra, R. K. (2023). Fresh Water availability and Its Global challenge. Br j multidiscip adv stud., 4(3): 1–78. https://doi.org/10.37745/bjmas.2022.0208

Mısır A, Arıkan OA, 2023. Zero waste management and circular economy. In: Cleaner Production, Green Consensus and Sustainable Waste Management, In: Aydın ME, Engin G. editors. Cleaner Production, Green Consensus and Sustainable Waste Management. Turkish Academy of Sciences Publication, Ankara, Türkiye, pp: 205-224. https://doi.org/10.53478/TUBA.978-625-8352-57-3.ch11

Nayanathara PGC, Pilapitiya T, Ratnayake AS. 2024.The world of plastic waste: A review. Cleaner Materials, 11: 100220. https://doi.org/10.1016/j.clema.2024.100220

Noutcha MAE, Damiete O, Johnny Jr. M, Ngozi O, Ezera CU, Okiwelu SN. 2016. Quantity and quality of water condensate from air conditioners and its potential uses at the University of Port Harcourt, Nigeria. Adv Appl Sci Res 7(6): 45-48. URL: https://www.primescholars.com/articles/quantity-and-quality-of-water-condensate-from-air-conditioners-and-its-potential-uses-at-the-university-of-port-harcourt-nigeria.pdf (accessed date: August 28, 2024)

Okeyinka OM, Ogundipe OO, Oloke DA, Adesogan SO. 2021. Reclaimed air conditioner condensate as alternative source of water in hot humid region. IOSR-JMCE, 18(6): 25-30. https://doi.org/10.9790/1684-1806012530

Rabbi K. 2021. E-waste creating employment electronic recycling. URL: https://urbanerecycling.com/e-waste-creating-employment/ (accessed date: August 28, 2024)

Ricci-Jürgensen M, Gilbert J, Ramola A. 2020. Global assessment of municipal organic waste production and recycling. In Sol Waste Assoc (ISWA). URL: https://www.altereko.it/wp-content/uploads/2020/03/Report-1-Global-Assessment-of-Municipal-Organic-Waste.pdf (accessed date: August 28, 2024)

Ritchie H. 2024. Air conditioning causes around 3% of greenhouse gas emissions. How will this change in the future? Published online at OurWorldinData.org. URL: https://ourworldindata.org/air-conditioning-causes-around-greenhouse-gas-emissions-will-change-future (accessed date: August 28, 2024)

Sabnis A, Kale M, Dhanorkar M, Kale S. 2020. Quality testing of air conditioner condensate and its potential in water conservation. JWARP, 12: 93-101. https://doi.org/10.4236/jwarp.2020.122006

Saraoğlu E. 2014. Arıtılmış atıksuların tarımsal sulamada yeniden kullanımı-ülkemizden ve dünyadan başarılı örnekler ve türkiye için uygulama önerileri. Uzmanlık Tezi, Çevre ve Şehircilik Bakanlığı, Ankara, pp: 1-105. https://webdosya.csb.gov.tr/db/destek/icerikler/ece_saraoglu_uzmanl-k-_tez--20191127122309.pdf (accessed date: December 27, .2024)

Sayğı H. 2022. Use of different agricultural wastes as plant nutrient material (organic fertilizer) in strawberry cultivation. In: Proceedings of the EurAsia Waste Management Symposium, October 24-26, İstanbul, Türkiye, p: 1-11. URL: https://www.eurasiasymposium.com/EWMS_2022/files/Hall2_2022/Session-4/157_Saygi.pdf (accessed date: August 28, 2024)

Sayğı H. 2023. Effect of municipal solid waste compost on yield, plant growth and nutrient elements in strawberry cultivation. Sustainability, 15(12): 9447. https://doi.org/10.3390/su15129447

Scalize P, Soares S, Alves A, Marques T, Mesquita G, Ballaminut N, Albuquerque A. 2018. Use of condensed water from air conditioning systems. Open Eng, 8(1): 284-292. https://doi.org/10.1515/eng-2018-0031

Seyhan N. 2023. AB'de döngüsel ekonomi üretim ve tüketim göstergelerinin değerlendirilmesi: MEREC Temelli MARCOS Uygulaması. SMAR, 4(3): 364-391. https://doi.org/10.54733/smar.1338423

Siam L, Al-Khatib IA, Anayah F, Jodeh S, Hanbali G, Khalaf B, Deghles A. 2019. Developing a strategy to recover condensate water from air conditioners in palestine. Water, 11(8): 1696. https://doi.org/10.3390/w11081696

Sırım V. 2018. İslam iktisadinda ihtiyaç kavrami. IBAD, 3(2): 910-919. https://doi.org/10.21733/ibad.478646

Snidvongs S, Vongsumran K. 2020. Air conditioner waste-water recovery. Green En Lif Sci, pp: 1-9. URL: https://www.researchgate.net/publication/341521299_Air_Conditioner_Waste-Water_Recovery (Accessed date: August 30, 2024)

Statista. 2024 Revenue of waste management and remediation services in the United States from 2010 to 2024. URL: https://www.statista.com/statistics/1386774/revenue-waste-management-industry-us/ (accessed date: August 28, 2024)

SUDER, 2024. Suyun önemi. SUDER (Ambalajlı Su Üreticileri Derneği). URL: https://suder.org.tr/saglikli-su-hidrasyon/suyun-onemi/ (accessed date: August 28, 2024)

The World Counts, 2024. Depletion of natural resources. URL: https://www.theworldcounts.com/stories/depletion-of-natural-resources (accessed date: August 28, 2024)

TÜİK. 2024. Atık istatistikleri, 2020. Türkiye İstatistik Kurumu (TUİK). URL: https://data.tuik.gov.tr/Bulten/Index?p=Atik-Istatistikleri-2020-37198 (Accessed date: August 30, 2024)

Uddin S, Omar A, Alam A. 2019. Assessment of quantity and quality of condensate water from air conditioners. In: Proceedings 2nd International Conference on Water and Environmental Engineering (iCWEE2019), 19-22 Jan, Dhaka, p: 84-93. URL: https://www.researchgate.net/publication/333015165_Assessment_of_Quantity_and_Quality_of_Condensate_Water_from_Air_Conditioners (accessed date: August 28, 2024)

Unesco. 2023. Partnerships and cooperation for water. The United Nations World Water Development Report 2023. p: 1-

12 URL: https://unesdoc.unesco.org/ark:/48223/pf0000384657 (accessed date: August 28, 2024)

UNEP. 2024. Global waste management outlook 2024: Beyond an age of waste–Turning rubbish into a resource. Co-produced with: International Solid Waste Association (ISWA), United Nations Environment Programme (UNEP). https://doi.org/10.59117/20.500.11822/44939

Usón AA, López-Sabirón AM, Ferreira G, Sastresa EL. 2013. Uses of alternative fuels and raw materials in the cement industry as sustainable waste management options. Enew, Sustain. Energy Rev, 23, 242-260. https://doi.org/10.1016/j.rser.2013.02.024

Wang F, Wong W-K, Wang Z, Albasher G, Alsultan N, Fatemah A. 2023. Emerging pathways to sustainable economic development: An interdisciplinary exploration of resource efficiency, technological innovation, and ecosystem resilience in resource-rich regions. Resources Policy, 85(PA). https://doi.org/10.1016/j.resourpol.2023.103747

Wang J, Azam W. 2024. Natural resource scarcity, fossil fuel energy consumption, and total greenhouse gas emissions in top emitting countries. Geoscience Frontiers, 15(2), 101757. https://doi.org/10.1016/j.gsf.2023.101757

WEF. 2023. Circular economy: The enormous opportunity of e-waste recycling. World Economic Forum (WEF). URL: https://www.weforum.org/agenda/2023/03/the-enormous-opportunity-of-e-waste-recycling/ (accessed date: August 28, 2024)

WHO. 1973. Reuse of effluents: Methods of wastewater treatment and health safeguards. Report World Health Organization. URL: https://iris.who.int/handle/10665/41032 (accessed date: December 27, 2024)

WHO. 1989. Health guidelines for the use of wastewater in agriculture and aquaculture. Report of World Health Organization. URL: https://iris.who.int/handle/10665/39401 (accessed date: December 27, 2024)

WHO. 2019. WHO Drinking water specifications. URL: https://cpcb.nic.in/who-guidelines-for-drinking-water-quality/ (accessed date: August 28, 2024)

Woods J, James N, Kozubal E, Bonnema E, Brief K, Voeller L, Rivest J. 2022. Humidity's impact on greenhouse gas emissions from air conditioning. Joule 6: 726–741, https://doi.org/10.1016/j.joule.2022.02.013

WWF. 2021. Plastics: The cost to society, the environment and the economy. A report for World Wide Fund for Natüre (WWF) by Dalberg, pp: 1-48. URL: https://europe.nxtbook.com/nxteu/wwfintl/tcops/index.php#/p/1 (accessed date: August 30, 2024)

WWF. 2023. Su kitliği kapimizda. 22 Mart Dünya Su Günü. URL: https://www.wwf.org.tr/?13200/dunyasugunu (accessed date: August 28, 2024).

Xu A, Wu YH, Chen Z, Wu G, Wu Q, Ling F, Huang WE, Hu HY. 2020. Towards the new era of wastewater treatment of China: development history, current status, and future directions. Water Cycle 1: 80–87. https://doi.org/10.1016/j.watcyc.2020.06.004

Yıldız NÇ. 2016. Suyun fiyatlandirilmasinda kavramsal çerçeve ve temel yaklaşimlar. SPD – Hidropolitik Akademi. URL: https://hidropolitikakademi.org/uploads/wp/2016/08/SUYUN-F%C4%B0YATLANDIRILMASINDA-KAVRAMSAL-%C3%87ER%C3%87EVE.pdf (accessed date: August 28, 2024).

Black Sea Journal of Engineering and Science
doi: 10.34248/bsengineering.1578563

Open Access Journal
e-ISSN: 2619 – 8991

Review
Volume 8 - Issue 2: 558-568 / March 2025

THERMAL SLAM: HARNESSING TEMPERATURE VARIATIONS TO ENHANCE OBJECT DETECTION AND TRACKING PERFORMANCE

Fathia SALEM[1]*, Osman Serdar GEDİK[1]

[1]*Ankara Yıldırım Beyazıt University, Faculty of Engineering, Department of Computer Engineering, 06460, Ankara, Türkiye*

Abstract: Thermal Simultaneous Localization and Mapping (SLAM) is a burgeoning field that collects robotics, computer vision, and thermal imaging. In this paper, we tried to present a thorough review of recent advancements in thermal SLAM, with a focus on its role in enhancing object detection and tracking. For better performance in low light, resistance to obstructions, and accuracy in bad weather, thermal SLAM systems work better with visual-based SLAM systems because they use changes in temperature in the environment. The review paper explains the fundamental principles of SLAM, including sensor technologies, data fusion techniques, and mapping algorithms. It then explores the methodologies used for object detection and tracking within the Thermal SLAM framework, encompassing classical approaches and deep learning techniques tailored for thermal imagery analysis. Additionally, the paper discusses challenges and limitations specific to thermal SLAM, such as thermal drift, sensor noise, and calibration issues, while also identifying potential areas for future research. The paper provides a comprehensive survey of applications that utilize thermal SLAM for object detection and tracking across various domains, including autonomous navigation, surveillance, search and rescue operations, and environmental monitoring. It synthesizes case studies and experimental results from relevant literature to demonstrate the effectiveness and practicality of thermal SLAM in complex scenarios where traditional visual-based methods struggle. Overall, this review emphasizes the role of thermal SLAM in advancing autonomous systems and enabling robust object detection and tracking in challenging environments. Examining recent developments, challenges, and applications, it sheds light on the progress made in this field.

Keywords: SLAM, Thermal camera, Object detection, Robust localization, Object tracking

***Corresponding author:** Ankara Yıldırım Beyazıt University, Faculty of Engineering, Department of Computer Engineering, 06460, Ankara, Türkiye
E mail: fafyalmnfy2014@gmail.com (F. SALEM)
Fathia SALEM https://orcid.org/0009-0000-9332-8125
O Serdar GEDİK https://orcid.org/0000-0002-1863-8614

Received: November 3, 2024
Accepted: January 28, 2025
Published: March 15, 2025

Cite as: Salem F, Gedik OS. 2025. Thermal slam: Harnessing temperature variations to enhance object detection and tracking performance, BSJ Eng Sci, 8(2): 558-568.

1. Introduction

Thermal Simultaneous Localization and Mapping (SLAM) is a developing discipline that integrates robotics, computer vision, and thermal imaging. This study presents a thorough examination of the latest developments in thermal SLAM, specifically highlighting its contribution to improving object detection and tracking. Thermal SLAM systems are more effective than visual-based SLAM systems in low light conditions, when there are obstructions, and during bad weather. This is because thermal SLAM systems rely on detecting changes in temperature in the surroundings.

In the field of robotics and autonomous systems, one of the most important tasks is using a technique known as Simultaneous Localization and Mapping (SLAM) that accomplishes estimation of robot's position in a generated map. The essential aim of this system is to offer assistance to a mobile agent in the process of navigating through an unfamiliar environment. The agent is able to simultaneously determine its location and then create a map to cover the adjacent "surrounding" area thanks to this capability. It is essential for autonomous systems to have an accurate estimation of the location and the surrounding map because it serves as a forerunner to a variety of other robotic operations, including navigation, exploration, and manipulation. The front end and the back end are the two fundamental components that make up a conventional structural localization and mapping architecture. The front end is tasked with acquiring sensor input and converting it into a more appropriate format for inference. Conversely, the back end utilizes the data obtained from the front end to calculate the agent's states. Additionally, the back end plays a vital role in generating an environment representation and optimizing the agent states that are consistent across the entire globe (Cadena et al., 2016; Li et al., 2019). Most front-ends used in SLAM systems primarily depend on either range sensor (such as depth or LIDAR sensors) or vision sensors (RGB cameras) to detect the adjacent environment. Noteworthy examples are ORB-SLAM as explored in the research by Mur-Artal et al. (2015) which employs RGB sensors, and LOAM by Zhang and Singh (2014) which utilizes LIDAR sensors as their respective SLAM front-ends. While both range-

This work is licensed (CC BY-NC 4.0) under Creative Commons Attribution 4.0 International License

based and vision-based SLAM systems generally perform effectively across different applications, their success significantly relies on ideal visibility circumstances. Nevertheless, the use of current sensors that are based on range, as well as vision for SLAM estimates, becomes challenging in the presence of unfavorable lighting conditions or airborne particulates like dust, soot, and smoke. For example, it is commonly recognized that RGB cameras are unable to operate in low light conditions; in contrast, cameras based on depth can be affected by bright illumination and glare (Debeunne and Vivet, 2020; Khattak et al., 2019b). Similar visual challenges arise when RGB or other sensors operate in environments with airborne particles (such as depth and LIDAR), as discussed by Bijelic et al. (2020) dense fog, or mist. Thermal imaging cameras, in contrast, are unaffected by most airborne pollutants and illumination conditions, as explored in the research by Brunner and Peynot (2014). The Long-Wave Infrared (LWIR) data released by nearby objects is captured by these cameras. The cameras that utilize properties of thermal imaging have distinct benefits that make them a practical alternative for SLAM applications in areas with limited visual information. However, the development of a complete thermal SLAM system poses a series of difficult obstacles. The key problem is to abstract or encode temperature data in a way that best supports the graph optimization process. The difficulty of this task stems from the fact that cameras utilizing thermal properties record the temperature distribution of the surroundings rather than their visual appearance and shape. The problem is exacerbated by the re-measurement accuracy of 8-bit thermal data, which reduces contrast and complicates the application of conventional feature identification and data binding techniques.

In addition, these types of thermal cameras require periodic halting of a process that takes between 0.5 and 1 second to perform Non-Uniformity Correction (NUC), often referred to as Flat Field Correction (FFC) (Mouats et al., 2015; Delaune et al., 2019). During this procedure, the sensor is exposed to a consistent temperature to calculate the correction values for fixed- pattern noise. Thermal cameras pose several additional challenges, including restricted resolution, deteriorating signal-to-noise ratio, and diminished contrast over time. These concerns suggest that the traditional approaches used for other optical sensors are not suitable for the usual front-end abstraction process in thermal SLAM systems, as explained by Wang et al. (2017). Thermal SLAM utilizes temperature fluctuations in the surroundings and enhances conventional visual-based SLAM systems by providing additional benefits, including better detection and tracking in low-light situations, resistance to obstructions, and improved accuracy in unfavorable weather conditions.

1.1. Non-Uniformity Correction (NUC)

Non-Uniformity Correction (NUC) is an essential preprocessing step in thermal imaging that compensates for the inherent inconsistencies in the response of thermal detectors Wu et al (2023). These inconsistencies can degrade image quality, which in turn affects the accuracy of subsequent tasks like localization and mapping in systems such as SLAM. Thermal cameras are susceptible to fixed pattern noise (FPN), a phenomenon caused by variations in the sensitivity of individual sensor elements. These variations arise due to manufacturing imperfections or external environmental factors, leading to a non-uniform thermal response across the camera's array of detectors.

To address these issues, NUC typically involves a brief pause in image capture, during which the thermal camera analyzes a uniform temperature source. This process allows the camera to adjust for sensitivity discrepancies, thereby improving the uniformity of the thermal images. However, this adjustment process can result in temporary data interruptions, halting image capture for a short period. As a result, real-time applications such as thermal SLAM, which require continuous data acquisition, are challenged by these interruptions.

The NUC process, if not properly executed, can introduce artifacts into the thermal images, such as blurred edges, a low signal-to-noise ratio, and inadequate texture representation. These artifacts negatively impact the clarity of thermal images and, consequently, the accuracy of localization and mapping tasks. To address these challenges, this study proposes a novel scene-based NUC method that is integrated with a monocular thermal SLAM system. This method not only reduces the data interruptions typically caused by NUC but also improves the overall quality of thermal images by taking advantage of real-time processing capabilities inherent in modern SLAM technologies. By incorporating advanced denoising algorithms along with optimized NUC strategies into our MonoThermal-SLAM framework, this approach aims to expand the use of thermal cameras in a variety of challenging environments. This integration ensures high-quality spatial localization and mapping, even in conditions that previously hindered real-time thermal imaging applications.

1.2. FFC (Flat Field Correction)

Flat Field Correction (FFC) is an essential preprocessing technique applied to thermal images to compensate for non-uniformities in sensor response, which can be exacerbated in challenging environments such as fire incidents as explored in the research by van Manen et al. (2023). The performance of thermal cameras can degrade due to various factors, including temperature variations and environmental conditions. In this study, FFC is particularly crucial given that inconsistent image quality may hinder feature extraction and pose estimation accuracy.

In the context of FirebotSLAM, a proactive triggering mechanism for FFC was employed based on several criteria: changes in temperature detected by the camera, the vehicle's turning rate, anticipated turns during navigation, and elapsed time since the last correction.

This adaptive approach ensures that corrections are performed at critical moments when inaccuracies are most likely to occur.

It was observed that timely application of FFC significantly contributes to maintaining consistent image quality throughout data acquisition phases during fire scenarios. The integration of FFC into FirebotSLAM enables better feature tracking by mitigating noise and enhancing overall imaging reliability. However, it is important to note that while effective during periods with stable environmental conditions or gradual changes in scene temperature, rapid fluctuations—such as those caused by dynamic fire sources—may still challenge traditional correction methodologies.

The authors highlight that further optimization of FFC routines could enhance system resilience against harsh thermal gradients encountered within smoke-filled environments while improving the robustness of extracted features for Odometry calculations.

1.3. LWIR (Long-Wave Infrared)

(Improving SLAM with Thermal Imagery)

Recent advancements in Simultaneous Localization and Mapping (SLAM) have encountered significant challenges when applied to Long-Wave Infrared (LWIR) imagery. Traditional visual SLAM methods often struggle in environments characterized by poor visibility or substantial illumination changes, such as those found at night or in adverse weather conditions. Keil et al. (2024) address these challenges by proposing a novel approach that integrates learned feature descriptors into existing Bag of Words (BoW) localization frameworks.

The authors highlight that thermal imagery experiences dramatic temperature-driven appearance changes from day to night, which complicates feature extraction and recolonization tasks within SLAM systems. They reveal that conventional feature descriptors such as ORB are not robust enough to maintain consistency across these diurnal variations, leading to failures in place recognition.

To mitigate these issues, the study employs Gluestick—a learning-based method for feature extraction and matching—to enhance robustness against illumination changes. The authors introduce an extensive dataset collected with FLIR Boson thermal cameras over 24-hour cycles, providing valuable resources for training and testing their proposed methodology.

The results show that their integrated approach significantly improves local tracking performance and successfully enables relocalization between day and night imagery—achieving high recall rates compared to traditional methods like ORB-SLAM3. This work represents a significant step towards achieving all-day autonomy for robotic systems utilizing LWIR cameras, ultimately paving the way for more effective long-term mapping solutions in diverse environments.

2. Simultaneous Localization and Mapping (SLAM)

Mapping is a crucial mechanism employed by mobile robots to create maps of the locations they operate in. These maps are utilized to determine their relative location within the environment, facilitating effective path planning (localization). The creation of Extended Kalman Filter SLAM (EKF-SLAM) technology is where SLAM got its start, as described by Leonard and Durrant-Whyte (1991). Initial efforts in integrating SLAM involved a wide range of sensors, such as LIDAR, ultrasonic, inertial sensors, and GPS. Montemerlo (2002) proposed FastSLAM, a hybrid approach that combines Particle Filter and Extended Kalman Filter algorithms. Later, the same team introduced an improved version called FastSLAM 2.0, as explored in the research by Montemerlo et al. (2003). Dellaert and Kaess (2006) made a significant contribution to the field by introducing Square Root Smoothing and Mapping is a crucial mechanism employed by mobile robots to create maps of the locations they operate in. These maps are utilized to determine their relative location within the environment, facilitating effective path planning (localization). The creation of Extended Kalman Filter SLAM (EKF-SLAM) technology is where SLAM got its start. Initial efforts in integrating SLAM involved a wide range of sensors, such as LIDAR, ultrasonic, inertial sensors, and GPS. Montemerlo (2002) proposed FastSLAM, a hybrid approach that combines Particle Filter and Extended Kalman Filter algorithms. Later, the same team introduced an improved version called FastSLAM 2.0, as explored in the research by Montemerlo et al. (2003). Dellaert and Kaess (2006) made a significant contribution to the field by introducing Square Root Smoothing and Mapping (SAM), a technique that uses square root smoothing to improve the optimization of the SLAM problem, resulting in improved mapping efficiency. Kim et al. (2007) introduced a method called Unscented FastSLAM (UFastSLAM) that utilizes unscented transformation. This method has been shown to have improved resilience and accuracy when compared to FastSLAM 2.0. The field of SLAM has recently experienced a significant increase in interest in camera-based systems to decrease the weight and complexity of the systems. Camera-based SLAM systems that rely exclusively on visual input are usually known as visual SLAM (vSLAM), as noted by Taketomi et al. (2017). Significantly, the field of literature has witnessed the development of low-computation methods specifically designed for unmanned aerial vehicles (UAVs) that have limited onboard resources. Among these methods, visual Odometry stands out as a common Simultaneous Localization and Mapping (SLAM) application for small UAVs. Initial inquiries examined the incorporation of both Long Wave Infrared (LWIR) and visible spectra to tackle difficulties presented by environmental elements like fog or smoke. Maddern and

Vidas (2012) introduced a technique for integrating 8-bit thermal and RGB images to facilitate UAV navigation. Their research uncovered notable daily fluctuations in the visible spectrum, which differed from the thermal spectrum's steady but less pronounced features. The integration of the combined spectrum resulted in enhanced outcomes compared to algorithms that rely exclusively on visual or thermal frames. Poujol et al. (2016) showed that significant improvements in performance can be achieved by integrating visual and thermal spectra in traditional visual Odometry methods. Their research utilized two image fusion methods: monochrome threshold-based image fusion (Rasmussen et al., 2009) and monocular visual Odometry, as explored in the research by Geiger et al. (2011). These techniques were applied to data gathered from an electric car navigating through an urban setting. The experimental results highlighted the enhanced value of fused images, which resulted in more resilient solutions. In a preliminary assessment, Brunner and Peynot (2010) examined the integration of optical and thermal cameras for determining position in settings filled with smoke or dust, with a specific emphasis on autonomous ground vehicles (AGVs). Although visual scans were not sufficient for determining relative movements, thermal imaging was able to offer estimates, albeit with less precision. Additionally, Brunner et al. (2013) suggested a technique to improve a Visual SLAM (VSLAM) algorithm by integrating LWIR and normal spectra. The SLAM architecture described by Chen et al. (2017) utilizes both thermal and visual data to create a color map of situations with low lighting conditions. One of the most widely approaches is Graph-based SLAM that used for Simultaneous Localization and Mapping (Grisetti et al., 2010), where the robot's trajectory and the environment map are represented as a graph as shown in Saputra et al (2020). In this method, robot poses are modeled as nodes, and the spatial relationships between them are represented as edges based on sensor measurements and motion constraints. Optimization techniques are applied to adjust the node positions, minimizing errors and refining both the robot's path and the map. This approach effectively handles large-scale environments and loop closures, ensuring accurate, consistent mapping and localization (Hoshi et al., 2024). In the study by Mouats et al. (2014), a method called multispectral stereo Odometry was presented. This method combines optical and thermal sensors and is specifically designed for ground vehicles. Khattak et al. (2019a) combined radiometric sensors, the FLIR Tau2, and a visual camera to facilitate the movement of a tiny quadrotor in poorly illuminated indoor situations contaminated with dust. The use of an Intel NUC-i7 computer for onboard processing, along with thermal frames, allowed for effective feature selection and Extended Kalman Filtering to estimate drone Odometry. This ensured consistent performance even in situations with poor visibility.

SLAM is vital for autonomous navigation and exploration, but current solutions struggle with performance consistency due to a lack of diverse, high-quality datasets and robust evaluation metrics. One major issue is the absence of high-quality datasets that cover diverse all-weather conditions and provide a reliable metric for assessing robustness. This limitation significantly restricts the scalability and generalizability of SLAM technologies, impacting their development, validation, and deployment. To address this Zhao et al. (2023), introduce SubT-MRS, a challenging dataset designed to enhance SLAM in all-weather environments. It includes over 30 diverse scenes, multimodal sensors (LiDAR, cameras, IMU, thermal), and various robot locomotion (aerial, legged, wheeled). We also propose new robustness metrics, offering valuable insights for advancing SLAM research.

The SLAM algorithm operates in an iterative fashion, where the robot continuously updates its position estimate and refines the map based on new sensor readings and previously acquired information. The overall architecture of the SLAM algorithm is shown in Figure 1, Tourani et al (2022). Building upon the foundational concepts of SLAM, we now move to the specific algorithmic procedures that enable simultaneous localization and mapping.

2.1. SLAM Specific Algorithmic Procedures Initialization

Sensor Data Acquisition: The robot gathers sensory information from its surroundings using sensors such as cameras, LiDAR, or sonar.

Initial Pose Estimation: The robot's initial position and orientation are estimated based on sensor data and prior knowledge.

2.1.1. Motion Prediction

Odometry: The robot estimates its current position and orientation based on its previous position and the movement commands it has executed.

Motion Model: A mathematical model is used to predict the robot's motion and account for potential errors in its movement.

2.1.2. Observation Update

Feature Extraction: Distinctive features are extracted from the sensor data, such as edges, corners, or planes.

Feature Matching: Corresponding features are identified between consecutive sensor readings to track changes in the environment.

Map Update: The robot updates its map of the environment based on the observed features and their locations relative to the robot's estimated position.

2.1.3. Data Association

Feature Tracking: The robot tracks the features it has previously observed to maintain consistency in the map.

Loop Closure Detection: If the robot revisits a previously mapped area, it detects and corrects accumulated errors in its position estimates.

2.1.4. Map Optimization

Pose Graph Optimization: The robot refines its position estimates and the map using optimization techniques to minimize errors and inconsistencies.

Bundle Adjustment: A more advanced optimization technique that jointly refines the robot's poses and the positions of landmarks in the map.

2.1.5. Output

Localization: The robot's current position and orientation are determined.

Mapping: A map of the environment is generated, which can be used for navigation, path planning, and other tasks.

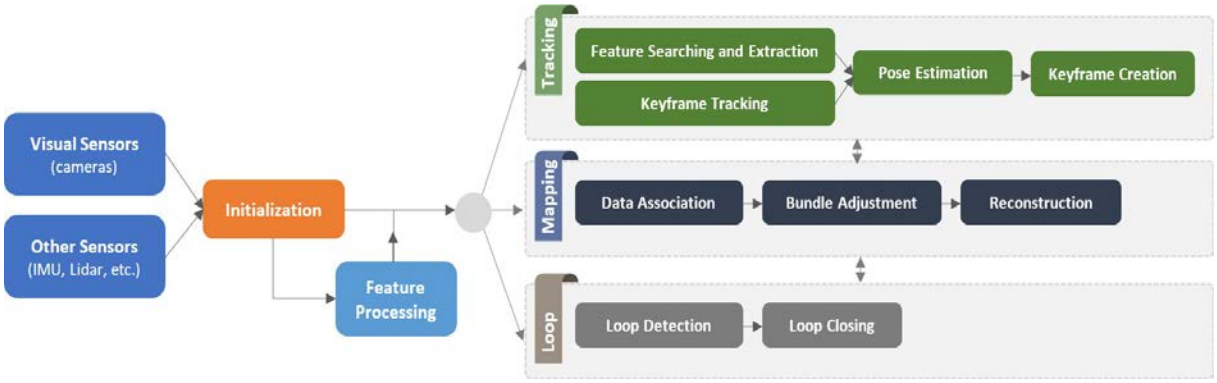


Figure 1. The flowchart of a standard visual SLAM approach, Tourani et al (2022).

3. Thermal SLAM

Thermal SLAM is an extension of traditional SLAM that uses thermal images or infrared sensors for both localization and mapping as shown in Figure 2, by Shin and Kim (2019) making it especially effective in environments where visibility is poor, such as smoke-filled areas, complete darkness, or obstacles that block traditional optical sensors. While Thermal SLAM leverages different sensor modalities, it is fundamentally based on the same core principles as conventional SLAM as we mentioned before:

Localization: This refers to determining the robot's position and orientation in the environment. In SLAM, localization is achieved by comparing the sensor data (in this case, thermal data) with the evolving map being built. The robot's location is continuously updated as it moves through the environment, helping it maintain an accurate representation of its surroundings.

Feature Mapping: In both traditional and thermal SLAM, the process of mapping involves detecting and tracking key features in the environment, such as temperature gradients, heat sources, or other thermal signatures. These features—often distinct in thermal images—are used to create and refine a 2D or 3D map, allowing the robot to both understand and navigate the environment.

Pose Estimation: Pose estimation involves calculating the robot's position and orientation within the map. This is critical for localization as it enables the robot to track its movements in space, updating its pose in real time as it encounters new thermal features. Accurate pose estimation ensures that the robot can navigate and maintain awareness of its surroundings, even in challenging conditions where optical data may be insufficient.

By relying on thermal data, Thermal SLAM overcomes the limitations of conventional SLAM in low-visibility environments while still maintaining the essential framework of localization, mapping, and pose estimation. Thermal SLAM is a recently developed field of research, with most discoveries published in the past ten years.

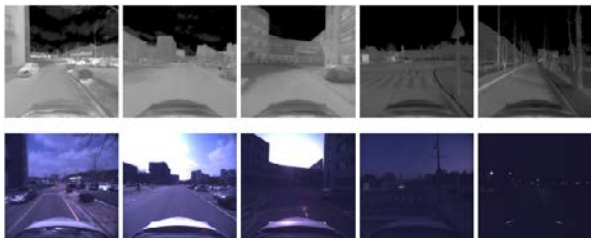


Figure 2. Set of Thermal-infrared (firstly) and RGB images (secondly), in contrast, RGB images, thermal images can capture overlook the time of captured (day or night) Shin and Kim (2019).

Thermal SLAM Research primarily concentrates on thermal Odometry, which involves using thermal cameras to calculate vehicle Odometry. However, thermal mapping, specifically the representation of thermal data in three dimensions, often requires overlaying thermal images onto point clouds created from other depth sources. A thermal-infrared SLAM system was first presented by Shin and Kim (2019) in Figure 3 who used full radiometric 14-bit raw data and LIDAR observations to estimate motion in six Degrees of Freedom (DoF). The experimental results demonstrated the advantages of the 14-bit system, overcoming restrictions related to the re-scaling procedure and showing increased resistance to data loss. Later, Khattak et al. (2020) suggested a thermal/inertial system that uses complete radiometric data to estimate Odometry. They emphasized that this system is resistant to data loss caused by sudden changes resulting from Automatic Gain Control (AGC) re- scaling. Although previous

research has shown positive outcomes, SLAM methods still require significant processing resources and often necessitate the use of high-resolution thermal images. Several of the previously mentioned studies depend on high-resolution thermal cameras like the FLIR Tau2, which involve significant expenses. Additionally, the incorporation of a small yet robust onboard computer system contributes to the financial costs, as well as the need to take into account factors like space, weight, and power usage.

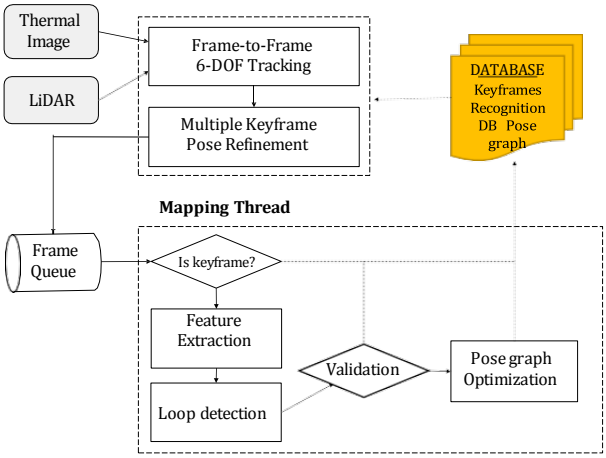


Figure 3. Thermal-Infrared SLAM Using Sparse Depth Information, Shin and Kim (2019).

3.1. Thermal Feature Extraction and Matching

Johansson et al. (2016) assessed how well several visual-based feature detectors and descriptors performed on thermal images using a dataset of image pairs taken in various textural and structural contexts. The dataset included pairs of images captured in different structural and textured environments. The images were initially resized using an 8-bit method, followed by histogram equalization prior to evaluation. The methods were tested under various image deformations, including changes in viewpoint and noise. The evaluation criteria were determined by considering recall, which measures the proportion of correct feature matches identified by RANSAC out of the total number of matches. The combination of the Hessian-affine extractor with the LIOP descriptor consistently demonstrated robust performance in various image deformations among floating-point descriptors. The SURF extractor and descriptor exhibited excellent performance, particularly in terms of their robustness against Gaussian blur and Gaussian white noise. Binary descriptors, when used in thermal imaging, provided performance comparable to floating-point descriptors, albeit with reduced computational expense. Combining binary descriptors like ORB with FREAK or BRISK produced competitive outcomes. Mouats et al. (2018) conducted another benchmark that specifically examined feature extraction and description algorithms for thermal features. This benchmark considered processing time, as it aimed at predicting UAV Odometry using thermal images. The datasets included video sequences captured in safe indoor and outdoor environments with a FLIR Tau2 LWIR camera. Overall, blob detectors like SIFT and SURF showed lower repeatability than corner detectors such as FAST and GFTT. Nevertheless, the characteristics of the blob displayed a more pronounced uniqueness, leading to elevated matching scores. The performance of SIFT feature extraction was subpar in various aspects. Surprisingly, the presence of motion blur had only a modest impact on feature extractors, and the SURF blob extractor had the highest performance. Although descriptors were relatively unaffected by Non-Uniformity Correction (NUC) as expected, it was observed that noise visibility was amplified in indoor situations with uniform temperatures. The authors suggested employing the SURF feature extraction technique in conjunction with the FREAK binary descriptor for thermal navigation applications. This combination provides a well-balanced compromise between match ability, repeatability, and real-time computing. The benchmarks were performed using datasets collected in controlled situations with consistent temperatures. However, environments with smoke or severe heat sources might have a major impact on the processes of extracting and describing features. Moreover, achieving a homogeneous dispersion of characteristics is essential for precise Odometry estimation. It is worth mentioning that the benchmark developed by Mouats et al. (2018) does not include a measurement for assessing the distribution of features across frames, which is crucial for accurately estimating thermal Odometry.

3.2. Thermal Image Processing

Over the past few years, techniques in image processing have been developed to address pattern noise in thermal imagery (Lu, 2020; Chen et al., 2021). Nevertheless, several conventional methods for reducing noise in thermal images fail to acknowledge the significant amount of time required for processing and encounter difficulties in successfully addressing the fundamental issues related to the measurement of light intensity in resized thermal images. To reduce the effects of Automatic Gain Control (AGC) operations on photometric changes, Mouats et al. (2015) suggested modifying the AGC threshold to minimize fluctuations in illumination. However, the core problem of photometric change remains unresolved, as this strategy merely postpones the eventual alteration in illumination. Brunner and Peynot (2010) and Vidas and Sridharan (2012) proposed a technique for histogram normalization of 14-bit thermal images to provide consistent illumination. In contrast, Papachristos et al. (2018) applied fixed interval re-scaling in familiar settings. Nevertheless, both approaches strongly depend on temperature priors that are peculiar to specific conditions, which restricts their practical usefulness. Recently, the use of deep neural networks in thermal image processing approaches has demonstrated potential. However, there is a lack of typical image processing methods specifically designed

to handle noise and AGC concerns simultaneously in rescaled low-contrast thermal images.

3.3. Feature Association on Thermal Images

Traditional feature-matching techniques, such as BRIEF (Calonder et al., 2010; Zhao et al., 2020), have proven useful in odometry and SLAM (Simultaneous Localization and Mapping) studies. Lucas and Kanade (1981) assessed various feature descriptors on rescaled images using thermal properties, which showed inferior matching ability compared to visible images. The difference in results might be ascribed to intrinsic challenges in thermal image quality, such as noise. Learning-based feature association methods have become increasingly popular in certain SLAM systems, demonstrating comparable performance to traditional techniques and often surpassing them in difficult circumstances. GCNv2 and DXS (Mouats et al, 2018; Tang et al., 2019) employ deep neural networks (DNNs) to identify features, extract them, and generate descriptors, with trials demonstrating improved resilience in environments with less texture. Zhao et al. (2020) created a method for monocular visual odometry by utilizing deep optical flow to compare consecutive frames. It is important to emphasize that the methods stated above are mostly intended for images visible to the naked eye and may not be directly suitable for infrared photographs. In the context of Super Thermal, Lu and Lu (2021) introduced a DNN that can find characteristics and calculate descriptors simultaneously. This study showcased the benefits of using a deep model for matching thermal features. However, this network has not been investigated within a comprehensive SLAM system, and its computational expense has not been discussed.

3.4. Thermal Odometry

The process of obtaining a high-accuracy estimate of rotational speed in SLAM systems that rely on thermal imaging is challenging because these cameras collect heat distribution instead of visual appearance and geometry. However, there have been attempts to create thermal Odometry, though these have mainly focused on short distances or have not achieved the same level of performance as RGB-based Odometry. Mouats et al. (2015) employed a Fast-Hessian feature extractor to compute the distance for thermal Odometry in UAV tracking, while Borges and Vidas (2016) developed a practical thermal Odometry system that includes an automated technique for scheduling the Nonuniformity Correction (NUC) operation. However, this system is limited to outdoor situations because it relies on road lane estimation to calculate scale. Recent progress in thermal Odometry has been made by combining it with other types of sensors. Delaune et al. (2019) used thermal and inertial sensors to track UAVs employing an Extended Kalman Filter (EKF) algorithm. They showed that this approach was effective in different illumination conditions by using FAST and KLT trackers. Similarly, Khattak et al. (2019a) devised a thermal-inertial Odometry system for monitoring UAVs. They utilized a direct technique based on key-frames to reduce radiometric errors between consecutive frames using raw radiometric data. Although there have been advancements in thermal-inertial Odometry, there is currently no published research on thermal-inertial SLAM. Vidas and Sridharan (2012) developed a portable thermal SLAM system that uses FAST-based feature tracking and bundle adjustment-based optimization. Nevertheless, it lacks a loop closure module, which is crucial in modern SLAM frameworks for producing coherent trajectories and maps. Moreover, the absence of a sensor not influenced by the environment, such as an Inertial Measurement Unit (IMU), complicates accurate estimation in diverse contexts. Shin and Kim (2019) introduced a feature-based LIDAR-thermal SLAM method that combines thermal data with sparse range measurements from LIDAR to enhance scale estimates. However, using their system in an autonomous driving environment, which often involves greater temperature variations than indoor settings, raises questions about its universal applicability.

3.5. Thermal Mapping

Vidas and Sridharan (2012) created a monocular SLAM system specifically designed for thermal cameras that are carried by hand. The program identifies corner features using the GFTT and FAST detectors and then tracks them using sparse Lucas-Kanade optical flow. To analyze the images with thermal properties, the original 14-bit thermal data is transformed into 8-bit data within a predetermined range centered on the average value between the lowest and maximum 14-bit intensity. Homography motion estimation utilizes matched SURF features to continue tracking following a Flat Field Correction (FFC). Local path refinements are conducted on every frame between two key-frames, and a new metric is introduced based on five factors to determine the selection of a new key-frame. Nevertheless, the technique frequently falls short of achieving a re-projection error below 1.5 for extended durations, especially during pure rotations. The authors did not disclose information about the accuracy of the resulting 3D thermal map. Shin and Kim (2019) integrated depth data from LiDAR and thermal data from a LWIR camera to generate a thermal map. A limited number of LiDAR points are transformed and mapped onto the 14-bit thermal image. These points are then monitored and traced in the next frame using a direct method. The loop closure, extracted through the bag of visual words technique, involves obtaining ORB features from the 8-bit transformed image. However, this method may lead to incorrect detections in settings with limited intricate patterns. To address this problem, supplementary geometric verification is introduced. The authors assert that they have created a visual SLAM system capable of accurately calculating a trajectory and generating a 3D thermal map throughout the day, regardless of outdoor illumination conditions. (Van Manen et al., 2023) developed Chameleon, a stereo thermal-inertial SLAM

system based on EKF-SLAM. Pose estimation depends on tracking up to thirty landmarks retrieved via SIFT feature extraction and description. Experiments conducted in both cold and heated conditions showed that relying solely on thermal-inertial data for localization is not feasible due to the lack of distinct differences in thermal images, especially in cold environments. While no specific margin of error is provided, the algorithm claims to approximate location within a few meters of a firefighting training facility where an active fire is present. Nevertheless, the limited mapping method cannot generate a clear and understandable representation of the building, and moisture formation on the lens in hot conditions negatively impacts the accuracy of determining position, resulting in a high dependence on inertial data. When only a thermal map is needed, it is typically preferable to overlay thermal data onto a 3D map created by a SLAM technique utilizing more widely used sensors. This is accomplished by acquiring the position and depth information via sensors like LiDAR, RGB cameras, or depth cameras. Subsequently, thermal data is incorporated into the 3D map by projecting map points onto thermal images. However, in environments filled with smoke or under fire conditions, secondary sensors may lose effectiveness, negatively impacting the accuracy and reliability of thermal mapping algorithms.

4. Thermal Inertial-SLAM Method

Visual SLAM's perform better in good weather conditions. However, in low visibility, foggy, stormy, blizzardy, or dark environments with poor visibility, such as darkness at night, enclosed environments, and tunnels, Visual SLAM's have difficulty reading the surrounding data due to their equipment (usually LIDAR).

TI-SLAM: Thermal-Inertial SLAM with Probabilistic Neural Networks for Adverse Conditions Saputra et al. (2021) introduced an approach called TI-SLAM that integrates neural network-based sensor abstraction with probabilistic pose graph optimization to improve pose accuracy in visibility-limited situations, such as darkness, smoke, or dust.

Neural Sensor Abstraction: The front-end uses Mixture Density Networks (MDN) to convert raw thermal and inertial data into a probabilistic format, optimizing the interpretation process for more accurate mapping and localization. TI- SLAM's neural network uses a ResNet 50 model to transform raw thermal data into distinctive 128-dimensional global descriptors. This structure is adapted for processing thermal images, which typically contain less feature variation than RGB images. For training, the network exploits triple loss with samples obtained from the Bag of Traced Words (BoTW) algorithm applied to RGB images. This method enables efficient training by focusing on generating high-quality outputs.

Robust Pose Graph Optimization: TI-SLAM is designed to perform under difficult conditions. This is achieved with thermal imaging and guidance that captures infrared radiation, which is unaffected by visible light conditions, as explored in the research by Khattak et al. (2019a). Thermal-inertial SLAM offers advantages compared to traditional SLAM methods due to its use of thermal and inertial data, robustness to environmental changes, reduced dependency on feature subtraction, robust predictions using Probabilistic Neural Networks (PNNs), graph-based optimization for consistent matching, and adaptability to different sensor configurations. Thermal and inertial data complement visual information, providing robustness to illumination changes and accurate motion estimation. Unlike traditional SLAM, it relies less on feature extraction algorithms using differential thermal signatures for matching. PNNs provide robust predictions by accounting for uncertainties in sensor measurements and motion estimates. Graph-based optimization reduces variance by providing globally consistent maps and trajectories. Furthermore, its modular nature allows for easy integration of additional sensors or adjustments to the sensor setup, increasing adaptability to various robotic platforms and application requirements.

Since the TI-SLAM algorithm is older compared to today's algorithms, we had to use specific versions of the additional packages needed for this algorithm to function, or versions of the packages that are still in use today. When we updated some packages, we encountered different errors in the algorithm, making the process more challenging than anticipated. Once we managed to run the TI-SLAM algorithm, the second major issue was the large size of the datasets used. The algorithm was able to reduce this dataset from 14 bits to 8 bits, but even this was taking up too much space in our virtual machine. Moreover, the size of these datasets caused the SLAM algorithm to generate output for an extended period. Additionally, to place these datasets in the correct file locations and provide them as input to the algorithm, the configuration file had to be configured separately for each dataset. Constantly updating the contents of this configuration file for each dataset was also a time-consuming problem for us. The last and biggest challenge we faced while running and testing this algorithm was that the machines we used were not equipped with sufficient hardware, such as RAM (Random Access Memory), required for large datasets. Although we ran this algorithm on our virtual machine with a high RAM size of 16 GB, we were unable to obtain output for many datasets. Due to the algorithm's large number of requirements for these datasets, our virtual machines were unable to meet this need, resulting in a "Process Killed" response for most of the large datasets. Despite all these problems, we tested our TI-SLAM algorithm on some datasets and achieved successful results. Thermal and inertial data complement visual information, providing robustness to illumination changes and accurate motion estimation. Unlike traditional SLAM, it relies less on feature extraction algorithms, using

differential thermal signatures for matching. Probabilistic Neural Networks provide robust predictions by accounting for uncertainties in sensor measurements and motion estimates. Graph-based optimization reduces variance by providing globally consistent maps and trajectories. Furthermore, its modular nature allows for easy integration of additional sensors or adjustments to the sensor setup, increasing adaptability to various robotic platforms and application requirements.

In summary, Thermal Inertial SLAM stands out for its ability to use thermal and inertial data, robust prediction using PNNs, and graph-based optimization, providing a robust and adaptable solution for mapping and positioning tasks in harsh environments.

5. Conclusion

Thermal SLAM, a new field, may improve object detection and tracking in challenging situations (Taketomi et al., 2017). Thermal SLAM leverages temperature fluctuations for robust operation in low light, adverse weather, and occlusions (Brunner and Peynot, 2014). Although Thermal SLAM seems promising, the low resolution of thermal cameras, signal-to-noise ratio deterioration, and low contrast in thermal images present distinct obstacles (Delaune et al., 2019). To overcome these constraints, the implementation of Thermal SLAM requires specialized feature extraction, matching, and image processing (Wang et al., 2017). For short-range applications, thermal Odometry has seen improvements (Lucas and Kanade, 1981; Lu and Lu, 2021). Thermal-inertial Odometry enhances performance (Borges and Vidas, 2016; Delaune et al., 2019), however, a complete thermal-inertial SLAM system with robust loop closure is still not achievable. Fusing thermal data with 3D maps from LiDAR is common in thermal mapping. While effective, this strategy may be limited in scenarios involving smoke or fire damage to secondary sensors (Maddern and Vidas, 2012).

Future studies should focus on developing processing methods for low-resolution, low-contrast thermal imagery, including feature extraction and matching techniques. Deep learning methods for Thermal SLAM are promising, potential for robust and dependable object recognition and tracking in complicated circumstances. In conclusion, Thermal SLAM could transform autonomous systems in visually challenged contexts (Papachristos et al., 2018). Additionally, approaches for thermal mapping that are independent of secondary sensors for smoke-filled environments should be investigated (Taketomi et al., 2017). Thermal SLAM has the potential to revolutionize autonomous navigation, search and rescue, and environmental monitoring by overcoming existing challenges and exploring new research areas. The future of Thermal SLAM is bright, and continuous research will unveil its full potential. Finally, Table 1 shows a summary of the works reviewed in this article.

Table 1. A summary of the works (methods)reviewed in this article

Method	Year	Authors	Limitations	Key Features
Thermal-Infrared SLAM	2019	(Shin and Kim, 2019)	Computationally expensive	Requires high-resolution thermal cameras and powerful computers.
Thermal/Inertial SLAM	2019	(Khattak et al., 2019a)	Computationally expensive	Uses full radiometric data for odometry.
Monocular thermal SLAM	2020	(Bijelic et al., 2020)	Lacks loop closure for consistent trajectories	Not suitable for large-scale environments or globally consistent maps.
Feature-based LiDAR-thermal SLAM.	2019	(Shin and Kim, 2019)	Requires additional LiDAR sensor, which may not be suitable for all environments.	Enhances thermal data with sparse range measurements from LiDAR for scale estimation.
Chameleon (Stereo thermal-inertial SLAM).	2023	(van Manen et al., 2023)	Limited effectiveness in low- contrast environments.	Relies heavily on inertial data, and potentially inaccurate thermal maps.
Visual and thermal Sensor Fusion (VSLAM+Thermal).	2012	(Maddern and Vidas, 2012)	Requires robust image fusion algorithms, and may be computationally expensive.	Combines visual and thermal spectra for navigation.
Multi-spectral Stereo Odometry.	2016	(Borges and Vidas, 2016)	Integrates optical and thermal sensors for ground vehicles.	Requires stereo camera setup (thermal and visual).
Thermal Radiometric SLAM with NUC.	2020	(Khattak et al., 2020)	Requires high-resolution thermal camera and powerful computer.	Integrates high-resolution thermal camera, powerful computer, and radiometric sensors.
Super thermal (Deep Learning).	2018	(Mouats et al., 2018)	Limited research on integration within a complete SLAM system, and computational cost needs evaluation.	Deep neural network for thermal feature matching.
Graph-Based Thermal- Inertial SLAM with Probabilistic Neural Networks.	2020	(Saputra et al., 2020)	May require significant computational resources for neural network operations.	Combines graph- based SLAM with probabilistic neural networks for enhancement. thermal-inertial navigation.
Graph-based SLAM.	2010	Grisetti et al., 2010)	Tutorial nature may limit depth in specific applications like thermal-inertial SLAM.	Provides a comprehensive overview of graph-based SLAM, a foundational technique in robotics
Only Look Once, Mining Distinctive Landmarks from ConvNet for Visual Place Recognition.	2017	(Chen et al., 2017)	Focused on visual place recognition, may not directly address thermal-inertial SLAM challenges.	Introduces a method extract distinctive landmarks from Convolutional Neural Networks for place recognition.
SubT-MRS Dataset: Pushing SLAM Towards All weather Environments.	2023	(Zhao et al., 2023)	Dataset-focused, may not provide a complete SLAM system.	Presents a dataset designed to challenge and improve SLAM systems in all-weather environments, potentially including thermal data.

Author Contributions

The percentages of the authors' contributions are presented below. All authors reviewed and approved the final version of the manuscript.

	F.S.	O.S.G.
C	50	50
D	50	50
S	50	50
L	50	50
W	50	50
CR	50	50
SR	50	50

C=Concept, D= design, S= supervision, L= literature search, W= writing, CR= critical review, SR= submission and revision.

Conflict of Interest

The authors declared that there is no conflict of interest.

Ethical Consideration

Ethics committee approval was not required for this study because of there was no study on animals or humans.

References

Bijelic M, Gruber T, Mannan F, Kraus F, Ritter W, Dietmayer K, Heide F. 2020. Seeing through fog without seeing fog: Deep multimodal sensor fusion in unseen adverse weather. In: Proceedings of the IEEE/CVF Conference on Computer Vision and Pattern Recognition, June 14-19, Seattle, WA, USA, pp: 11682-11692.

Borges PVK, Vidas S. 2016. Practical infrared visual odometry. IEEE Trans Intell Transp Syst, 17(8): 2205-2213.

Brunner C, Peynot T. 2010. Visual metrics for the evaluation of sensor data quality in outdoor perception. In: Proceedings of the 10th Performance Metrics for Intelligent Systems Workshop, September 28-30, Baltimore, MD, USA, pp: 55-61.

Brunner C, Peynot T. 2014. Perception quality evaluation with visual and infrared cameras in challenging environmental conditions. In: Experimental Robotics: The 12th International Symposium on Experimental Robotics, March 17- 20, Tokyo, Japan, pp: 231-240.

Brunner C, Peynot T, Vidal-Calleja T, Underwood J. 2013. Selective combination of visual and thermal imaging for resilient localization in adverse conditions: Day and night, smoke and fire. J Field Robot, 30(4): 641-666.

Cadena C, Carlone L, Carrillo H, Latif Y, Scaramuzza D, Neira J, Leonard JJ. 2016. Past, present, and future of Simultaneous Localization and Mapping: Toward the robust-perception age. IEEE Trans Robot, 32(6): 1309-1332.

Calonder M, Lepetit V, Strecha C, Fua P. 2010. Brief: Binary robust independent elementary features. In: Proceedings of the Computer Vision– ECCV 2010:11th European Conference on Computer Vision. Springer- Verlag, September 5- 11, Heraklion, Crete, Greece, pp: 778-792.

Chen X, Liu L, Zhang J, Shao W. 2021. Infrared image denoising based on the variance-stabilizing transform and the dual-domain filter. Digit Signal Process, pp: 113-128.

Chen Z, Maffra F, Chli M. 2017. Only look once, mining distinctive landmarks from convnet for visual place recognition. In: Proceedings of the 2017 IEEE/RSJ International Conference on Intelligent Robots and Systems (IROS), September 24-28, Vancouver, BC, Canada, pp: 6435-6441.

Debeunne C, Vivet D. 2020. A review of Visual-LiDAR fusion based Simultaneous Localization and Mapping. Sensors, 20(7): 20-68.

Delaune J, Hewitt R, Lytle L, Sorice C, Thakker R, Matthies L. 2019. Thermal-inertial odometry for autonomous flight throughout the night. In: Proceedings of the 2019 IEEE/RSJ International Conference on Intelligent Robots and Systems (IROS), November 4-8, Macau, China, pp: 1090- 1097.

Dellaert F, Kaess M. 2006. Square Root SLAM: Simultaneous Localization and Mapping via square root information smoothing. Int J Robot Res, 25(12): 1181-1203.

Geiger A, Ziegler J, Stiller C. 2011. Stereoscan: Dense 3D reconstruction in real-time. In: Proceedings of the 2011 IEEE Intelligent Vehicles Symposium (IV), June 5-9, Baden-Baden, Germany, pp: 963-968.

Grisetti G, Kümmerle R, Stachniss C, Burgard W. 2010. A tutorial on graph-based SLAM. IEEE Intell Transp Syst Mag, 2(4): 31-43.

Hoshi M, Hara Y, Nakamura S. 2024. Graph-based SLAM using wall detection and floor plan constraints without loop closure. ROBOMECH J, 11(1), 18-32.

Johansson J, Solli M, Maki A. 2016. An evaluation of local feature detectors and descriptors for infrared images. In: Proceedings of the Computer Vision–ECCV 2016 Workshops: October 8-10, Amsterdam, Netherlands, Proceedings, Part III, pp: 142.

Keil C, Gupta A, Kaveti P, Singh H. 2024. Towards Long-Term SLAM on Thermal Imagery. arXiv preprint arXiv: 2403.19885.

Khattak S, Papachristos C, Alexis K. 2019a. Keyframe-based direct thermal–inertial odometry. In: Proceedings of the 2019 International Conference on Robotics and Automation (ICRA), May 20-24, Montreal, QC, Canada, pp: 6197-6203.

Khattak S, Papachristos C, Alexis K. 2019b. Visual- thermal landmarks and inertial fusion for navigation in degraded visual environments. In: Proceedings of the 2019 IEEE Aerospace Conference, March 2-9, Big Sky, MT, USA, pp: 1-9.

Khattak S, Papachristos C, Alexis K. 2020. Keyframe- based thermal–inertial odometry. J Field Robot, 37(4): 552-579.

Kim C, Sakthivel R, Chung WK. 2007. Unscented FastSLAM: A robust algorithm for the simulataneous Localization and Mapping problem. In: Proceedings of the 2007 IEEE International Conference on Robotics and Automation, April 10-14, Rome, Italy, pp: 2439-2445.

Leonard JJ, Durrant-Whyte HF. 1991. Mobile robot localization by tracking geometric beacons. In: Proceedings of the 1991 IEEE International Conference on Robotics and Automation, April 9- 11, Sacramento, CA, USA, pp: 376-382.

Li J, Li Z, Feng Y, Liu Y, Shi G. 2019. Development of a human–robot hybrid intelligent system based on brain teleoperation and deep learning SLAM. IEEE Trans Autom Sci Eng, 16(4): 1664-1674.

Lu C. 2020. Stripe non-uniformity correction of infrared images using parameter estimation. Infr Phys Tech, 107(1), pp: 1-7.

Lu Y, Lu G. 2021. Superthermal: Matching thermal as visible through thermal feature exploration. IEEE Robot Autom Lett, 6(2): 2690-2697.

Lucas BD, Kanade T. 1981. An iterative image registration technique with an application to stereo vision. In: Proceedings of the IJCAI'81: 7th International Joint Conference on Artificial Intelligence, August 24-28, Vancouver, BC, Canada, pp: 674-679.

Maddern W, and Vidas S. 2012. Towards robust night and day place recognition using visible and thermal imaging. In:

Proceedings of the RSS 2012 Workshop: Beyond laser and vision: Alternative sensing techniques for robotic perception, July 9, Sydney, Australia, pp: 1-8.

Montemerlo M. 2002. FastSLAM: A factored solution to the Simultaneous Localization and Mapping problem. In: Proceedings of AAAI02, July 28- August 1, Edmonton, Canada, pp: 593-598.

Montemerlo M, Thrun S, Koller D, Wegbreit B. 2003. FastSLAM 2.0: An improved particle filtering algorithm for Simultaneous Localization and Mapping that provably converges. In: Proceedings of the IJCAI, August 9-15, Acapulco, Mexico, pp: 1151-1156.

Mouats T, Aouf N, Chermak L, Richardson MA. 2015. Thermal stereo odometry for UAVs. IEEE Sens J, 15(11): 6335-6347.

Mouats T, Aouf N, Nam D, Vidas S. 2018. Performance evaluation of feature detectors and descriptors beyond the visible. J Intell Robot Syst, 92: 33-63.

Mouats T, Aouf N, Sappa AD, Aguilera C, Toledo R. 2014. Multispectral stereo odometry. IEEE Trans Intell Transp Syst, 16(3): 1210-1224.

Mur-Artal R, Montiel JMM, Tardos JD. 2015. ORB- SLAM: A versatile and accurate monocular SLAM system. IEEE Trans Robot, 31(5): 1147-1163.

Papachristos C, Mascarich F, Alexis K. 2018. Thermal-inertial localization for autonomous navigation of aerial robots through obscurants. In: Proceedings of the 2018 International Conference on Unmanned Aircraft Systems (ICUAS), June 12-15, Dallas, TX, USA, pp: 395-401.

Poujol J, Aguilera CA, Danos E, Vintimilla BX, Toledo R, Sappa AD. 2016. A visible-thermal fusion-based monocular visual odometry. In: Proceedings of Robot 2015 Second Iberian Robotics Conference: Advances in Robotics, November 19-21, Lisbon, Portugal, pp: 213-225.

Rasmussen N. D, Morse B. S, Goodrich M. A, Eggett D. 2009. Fused visible and infrared video for use in wilderness search and rescue. In: Proceedings of the 2009 Workshop on Applications of Computer Vision (WACV), December 7-8, Snowbird, UT, USA, pp: 1-8.

Saputra MRU, De Gusmao PP, Lu CX, Almalioglu Y, Rosa S, Chen C, Trigoni N. 2020. Deeptio: A deep thermal-inertial odometry with visual hallucination. IEEE Robot Autom Lett, 5(2): 1672- 1679.

Saputra MRU, Lu CX, de Gusmao PPB, Wang B, Markham A, Trigoni N. 2021. Graph-based thermal-inertial SLAM with probabilistic neural networks. IEEE Trans Robot, 38(3): 1875-1893.

Shin YS, Kim A. 2019. Sparse depth enhanced direct thermal-infrared SLAM beyond the visible spectrum. IEEE Robot Autom Lett, 4(3): 2918- 2925.

Taketomi T, Uchiyama H, Ikeda S. 2017. Visual SLAM algorithms: A survey from 2010 to 2016. IPSJ Trans Comput Vis Appl, 9: 1-11.

Tang J, Ericson L, Folkesson J, Jensfelt P. 2019. GCNv2: Efficient correspondence prediction for real-time SLAM. IEEE Robot Autom Lett, 4(4): 3505-3512.

Tourani A, Bavle H, Sanchez-Lopez JL, Voos H. 2022. Visual slam: What are the current trends and what to expect? Sensors, 22(23): 9297-9326.

van Manen BR, Sluiter V, Mersha AY. 2023. FirebotSLAM: Thermal SLAM to increase situational awareness in smoke-filled environments. Sensors, 23(17): 7611-7636.

Vidas S, Sridharan S. 2012. Hand-held monocular SLAM in thermal-infrared. In: Proceedings of the 2012 12th International Conference on Control Automation Robotics and Vision (ICARCV), December 5-7, Guangzhou, China, pp: 500-506.

Wang S, Clark R, Wen H, Trigoni N. 2017. Deepvo: Towards end-to-end visual odometry with deep recurrent convolutional neural networks. In: Proceedings of the 2017 IEEE International Conference on Robotics and Automation (ICRA), May 29-June 3, Singapore, pp: 2043-2050.

Wu Y, Wang L, Zhang L, Bai Y, Cai Y, Wang S, Li Y. 2023. Improving autonomous detection in dynamic environments with robust monocular thermal SLAM system. ISPRS J Phot Remote Sens, 203: 265-284.

Zhang J, and Singh S. 2014. LOAM: Lidar odometry and mapping in real-time. In: Proceedings of Robotics: Science and Systems (RSS), July 12-16, Berkeley, CA, USA, pp: 109-117.

Zhao S, Singh D, Sun H, Jiang R, Gao Y, Wu T, Xu J. 2023. Subt-mrs: A subterranean, multi-robot, multi-spectral and multi-degraded dataset for robust SLAM. arXiv preprint arXiv:2307.07607.

Zhao S, Wang P, Zhang H, Fang Z, Scherer S. 2020. Tp-tio: A robust thermal-inertial odometry with deep thermal point. In: Proceedings of the 2020 IEEE/RSJ International Conference on Intelligent Robots and Systems (IROS), October 25-29, Las Vegas, NV, USA, pp: 10321-10328.